



# Towards an automated framework for coronary lesions detection and quantification in cardiac CT angiography

Imen Melki

## ► To cite this version:

Imen Melki. Towards an automated framework for coronary lesions detection and quantification in cardiac CT angiography. Computer Science [cs]. Université Paris Est, 2015. English. NNT: . tel-01273806v1

**HAL Id: tel-01273806**

**<https://theses.hal.science/tel-01273806v1>**

Submitted on 13 Feb 2016 (v1), last revised 7 Mar 2016 (v2)

**HAL** is a multi-disciplinary open access archive for the deposit and dissemination of scientific research documents, whether they are published or not. The documents may come from teaching and research institutions in France or abroad, or from public or private research centers.

L'archive ouverte pluridisciplinaire **HAL**, est destinée au dépôt et à la diffusion de documents scientifiques de niveau recherche, publiés ou non, émanant des établissements d'enseignement et de recherche français ou étrangers, des laboratoires publics ou privés.



University Paris Est  
Laboratory of Informatics Gaspard-Monge  
Department of Informatics

## THESIS

to obtain the Doctor of Philosophy grade of the University Paris-Est with  
specialization in Informatics

**Imen MELKI**

---

**TOWARDS AN AUTOMATED FRAMEWORK FOR CORONARY  
LESIONS DETECTION AND QUANTIFICATION IN CARDIAC CT  
ANGIOGRAPHY**

---

### COMPOSITION OF THE JURY:

**Director:** Laurent Najman, ESIEE Paris

**Supervisor:** Hugues Talbot, ESIEE Paris

**Co-supervisor:** Laurent Launay, GE Healthcare

**Co-supervisor:** Jean Cousty, ESIEE Paris

**Referee:** Gregoire Malandain, INRIA

**Referee:** Frédérique Frouin, Faculté de Médecine Pierre et Marie Curie

**Examinator:** Wiro Niessen, Erasmus MC

**Examinator:** Leo Grady, HeartFlow

Champs-sur-Marne, France

22 June 2015





---

# Abstract

## **Towards an automated framework for coronary lesions detection and quantification in cardiac CT angiography**

Coronary heart diseases (CVDs) are the group of disorders that affect the coronary artery vessels. They are the world's leading cause of mortality (7.3 million deaths worldwide). Therefore, early detection of these diseases using less invasive techniques provides better therapeutic outcome, as well as reduces costs and risks, compared to an interventionist approach. Recent studies showed that X-ray computed tomography (CT) may be used as an alternative to accurately locate and grade heart lesions in a non invasive way. However, analysis of cardiac CT exam for coronaries lesions inspection remains a tedious and time consuming task, as it is based on the manual analysis of the vessel cross sections. High accuracy is required, and thus only highly experienced clinicians are able to analyze and interpret the data for diagnosis. Computerized tools are critical to reduce processing time and ensure quality of diagnostics. The goal of this thesis is to provide automated coronaries analysis tools to help in non-invasive CT angiography examination. Such tools allow pathologists to efficiently diagnose and evaluate risks associated with CVDs, and to raise the quality of the assessment from a purely qualitative level to a quantitative level. The first objective of our work is to design, analyze and validate a set of automated algorithms for coronary arteries analysis with the final purpose of automated stenoses detection and quantification. We propose different algorithms covering different processing steps towards a fully automated analysis of the coronary arteries. Our contribution covers the three major blocks of the whole processing chain and deals with different image processing fields. First, we present an algorithm dedicated to heart volume extraction. The approach extracts the heart as one single object that can be used as an input masque for automated coronary arteries segmentation. This work eliminates the tedious and time consuming step of manual removing obscuring structures around the heart (lungs, ribs, sternum, liver...) and quickly provides a clear and well defined view of the coronaries. This approach uses a

geometric model of the heart that is fitted and adapted to the image data. Quantitative and qualitative analysis of results obtained on a 114 exam database shows the efficiency and the accuracy of this approach. Second, we were interested to the problem of coronary arteries enhancement and segmentation. In this context, we first designed a novel approach for coronaries enhancement that combines robust path openings and component tree filtering. The approach showed promising results on a set of 11 CT exam compared to a Hessian based approach. For a robust stenoses detection and quantification, a precise and accurate lumen segmentation is crucial. Therefore, we have dedicated a part of our work to the improvement of lumen segmentation step based on vessel statistics. Validation on the Rotterdam Coronary Challenge showed that this approach provides state of the art performances. Finally, the major core of this thesis is dedicated to the issue of stenosis detection and quantification. Two different approaches are designed and evaluated using the Rotterdam online evaluation framework. The first approach get uses of the lumen segmentation with some geometric and intensity features to extract the coronary stenosis. The second is using a learning based approach for stenosis detection and stenosis. The second approach outperforms some of the state of the art works with reference to some metrics. This thesis results in a prototype for automated coronary arteries analysis and stenosis detection and quantification that meets the level of required performances for a clinical use. The prototype was qualitatively and quantitatively validated on different sets of cardiac CT exams.

**Keywords.** : Coronary arteries diseases, Stenosis detection, Automated detection, CT angiography, Image processing

---

# Resumé

## **Vers un système automatisé pour la détection et la quantification des lésions coronaires dans des angiographies CT cardiaques**

Les maladies coronariennes constituent l'ensemble des troubles affectant les artères coronaires. Elles sont la première cause mondiale de mortalité. Par conséquent, la détection précoce de ces maladies en utilisant des techniques peu invasives fournit un meilleur résultat thérapeutique, et permet de réduire les coûts et les risques liés à une approche interventionniste. Des études récentes ont montré que la tomodensitométrie peut être utilisée comme une alternative non invasive et fiable pour localiser et quantifier ces lésions. Cependant, l'analyse de ces examens, basée sur l'inspection des sections du vaisseau, reste une tâche longue et fastidieuse. Une haute précision est nécessaire, et donc seulement les cliniciens hautement expérimentés sont en mesure d'analyser et d'interpréter de telles données pour établir un diagnostic. Les outils informatiques sont essentiels pour réduire les temps de traitement et assurer la qualité du diagnostic. L'objectif de cette thèse est de fournir des outils automatisés de traitement d'angiographie CT, pour la visualisation et l'analyse des artères coronaires d'une manière non invasive. Ces outils permettent aux pathologistes de diagnostiquer et évaluer efficacement les risques associés aux maladies cardio-vasculaires tout en améliorant la qualité de l'évaluation d'un niveau purement qualitatif à un niveau quantitatif. Le premier objectif de ce travail est de concevoir, analyser et valider un ensemble d'algorithmes automatisés utiles pour la détection et la quantification de sténoses des artères coronaires. Nous proposons un nombre de techniques couvrant les différentes étapes de la chaîne de traitement vers une analyse entièrement automatisée des artères coronaires. Premièrement, nous présentons un algorithme dédié à l'extraction du cœur. L'approche extrait le cœur comme un seul objet, qui peut être utilisé comme un masque d'entrée pour l'extraction automatisée des coronaires. Ce travail élimine l'étape longue et fastidieuse de la segmentation manuelle du cœur et offre rapidement une vue claire des coronaires. Cette approche utilise un modèle géométrique du cœur ajusté aux données

de l'image. La validation de l'approche sur un ensemble de 133 examens montre l'efficacité et la précision de cette approche. Deuxièmement, nous nous sommes intéressés au problème de la segmentation des coronaires. Dans ce contexte, nous avons conçu une nouvelle approche pour l'extraction de ces vaisseaux, qui combine ouvertures par chemin robustes et filtrage sur l'arbre des composantes connexes. L'approche a montré des résultats prometteurs sur un ensemble de 11 examens CT. Pour une détection et quantification robuste de la sténose, une segmentation précise de la lumière du vaisseau est cruciale. Par conséquent, nous avons consacré une partie de notre travail à l'amélioration de l'étape de segmentation de la lumière, basée sur des statistiques propres au vaisseau. La validation avec l'outil d'évaluation en ligne du challenge de Rotterdam sur la segmentation des coronaires, a montré que cette approche présente les mêmes performances que les techniques de l'état de l'art. Enfin, le cœur de cette thèse est consacré à la problématique de la détection et la quantification des sténoses. Deux approches sont conçues et évaluées en utilisant l'outil d'évaluation en ligne de l'équipe de Rotterdam. La première approche se base sur l'utilisation de la segmentation de la lumière avec des caractéristiques géométriques et d'intensité pour extraire les sténoses coronaires. La seconde utilise une approche basée sur l'apprentissage. Durant cette thèse, un prototype pour l'analyse automatisée des artères coronaires et la détection et quantification des sténoses a été développé. L'évaluation qualitative et quantitative sur différents bases d'examens cardiaques montre qu'il atteint le niveau de performances requis pour une utilisation clinique.

**Mots-clefs.** : Maladies des artères coronaires, Detection de sténoses, Détection automatique, Tomodensitométrie, Traitement d'images

---

# Acknowledgments

First and foremost, I would like to express my endless gratitude to my supervisor Laurent Najman for supporting me during the course of this thesis. Apart from his scientific knowledge and contributions of time and ideas, I am grateful for the kind advices and words he told me to encourage me and motivate me to finish this work. Laurent, working with you was not only an honor but also a pleasure. Without you encouraging my work and supporting me during tough times, this thesis would not have been possible. Thank you so much!

This PhD thesis was realized in collaboration with GE Healthcare in the context of a CIFRE convention. I would like to thank Laurent Launay, my manager and co-supervisor, who gave me the opportunity to work on my thesis in such a fruitful and interesting context. I am very grateful for all the effort and time he spent on various bureaucratic issues hence allowing this thesis to take place. Besides, I thank him for his scientific feedback and the constructive discussions on the proposed methods and the evaluation process.

I am also very grateful to my second co-supervisor, Hugues Talbot, for all the help, time and effort he has devoted to this joint work. He was of great help during critical phases of this thesis. In addition to supervising, helping in code writing and contributing in algorithms design, I appreciated his continuous support and friendship. Moreover, I would like to thank Jean Cousty for his insights and his involvement in major parts of my work. Thank you both for reviewing this manuscript and helping me to improve it.

Likewise, I thank my two former colleagues Céline Pruvot and Nicolas Gogin for their scientific feedback and valuable ideas. Céline, it is thank to your support, supervision and the insightful and detailed discussions we had that I was able to apprehend and appreciate the area of cardiac images analysis. Our discussions of the topic of coronary arteries analysis and stenosis detection initialized the second and third parts of this thesis. Thank you for

sharing your knowledge and expertise in such a challenging domain. Also thank you for all the provided materials and your help in evaluating some of the proposed algorithms. Nicolas, you have always found the time to talk to me and propose consistent and excellent ideas and improvements of the proposed algorithms. Your scientific knowledge and insights were very valuable and helpful to me, specially in the area of machine learning. I owe a lot of gratitude to both of you! Your encouragement, immense knowledge and insights were key motivations throughout my PhD.

Furthermore, I take this opportunity to express my gratitude to the AW team for hosting me during these 3 years. I thank all my colleagues for providing many valuable discussions and ideas as well as a lot of fun. This made this experience a memorable pleasure. Namely I want to thank Julien Wojak, Fayçal EL Amrani, Guillermo Ruiz for their valuable help in code writing, brain storming, and the many fruitful and encouraging discussions we had. Special thanks to Jérôme Knoploch for his consistent comments and contributions to this work. I also want to thank Maxime Teisseire for the time and efforts he dedicated to manually generate the needed ground truth. Finally, I thank Caroline Foubert for her endless kindness and the effort she made in organizing the different team events.

I also want to thank the interns I coached during my PhD thesis: Peter Schaeffer, who contributed to the work on coronary arteries enhancement. Cyril Cardon and Antoine Bordes who worked on the topic of stenosis detection. Working with you was such an enriching experience to me. Thank you for your motivation, involvement and work!

Moreover, I would like to thank my thesis referees Frédérique Frouin and Grégoire Malandain for kindly accepting this demanding role. I am very grateful for their time and efforts to review this thesis and honored by accepting to be part of my jury. Thank you for your insightful feedback and constructive comments helping to improve the content of this manuscript.

I would like to thank Wiro Niessen and Leo Grady for accepting to sit in the jury of this thesis. I am honored by this and grateful for their time and effort.

The completion of this thesis would not have been possible without the encouragement and support of several people. I would thank my friends who were there for me and who are still supporting me, specially Abir. I am eternally grateful to my family: My parents, brothers and sister for their unconditional love and support. Without you being by my side during my whole life, I would never be able to become what I am and accomplish my dreams. Besides, I would never be able to finish this dissertation without the support and love of my husband and son. Chahir you were always there cheering me up, stood by me through the good and specially bad times. You have been extremely patient, supportive and helpful with our little boy. Dear Anas, you made this experience more challenging and interesting. You both gave

me courage and energy to finish this work and motivated me to keep reaching for excellence. Thank you for patience and for what you endured during the last stages of the redaction of this manuscript.

I specially dedicate this work to the memory of my beloved father, who passed away recently. I deeply regret that he is not able to share this with me but hope that he can be proud of me.





---

# Contents

<b>Abstract</b>	<b>i</b>
<b>Resumé</b>	<b>iii</b>
<b>Acknowledgments</b>	<b>v</b>
<b>List of Figures</b>	<b>xvii</b>
<b>List of Tables</b>	<b>xxxv</b>
<b>I Introduction and Review</b>	<b>1</b>
<b>1 Introduction</b>	<b>1</b>
1.1 Cardiac Anatomy . . . . .	3
1.1.1 The Cardiovascular System Anatomy . . . . .	3
1.1.1.1 The blood vessels . . . . .	5
1.1.1.2 The blood . . . . .	6
1.1.1.3 The heart . . . . .	7
1.1.2 Cardiovascular Lesions . . . . .	11
1.1.2.1 Atherosclerosis Genesis . . . . .	12
1.1.2.2 Artery Modeling . . . . .	15
1.1.3 Treatments . . . . .	17
1.2 Cardiac Medical Imaging . . . . .	18

1.2.1	Conventional Coronary Angiography . . . . .	20
1.2.2	Intra Vascular UltraSound . . . . .	21
1.2.3	Computed Tomography Angiography . . . . .	22
1.2.3.1	Basics of CT Angiography . . . . .	22
1.2.3.2	Cardiac CT Development . . . . .	25
1.3	Cardiac Computed Tomography . . . . .	30
1.3.0.3	Accuracy of Cardiac CT for Coronary Artery Plaques Assessment	30
1.3.1	Cardiac CT: Advantages and Limitations . . . . .	32
1.3.2	Coronary Assessment using CT Angiography . . . . .	35
1.3.2.1	Basic Visualization Techniques . . . . .	37
1.3.2.2	Advanced Visualization Techniques . . . . .	39
1.3.2.3	Stenosis Assessment using Coronary CT . . . . .	42
1.4	Our Approach . . . . .	45
1.4.1	Context of the thesis . . . . .	45
1.4.2	Our Contribution . . . . .	46
1.4.2.1	Literature review . . . . .	46
1.4.2.2	CT image processing for coronary an efficient coronary analysis	47
1.4.2.3	Stenosis detection and quantification . . . . .	49
1.4.2.4	Validation process . . . . .	49
1.4.3	Thesis Outline . . . . .	51
<b>2</b>	<b>Cardiac CTA Processing for Coronary Arteries Analysis: A review</b>	<b>53</b>
2.1	Image Pre-processing . . . . .	54
2.1.1	Downsampling . . . . .	54
2.1.2	Image filtering for noise reduction . . . . .	55
2.1.3	Tubular structures enhancement . . . . .	55
2.2	Image Pre-segmentation . . . . .	57
2.2.1	Delineation of anatomical region of interest . . . . .	57
2.2.2	Abnormalities removal . . . . .	58
2.2.3	Seeds extraction . . . . .	58
2.3	Vessel modeling . . . . .	60
2.3.1	Intensity Models . . . . .	60
2.3.2	Geometry Models . . . . .	62
2.3.3	Hybrid Models . . . . .	63
2.4	Vessel features extraction . . . . .	64

2.4.1	Centerline extraction . . . . .	67
2.4.1.1	Optimization Approaches . . . . .	67
2.4.1.2	Vessel Tracking . . . . .	69
2.4.1.3	Skeletonization . . . . .	72
2.4.2	Vessel extraction . . . . .	73
2.4.2.1	Volume-based Approaches . . . . .	73
2.4.2.2	Contour-based Approaches . . . . .	77
<b>II</b>	<b>CT angiography segmentation</b>	<b>83</b>
<b>1</b>	<b>Automated Heart Mask Extraction</b>	<b>85</b>
1.1	Prior Knowledge and Challenges . . . . .	87
1.1.1	Prior Knowledge: Anatomic and Appearance Priors . . . . .	87
1.1.2	Heart Isolation Challenges . . . . .	88
1.2	Related Work . . . . .	90
1.3	Overview of the Proposed Approach . . . . .	94
1.3.1	Pre-processing Step . . . . .	95
1.3.1.1	Lungs and Descending Aorta Volumes Extraction: . . . . .	96
1.3.1.2	Heart Center Extraction . . . . .	97
1.3.2	Heart Model Fitting . . . . .	99
1.3.2.1	Heart Shell Cloud Extraction . . . . .	99
1.3.2.2	Ellipsoid Fitting: A WLSQ approach . . . . .	106
1.3.3	Heart Volume Extraction . . . . .	113
1.3.3.1	Graph-Based Approaches . . . . .	113
1.3.3.2	Heart Surface Segmentation . . . . .	116
1.3.3.3	Extra Bones Removal . . . . .	119
1.4	Experiments . . . . .	120
1.4.1	Data . . . . .	120
1.4.2	Manual Segmentation . . . . .	120
1.4.3	Evaluation measures . . . . .	122
1.4.3.1	Quantitative Evaluation . . . . .	122
1.4.3.2	Qualitative Evaluation . . . . .	123
1.5	Results . . . . .	125
1.5.1	Computational time . . . . .	125

1.5.2	Parameters Optimization . . . . .	125
1.5.3	Quantitative evaluation results . . . . .	128
1.5.4	Qualitative evaluation results . . . . .	130
<b>2</b>	<b>Coronaries Artery Segmentation</b>	<b>135</b>
2.1	Coronary arteries segmentation: A brief Review . . . . .	136
2.1.1	Direct segmentation approaches . . . . .	136
2.1.2	Centerline-based segmentation approaches . . . . .	139
2.2	A Coronary Enhancement Filter using the Shape Tree and Path Openings . . .	144
2.2.1	Preliminaries . . . . .	144
2.2.1.1	Hessian based enhancement filter . . . . .	145
2.2.1.2	Path Openings . . . . .	146
2.2.1.3	Shape Tree . . . . .	149
2.2.2	The enhancement filter . . . . .	155
2.2.2.1	Evaluation process . . . . .	156
2.2.2.2	Shape Tree construction . . . . .	157
2.2.2.3	Image filtering for noise reduction using robust path openings .	160
2.2.3	Preliminary Results and Discussion . . . . .	163
2.3	Statistic-based Vessel Lumen Segmentation . . . . .	164
2.3.1	State of the art coronary arteries segmentation and lumen extraction . .	165
2.3.2	Vessel lumen mask extraction using adaptive statistics . . . . .	167
2.3.2.1	Reformatted vessel volume extraction . . . . .	169
2.3.2.2	Vessel lumen marker extraction . . . . .	169
2.3.3	Vessel Segmentation and evaluation results . . . . .	173
2.3.3.1	Vessel segmentation using seed-based algorithms . . . . .	173
2.3.3.2	Quantitative evaluation results . . . . .	175
2.3.4	Conclusions and future work . . . . .	179

### III Methods for Automated Coronary Arteries Stenosis Detection 181

<b>1</b>	<b>Previous work and Evaluation framework</b>	<b>183</b>
1.1	Coronary Arteries Lesions Detection . . . . .	185
1.1.1	Pathology Models . . . . .	185
1.1.1.1	Stenosis . . . . .	185

1.1.1.2	Calcification . . . . .	186
1.1.1.3	Aneurysm . . . . .	186
1.1.2	Rule-based Approaches . . . . .	187
1.1.2.1	Lumen Segmentation based Approaches . . . . .	188
1.1.2.2	Intensity-based Approaches . . . . .	191
1.1.2.3	Second Derivative based Approaches . . . . .	192
1.1.2.4	FFRs Estimation Approaches . . . . .	195
1.1.3	Learning-based Approaches . . . . .	196
1.1.4	Discussion . . . . .	201
1.2	Materials and Evaluation Framework . . . . .	203
1.2.1	Data . . . . .	204
1.2.2	Reference Standards . . . . .	204
1.2.3	Evaluation Measure for Stenosis Detection and Quantification . . . . .	205
1.2.3.1	Definitions . . . . .	205
1.2.3.2	Evaluation measures . . . . .	207
<b>2</b>	<b>A two-stage Automatic Coronary Arteries Stenoses Detection</b>	<b>211</b>
2.1	Artery Coronaries Tree Construction . . . . .	212
2.2	Vessel Lumen Contours Extraction and Diameter Quantification . . . . .	216
2.3	Stenosis Detection . . . . .	217
2.4	Evaluation for MICCAI 2012 coronary artery stenosis detection challenge . . . . .	224
<b>3</b>	<b>Learning-based Detection of Severe Coronary Stenoses</b>	<b>229</b>
3.1	Machine Learning Approaches in Medical Context . . . . .	230
3.1.1	Supported Vector Machines . . . . .	232
3.1.2	Boosting Algorithms . . . . .	233
3.1.3	Random Forests . . . . .	234
3.2	Features Extraction for Coronary Lesions Modeling . . . . .	242
3.2.1	Vessel sampling using the cylindrical pattern . . . . .	243
3.2.2	Features selection . . . . .	249
3.2.2.1	Local Features . . . . .	250
3.2.2.2	Global Features . . . . .	253
3.3	Stenosis detection using the Random Forest Classifier . . . . .	256
3.3.1	Training Step . . . . .	257
3.3.2	Testing Step . . . . .	262

3.3.2.1	Stenotic regions flagging . . . . .	263
3.3.2.2	Stenosis center extraction . . . . .	265
3.3.3	Stenosis Quantification . . . . .	266
3.3.4	Implementation . . . . .	268
3.4	Experiments and Results . . . . .	274
3.4.1	Parameter Tuning and Experimental Setup . . . . .	275
3.4.1.1	Features Selection . . . . .	275
3.4.1.2	Training database creation . . . . .	276
3.4.1.3	Random Forest classifier parameters selection . . . . .	281
3.4.1.4	Output probability profile processing . . . . .	282
3.4.1.5	Stenosis threshold optimization . . . . .	285
3.4.2	Results . . . . .	289
3.4.2.1	Evaluation on the Rotterdam Coronary Artery Algorithm Eval- uation Framework . . . . .	289
3.4.2.2	Evaluation on a GE database . . . . .	297
<b>IV</b>	<b>Conclusions and Future Work</b>	<b>303</b>
<b>1</b>	<b>Achieved work</b>	<b>307</b>
1.1	Automated heart delineation . . . . .	307
1.2	Coronary arteries extraction . . . . .	308
1.3	Automated coronary stenosis detection . . . . .	308
1.3.1	A two-stage Automatic Coronary Arteries Stenoses Detection . . . . .	308
1.3.2	Learning-based Detection of Severe Coronary Stenoses . . . . .	308
<b>2</b>	<b>Limitations and Perspectives</b>	<b>311</b>
2.1	Automated heart delineation . . . . .	311
2.2	Coronary arteries extraction . . . . .	312
2.3	Automated coronary stenosis detection . . . . .	312
2.3.1	A two-stage Automatic Coronary Arteries Stenoses Detection . . . . .	312
2.3.2	Learning-based Detection of Severe Coronary Stenoses . . . . .	313
<b>V</b>	<b>Appendix</b>	<b>315</b>
<b>A</b>	<b>Publications</b>	<b>317</b>

<b>B American Heart Association Coronary segmentation</b>	<b>319</b>
B.1 Left ventricle segmentation . . . . .	319
B.2 Coronary arteries territories assignment . . . . .	320
<b>C Measures for Automated Segmentation Evaluation of medical imaging</b>	<b>325</b>
C.1 Volume Based Measures . . . . .	325
C.1.1 Statistical measures . . . . .	326
C.1.1.1 Sensitivity . . . . .	326
C.1.1.2 Specificity . . . . .	327
C.1.1.3 Positive productive value . . . . .	327
C.1.1.4 Negative productive value . . . . .	327
C.1.1.5 Fraction of false negative . . . . .	327
C.1.1.6 Fraction of false positive . . . . .	328
C.1.1.7 Receiver Operator Characteristic curve . . . . .	328
C.1.2 Overlap Measures . . . . .	329
C.1.2.1 Dice similarity coefficient . . . . .	329
C.1.2.2 Jaccardi Index . . . . .	330
C.2 Distance based measures . . . . .	330
C.2.1 Distance of Hausssdorf . . . . .	330
C.2.2 Mean absolute distance . . . . .	331
<b>Bibliography</b>	<b>333</b>





---

## List of Figures

1.1	Human cardiovascular system: systemic and pulmonary circulations (Copyright © Addison Wesley Longman, Inc.) . . . . .	4
1.2	Blood Vessel Layers [4] . . . . .	6
1.3	Location of the heart in the Chest [36] . . . . .	8
1.4	Heart Cavities and blood flow: A cross-section of a heart showing its four chambers and the circulation of the blood in the left and right sides. Oxygen rich blood arrives from the lungs to the left ventricle to be pumped through the aorta to the rest of the body (red arrow). Oxygen-poor blood flows from the body to the lungs through the vena cavae and the right chambers. [327] . . . . .	9
1.5	Anterior view of coronary arteries and major blood vessels connected to the heart [327] . . . . .	10
1.6	Coronary artery segments according to the American Heart Association classification [21] . . . . .	11
1.7	The atherosclerosis progression steps resulting in the plaque rupture (Illustration from [87]). . . . .	13
1.8	Calcified and Soft plaques visualization in CT Angiography: arrow 1 shows a soft plaque, arrow 2 points to a calcified one and arrow 3 shows a mixed plaque . . . . .	14
1.9	Heart infarction caused by a blockage of a coronary artery by a blood clot [323] . . . . .	16
1.10	Coronary artery balloon angioplasty [329] and stent placement [330]. . . . .	18
1.11	Coronary artery Bypass Grafting: The figure shows how the vein and the artery are grafted to the heart [328]. . . . .	19

1.12	Angiograms of the LCA (left) and RCA (middle) with an observed stenosis of 80% and 50% (black arrows) respectively. The right image shows the stenosis of the RCA being stented (black arrow). PCI indicates percutaneous coronary intervention (© 2010 American Heart Association, Inc.) . . . . .	20
1.13	Intravascular ultrasound image of a left coronary artery with a soft plaque [456]. In the right image we can view the external vessel border (blue), the lumen border (yellow) and the plaque burden (green). . . . .	21
1.14	An example of a CT 3D volume . . . . .	23
1.15	Turning points in the computed tomography imaging history. Illustrations from [90]. . . . .	26
1.16	The common Hounsfield density value ranges for some human body tissues. Adapted from [90] and [345] . . . . .	27
1.17	Prospective ECG-triggering with a 16 slices CT scanner. Only a single 16-slice scan can be acquired during a heart cycle because of the long acquisition time. Thus, different sequential scans are performed during the same heart cycle phase to cover the whole heart volume. Illustration from [332] . . . . .	29
1.18	Retrospective ECG-triggering using a spiral multi-slices CT scanner. Continuous scans are acquired during the whole heart cycle. Thus, images of different heart cycle phases can be reconstructed [332] . . . . .	29
1.19	CT density value ranges for different plaque types (lipid rich, fibrous and calcified) and vessel lumen. Each box represents the <i>mean</i> $\pm$ <i>std</i> range of the HU value. Extreme values are displayed on the whiskers start and end points. Values from [312]. . . . .	32
1.20	Different Plaque types visualization in CT: (a) An atherosclerosis plaque with an extensive lipid accumulation. In the corresponding CTA the plaque appears as a soft tissue with a HU density of 40. (b) A soft purely fibrous non calcified plaque appears with a higher density of 90 HU. (c) A hard plaque with a calcified core that appears as a brilliant spot in CTA with a density around 110 HU. Illustrations from [28] . . . . .	33

1.21	Visualization of different atherosclerosis coronary plaques using computed tomography angiography. (A) A soft plaque (non calcified) of the proximal RCA showing a positive remodeling of the artery wall. (B) A mixed plaque of the left main artery ( the large arrows show the calcified and the soft cores of the plaque), Moreover, a soft plaque can be seen along the proximal and medial LAD (the double arrows) (C,G) Multiplanar reformatted reconstruction along the diseased coronary allowing an accurate visualization of the soft plaque extent and the stenosis degree, and the corresponding conventional coronary angiography confirming the presence of the stenosis. (E,D) A maximum intensity projection (a 5 mm slab) showing a partly calcified plaque of the proximal left descending artery and the corresponding conventional coronary angiography. (F) A 3D volume rendering of the stenosis illustrated in (C) and (G). Illustrations form [5]. . . . .	36
1.22	Examples of main visualization techniques of a cardiac CT angiography: (a) Axial view (b) Sagittal view (c) Coronal view (d) Oblique view (e) Volume Rendering of the raw image (f) MIP view on the oblique view showing the proximal and medial segments of the right coronary artery (RCA). . . . .	40
1.23	Coronary artery visualization for stenosis assessment. Images from a AW workstation of GE Healthcare. . . . .	42
1.24	Stenosis assessment using double reference site selection. Images produced on a AW workstation of GE Healthcare . . . . .	44
1.25	3D rendering volume of a diseased heart with several severe stenoses (>70%) caused by soft, calcified and mixed plaques (showed by the arrows). (a) The original volume. (b)-(d) The isolated heart volume allows a robust visualization of all the pathological coronary segments. . . . .	48
1.26	Automatic Stenosis detection on two diseased branches from two different cases: Patient 08 (First row) and Patient 14 (second row). 3D View of the artery coronary tree with marked detected stenosis (left), Lumen view of a diseased branch showing the probability profile in green with a peak at a severe stenosis (right). . . . .	50
1.27	The overall automated coronary stenosis detection and quantification flowchart.	52

2.1	Log-spectrum of a 512x512 image slice. The spectral power can be found in frequencies less than $\Pi/2$ . Hence, one can downsample by a factor 2 without losing information. Illustration from [152] . . . . .	55
2.2	Vessel intensity enhancement: (left) Initial image, (center) Enhanced image, (right) Gaussian look up table. Illustration from [299]. . . . .	56
2.3	The original image (left) is filtered using a greyscale threshold and an island removal algorithm, the result is a vessel with a hole inside (middle), An opening operation removes the vessel wall behind the calcifications (right). Illustration material from [453] . . . . .	58
2.4	The core point sets corresponding to the centers of intensity plateaus in 2D [406] . . . . .	59
2.5	The 3D heart model (left) matched to a Cardiac CT data (middle). The coronaries search regions defined using the four landmarks $A_1$ , $A_2$ , $R$ and $L$ [483] . . . . .	59
2.6	Examples of vessel intensity models: (a) Results of applying different threshold values to segment the right carotids volume. Illustration from the work of Boskamp et al. [45]. (b) Intensity plots of orthogonal 2-D slices through vessels with different sizes in 3-D MR images, and their corresponding generated 3-D images using the cylindrical intensity model as proposed in [467]. . . . .	61
2.7	Shape space from [149] and [261] defined based on the Hessian matrix eigenvalues variations. Vessels are typically matched to the bright string prototype. Illustration based on material from [261]. . . . .	65
2.8	Vessel centerline extraction using fast-marching optimization. Comparison of the two paths obtained using a normal (a) and a centering (b) potential. Illustration material from [109]. . . . .	68
2.9	3D vessel tree extraction using minimal paths: (a) Initial image, (b) minimal action map, (c) obtained tree and (c) final tree after thresholding on the geodesic voting scores. Illustration based on material from [299]. . . . .	69
2.10	Ellipsoid Fitting in a tracking scheme. [425] . . . . .	71
2.11	The iterative centerline correction process proposed in [453]. At each iteration, a new center point is defined using the centers of gravity of each two opposite points on the vessel 2D border. The final point is closer to the real center than the initial one. . . . .	71

2.12	Vessel segmentation using the Region Growing approach. Starting from a seed point ( in red in (a)), neighboring voxels are added to the segmented region if they meet some defined inclusion criteria (generally computed using the voxel gray value). . . . .	74
2.13	Vessel Wall extraction using a flexible B-spline. a) User selected start points b)Initial geodesic path computed between the two points, c) Evolution of the geodesic path inside the vessel and initialization of the vessel surface, d) Resulting vessel wall after deformation [149] . . . . .	79
2.14	Brain Vessel Segmentation Using: (left) Curves [268] and (right) CAC [473] .	80
2.15	Vessel Center Extraction: (a) Original CT Image (b) Correspondent center likelihood inside the black square (c) Rays used for the estimation of the maximum center likelihood, Illustration from [460] . . . . .	81
1.1	Surrounding structures of the heart. (a) Axial view of a cardiac CT showing the heart main structures (the four chambers and the main coronary arteries) and its surrounding organs (lungs, sternum, spine, descending aorta and the ribs). (b) Coronal view of the heart showing the contact surface with the liver. Heart coronaries are marqued with dark arrows. . . . .	86
1.2	3D rendering volume of a diseased heart with several severe stenoses (>70%) caused by soft, calcified and mixed plaques (showed by the arrows). The isolated heart volume allows a robust visualization of all the pathological coronary segments. . . . .	86
1.3	Exemple of heart isolation including important part of the liver. . . . .	89
1.4	Heart isolation algorithm workflow . . . . .	95
1.5	The Hounsfield scale. . . . .	95
1.6	Lungs volume extraction steps: (a) A cross section slice of the original volume. (b) Air class thresholding result. (c) The connected components corresponding to the right and left lungs. (d) Holles closing of the previous connected components. (e) A 3D rendering of the extracted lungs volume. . . . .	96
1.7	Aorta volume extraction steps: (a) A cross section slice of the original volume. (b) Blood pool class volume. (c) Eroded blood pools. (d) The connected component corresponding to the descending aorta. (e) Dilation of the previous connected componenet to include the aorta wall. (f) A 3D rendering of the extracted descending aorta. . . . .	97

1.8	Heart center extraction steps: (a) Axial slice of bright structures class. (b) 3D rendering volume of bright structures (c) 3D rendering of heart cavities. (d) and (e) Estimated heart center on a 3D and axial views. . . . .	98
1.9	Heart shell points extraction: Axial (a) and (b) coronal views of the detected points by the 3D ray casting. . . . .	100
1.10	Heart shell points analysis: (a) The original 3D heart shell points $\mathcal{P}_o$ (mainly heart/lungs contact points). (b) XY projection of the set $\mathcal{P}_o$ showing the two types of outliers (example G and B). . . . .	104
1.11	Outliers Detection: (a) X coordinate variation in the original set of points following the scanning order. (b) Sorted X coordinates of the 3D points. (c) LBP and RBP detection using the second derivative values threshold around the tails of the curve. Left and right breaking points corresponds to the limits of the inliers interval. . . . .	105
1.12	Outliers Detection: (a) Breaking Points detection using Y $2^{nd}$ derivative for the detection of type $O_2$ outliers. (b) Detected outliers ( $O_1$ are marked in green and $O_2$ in blue). . . . .	107
1.13	Ellipsoid fitting: (a) An LSQ Ellipsoid fitting on the 3D initial Data $\mathcal{P}_o$ . (b) An LSQ Ellipsoid Fitting on the clean data $\mathcal{P}_c$ after outliers removal . . . . .	108
1.14	Ellipsoid fitting: (a) The LSQ fitting result, (b) The Direct Least Square fitting (DLSQ)[165] . . . . .	110
1.15	Iterative Ellipsoid fitting: (a) The first fitting result (before outliers removal), (b) The second fitting (after outliers removal), (c) The final fitting result (after the WLSQ iterative approach), (d) 3D rendering of the heart ellipsoid . . . . .	112
1.16	Heart labels creation: (a) and (b) Axial and coronal views of the heart inside labels. (c) and (d) Axial and coronal views of the heart background labels. . .	117
1.17	An example of automated heart isolation: Axial (first row), coronal (second row) and 3D rendering (third row) views of the heart volume labeled on the original volume.. . . .	118
1.18	Modifying threshold value for sternum removal. The peripheral bones are removed but this induces some heart structure removal too. . . . .	119
1.19	Extra bones removal: (a) - (f) 2D axial views showing te different processing steps. (g) 3D rendering of the detected bones. (h) - (k) 3D rendering views of the heart volume before and after bones removal. We clearly can state the impact of removing bones on clearing the heart surface views. . . . .	121

1.20	ROC Curve of heart segmentation: the different ROC points are obtained by varying the random walker threshold and the dilation size . . . . .	127
1.21	ROC Curve of heart segmentation: the bones removal step improves the heart segmentation quality (green point). . . . .	127
1.22	Box plots of volume based evaluation metrics for data sets $S_1$ and $S_2$ . . . . .	129
1.23	Box plots of DICE coefficient, Hausdorf distance, FNVF and FPVF metrics for data sets $S_1$ and $S_2$ . . . . .	129
1.24	Distance maps of some segmented heart volumes exhibiting relatively high distance errors. . . . .	131
1.25	Qualitative Evaluation: distribution of the different grade classifications over the data set. . . . .	131
1.26	Qualitative Evaluation: Segmentation quality grade classification for all the database. . . . .	132
1.27	Examples of heart segmented volumes. . . . .	133
2.1	Examples of adjacency graphs: (a) SW-NE 90° graph (b) SE-NW 90° graph (c) S-N 90° graph . . . . .	147
2.2	A valid path of length 6 on a S-N 90° graph. . . . .	148
2.3	A 2D example of a set $X$ and its path opening $\alpha_5(X)$ : (a) The initial set $X$ (in black) defined on a S-N 90° graph. (b) The path opening result in green. Eliminated points are highlighted in red. . . . .	149
2.4	A toy example of extraction of a disconnected linear bright path using path opening and robust path opening: (a) Disconnected path (b) Path opening with $L = 5$ (c) Robust path opening with $L = 5$ and $K = 2$ . . . . .	149
2.5	A toy example of the extraction of the max tree of a grey level image: (a) Input Image (b)- (e) Different connected components of the image at different threshold values (f) Correspondent max tree. . . . .	153
2.6	Image filtering using the classical connected operators (the black path) and the shape space based approach (the black+red path). Illustration material from [472]. . . . .	154
2.7	Cardiac CT angiography filtering using the elongation attribute computed on the max tree. . . . .	156
2.8	Image filtering using the max tree and the elongation attribute with a connectivity $C_6$ : (a) $h = 2$ (b) $h = 5$ . . . . .	159
2.9	Filter on masque . . . . .	160



2.10	The 7 directions used for the robust path opening. . . . .	161
2.11	Image pre-filtering using the hessian and the robust path opening filters. Results of the extraction of the coronary arteries are obtained by applying a shape space filtering on the pre-filtered image: (a) Image filtered using no pre-filtering step (b) Image filtered using the hessian enhancement filter and the RPO based enhancement filter (c). . . . .	161
2.12	Noise reduction using weighted elongation attribute with the component volume ((e), (f)). Results of image filtering using the original image with no enhancement with the elongation attribute ((a), (b)) and the RPO based enhancement filter with the elongation attribute ((c), (d)). . . . .	162
2.13	The cardiac image filtering for coronary segmentation flowchart. . . . .	163
2.14	Challenging case with several calcified plaque disconnecting the coronary arteries (a) Coronary tree ground truth (b) Automatically segmented coronary tree. An post-processing step was applied to remove the remaining heart cavity. . . . .	163
2.15	Overlap measure obtained on the 11 cardiac datasets. . . . .	164
2.16	Coronary artery tree segmentation: (a) The provided coronaries centerlines used as vessel markers to initiate the watershed process. (b) The resulting coronary arteries lumen volume used to compute the lumen contours. (c) The coronary arteries tree rendering with the centerlines and the ascending aorta. . . . .	166
2.17	Vessel lumen Quantification: For each vessel cross section a 2D ray casting is used to find the starting point of the section contour, i.e. the first point outside the watershed volume. Then, we look for the next contour point in a restricted neighborhood of the current point. The process stops when the starting point is reached for the second time. . . . .	166
2.18	2D vessel cross section intensity profiles are shown for normal (a)-(c) and pathological (b)-(d) cases with the corresponding ray directions. Normal ray profiles has maximal intensity values near to the vessel center and lower values near the lumen border. Intensity profiles along pathological tissues show different patterns. For calcified lesions, a second and higher peak is detected at the center of the calcified region. On the contrary, soft lesions showed lower intensity values than the vessel lumen hence involving a drop of the ray intensity profile. The two borders can be delineated by using adequate threshold values. . . . .	168

2.19	Vessel reformatted volume generation: (a) The provided vessel centerline. (b) The resampled centerline. (c) The 2D vessel cross-sections stacked to contract the final vessel warped volume (d). . . . .	169
2.20	Ascending aorta extraction (b) from image (a), followed by histogram extraction and smoothing (c) for initial vessel statistics computation. . . . .	170
2.21	Adaptive thresholds for calcified and non calcified plaques extraction for a healthy (a) and diseased vessel (b). . . . .	171
2.22	2D lumen boundaries extraction using adaptive thresholds: (a) Rays of a maximum radius $R$ are traced around the vessel centerline point. (b) A point on the ray and the associated neighboring pattern to detect lumen border. . . . .	172
2.23	A post smoothing step to avoid noisy contours: Original (a) and smoothed (b) contour. . . . .	173
2.24	Examples of coronary vessels masks extraction using static patient specific thresholds ((a) (c) (e)) and adaptive patient specific thresholds ((b) (d) (f)). Adaptive thresholds allow to obtain more accurate vessel lumen markers by removing leakage and lesion inclusion. . . . .	174
2.25	Overall lumen segmentation flowshart. . . . .	175
2.26	3D example of coronary lumen segmentation results of datasets 16, 14, 13, 12, 01 and 05. . . . .	176
1.1	2D Ray-casting to detect vessel wall points while excluding the calcified plaques using a gradient threshold. Illustration from the work of Wink et al. [460]. . . . .	186
1.2	Stenosis detection using hessian based approach: (Left) The non-redundant shape-space for second order 3D variations proposed by [262]. (Right) Maximum Intensity Projection (MIP) of two stenotic regions in an MRA dataset, wire-frame representation with stars denoting the stenotic area. . . . .	193
1.3	Two cases showing the accuracy of $FFR_{CTA}$ compared to invasive FFR. Case (a) shows a nonfunctionally significant stenosis at the LAD with a computed $FFR_{CTA}$ of 0.62. This value is confirmed using invasive angiography that shows an FFR of 0.65. Case (b) shows a non hemodynamically significant stenosis with an $FFR_{CTA}$ of 0.87. The FFR measured using invasive angiography was of 0.86. Illustrations from [414]. . . . .	196

1.4	Automatic calcified coronary lesions extraction and quantification pipeline: First, the algorithm starts by identifying a set of calcification candidates. Appropriate features are computed to describe each of the previous candidates. Following, a trained classifier is used to distinguish between true calcifications and false detections. A review step is proposed in order to validate/supress suspicious calcification that the classifier could not label with a high confidence. The final calcium score can thus be computed. Illustration from [463] .	198
1.5	An overview of the proposed workflows in the previously published works on coronary arteries plaque lesions detection and quantification. . . . .	203
1.6	Matching procedure of the reported stenosis to a segment and lesion number. Illustration from reference [215] . . . . .	209
2.1	Examples of different target lesions to be detected in the challenge database. Calcified plaques are highlighted in yellow, soft plaques in red and mixed plaques in blue. . . . .	213
2.2	Overview of the lumen based stenosis detection approach . . . . .	214
2.3	Example of merging 3 different branches with overlapping segments. . . . .	214
2.4	Coronary artery tree merging. (a) The original coronaries centerlines presenting overlapping segments with multiple centerline points (each branch is illustrated using a different color). (b) Resulting coronary arteries tree organized in a set of disjoint segments (each segment is represented by a different color). . . . .	215
2.5	Geometry definition for each centerline points. $R_1$ and $R_2$ are used to define the cross section planes. . . . .	216
2.6	Vessel area quantification: for each center point the correspondent section area is set to the median value of all the section area inside the box of height H. .	217
2.7	Examples of vessel lumen quantification showing the real (in blue) and the smoothed (in red) vessel lumen cross sections area profiles. . . . .	218
2.8	Vessel area profile reconstruction: Original and smoothed vessel area profile per 2D section (in red and blue respectively). The vessel theoretic profile is constructed using a robust linear regression (in green). . . . .	220
2.9	Stenoses detection and quantification using the healthy reconstructed vessel lumen cross section area profile. Several stenosis are detected but only five of them are flagged as severe stenosis. . . . .	221
2.10	Examples of computed intensity variations along some diseased branches. . .	222

- 
- 2.11 Stenosis detection for dataset 09: (a) 3D rendering of the coronary tree with detected stenosis highlighted in red. (b) Lumen views of the left anterior descending artery and the right artery coronary (c) Curved view of the left anterior artery and the right. Detected stenotic areas are marked in between two red segments. . . . . 223
- 2.12 Coronary arteries severe stenosis detection performance: True positive (TP), false positive (FP), false negative (FN) and true negative (TN) rates with reference to the QCA (a) (segment-based analysis) and CTA (b) (segment-based analysis) reference standards. Values are illustrated for the training and the testing databases as well as for the whole database. . . . . 225
- 3.1 Supported vector machines classifier: (a) A 2D example of linearly separable data. (b) The two classes could be separated using multiple lines. But being too close to some training data such lines are more sensitive to noise and will not generalize correctly. (c) The better hyperplane separating the two training subsets is the one maximizing the margin distance as it will be able to better classify new samples that are close to the current decision boundary. . . . . 233
- 3.2 Boosting algorithm: (a) A 2D example of training data for a 2-class classification. (b)- (e) Examples of some weak classifiers iteratively created by the boosting algorithm to construct the final strong classifier. After each weak classifier, the training data is re-weighted giving a higher weight to miss-classified samples. (f) The final strong classifier as a weighted combination of weak hypothesis allowing to accurately separate the two classes. . . . . 235
- 3.3 Decision tree constitutes a set of hierarchically organized nodes (gray) with ending leaves (blue). Each node corresponds to a test function ( $h_i$ ) used to decide whether to send the input data to the left child node or to the right one. Each path on the tree leads to a leaf point corresponding to a final decision  $D_i$  (prediction) on the input object. . . . . 236

3.4	Training stage: (a) Each tree is trained using a <i>randomly</i> selected subset of input labeled data. The trees are grown separately until reaching a stopping condition (details in the text). (b) To train a single decision tree, a subset of learning data is used as input (here denoted $S_0$ ). For each node $i$ , a set of <i>randomly</i> selected features of the vector $\vec{x}$ is employed for optimizing the parameters of the split function $h_i$ by maximizing a given energy function $IG$ . The input data set $S_i$ is then split into two disjoint sets $S_i^R$ and $S_i^L$ , subsequently used to grow the children nodes. Internal nodes are illustrated in gray and final leaves in blue. . . . .	240
3.5	Random Forest testing stage . . . . .	241
3.6	Example of a lesion located at the bounding of two successive patterns $C_{i-1}$ and $C_{i+1}$ . Adding an overlapping pattern $C_i$ allows to insure that at least on of the cylindrical patterns includes the lesion and thus it could be captured by the extracted features. . . . .	244
3.7	Example of vessel with different plaque types (soft and calcified). Cross sections A, B, C and D of the vessel are shown on the right images. The slices shows a healthy section (A), two calcified sections (B and D) and a section with a soft plaque (C). The vessel cross section are fairly approximated by circular sections. . . . .	245
3.8	Vessel sampling pattern: (a) A straight cylindrical pattern with varying height $H_i$ and width $D_i$ . This model is not accurate to sample highly curved segments of the vessel (examples in dashed lines). (b) To deal with curved regions along the vessel, we propose to use a curved cylindrical model that locally fits the vessel curvature. This allows to avoid including undesirable surrounding structures and missing some vessel regions which could bias the classification of the corresponding point. . . . .	246
3.9	Schematic vessel sampling using the (a) straight and (b) curved cylindrical patterns. The curved varying pattern offers a better overlap with the vessel volume while minimizing the inclusion of undesirable surrounding structures (specially at distal segments of the vessel). . . . .	247
3.10	Schematic illustration of the different sub-regions (radial on the left and longitudinal on the right) defined in the cylindrical pattern. . . . .	248
3.11	An illustration of the sampling of a 2D slice of the cylindrical pattern. The sampling results in 4 points per 2D sub-region. . . . .	249

- 
- 3.12 Mean gray values extraction and sorting in order to create a rotational invariance of these features. Each feature value corresponds to the mean intensity value inside of one of the sub-regions. Higher values are represented with darker colors. The set of feature values is sorted and then added to the feature values vector. . . . . 250
- 3.13 Intensity variation of 2-D cross sections of some coronary arteries - First column presents a normal cross-section (a), a cross-section with a calcification (a) and a cross-section with a soft plaque (a). 2D views of pseudo-color intensity plots of the same cross sections are shown in column 2. The third column shows a 3D view of the same intensity plots. Pseudo-color maps are generated by scaling the cross section data between its minimum and maximum values. 251
- 3.14 Illustration of radial gradients features calculation using Haar-like patterns. The difference between the two dark regions is computed as a feature for each pair of regions. The difference intensity value between the light crown and the su of the two dark ones is also used as a Haar-like feature. . . . . 253
- 3.15 Cylindrical pattern rotation to enhance the rotation invariance around the vessel center. . . . . 253
- 3.16 Illustration of longitudinal gradients features calculation similar to the well known Haar-like features. For the left, the difference between the dark and light regions is computed as a feature to assess the presence of a lesion inside one of the two sub-regions. For the right, the feature corresponds to the difference intensity value between the two bright sub-regions and the dark one. This allows to capture a lesion located at the center of the pattern. . . . 254
- 3.17 Intensity histogram of a sampling pattern located at a diseased vessel segment with (a) normal, (b) calcified, (c) soft and (d) mixed plaque. All the histograms contain 40 bins ranging form 0 HU to 600 HU. . . . . 255
- 3.18 Distribution of the reported coronary lesions by the CTA observers over the different lesion types and stenosis degrees. Only 27 over 103 lesions correspond to severe stenoses. . . . . 260
- 3.19 The structure of the training dataset. . . . . 262

- 3.20 Output probability profile processing: (a) The output probability profile for the pathological class along a vessel branch (i.e. the horizontal axis corresponds to the point position along the vessel path). (b) The smoothed probability profile after applying the Hann filter. (c) The severe stenosis ground truth (green line) displayed on the smoothed profile. We can see that the annotated stenosis correspond to peak of the probability profile. Hence the classifier is able to recognize the marked stenosis. This profile is obtained on an annotated dataset that was excluded from the training database (cross validation leaving-one-out process). . . . . 263
- 3.21 Stenotic regions detection using a single threshold. Using a threshold value of 50 (red line) allows to detect all the stenosis reported by the consensus of readers (the detected regions are marked in green) but it also leads to the detection of three false detections marked in red. The ground truth stenosis are shown using the green line. . . . . 264
- 3.22 Stenotic regions detection using hysteresis thresholding. A first high threshold allows to select the surely stenotic regions (in dark green). Second the selected connected components are propagated to including neighboring stenotic point with a probability higher than  $T_{prob2}$  (in light green). Using such approach false positives are eliminated thanks to the first high threshold. The ground truth stenosis are shown using the green line. . . . . 264
- 3.23 Stenosis Center Extraction: The probability profile is illustrated in blue. In (a), the center point is defined as the vessel point showing the minimum cross section area value. The flagged stenotic region is displayed in green and the corresponding cross section area profile is drawn in purple. The straight line indicates the extracted stenosis center. In (b), the center point is extracted as the point having the maximum probability value. The two approaches give two distinct points. . . . . 265
- 3.24 Stenosis quantification for (a) the CTA (per lesion) and (b) QCA (per segment) evaluation. (c) The segment stenosis corresponds to the maximum lumen narrowing induced by all the stenosis located at that segment. . . . . 267
- 3.25 The prototype flowchart developed for the automated coronary stenosis detection. . . . . 270
- 3.26 The prototype is launched by clicking on the icon (2) after selecting the wanted exam from the list of available exams in (1). This work is developed as a prototype of the Volume Viewer software. . . . . 272

3.27	proto . . . . .	273
3.28	Automatic Stenosis detection on two diseased branches from two different cases: Patient 08 (First row) and Patient 14 (second row). 3D View of the artery coronary tree with marked detected stenosis (left), Lumen view of a diseased branch showing the probability profile in green with a peak at a severe stenosis (right). . . . .	274
3.29	7 different sets of features have been extracted over the training data sets. The sets are compared using the per lesion (CTA) and per segment (QCA) evaluations. (a) and (a) shows the QCA and CTA true positives, false positives and false negatives rates. In (c) the false positive per patient rates (compared to the QCA and CTA references) are shown. . . . .	277
3.30	Sensitivity and PPV values compared to the QCA and CTA references for the 7 sets of features. $F_5$ shows the best overall performances. . . . .	278
3.31	Composition of different training databases for stenosis detection. (a) All the healthy points are included into the training database with the pathological points ( $S_1$ ). (b) The non pathological class is constructed used only the stenotic points with a degree lower than 50% ( $S_2$ ). (c) A set of N points selected from healthy and non severe stenotic points is used as non pathological samples ( $S_3$ ). Finally (d), a set of N points selected only from the healthy class is selected to designate the non pathological class ( $S_4$ and $S_5$ ). . . . .	279
3.32	Comparison of different training databases for stenosis detection: (a) shows the distribution of the segments detected as diseased over the TP, FP and FN classes (i.e. per segment analysis) for different training databases ( $S_1$ to $S_5$ ). In figure (b) the distribution of the detected lesions (i.e. per lesion analysis), by the proposed approach, over the TP, FP and FN classes is illustrated using the same training databases. The sensitivity and PPV for both the CTA and QCA based analysis for each training database are presented in figure (c). . .	280
3.33	Obtained ranks by the different training databases. The best overall rank is obtained by subset $S_5$ . . . . .	281
3.34	ROC Curves used to optimize the Random Forest classifier parameters. Each curve corresponds to a set of parameters from table 3.4. Parameters value presented by the blue curve gives the better performance. . . . .	282



3.35	Optimization of the Random Forest classifier intrinsic parameters over the training data sets. The rates of the per lesions and per segments TP, FP and FN are shown in (a) and (b). The CTA and QCA sensitivity and PPV values are shown in (c). . . . .	283
3.36	Severe and non severe stenosis classification performances for three different smoothing parameters. The per lesion and per segment sensitivity and PPV values are presented for the three submissions. . . . .	284
3.37	Optimization of the probability threshold value for stenosis detection. FP, TP and FN rates are shown for both a per segment (a) and a per lesion (b) evaluation for different threshold values. The corresponding sensitivity and PPV values are presented in (b). . . . .	286
3.38	Stenotic regions detection by using a two-thresholds based approach. FP, TP and FN rates as well as the FP per patient rates, are shown for both a per segment (a) and a per lesion (b) evaluation for different couples of threshold values. The corresponding sensitivity and PPV values are presented in (b). . . . .	287
3.39	Stenosis center extraction strategy selection: FP, TP and FN rates are shown for both a per segment (a) and a per lesion (b) evaluation of both of the strategies. The corresponding sensitivity and PPV values are presented in (c). The maximum probability strategy gives a better classification result. . . . .	288
3.40	Sensistivity and PPV values distribution as compared to QCA and CTA reference standards. . . . .	294
3.41	A slice-based evaluation scheme: Blue slices refers to the reference standard annotated by the observers. True Positive slices (reported by the method) are marked in green while false negative ones are depicted in yellow. False positive detections are marked in red and true negative slices (non diseased) are depicted in grey. . . . .	297
3.42	Coronary lesions detection results on a diseased LAD branch showing soft and calcified plaques. Detected lesions are marked using blue bookmarks. The proximal and distal references as well as the minimum lumen narrowing are marked. . . . .	300
3.43	Coronary lesions detection results on a diseased RCA branch showing soft plaques. Two different lesions are detected and are marked in purple and red bookmarks. The proximal and distal references as well as the minimum lumen narrowing of each lesion are shown. . . . .	300

3.44	Coronary lesions detection results on a diseased RCA branch with mixed, calcified and soft plaques. The different lesions are detected and are marked using a red bookmark. The proximal and distal references as well as the minimum lumen narrowing of each lesion are shown. . . . .	301
3.45	Coronary lesions detection results on a diseased RCA branch with calcified plaques and a stent that covers the proximal segment. The detected stent is marked using a blue bookmark. . . . .	301
A.1	Views of the long vertical axis, long horizontal axis and the short axis planes showing the recommended basal, mid-cavity and basal slices with the corresponding 17-segments. Illustration from [?] . . . . .	321
A.2	Assignment of the 17 segments of the left ventricle to the RCA (red), LAD (blue) and LCX (green). A1, A2 and A3 shows the axial views of the basal, mid-cavity and the apical thirds of left ventricle on a CT angiography with the corresponding AHA segments. B and C shows the horizontal and vertical long axis of the left ventricle displaying the ventricle apex (segment 17). Bottom: Segmental anatomy of coronary arteries corresponding to the modified AHA 17-segment model of the left ventricle. With considering that there is a great variability in blood supply of different segments, the individual segments are assigned to each coronary artery territories. Illustration from [?] . . . . .	322
A.1	An exemple of a segmentation with the distribution of false positives, true positives, true negtaives and false negatives. Both the segmentation S (green) and the ground truth G (blue) are illustrated. . . . .	326
A.2	A ROC curve illustration showing particluar classification cases. . . . .	329



---

## List of Tables

1.1	Normal lumen diameter (mean $\pm$ STD) of human coronaries for the main arteries. Values measured in a group of 83 patients. (Adapted from [120]) . . . .	12
1.2	Accuracy of severe coronary stenosis detection with 16-slices, 64-slices and dual source CT angiography. Sensitivity, Specificity, PPV and NPV values are reported per patient, per vessel and per segment analysis. . . . .	31
1.3	Main imaging characteristics of CT angiography compared to conventional CA and IVUS. . . . .	37
1.4	Coronary arteries stenosis qualitative and quantitative grading using CT angiography. Adapted from [351] . . . . .	45
1.1	Comparison of previous works on heart isolation in MR and CT angiography. <i>Error</i> refers to the mean distance error between the manual and automated heart segmentation. <i>Jl</i> is the Jaccard index. <i>Dice</i> refers to the Dice Similarity Coefficient. . . . .	93
1.2	Ellipsoid fitting using linear least squares (LSQ) and direct least square (DLSQ)	109
1.3	Iterative Ellipsoid fitting using linear least squares (LSQ): Average Fitting Deviation and eccentricity of the three fitted ellipsoids. . . . .	111
1.4	Qualitative evaluation: Overall segmentation quality classification . . . . .	124
1.5	Automated heart segmentation: computational time for each processing part .	125
1.6	Automated heart segmentation: Parameters settings . . . . .	126
1.7	Quantitative evaluation: Sensitivity, specificity, PPV and NPV mean values and standard deviations for $S_1$ , $S_2$ and the overall database . . . . .	128

1.8	Quantitative evaluation: DICE overlap measure and Hausdorf distance values for $S_1$ , $S_2$ and the overall database . . . . .	130
1.9	Qualitative evaluation: Mean grade value of the different evaluation metrics .	132
1.10	Comparison of the previous works on heart isolation CT angiography . . . . .	134
2.1	An overview of the qualitatively and quantitatively evaluated CTA coronary artery segmentation approaches. For qualitative evaluation “Visual inspection” indicates that the quality of the segmentation result was assessed visually and judged as satisfactory or not. For qualitative evaluation the metric used is mentioned. . . . .	143
2.2	Coronary arteries filtering using different attributes on the tree of shapes . . .	159
2.3	Vessel lumen mask extraction using different k values. . . . .	177
2.4	Vessel lumen segmentation performances evaluation using the reformatted vessel volumes and the original images. . . . .	178
2.5	Comparison of state of the art approach and the proposed one. . . . .	178
2.6	Coronary lumen segmentation performances as compared to state of the art approaches and the three observers. . . . .	178
1.1	Ad hoc approaches for (semi-)automated detection of coronary arteries lesions. SP refers to soft plaques and CP to calcified ones. . . . .	194
1.2	Learning based approaches for (semi-)automated detection of coronary arteries lesions . . . . .	200
1.3	Definition of TP, TN, FP and FN measures proposed in the literature for stenosis detection evaluation in CT angiography. . . . .	206
1.4	Segment-based (compared to QCA reference standards) and lesion-based (compared to CTA reference standards) definitions of TP, TN, FP and FN detections for coronary arteries significant stenosis detection using the framework described in [215]. . . . .	208
2.1	Performance of the proposed approach for severe stenosis detection on the training database. Results are compared to the three observers and their consensus. Evaluation is performed by segment (compared to QCA) and lesion analysis (compared to CTA). . . . .	224

2.2	Performance of the proposed approach for severe stenosis detection on the testing database. Results are compared to the three observers and their consensus. Evaluation is performed by segment (compared to QCA) and lesion analysis (compared to CTA). . . . .	226
2.3	Performance of the proposed approach for severe stenosis detection on the 48 datasets. Results are compared to the three observers and their consensus. Evaluation is performed by segment (compared to QCA) and lesion analysis (compared to CTA). . . . .	226
2.4	Evaluation of the first and second steps results on the training datasets. The first step corresponds to the stenosis candidates extraction using only the lumen area reduction. The second step corresponds to the false positive removal step using appearance properties. . . . .	226
3.1	Coronary plaque types distribution over the 18 training data sets. . . . .	258
3.2	Coronary stenosis degrees distribution over the training data sets. . . . .	259
3.3	Composition of 7 tested features sets using the partitioned cylindrical pattern. . . . .	276
3.4	Random Forest parameters setting . . . . .	281
3.5	Random Forest output probability profile smoothing. Variation of the window width and comparison of the classification results over the training database. The overall rank of the submission is modified in order to compare only these three submissions. . . . .	284
3.6	Per segment evaluation results (TP, FP, FN and FP/Pat values) of severe stenosis detection obtained by the two approaches $V_1$ and $V_2$ on the training and testing databases of the Rotterdam Coronary Artery Algorithm Evaluation Framework . . . . .	289
3.7	Per lesion evaluation results (TP, FP, FN and FP/Pat values) of severe stenosis detection obtained by the two approaches $V_1$ and $V_2$ on the training and testing databases of the Rotterdam Coronary Artery Algorithm Evaluation Framework . . . . .	290
3.8	Per segment and Per lesion evaluation results (Sensitivity and PPV values) of severe stenosis detection obtained by the two approaches $V_1$ and $V_2$ on the training and testing databases of the Rotterdam Coronary Artery Algorithm Evaluation Framework . . . . .	290
3.9	Evaluation results of the three proposed methods on severe stenosis detection compared to the observers' consensus. . . . .	291

3.10	Results of severe stenosis detection of the Rotterdam Coronary Challenge: comparison of the 16 submitted methods. Evaluation was performed on the 30 testing data sets. . . . .	292
3.11	Results of severe stenosis detection of the Rotterdam Coronary Challenge: comparison of the 16 submitted methods. Evaluation was performed on the 48 training and testing data sets. . . . .	293
3.12	(Semi-) Automated severe stenosis detection performance of the 16 public methods submitted to the evaluation framework. . . . .	293
3.13	Lesion distribution within the two testing databases. . . . .	298
3.14	Per Branch and Per patient evaluation results using $B_1$ . . . . .	298
3.15	Per segment, Per Branch and Per patient evaluation results using $B_2$ . . . . .	299
A.1	The 17 myocardial segments with the recommended nomenclature for the left ventricle and the corresponding coronary arteries segmentation for tomographic imaging of the heart . . . . .	323
A.1	Confusion matrix . . . . .	326

---

# Abbreviations

**AHA** American Heart Association. [10](#), [105](#), [106](#)

**AM** acute marginal arteries. [10](#)

**CBCT** Cone-Beam Spiral Computed Tomography. [25](#)

**CCA** Conventional Coronary Angiography. [1](#), [2](#), [20](#), [21](#), [33](#)  
[. 31](#)

**CCT** cardiac computed tomography. [3](#)

**CHD** Coronary Heart Disease. [1–3](#), [16](#), [31](#), [33](#)

**cMPR** curved multi-planar reformatting. [39](#), [42](#)

**CPR** curved plane reformatting. [2](#)

**CT** computed tomography. [2](#), [3](#), [22](#)

**CTA** computed tomography angiography. [2](#), [12](#), [14](#)

**CVD** Cardiovascular Disease. [1](#)

**DSC** Dice similarity coefficient. [88](#)

**DSCT** Dual source CT. [25](#), [29](#), [32](#), [35](#)

**EBCT** Electron Beam Spiral Computed Tomography. [27](#), [28](#)



**FN** False Negative. [88](#), [112](#)

**FOV** Field Of View. [36](#)

**FP** False Positive. [88](#), [112](#)

**GC** Graph Cuts. [79](#)

**HU** Hounsfield Unit. [24](#)

**IVUS** Intra Vascular UltraSound. [20](#), [21](#), [31](#)

**LAD** left anterior descending artery. [10](#), [106](#)

**LCA** left coronary artery. [9](#)

**LCX** left circumflex branch. [10](#), [106](#)

**LM** The left main artery. [10](#)

**MIP** Maximum Intensity Projection. [39](#)

**MPR** Multi-planar reformatting. [39](#), [42](#)

**MRI** Magnetic Resonance Imaging. [56](#)

**MSCT** Multi-slice spiral computed tomography. [2](#), [25](#), [31](#), [32](#), [35](#)

**OMPR** oblique multiplanar reformatting. [2](#)

**PDA** right posterior descending artery. [10](#)

**RCA** The right coronary artery. [10](#), [106](#)

**RW** Random Walker. [79](#)

**TN** True Negative. [88](#), [112](#)

**TP** True Positive. [88](#), [112](#)

**VR** Volume Rendering. [39](#), [40](#)

**WHO** The World Health Organization. [1](#)

---

## Glossary

**angina** Angina pectoris is the result of myocardial ischemia caused by an imbalance between myocardial blood supply and oxygen demand. It is a common presenting symptom (typically, chest pain) among patients with coronary artery disease (CAD). (From <http://emedicine.medscape.com/article/150215-overview>) [11](#)

**apex** The lowest superficial part of the heart, formed by the inferolateral part of the left ventricle ( From <http://medical-dictionary.thefreedictionary.com/apex+of+the+heart>). [7](#)

**myocardium** The thick middle layer of the heart that forms the bulk of the heart wall and contracts as the organ beats. (From <http://medical-dictionary.thefreedictionary.com/myocardium>) [4](#), [9](#)

**catheter** A thin tube that can be inserted in the body to treat diseases or perform a surgical procedure. A balloon catheter is a catheter whose tip has an inflatable balloon that holds it in place or can dilate the lumen of a vessel, such as in angioplastic procedures. An injection catheter is a catheter through which a contrast medium is injected for visualization of the vascular system of an organ (From <http://medical-dictionary.thefreedictionary.com/catheter>) [17](#), [20](#)

**contrast agent** Radiocontrast agents are a type of medical contrast medium used to improve the visibility of internal bodily structures in X-ray based imaging techniques such as computed tomography (CT) and radiography (commonly known as X-ray imaging). Radiocontrast agents are typically iodine or barium compounds.(From <http://en.wikipedia.org/wiki/Rac>) [20](#)

**stenosis** The narrowing of an opening or passage-way in the body. In arteries, stenosis is caused by a build-up of atherosclerotic plaque, disease, or other disorder. (<http://medical-dictionary.thefreedictionary.com/stenosis>) 2, 14

**stent** A tube designed to be inserted into a vessel or passageway to keep it open. Stents are inserted into narrowed coronary arteries to help keep them open after balloon angioplasty. The stent then allows the normal flow of blood and oxygen to the heart. Stents placed in narrowed carotid arteries (the vessels in the front of the neck that supply blood to the brain) appear useful in treating patients at elevated risk for stroke. Stents are also used in other structures such as the esophagus to treat a constriction, the ureters to maintain the drainage of urine from the kidneys, and the bile duct to keep it open. (From <http://www.medterms.com/script/main/art.asp?articlekey=5554>) 17

**thrombosis** Formation of a clot in the blood that either blocks, or partially blocks a blood vessel. The thrombus may lead to infarction, or death of tissue, due to a blocked blood supply. (From <http://medical-dictionary.thefreedictionary.com/thrombosis>) 12

**thrombus** A clot consisting of fibrin, platelets, red blood cells, and white blood cells that forms in a blood vessel or in a chamber of the heart and can obstruct blood flow. The rupture of atherosclerotic plaques can cause arterial thrombosis (the formation of thrombi), while tissue injury, decreased movement, oral contraceptives, prosthetic heart valves, and various metabolic disorders increase the risk for venous thrombosis. A thrombus in a coronary artery can cause a heart attack. (From <http://medical-dictionary.thefreedictionary.com/thrombosis>) 12

# Part I

## Introduction and Review



---

---

# Chapter 1

---

## Introduction

Cardiovascular Diseases (CVDs) are the group of disorders that affects the cardiovascular system mainly Coronary Heart Diseases (CHDs), cerebrovascular diseases and peripheral arterial disease. According to The World Health Organization (WHO), CHDs remain the world's leading cause of mortality specially in developed countries. In 2008, coronary arteries diseases claimed 7.3 million lives worldwide representing more than 12% of total deaths [3]. They are the largest cause of death in Europe and United States, and account for one sixth of deaths per year. For instance, more than 600 000 deaths are caused by CHDs in Europe and approximately 500 000 in the US [19]. By 2030, almost 23.6 million people will die from CVD, mainly from heart disease and stroke. These diseases are projected to remain the single leading causes of death with the largest percentage increase in the Eastern Mediterranean Region. Considering the previous statistics, early detection and diagnosis of these diseases would help providing better therapeutic monitoring by clinicians and improve aftercare for patient suffering from CHDs. In the context of treatment of acute phases of illness, quality of interventional choice improves the success rate acts and reduces costs and risks.

Conventional Coronary Angiography (CCA) is the standard routine for vessel investigation and CHD diagnosis. The main advantage of this modality is that the intervention can be performed directly when a lesion is located by X-ray. However, its invasive nature leads to a non-negligible risk for the patient's health [485] and a related important cost for the intervention, specially when the patient shows some symptoms but doesn't exhibit a high likelihood for CHDs. In fact, in Europe and USA only 40% of conventional coronary angiographic examinations are followed up by a subsequent interventional or surgical procedure, when the rest of angiograms are performed only for the purpose of ruling out CHDs [93]. Thus, it is preferable for a patient to avoid undergoing an unnecessary risky invasive exam only for diagnosis of CHDs. The previous

facts show the importance of and the need for a reliable noninvasive alternative to visualize the coronary arteries and rule out cardiac diseases.

The continuous and rapid development of X-ray [computed tomography \(CT\)](#) imaging over the last 10 years has made the dream of imaging heart coronaries using a reliable, widely available and non invasive modality come true. In fact, the introduction of the [Multi-slice spiral computed tomography \(MSCT\)](#) in 1998 made possible the acquisition of the heart and the coronary arteries with a high temporal and spatial resolution. Recent studies [281] showed that [MSCT](#) may be used as an alternative to accurately locate and grade heart lesions in a non invasive way. In fact, cardiac [computed tomography angiography \(CTA\)](#) has become a standard technique to inspect coronaries and rule out significant lesions at a quality comparable to [CCA](#). For cardiologists, this represents a valuable tool for diagnosis and necessary intervention planning with minimal related risk and costs. Nevertheless, analysis of cardiac [CT](#) exams for [CHDs](#) inspection remains a tedious and time consuming task, considering the manual clinical work-flow as well as the increasing number of patients and the resulting angiographies to be assessed. High accuracy is required, and thus only highly experienced clinicians are able to analyze and interpret the data for diagnosis. Consequently, conventional invasive angiography is still the standard procedure for [CHD](#) diagnosis. Therefore, it is highly recommended to develop computerized tools to reduce the amount of data to be reviewed and assist the cardiologist in the diagnosis process. This would reduce processing time and ensure quality of diagnostics. As a result, clinicians can more concentrate on the interpretation of relevant data and several patients can be diagnosed at the same time thus highly reducing the cost of such examinations on the healthcare system. Therefore an automatic coronary analysis tool would help in [CTA](#) examination, allowing pathologists to efficiently diagnose and evaluate risks associated with [CHDs](#), and raise the quality of the assessment from a qualitative level to a quantitative level.

Even though [CTA](#) has been established as a reliable alternative to the standard [CCA](#), the complexity of the resulting data is still the main limitation to the use of this modality. Commonly, the clinical work-flow is mainly manual based on the analysis of original slices combined to the [oblique multiplanar reformatting \(OMPR\)](#) and [curved plane reformatting \(CPR\)](#) views (see section 1.3.2). Which makes the assessment of the coronary arteries and the quantification of [stenosis](#) a time-consuming task. Our objective is to propose (semi)-automatic tools for [CTA](#) data analysis to ease the cardiovascular lesion diagnosis stage. Those tools are also meant to reduce the intra- and inter-observer variability and the dependance of the quality of the diagnosis on the degree of the clinical experience. This thesis presents tools to rapidly and efficiently detect and quantify coronaries stenoses in [CTA](#). Our methods are completely automated in order to reduce the user interaction and thus guarantee a high reproducibility. A

prototype is developed for each method and the proposed algorithms have been evaluated on different clinical databases compared with reference data provided by experts.

This introductory chapter addresses the needed background knowledge to better understand the clinical context of our work. We first propose a description of basic human cardiac anatomy aspects in Section 1.1. Coronary arteries lesions anatomy are described in Section 1.1.2 to apprehend their nature and understand the various anatomical properties likely to be used in the development of lesion detection methods. We also assume that minimal knowledge on medical imaging techniques is required to deal with the issue. In section 1.2 main cardiac medical imaging are exposed. We will mainly focus on the characteristics of CT modality (section 1.2.3), list some of cardiac computed tomography (CCT) advantages and limitation and finally explain the use of this modality for CHDs assessment and diagnosis (section 1.3.2). Section 1.4.2 presents the contribution of this thesis in order to offer fully automated tools for coronary arteries inspection. Finally, we expose the overall organization of the manuscript in section 1.4.3.

## 1.1 Cardiac Anatomy

In this section we present to the reader the clinical context of our work and explain the different medical terms related to the detection of CHDs. The first part is an overview of the human cardiovascular system and the heart anatomy (section 1.1.1). The second part, (section 1.1.2), describes the pathology of the atheromatous plaque: Its origin, its different types and its consequences on the heart system. Medical non-invasive and invasive treatments used to reduce coronary diseases related risks are exposed in section 1.1.3.

### 1.1.1 The Cardiovascular System Anatomy

The cardiovascular system is the body system that supplies all the organs with the proper amount of oxygen and nutrients, and discharge them from carbon dioxide and other waste products. It is a closed system constituted by the heart which pumps the blood and the blood vessels including arteries, veins and capillaries which carry blood, nutrients, oxygen and other gases, and hormones to and from the body cells (FIG. 1.1).

The blood is carried in the body throw two different circuits:

- *Pulmonary circulation* (also called the small circulation): It transports the oxygen-depleted blood from heart to lungs and return oxygenated blood to the heart again.



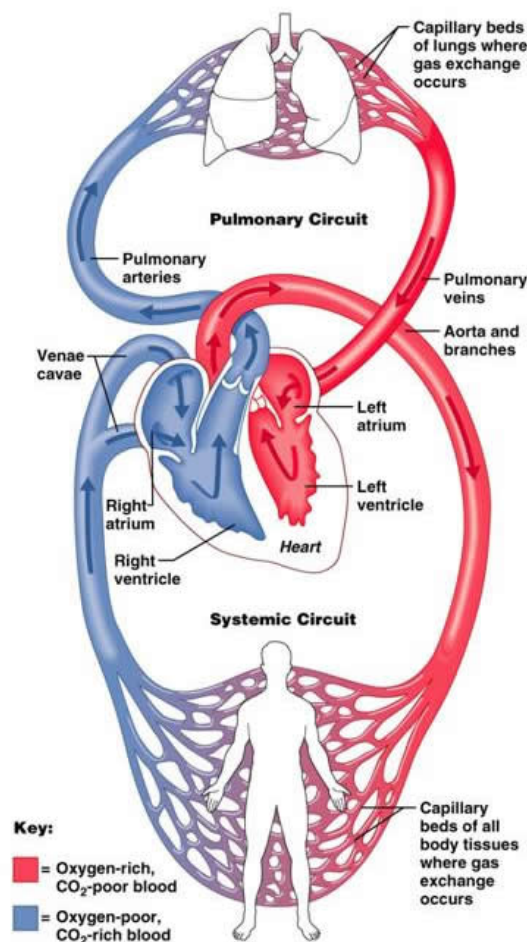


**Figure 1.1** – Human cardiovascular system: systemic and pulmonary circulations (Copyright © Addison Wesley Longman, Inc.)

- *Systemic circulation* (also referred to as the great circulation): This circulation portion transports the blood away from the heart through arteries to all body tissues and returns oxygen-depleted blood back to the heart through the veins.

The small and great circulations depend on one another, and both start from the heart. The heart muscle ([myocardium](#)) is irrigated by its own blood vessel network (Coronary Vessels). The coronary circulation is considered to be part of the systemic circulation. It supplies the heart with oxygen and nutrients rich blood and carries waste materials away from the heart muscle cells.

### 1.1.1.1 The blood vessels

They are the part responsible for transporting the blood through out the body. The central opening of a blood vessel, the *lumen*, is surrounded by a wall formed by three layers (figure 1.2) :

- **The tunica intima:** This is the thinnest layer. It delimits the vessel wall towards the lumen of the vessel and comprises its endothelial lining (typically simple, squamous) and associated connective tissue. Beneath the connective tissue, we find the internal *elastic lamina*, which delimits the *tunica intima* from the *tunica media*.
- **The tunica media:** This tunica is formed by a layer of circumferential smooth muscle and variable amounts of connective tissue. A second layer of elastic fibers, the external elastic lamina, is located beneath the smooth muscle, delimiting the tunica media from the *tunica adventitia*.
- **The tunica adventitia:** It consists mainly of connective tissue fibers. The tunica adventitia blends with the connective tissue surrounding the vessel. It also contains nerves that supply the vessel as well as nutrient capillaries in the larger blood vessels. The definition of the outer limit of the tunica adventitia is therefore somewhat arbitrary.

There are three major kinds of blood vessels forming the whole network: The arteries, the veins and the capillaries.

- Arteries** They are elastic vessels which carry the oxygenated blood from the heart (except in the case of pulmonary arteries). They can be subdivided into three types according to the composition of the elastic and muscular tissue in their tunica media as well as their size: *elastic arteries*, *muscular arteries* and *arterioles*. Arteries and arterioles have relatively thick muscular walls because they must adjust their diameter to maintain the blood pressure constant and control the blood flow.
- Veins** They are elastic vessels that transport blood to the heart. Smooth muscle in the walls of veins can expand or contract to adjust the flow volume returning to the heart and make more blood available when needed. Similarly to arteries we count three kind of veins: *veins*, *venules* and *postcapillary venules*. Veins and venules have much thinner, less muscular walls than arteries and arterioles, largely because the pressure in veins and venules is much lower; veins may dilate to accommodate increased blood volume.

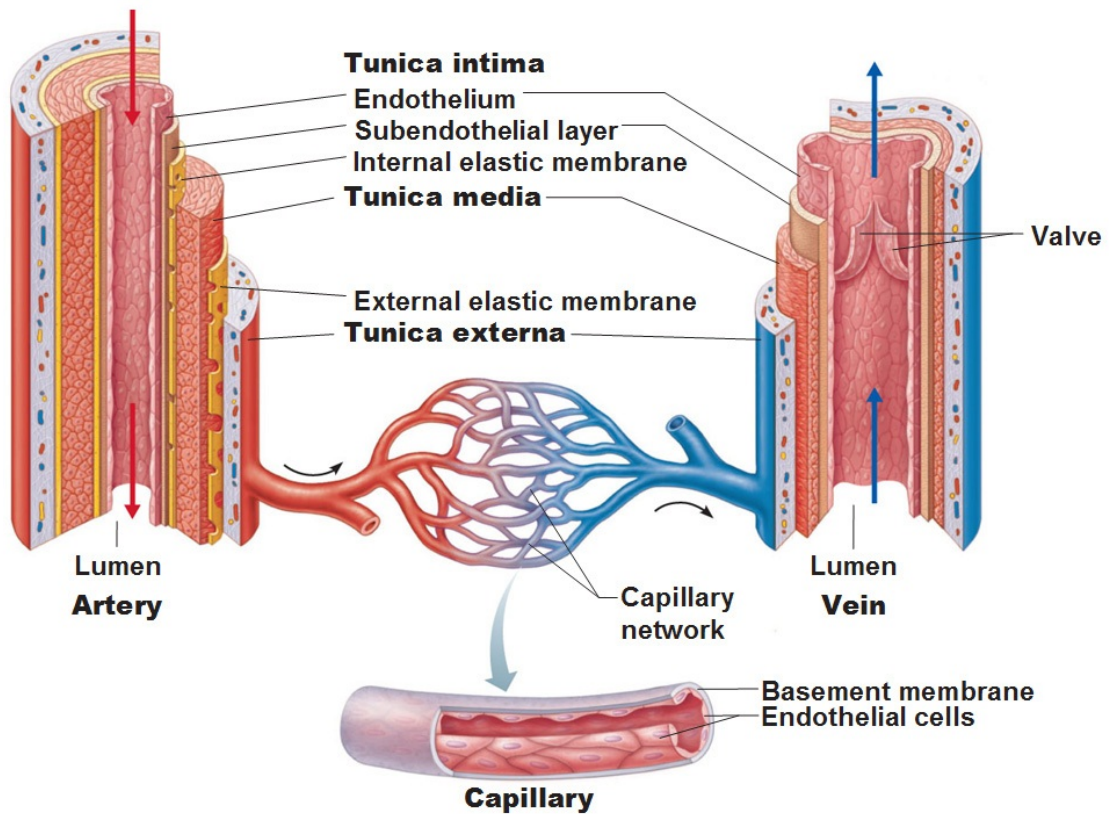


Figure 1.2 – Blood Vessel Layers [4]

- iii. **Capillaries** Capillaries are extremely narrow blood vessels located within the tissues and thus forming dense interweaving networks called *capillary beds* that transport blood from the arteries to the veins. Only the tunica intima is present in these walls, and some walls consist exclusively of a single layer of endothelium. They have a size of approximately 5-20  $\mu$ -meters, to aid fast and easy diffusion of gases, sugars and other nutrients to surrounding tissues while allowing carbon dioxide and wastes into the capillaries.

#### 1.1.1.2 The blood

It is a specialized bodily fluid that delivers necessary substances to the body's cells such as nutrients and oxygen and transports waste products away from those same cells. It is composed of *blood cells* suspended in a liquid called *blood plasma*. Plasma, which constitutes 55% of blood fluid, is mostly water (92% by volume), and contains dissolved proteins, glucose, mineral ions, hormones, carbon dioxide (plasma being the main medium for excretory product transportation), platelets and blood cells themselves. The blood cells present in blood are mainly red

blood cells (also called RBCs or erythrocytes) and white blood cells, including leukocytes and platelets. The most abundant cells in vertebrate blood are red blood cells.

Blood insures many vital functions in the body such as:

- Supply of the oxygen and nutrients such as glucose and fatty acids to the body's tissues
- Removal of waste such as carbon dioxide and lactic acid
- Immunological functions (circulation of white cells, detection of foreign materials by antibodies..)
- Coagulation, part of the body's self-repair mechanism (blood clotting after an open wound in order to stop bleeding)

#### 1.1.1.3 The heart

The human heart is a muscular cone-shaped organ located in the chest cavity (*mediastinum*) between the lower borders of lungs behind the sternum and above the diaphragm, with its pointed end (the [apex](#)) pointing toward the left. It is surrounded by a fluid filled sac called the *pericardium* ( see figure [1.3](#)) facilitating the movement of the heart and preventing its distension. The weight and size varies among individuals depending on age, gender, fitness and pathology. It is about the same size as two clenched fists of the same person (just one fist of the person is a kid). Roughly we can estimate its length to 12 cm and the width to 8 cm. The heart weight varies from 230 to 280 gr for women and 280 to 320 in men averages.

The Heart is divided into right and left sections, separated by the *inter-ventricular septum*. Each of these (right and left) sections is also divided into upper and lower compartments known as *Atria* and *Ventricles*, respectively (figure [1.4](#)). The right and the left ventricles act as two separate but synchronized pumps. The right side is responsible of pumping the deoxygenated blood to the lungs through the pulmonary arteries. Meanwhile, the left side pumps the oxygenated blood received from the pulmonary veins to the rest of the body through the aorta. As a result, and since in the rest of the body the blood flow is higher, the left ventricle has to work harder to maintain the some blood flow rate as in the right side.

The heart is one of the most important organs in the human body. Its function is to pump blood throughout all body vessels, even against gravity, in order to allow the normal gas exchange between oxygen and carbon dioxide in every body district. The full heart cycle is composed of a *systole* (fatigue) and *diastole* (contraction) phases. During the systole phase, the right and left ventricles contracts, and the pulmonary and aortic valves open thus allowing

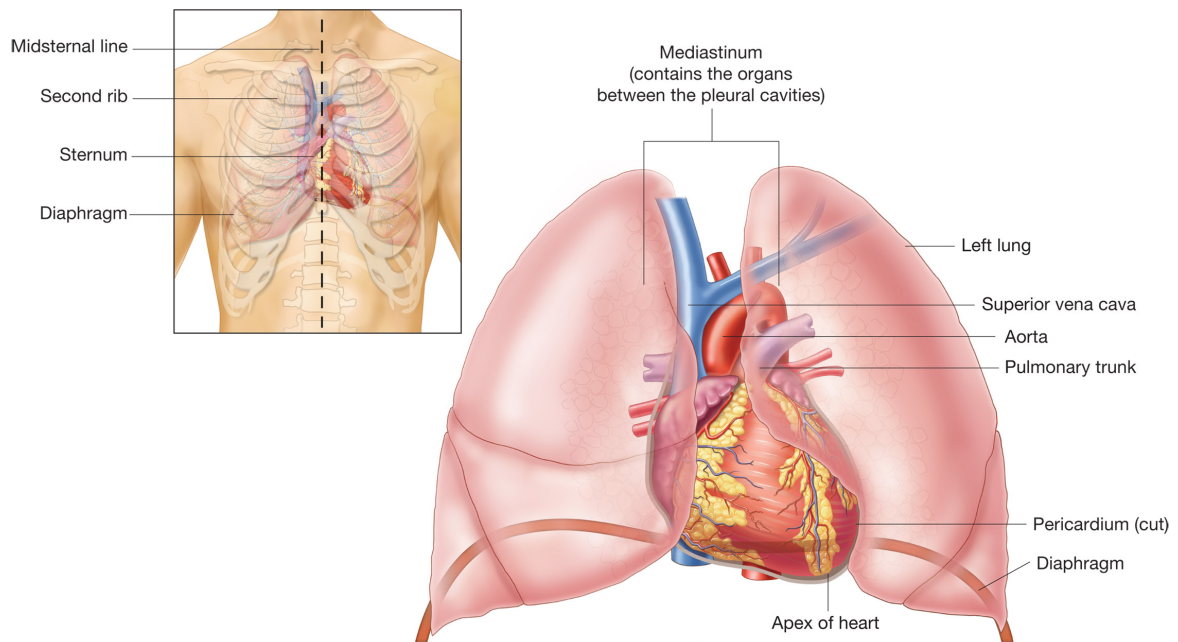


**Figure 1.3** – Location of the heart in the Chest [36]

the ejection of the blood into the pulmonary artery and the aorta respectively. Meanwhile, the atrioventricular valves are closed to prevent the blood from entering the ventricles. During the diastole stage, the heart ventricles relax allowing the chambers to be filled with blood. The atrioventricular valves open and the blood flows from the left and right atria to the left and right ventricles. By the end of this phase the two ventricle are filled with blood and a new heart cycle starts. The whole heart cycle takes about 0.8 seconds under normal circumstances. The contraction of the heart are caused by electrical impulses produced by specialized heart cells located in the [myocardium](#). Therefore, it is very important for the heart muscle to get its needed supply of oxygen in order to be able to work correctly.

We refer to the vessels that deliver oxygen-rich blood to the [myocardium](#) as *Coronary Arteries*. They branch from the ascending aorta root after the aortic valve at two opening called *coronary ostia* and form two main coronary trees. Forming a crown around the heart, they mainly run on the heart surface embedded within the epicardial fat and have small branches that dive into the myocardium to irrigate it as shown in figure 1.5. The exact anatomy of the myocardial blood supply system varies considerably from person to person. In general, there are two main coronary arteries (figure 1.5):

- **left coronary artery (LCA)** It originates from the left aortic sinus, just above the aortic valve and supplies the heart left ventricle and atrium with their demands of blood. It runs for 10 to 25 mm ([The left main artery \(LM\)](#)) before giving rise to the [left anterior](#)

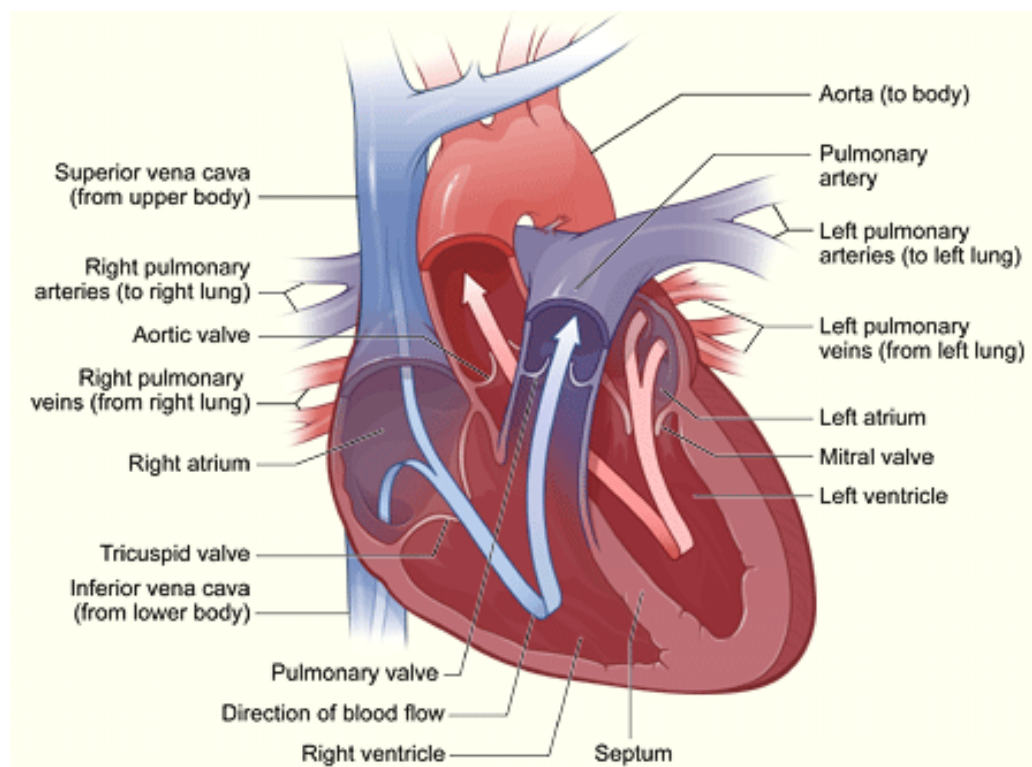


**Figure 1.4** – Heart Cavities and blood flow: A cross-section of a heart showing its four chambers and the circulation of the blood in the left and right sides. Oxygen rich blood arrives from the lungs to the left ventricle to be pumped through the aorta to the rest of the body (red arrow). Oxygen-poor blood flows from the body to the lungs through the vena cavae and the right chambers. [327]



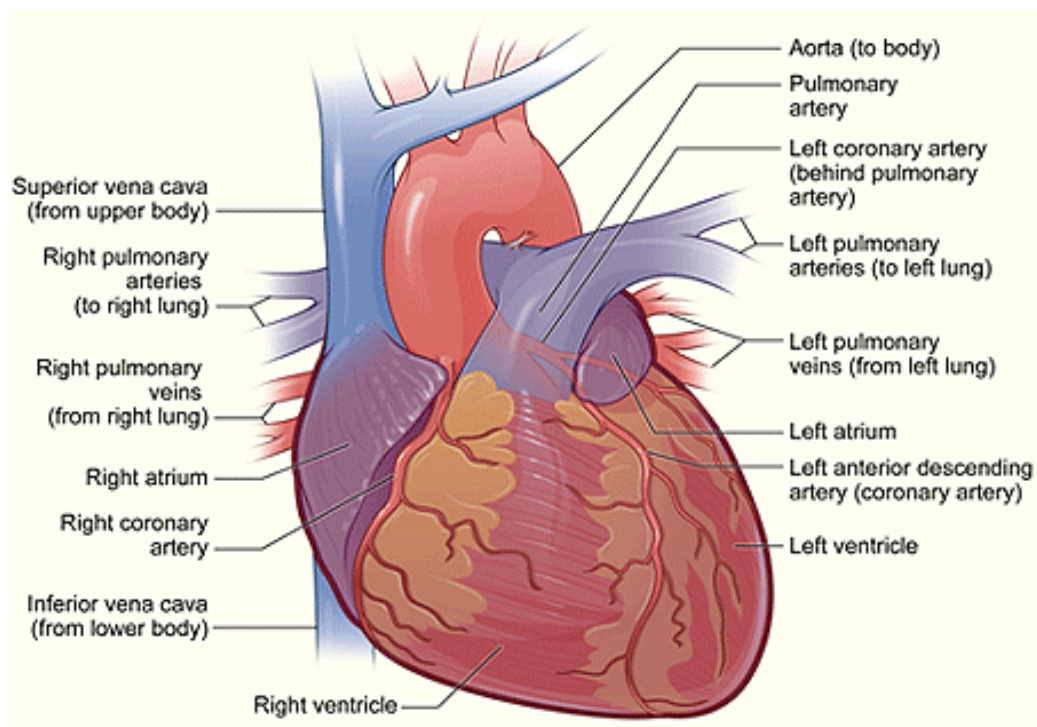


**Figure 1.5** – Anterior view of coronary arteries and major blood vessels connected to the heart [327]

descending artery (LAD) and the left circumflex branch (LCX). Their roles is to supply the lateral side and back of the heart, and the front of the left side of the heart respectively. The LAD coronary artery measures from 10 to 13 cm in length, whereas the LCX measures about 6 to 8 cm in length.

- **The right coronary artery (RCA)** It originates from the right aortic sinus. Divided into the right posterior descending artery (PDA) and acute marginal arteries (AM), it supplies blood to the right ventricle, right atrium, and the sinoatrial nodes which regulate the heart rhythm. It is about 12 to 14 cm in length before bifurcation.

The main coronary arteries can further bifurcate in smaller branches as the obtuse marginal (OM), and diagonals. For a better analysis of the function of the left ventricle and the myocardial perfusion the American Heart Association (AHA) proposed to divide the ventricle muscle into 17 segments (Appendix B). Figure 1.6 shows the assignment of the 17 myocardial segments to the LAD, the LCX and the RCA territories.

The normal (healthy) diameter of human coronary arteries could not be assessed precisely and there is no data available that states those values. In fact, several factors might lead to different healthy lumen diameters. The anatomic distribution of the arteries (right or left

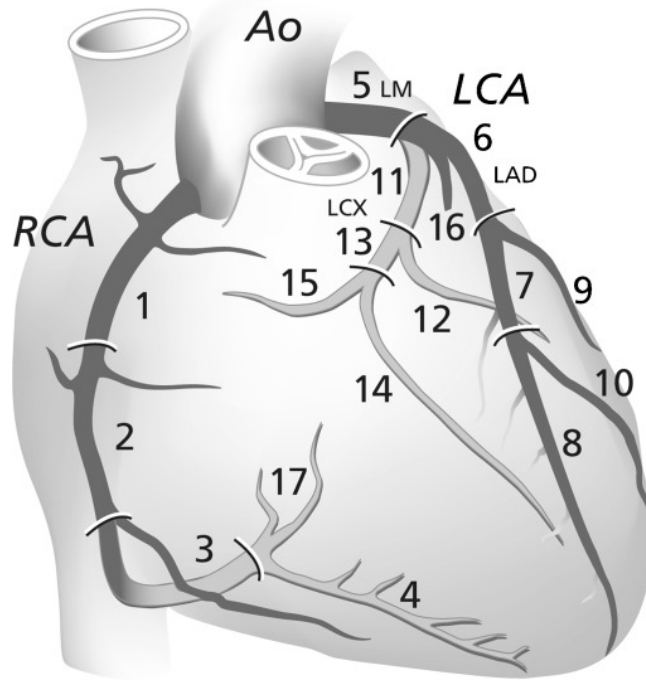


**Figure 1.6** – Coronary artery segments according to the American Heart Association classification [21]

dominant), the age, the sex as well as the pathological state of the patient influence the real size of the lumen [120]. Table 1.1 lists the normal lumen diameter of the main coronary arteries for healthy men and women.

Unfortunately, these narrow vessels are subject to be affected by a pathology named *atherosclerosis* which commonly cause an important lumen narrowing. This is very critical since those arteries are the only responsible for the heart supply and thus any blockage could lead to a dysfunction of this organ and severe impact on the patient's health.

### 1.1.2 Cardiovascular Lesions

Cardiovascular diseases or heart diseases are the class of pathologies that affects the heart and the blood vessels. This term is usually used to refer to arterial diseases: The Atherosclerosis.

*Atherosclerosis* (also known as atherosclerotic vascular disease or ASVD) is a hardening of the arteries as the result of a build up of fatty materials like cholesterol and calcium along the vessel walls [29]. This syndrome affects principally the large and medium-sized elastic and muscular arteries. It is a chronic inflammatory response in the walls of arteries, in large part due to the accumulation of macrophage white blood cells and promoted by low-density lipo-proteins (plasma proteins that carry cholesterol and triglycerides) [260] without adequate



Coronary Segment	Diameter (mm)	
	Men	Women
<b>Left Main</b>		
Proximal	4.5±0.6	4.0±0.5
Middle	4.5±0.5	3.9±0.4
Distal	4.5±0.4	3.8±0.3
<b>Left Anterior Descending</b>		
Proximal	3.7±0.5	3.3±0.4
Middle	2.3±0.4	2.2±0.5
Distal	1.1±0.4	0.9±0.3
<b>Left Circumflex</b>		
Proximal	3.4±0.5	2.9±0.5
Middle	2.8±0.6	3.1±0.4
Distal	1.3±0.5	1.2±0.6
<b>Right Coronary Artery</b>		
Proximal	4.0±0.6	3.4±0.7
Middle	3.2±0.5	2.9±0.7
Distal	1.9±0.6	1.7±0.5

**Table 1.1** – Normal lumen diameter (mean ±STD) of human coronaries for the main arteries. Values measured in a group of 83 patients. (Adapted from [120])

removal of fats and cholesterol from the macrophages by functional high density lipo-proteins (HDL). For the coronary arteries, these lesions can cause a lumen narrowing or even an occlusion thus restricting the blood flow to the corresponding heart muscle territory.

Atherosclerosis is typically a silent disease until one of the many late-stage vascular manifestations intervenes [1]. Some people with atherosclerosis may experience [angina](#) (chest pain) due the insufficient blood supply (hence a lack of oxygen supply) of the heart muscle. It mainly occurs during times of physical activity or strong emotions, when the heart needs more oxygen supply, and disappears when the person is at rest.

The advanced lesion of atherosclerosis may lead to further pathological changes including focal rupture, ulceration or erosion, hemorrhage into a plaque and superimposed [thrombosis](#).

Different risk factors were identified [274] with different relative importance:

- Some diseases such as: hyperglycemia, hypertension, Diabetes, Obesity
- Behavior factors: Tobacco smoking, physical inactivity
- Genetic factors: sex and heredity

### 1.1.2.1 Atherosclerosis Genesis

Several theories of atherosclerosis genesis were proposed. A unifying theory assumes that vascular injuries are supposed to be the key event of atherosclerosis's formation by : The response-to-vascular injury theory [362, 363]. According to this theory, the local disturbances

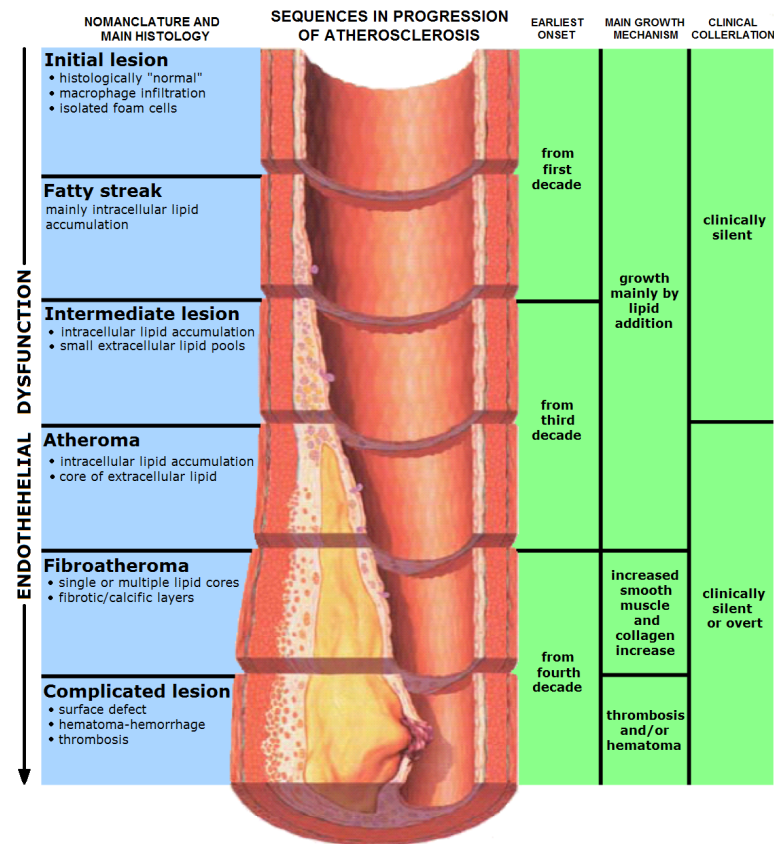


**Figure 1.7** – The atherosclerosis progression steps resulting in the plaque rupture (Illustration from [87]).

of blood flow around branching or high angulated points along with the risk factors lead to the succession of a series of events that culminate in the development of atherosclerosis plaques.

In fact, the endothelium injury allows adhesion and migration of monocytes to become macrophages as a reaction to the inflammation. Then the accumulation of the lipid into those cells produces a lesion called a fatty streak. The core of the fibro-fatty lesion is formed by the dead macrophages and smooth muscle cells and further accumulation of lipid (see figure 1.7).

The atheromatous plaque is basically composed of:

- The atheroma: An accumulation of a soft, flaky and yellowish material at the center of large plaques.
- An underlying area of cholesterol crystals
- Calcification at the outer base of the older lesions, the most advanced ones.

There are two main types of plaques:

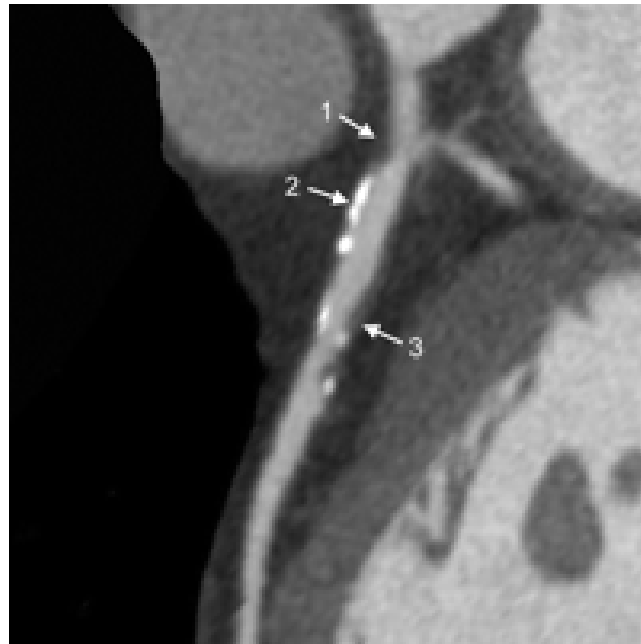


**Figure 1.8** – Calcified and Soft plaques visualization in CT Angiography: arrow 1 shows a soft plaque, arrow 2 points to a calcified one and arrow 3 shows a mixed plaque

- i. Soft plaques: They are mainly composed of lipid molecules and contain low amount of calcium. They represent the early stage of development of the atheromatous plaque. Lipid-rich plaque is more dangerous as it is more unstable and therefore more prone to rupture causing a [thrombus](#) formation [441]. It is very difficult to visualize in [CTA](#). Depending on its extent and size, it can be detected based on vessel lumen narrowing. Soft plaque inspection in [CTA](#) highly depend on the image contrast and quality and can be improved using image processing tools to detect and highlight those lesions.
- ii. Calcified plaques: Also known as hard plaques. They are collagen-rich plaques representing an advanced stage of the plaque formation. Calcified plaque are more stable than soft plaque and exhibit a lower risk of rupture. This type of plaque is easy to visualize in contrasted and non contrasted [CTA](#). See figure 1.8.

Atherosclerosis plaques may require 10 to 15 years for full development. Over time, atheroma progresses inducing a compensatory remodeling of the surrounding muscular tissue .

### 1.1.2.2 Artery Modeling

The vessel is not just a passive housing of the atherosclerotic plaque. The whole vascular system does react to the process of plaque formation. In fact, as a result of the plaque progression the vessel morphology evolves in a process called the *arterial remodeling* [213, 448]. Two types of modeling occur: (1) The wall remodeling and (2) The lumen remodeling leading to *aneurysm* and *stenosis* formation. This results are often observed, at different locations, with the same individual.

**1.1.2.2.1 Artery wall enlargement** Atheroma and changes in the artery wall result first in small outward enlargements (*aneurysms*) of the artery wall, just enough to compensate for the occupied volume (the *Glagov phenomenon*) while the lumen diameter remains non compromised. A less common outcome is that the enlargement can continue to 2 or 3 times the healthy vessel diameter, usually over decades of living. This causes the thinning of the muscular wall and a gross aneurysmal enlargement of the artery occurs, commonly in the abdominal region of the aorta.

This might lead to sudden hemorrhage (bleeding) and often a rapid death with just the stress of the pulse. In the other hand, atheroma within aneurysmal enlargement are more prone to rupture (vulnerable plaques) and shower debris of atheroma and clot downstream than causing flow limitation due to lumen narrowing. In fact, such plaque grows further and does not begin to encroach on the lumen until it occupies 40% of the cross-sectional area while the encroachment must be 70% or greater to cause flow limitation.

**1.1.2.2.2 Lumen narrowing** Many of the plaques with an initial wall remodeling eventually progress to the vascular lumen narrowing as we said above: The caliber of the artery opening (lumen) remains unchanged until typically over 50% of the artery wall cross sectional area consists of atheromatous tissue. In fact, if the muscular wall enlargement fails to keep up the enlargement of the plaque volume then the lumen begins to narrow (*stenosis apparition*). In fewer cases, the atheroma grows inward without any compensatory vascular dilation, thus causing a gradually luminal diameter decrease and eventually a total occlusion of the artery. This leads to a flow limitation causing the death of the tissues fed by the artery in approximately 5 minutes (myocardial ischemia). This is a non reversible phenomena called a *myocardial infarction* (necrosis of downstream myocardium), commonly known as heart attack (figure 1.9). The injured heart muscle will not be able to work correctly thus threatening the patient's life.

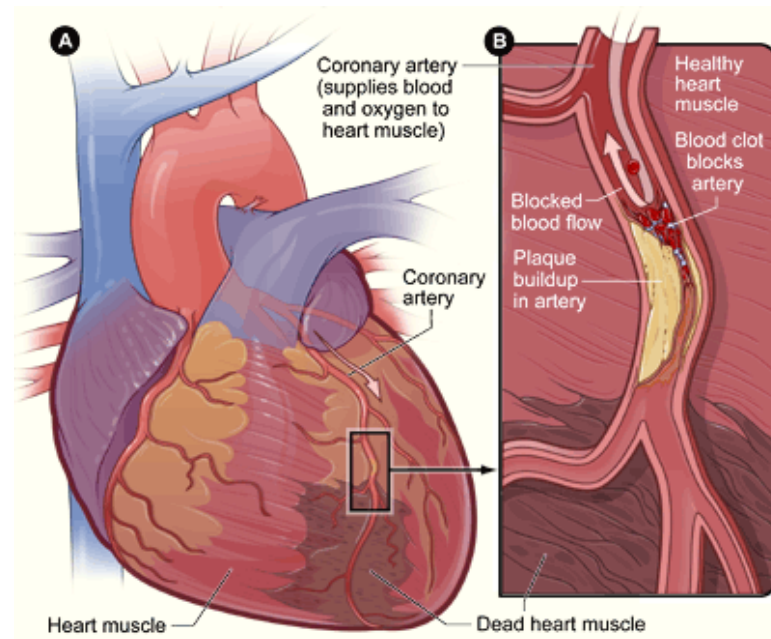


**Figure 1.9** – Heart infarction caused by a blockage of a coronary artery by a blood clot [323]

An other reason of the lumen narrowing and occlusion would be the repeated ruptures of the covering tissues separating the atheroma from the blood stream, a common event after decades of living. In fact, if a rupture occurs of the endothelium and fibrous cap of the plaque, then a platelet and clotting response over the rupture rapidly develops. This accumulation usually produces narrowing/closure of the lumen. Additionally, the rupture may result in a shower of debris which might cause the occlusion of smaller downstream vessels. A stenosis is considered to be severe if the narrowing is higher than 70% of the artery lumen, moderate if it is between 50% and 70% and non significant bellow 50% [54].

As a conclusion, stenosis less than 60% are the ones at greater risk of sudden occlusion. In fact, lumen occlusion is more the result of young plaque rupture and thrombosis than the vessel gradually narrowing following the plaque growth. This occurs because of the relatively higher lipid content of the lipid core, and the increased leukocyte activity at the shoulder regions of such plaques. However, this kind of plaques (*vulnerable*) is the most difficult to detect because it's an early and silent stage of atheroma development. There is no imaging modality that allows a reliable detection of such plaques. But the analysis of the composition of the plaque and its structure helps the clinicians to estimate the development stage of this plaque and its risk of rupture.

### 1.1.3 Treatments

Treatment of [CHDs](#) aims to reduce the related risk of having a heart attack and relief the different symptoms. It usually involves lifestyle changes, and if necessary medicine and some medical procedures.

The first step to consider toward promoting healthier heart arteries, is to make healthy lifestyle changes. Indeed, healthy habits can slow down and even stop the development of heart diseases. This includes:

- Stopping smoking
- Having heart healthy diet
- Maintaining a healthy weight
- Getting regular exercise
- Managing stress

If lifestyle changes are not enough, drugs can be used to:

- Help lower cholesterol amount in the blood (specially the low-density lipoprotein one at the origin of the atheromatous plaque)
- Decrease the blood pressure and the heart rate thus decreasing the heart demand of oxygen
- Prevent the formation of blood clots by making the blood thinner.
- Reduce the chest pain by reducing the heart demand in blood.

If the angina symptoms are getting worse, interventional procedures can be considered to treat the arteries lesions and improve the blood flow of the heart. There are two different possibilities:

1. **Angioplasty:** This is a non surgical procedure to open blocked or narrowed coronaries. A thin soft tube called a [catheter](#) is inserted into a peripheral blood vessel (arm, groin or wrist) and threaded into the diseased portion of the artery. A guide wire with a balloon is carried to the narrowed area through the catheter. Once the catheter reaches the blocked portion, the balloon is inflated to press the plaque against the vessel wall, hence enlarging the vessel lumen and improving the local blood flow. Usually, a small and expandable

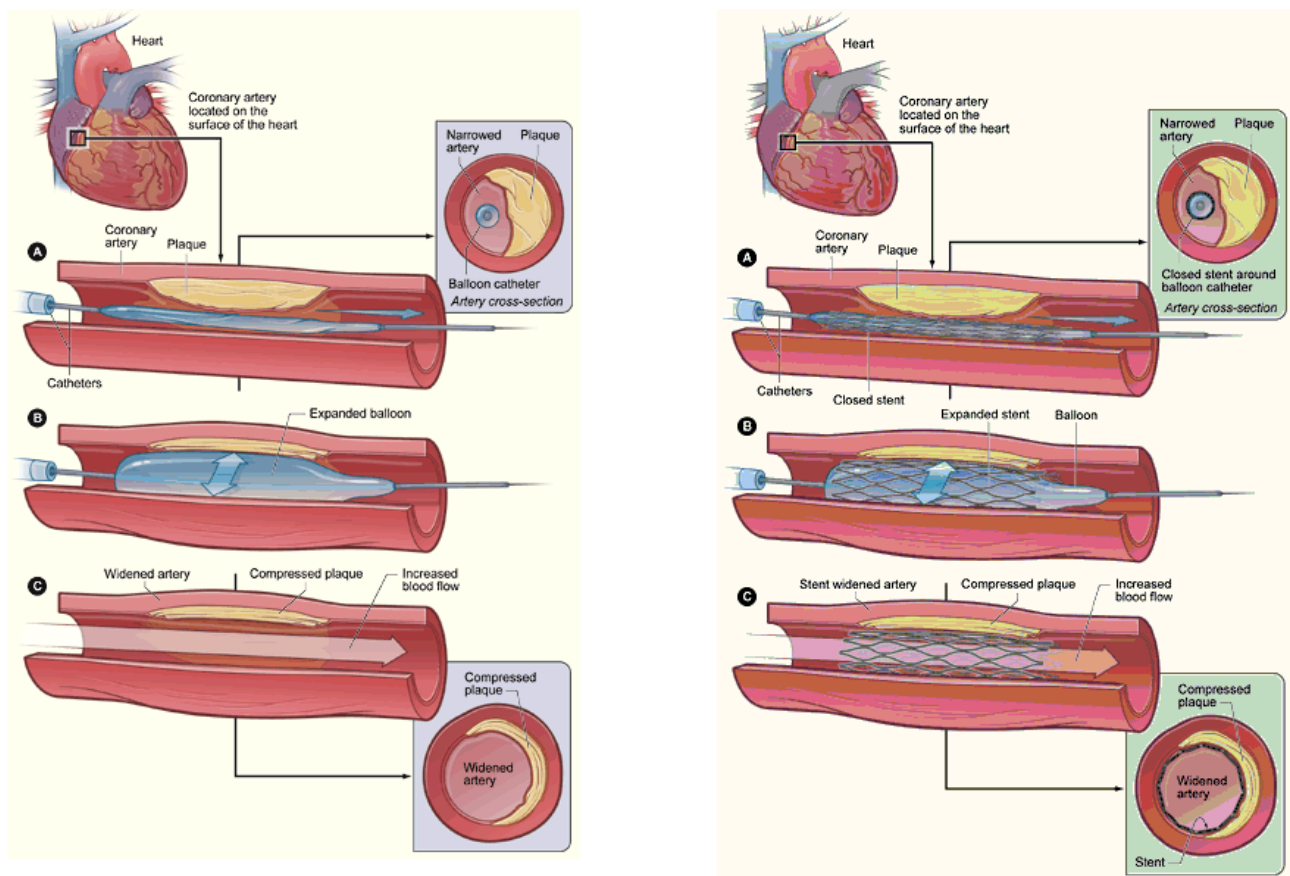


**Figure 1.10** – Coronary artery balloon angioplasty [329] and stent placement [330].

**stent** is left inside the artery to keep it open (figure 1.10). An X-Ray screen is used to observe the movement of the catheter through the vessels .

2. **Coronary Artery Bypass Grafting (CABG):** It is a type of surgery used to reroute blood to the diseased heart muscle territory. A vessel from another part of the body (a vein or an artery) is grafted to bypass the narrowed coronary artery (figure 1.11). Thus, oxygen rich blood is rerouted from the aorta to irrigate the heart muscle. This procedure improves the heart blood flow, relieves chest angina and prevents heart attacks. It is most often used when several coronary arteries are narrowed/blocked.

## 1.2 Cardiac Medical Imaging

In this section we present an overview of the commonly used medical imaging modalities for coronary arteries lesions diagnosis and follow up. We will focus on contrast enhanced CT



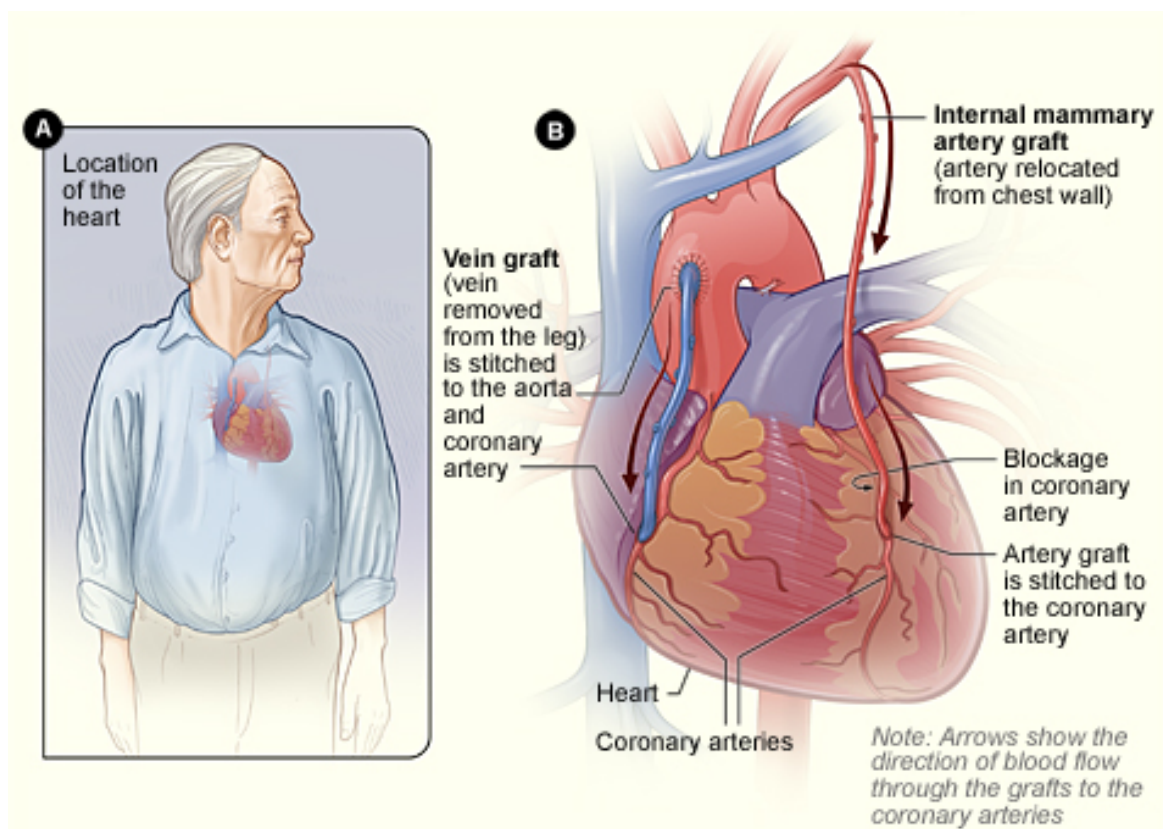


**Figure 1.11** – Coronary artery Bypass Grafting: The figure shows how the vein and the artery are grafted to the heart [328].



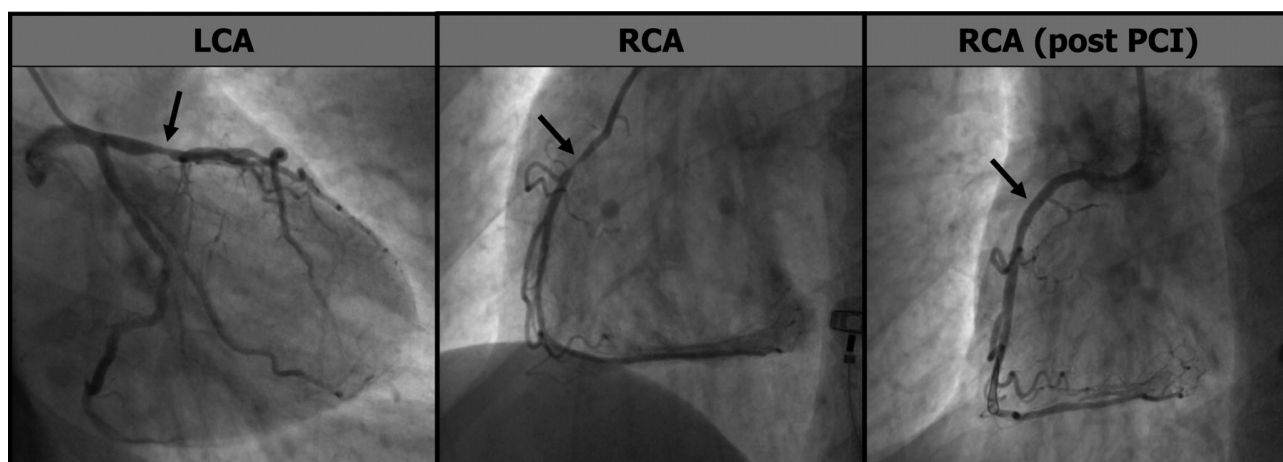


**Figure 1.12** – Angiograms of the LCA (left) and RCA (middle) with an observed stenosis of 80% and 50% (black arrows) respectively. The right image shows the stenosis of the RCA being stented (black arrow). PCI indicates percutaneous coronary intervention (© 2010 American Heart Association, Inc.)

angiography as the algorithms we propose in this thesis are dedicated to this modality.

### 1.2.1 Conventional Coronary Angiography

Since the 1960's, [CCA](#) has been the most common angiography performed for coronary arteries inspection. It is a minimally invasive procedure in which a dedicated [catheter](#), typically with a 2.0 mm in diameter, is inserted through a peripheral artery (generally in the leg) and guided through the arterial system to the opening of one of the coronary arteries. An X-Ray [contrast agent](#), called X-Ray dye, is then administrated and mixed with the blood circulating within the heart arteries. It is used to highlight the vessel network to be visualized. An X-ray motion image of the blood flowing inside the arteries with the transient contrast agent is recorded allowing to visualize the size of the arteries lumen [1.12](#). The X-ray dye is rapidly washed away from the heart arteries. Therefore, the contrast agent needs to be re-injected to make the blood flow visible for 3 to 5 seconds.

However, since the late 1980's, it has been established that CCA does not allow to recognize the presence or the absence of the coronary atherosclerosis in the vessel walls. It only allows the visualization of the resulting luminal narrowing, the final stage of plaque progression. If a stenotic region is suspected, [Intra Vascular UltraSound \(IVUS\)](#) can be used to closely inspect the coronary lesion. The advantage of this approach is that in complex and urgent cases where a narrowed/blocked artery is revealed, an angioplasty (with or without stenting) might be performed to open the lumen. The major drawbacks of this modality are mainly its invasive nature, the related costs and the need for a subsequent procedure to evaluate the plaque type

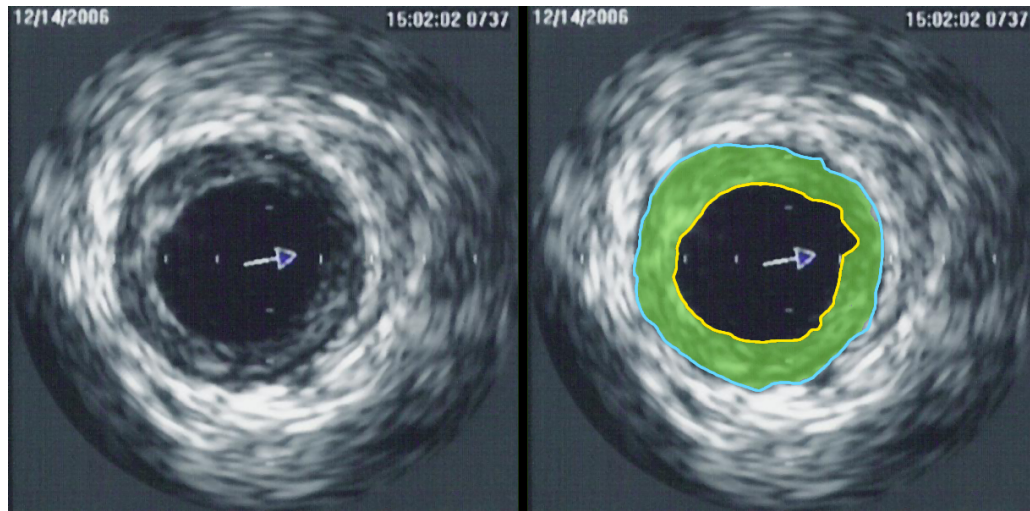


**Figure 1.13** – Intravascular ultrasound image of a left coronary artery with a soft plaque [456]. In the right image we can view the external vessel border (blue), the lumen border (yellow) and the plaque burden (green).

and extent. However, [CCA](#) is still the standard routine for coronary heart diseases diagnosis thanks to its spatial and temporal resolution. Moreover, if needed, interventional therapeutic procedures can be performed simultaneously.

### 1.2.2 Intra Vascular UltraSound

[IVUS](#) is an invasive medical imaging modality used to see inside the vessel. A catheter, with a tiny ultrasound wand attached to its distal part, is guided through the body and positioned into the vessel segment to be imaged using angiography techniques. The small tip of the catheter emits ultrasound waves that are reflected by the surrounding tissues mainly the vessel inner wall and the atheromatous deposit. The echos are converted to electrical signal and sent to an external computerized ultrasound system to be processed. The final image is a real time 2D section views of the vessel part surrounding the catheter tip (figure 1.13).

This modality is frequently used to visualize the coronary arteries inner wall during an angioplasty to determine where the stent should be placed and verify that it was placed correctly at the end of the procedure. It can be used to assess coronary arteries lesions. This allows to estimate the volume of atheromatous plaques within the vessel wall as well as their compositions. IVUS is also used to precisely determine the related vessel lumen narrowing. It can be useful to visualize some challenging artery segments or regions that other angiographies failed to reliably visualize such as ostia area and overlapping arteries [1]. This modality also allows to follow up the results of some therapeutic procedures over time. It has also played an important role in

understanding the evolution process of the atheromatous plaque and the patho-physiology of this lesion. It also helped in research and the development of novel drugs and improvement of therapeutic devices. It helped for example to understand stent re-stenosis.

IVUS is considered as the gold standard for plaque visualization and assessment. It provides cross sectional images of the vessel depicting the wall composition and providing precise quantitative measures (extension of the plaque, area of the lumen...). However, because of its invasive nature and the cost of the procedure, clinicians try to use other alternative modalities to visualize coronaries arteries.

### 1.2.3 Computed Tomography Angiography

CT is a non-invasive medical imaging technique in which a three-dimensional image of a body structure is constructed by computer from a series of 2D plane cross-sectional X-ray images taken along a single axis of rotation allowing to see inside the body without cutting into it [181]. Each cross section image represents a slice of the body part being imaged as if we look into a loaf of bread by cutting it into thin slices.

Computed tomography angiography (CTA) is a computed tomography technique used to visualize the body blood vessels (veins and arteries). It is commonly used as a diagnostic tool to examine the brain, neck, heart and other organs' vessels. It is also used as a guide for interventional procedures and as a follow up tool after the intervention.

The different body structures are visualized based on their ability to block the X-ray beam (figure 1.14). A contrast material is used to highlight the vascular structures that would be difficult to delineate from their neighborhood otherwise. The contrast material can also help in obtaining functional information about tissues. The injected dose and mode depends on the anatomy to be imaged [195, 196].

The introduction of X-Ray computed tomography in 1968 by GODFREY HOUNSFIELD was the beginning of a new era of medical imaging providing a 3D representation of the body organs instead of only 2D projections [191]. It has been established as a reliable non invasive imaging modality for various diagnostic and therapeutic purposes. Indeed, the usage of this modality has dramatically increased during the two last decades all over the world. For instance, over 80 million CT scan has been performed in the USA in 2011 [102].

#### 1.2.3.1 Basics of CT Angiography

The basic idea of CT scanning is to set the subject to be imaged on a table between an X-Ray beam and an electronic detector to measure the amount of radiation absorbed by the different

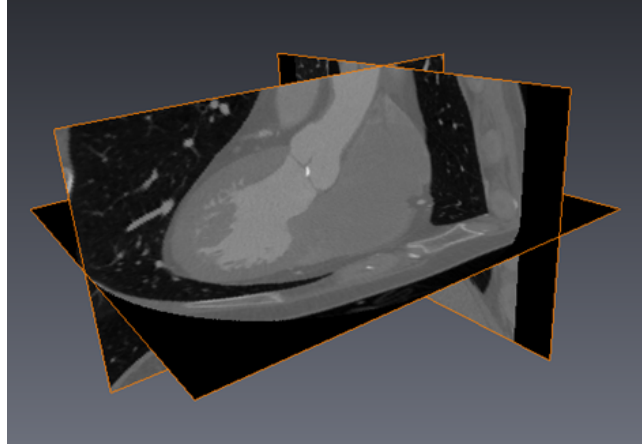


**Figure 1.14** – An example of a CT 3D volume

organs. To reconstruct a 2D cross section of an object, the X-rays should be projected in all angles around it. After passing through different body tissues, the radiation intensity is attenuated several times. In fact, each material has a specific attenuation coefficient. Thus, for one single ray projection along a path  $U$ , the detected radiation intensity  $I$  can be expressed as following:

$$I = I_0 \cdot e^{\int_U \mu(x,y) du} \quad (1.1)$$

with  $I_0$  being the initial emitted radiation intensity and  $u(x,y)$  the function defining the material specific attenuation coefficient at the position  $(x,y)$  of the object cross section. The obtained data corresponds to the projection of the object following the different X-rays passing through it. It corresponds to the *Radon transform* of the object's slice [350]. Computing the attenuation coefficient  $u(x,y)$  for all the samples of the object allows a reconstruction of the corresponding 2D cross section. Mathematically, this consists of solving the inverse Radon transformation of the projected data [90]. Several reconstruction algorithms were used to solve this back projection problem since the apparition of the first CT scanner. The earlier scanners used algorithms based on *algebraic reconstruction techniques (ART)*. However, because of its high complexity and the limited computer technology available at the time, this approach was not suitable for this problem. Later, the *filtered back-projection* algorithm was established to be the state of the art technique to solve the problem. But this method is not suited for the later scanners generation (with fan-beam X-Rays and complex physics) which leads to several artifacts and a high noise amount in the reconstructed image. But with the apparition of spiral multi-slices scanners, newer sophisticated iterative reconstruction algorithms have been

designed to address the problems due to the spiral movement of the X-Ray source and its fan shape hence allowing for a higher image resolution and lower noise and artifacts. For more details about the algorithms the reader can refer to [90].

Once the specific attenuation coefficient are computed for each sample of the image, the final pixel values are converted in the **Hounsfield Unit (HU)** scale. This is a normalized quantitative scale used in medical imaging to express the radio-density values of the scanned organs. It is a linear transformation that maps the original attenuation coefficients into 12-bits values with 0 HU corresponding to the value affected to the water and  $-1000$  HU being the air intensity value. The linear transformation is formulated as following:

$$HU = \frac{\mu - \mu_{water}}{\mu_{water}} * 1000 \quad (1.2)$$

Since the apparition of the first CT scanner in 1971, several generations of scanners have succeeded to trace the computed tomography medical imaging (figure 1.15). The first CT scanner generation used a single pencil-like X-ray beam and a single detector at the opposite side of the patient. The X-ray source emits a beam that traverse the body and is collected by the sensors at the opposite side. To acquire one single cross sectional slice, the source/detector assembly is translated across the body and is rotated around the patient afterward. The same process of parallel acquisitions is performed from different angles. The different acquisitions (sets of detected rays at the different angles) are sent to a computerized system to reconstruct one or different 2-dimensional slices. However this mechanical process was time consuming; It can take from several minutes to several hours to perform one single CT scan with a resolution of 80x80 pixels per slice [345]. The second generation of scanners uses a small angle fan-shaped beam of X-rays with multiple sensors thus allowing to reduce the number of rotations previously needed. This type of scanners permits to reduce the acquisition/processing time needed for a slice reconstruction to the order of some minutes. Furthermore, the angle of the fan beam as well as the associated detectors have been increased to be able to cover all the body. Thus, the system does not need to translate across the patient body anymore but only rotates around it. This makes the acquisition process faster (only 3 seconds to take a picture) [191]. For the fourth generation, the moving detectors are replaced by a stationary circular ring detector. This new generation have encountered several problems mainly the cost of the ring detector and the reduced image quality due to X-ray scattering problems. This yields to further improvement of third generation scanners at the late of the 1980s and the invention of the helical or spiral CT scanners. In fact, the state of the art scanners use the some rotating emitter/detector system of the third generation. The system is continuously rotated around the patient while the table

slides slowly into the X-ray scan field (the gantry) allowing the acquisition of a full 3D volume. Those machines have been subsequently developed by using multiple rows of detectors (between 8 to 32 rows) and hence detecting multiple slices simultaneously. This gave birth to the [MSCT](#) in 1998. In 2001, [Cone-Beam Spiral Computed Tomography \(CBCT\)](#) was introduced. It uses a cone shaped beam allowing the use of more detectors (from 16 to even 320 rows of detectors). Up to 256 slices can be acquired simultaneously with those scanners. The apparition of this new generation of CT scanners allowed for faster scan acquisition (less than two minutes to finish a complete scan including the reconstruction step) resulting in a shorter radiation exposure time and a higher image resolution ( 0.23 mm) [90]. The last decade have also witnessed the apparition of new CT scanners generation: the [Dual source CT \(DSCT\)](#) scanners [203], the High Definition CT scanner (HDCT) [137], and the Revolution CT scanner in 2013 able to take an image in less than one second thus producing clear images for beating heart and coronary arteries [138].

Besides the fact that CT angiography allows to reconstruct a 3D visualization of the body structures, it's better than traditional 2D medical radiology because it completely eliminates the superimposition of images of structures outside the area of interest. Depending on the diagnostic task, the CT imaging offers the possibility to view the images in three different planes (axial, coronal and sagittal). In addition, thanks to the high contrast resolution of CT, tissues with less than 1% difference in physical density can be distinguished. In fact, referring to the Hounsfield scale for tissue densities in CT images, we can discriminate between different organs only based on the appearance properties. See figure 1.16 for the detailed Hounsfield Scale.

However this modality suffers from a major drawback which is the important radiation doses needed for a higher resolution images. In fact, decreasing the dose of radiations while keeping the same resolution results in noisy images. High radiations exposure is known to increase the risk of cancer and is particularly harmful for children [60]. However thanks to new technologies, software solution are available to filter this random noise and thus reducing the radiation doses during CT examinations without compromising the image quality.

### 1.2.3.2 Cardiac CT Development

Cardiac Imaging is a specific challenging task because of the continuous movement of this organ and the particularly small scale of its structures (e.g. coronary arteries). High temporal and spatial resolution are therefore required to offer a clear image of the heart without moving artifacts. In fact, several studies have shown the relationship between the heart rate and the



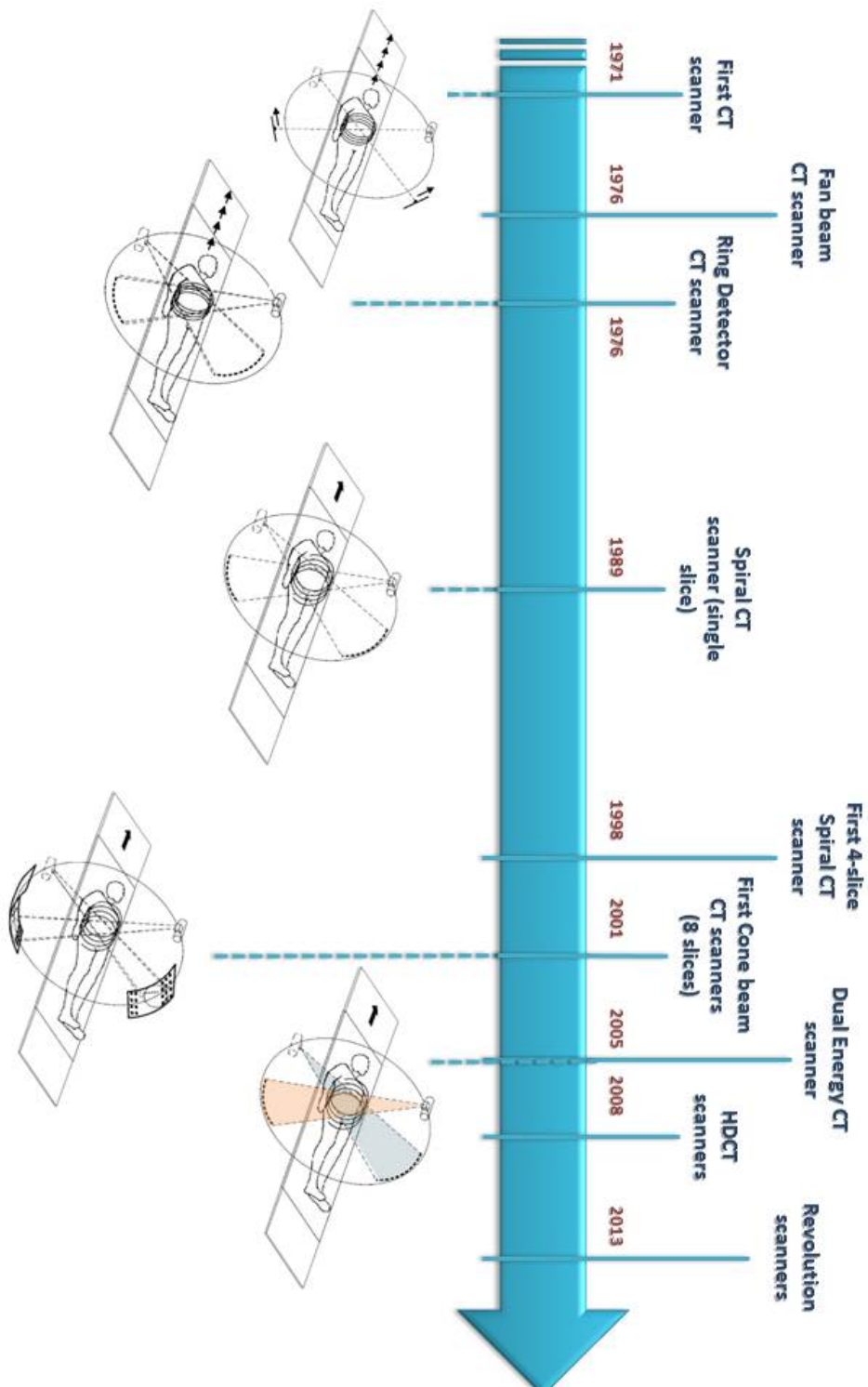


**Figure 1.15** – Turning points in the computed tomography imaging history. Illustrations from [90].

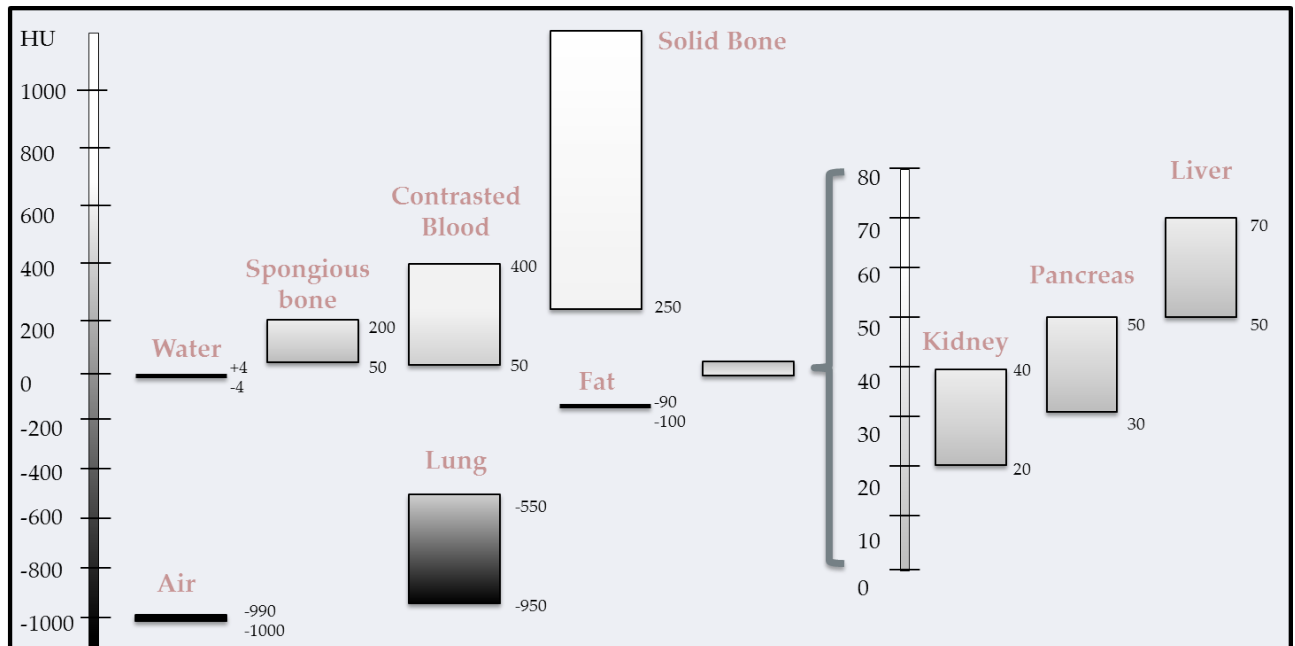


**Figure 1.16** – The common Hounsfield density value ranges for some human body tissues. Adapted from [90] and [345]

quality of the scanned image [53, 160, 202]. Thanks to the continuous progress during the last 4 decades, CT imaging has vastly improved. The great improvements in spatial resolution, speed of acquisition and the resulting image quality has made the dream about cardiac imaging clinically possible. In fact, modern multi-slice scanners reach sub-voxelic resolutions enabling the accurate visualization of small challenging arteries, e.g. coronaries. CTA acquisitions enables not only the visualization of the vascular lumen but does also reveal the presence and the extent of calcified and soft plaque which may be clinically relevant cues for risk assessment (figure 1.8).

With the first generation of CT scanners, precise heart imaging was not possible due to the relatively long time of acquisition (about 10 seconds per slice) compared to the rapid heart motion (more than 10 beats per 10 seconds). Only high scale details, such as the heart surface lesions, can be detected with the earlier equipments [191]. In early 1980s, **Electron Beam Spiral Computed Tomography (EBCT)** have been introduced specially to offer better beating heart images [48]. Unlike the conventional CT machines, the X-Ray source of **EBCT** is not swept mechanically but rather electronically hence allowing for a faster image acquisition (in 50 to 100 msec). Thanks to this considerably short time of acquisition, virtual motion free images of the heart was acquired. The sequence of 2D cross sections scanning was synchronized with



the heart beat, using an electro-cardiograph (ECG gating), to be processed during the diastole phase. Since the early 1990s, several studies have established the accuracy of this technology for cardiac imaging and coronary calcification assessment [13, 16, 56, 367]. Subsequently, several studies have shown that non invasive coronary lumen visualization was possible with EBCT using an intravenous injection of contrast agent [68, 311, 353] which allows for an accurate severe stenosis detection [6]. Despite those facts, various issues have limited the use of this technology (around only 120 scanners available worldwide). This includes the high cost of manufacturing and the low production volume of this modality.

Meanwhile, the development performed in traditional CT scanners leading to the apparition of the sub-second single slice spiral scanners wasn't sufficient enough to generate satisfactory heart image quality. Studies showed that the resulting images with motion artifact had limited clinical application and are not reliable for stenosis detection. Reliable cardiac scanning era has started after the introduction of the first multi-slice (2, 4 and 8 slices simultaneously) spiral CT scanners in the late 1990s. Multi-slices CT allowed for a better volume coverage of the heart and a better spatial and temporal resolution than single slice CT scanners. Despite first experience studies revealed limited coronary detection rate because of heart motion related artifact, this was overcome using ECG-correlated scanning sequences (*prospective ECG-triggering*) to capture specific heart cycle phase [7] (see figure 1.17). However, the acquisition time was still too long and the spatial resolution was too coarse for an accurate coronary arteries assessment. Further progress in CT scanner technologies lead to the use of more detectors and the apparition of 16-, 64 and 320-slices spiral scanners.

Since 2002 and until now, rapid and continuous progress in multi-slice spiral CT scanners hardware with robust reconstruction algorithms have introduced a new scanner generation permitting thinner slices generation and a better spatial (0,2 to 0.6 mm) and temporal (less than 100ms) resolution. Hence motion free heart images can be acquired in less than 5s with reduced radiation exposure time and higher image quality. In some cases, Beta blockers medication are still subsequently injected in order to lower the beat rate and reduce the motion artifacts. An other approach for more robust image motion free reconstruction is the use of simultaneous ECG-signal recording during the continuous acquisition of the heart volume slices with the spiral movement (*Retrospective ECG-triggering*: see figure 1.18). This allowed for a rapid reconstruction of the heart image in a single cardiac cycle phase with selecting the desired slices to reconstruct the final image. Even if this leads to higher stored slices than the prospective ECG-triggering, it is much more flexible and rapid. Moreover, images of the heart in multiple phases can be generated which is useful for functional assessment of the heart.

The introduction of the dual source multi-slice spiral scanners DSCT has subsequently

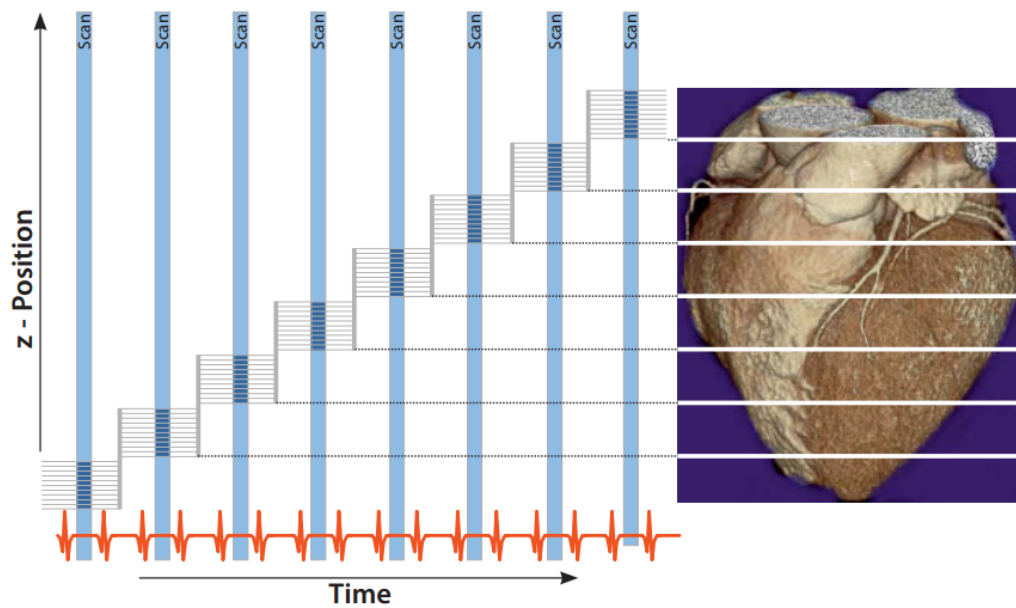


**Figure 1.17** – Prospective ECG-triggering with a 16 slices CT scanner. Only a single 16-slice scan can be acquired during a heart cycle because of the long acquisition time. Thus, different sequential scans are performed during the same heart cycle phase to cover the whole heart volume. Illustration from [332]

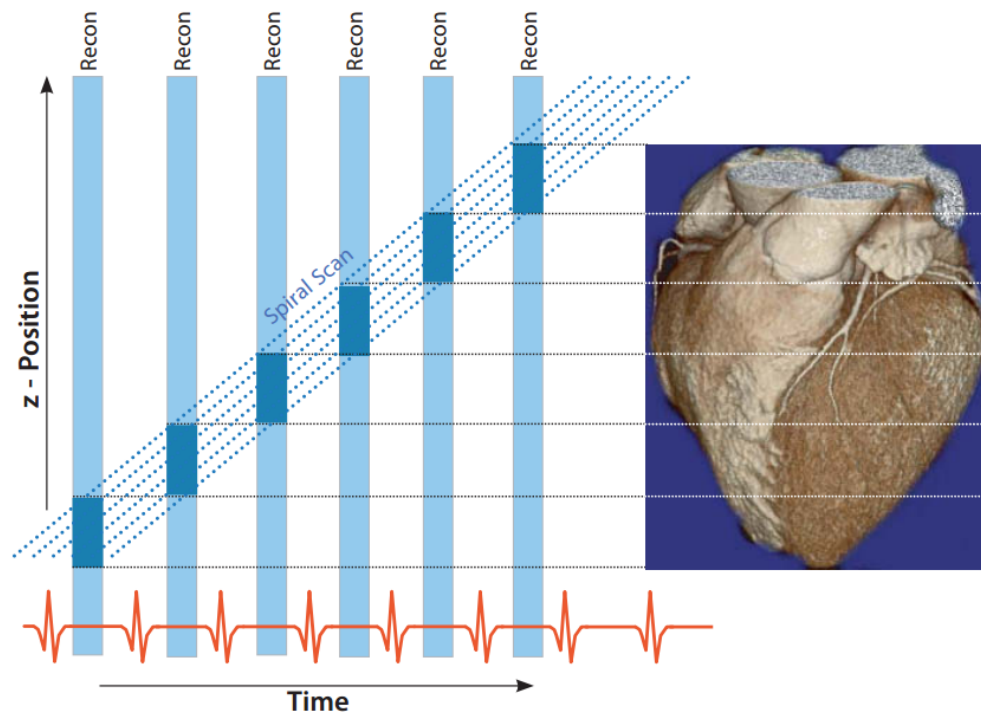


**Figure 1.18** – Retrospective ECG-triggering using a spiral multi-slices CT scanner. Continuous scans are acquired during the whole heart cycle. Thus, images of different heart cycle phases can be reconstructed [332]

improved the temporal resolution of cardiac imaging ( $82ms$ ) [202]. In fact, using two different X-ray sources with a  $90^\circ$  offset permits to double the temporal resolution of a one single x-ray source with the same rotation speed. As a result the entire heart volume can be scanned in real time during one single heart cycle for almost all the patients and discard the use of beta blockers in clinical practice. Besides, important improvements in image reconstruction algorithms (real time reconstruction, motion artifact reduction) has allowed for a better cardiac and specially coronary CT imaging [317].

## 1.3 Cardiac Computed Tomography

### 1.3.0.3 Accuracy of Cardiac CT for Coronary Artery Plaques Assessment

Current state-of-the-art CT scanners allow to acquire motion free images for almost all patients with reduced X-ray radiation doses ( $<1mSv$ ). The latest improvements during the last 10 years leading to a better spatial resolution made this modality a reliable non invasive tool for coronary assessment and lesion detection and quantification [5]. Two different CT diagnostics imaging procedures are used for coronary lesions assessment: *native coronary CT* and *contrast enhanced coronary CT*. For the first technique, the CT scan of the heart is performed without using a contrast agent. It is basically used to assess the [Coronary Calcium Score \(CCS\)](#), a reliable risk indicator for coronary arteries atherosclerosis [134]. In fact, it has been proved that severe coronary events can be predicted using the [CCS](#) [111, 450]. However, coronary plaques presents a striking heterogeneity and are most likely composed of non calcified tissues [440]. Thus, exhibiting a low [CCS](#) does not exclude the fact that the patient may have soft plaques, the most vulnerable ones (see section 1.1.2). Therefore, there is a need for a procedure that allows a more precise assessment of coronary arteries plaque burden and composition in a non invasive way. Hence, contrast enhanced coronary CT approach is being used as an alternative to the traditional invasive coronary angiography. A non-ionic water-soluble contrast agent is injected to enhance the vascular structures. This allows to reduce the related risk of the catheterization procedure on the patient's health and improves the risk stratification for coronary artery events in asymptomatic patients [5].

Several studies have been dedicated to validate the clinical feasibility and the diagnostic accuracy of the [MSCT](#) for coronary stenosis assessment compared to intravascular ultrasound ([IVUS](#)) reference standards [167, 245, 247, 383, 400]. The reported sensitivity and specificity values depends on the CT scanner generation used for the study in addition to the patient selection criteria, the readers' experience and the reference standard used for validation. Gen-

	16-slices CT [280, 321]			64-slices CT [320]			Dual source CT [488]		
	<i>per patient</i>	<i>per vessel</i>	<i>per segment</i>	<i>per patient</i>	<i>per vessel</i>	<i>per segment</i>	<i>per patient</i>	<i>per vessel</i>	<i>per segment</i>
Sensitivity	94.0	95	70.0	98.4	93.7	95.0	93.9	90.2	84.2
Specificity	86.0	86	96.0	89.1	92.7	97.7	93.5	97.1	99.1
PPV	91.0	80	72.0	96.0	90.6	90.6	97.5	95.2	93.3
NPV	91.0	97	96.0	95.3	95.2	98.8	85.3	93.9	97.7

**Table 1.2** – Accuracy of severe coronary stenosis detection with 16-slices, 64-slices and dual source CT angiography. Sensitivity, Specificity, PPV and NPV values are reported per patient, per vessel and per segment analysis.

erally, state of the art scanners offer high sensitivity and specificity values for severe stenosis detection ( $>50\%$ ). Using recent generations of 16-slice CT scanners, studies reports a sensitivity value ranging from 86 to 99 % and a specificity of 86-98 % [177, 234, 280, 321]. Using 64-slice CT, sensitivity between 73 and 99% and specificity from 93 to 97% were reported [112, 275, 285, 300, 320]. In those studies, results of lesion detection was assessed on vessel segments with a diameter higher than 1.5 mm. Depending on the study, results of detection are reported per patient [225, 300, 488], per vessel [205, 321] or per segment analysis [156, 189, 234]. Table 1.2 presents the *sensitivity*, *specificity*, *positive predictive value* and *negative predictive value* of different scanners types for severe stenosis detection.

In [285], a multicenter multivendor study using different 64-slice scanners was performed to evaluate the detection of significant CHD. The obtained sensitivity to detect severe coronary lesions was 99%. The study showed also that CT has a negative predictive value of 97%. However, lower values of specificity (64%) and positive predictive value (86%) was reported compared to previous studies. This is mainly due to the overestimation of the degree of calcified stenosis. In fact, the calcified core can cause some blurring effects and thus obscure the underlying coronary lumen visualization [489]. Recent studies shows that using DSCT, higher sensitivity (99%) and specificity (89%) can be achieved [62, 108, 114, 369, 488]. Those data shows that a negative coronary CT exam is reliable to exclude a significant coronary stenosis. Meanwhile, lesions detected on CT angiography need further assessment using a more reliable procedure for coronary plaque characterization and quantification.

According to previous studies, it is stated that compared to IVUS, coronary CT is able to assess different coronary plaque types with high accuracy. Based on an *ex vivo* study on heart specimens, showed that advanced stages of heart plaques can be detected using MSCT (figure 1.20). In [245, 383], a high correlation between IVUS echogenicity of the plaque and the corresponding measured CT densities was observed. Moreover, it is shown that coronary CT is able to differentiate the composition of coronary atherosclerosis plaques. CT angiography

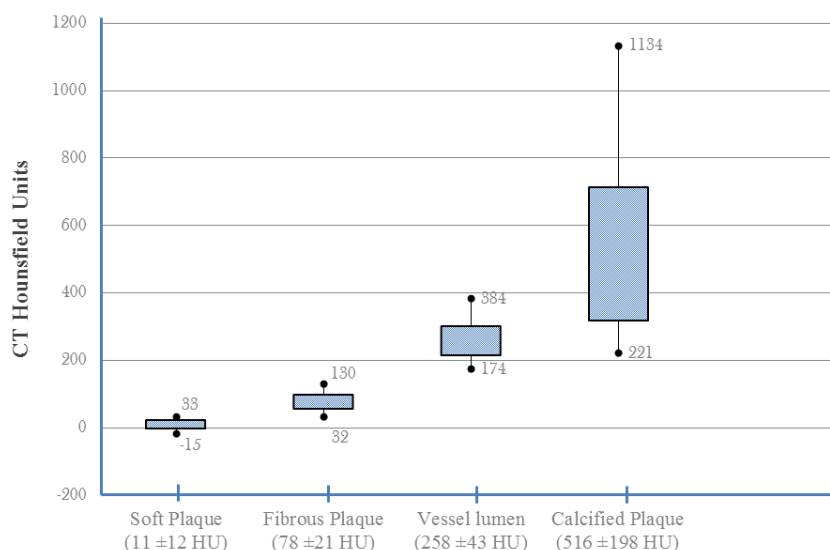


**Figure 1.19** – CT density value ranges for different plaque types (lipid rich, fibrous and calcified) and vessel lumen. Each box represents the *mean*  $\pm$  *std* range of the HU value. Extreme values are displayed on the whiskers start and end points. Values from [312].

can differentiate between three main categories of plaques; *calcified*, *soft* and *mixed* plaques. Coronary CT presents different density ranges for the different plaque types which allow a coherent plaque type assessment (see figure 1.19).

As discussed previously, CT enables an accurate visualization and quantification of calcified plaques. CT presents a sensitive value of 95% and a specificity of 91 % for calcium rich plaque detection. Although it is harder for CT to distinguish between different soft plaque types, this modality presents reasonable sensitivity and specificity values for non calcified plaque detection near to 78% and 86% respectively [8, 247]. However, even if CT is not capable of characterizing the precise composition of the plaque, it is able to offer other significant indicators for eventual future coronary events that can be caused by the detected lesions. Those features include the 3D plaque extent, the plaque volume, the artery remodeling and the stenosis degree [8, 246].

### 1.3.1 Cardiac CT: Advantages and Limitations

Cardiac Computed Tomography exhibits several interesting advantages that make it a possible alternative to the invasive coronary angiography. The first advantage making CT preferable for ruling out severe CHDs is its non-invasive nature that leads to lower risks of complications

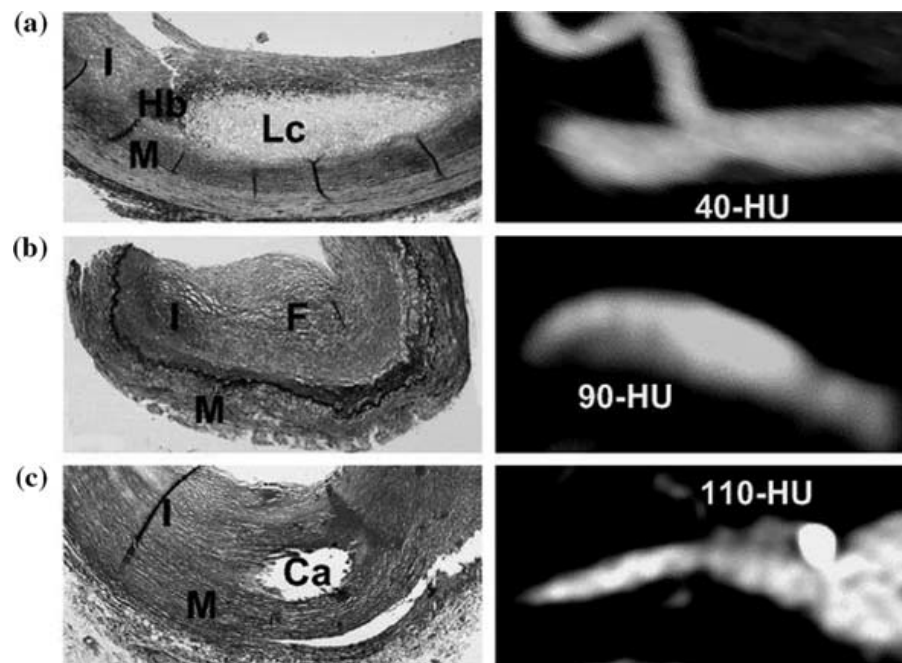


**Figure 1.20** – Different Plaque types visualization in CT: (a) An atherosclerosis plaque with an extensive lipid accumulation. In the corresponding CTA the plaque appears as a soft tissue with a HU density of 40. (b) A soft purely fibrous non calcified plaque appears with a higher density of 90 HU. (c) A hard plaque with a calcified core that appears as a brilliant spot in CTA with a density around 110 HU. Illustrations from [28]

on patients than catheterization. Thanks to its availability and its rapidity, CTA presents a cost-effective alternative for patient at low risk for CHDs (positive stress test, no symptoms). Thanks to the high positive predictive value of CT, a preliminary CT coronary angiography would allow to eliminate the unnecessary cost of invasive angiography. This makes it a valuable non invasive tool to get prognostic information in patient who does not exhibit a high pretest likelihood for coronary stenosis [401]. This allows to decide whether an invasive coronary angiography is necessary or not; If the CT shows clearly healthy coronary arteries, there is no need for an invasive procedure and the cost of CA can be avoided. Using preliminary CTA on patient with a risk for severe stenosis lower than 50% helps saving around \$780 [172].

A major advantage of coronary CT compared to CCA is the ability to visualize the vessel wall composition in addition to the vessel lumen which is more relevant for preventing coronary acute events. It allows to determine the extent, the type and the composition of the plaque which is not possible when using CCA without the use of intravascular ultrasound [383]. Moreover, it is able to detect non-stenotic plaques missed by conventional coronary angiography. Coronary CT is also capable to differentiate between soft and calcified plaques [244]. This comprehensive assessment of the wall represents a valuable tool to improve the risk prediction combined to the usual risk measures [383] and offers a non invasive alternative for coronaries diseases monitoring. Moreover, coronary CT offers a 3D volume of coronary vessels. Therefore, it is easier to estimate the real extent of the plaque in 3D than using CCA. Moreover, this modality offers the possibility to visualize the vessel with its surrounding tissues in any plan unlike CA. It is, thus, more accurate for estimating the real lumen narrowing specially in case of eccentric plaques [158]. Besides, this 3D information avoids all the superimposition and shadowing problems related to the 2D projection of the CCA. Subsequently, coronary CT offers a larger field of view compared to CA which represents a valuable information of other non coronary cardiac (myocardium, heart ventricles, valves, aorta, pulmonary veins) and thoracic organs (lungs, bones). This information might be useful for exclusion of non-cardiac origins for chest pain (a symptom for coronary arteries lesions) and thus enables early and safe triage for patients showing some severe cardiac lesions' symptoms [169, 190]. This is very valuable to reduce the time and the cost of assessing patients with chest pain. Besides, thanks to the recent advances in CT images scanning and reconstruction, 4D CT images of the heart can be provided and used to analyze the function of the heart organs (ventricles, valves...) [368].

Nowadays, coronary CT is not expected to totally replace invasive coronary angiography. This modality still raises some concerns because of the higher amount of radiation to which the patient is exposed compared to the conventional coronary angiography. Further efforts should be dedicated to reduction of radiation doses while keeping a coherent diagnosis accuracy. In



addition to some image quality limitation (calcification blurring and heart motion), several patients with contraindication to CT scanning (renal failure, atrial fibrillation, allergy to iodine ...) cannot be studied with the state-of-the-art equipments. Obtaining accurate image quality for coronary pathology assessment is still challenging also for patient with high heart rates ( $>65$  beats per minute). Despite the significant improvements achieved since the first apparition of CT angiography, there is still a high demand on a better temporal resolution to be able to rapidly acquire good quality cardiac images with no need to control the heart rate. In fact, despite the high temporal resolution ( $75ms$ ) that offers recent **DSCT** scanners, heart rate control is still mandatory to provide cardiac image with appropriate quality for coronary assessment. Besides, **MSCT** (16-, 256- and 320-slices) have also limited temporal resolution ( $> 165ms$ ) compared to invasive coronary angiography ( $< 20ms$ ). Therefore, beta blockers are still used to lower the heart rate when using those scanners.

Moreover, this modality suffers from its failure to accurately assess the vessel lumen with the presence of important calcified plaques because of blooming artifacts which leads to an overestimation of the stenosis degree [313, 400]. Therefore, CT angiography is usually not recommended for patient with high Agatston calcium score [300]. Another limitation of coronary CT is the cut-off value for severe stenosis detection, set to 50%. This value is usually used for evaluating the diagnostic performance of CTA in most of the studies. However, it has been established that using a cut-off value of 60%, performance of detecting significant stenosis is optimal and equivalent to invasive coronary [124]. Besides, even if CT angiography is able to determine the plaque volume, burden and the lumen remodeling, it is not able to identify vulnerable plaques because of the considerable overlap between fibrous and lipid rich plaques attenuation ranges [282]. Furthermore, because of the current spatial resolution of CT, assessment of coronary lesions is not possible in distal thin vessels ( $<1$  mm).

### 1.3.2 Coronary Assessment using CT Angiography

After the acquisition and reconstruction steps, the scanned images are sent to a digital workstation for further post-processing and coronary specific visualization. Coronary CT results in a 3D volume image of the heart and, probably, some of its surrounding organs. The 3D volume is constructed of a stack of  $512 \times 512$  pixel 2D images. The number of stack images can range from 200 up to 500. The 2D image resolution depends on the chosen **Field Of View (FOV)**: To have a better resolution for accurate coronary stenosis assessment, a reduced FOV would be more suitable. Usually, a FOV between  $180 - 200mm$  that encompasses mainly the heart is recommended for coronary CT evaluation. This allows for a resolution around  $0.3mm$



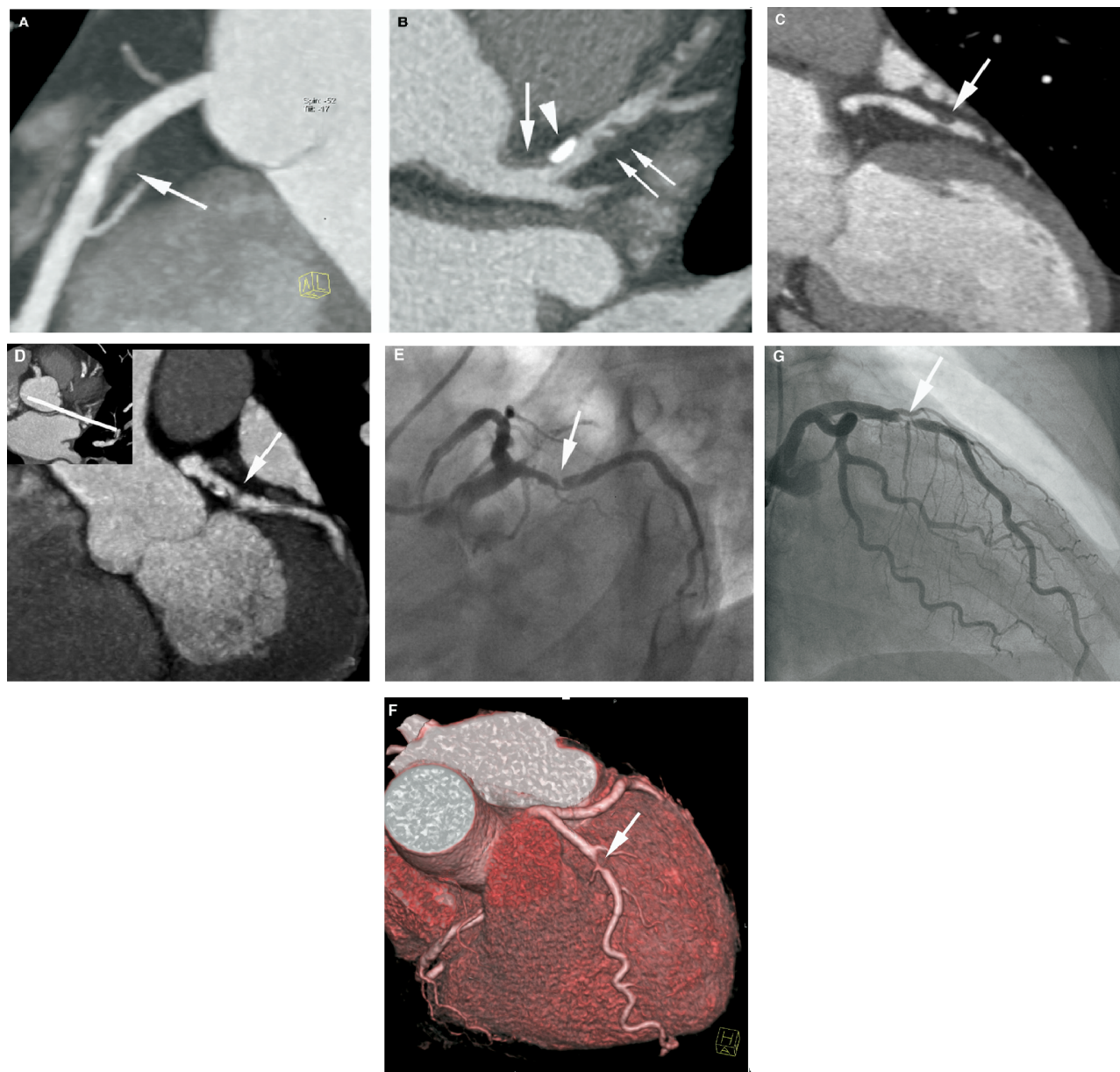


**Figure 1.21** – Visualization of different atherosclerosis coronary plaques using computed tomography angiography. (A) A soft plaque (non calcified) of the proximal RCA showing a positive remodeling of the artery wall. (B) A mixed plaque of the left main artery ( the large arrows show the calcified and the soft cores of the plaque), Moreover, a soft plaque can be seen along the proximal and medial LAD (the double arrows) (C,G) Multiplanar reformatted reconstruction along the diseased coronary allowing an accurate visualization of the soft plaque extent and the stenosis degree, and the corresponding conventional coronary angiography confirming the presence of the stenosis. (E,D) A maximum intensity projection (a 5 mm slab) showing a partly calcified plaque of the proximal left descending artery and the corresponding conventional coronary angiography. (F) A 3D volume rendering of the stenosis illustrated in (C) and (G). Illustrations form [5].

Parameters	CCTA	CCA	IVUS
<b>Temporal Resolution</b>	42-165ms	5-10ms	NA
<b>Spatial Resolution</b>	0.25-0.5 mm	0.2 mm	0.08 - 0.1 mm
<b>Provided Image</b>	3D image	2D projection	2D cross sections and longitudinal views
<b>Plaque type</b>	calcified, non calcified, mixed	no information	fibrous, lipid rich, calcified
<b>Stenosis Assessment</b>	+	-	+++
<b>Coronary visualization</b>	lumen and vessel wall (All segments)	lumen	lumen and vessel wall (Limited segments)
<b>Radiation dose</b>	0.8-20 mSv	5-10 mSv	5-10 mSv (associated to CCA)
<b>Cost</b>	low	high	high
<b>Acquisition type</b>	non invasive	invasive	invasive

**Table 1.3** – Main imaging characteristics of CT angiography compared to conventional CA and IVUS.

which is coherent for thin coronary artery visualization ( $<1.5$  mm). In general, CT results on anisotropic volumes, i.e. the in-plane (in the slice) resolution is slightly different from the out-of-plane one (between the slices) [345]. The resulting 3D volume is too dense to allow an effective and rapid coronary vessels analysis using basic visualization approaches. Generally workstations offers a set of post-processing tools to help the radiologist investigating the coronaries with high confidence and more easily [339]. This results on advanced visualization techniques proper to coronary vessels that permit a robust display of the vessel lumen and surrounding tissues. Those are valuable tools for helping saving time of the diagnostic steps and making more efficient the coronary stenosis detection using CT angiography. This section aims to review the basic visualization approaches for coronary inspection and lesions ruling out. We will also give some details on advanced reconstructed views commonly used by reviewers and available on most of the workstations.

### 1.3.2.1 Basic Visualization Techniques

Basic visualization of coronary arteries uses the unprocessed 2D images stack (raw data) of the CT angiography. It consists of a set of visualization techniques that are routinely used to quickly scan the CT exam for lesion inspection (figure 1.22).

**1.3.2.1.1 Transaxial Images** Transaxial images are the output raw data reconstructed from the CT scanner (figure 1.22.a ). They consists of a set of two dimensional images of the scanned body area stacked in the longitudinal direction of the acquisition (the z-axis).

The first step of the analysis of CT angiographies is browsing the stack of images by scrolling through the different slices. This allow for a rapid investigation of the scanned volume and the detection of possible anomalies. The main advantage of this type of views is that they represent the original raw data without any distortion or artifact that might occur following a post-processing step and with a maximum resolution and grey values display [351]. However, the interpreter should rely on his own imagination to reconstruct a 3D view of the cardiac anatomy. In fact, establishing the anatomic connection between the different arteries branches and the heart components based on only 2D views is a tedious and time consuming task that requires highly experienced interpreter. Besides, tracking tortuous vessels in 2D axial images might be particularly challenging and requires more investigation to accurately follow the vessel.

**1.3.2.1.2 Multi-Planar Reformatting** [Multi-planar reformatting \(MPR\)](#) allows a high-resolution reconstruction of planar oblique views of the scanned object at any plane of the 3D volume. The two basic reconstructions are the *sagittal* and *coronal* views (figures 1.22.b and 1.22.c ). This kind of visualization is interesting as it allows the selection of the optimal plane for the best display of a given organ (figure 1.22.d). MPRs could be generated interactively (the user can choose the plane of display on the view) or automatically (based on the segmentation and the analysis of the object of interest); See section 1.3.2.2.

**1.3.2.1.3 Maximum Intensity Projection** A commonly used visualization technique for vascular structures is the [Maximum Intensity Projection \(MIP\)](#) (figure 1.22.f ). It is a projection of a 3D information contained in a slab of slices on a 2D plane. The technique performs a parallel ray casting from the view plane along the selected slab of slices in the direction of the view camera [345]. The resulting 2D image voxels display the maximum intensity falling along the traced rays. Therefore, contrast enhanced structures (usually the brighter ones), e.g. vascular structures, can be assessed easily as all the other structures will be eliminated from the display view. For coronaries visualization, the orientation and the thickness of the slab can be adjusted in order to include all the vessel lumen and wall and avoid the overlap with unwanted structures (heart chambers for example). Typical slab thickness for coronary display ranges from 3 to 10 mm depending on the vessel size [332]. Hence, a larger vessel segment can be displayed compared to MPR. Combined to [curved multi-planar reformatting \(cMPR\)](#), MIP provides a more comprehensive view of all the vessel volume. This technique is commonly used because it offers a global overview of the vessel with minimal interaction. However, one major outcome of the use of this display technique is the absence of the depth information and the lack of details about the vessel cross section which is relevant for stenosis analysis. Moreover,

the interpretation quality depends on the slab thickness; An overestimation of this parameter might lead to missing some stenosis because being shadowed by adjacent bright structures. On the other hand, selecting a small slab thickness might prevent the user from visualizing relevant calcifications. Thus, MIP should be used in addition to other visualization techniques in order to ensure a better analysis of the vessel [354].

**1.3.2.1.4 Volume Rendering** [Volume Rendering \(VR\)](#) is a widely used technique that offers an integer 3-dimensional colored visualization of the volumetric CT data. A transfer function is used to map each voxel into a color and opacity according to its HU value [332]. Using a simple camera model, a ray is generated for each single pixel of the resulting 2D image starting from the center of the projection of the camera and traversing the whole volume. All the pixels lying along this ray contribute on the final pixel value: the opacity of all visited pixels of the volume is summed using some weighting factors. If a pixel with an opacity of 1 is encountered (totally opaque) the ray is stopped and only this pixel will be displayed in the resulting image [73, 332]. By properly selecting HU values ranges, different tissues can be rendered with different mapping (figure 1.22.e ). This approach is not useful for coronary artery stenosis assessment as it offers only an outside of the vessel wall. Besides the thickness of the vessel depends on the parametrization of the volume rendering.

### 1.3.2.2 Advanced Visualization Techniques

Recently, some sophisticated visualization techniques became available for a more detailed analysis of the cardiac anatomy. Those techniques generally needs further (semi-)automatic image processing to extract cardiac regions of interest as the heart and the coronaries volume. They usually adapt the basic visualization techniques (MPR, MIP and VR) to offer an optimal and simplified clinical workflow for coronary lumen analysis and lesions detection and quantification (figure 1.23).

**1.3.2.2.1 Heart Volume** A first step for a simplified visualization of cardiac CT data, is to keep only relevant structures for vascular lesions diagnosis. This could be manually performed using manual segmentation tools to remove the unwanted shadowing structures as the ribs, the lungs and the liver. The goal is to keep only the heart volume with the main great vessels. Today, all the commercialized workstation provides semi-automatic or fully automatic tools for heart isolation. A review of some of heart extraction algorithms is presented in section 2.2.1. The heart volume is usually displayed using the [VR](#) techniques thus providing an overview of the coronary arteries running on the heart surface. This volume rendering offers a valuable



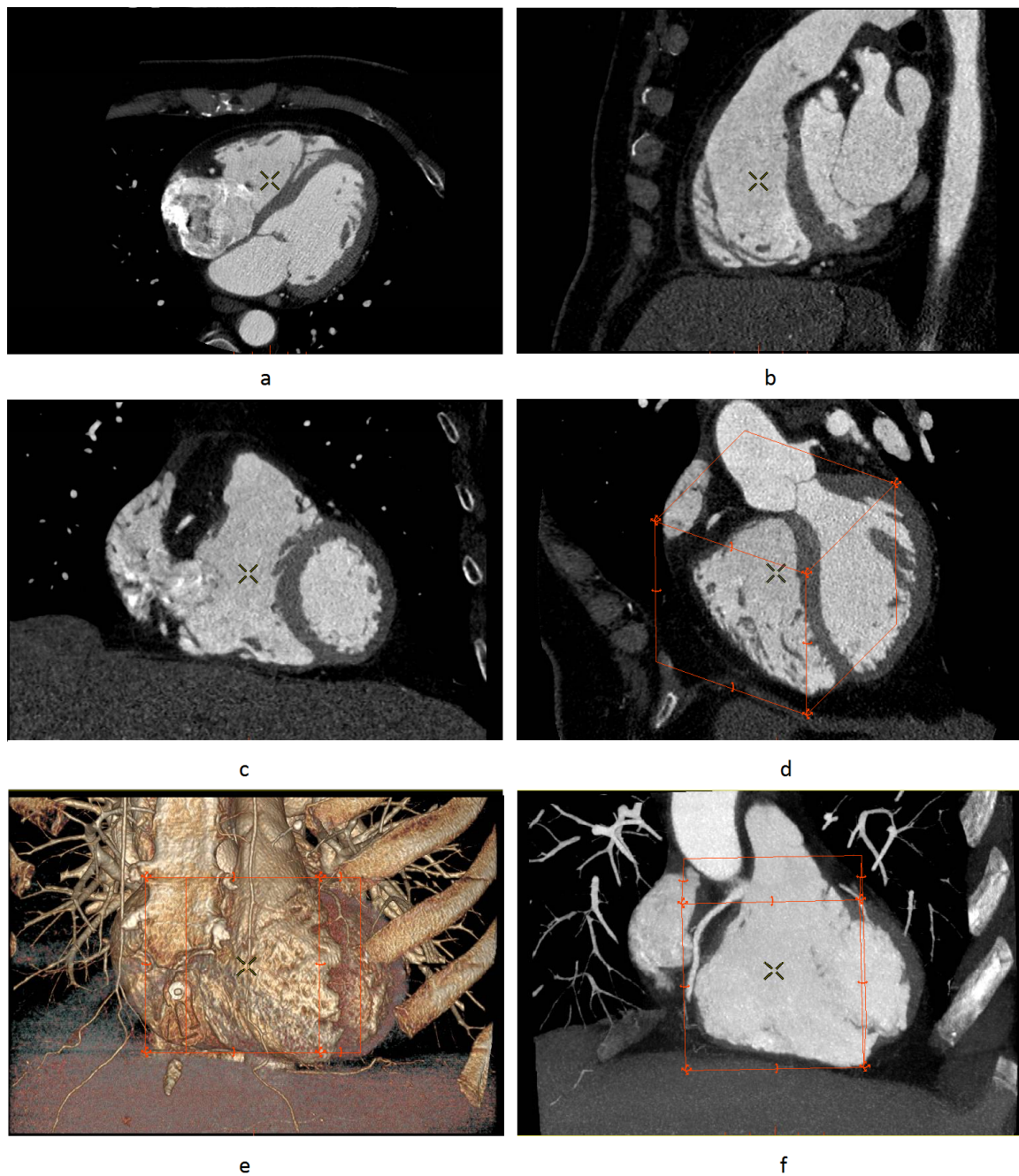


**Figure 1.22** – Examples of main visualization techniques of a cardiac CT angiography: (a) Axial view (b) Sagittal view (c) Coronal view (d) Oblique view (e) Volume Rendering of the raw image (f) MIP view on the oblique view showing the proximal and medial segments of the right coronary artery (RCA).

insight of the 3D anatomic relationships and helps highlight aberrant coronary anomalies and the presence of stents or coronary bypass grafts [351].

**1.3.2.2.2 Coronaries Tree VR** In order to enable an accurate visualization and analysis of coronary arteries, the coronary tree is often segmented after the heart volume has been extracted. This offers a more comprehensive 3D overview of the heart coronary tree and allow a rapid highlight of probable lesions and anomalies. Different segmentation approaches can be used for coronary vessel segmentation. For an overview of these approaches please refer to section 2.1. Similarly to the heart volume, the coronary tree is usually visualized using volume rendering. Thus calcifications can be highlighted if proper HU ranges are set. Hence, the user can rotate the coronary tree to inspect lesions and plaques in different angles of view. Coronary anomalies can be analyzed regarding their origin, their extent and their impact on cardiac structures like the heart chambers or myocardium [351]. Branches names are automatically detected. If some of the common branches are missed interactive tools are provided to complete the segmentation and label the missed branches segments [332].

**1.3.2.2.3 Multiplanar reformatted views of vessel volume** An other important and relevant feature for accurate coronary analysis is the centerline extraction. In fact, the vessel centerline extraction is an important pre-processing step for stenosis detection and quantification. Coronary centerlines can be rather automatically generated from the previously extracted coronary tree, or extracted between two seed points manually set by the user. It allows the reconstruction of MPR and cMPR view of the vessel. Most of the advanced workstations provides MPRs of the coronary arteries. A lumen view is automatically computed using the vessel's centerline by reconstructing a cut plane of the vessel lumen parallel to the centerline. The user can rotate the vessel on its longitudinal axis allowing to visualize all the vessel volume. Moreover, the interpreter can scroll through the stack of 2D cross sections of the artery (coronary transaxial views) which allow an accurate visualization of the vessel lumen as well as the atherosclerosis plaque. The user generally dispose of a set of tools to manually delineate the plaque and quantify the stenosis on both of the views. Moreover, curved MPR views representing a straightened display of the vessel and allowing for quantitative analysis of the vessel are provided. The cMPR view is generally used to follow the course of tortuous vessels which cannot be displayed on a single MPR view [339]. A correct centerline is required for an accurate curved MPR generation. The centerline is usually extracted using an (semi-)automatic approach (see section 2.4.1.2) and further adjusted by the user. In fact, artifact lesions can be visualized if the centerline is not correct. Thus, the user should pay attention to the robustness



**Figure 1.23** – Coronary artery visualization for stenosis assessment. Images from a AW workstation of GE Healthcare.

of the vessel centerline and eventually correct it before interpreting the cMPR view.

Basic visualization techniques cannot be used solely for coronary arteries analysis as they are not able to offer a comprehensive view of the complex vascular structure. Advanced reconstruction methods are today available thanks to the achieved progress in software and hardware making possible more sophisticated visualization techniques in real time. Post-processing based visualization approaches (cMPR, Lumen view, cross sections) are valuable tools for a rapid and reliable coronary stenosis investigation using CT angiographies. Nevertheless, considering the increasing number of CT angiographies to be examined per day specially in emergency rooms, more automated tools for stenosis ruling out will help saving diagnosis time and cost. In fact, taking advantage of the potential of cardiac CT angiography to accurately detect, characterize and quantify coronary lesions, advanced processing tools are being proposed for automated coronary plaques detection and quantification. Even if the clinical relevance of those plaque detection and quantification tools are still need to be studied, they probably would help getting more quantitative information on plaque burden and simplify monitoring the therapeutic response of diseased patients under treatment.

### 1.3.2.3 Stenosis Assessment using Coronary CT

Today, several ways are available permitting to analyze coronary arteries for stenosis assessment using CT angiography [17, 351]. Commonly, the first step toward an accurate stenosis detection is artifact preview to estimate the image quality. In fact, motion artifacts, calcification and metal blooming, and image noise might lead to an erroneous stenosis grading [5, 351]. Once the relevant artifacts have been detected, a systematic review of the coronary arteries in different

view and axis is necessary. The course and the branching of the main coronary arteries should be examined to verify the readability of the different coronary segments. If a segment is absent or not readable for some reason, it should be mentioned by the viewer. Then, the reader shall examine the eventual coronary anomalies with reference to their origin, extent (proximal and distal) and their impact on important cardiac structures. The reported coronary lesions should be classified with reference to their anatomic segment (B) for a clear communication of the results. Besides, the segmental position of coronary lesions have to be considered in order to estimate the associated impact on the myocardium [351]. The resulting luminal narrowing should be reported by estimating the minimal luminal diameter along the detected plaque extent. The use of MPRs views allows to visualize the lumen volume in different angles and thus facilitates the estimation of this feature. The user can use the (semi-)automated lumen contour extraction usually available on the workstation used to review the scan. Otherwise, he can define the lumen contour using manual tools. Even if the minimal lumen diameter is routinely reported in clinical practice, minimal lumen area seems to be more relevant to grade the stenosis degree. In fact, the use of minimal lumen area reduces the grading errors related to irregular shapes of the lumen which tends to bias the minimal diameter estimation. Moreover, luminal area is more correlated with the associated blood flow that circulates through the stenotic area. However, despite of the relevance of luminal area use for accurate stenosis grading, diameter based grading is still the preferred one as it allows to reproduce the same measure as the gold standard coronary angiography. Stenosis degree estimation using MDCT is still mainly visual. After visualizing the lesion in different planes and defining the minimal diameter section. The user manually selects a non diseased section at the proximity of the diseased area to be used as a reference section for stenosis quantification. Then, a qualitative visual estimation of the degree of the stenosis is reported. Reference site selection is a subsequent factor affecting stenosis grading and introducing more variability and bias between the different readers and modalities. In fact, stenosis quantification is directly related to the chosen reference sites selection approach. 3 different approaches are possible: Single reference, double references and healthy lumen reconstruction. Single reference consists in selecting one normal reference lumen section within the same artery segment to estimate the lumen narrowing. For double references selection, two non-diseased lumen sections are selected on both sides of the stenotic lumen section. A third approach consists in reconstructing a healthy lumen at the diseased point to be used as a reference site. More commonly, double references selection is used for quantitative assessment of stenosis [17]. Generally, advanced workstations offer semi-automated tools for quantitative stenosis grading (see figure 1.24). Due to the limited spatial resolution of MDCT angiography, the obtained % stenosis should be rounded to the corresponding quartile between 0 and 100% of



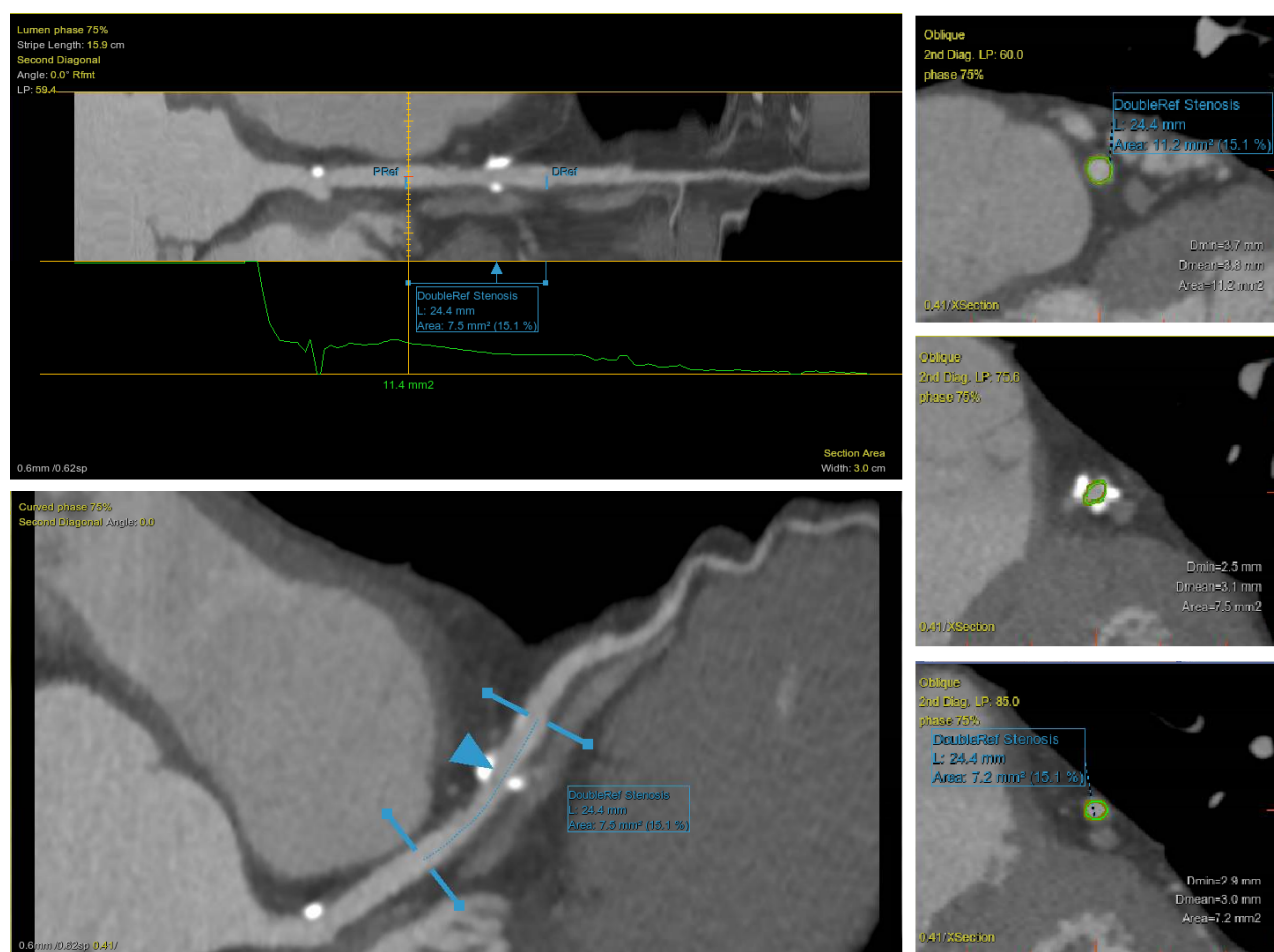


**Figure 1.24** – Stenosis assessment using double reference site selection. Images produced on a AW workstation of GE Healthcare

stenosis. The different recommended qualitative and quantitative stenosis grades are illustrated in table 1.4. In addition to the stenosis degree, the type of the associated plaque should be examined and reported by the user. Since CTA does not allow a precise characterization of the anatomic pathology of the plaque, the description of the plaque should be reported as *calcified*, *non-calcified* or *mixed* plaque according to the Society of Cardiovascular Computed Tomography [351]. Thus, the interpreter should provide a final summary report containing: (1) Patient's clinical information (sex, height, weight, ...), (2) Image acquisition parameters and quality (radiation dose, timing contrast, heart rate, artifacts, ...), and (3) Coronary findings and interpretation (stenosis location, extent, severity, plaque type, ...).

Luminal stenosis descriptors	Qualitative Grading	Quantitative Grading
<b>Normal</b>	Absence of plaque and no luminal stenosis	Absence of plaque and no luminal stenosis
<b>Minimal</b>	Plaque with negligible impact on lumen	Plaque with <25% stenosis
<b>Mild</b>	Plaque with no flow-limiting stenosis	25%–49% stenosis
<b>Moderate</b>	Plaque with possible flow-limiting disease	50%–69% stenosis
<b>Severe</b>	Plaque with probable flow-limiting disease	70%–99% stenosis
<b>Occluded</b>	Plaque with total flow-limiting disease	100% stenosis

**Table 1.4** – Coronary arteries stenosis qualitative and quantitative grading using CT angiography. Adapted from [351]

## 1.4 Our Approach

Motivated by the need of a faster and accurate cardiac CT data analysis, we devoted our work to the development of automated tools to facilitate and simplify the diagnostic clinical framework. Our main attention was focused on offering completely automated solutions to help the clinician improve the stenosis detection accuracy using multi-slice CT angiography.

### 1.4.1 Context of the thesis

This PhD thesis was performed in the context of CIFRE (Industrial Conventions Research Training). It is a collaboration between the A3SI team at ESIEE Paris and the AW team at GE Healthcare. In the context of this collaboration, I held a position of CIFRE engineer at GE Healthcare since June 2011. At the beginning, more time was dedicated to my PhD activities at ESIEE including literature review, brainstorming and teaching. This also allowed to propose new techniques to solve the treated problems. Then more time was spent at GE for image processing algorithms development, and their evaluation in a clinical setting.

The collaboration with GE allowed to work on an industrial product, the Advantage Workstation VolumeShare product. I worked in particular on the Volume Viewer module. It provides a rich set of tools for multi-modality 3D image processing and visualization. To develop the proposed algorithms we utilized the associated C/C++ image processing library named the Voxtool Library. It is the commonly used library for the development of the different VolumeShare protocols. Using this environment, we provided a fully automated prototype for

coronary artery lesions detections and quantification. The proposed prototype utilizes some existent components of image processing, such as vessel centerline extraction, while including new ones mainly related to the stenosis detection step.

Working in such an industrial and clinical context added an application-driven dimension to my work and urged me to provide result-oriented solutions. In fact, the main goal of this PhD thesis is to develop, evaluate and validate medical applications to support clinicians during the coronary pathologies diagnosis. Hence, I benefited from the available hardware/software platform to efficiently develop new techniques, evaluate them in a clinical setting and adapt the final solutions into industrial products. Therefore, in order to reach the expected level of performance for an industrial product, special care was dedicated to the validation of each proposed approach on real and representative sets of clinical data. The size of used sets varies from 10 to more than 100 images depending on the proposed technique.

Depending on the performances of state of the art tools of the used platform, I treated different problems related to the topic of coronary stenosis detection and quantification. I started with heart segmentation (chapter 1 of part II), coronary segmentation and lumen contours extraction (chapter 2 of part II) and finally focused on stenosis detection and quantification (part III). Some of this work and obtained results presented in this thesis has already been the subject of a publication [289–292]. Recent results will be published soon. Following we present the main contributions of this PhD thesis and the organization of this manuscript.

## 1.4.2 Our Contribution

The major contribution of this thesis is to propose efficient tools with the main purpose of aiding clinicians in CT image studies by providing more precise data (e.g. the heart volume) with qualitative and quantitative information. The most significant contributions of this thesis can be classified into four major topics: Literature review, CT image processing for coronary an efficient coronary analysis, Stenosis detection and quantification and Validation process.

### 1.4.2.1 Literature review

The first contribution of this thesis is the review of the recent works on the different medical image processing related topics. We have first presented an overview of the literature on cardiac CTA images processing for coronary arteries extraction and analysis. We summarized the different used vessel models and we recall the most recent and successful approaches proposed for vessel extraction. The approaches were organized, following the target feature to be extracted, into two major categories. Each category was further refined into subcategories with reference

to the character of the employed algorithm and the level of knowledge involved in the design of the technique. The presented approaches were commented based on the used validation process and obtained results. Such a study helped as to better apprehend vessel segmentation related challenges, and in our choice of techniques for solving such issues.

Subsequently, at each chapter we recall the most recent works related to the topic in question. More details on the proposed approaches, the involved user interaction, the validation process, the used data and obtained results are given. This allowed to compare our proposed method to state of the art ones.

#### 1.4.2.2 CT image processing for coronary an efficient coronary analysis

An important proportion of this thesis deals with cardiac CT image processing tools for an efficient coronaries analysis. We propose new technical elements that deal with this fields. We evaluate their performances and validate them on clinical cases.

First, we propose a fully automated heart segmentation approach in chapter 1. Unlike most of previously presented approaches, this method segments the heart as a compact object. The extracted volume can be used in a variety of medical applications such real-time interventional procedures guiding, radiotherapy treatment planning and heart cavities investigation. The heart volume can also be used to reduce the required effort and time for cardiac CT data analysis by providing an accurate and fast visualization of coronary arteries.

One common issue with heart segmentation is the elimination of obscuring structures with common appearance proprieties, like the liver. In fact, non constrained segmentation failed to separate the heart volume from the liver because such regions suffer from weak or absent boundaries. We utilize a geometric model of the heart to extract a first approximation of the cardiac volume and constraint the segmentation around challenging regions. The heart can be roughly represented by 3D ellipsoid. Previous work using such model, proposed predefined geometric model to represent the heart, with fixed axis or size. However, such a choice is not suitable because of inter-patient variability of the heart size and shape. In order to overcome such limitation, we propose to extract the ellipsoid that fits the best a set of points on the heart surface by using a minimization scheme of the weighted least squares residuals. The obtained approximation is further refined to extract the final heart segmentation. We demonstrate the usefulness of this model to correctly extract the heart volume and eliminating obscuring structures (figure 1.25), on a large database of cases in a quantitative and qualitative manner. This work has been presented during the ICIP conference [289] and published in the IJCARS journal [290].

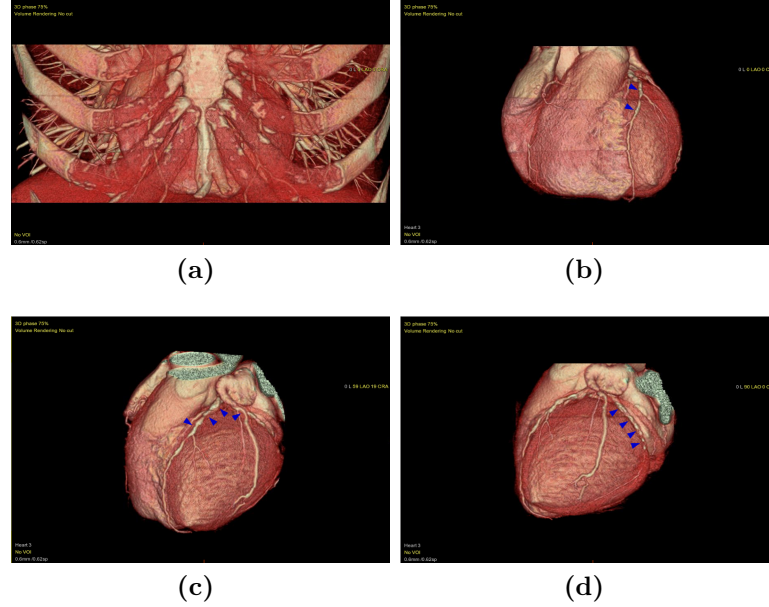


**Figure 1.25** – 3D rendering volume of a diseased heart with several severe stenoses ( $>70\%$ ) caused by soft, calcified and mixed plaques (showed by the arrows). (a) The original volume. (b)-(d) The isolated heart volume allows a robust visualization of all the pathological coronary segments.

To further improve the visualization of coronary arteries, we propose a novel approach for coronaries enhancement and extraction in section 2.2. It takes advantages of the recently introduced technique for linear structures enhancement; The Robust Path Openings [92]. This allows to overcome the usually used Hessian based filter limitations as the scale and local variation dependency. Then, to extract the coronaries connected components in the enhanced volume, we use a new shape-space based morphological filter by combining appropriate attributes. Preliminary results show that the proposed approach is robust against noise and is very promising for coronary arteries extraction. Further improvements are planned in order to provide a tool for coronary tree segmentation useful in a clinical context.

Our contributions in automated coronary analysis also encompass coronary arteries lumen extraction. In section 2.3, we present a statistical based approach for accurate lumen extraction. The proposed approach delineate the lumen contours by using patient specific statistics in order to exclude coronary lesions from the extracted volume. The method is evaluated using the online evaluation framework presented in [215] and provide state of the art performances. It can be used for an accurate extraction of coronary stenosis and quantification with high confidence.

### 1.4.2.3 Stenosis detection and quantification

In the context of coronary lesions detection and quantification, we propose two different automated approaches. The first method relies on the vessel lumen segmentation and quantification to extract stenotic regions candidates based on the lumen area profile (Chapter 2). This set is further processed to eliminate erroneous detections by analyzing intensity and geometry features. This approach was submitted to participate to the Coronary Artery Stenoses Detection and Quantification Challenge and ranked third during the on site challenge. This work was published in the challenge proceedings [291].

In chapter 3, a second approach for stenosis detection and grading, utilizing machine learning, is described. The main motivation of this work is prove that learning based approaches are able to overcome the limitation of rule-based techniques for detecting all coronary pathologies types (using one single approach). In fact, such explicit approaches usually detect stenoses based on lumen segmentation. This makes the robustness of the detection approach tightly conditioned by the segmentation step accuracy. We used intensity-based and geometric features that best captures the different stenosis configurations at variant scales. A large set of features are tested and evaluated on the training database using a cross validation process. Only meaningful and discriminant ones are kept. A major limitation for previous works using machine learning approaches is the use of a vessel pattern with pre-determined size and shape. In order to ensure a rotation and scale invariance, we designed a deformable vessel pattern with variable size and direction. This allows to the shape model to include the local vessel volume while ensuring that the surrounding tissues are excluded.

The proposed algorithm was evaluated and validated using the online coronary stenosis detection and quantification framework [215]. Furthermore, it was extended and improved in order to reduce false detection amounts. Finally, a fully automated prototype was developed based on this approach. Quantitative and qualitative evaluation results on a GE database show that the tool can be used as a first reader to quickly highlight and grade coronary severe stenoses (figure 1.26). This work has been presented during the SPIE conference 2013 [292].

### 1.4.2.4 Validation process

Finally, a significant effort was dedicated during this thesis to the evaluation and validation of the different proposed algorithms, in a clinical context. The automated heart extraction segmentation was qualitatively and quantitatively validated on 133 healthy and pathological CT cardiac images. For the quantitative validation, we compared the automatically extracted hearts to ground truth manual segmentation. Therefore, we used volume-based and distance-

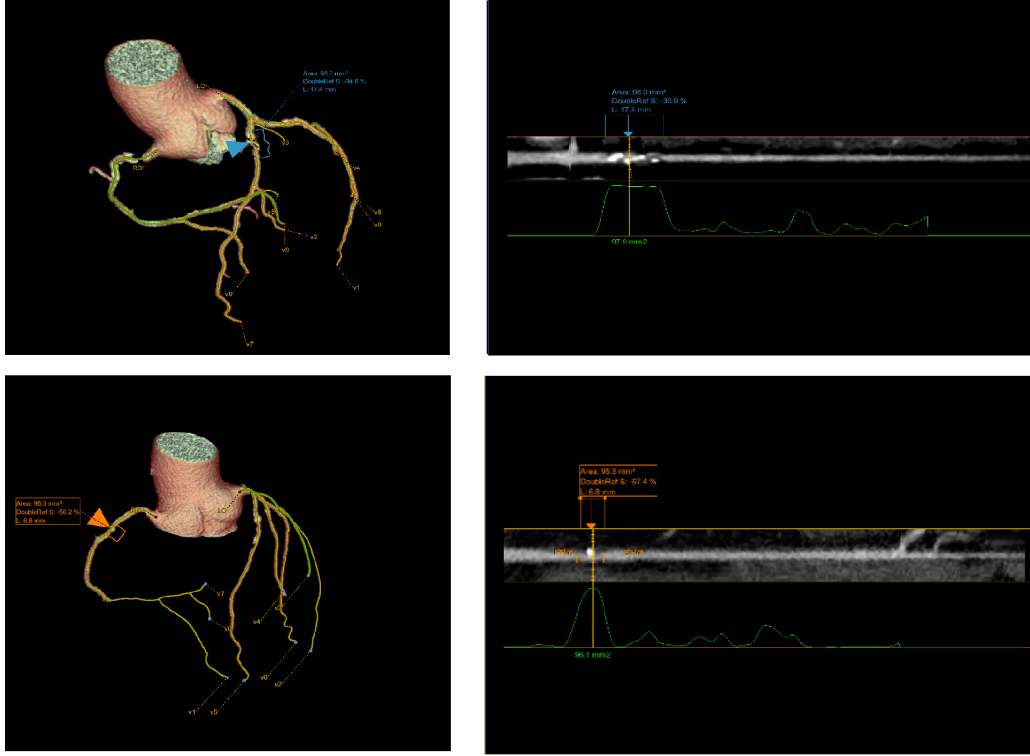


**Figure 1.26** – Automatic Stenosis detection on two diseased branches from two different cases: Patient 08 (First row) and Patient 14 (second row). 3D View of the artery coronary tree with marked detected stenosis (left), Lumen view of a diseased branch showing the probability profile in green with a peak at a severe stenosis (right).

based validation methodology as described in section 1.4.3. Subsequently, an expert has visually inspected the segmentation result on a subset of the database. This required the design of an appropriate measurement methodology to quantify the approach performances. The proposed metrics are designed with reference to accuracy criteria, detailed in section 1.4.3.2.

We have extensively used the online evaluation framework for coronary arteries segmentation and stenosis detection quantification [215] to evaluate different proposed approaches (i.e. lumen segmentation technique, stenosis detection and quantification). The major asset of this framework is that it offers a common representative database allowing to fairly evaluate a new approach and compare it to state of the art methods (that have been submitted to the framework). It uses common validation measures to quantify the algorithm performances. This is very interesting in order to be able to judge a new algorithm. Eventually, the framework suffers from some limitations but it is the only publicly available tool for this purpose until now.

Furthermore, to provide a more qualitative evaluation of the cardiac lesion detection prototype, we designed our own metrics that allow to assess the amount of correctly classified



coronary arteries. Therefore, we used a local 31 CT exam database coming from a GE CT scanner. The major challenge of the task of designing an assessment metric is to accurately translate the target performances expected by the clinician into a measurable quantity. Therefore, an interaction with experts and the product users are mandatory to efficiently design such metrics. Moreover, we believe that for an accurate evaluation and validation of a given approach intended to be used in a clinical context, both quantitative and qualitative evaluation should be performed. In fact, although a quantitative evaluation allows to rapidly compare the proposed algorithm results to a given ground truth on a large database, it does not provide a precise assessment on the segmentation quality. Only an experimented expert, based on a visual inspection, can judge if a segmentation result is satisfactory or not, with reference to the clinical context needs. We thus believe that both of the evaluations must be performed for any algorithm dedicated to clinical use.

### 1.4.3 Thesis Outline

The content of this thesis addresses the problem of coronary artery analysis and lesions detection, and related topics:

- **Part 2:** Presents algorithms for automated cardiac CT images segmentation. This part is divided into two chapters. Chapter 1 presents a fully automated algorithm for heart volume extraction based on geometric model fitting. We first review and compare most recent works dealing with this issue. Then, the algorithm is described. Finally, details of the validation process and qualitative and quantitative evaluation results are presented. Chapter 2 of this part deals with coronary arteries detection and lumen segmentation topics. A review of the related literature is proposed. Approaches are divided into two distinct categories based on the input knowledge used in the proposed algorithm. Then, we propose a new approach for coronary arteries segmentation based on robust path openings and component tree filtering. Preliminary results of this approach are presented and discussed. Afterward, we present and discuss a statistical based technique for vessel lumen segmentation improvement. This technique allows to take into account the intensity variability between patients and along the vessel. Validation on the online Rotterdam evaluation framework shows that the approach provides an accurate segmentation of healthy and pathological vessel lumen.
- **Part 3:** Presents methods for automated Coronary arteries stenosis detection and quantification. In chapter 1 of this part, we review the details of previous work on coronary



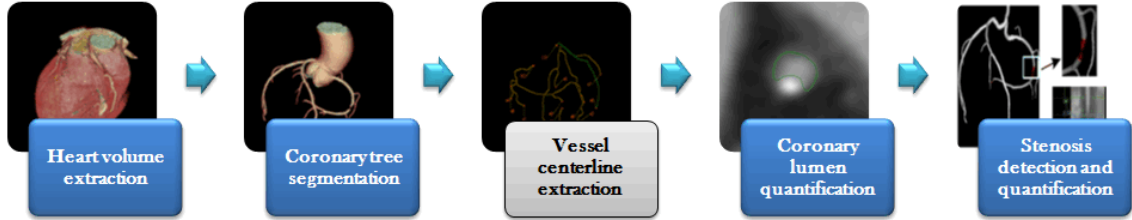


**Figure 1.27** – The overall automated coronary stenosis detection and quantification flowchart.

lesions detection and quantification. We also present the evaluation framework used to validate the two approaches, and compare our results to state of the art methods. Used material and evaluation metrics are explained. In chapter 2, we present a two-stages automated coronaries stenoses detection. Based on the vessel lumen segmentation, stenosis candidates are extracted. Furthermore, false positive candidates are removed by combining local intensity and geometric features. This approach ranked third during the Rotterdam Coronary arteries challenge hold during the MICCAI conference (2012). In chapter 3, we investigate a new approach for stenosis detection and quantification based on Random Forest. A set of variant features is tested. Parameters optimization and performance evaluation using the Rotterdam online framework are presented and discussed. Finally, this approach is extended and adapted to present a fully automated prototype for severe stenosis detection and grading.

The different parts and chapters are organized following a logic flowchart of an automated tool for stenosis detection and quantification as presented in figure 1.27. In the context of this thesis, we did not focus on the problem of centerline extraction. The first part is dedicated to preliminary processing needed for an automated coronary arteries lesions detection: This includes heart masque extraction and coronary arteries detection and segmentation. The following part, presents the work on automated stenosis detection, using some of the work presented in previous chapters. Each part is organized in an independent way (Introduction, review of literature and background, methods, results and discussion) and can hence be read independently from the others. However, we encourage the reader to follow the proposed organization of the manuscript for a better comprehension.

---

---

## Chapter 2

---

# Cardiac CTA Processing for Coronary Arteries Analysis: A review

The core of the different practical applications in medical imaging is vessel segmentation. In fact, this processing is required for visualization systems, vessel diagnosis and even in therapeutic tools such as computer-guided surgery. However, vessel segmentation is still an open problem even if many methods have been proposed depending on the image modality, the user interaction required, the prior knowledge on vessels we aim to extract and many others factors. Vascular structures segmentation has turned out to be a very challenging task, even when a contrast agent is injected to improve the image contrast resolution. The major difficulties include:

- The vessels intensity: Overlap with other nearby anatomical structure such as bone for high contrasted vessels or muscle for low contrasted ones. An other problem is related to the intensity inhomogeneity within the vessel itself, i.e MRA cases.
- The intra-patient variability of vessels' topology and appearance characteristics.
- The presence of pathologies such as calcifications, aneurysms and tumors besides some implants such as stents and bypasses.

The manual segmentation is a tedious and time consuming task. It is also user dependent and error prone which makes it impractical for routine clinical practices.

A general vessel extraction scheme contains usually three main steps: 1) A pre-processing step to simplify the image content and improve the image quality, 2) A pre-segmentation step to reduce the region of interest and approximate the localization of vessels, and 3) A vessel features

extraction step aiming to define the vessel volume and quantify some relevant characteristics (e.g. centerline, lumen contours, lumen radii). The extracted features depend on the complexity of the target task. For instance, for simple and rapid visualization tasks only the vessel volume is necessary. Meanwhile, for computer assisted diagnosis tools more detailed information is needed as the vessel centerline, the lumen contours and the vessel radii.

Hereafter, we will briefly present and discuss some of the proposed schemes bases for vessel segmentation from 3D angiography data, ranging from interactive to fully automatic approaches. The first section 2.1 is dedicated to the pre-processing step aiming to improve the vessel segmentation results. In this part we will discuss approaches for image quality enhancement and noise reduction. In section 2.2, some of the pre-segmentation steps used to extract region of interests and roughly approximate the target structure are detailed. Finally, we will focus on vessel features extraction schemes. We will first review the most used vessel models defined to segment vascular structures in 3D data sets. Then we will discuss the approaches defined to extract the vessel. Two categories are hence identified: 1) Centerline extraction dedicated approaches and, 2)Vessel volume and contours modelling.

## 2.1 Image Pre-processing

### 2.1.1 Downsampling

3D angiography results in a tremendous amount of information that needs to be simplified. Downsampling could be performed to accelerate the processing and reduce the memory use without losing the accuracy of the image, as in [152, 299, 464]. In their work on carotids extraction and stenosis grading, Wong et al. [464] down-sampled every image slice by a factor of two to save computational power, hence images are resampled to a resolution comparable to their real in-plane resolution. In [152], downsampling is performed after an inspection of the image spectra as shown in figure 2.1 to be sure that this pre-processing step can be performed without losing information.

The main motivation behind 3D angiography pre-processing is to simplify the amount of information embedded in such images. An other goal of image pre-processing is to increase both the accuracy and the interpretability of the digital data during the image processing phase by *denoising* or/and *filtering* the image. Improving the image quality could be done by reducing the noise while preserving the vessels or enhancing the vascular structures while avoiding noise amplification.

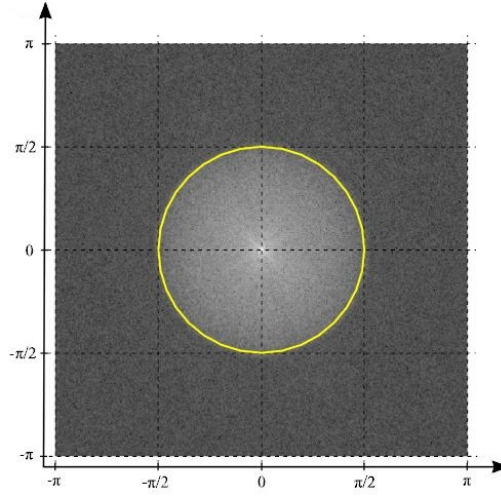


**Figure 2.1** – Log-spectrum of a 512x512 image slice. The spectral power can be found in frequencies less than  $\pi/2$ . Hence, one can downsample by a factor 2 without losing information. Illustration from [152]

### 2.1.2 Image filtering for noise reduction

Noise is a common problem for all imaging modalities especially CT angiography. Classical denoising approaches, based on an assumed model of the noise, process isotropic filtering and thus removes not only the noise but also the small objects and is not suited for vessel segmentation applications. A robust NL-means algorithm was proposed in [125] and used in [506] to remove the noise from the 3D CT image. To cope with this issue, a family of vessel-dedicated anisotropic filters were also defined [34, 84, 106, 227, 263, 340, 341]: The main idea is to process the filtering locally in the direction of the linear structures (vessels) in order to avoid blurring the boundaries and to preserve small objects. For this we need to define the orientation of the objects first. Several works related to this topic could be found: In [227] and [279], the direction of the least curvature were used to carry out the anisotropic diffusion. Structure tensors [340, 452] and gradient flux [229] were also used to define the local anisotropy of the data. Morphological approaches could also be used to extract the diffusion direction: in [432] this direction is defined to be the one giving the strongest response to a crest detection operation using linear structures.

### 2.1.3 Tubular structures enhancement

Numerous filters were proposed for vessel enhancement and noise reduction. This includes derivatives filters as proposed in [222] and in [344], and mathematical morphology based filters as proposed in [457, 484]. Additionally, the well known Hessian based filters were widely

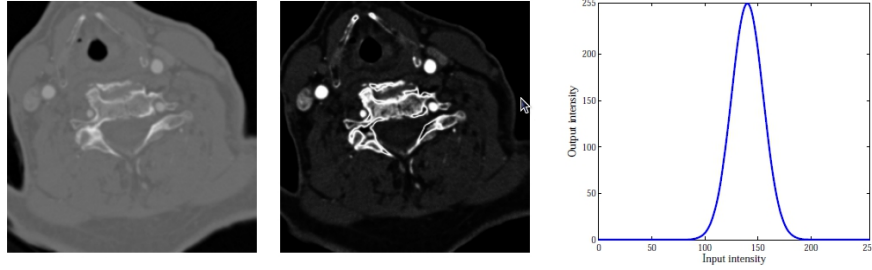


**Figure 2.2** – Vessel intensity enhancement: (left) Initial image, (center) Enhanced image, (right) Gaussian look up table. Illustration from [299].

used as vessel enhancement filters. According to defined shape models, those filters exploit the Hessian eigenvalues to discriminate between plane-, blob- and tubular-like structures [149, 231, 255, 261, 373]. In [393], the vesselness measure were used for the pulmonary arteries segmentation. Wang and Smedby uses this approach to enhance the coronaries centerline [443]. As an alternative for the second order derivative analysis, we can cite the structure tensor analysis based on the exploitation of the covariance of the image gradient vectors [11, 12] or the spherical flux based filters proposed in [240, 241]. Other enhancement filters are derived from mathematical morphology such as the top-hat filter from [484] or the technique proposed in [457] and based on the application of an elongation criteria to the connected component tree of the grey scale image. The recent work of Tankyevych [411] is a combination of the Hessian matrix analysis and morphological filters to enhance vascular structures. The filter processes a vascular structures reconnection by applying morphological closing guided by the Hessian-based direction information.

Other approaches based on the voxel values redefinition were proposed in order to enhance vessel structures and remove eventual noise. Voxel value normalization were used in [406] to reduce common artifacts of CT scans such as variation of contrast between neighboring slices. The idea is to map all the slice voxels with  $\max(\mathbf{0}, \frac{l-1}{\mu-1})$ ,  $l$  being the low boundary of the heart intensity values and  $\mu$  the mean value of all voxels greater than  $l$ . A smoothed image  $\nu_1$  is obtained by applying a  $\sqrt{2}$  width Gaussian filter to the resulting image. A Gaussian look up table was used in [299] to enhance bright structures in the CT image 2.2.

In general, efforts have been intensively dedicated to design vessel-specific schemes aiming to enhance thin and tubular structures while reducing noise and irregularities. For a more comprehensive review and evaluation of the denoising methods and vessel enhancement approaches one can refer to [66, 286, 402].

## 2.2 Image Pre-segmentation

Working on the initial 3D data involves processing a huge amount of non-useful information and thus slowing down the processing and inducing false positive detection. Therefore, several works proposed approaches of image pre-segmentation to simplify the image content and approximate [Region of Interest \(ROI\)](#). For this purpose prior anatomical knowledge is required for a rough localization of the structure of interest. Some other efforts were dedicated to remove abnormalities before processing the data in order to increase the robustness of the proposed approach against false positive detections. Image pre-segmentation could also be considered to extract some information about the target structure in order to automate the whole processing system.

### 2.2.1 Delineation of anatomical region of interest

The first approach for ROIs selection is the definition of anatomical masks. For instance, several works focused on automatic or semi-automatic heart mask delineation for coronaries segmentation. Intensity information was directly exploited for this purpose in [470] and [78]. In [78], the heart mask was extracted based on a combination of thresholds of the heart densities (i.e. corresponding to the different cavities) and a set of morphological operations [386]. A more sophisticated approach is to apply the threshold on a mixture probability map extracted from vessel enhanced images [11, 12, 393] or estimated through Expectation-Maximization of a probabilistic model as in [155, 176]. In [219] the gradient information was exploited to process a 2D model balloon inflation for detecting the heart wall. Florin et al. [143] used an algorithm driven from the graph cuts optimization technique with a shape constraint to segment the heart surface [50]. More sophisticated approaches for heart mask extraction for coronary arteries analysis are detailed in section 1.1.2.

For pulmonary arteries extraction, lungs mask extraction was performed in [393] based on thresholding and labeling. Anatomical atlas-based approaches could be employed to define ROIs in medical imaging when reliable statistical information is provided, as performed in [337] for brain vessels segmentation. A more precise mask of the vascular structure were defined in [184] using a seeded region growing approach to segment the vessels as well as eventual calcified plaques.

ROIs could also be selected by removing all the structures that do not match to the target anatomy. In the context of coronaries detection, removing the lungs from the working volume was an easy alternative to reduce the working volume and thus reduce false positives. In [406],



**Figure 2.3** – The original image (left) is filtered using a greyscale threshold and an island removal algorithm, the result is a vessel with a hole inside (middle), An opening operation removes the vessel wall behind the calcifications (right). Illustration material form [453]

lungs removal was done by applying a second order Gaussian filter to the original image  $\nu_1$  with a width of  $6\sqrt{2}$  thus obtaining a second images  $\nu_2$ . A final image  $\nu_3$  is obtained by setting to 0 all the voxels of  $\nu_1$  having a value less than 0.5 in  $\nu_2$ . Krissian et al. [232] removed the lungs vessels by processing a set of thresholding and morphological openings on the initial image. In [464], irrelevant regions are excluded to speed the extraction of carotids centerlines and stenosis detection. Hence, each dataset is cropped to a rectangular region including the three main carotid segments of interest. This rectangular region is defined based upon the three given input points, marking the extremities of the three segments, and their centroid.

## 2.2.2 Abnormalities removal

Some pre-segmentation schemes includes removing abnormalities from the original data in order to increase the robustness of the proposed method. For instance, in the context of coronary lumen segmentation, calcifications exclusion is one of the pre-segmentation goals in order to avoid including them within the final vessel lumen. With refer to their appearance model (very bright structures) a simple way to extract them would be a simple thresholding [152, 453]. Similarly, calcium was removed from Cardiac CT in [78] by darkening the corresponding voxels, i.e. above a defined threshold. A seeded gray-scale thresholding was used in [453] to set vessel out-range voxels values to 0. For this purpose two thresholds (High and Low) were defined based on the start point value. Calcifications were so excluded by first applying an island removal filter on the precedent volume and then an opening operation to eliminate calcification borders (fig. 2.3).

## 2.2.3 Seeds extraction

Pre-segmentation could also be used to automatize the extraction process by initializing it without the user interaction. In [219], starting points for a tracking process to extract the coronaries were detected by an automatic extraction of the 2D aorta section (Hough transform)

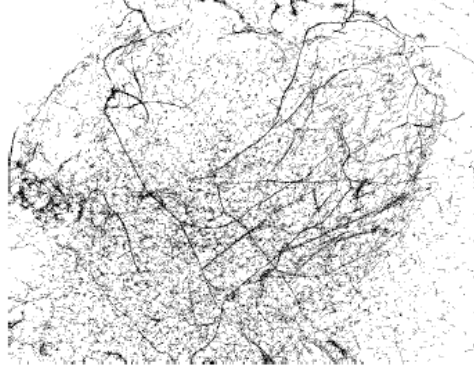


**Figure 2.4** – The core point sets corresponding to the centers of intensity plateaus in 2D [406]

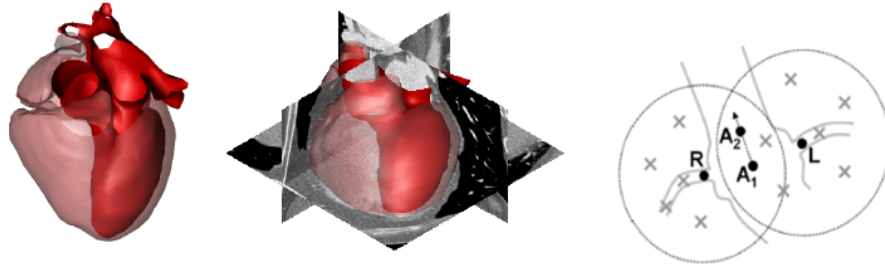


**Figure 2.5** – The 3D heart model (left) matched to a Cardiac CT data (middle). The coronaries search regions defined using the four landmarks  $A_1$ ,  $A_2$ ,  $R$  and  $L$  [483]

then applying a propagation algorithm to detect the ostia points (depart points of the LCA and RCA from the aorta). Robust maxima were also selected as seed points for tracking approaches as in [248]. Similarly, in [405] initial point candidates, for a graph-based workflow for coronary segmentation from cardiac CTA, were obtained as local maxima of intensity. Centers of intensity plateaus in two dimension slices were selected as an initiation for vessel centerline points in [406](see figure 2.4). In [143], rays are cast from the heart center to detect the intensity peaks likely corresponding to the coronaries points.

In [483], a 3D model of the heart is matched to cardiac CT exams for detecting the approximate position of the heart. Based on this information and a symmetry measure, candidates for coronary artery seeds (RCA and LCA) are calculated inside a defined region of search (see figure 2.5). An automatic seeding algorithm for coronary arteries segmentation is presented in [443] including rib cadge removal, ascending aorta tracing and an initial seeding of the coronaries. Aorta segmentation was also performed to define the initial direction points for a tracking algorithm in [78].

Pre-segmentation approaches, if well performed, allow the reduction of the false positive and



the computation cost. However, most of those methods are pixel-wise based and so they are prone to failure by generating false negative, false positive and disconnected results. Topological properties and spatial coherence could be embedded to improve their outputs.

In the next section, we propose to review the most popular and meaningful vessel models introduced in the literature to represent vascular structure in medical images. The proposed models are generally designed to capture the vessel features.

## 2.3 Vessel modeling

Vessel segmentation represents a wide area of medical image analysis and visualization literature that has attracted the interest of the image analysis society. In fact, a large number of works related to vascular structures segmentation in CTA and MRA data have been published. Proposed algorithms varies from general image segmentation techniques to specific vessel model-based extraction approaches.

Prior information on the target structure could be assumed and embedded in vessel models to facilitate the extraction task. In the last decades, the increasing knowledge about human anatomy and the continuous improvement of medical imaging have allowed to get precise information about the target organ such as appearance properties, shape and size. In fact, vessels appears as *bright tubular* structures in contrast-enhanced angiography (CT and MRA). Those two properties have been encoded in more or less complicated models. Hereafter we will briefly discuss those models based on their complexity: Simple Models (including intensity and geometry models) and Hybrid Models (combining the two kinds of information).

### 2.3.1 Intensity Models

The first exploited prior information on vessels is their theoretical appearance in contrast-enhanced angiography (CT and MRA). In fact, in this modalities vessels are bright structures surrounded by darker background. The information about the specific vessel intensity ranges was directly embedded to extract vessels in several works [45, 219, 230, 406, 453] in CT angiography. Passat et al. [337] used two adaptive thresholds to segment vessel in MRA brain images. However, it is difficult to guaranty the steadiness of the contrast agent homogeneity along the hole vessel structure and concentration for the different patients. An other problem related to the MRA modality consists of the variability of the blood flow along large vessels which results in variable vessel intensity. To cope with this problem, some authors proposed to exploit the theoretical statistical distribution of the intensity inside the vessel rather than

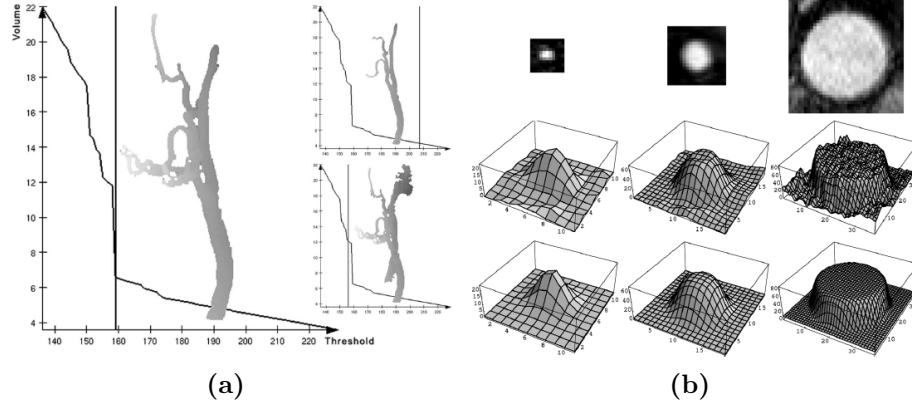


**Figure 2.6** — Examples of vessel intensity models: (a) Results of applying different threshold values to segment the right carotids volume. Illustration from the work of Boskamp et al. [45]. (b) Intensity plots of orthogonal 2-D slices through vessels with different sizes in 3-D MR images, and their corresponding generated 3-D images using the cylindrical intensity model as proposed in [467].

the density values with refer to the image modality properties. This distribution was modeled in MRA images especially by a Gaussian model as in [88, 174, 176]. A linear combination of discrete Gaussians was proposed in [133] to deal with laminar and turbulent blood flow near to pathology. Chung et Noble [89] modeled the vessel intensity distribution using a Rician model. A 2D cylindrical parametric intensity model was proposed by [468] to represent the intensity distribution on the cross section of the vessel. The model was fitted to the image using a Kalman Filter. Some papers proposed also a distribution model for CT modality such as Cauchy [11] or Gaussian [144] models.

To more precisely characterize vascular structures, some approaches define a mixed model considering information on the vessel structure and surrounding tissues. Local neighborhood intensities are considered in a spherical polar coordinate system in order to capture the common properties for the different types of vascular points in [349]. The more intuitive mixed model assumes that vessels are brighter than their background [144, 378, 425] with constant intensity values. Statistical mixture were proposed to improve the result of this approaches and model both of the vessel and background in a more accurate way [119, 176, 277, 475]. Because of the possible presence of vascular pathologies, the explicit assumption on the homogeneity of the background would fail. Schaap et al. [377] assumes that vessels are more homogeneous than their background which allows the improvement of the results near the pathological regions.

Because of their dependency on the image modality and the weakness to correctly model the vessel in the presence of artifacts, pathologies or loss of signal, appearance models could not be reliable for accurate vessel segmentation tasks.

### 2.3.2 Geometry Models

The second property of vessels are their characterizing shape. In fact, vessels have always been modeled by thin elongated tubular structures in 3D angiography. Depending on the target application, those models take in account different specific geometric properties. In the literature, vessels have always been described using two different features: Their surface and their main axis (i.e. centerline). Hereafter, we will distinguish between geometric models designed for the vessel surface and those for the vessel centerline.

- **Surface Model:** Vessel wall could be modeled based on its local tubular shape. This assumption was exploited to extract the vessel borders by 3D or 2D models. A cylindrical model was proposed in [149] to enhance vascular structure. A more general model was introduced in the work of Sato et al. [373] including elliptical shapes. Deformable models were used to fit an initial curve to the vessel surface based on the regularity assumption of the vessel surface to define the evolution forces. The vessel wall was extracted by using a 3D B-spline in [147] and [146], and an active shape model in [103, 104, 299]. An other approach was to extract the vessel surface by defining a 2D cross section models. Circular, elliptical and star patterns were proposed to extract the 2D vessel contours in [326, 460] as well as parametric curves used in [185, 256]. Further discussion of those techniques are presented in the section 2.4.2.2.
- **Centerline Model:** In some works the vessel structure was modeled by a 1D curve: the centerline, i.e the centered curve inside the vessel lumen. In fact, the centerline has become a powerful tool in various applications such as visualizing tasks or pathology detection. The most intuitive way to reduce a 3D structure to a 1D presentation while preserving its topology is the skeletonization. Several works has been presented dealing with this topic based on the definition of medial axis [38], the distance map transform [46] or the Gradient Vector Flow as in [26, 175]. The definition of simple points [33] helped to exploit a new approach of skeleton extraction: the Morphological Thinning [43, 46, 335]. The centerline is obtained by removing all simple points from the vessels volume with respect to some defined constraints. Parametric models such as B-splines [46, 147] and cardinal Splines [466] has been proposed to represent the vessel centerline. In [147], an initial curve was fitted to the image driven by the hessian eigenvalues analysis. Prediction Schemes relying on assumption on the local regularity of the vessel centerline were designed making possible the estimation of the next vessel position and attributes only based on the previously extracted ones. In [467], the Kalman filter is used to predict

the direction and radius of the vessel from previously estimated values in a tracking process. However this approach would fail because of the characteristics of vessels such as high curvature regions, abrupt radius changes and bifurcations. In fact, stochastic schemes has been presented as an alternative to this solution allowing to deal with the non linear changes eventually present during the tracking process. Florin et al. [142, 144] has designed an extraction scheme using the Particle Filter (The Sequential Monte-Carlo Technique) considering this filter as a direct tracking approach. The Markov Marked Point Process was adapted in [237] to vessel extraction. The vessel was defined as a set of pice-wise linear segments randomly initialized on the image and evolved through a reversible jump Markov chain Monte-Carlo scheme. However, despite of the accuracy of the result these approaches offer, they are still not suited for today's clinical standards because of their high computational cost.

Some approaches combines surface and centerline models to modelize the vessel. The vessel wall contour is represented with respect to the centerline curve using generalized cylinders [35]. The vessel wall is hence represented by 2D cross section contours defined along the vessel centerline. Geometric models of the cross sectional contours are the same mentioned above. There exists different ways to define the generalized cylinder by combining different curves and cross section patterns. Some models are rigid and do not allow a great variance between the 2D cross sections as the straight homogeneous generalized cylinder model presented in [487]. Some other extensions of generalized cylinders handle curved centerlines and varying cross section shapes as in [325]. To enhance the 3D coherence of the object and avoid torsion artifacts and other limitation to the 2D cross section model of the vessel wall, some authors proposed to modelize the vessel surface using a 3D surface evolving from the vessel axis. In [146], the vessel wall is modeled using a 3D B-spline that evolves to fit the vessel wall starting from the vessel centerline. A similar approach is proposed in [307] where a 3D active surface is used instead.

### 2.3.3 Hybrid Models

Hybrid models were designed to combines both appearance and geometric information about the target vessel.

As vessel are highly variable structures, hybrid models aims to locally describe the vessel shape while modeling the intensity distribution inside the approximated shape. Usually, radial variation in the cross section of the geometric model are used to describe the intensity distribution. In practice, parabolic profiles [399] and Gaussian like profiles [231, 359] are used to approximate the intensity variation. Bar-like profiles are proposed in [41, 222] to describe the

plateau-like radial intensity profiles especially of large vessels. However, such profiles do not consider blurring and partial volume effects. To deal with this limitation, authors proposed to use modified bar-like profiles by using Gaussian-based error function to estimate such effects as in [231, 467, 469].

Similarly, a common strategy to detect vascular structures, in the literature, is the use of second order derivatives of the image intensity. By analyzing the local image geometry, vessels are identified as bright tubular structures showing an orientation with a low curvature (i.e. the vessel direction) and a plan with high curvatures (i.e. the vessel cross section). Therefore, a fair amount of works have been dedicated to define tubular structure patterns using the Hessian matrix [149, 256, 261, 267, 373, 393]. All these works define filters using the Hessian eigenvalues to enhance vascular structures. In [149], the authors proposed a shape space based on the second order variation of the image intensities as shown in figure 2.7. The hessian-based vesselness measure proposed in this work is considered as the most used hybrid template to model vessel structures. Similarly, Sato et al. [373] defined a vesselness function using the relative variation Hessian eigenvalues. An other shape space has been defined in [185] using the inertia moments. Similarly to Hessian based filters, the proposed vesselness filter is designed using ratios of the eigenvalues of the inertia matrix.

An other hybrid vessel model family includes the use of 3D geometric structures with an associated local intensity model. In [425], the authors proposed local superellipsoids to describe the vessel local geometry using a piece-wise constant intensity model. Similarly, in [152] 3D cylinders are used for modeling the vessel shape combined to a linear Gaussian appearance model. Contrary to the previous image tensor-based approaches, the model parameters are explicitly optimized locally.

Hereafter, we will briefly present and discuss the main approaches proposed to extract vascular structures features using CT and MR angiography.

## 2.4 Vessel features extraction

As mentioned previously, vessel segmentation is a feature key for advanced angiography analysis and computer aided diagnosis tasks. Therefore, a large number of approaches have been published to deal with different vessel segmentation challenges. Several reviews of vessel segmentation approaches exists in the literature. One could refer to the two works [214] and [250]. Despite the continuous efforts to propose a clear and comprehensive classification of vessel segmentation and extraction methods, this task is still very challenging regarding the complexity

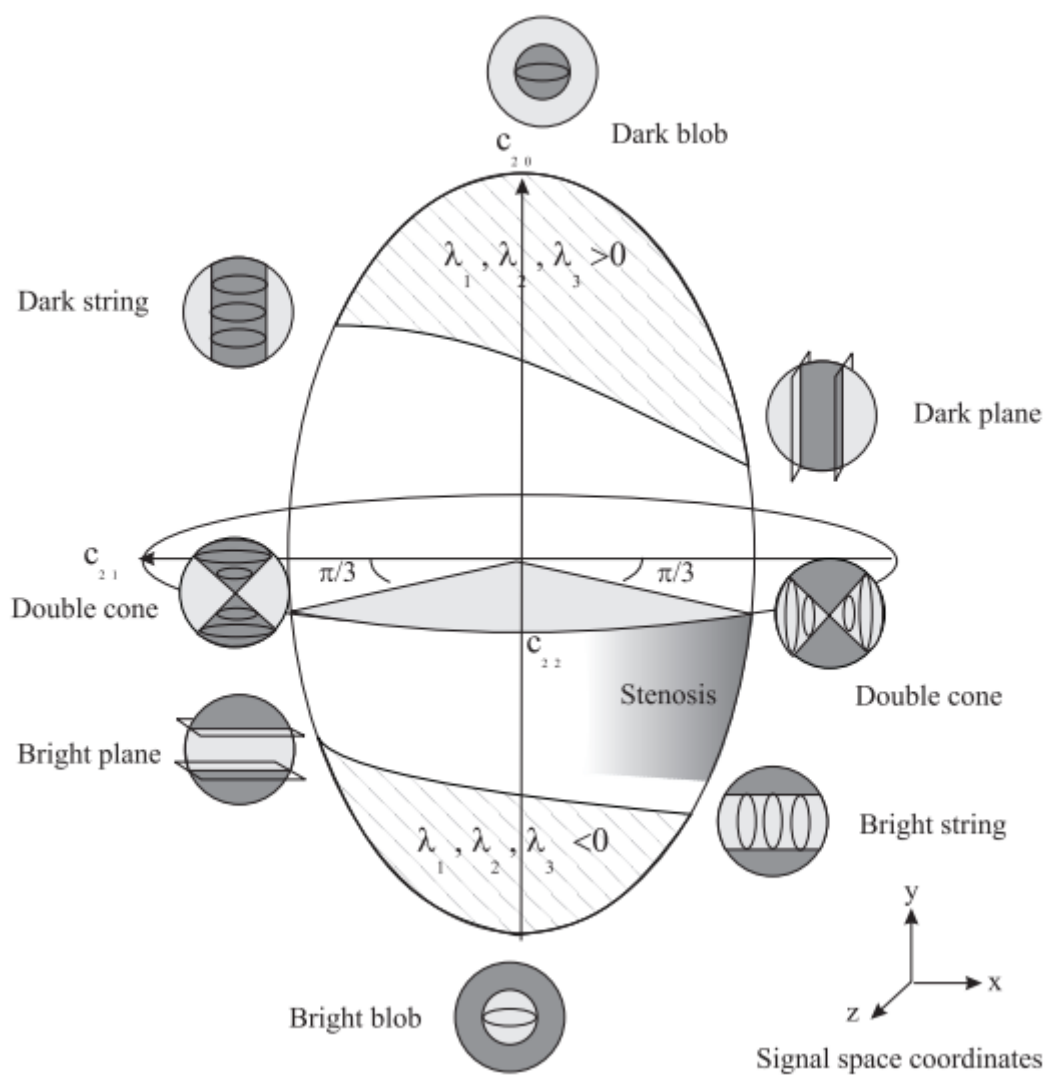


**Figure 2.7** – Shape space from [149] and [261] defined based on the Hessian matrix eigenvalues variations. Vessels are typically matched to the bright string prototype. Illustration based on material from [261].

of the proposed approaches. The classical categorization schemes focus on the employed algorithm characteristics rather than the employed vessel model or the target features. In the review proposed by [LESAGE \[250\]](#), vessel segmentation approaches are analyzed based on three aspects: The hypothesis made on the target vessel model, image information used to extract the vessel, and the segmentation techniques employed to obtain the final segmentation results. This classification seems to present the most complete way to categorize the different works. However, it results in a complicated networks making the analysis of a vessel segmentation approach not straightforward as an algorithm may combine different techniques related to the three aspects. In fact, the concepts of vessel models and image features could be confused when trying to categorize a new segmentation algorithm. A possible categorization scheme could be based on the information level that the proposed algorithm provides. High level segmentation techniques would refer to approaches that offer only a rough segmentation of the vascular structure such as thresholding and region growing based algorithms. Low level extraction techniques include algorithms that provide more precise information about the target vessel such as the vessel centerline, the lumen radii and other quantitative information.

Hereafter, we provide a brief review of vessel segmentation and extraction techniques. We propose to separate the segmentation algorithms into two main classes based on a simple observation. A vessel can be easily presented by two basic features: a centerline that describes the vessel path, and a contour delimiting the vessel volume. Depending on the target task, one could classify an approach to one of the previous categories. For some schemes, one single approach may provide both tasks by combining two techniques. Typically such a scheme could be designed as following:

- A first step of vessel segmentation followed by a step of centerline extraction from the vessel segmentation
- A first step of vessel centerline extraction followed by a second one of vessel surface extraction
- One single step of iterative centerline points detection and vessel cross section extraction

Furthermore, each category will be organized on sub-categories depending on the knowledge level involved in the design of the proposed approach as well as the character of the employed algorithm. Because of the large number of works dealing with vessel segmentation challenge, we are not able to list all the published method. We will present some of the most used ideas to illustrate each class.



### 2.4.1 Centerline extraction

The computerized assessment of cardiovascular diseases is strongly dependent on the extraction of the vascular tree centerline. In fact, vessel centerline is the foundation of some advanced visualization techniques such as the curved views and multi-planar views (see section 1.3.2.2). Besides its importance for visualization tasks [24, 70], vessel centerline is necessary for accurate measure of the vessel lumen diameter and automatic quantitative analysis such as stenosis or aneurysm grading and plaques volume measuring.

In the literature, we can distinguish between three main approaches for vascular (tubular) structures centerline extraction: 1) Optimal paths extraction methods aiming to find an optimal path between two (or more) seed points, 2) Tracking algorithms operating locally to extract the vessel centerline based on the local structure geometric specificity (e.g. tubularity, orientation) and 3) Skeletonization of a pre-segmented vessel mask.

#### 2.4.1.1 Optimization Approaches

Several authors proposed the use of optimal cost path approaches on the original or pre-filtered image to (semi-)automatically extract vessel centerline. Indeed, the problem of vessel axis extraction can be expressed as the definition of an optimal path in a weighted graph modeling the image voxels, as well as their neighborhood relations and intensity. However, the centerline correct location is favored by the design of appropriate cost metrics to be optimized. Optimal cost path approaches need the definition of at least two points (e.g. the vessel extremities). Such start and end points might be defined manually by the user or extracted automatically using image segmentation or pattern recognition approaches. Moreover, some subsequent user-interaction can be added to guide/correct the vessel centerline in challenging configurations (e.g. presence of plaques, moderate image quality).

The minimal path could be extracted with the standard minimal path search technique: the Dijkstra Algorithm [117] for the discrete  $L_1$  path optimization schemes [170, 334, 461]. However, the limitation of this approach is its discrete nature which could lead to metrication errors. An alternative for the continuous formulation of the minimal path problem was the optimization schemes based on the fast-marching algorithm [388]. It approximates the Euclidian cumulative cost, yielding sub-voxel accurate paths. This approach was applied in [109] with a proposed heuristic to obtain a centered path inside the vessel (see figure 2.8). In [230, 232], the centerline was extracted using a fast marching starting from the end point of the vessel to the root followed by a backtracking of the front propagation using the local intensity gradient of the geodesic distance transform. The level-set approach has been generalized to avoid the backtracking step



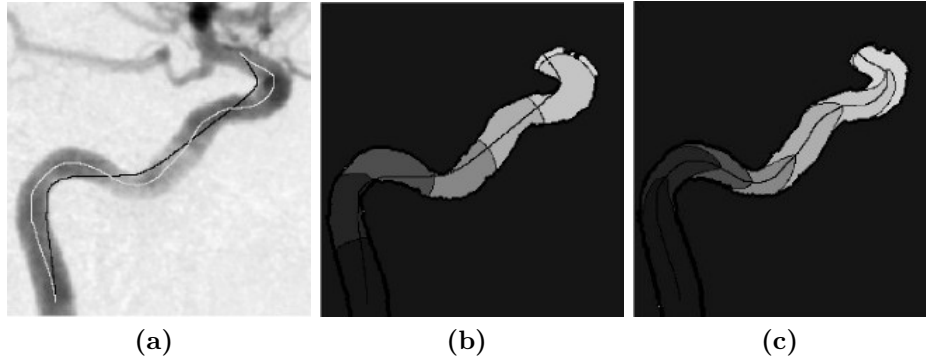


**Figure 2.8** – Vessel centerline extraction using fast-marching optimization. Comparison of the two paths obtained using a normal (a) and a centering (b) potential. Illustration material from [109].

in [268]: The algorithm directly provides the geodesic path as the zero-level set of a higher dimensionality function (co-dimension two).

As mentioned before the design of an appropriate cost metric to be optimized is crucial for a robust centerline extraction. Several metrics has been defined for the minimal path computation in the context of centerline extraction. In [415], a *Medialness* measure based on multi-scale cross-sectional vessel modeling and boundary measure was defined [228]. The vessel axis is then extracted by a minimal cost path search on the medialness image between two given points [109]. Similarly, the Dijkstra algorithm was used in [170] with a medialness based cost function. A distance map was computed in [428] for the minimal path extraction. Zhang et al. [490] proposed a cost metric defined from the Sato vesselness measure. The path is then extracted using a live wire algorithm. In [118], an Axial Symmetry Image was constructed using a two stage hough-like election to enhance axial symmetries. The centerline is extracted by searching the minimal path between a supplied distal point and a point on the aorta in the symmetry image. Furthermore, Li and Yezzi [252] and Wink et al. [462] proposed minimum cost path techniques in which scale is included as an additional dimension in the cost image. In [461], the proposed method is an extension of the minimum cost path search based on a multiscale vessel enhancement filter [462], but propagates the wave front through the filter response at a range of scales instead of through the maximum response of the filter, thus, inherently providing scale selection.

Minimal path approaches are usually employed in interactive frameworks. In fact the process needs the definition of start and end points for each vessel segment. To cope with the end point definition, some works defined automatic stop criteria. One can cite, for example, the heuristic thresholds on the medialness values in [415] or the exploitation of the geodesic distance increase rate to stop the propagation in [109].

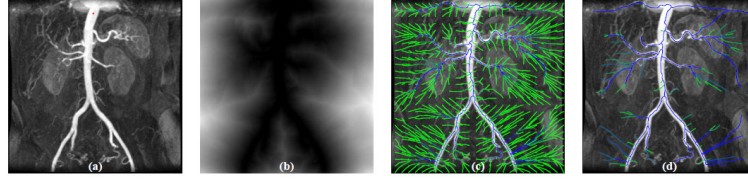


**Figure 2.9** – 3D vessel tree extraction using minimal paths: (a) Initial image, (b) minimal action map, (c) obtained tree and (d) final tree after thresholding on the geodesic voting scores. Illustration based on material from [299].

The whole vessel tree could also be extracted using the minimal path approach to extract the different vessels and then merge the resulting paths in a single tree. The different paths could be backtracked to a proximal single seed as in [170]. The geodesic voting is an approach relying on the assumption that vessels axis converge in a highly anisotropic region. This approach helps selecting the accurate vessel centerlines located in a high path density region [299] (see figure 2.9).

Despite their low theoretical algorithmic cost, the practical computational cost of the minimal path search based methods could be a limitation for their clinical use. The choice of computing the path starting simultaneously from both sides could reduce this cost.

Other optimization schemes for centerline extraction rely on model fitting with respect to the images' embedded data. Frangi et al. [147] proposed a fitting approach based on an initialization of the vessel axis as a geodesic path on the vessel wall and the attract this path inside the vessel using the vesselness values. The cardinal spline were preferred in [465] for their intuitive geometrical behavior. The robustness of this approach is highly dependent on the defined model and thus the local minima issues tending to affect the optimization process could be mitigated.

#### 2.4.1.2 Vessel Tracking

Centerline tracking algorithms works locally without pre-processing the whole image. In fact, such approaches define the centerline as a self-contained structure and do not require any preliminary image processing step. The main idea of a tracking approach is to extract the object of interest (e.g. the centerline) by iterative prediction and correction steps. Starting from a seed point inside the vessel, a candidate point is predicted using an estimated vessel direction. The vessel direction might be determined using a ray casting approach [460], model fitting [153] or vesselness measurement [261]. The new position is the defined by moving forward with a predefined step. The step could be fixed or depend on the vessel scale, and hence is adjusted locally in order to avoid getting out the vascular structure. The predicted position is

then adjusted using some medialness or vesselness measure, and added to the vessel centerline. The centerline extraction is usually performed while traversing the vessel by looking to the 2D orthogonal plane to the current vessel direction. Vessel models (intensity or geometry) could be used for centerline points and direction prediction and correction.

*Prediction process* consists in the search of the next vessel center and direction. The estimation of the new position is highly constrained to the new direction choice. In fact, forwarding in a wrong direction could lead to tracking failure and premature ending of the process. The new vessel direction is predicted referring to the image features or geometric models. From a given vessel point, a new position could be predicted by conserving the same vessel model and extrapolating it in the direction of the current vessel [425] (fig. 2.10). Around high curvature or branching points this assumption would fail. To increase the robustness, a range of predictions could so be considered. In [152, 153], a collection of possible vessel continuations is generated from the current vessel segment. Those continuations are placed on a sphere defined by an angle of deviation from the current vessel direction. Filtering the next vessel position and direction has also been proposed [140, 460] using a sliding volume to detect branching vessels. A b-spline model was then used to interpolate the centerline points. Based on Gaussianity and linearity assumptions, Kalman filtering has been applied for this purpose in several works [163, 467–469].

The local geometry feature of the vessel was used to estimate the vessel direction and improve robustness. In [70], a hessian-based estimation was performed to extract the principle direction (corresponding to the small eigenvalue). An analogy could also be established between voxel intensity and mass as an alternative to the use of second order derivatives. A simple tubularness criterion would state that the gravity center of the region of interest (e.g. the vessel segment) should be located near to the centerline. Moments of inertia has been used in [41, 185, 192]. Agam et al. used the gradient vector distribution to estimate the vessel orientation [11, 12]. However the use of complex geometric models, that depend on several parameters, could lead to the process failure and premature stopping specially near pathologies and bifurcations where the vessel model is often not suited.

The prediction step is usually followed by a *correction* one to improve the tracking robustness. The predicted point could be refined (i.e. centered) with refer to a sphere-based geometric model. The re-centring scheme aims to search the best point that fits the best to a spherical neighborhood model relying on local threshold [76] and inertia moments [75, 184]. In [75], the process is based on a minimization of a criterion that combines the intensity variance with the spatial inertia moments. Correction could also be performed using 2D active contours to extract a robust segmentation of the cross section [248]. One of the main problems encountered

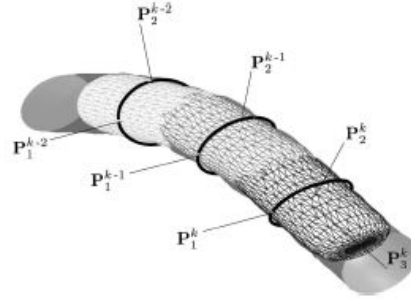


**Figure 2.10** – Ellipsoid Fitting in a tracking scheme. [425]

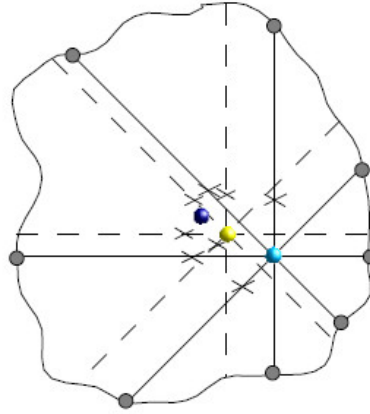


**Figure 2.11** – The iterative centerline correction process proposed in [453]. At each iteration, a new center point is defined using the centers of gravity of each two opposite points on the vessel 2D border. The final point is closer to the real center than the initial one.

during the vessel point prediction is that the predicted center could be located outside the vessel lumen which needs a robust recentering. This is guaranteed when applying the recentering schemes in a local neighborhood [23, 460].

Medialness feature optimization could also be useful for recentering the predicted vessel center [415]. We can simply re-center the point as the center of mass of the 2D cross section contour points detected with a ray casting approach as in [453] (see figure 2.11). Several works have exploited the 2D cross features to correct the prediction result [23] [322] [460]. 3D models were also locally optimized to correct the predicted vessel center as an alternative to 2D re-centering [152] [425] [469].

Usually, the tracking process needs the interaction of the user to define the starting point(s). Some papers propose a fully automatic tracking scheme. In [219] starting points are initialized using the fast marching level set method. To ensure a best tracking result the definition of

robust termination criteria is important specially when end points are not predefined. We can so prevent the detection of false positive and stop the tracking once we go out the vessel. Those criteria are mainly based on intensity statistics' changes (intensity standard deviation, mean value, gradient...) around the current vessel segment [184, 483] estimated on a spherical or radial neighborhood. Other assumption on the length of the tracked vessel or the quality of the extracted centerline might be used to stop the tracking process.

Generally, tracking schemes follow a single vessel. To extract the whole tree one can manually reside starting point and the merge the resulting centerlines. Automatic approaches were proposed to deal with the whole vessel tree extraction. A simple process would be based on topological knowledge: the storage of bifurcation points encountered during the tracking of a selected branch and then tracking the branching vessels starting from those seeds [76, 140]. Several starting points could also be initiated as in [219, 230, 232] using a fast marching level set method starting from the aorta and reaching the distal ends of coronaries. The tracking is then performed by backtracking the front propagation starting from the end points.

Thanks to their local search approach, tracking schemes represent low computational cost which make them suitable for large 3D datasets and rapid clinical tasks. However, the limitation of such methods is their tendency to fail in correctly tracking vascular structures in the presence of high curvatures, bifurcations or vascular abnormalities (e.g. stenoses or aneurysms). This usually cause the premature stopping of the tracking process. Moreover, when tracking one single branch, the algorithm may be attracted by an other nearby vessel or goes on a non desired branching vessel. Therefore, most of the workstation propose manual edition and control tools to allow the user to correct the tracking result if needed.

### 2.4.1.3 Skeletonization

The third category extracts the centerline from a pre-segmented vessel lumen. After a binarization of the segmented vessel volume, the centerline is obtained by applying a skeletonization step. Several works have been presented dealing with this topic. Most generally, skeleton extraction approaches are based on the definition of the medial axis [38] and the distance map to extract the centerline points (i.e. lighter pixels in the distance transform image)[46] by removing points in a particular order. The Gradient Vector Flow was used in [175] to extract the skeleton as an alternative to the distance transformation. In fact, the GVF vanishes at center curves independent of the object shape which allows a robust extraction of the centerline near to junctions. Similarly, in [26], the skeleton was extracted based on properties of the Gradient Vector Flow to derive a tube-likeness measure combined to a medialness measure. This work

is applied in [25] to extract coronary centerlines using ridge-traversal. Besides, gray values and centerline length are used to select correctly tracked coronary centerlines. In [443], the coronary tree skeleton is detected by iteratively finding the next point (corresponding to the strongest neighbor) on the fuzzy connectedness tree.

A second general approach for skeletonization is the morphological thinning based on the definition of simple points and their deletion while preserving the object topology [43, 46, 335]. However this approach is noise sensitive and requires a careful spurious branches pruning. Several post processing steps of the resulting skeleton could then be applied to improve the robustness [45, 46, 442]. Skeletons could be filtered by removing some points without changing its topology. Several criteria could be used such as the the curve length, the curvature and the quantity of information from the original shape contained in each part of the skeleton [438].

Inhibitor sets could be defined to preserve the visual aspect of the initial shape in the skeleton and thus compensate for the generation of insignificant branches. Those points should not be removed while the thinning process and will then result on a satisfactory visual result. In [98], this set of points was defined using the discrete bisector function.

## 2.4.2 Vessel extraction

This section is dedicated to review the different approaches for vascular lumen segmentation techniques. We can distinguish between two categories: 1) Volume segmentation dedicated approaches and 2) Contours extraction techniques. The first category of techniques offers a volumetric description of the vessel's lumen. The second category aims to delineate the vascular lumen by searching extracting its surface applying 2D or 3D contour extraction schemes. The first class of approaches provides a rough segmentation of the vessel volume generally used for visualization and rendering tasks. This type of approaches generally uses classical segmentation techniques not specifically designed for vessel extraction. The last class contains techniques providing a more detailed description of the vessel volume by extracting the precise 2D or 3D vessel wall contours. Hence, additional quantitative information might be easily extracted (e.g. vessel cross section area and mean radii, vessel orientation). Such approaches are usually proposed for an advanced vessel analysis framework.

### 2.4.2.1 Volume-based Approaches

This class of techniques employs generic segmentation algorithms borrowed from image segmentation literature and adapted to vascular structures segmentation. The proposed approaches

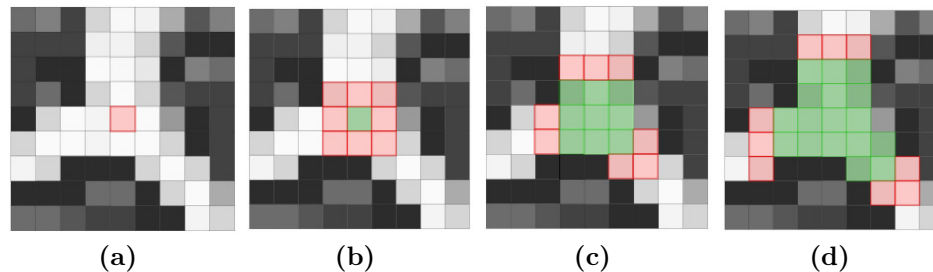


**Figure 2.12** – Vessel segmentation using the Region Growing approach. Starting from a seed point (in red in (a)), neighboring voxels are added to the segmented region if they meet some defined inclusion criteria (generally computed using the voxel gray value).

aim to extract a 3D volume describing the vascular structure. This class generally includes the well known propagation based techniques, thresholding and clustering approaches.

#### 2.4.2.1.1 Region growing approaches

Region-growing is one of the most commonly used and oldest techniques for vascular structure segmentation [504]. They proceed by successively including neighboring voxels starting from seed points assumed to belong to the vessel (inside of the vessel, on the root or the distality) [10]. The including process is based on defined propagation criteria to ensure the correct segmentation of the vessel (intensity or geometry criteria).

Generally the seed points are provided manually and for specific schemes they should be located in particular regions (the root of the vessel tree, end vessel points..). In the case of a fully automatic framework, seeds could be extracted automatically thanks to a pre-processing step [314]. In [219], the segmentation of the coronaries was preformed by a region-growing approach from the starting points of the LCA and the RCA. The two ostia were extracted thanks to an automatic aorta segmentation (2D Hough transform and then an intensity based propagation). Similarly, seeds selection from a blood pool class was proposed in [232] to automatically segment the aorta in a 3D CT angiography. Bouraoui et al. [47] proposed a fully automatic method of segmentation of the coronary arteries in X-ray images by combining the gray-level hit-or-miss transform and the region-growing. First, the aorta is segmented by application of a gray scale hit-or-miss transform followed by a region-growing. Then, the coronary arteries are detected using a hit-or-miss based region-growing initialized from the aorta.

It's also possible to define several seeds for different vessels. This would be useful in case of vessel separation or artery/vein discrimination. Ad hoc propagation criteria could be used to perform this competitive region growing. By duality to skeletonization, the region growing



process was used to segment vessels with seed points located in the background (could be easily automatically defined). Simple points are added to the background with respect to intensity and topological criteria [121, 337].

Propagation criteria could simply be defined based on the vascular intensity model. A first segmentation was performed in [45] using a simple intensity threshold, which makes the process very sensitive to noise, loss of signal and contrast agent inhomogeneity. Region growing using two adaptive threshold for stopping criteria was proposed in [337]. To define those thresholds for each region an atlas has been constructed from MRA brain images. Prior information on the vessel could also be used to guide the propagation such as the vessel shape and size [315].

Region-growing approaches are specially popular for their simplicity (low-level information, simple inclusion criteria) and their computational efficiency (generally linear computational cost). Indeed, this technique is commonly used in most commercial software for vessel analysis. Their local exploration of the volume makes them perfectly suitable for large datasets segmentation. However, because of its voxel-wise approach, region growing is prone to leakage (false positive) and holes (false negative) issues. In fact, the method could eventually fail to extract connected vessel with presence of a signal loss. Trying to deal with this issue by using permissive criterion could cause false positive detection and an over-segmentation of the vessel tree. To reduce the false positive risks, a growth limitation could be used based on the size of the target object to stop propagation once a fixed size is reached [294]. An other approach to prevent leakage was the use of a competitive region growing approach to segment simultaneously the object and its background in [478]. The work of Wesarg and Firle in [453] could also be considered as an interesting approach of region growing in which the vessel wall is searched along a 1D discrete ray following filtered 3D direction.

#### 2.4.2.1.2 Wave Propagation

Wave Propagation strategies have been introduced as approaches to segment the vessel volume while propagating along the vessel direction [481]. It consists in evolving a front inside the vessel which is constrained to remain normal to the vessel direction at each step.

They offer a spatial coherence during the propagation process which is not afforded with classical region growing approaches besides of an advanced topological analysis. Several works have been devoted to the use of discrete waves such as [214, 481]. In those cases the propagation scheme is similar to an ordered region growing process in which the candidates are included in an order to respect a correct front geometry [481]. An other alternative to an ordered wave propagation is the fast marching algorithm [232, 387]: The voxels are visited in an order



according to their geodesic distance from the vessel seed, given an adequate vessel-dedicated potential.

Different wave speed function was used in the propagation schemes: Uniform Euclidean speed and binary inclusion was used in [266], a weighted geodesic speed was defined in [384] and a dynamically adapted speed in [277].

### 2.4.2.1.3 Thresholding

In CT and MR angiography, vessel voxels have relative higher intensity values compared to surrounding tissues. Based on this observation, vascular structures could be separated from other non vascular structures using appropriate threshold values. In an ideal world, one single threshold value might be used to separate the two classes. However, due to image artifacts, noise, image intensity overlap between different tissues and the non homogenous diffusion of the contrast agent inside the vessel, the resulting segmentation from applying one single threshold is not satisfactory in real cases. Meanwhile, as thresholding only classifies a voxel depending on its intensity value, it is a very time efficient technique allowing real time interactivity. Therefore, most of commercial systems propose a manual tool for thresholding. For better isolation results, a threshold range could be defined by the user to extract vascular structures. Generally, the selection of the appropriate threshold value(s) is the key issue for a good segmentation result. Therefore, many works have been dedicated to the automatic selection of the optimal threshold value as in [477]. Furthermore, to overcome the limitation of conventional thresholding (e.g. sensibility to noise and miss-classification of non vascular high intensity structures), locally adaptive thresholding could be used to segment vessels as proposed in [458]. In fact, local thresholding seems to be promising for vessel structures segmentation with a varying background and object intensities, which is very common in medical images.

Apart from its use as a standalone segmentation tool, thresholding may be incorporated with some other more advanced methods. It may be used in a pre-processing step to limit the computation of the remaining steps. For a better selection of the voxels inside vascular structures, thresholding can be applied on vascular-specific features as the vesselness measure computed using the Hessian eigenvalues [149, 261, 373]. In fact, using vessel enhancement filters before thresholding reduces the missclassification error. Although the result is still not perfect, as different anatomical structures may present a tube-like shape and as vessel may deviate from a perfect tubular shape (e.g near bifurcation and pathological points), it allows a better selection of tubular structures that could be used as a start point for further processing.

#### 2.4.2.1.4 Clustering

Clustering aims to find a “natural” partitioning of the image structures by assigning each point to the “nearest” cluster. Two commonly used clustering algorithms are K-mean [459] and Fuzzy C-means [304]. The K-mean clustering method is usually used to hardly separate the image into different homogenous classes. The algorithm automatically partitions the image by minimizing the average distance from each voxel to the centroid of the nearest cluster. On the other hand, Fuzzy C-mean provides a soft segmentation of the image by assigning to each voxel a degree of belonging to the different clusters. A hard segmentation could be extracted by allowing the voxels to have membership of cluster in which they have the maximum value of membership coefficients. Different similarity measures can be defined to construct the different cluster depending on the target application. For image segmentation, connectivity, distance and intensity are commonly used to form the clusters [151]. More sophisticated similarity measures are based on the calculation of a texture feature vector around the voxel neighborhood and hence the point is classified into the most similar region.

The strength of these approaches is that they are perfectly suitable for multidimensional data. However, it could suffer from the same weakness as thresholding method (e.g. noise and intensity overlap between different tissues). Moreover, clustering algorithm are sensitive to the initial partition and the stopping criteria.

#### 2.4.2.2 Contour-based Approaches

Contour-based approaches aims to extract a surface describing the vessel wall rather than extracting the vessel volume. They provide a more precise representation of the vessel and are usually preferred when we need further quantification of the vessel lumen diameter or area. Some of these approaches are applied after a volume based extraction of the vessel to define the vessel wall.

##### 2.4.2.2.1 Active Contours

Active contours (also known as deformable models) are techniques aiming to fit a geometric hypersurface to the image to segment a defined object. The shape of hypersurface is deformed from an initial model guided by several forces. A general evolution scheme uses two antagonistic forces (eventually combined of several ones): a "model-driven" force (internal force) dedicated to preserve the model geometric properties as smoothness and a "data driven" related to the image contents. Deformable models have been intensively used for segmentation of several object types. In fact they allow the representation of any arbitrary shape and offer a topological

adaptivity to the target object besides of a sub-pixel precision making them suited for small object segmentation.

- **Explicit Active contours :** Active contours, usually named Snakes, are one of the most classical methods used for contour extraction [210]. They rely on an explicit Lagrangian formulation of a contour evolution driven by an external force, derived from the image, and an internal model-based force. The external force attracts the contour to the region of maximum gradient corresponding to the object contour, hence minimizing the external energy. Meanwhile, the internal force controls the smoothness of the obtained contour by minimizing the internal energy. The internal energy is minimized when the curvature of the contour is null. This force allows to avoid leakage into neighboring image regions when confronted with weak edges. It also allows to accurately segment objects on noisy background.

Their simplicity and computational efficiency in 2D case, make them very useful to extract the vessel cross section contours as in [185] and [256]. Generally, they are used to extract 2D cross-section contours from the vessel centerline (obtained with one of the techniques explained in section 2.4.1). Moreover, active contours can achieve subvoxelic precision which is desirable when segmenting relatively small vessels. To overcome local minima issues, Rueckert et al. [366] proposed to use active contours coupled to stochastic relaxation.

The parametrization becomes more complex for 3D cases and the implementation of simple active contour is not suited for vessel extraction as they prevent the extraction of thin and elongated surfaces. For this purpose specific refinements were proposed. One can mention for example, the work of Toledo and al. [420, 421] specifically designed for vessel segmentation: The Eigen-Snakes. The direction of the target vessel, estimated using the analysis of the principal component of the gradient vector direction, was exploited to formulate the energy to minimize. A deformable tubular model, is introduced in [480] where a surface mesh is optimized with respect to the centerline curve in a tubular coordinate system. Frangi et al. [146, 147] used a B-Spline tensor surface to extract the vessel surface optimized using explicit control points and an incremental optimization schemes for more refinements 2.13. More recently, a new local region-based energetic formulation was introduced by Mille and Cohen in [298]. The proposed parametric model evolves a centerline curve with varying radius and was extended to 3D cases in [299].

An other variety of active contours are the topology-adaptive snakes introduced by McInerney and Terzopoulos in [284]. The T-snakes offer the possibility of controlling contour

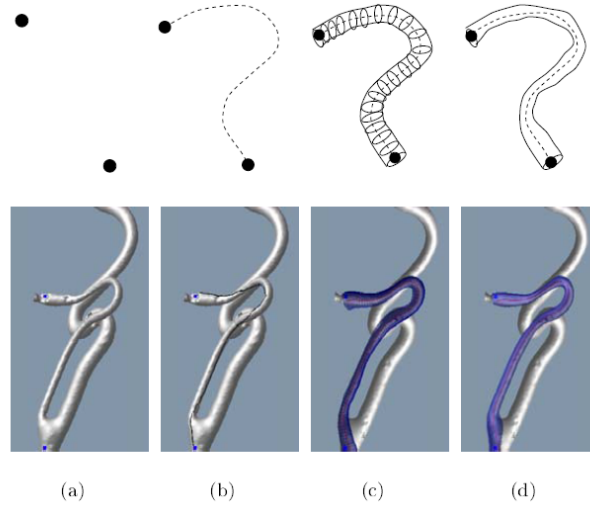


**Figure 2.13** – Vessel Wall extraction using a flexible B-spline. a) User selected start points b) Initial geodesic path computed between the two points, c) Evolution of the geodesic path inside the vessel and initialization of the vessel surface, d) Resulting vessel wall after deformation [149]

splitting and merging which allow a better extraction of thin and branching vessels with a specific re-parametrization scheme. In [31], a new prior based on the appearance of the target object was incorporated within the geodesic active contour framework with shape priors, seeking for the object whose boundaries lie on high image gradients and that best fits the shape and appearance of a reference model. The output contour results from minimizing an energy functional built of these three main terms.

- Level Sets and implicit active contours:

An other classical type of deformable models are the implicit active contours. Implicit (Geometric) active contours are represented implicitly as level sets of two-dimensional distance functions which evolve according to an Eulerian formulation of contour evolution through partial derivative equations. They are based on the theory of curve evolution implemented via level set techniques. The contour is represented by the zero-level of the higher dimension function (level set). This representation of active contours allows to handle changes of the target objects.

A vessel dedicated level set scheme was proposed in [268]. The theoretical core of this approach is to evolve a 1D curve in a 3D domain. Its based on the evolution of an initial boundary curve estimate toward the true vessel wall using partial differential equations. This scheme uses a codimension-two regularization force with the definition of a new energy term related to the vessel direction (the lowest curvature). More accurate results

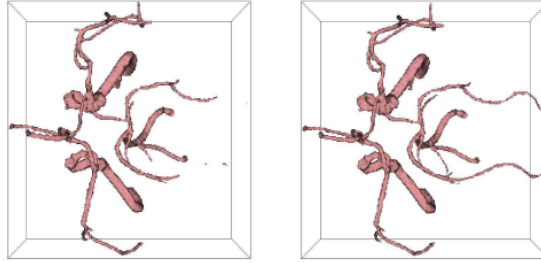


**Figure 2.14** – Brain Vessel Segmentation Using: (left) Curves [268] and (right) CAC [473]

are obtained in [473] using the Capillary Active Contours (CAC) which uses an alignment edge term to evolve the surface into thin branches of blood vessels 2.14. In order to efficiently steer the level set into the vessel boundaries, background and vessel intensity were estimated in [278] from the intensity histogram.

The most important advantages of level set approach are its ability to follow topological changes while surface evolution and it does not suffer from the problems of parametrization due to its implicit formulation. However, Level sets techniques induce an additional computational cost and the critical issue of stability and convergence of this method requires a specific care in the implementation.

Several works were dedicated to best adapt deformable models to vascular structures extraction. An idea was to use the flux maximization instead of curvature-based regularization. This aims to align the surface normals with an appropriate data-based vector field (e.g. the gradient field) and thus using the direction information besides of the magnitude one. This idea was exploited using the derivative of a multiscale gradient flow in [434] and multiscale Hessian-based flow in [110]. Local variances, measured with first order derivatives, were used in [242] to improve the robustness near adjacent structures and get more stable and accurate results than Hessian-based measures.

Deformable models are very appreciated for their flexible framework allowing the integration of several regularization forces. Besides these methods are robust against weak edges and noisy structures. However, due to spurious local minima present inside the vessel, the contour evolution could stop at insignificant regions where we notice some intensity variation resulting in significant gradients. A possible way to deal with this issue is the definition of an initial contour close to the desired result coupled to a robust optimization scheme. Furthermore, the use of vessel dedicated features incorporated in the internal and external forces should help overcoming such issues. However, the major limitation of the use of the level set methods on 3D clinical data is the long associated computational time compared to explicit active

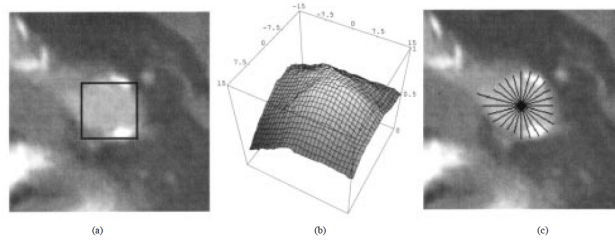


**Figure 2.15** – Vessel Center Extraction: (a) Original CT Image (b) Correspondent center likelihood inside the black square (c) Rays used for the estimation of the maximum center likelihood, Illustration from [460]

contours methods. Some efforts have been made to accelerate the performance by limiting the computation of the level-set function to a band of few [9] or one single pixel wide [455].

#### 2.4.2.2.2 Ray Casting

Ray casting is one of the most used techniques for 2D cross section contour extraction [322], [453], [460], [170]. Their theory is based on the detection of the vessel boundary on equi-angular rays thrown from a provided point inside the vessel. Rays are drawn on the 2D cross section perpendicular to the estimated vessel centerline at that point. The center of the vessel could after be computed using the extracted contour point. The contour search is hence performed along 1D rays which increase the level of computational performance compared to other contour based approaches.

Contour candidate points are generally detected along the ray using intensity [453] or gradient based criteria [460]. The robustness and coherence of the approach is clearly related to the number of rays used to detect contour points. To improve the results additional constrains could be embedded to ensure a radial coherence between the neighboring contour points. Dynamic programming has been used as an optimization scheme to extract the best contour from a set of detected point as in [435].

Usually, the position of the starting point (the point on the vessel axis) is refined. A new center point is estimated as the center of mass of the candidate contour points [322, 435, 453, 460] (see figure 2.15). The process of ray casting and recentering might be repeated until a robust contour/center are obtained [435]. Ray casting was also used to compute a multiscale medialness measure by summing the responses along rays in a distance-wise manner as in [170]. The polarity of the gradient sign was used to decrease the influence of eventual hyper intense nearby structure such as calcification or bones. Gradient polarity was also employed in the work of [453] and [460].

### 2.4.2.2.3 Morphological Approaches

Mathematical morphology techniques tries to fit a “structuring element” (binary or gray-scale) to every voxel of a selected region of the image. Basic operation are erosion (removing points of the object where the structuring element does not fit) and dilation (removing points of the background where the structuring element does not fit). Interesting morphological filters used for segmenting vessels are mainly opening, closing and thinning. The opening and closing operation enable, respectively, the filtering of small bright structures in a dark background and the removal of small dark objects over a light background. Using such basic mathematical morphology operations, other high level approaches are designed for medical images segmentation. Popular approaches used for 3D vascular segmentation includes Watersheds [338], the grey-level hit-or-miss transform [47, 316] and the connected filters [72, 457].

Thin objects could be filtered using morphological operation with appropriate structuring element like segments or paths. To detect arbitrary oriented objects we can consider a family of oriented segments and compute a supremum of openings or an infimum of closings. The use of family of paths (elongated, not necessarily straight structuring element) could also be used to filter out long thin objects [15]. Some works have taken in account for noise and disconnections using families of incomplete segments or the incomplete paths [408]. In [412] the use of path and segment morphological operators gives better results than linear and steerable filters for 2D thin structures segmentation. In [78] vessel candidate points are iteratively selected using a local gray scale morphological 3D reconstruction. Starting from a point P on the vessel, the local neighborhood is reconstructed using a Top Hat opening with a sphere of radius similar to the vessel width as structuring element. Hence, only bright sections of tubular like structures with a gray level and a width matching those of a typical vessel are extracted. In [129], two vessel segmentation and filtering techniques based on recent advances in mathematical morphology are presented. The first filtering technique is an extension of the work presented in [412]. It combines a spatially variant mathematical morphology approach and a derivative based approach to segment 3D vascular structures. Then, the work described in [128] presenting an example-based interactive vessel segmentation algorithm using a component-tree-based technique is described. The two approaches are evaluated on synthetic data and real cases. However, additional qualitative evaluation on clinical data is mandatory in order to assess the robustness of the proposed approaches for clinical use. Challenging cases (e.g. thin and pathological vessels) should be also tested.

## Part II

# CT angiography segmentation





---

# Chapter 1

---

## Automated Heart Mask Extraction

Depending on the field of view, cardiac CTA data sets can include extra-cardiac thoracic information (aortic and pulmonary vascular structure, lungs and liver, spine, sternum and some ribs, ...). See figure 1.1. Thus, interpreting and analyzing such a wide breadth of information in the context of coronary arteries lesion assessment is a time consuming task. A robust heart anatomy analysis demands the removal of all non cardiac obscuring structures (e.g., lung, liver, and rib cage) to clear the heart 3D view and enforce attention to its structures. With the increasing number of CT images to be processed per day, automated tools for heart contours extraction would be appreciated to reduce the required effort and time for such data analysis. Hence, automated heart isolation would afford an accurate and fast visualization of coronary arteries. In fact, this helps physicians to efficiently localize suspicious coronary segments and thus eliminates the tedious task of manually removing the heart's surrounding organs in CT volumes (see figure 1.2). Moreover, such automated heart delineation tools allow to eliminate the inter- and intra-observers variability.

Besides, robust heart segmentation could be used in different clinical applications such as cardiac and vascular diseases investigation or the study of cancer in thoracic region. The result of heart segmentation could be used to define the heart short and long axis and thus generate more accurate views of the heart chambers (see section 1.3.2.2). Heart volume delineation can also be useful for real-time interventional procedures guiding. Similarly, the heart segmented volume would be useful for radiotherapy treatment planning in order to prevent it from being irradiated. In fact, for lungs or liver cancer treatment, the heart should be excluded. Usually, the radiotherapist manually defines a large margin around sensitive organs that must not be affected by radiation. Heart volume delineation can also be considered as a pre-processing step for automated cardiac structures segmentation (coronaries and heart chambers): the heart



volume could be used as a region of interest which would reduce the overall processing time as well as the amount of false detections. Heart volume can also be used as a reliable landmark in a multi-modality image registration frameworks: computed tomography, magnetic resonance imaging (MRI), positron emission tomography (PET) or single photon emission computed tomography (SPECT) registration [74].

However, automated heart isolation is a not an easy task to do. Several challenges, mainly related to the heart anatomy and the image characteristics make this task difficult.

## 1.1 Prior Knowledge and Challenges

### 1.1.1 Prior Knowledge: Anatomic and Appearance Priors

Regarding its complex and variable shape, prior knowledge on the heart anatomy is mandatory to be able to reliably delineate this organ's volume in CT angiography. The most important prior information about the heart is its "*conical shape*" [397]. Besides, the approximate location of the heart can be considered as a prior knowledge for heart segmentation. The heart lies between the right and left lungs behind the sternum [397]. It also lies on the diaphragm with its apex pointing to the left thoracic cavity. The size of the heart could also be used as a prior knowledge to guide the segmentation and avoid over-estimations (see section 1.1.1.3). Besides, prior knowledge on other non cardiac structures (lungs, liver, spine, aorta) provides very useful information for heart segmentation. For instance, characteristics of the lungs (position and size) could be used to extract their mask in order to constrain the heart isolation process.

Appearance knowledge about the heart structures and its surrounding organs are also a valuable information enabling a better segmentation. Depending on the imaging modality, this kind of knowledge helps to capture the main features of the heart and other organs. For instance, using CT, lungs and bones can be detected easily based on their intensity properties. Moreover, heart chambers and other blood pools (e.g. aorta and coronaries) could be extracted in enhanced CT using appropriate intensity values (see section 1.2.3.1). Available information about heart muscle intensity could also be used to guide the segmentation process and avoid including non cardiac structures in the final result.

Those prior information must be used carefully. In fact, some properties may differ from one patient to another for different reasons. As stated in section 1.1.1.3, the heart size and shape could vary between individuals and during the heart cycle. Therefore a single rigid heart model could not be used to represent the heart in such cases. Images coming from different scanners with different acquisition parameters and reconstruction algorithm results also in

different appearance properties of the structures of interest. Thus, prior knowledge should be considered carefully in order to guide the segmentation process and make it more robust while keeping a freedom degree, to be able to capture all the possible configurations of the object.

### 1.1.2 Heart Isolation Challenges

As stated in section 1.1.1.3, the heart is a very complex organ composed of different heterogeneous structures (e.g. ventricles, myocardium, vessels, atria). The first major challenge to be considered is related to the wide inter- and intra-patient shape variability of the heart. In fact, heart shape varies among individuals depending on the patient age, sex, breed and fitness. Besides, variations in shape exist due to acquisition and contrast agent injection timing during the heart cycle and hence resulting in variable contrast between the different heart cavities and surrounding organs. Moreover, presence of cardiac pathologies (vessel diseases, presence of bypass graft, etc) does include further variations in heart shape. This should be considered when creating prior heart model to be able to capture all the possible configurations. For training based algorithm, this means that the training sets should be large enough to include the different heart shapes.

Secondly, the final heart segmented volume should include all the coronary vessel segments specially the proximal and median ones - the most relevant for pathological segment identification. In fact, significant coronary lesions are mainly located at the first segments of the coronaries and around branching points. This represents a big challenge to heart segmentation algorithms as the coronaries are located on the surface of the heart and any underestimation of the heart volume could lead to a truncated part of these relevant features.

Moreover, several major vessel trunks link the heart cavities to the other organs (e.g. vena cava, aorta, pulmonary veins and arteries). The proposed approach should be able to cut those trunks to offer a clearer view of the heart coronaries' roots. However, these structures are not physically separated from the heart cavities (figure 1.4). As a consequence, there is no visible image boundaries at the departure of these trunks. Anatomical knowledge shall be used to define those cutting planes instead. For example, valve planes could be used to define such unseen boundaries.

Heart segmentation algorithms should also deal with a subsequent problem related to structures boundary visibility; In cardiac CT images, for some adjacent anatomical structures of the heart, the intensity distribution is very similar and the boundaries separating such organs are so weak (even invisible due to partial volume effects). In fact, the liver as well as the surrounding body muscles of the heart present identical intensity values to the heart myocardium. There-

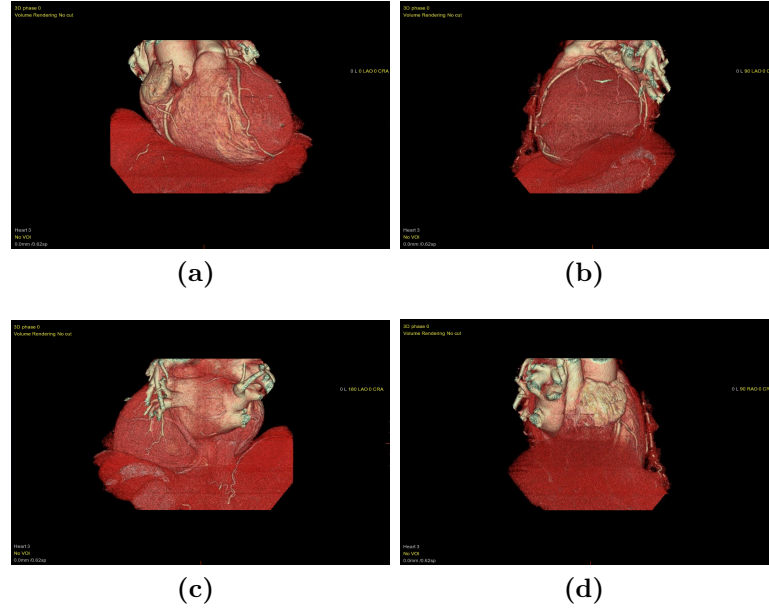


**Figure 1.3** – Exemple of heart isolation including important part of the liver.

fore, separating such similar regions based only on appearance properties would be difficult and would certainly lead to false detections (figure 1.3). Hence, the detection of these indistinct boundaries demands the use of anatomical prior knowledge to guide the segmentation process.

To conclude, an automated heart isolation algorithm must satisfy the following constraints:

- Include all main cardiac features : heart cavities, ascending aorta, coronaries and possibly bypass grafts.
- Remove obscuring structures : liver, sternum and ribs, spine, descending aorta.

Heart shape variation and weak boundaries with adjacent structures are the main challenges for any automated heart segmentation algorithm. Generally, the proposed approaches in the litterature use prior knowledge on heart shape and appearance models to control the segmentation process. These models are usually formulated and presented through *atlas* or *deformable models* and then fitted to unseen data. To obtain smooth and coherent final segmentation, the fitted model should be further refined to better fit the heart boundaries. The next section deals with the most important published works on heart volume delineation on cardiac CT angiography.

### 1.2 Related Work

3D Cardiac images processing has become one of the most active research areas in the last two decades. The fast and continuous development of the cardiac imaging modalities (mainly CT and MRI) is one of the motivations of such works. In fact, the progress made in the spatial and temporal resolutions results in a large amount of information for one single cardiac examination. Therefore, there is an increasing need for efficient algorithms to process those data sets and thus make the diagnostic task less laborious. Several approaches have been proposed for image analysis and cardiac shape and function parameters extraction.

Heart segmentation related works have mainly focused on heart cavities extraction, i.e, the left and right ventricles to extract relevant functional parameters as in [273, 283, 302, 324, 385, 430, 503]. For a full review of the model based heart cavities extraction schemes in different cardiac modalities (CT, MRI, ultrasound, Nuclear and X-rays), the reader could refer to [148], [403] and [342]. Most presented approaches were dedicated to functional heart parameter analysis in cardiac [Magnetic Resonance Imaging \(MRI\)](#) as in [273, 324, 385, 503] or ultrasound images [302]. In [324], a non-rigid registration model in a polar coordinate system is used to delineate the myocardial contour in cardiac MR. A clustering approach using the K-means algorithm is proposed in [273] to extract the left ventricle cavity. However, the previous techniques are not adapted for CT cardiac images segmentation as they rely on models extracted from MR images.

Fewer works have focused on heart cavities extraction in cardiac CT volumes [346, 430, 494]. A 3D active shape model was used in [430] to segment the left ventricle. [Prem et al.](#) [346] presented an automatic model-based approach for the segmentation of the heart cavities (a 4-chamber model) and the attached great vessels in CT data sets. Similarly, [Zheng et al.](#) [494] proposed an approach for automatic heart chamber segmentation in 3D CT volumes based on marginal space learning and steerable features. However, such approaches are not suited for coronaries visualization as they do not extract the heart cavities, the myocardium and coronaries as a single object. In fact, as stated previously, heart isolation in cardiac CT as a whole is an important step for several applications (radiotherapy planning, cardiac and vascular pathologies inspection, modalities registration).

Few works have been published on heart isolation. Proposed methods included atlas based segmentation, model based segmentation and machine learning approaches. Atlas bases approaches were proposed to automatically segment the heart as a whole in cardiac images [199, 216, 249, 431]. In [249], a hierarchical anatomical modeling and matching of thoracic organs is proposed to segment major organs (e.g. lungs and heart) in thoracic MR data (a

fuzzy atlas of thoracic organs). It takes 5 to 20 minutes to provide a coarse segmentation of the different organs. The organ surfaces were estimated within a margin of 10 mm. Thus, this approach can only provide a rough initialization for organ segmentation that needs to be further refined using more accurate techniques. In [431], the authors presented an adaptive local multi-atlas segmentation method to isolate the heart on non-contrast volumetric chest CT scans. The algorithm allows for a heart segmentation with a mean overlap of 87 % but requires around 30 minutes for segmenting a complete scan which is not practical for clinical applications. Multi atlas based segmentation was also used in [199]. Authors proposed an atlas selection procedure equivalent to sequential forward selection from statistical pattern recognition theory. This allows a more coherent and rapid registration than the method previously proposed in [431]. Kirisli et al. [216] presented a fully automatic algorithm to segment the cardiac chamber as well as the whole heart volume from CT data sets. The algorithm is also based on a multi-atlas segmentation approach using a non-rigid registration framework. The approach was evaluated on a large database and presented a mean DICE coefficient of 0.93. The major drawback of atlas based approaches is the relatively high computation time which is not suitable for most of clinical applications. In fact, this type of techniques seems to be very time consuming especially when a high number of atlases are used. An alternative to reduce the overall processing time is to work in down-sampled volumes without compromising the final segmentation accuracy. However, the obtained computation time (around 20 minutes to process a cardiac CT) is still not satisfactory for rapid clinical applications.

Model based segmentation with geometric and appearance prior knowledge has also been used for (semi-)automatic heart delineation. Prior knowledge on the heart position between the right and left lungs are used to define a heart model in [309, 310]. A fuzzy formalism of this anatomical prior knowledge is proposed and used to drive the evolution of a deformable model for heart segmentation. However, this approach suffers from the high computational time (17 hours for a non down-sampled volume) and a relatively high distance error ( 6 mm) compared to other approaches. In [132], the whole heart (i.e., four chambers, myocardium, and great vessels) was segmented in CT images by a 3-D model-based approach. Model adaption is performed with a coarse-to-fine adaptation process that progressively relaxes the constraints on the allowed deformations. This approach was validated on 28 CT data set and showed satisfactory results (a mean distance of 0.82 was accomplished) combined to a low computational time ( 10-30s).

In [143], the author used an algorithm driven from the graph cuts optimization technique with a shape constraint to segment the heart shell [51]. A distance map computed on the result of the graph cut is used to fit a simpler geometric model to the heart (a bi-axial ellipsoid ). In [331], a 3-D semi-automatic algorithm using a 3-D super-ellipsoid model of the heart was



presented. Similarly, [154] proposed a graph cut based algorithm for heart isolation for coronaries visualization in CT angiography. A 3D balloon inflation approach is used to determine the ellipsoid of maximum volume inside the heart. This ellipsoid is used as initialization of the graph cut algorithm. They also introduced a "blob" constraint term in the energy formulation to prevent leaking in the aorta or other pulmonary vessels. An other approach for heart isolation in cardiac MR images was presented in [166]. The algorithm starts with a manual selection of a 2D axial section that contains the heart. A hierarchical approach is used to recognize all other organs in this slice (torso, lungs, background). The heart borders are then estimated based on the lungs fields. The final cardiac contour is then propagated to adjacent slices and used as an initialization for further segmentation. A similar approach was proposed in [219]. An initial contour of the heart was computed using a 2D model balloon inflation. The gradient information was exploited to fit the balloon to the heart wall. This contour is then copied to the neighboring slices to perform the same extraction scheme. This process is then repeated until all the slices are processed which could lead to an over segmentation of the heart as the contours would be copied in liver slices. In [495, 497] a marginal space learning technique is used to initialize the heart model in CT volumes. Subsequently, this model is refined using local data-driven voxel-based refinements to produce a more accurate heart mask boundaries. In [497], the left atrial appendage (LAA), the pulmonary arteries (PA) and pulmonary veins (PV) are subsequently removed from the final heart mask to clear the left coronary artery (LCA) tree view. This approach allows for automated heart delineation in CT volumes with a mean distance error of 1.91 mm.

Some other works focused on automatic or semi-automatic heart mask delineation for further coronaries segmentation. In [78], the heart mask was segmented based on a combination of threshold of the heart densities and a set of morphological operations [386]. A 3D model of the heart, built based on a set of manually set landmark points, is matched to cardiac CT exams for detecting the approximate position of the heart in [483]. Those works do not focus on perfectly removing the obscuring structures around the heart and thus the resulting segmentation could contain important parts of the liver or other obscuring structures. Moreover, no qualitative or quantitative validation of those approaches have been presented.

**Table 1.1** – Comparison of previous works on heart isolation in MR and CT angiography. *Error* refers to the mean distance error between the manual and automated heart segmentation. *Jl* is the Jaccard index. *Dice* refers to the Dice Similarity Coefficient.

Work	Approach	Automatic	Modality	Patients	Evaluation	Measures	Processing time
<a href="#">Gregson [166]</a>	Adaptive thresholding + Mathematical morphology	Auto.	MR	N/A	N/A	N/A	N/A
<a href="#">Lelieveldt et al. [249]</a>	Atlas based approach: Fuzzy implicit surface model and hierarchical modeling of thoracic organs	Semi-Auto.	MR	15	Qualitative	Error = 10 mm	5-10 min
<a href="#">Moreno et al. [310]</a>	Fuzzy representation of the between relationship + deformable models	Auto.	CT	10	Quantitative	Error = 6.4 mm	4min (down-sampled)
<a href="#">van Rikxoort et al. [431]</a>	Adaptive local multi-atlas segmentation	Auto.	CT	29 data set (15 atlas + 14 target images)	Quantitative	$Jl = 0.8733 \pm 0.0363$	30 min
<a href="#">Ecabert et al. [132]</a>	3D deformable models	Auto.	CT	28	Quantitative (Leave One Out)	Error = $0.82 \pm 1.00$ mm	10-30 sec
<a href="#">Isgum et al. [199]</a>	Multi-Atlas-Based Segmentation	Auto.	CT	29 data set (15 atlas + 14 target images)	Quantitative	$Jl = 0.88 \pm 0.03$	15 min
<a href="#">Funka-Lea et al. [154]</a>	Graph cuts with elliptic heart model	Auto.	CT	70	qualitative (70 cases) and quantitative (9 cases)	Error = 5.5 mm	20 sec
<a href="#">Kirisli et al. [216]</a>	Multi-Atlas-Based Segmentation	Auto.	CT	251	qualitative (243 patients) and quantitative (8 patients)	Error = $1.25 \pm 1.73$ mm, Dice = 0.95	25 min
<a href="#">Oghli et al. [331]</a>	2D Supper-ellipsoid fitting	Semi-Auto.	CT	20	quantitative	Dice = 0.85, $Jl = 0.76$	1 sec
<a href="#">Zhong et al. [497]</a>	Marginal space learning + data-driven model deformation	Auto.	CT	589 (288 patients)	quantitative (four-fold cross-validation)	Error = 1.91 mm	1.5 sec

Following, we present a hybrid algorithm for automated heart volume delineation in 3D cardiac CT data sets for coronary arteries visualization. Our work eliminates the tedious and time consuming step of manual removing obscuring structures around the heart (lungs, ribs, sternum, liver...) and quickly provides a clear and well defined view of the coronaries. So far, works related to heart segmentation have mainly focused on heart cavities delineation, which is not suited for coronaries visualization and/or segmentation. In contrast, our algorithm extracts the heart cavities, the myocardium and coronaries as a single object. The proposed approach is based on the fitting of a geometric model of the heart to a set of automatically extracted 3D points lying on the heart shell. A two-stage fitting scheme is used to improve the robustness to the outliers. The fitting result is refined using a Random Walker (RW) segmentation approach. Quantitative and qualitative analysis of results obtained on a 114 exam database shows the efficiency and the accuracy of our approach. Preliminary quantitative results of this approach have been published in [289, 290].

### 1.3 Overview of the Proposed Approach

The automated heart delineation algorithm presented in this chapter is based on a combination of several processing steps. The algorithm main steps are summarized in figure 1.4. It can be divided in three main steps: (1) Pre-processing step, (2) Heart model fitting and (3) Final heart delineation. The first step consists in extracting prior information about lungs and descending aorta volumes as well as estimating the heart center position. This information is mandatory to accurately perform the heart geometric model fitting to the image data. Secondly, a prior geometric model of the heart is fitted to the image in order to estimate the heart volume and position. Therefore, a cloud of 3D points lying on the surface of the heart is extracted using a ray casting starting from the heart center and constrained by the lungs volume. This represents a subset of the heart shell points that will be used to fit the heart model. However, this set of points is contaminated by some outliers that need to be eliminated in order to get a coherent heart model estimation. A backward outliers removal step is performed to eliminate the contaminated data based on the data sparsity analysis. The remaining set of points is then used to fit a geometric model (elliptic model) to the heart: a novel two-stage ellipsoid fitting is proposed to estimate the best ellipsoid covering the heart volume. Subsequently, as the heart is not perfectly elliptic, we use a supervised graph based technique using Random Walkers (RW) to refine the heart's delineation. The resulting mask may include some extra ribs and parts of the sternum and/or the spine. Therefore, a final step of extra bones removal is applied to clean

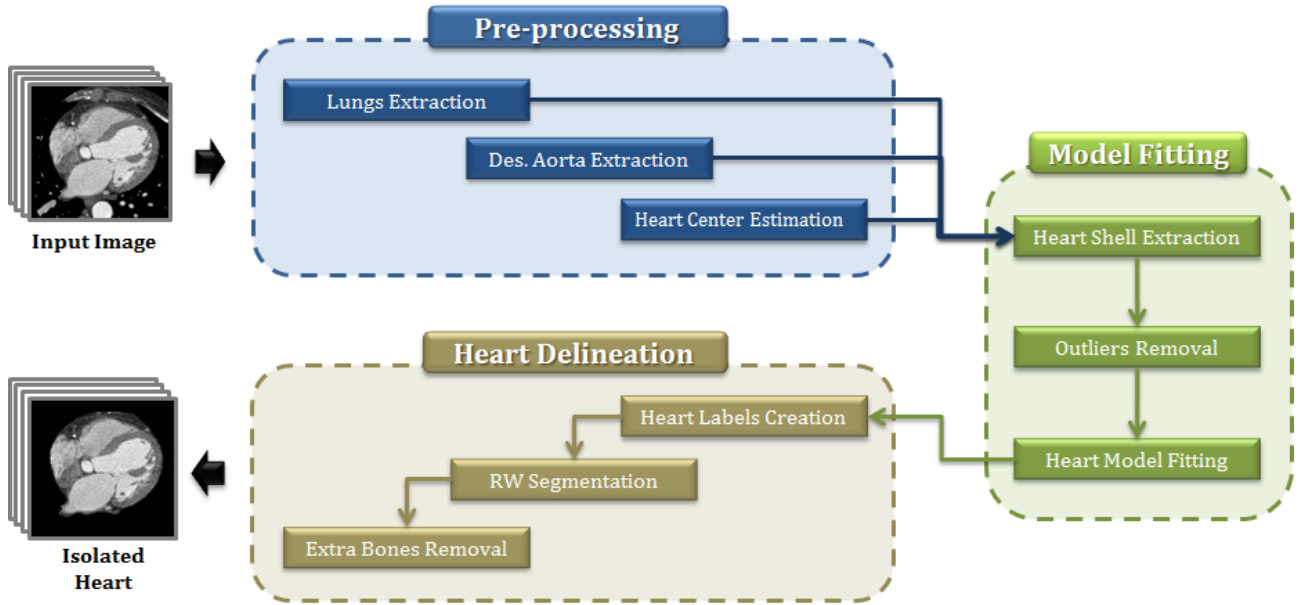


**Figure 1.4** – Heart isolation algorithm workflow

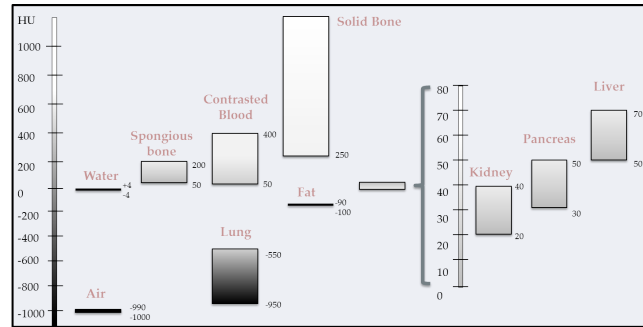


**Figure 1.5** – The Hounsfield scale.

up the final heart volume.

### 1.3.1 Pre-processing Step

This step aims to prepare the input data needed by the algorithm to extract the heart shell points. In fact, to perform the heart surface cloud extraction, the lungs and the aorta volumes and the heart center are required. In this pre-segmentation section, we mainly focus on the appearance characteristics of each feature in CT angiography. As shown in the figure 1.5, one can easily discriminate between air and blood pools as they cover two different ranges of intensity in Hounsfield Scale.

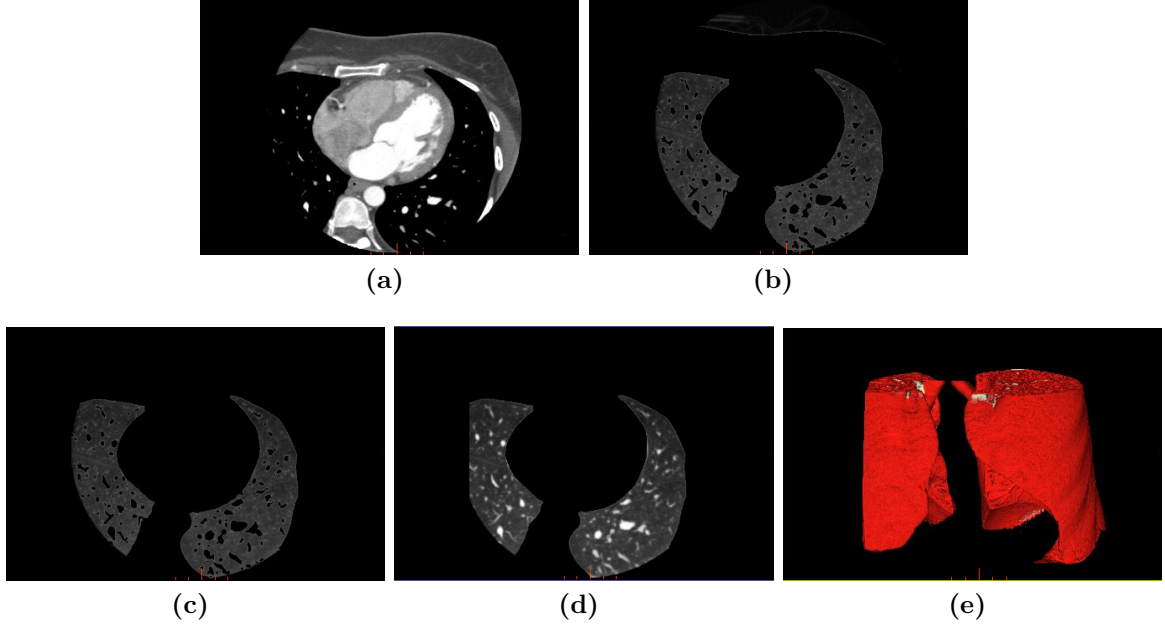


**Figure 1.6** – Lungs volume extraction steps: (a) A cross section slice of the original volume. (b) Air class thresholding result. (c) The connected components corresponding to the right and left lungs. (d) Holles closing of the previous connected components. (e) A 3D rendering of the extracted lungs volume.

### 1.3.1.1 Lungs and Descending Aorta Volumes Extraction:

The lungs volume is used to extract the heart wall relevant points. In facts, the heart being mainly surrounded by the lungs, the most reliable points we could use for any model fitting would be the heart/lungs contact points. One can use a simple threshold value to detect these contact points and stop the ray casting (see section 1.3.2.1) as in [154]. Instead, we prefer to extract the correct lungs volume, using additional processing steps, in order to avoid false positive detection related to noisy points. To extract the lungs volume, we first apply a threshold to the input image to keep only voxels with a CT intensity ranging between  $T_{air}$  and  $T_{lungs}$ . We then perform a set of mathematical morphology operations to extract the two connected components corresponding to the lungs air volume. Therefore, we apply a size based filtering to keep only connected components with a volume higher than  $V_{lungs}$  to eliminate small structures that probably contain air and do not correspond to lungs connected components. Finally, to include the pulmonary vessels in the lungs mask we apply a 2D hole closing step. Those different steps are illustrated in figure 1.6.

Subsequently, we perform an automated descending aorta volume extraction. This mask is useful for: 1) the heart center estimation and 2) the heart wall points extraction steps. First, we apply a threshold ( $T_{bright1}$ ) to the input volume to extract bright structures (e.g.

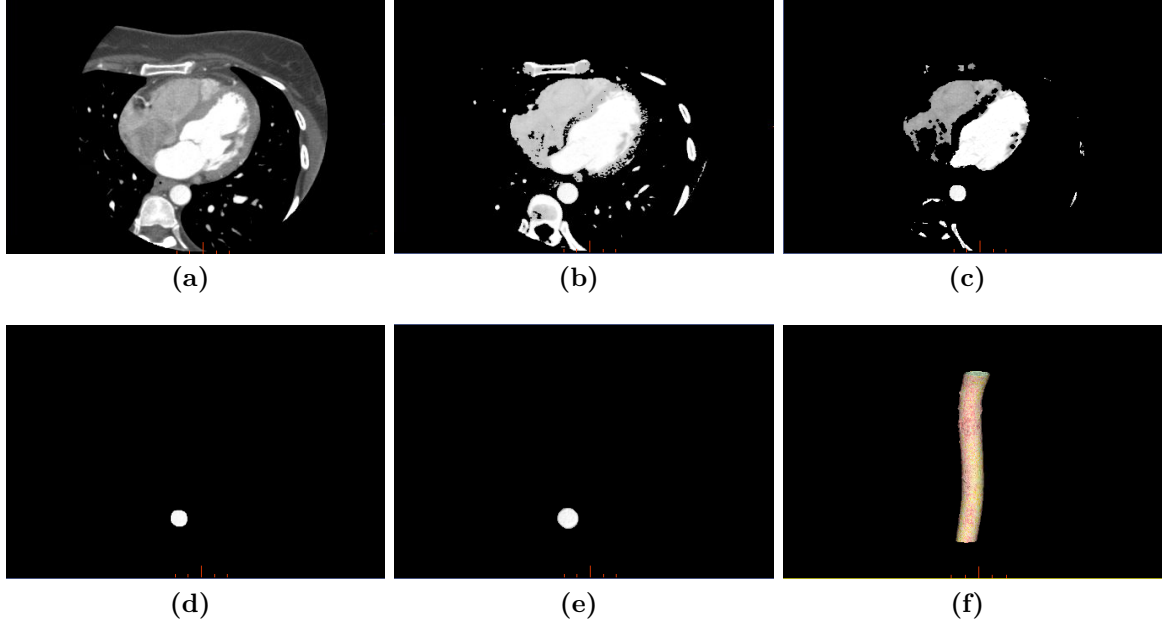


**Figure 1.7** – Aorta volume extraction steps: (a) A cross section slice of the original volume. (b) Blood pool class volume. (c) Eroded blood pools. (d) The connected component corresponding to the descending aorta. (e) Dilation of the previous connected component to include the aorta wall. (f) A 3D rendering of the extracted descending aorta.

blood pools and bones). The resulting mask is then eroded (with a structuring element of size  $S_{SE}$ ) to separate the adjacent connected component. In fact, the spine vertebrae and the descending aorta could remain connected after this threshold step. Once the different components are separated, we compute some geometric features (e.g. circularity and size) for all the 2D connected components. Thereafter, we filter the circular connected components with a size corresponding the aorta's size range values ( $S_{aorta1}$  and  $S_{aorta2}$ ). The descending aorta is thus extracted as the biggest 3D connected component remaining in the volume. Finally, the aorta volume is dilated to reconstruct the vessel wall eliminated during the erosion step. Figure 1.7 illustrates the different previous steps.

#### 1.3.1.2 Heart Center Extraction

In this step, we estimate the heart center position  $C$ . This point will be used to launch the ray casting. It should be well centered inside the heart volume to allow the points cloud to be well scattered on the heart surface. In fact, its location affects the density of the points cloud and thus could bias the fitting result; The more centered inside the heart it is the best the result fitting would be.  $C$  could be estimated as the center of the heart blood pools. Therefore,

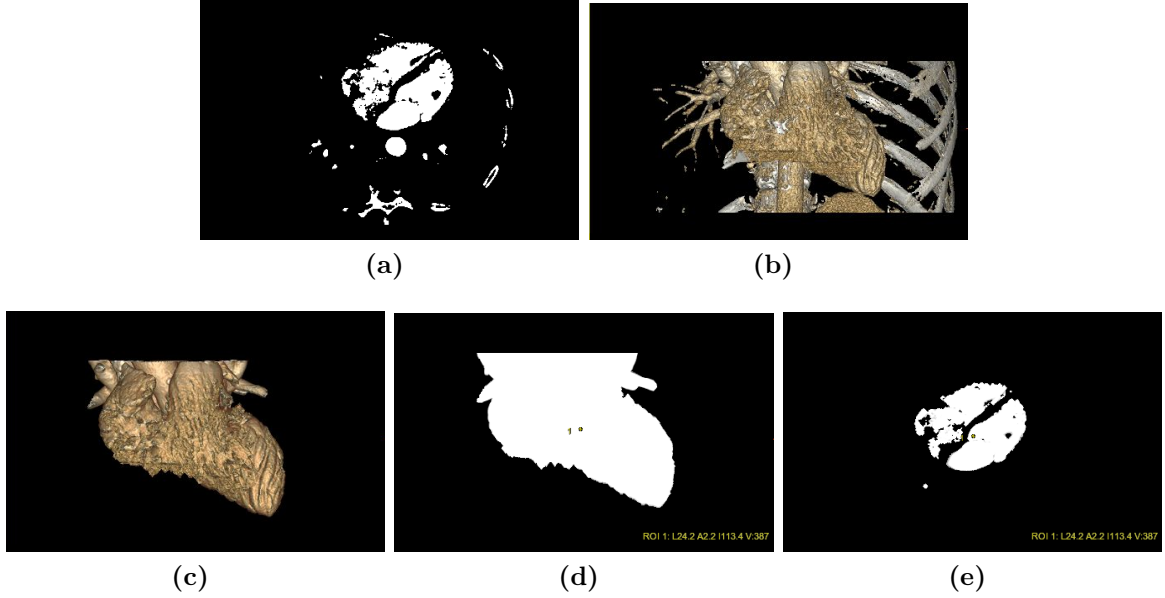


**Figure 1.8** – Heart center extraction steps: (a) Axial slice of bright structures class. (b) 3D rendering volume of bright structures (c) 3D rendering of heart cavities. (d) and (e) Estimated heart center on a 3D and axial views.

to automatically extract the heart center, we mainly focus on the intensity characteristics of the heart cavities. As shown in the figure 1.1, bright structures mainly corresponds to blood pools and bones. Defining the heart center as intensity weighted barycenter, as in [154], would fail if the field of view does not include the whole chest bone. We propose a more elaborated heart center extraction in CT exams. First, we apply a bright structure threshold ( $T_{bright2}$ ) on a down-sampled version of the 3D image. This results in keeping mainly the bone, the heart chambers and the aorta. We prefer to work on a down-sampled version as it accelerates the processing and eliminates the small unwanted details (e.g. vessels). Moreover, the aorta volume extracted in section 1.3.1.1 is removed from the thresholded volume to insure that the final point is centered inside the heart and not biased by the descending aorta. The heart cavities are thus extracted by filtering the biggest connected component in the resulting thresholded volume after subtracting the aorta volume. Heart center is set as the center of mass of the resulting cavities. To ensure that  $C$  is well centered within the heart, we readjust it with a ray casting pass; We detect the heart/lungs contact points and then redefine the heart center as the center of gravity of these points. All the previous steps are illustrated in figure 1.8

We end this pre-processing step with the extraction of the heart box (named  $H_{Box}$ ) from the 3d volume. The aim from this step is to reduce the processing to the heart windows thus reducing the processing time and increasing the robustness of the approach. The detection of

the heart box is mainly based on the detection of the first slice where the aorta starts. To avoid false positives, we select the first slice followed by two slices containing the two connected components of the aorta (the ascending and the descending). The ending slice is fixed to be at 160 millimeters from the starting one.

## 1.3.2 Heart Model Fitting

The aim of this part is to define a geometric model of the heart anatomy to be used as a constraint to the heart segmentation. The motivation of this constraint is to perform an accurate segmentation around heart regions suffering from weak or absent boundaries such as the heart/diaphragm boundary. In fact, any non-supervised segmentation technique would fail to extract such boundaries because of the lack of information in this area separating two structures with common appearance proprieties.

The heart anatomy could be simply approximated by an ellipsoid shape [143, 154]. Based on this assumption, we would like to extract the best ellipsoid that fits the heart volume for each exam. In [154], the ellipsoid was extracted by inflating a 3D balloon inside the heart. A threshold is used to detect the contact points with the heart wall and thus continue the inflation in the opposite direction. The ellipsoid axis are set to be the X, Y and Z axis of the volume. If the extracted ellipsoid is too small to be a region within the heart than the algorithm terminates. In [143], a bi-axial ellipsoid was proposed instead of a tri-axial one. The ellipsoid parameters were defined using the extracted heart shell from the graph cut algorithm. The center was defined as the center of gravity of the extracted surface. The two axis are defined with reference to the nearest and the farthest point on the heart shell. We want to avoid setting in advance the parameters of the heart ellipsoid. Our method is based on ellipsoid fitting by minimizing the weighted least squares residuals applied on an automatically extracted set of point on the heart surface.

### 1.3.2.1 Heart Shell Cloud Extraction

**1.3.2.1.1 Heart Shell Points Extraction: A Ray Casting Approach** Relevant heart wall points could be defined as the heart's contact points with its surrounding anatomies: lungs and aorta. To extract the relevant points we perform a 3D ray casting from the heart center  $C$  and detect the contact points with these two structures. The ray casting is constrained to remain inside the heart box  $H_{Box}$  to avoid going far from the heart region of interest and thus decrease the number of outliers. For each ray, starting from the heart center  $C$ , we move on the corresponding direction with a unit step until reaching a contact point with the previously



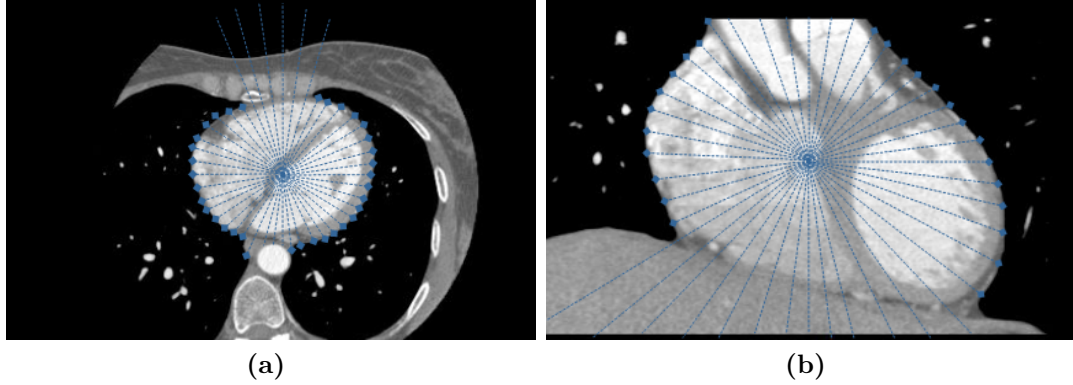


**Figure 1.9** – Heart shell points extraction: Axial (a) and (b) coronal views of the detected points by the 3D ray casting.

detected lungs or aorta volumes. If so, the point is stored in the heart wall cloud points and we move to the next direction. The density of the extracted cloud depends on the angular sampling  $\theta$  of the ray casting. This value has been optimized to allow getting enough points for a robust fitting of the geometric model. An example of the extracted points set is shown in 1.9.

Before we begin the processing of the resulting data, we should pay attention to the presence of eventual outliers that could contaminate the whole set of points and thus bias the model estimation. In the remainder, let  $\mathcal{P}_o$  refer to the original extracted set of points.

**1.3.2.1.2 Outliers removal: A review** A coherent specification of a model based on a given data requires first a detection of aberrant samples that could lead to biased parameter estimation. Therefore, it is very important to detect and remove those outlying observations before any other processing step.

An *outlier* is an observation “that appears to deviate markedly from other members of the sample in which it occurs” [168]. In [178], an outliers is defined to be “an observation that deviates so much from other observations as to arouse suspicion that it was generated by a different mechanism”. A prior knowledge on the data structure could yield to more specific definition of what an outlier could be. Detecting outliers is a critical step, that was processed for centuries, in several domain applications such as fraud detection, satellite images analysis, motion detection, detecting mislabeled entries in a data base for training and many other fields [188]. A wide variety of techniques covering the full gamut of statistical, neural and machine learning techniques has been elaborated to estimate the outliers in a given data set. For a full review of the outliers detection methodologies the reader could refer to [197], [188] and [32].

### 1.1.3 Overview of the Proposed Approach

---

Hereafter, we will focus on methods that are adapted to euclidean data. Several classifications are possible. *Global* versus *Local* classification consider the resolution of the reference compared to which the “outlierness” measure would be determined (the whole data or a subset of it). An other possibility is to consider the techniques with refer to their output: *Scoring* versus *Labeling* approaches: the output would be a binary information labeling the datum as *outlier* or *inlier*, or a score of the “outlierness”.

One could also classify those techniques based on their modeling properties. With no prior information on the data model, distance-based and density-based approaches are often used to detect the outliers. Distance-based approaches judge a point with reference to the distance to its neighborhood based on the assumption that ‘normal’ data are in very dense neighborhood and that outlier observations could be characterized as low density neighborhood points. A distance-based definition of outliers was first proposed by Knox and Ng [221] where an *DB-outlier* is defined as “An object O in a dataset T is considered a DB(p,D)-outlier if at least a fraction p of the objects in T lies greater than distance D from O”. Ramaswamy et al. in [352] proposed to take the *K-Nearest Neighbors* (k-NN) distance of a point as its outlierness score and used a partition-based algorithm to efficiently mine top-N outliers from a large database: “The outliers are the top n data elements whose distance to the  $k^{th}$  nearest neighbor is greatest”. In [136], the authors defined a Resolution based Outliers Factor (ROF) to score each point in the data set. Varying the resolution from  $R_{max}$  (the maximal distance threshold when all points are clustered) and  $R_{min}$  (the minimal distance threshold for which all points are outliers), the ROF of an object O is defined as the accumulated ratios of sizes of the clusters containing O in two consecutive resolutions. However, distance based approaches would fail if the data presents different density per area. To deal with this issue a Local Outlier Factor (LOF) was proposed by Breunig et al. [61] depending on how the data points are closely packed in an object’s local reachable neighborhood. To overcome the problem of low density regions where it would be difficult to detect outliers, a new variant of the LOF based on the connectivity (COF) was introduced in [410]. For other variants of density based outliers scoring algorithms, we can refer to [201, 336]. The major limitation of the proximity based approaches is the exponential computational growth that is directly related to the dimensionality of the data and the number of the recorded observation.

Model-based approach assume that the data follow a specific distribution model. Those approaches are highly accurate if we know the data fits a pre-selected distribution model. Two similar approaches aims to extract the outliers by defining a boundary around the densely populated normal data: The Minimum Volume Ellipsoid estimation (MVE) and the Convex Peeling [365]. The MVE fits the smallest permissible ellipsoid volume around the majority

of the data. The Convex Peeling process by removing the records on the data's convex hull assuming that the outliers remain at the border of the data's space. An other peeling approach uses the least square standard regression, by minimizing expression (1.1), to measure the effect of the deleted point on the fitted model [422].

$$\sum_{i=1}^n (y_i - \hat{y}_i)^2 \quad (1.1)$$

where  $\hat{y}_i$  is the estimated value. The authors repeatedly fit the model to the data after deleting the point with the greatest deviation and stop when the maximum deviation falls below a threshold value. This method is not very robust as the outliers not yet removed are considered to fit the model and could bias the result.

Other model based approaches dedicated for the uni-variate variables assume that the data follow an approximate normal distribution. Then outliers are defined as observations that saliently deviates from the model based on mean and standard deviation [226]. The Z-score of a sample is defined as:

$$Z_i = \frac{y_i - \bar{y}}{\sigma} \quad (1.2)$$

where  $\bar{y}$  is the mean value of all the observations and  $\sigma$  the standard deviation of the observations. It estimates how many standard deviation does the observation i deviates from the mean value. It's not recommended to use the mean and the standard deviation for data containing a big amount of outliers as the values would be distorted. The use of the Median Absolute Deviation (MAD) is a robust alternative to measure the variation of a uni-variant data with presence of outliers:

$$MAD = median(|y_i - \tilde{y}|) \quad (1.3)$$

where  $\tilde{y}$  is the median value of all the observations. In [197], a modified Z-score based on MAD was defined as:

$$M_i = \frac{0.6745(y_i - \tilde{y})}{MAD} \quad (1.4)$$

Observations with a modified Z-score greater than 3.5 are recommended to be labeled as outliers. Several other tests based on "the distance from the mean" are present in literature for single or multiple outliers detection: The Grubb's test [168], Dixon's Q test [105] and The Tietjen-Moore test [418].

As we have stated, there is no unique outliers removal/detection approach that is accurate for all situations; It depends on the data and the kind of outliers we want to remove. In the following, we propose a prior-knowledge approach to detecting the outliers in  $\mathcal{P}_o$ .

**1.3.2.1.3 Outliers removal from the heart shell points** A prior knowledge on the generating process of the data is very desirable to improve the robustness of outliers removal step. Points lying on the heart surface correspond to a blob shape. Based on this observation, we would like to detect points that saliently deviate from this shape. The analysis of our data set  $\mathcal{P}_o$  leads to the identification of two different types of outliers with reference to the X and Y axes respectively (coronal and sagittal axes): Let  $O_1$  be the outliers, along the X axis, far from the heart cloud (for example point G in figure b) and  $O_2$  be the outliers, along the Y axis, corresponding to the spin/lungs contact points closer to the upper heart wall points (for example point B in figure b). We will concentrate our research of outliers on the 2D projection of  $\mathcal{P}_o$  on the XY plan. This choice is motivated by the fact that no outliers have been detected along the Z coordinates as the ray casting was constrained by the heart box (see section 1.3.1.2).

Isolated points could be removed using any proximity based approach. However, the computing cost of this choice is not very encouraging and this approach would fail to detect some closer false detections to the heart shell points. For the explanation, we will focus on the detection of outliers of type  $O_1$ . The same approach is used to detect outliers of type  $O_2$  as well. As we can see on the 2D projection of the data (figure b), these outliers are located in two sides of the heart (the right and the left one) and have a lower X neighborhood density than the rest of the points lying on the heart wall. Figure a shows the variation of the X coordinates in the original set of data  $\mathcal{P}_o$ . In this figure, the points (on the abscissa axis) are presented in the same order as the ray casting scanning. It is hard to define the outliers based on this observation. Standard deviation based approaches failed to extract the appropriate outliers as the standard deviation value was contaminated by this erroneous points. Similarly, the modified Z-score proposed in [197] was not a robust choice for our case.

We choose to work on the sorted values of the X coordinates in the set of data to remove the type  $O_1$  outliers (see figure b). In fact, we can assume that the X variation in our data follow a normal distribution and that outliers are located at the tails of the sorted values of X. Those outliers are characterized as points belonging to low density regions in the set of points. So if we track the sorted X variation speed, we will be able to detect those erroneous observations by detecting the two breaking points (BP) on this curve. In other words, if we scan the 2D projection in the X increasing direction with computing the variation between two successive points we will notice a bigger variation when we move from an outlier to an inlier (and vis

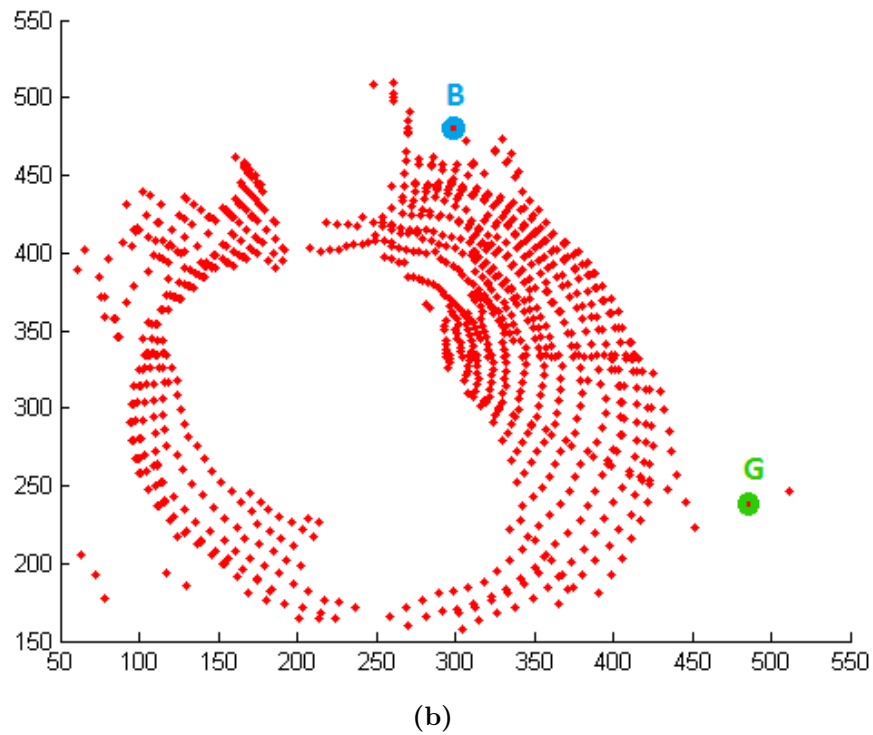
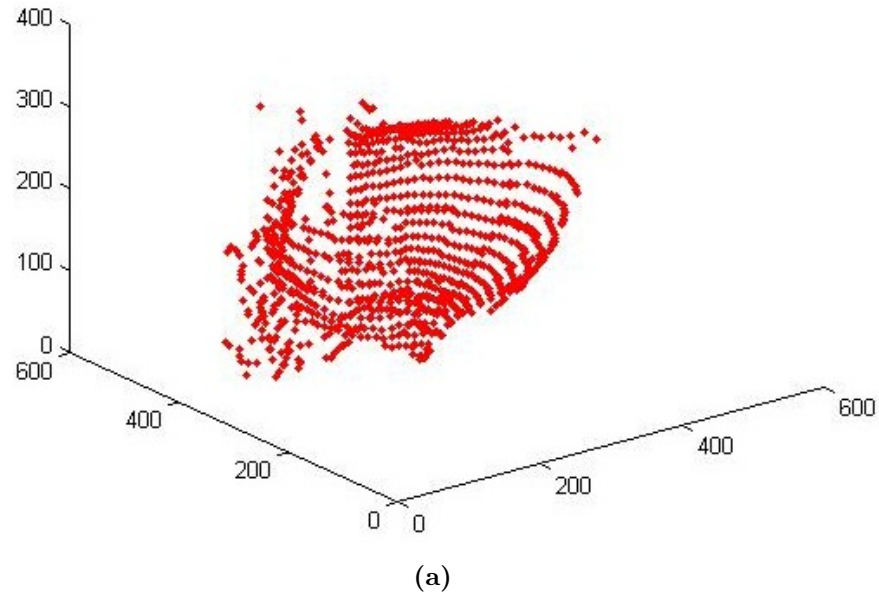


**Figure 1.10** – Heart shell points analysis: (a) The original 3D heart shell points  $\mathcal{P}_o$  (mainly heart/lungs contact points). (b) XY projection of the set  $\mathcal{P}_o$  showing the two types of outliers (example G and B).

### 1.1.3 Overview of the Proposed Approach

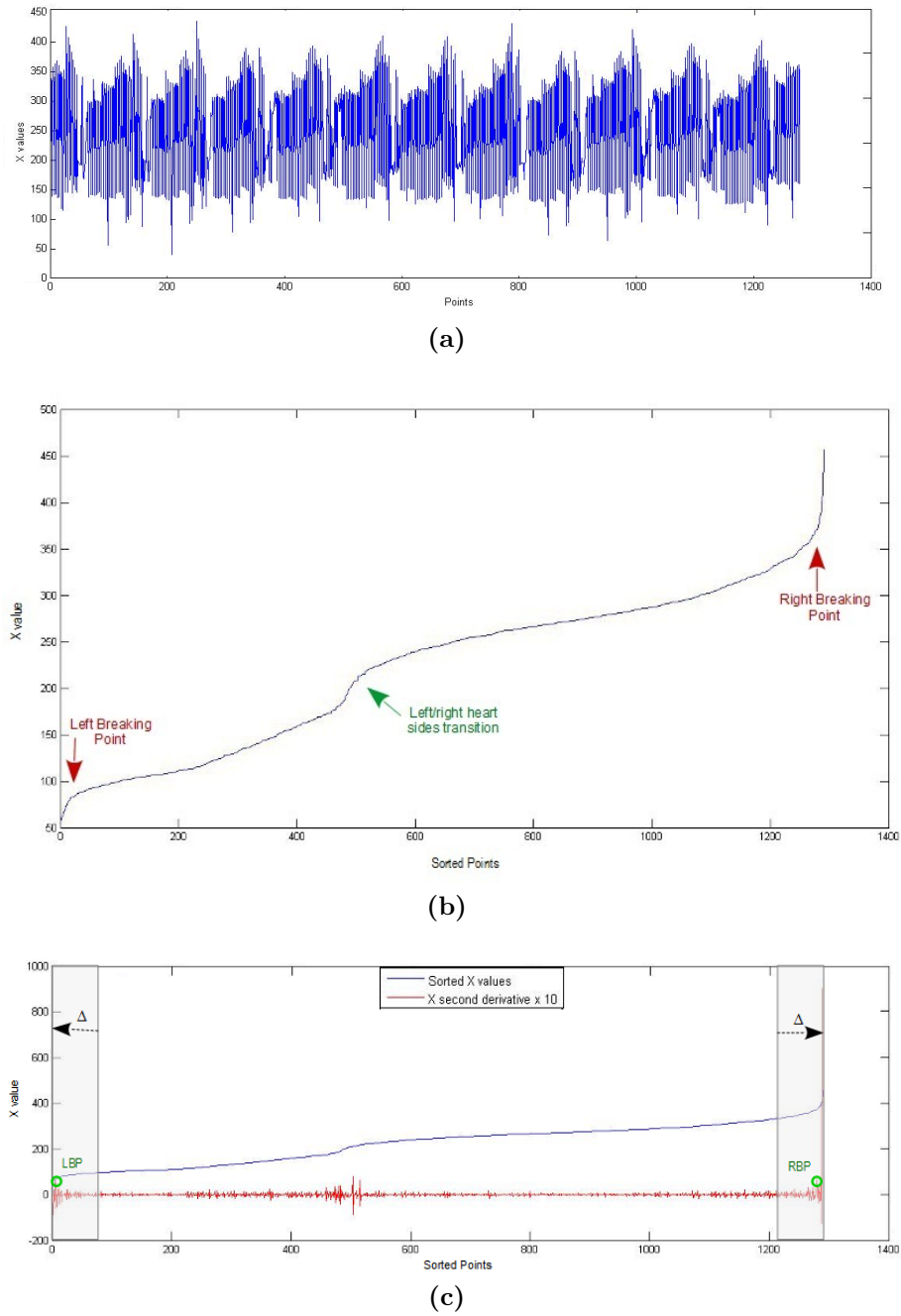


**Figure 1.11** – Outliers Detection: (a) X coordinate variation in the original set of points following the scanning order. (b) Sorted X coordinates of the 3D points. (c) LBP and RBP detection using the second derivative values threshold around the tails of the curve. Left and right breaking points corresponds to the limits of the inliers interval.

versa) and a smaller variation between inliers (points on the surface of the heart).

To detect the two breaking points (corresponding to the beginning of the left and right outliers regions) , we have to detect the change of the speed of X variation. That's why we choose to compute the second derivative of X in order to detect those changing points. Assuming that at most a proportion  $\alpha$  of  $\mathcal{P}_o$  are outliers, we define a search depth  $\Delta = n\alpha$  at both sides of the curve, where  $n = |\mathcal{P}_o|$ . As the left and right breaking points (LBP and RBP) correspond to a fast variation of X, we compute the second derivative of this curve and detect the first value higher than a given threshold  $T_d$  for both left and right sides. The search process starts at  $i = \Delta$  ( left side) and  $i = n - \Delta$  (right side). Outliers are defined as points falling outside of the [LBP RBP] interval.

For  $O_2$  outliers, we process similarly. Those outliers results from the an erroneous detection of lungs/spin contact points in the ray casting process. They are located at the top of the heart (i.e. with the Y attribute). Figure a shows the variation of the Y attribute along the 2D projection and its second derivative. Using this two stage approach we were able to remove efficiently and quickly the erroneous observations in our data (see figure b).

### 1.3.2.2 Ellipsoid Fitting: A WLSQ approach

Ellipsoid fitting was widely used to model 3D shapes in several fields (e.g. pattern recognition, computer vision and orbit estimation in observational astronomy). We can classify the techniques presented in the literature to *clustering methods* (Hough transform [243, 318] and *Least Squares minimization approaches*.

Hough transform based approaches suffers from the storage and computational requirements, despite the several modifications proposed to overcome those limitations [86]. The Least square techniques aims to find the best fit to the given data by minimizing a distance measure between all the points and the estimated ellipsoid. Different algorithms have been used, some being more robust to the presence of contaminated data than others. In [139], a method was proposed to fit an elliptical model to 2D scattered data. The idea is to fit the general equation of a conic to the given data, subject to a constraint which forces the conic to be an ellipse. This work has been extended to 3D data in [165] to approximate a general set of 3-D points using a 3-D ellipsoid for head tracking.

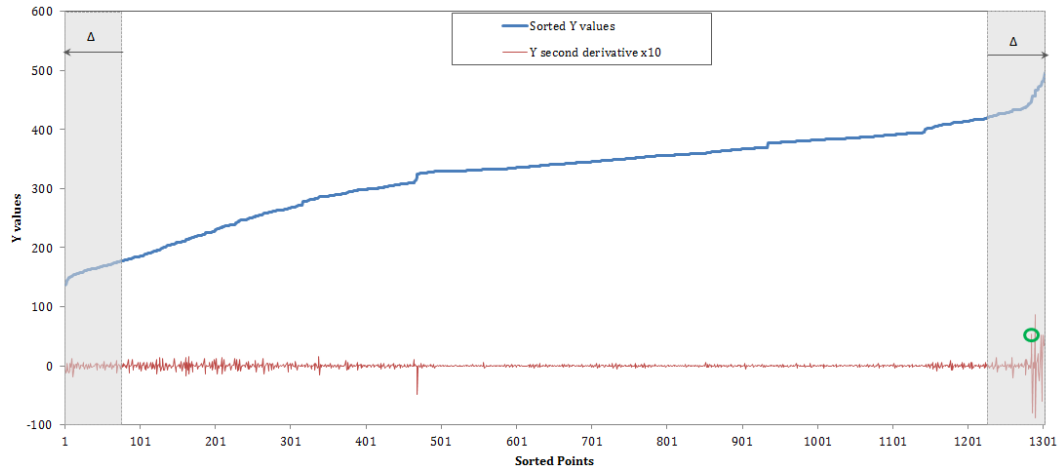
For a 3D conic, the equation is given by:

$$F(\mathbf{a}; \mathbf{x}) = \mathbf{a} \cdot \mathbf{x} = ax^2 + bxy + cy^2 + dxz + eyz + fz^2 + gx + hy + iz + j = 0 \quad (1.5)$$

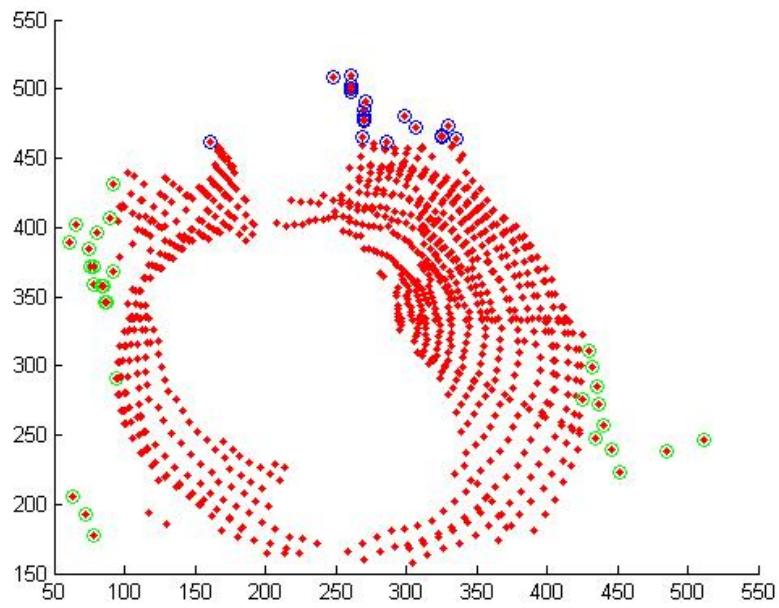
with  $\mathbf{a} = [a \ b \ c \ d \ e \ f \ g \ h \ i \ j]^T$ ,  $\mathbf{x} = [x^2 \ xy \ y^2 \ xz \ yz \ z^2 \ x \ y \ z \ 1]^T$ .



### 1.1.3 Overview of the Proposed Approach



(a)



(b)

**Figure 1.12** – Outliers Detection: (a) Breaking Points detection using  $Y$   $2^{nd}$  derivative for the detection of type  $O_2$  outliers. (b) Detected outliers ( $O_1$  are marked in green and  $O_2$  in blue).



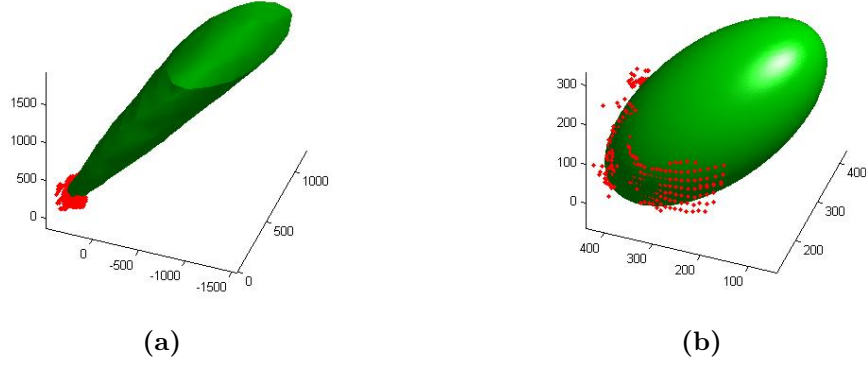


**Figure 1.13** – Ellipsoid fitting: (a) An LSQ Ellipsoid fitting on the 3D initial Data  $\mathcal{P}_o$ . (b) An LSQ Ellipsoid Fitting on the clean data  $\mathcal{P}_c$  after outliers removal

The fitting of the general conic could be estimated by minimizing the sum of the squared *algebraic distances*:

$$E = \|\mathbf{D}\mathbf{a}\|^2 = \sum_{i=1}^n (F(\mathbf{a}; \mathbf{x}_i))^2 \quad (1.6)$$

with  $\mathbf{D} = [\mathbf{x}_1 \ \mathbf{x}_2 \ \dots \ \mathbf{x}_n]^T$  being the design matrix defined by the set of the heart wall points and  $F(\mathbf{a}; \mathbf{x}_i)$  is the algebraic distance of the point  $(\mathbf{x}_i)$  to the conic  $F(\mathbf{a}; \mathbf{x}) = 0$ .

The vector  $\mathbf{a}$  could be constrained in order to avoid the trivial solution  $\mathbf{a} = \mathbf{0}_9$ . Therefore, several approaches have been proposed in the literature with linear ( $a + c = 1$  [449],  $f = 1$  [361]...) or quadratic ( $\|\mathbf{a}\| = 1$ ) constraints applied to the system parameters. In [139] a *direct least squares* fitting is used to fit a 2D conic to a set of scattered points while forcing this conic to be an ellipsoid; The author imposes the equality  $4ac - b^2 = 1$ . In fact, to be an ellipsoid the conic should verify the discriminant equality  $b^2 - 4ac < 0$  which could be replaced by the previous constraint thanks to the freedom to arbitrarily scale the parameters. A similar constraint is proposed in [165] for 3D conic fitting.

The minimization problem 1.6 could be solved by considering the generalized eigenvalue system [42]:

$$\mathbf{D}^T \mathbf{D} \mathbf{a} = \lambda \mathbf{C} \mathbf{a} \quad (1.7)$$

with :

### 1.1.3 Overview of the Proposed Approach

**Table 1.2** – Ellipsoid fitting using linear least squares (LSQ) and direct least square (DLSQ)

	Average Fitting Deviation	Radii	Center
LSQ	0.0159	245 135 124	273 239 134
DLSQ	2.0	936 491 419	277 199 114

$$C = \begin{bmatrix} 0 & 0 & 2 & 0 & 0 & 0 & 0 & 0 & 0 \\ 0 & -1 & 0 & 0 & 0 & 0 & 0 & 0 & 0 \\ 2 & 0 & 0 & 0 & 0 & 0 & 0 & 0 & 0 \\ 0 & 0 & 0 & 0 & 0 & 0 & 0 & 0 & 0 \\ 0 & 0 & 0 & 0 & 0 & 0 & 0 & 0 & 0 \\ 0 & 0 & 0 & 0 & 0 & 0 & 0 & 0 & 0 \\ 0 & 0 & 0 & 0 & 0 & 0 & 0 & 0 & 0 \\ 0 & 0 & 0 & 0 & 0 & 0 & 0 & 0 & 0 \\ 0 & 0 & 0 & 0 & 0 & 0 & 0 & 0 & 0 \end{bmatrix}$$

Hence,  $\mathbf{a}$  is the generalized eigen-vector of 1.7 corresponding to the smallest positive eigen-value. We can then define the ellipsoid parameters (center and radii) from the algebraic formula of the 3D conic 1.5.

An other approach consists in fitting the ellipsoid to the 3D scattered data points using the *linear least squares* with the linear constraint proposed in [361] to set the  $j$  parameter to 1. Thus, the generalized problem to be considered is:

$$\mathbf{D}^T \mathbf{D} \mathbf{a} = \mathbf{D}^T \mathbf{1}_n \quad (1.8)$$

We have compared both of the previous approaches on our data for extracting the 3D ellipsoid after the step of outliers removal. Figure 1.14 shows the fitted ellipsoid using the two methods. As detailed in table 1.2, the first fitting (LSQ) is more accurate for our data as it fits the best to the whole set of points (the resulting median algebraic distance overall the data points is equal to 0.0159) and the resulting ellipsoid is closer to the heart geometry (the heart long axis being around 12 14cm).

To improve the performance of the fitting step, we process an iterative weighted LSQ fitting approach to prune points that saliently deviates from the estimated model for each iteration. First, we define the *Average Fitting Deviation* (AFD)  $\sigma$  as following:

$$\sigma = \sqrt{\frac{1}{|\mathcal{P}|} \sum_{i \in \mathcal{P}} F(a; x_i)} \quad (1.9)$$

with  $\mathcal{P}_c$  being the set of the heart shell points kept after the first step of outliers removal (see

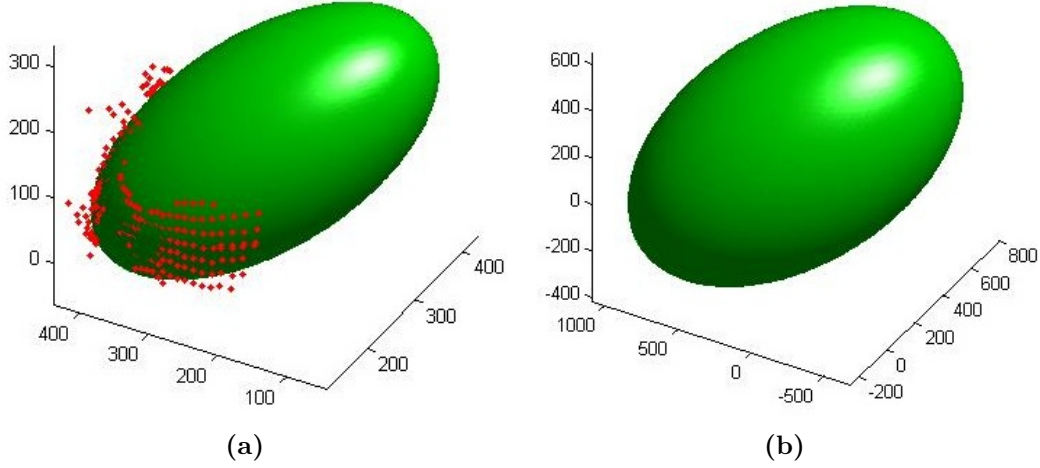


**Figure 1.14** – Ellipsoid fitting: (a) The LSQ fitting result, (b) The Direct Least Square fitting (DLSQ)[165]

previous section 1.3.2.1) and  $F(a, x) = 0$  the result of the LSQ fitting on  $\mathcal{P}_c$ . AFD is thus used to define the mean error of fitting. This value is low for an accurate fitting and considerably high for a bad fitting result. Hereafter, we use the AFD for a fitting to determine a new set of outliers with reference to the resulting estimated ellipsoid. First, we scan all the points included in  $\mathcal{P}_c$ : A null weight  $w$  is affected to points that deviates from the fitted model more than  $\nu$  times the AFD. Then a new fitting is processed on the remaining set of points. The iterative process stops when all the remaining points (with a non-zero weight value) are at a distance lower than  $\nu \cdot \sigma$  from the ellipsoid.

To summarize the approach of the ellipsoid fitting, algorithm 1 illustrates the main steps described previously. Figure 1.15 shows the different fitted ellipsoids before outliers removal ( $E_{l_0}$ , figure a), after the model-based outliers removal ( $E_{l_1}$ , figure b) and after the iterative fitting step ( $E_{l_2}$ , figure c). Table 1.7 shows the variation of the AFD and the eccentricity of the three fitted ellipsoids. Using our outliers removal both the AFD and the eccentricity of the fitted ellipsoid are improved. The iterative approach for detecting and removing the nearest outliers provides a better result. Indeed, the final ellipsoid features the best AFD and eccentricity compared with the other ellipsoids.

This approach was tested on 137 3D CT scan sets. Four failure cases were detected because of an erroneous 3D set of points. For 3 cases, the failure is due to an erroneous heart center estimation. The last failure case was because of a lack of contact points between the heart and lungs (about half of the heart volume was surrounded by the liver).

---

**Algorithm 1:** Extract the heart ellipsoid

---

**input** : Lungs volume  $LV$ , descending aorta volume  $DAV$ , heart center  $C$

**output:**  $E_l$  that fits the best heart volume

$\mathcal{P}_o = \text{extract\_heart\_shell\_points}(LV, DAV, C)$

$\mathcal{P}_c = \text{remove\_outliers}(\mathcal{P}_o)$

$first \leftarrow true$

**while**  $\mathcal{P}_{out} \neq \emptyset$  **do**

**if**  $first$  **then**

$first \leftarrow false$

**else**

$\mathcal{P}_c \leftarrow \mathcal{P}_c \setminus \mathcal{P}_{out}$

**end if**

$E_l \leftarrow \text{fit\_ellipsoid}(\mathcal{P}_c)$

$\sigma \leftarrow \text{average\_fitting\_deviation}(E_l, \mathcal{P}_c)$

**for all**  $x \in \mathcal{P}_c$  **do**

**if**  $\text{Dist}(E_l, x) > \nu \cdot \sigma$  **then**

$w_x = 0$

**else**

$w_x = 1$

**end if**

**end for**

$\mathcal{P}_{out} := \{x \in \mathcal{P}_c, w_x = 0\}$

**end while**

**Return**  $E_l$

---

**Table 1.3** – Iterative Ellipsoid fitting using linear least squares (LSQ): Average Fitting Deviation and eccentricity of the three fitted ellipsoids.

	Average Fitting Deviation	Eccentricity
$E_{l_0}$	0.0368	0.895
$E_{l_1}$	0.0190	0.797
$E_{l_2}$	0.0121	0.759

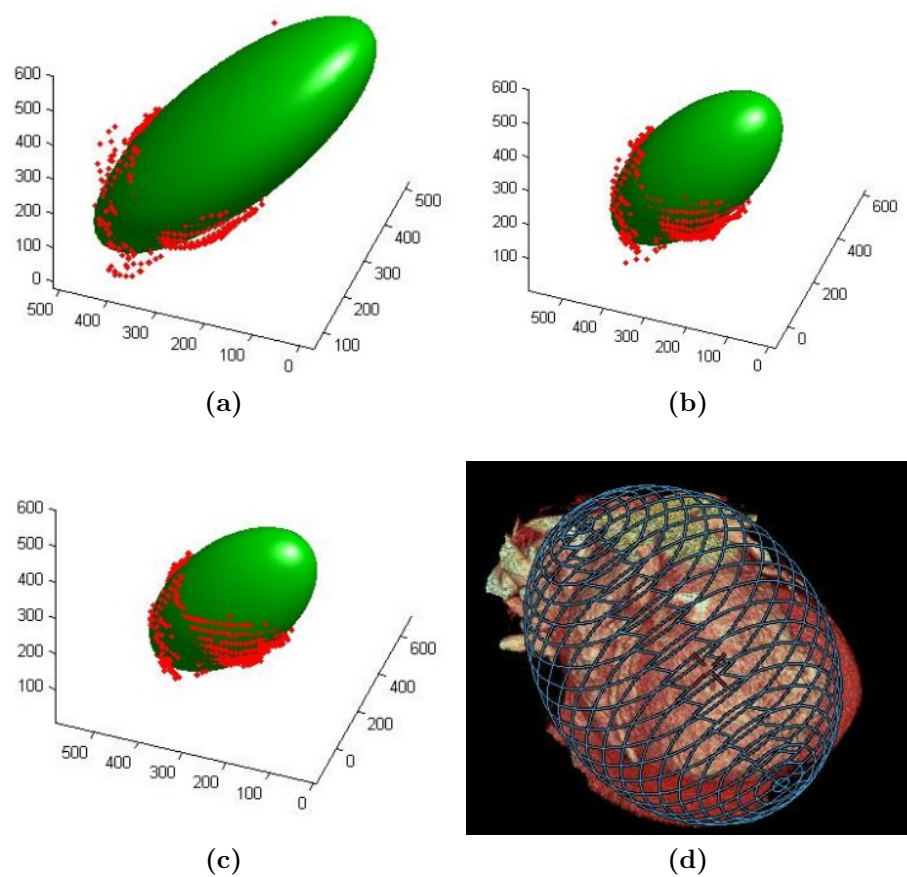


**Figure 1.15** – Iterative Ellipsoid fitting: (a) The first fitting result (before outliers removal), (b) The second fitting (after outliers removal), (c) The final fitting result (after the WLSQ iterative approach), (d) 3D rendering of the heart ellipsoid

### 1.3.3 Heart Volume Extraction

Once we have estimated the best fitting ellipsoid of the heart, we move to the final step of the heart wall delineation. Since the heart is not perfectly elliptic, the fitting result needs to be refined to match the real heart contours. Therefore, we define two labels for the heart (H) and the background (B) by applying separately an erosion and a dilation to the heart ellipsoid. The final segmentation is obtained using a supervised graph-based approach.

#### 1.3.3.1 Graph-Based Approaches

Graph based segmentation approaches interpret an image as a graph, whose nodes are the image pixels (voxels in 3D) and edges are defined by some adjacency relationship. They provide different topologies to exploit optimum connectivity between pixels for effective delineation by taking advantage of a solid mathematical background from graph theory. Earlier works date back over 30 years with the work of Zahn [482] where a family of graph-theoretical algorithms based on the minimal spanning tree for detecting several kinds of cluster structure in arbitrary point sets were proposed.

**1.3.3.1.1 Watershed Transform** The watershed algorithm is a popular segmentation framework, coming from the field of mathematical morphology. It has been widely used in different fields including medical imaging segmentation, due to several advantages (e.g. simplicity, possibility to be parallelized, ability to always detect a contour even if the contrast is poor). A grey level image could be interpreted as a topographic relief, where the altitude of each point is relative to its gray value. If we imagine that some drops of water are falling on this topographic relief, they will flow until reaching a local minima. The watersheds of this image corresponds to the limits of the *catchment basins* of the different drops. The watershed transform is computed on a function of the original image used to split the different regions (generally defined as the image gradient). Hence, the watershed lines are located at high gradient points and the catchment basins corresponds to homogenous grey level regions in the original image.

Several definitions of the watershed transform have been proposed in the literature, leading to different algorithms to compute the watershed on a given discrete image [100, 295, 437]. A review of the different definitions and algorithms is provided in [358]. The approach introduced by Meyer in [295] is based on the topographical distance. Starting from a set of selected and labeled seeds, the algorithm successively floods the grey value relief corresponding to the gradient image of the original image and watersheds with adjacent catchment basins are created.

However, segmentation results from watershed transform may suffer from leaks and degeneracy of the solution in the presence of weak boundaries.

**1.3.3.1.2 Graph Cuts** **Graph Cuts (GC)** techniques have been developed as a method for interactive seeded segmentation originally produced by [Boykov and Jolly \[52\]](#). It is based on the labeling of some nodes belonging to the background and others to the foreground (object to be segmented). The algorithm finds the minimum-weighted cut separating the two labels by performing a max flow/min cut analysis. This work has been extended to overcome speed issues [\[257, 264\]](#), to propose additional image features [\[37\]](#) and to address problem of user interaction [\[364\]](#). We note two major concerns associated to the GC algorithm, the metrication errors and the shrinkage bias. Successful works for addressing the metrication errors were proposed using continuous maximum flows, additional edges or total variation [\[49, 407, 426\]](#). However, they induce a greater memory and computation time costs than the original algorithm. Similarly, shrinkage bias has been solved [\[49, 407, 436\]](#) in some works but requiring additional computation and parameters.

**1.3.3.1.3 Random Walkers** **Random Walker (RW)** is an other supervised segmentation algorithm developed by [Grady \[164\]](#) trying to capture the benefits of the previous graph based methods while overcoming their disadvantages. The approach combines robustness to weak or missing boundaries and noise in the image while avoiding trivial solutions [\[164\]](#). It allows to overcome blocky surfaces or segmentation leaking possible when using Graph Cuts or Watershed based approaches.

Following, the image will be represented by a graph  $G = (V, E)$  where each node  $v_i \in V$  corresponds to a voxel of the image and each edge  $e_{ij} \in E$ , connects the two nodes  $v_i$  and  $v_j$ . A weight  $\omega_{ij}$  is affected to the edge  $e_{ij}$  to reflect a dissimilarity measure between the two nodes based on intensity changes. A common used expression for the weight function is:

$$\omega_{ij} = \exp(-\beta(g_i - g_j)^2) \quad (1.10)$$

with  $g_i$  being the intensity of the voxel  $i$  and  $\beta$  a free parameter of the algorithm. We also define the degree of a node  $i$ , denoted by  $d_i$  as the sum of the weights of all the incident edges on  $v_i$ :

$$d_i = \sum(\omega_{ij}) \quad (1.11)$$

Although the algorithm was initially motivated by sending random walkers from each unlabeled

### 1.1.3 Overview of the Proposed Approach

---

beled pixel and computing the first seed (foreground/ background) they reach, it is impractical to solve the problem based on this approach. Practically, the probability for each random walker to reach first a voxel of a particular label is computed by solving the **Dirichlet problem** [22]. A Dirichlet integral is defined by:

$$D[u] = \frac{1}{2} \int_{\Omega} |\nabla u|^2 d\Omega \quad (1.12)$$

for a field  $u$  and a region  $\Omega$ . The Dirichlet problem consists in finding the *harmonic* function subject to its boundary values. A harmonic function is a function that satisfies the **Laplace Equation**:

$$\nabla^2 u = 0 \quad (1.13)$$

In fact, the harmonic function satisfying the boundary conditions minimizes the dirichlet integral [99]. The Laplacian matrix  $L$  is usually used to model the interaction between the image voxels. This matrix is defined by:

$$L_{ij} = \begin{cases} d_i & \text{if } i = j \\ -\omega_{ij} & \text{if } v_i \text{ and } v_j \text{ are adjacent nodes} \\ 0 & \text{otherwise} \end{cases} \quad (1.14)$$

The combinatorial formulation of the Dirichlet integral is:

$$D[x] = \frac{1}{2} x^T L x = \frac{1}{2} \sum_{e_{ij} \in E} \omega_{ij} (x_i - x_j)^2 \quad (1.15)$$

with  $x$  being the combinatorial harmonic function minimizing (1.15).

As the laplacian matrix is positive semi-definite, the critical points of  $D[x]$  corresponds to its minima. If we partition the set of vertices into two sets seeded/unseeded nodes the equation 1.15 could be rewritten as following:

$$D[x] = \frac{1}{2} \begin{bmatrix} x_M^T & x_U^T \end{bmatrix} \begin{bmatrix} L_M & B \\ B^T & L_U \end{bmatrix} \begin{bmatrix} x_M \\ x_U \end{bmatrix} \quad (1.16)$$

U and M referring to *unseeded* and *marked* vertices. B is the laplacian matrix part corresponding to the labelled vertices. To find the critical points we differentiate (1.16) with refer to  $x_U$  which yields to:

$$L_U x_U = -B^T x_M \quad (1.17)$$



To define the probabilities for a label  $s$ , the solution could be found by solving the system:

$$L_U x^s = -B^T m^s \quad (1.18)$$

with  $m^s$  the set of seeds of the label  $s$ .

The solution for all the labels is found by solving the system:

$$L_U X = -B^T M \quad (1.19)$$

with  $X$  having  $K$  columns corresponding to the number of the labels.  $M$  is called the boundary condition matrix containing the labels for each seed point ( $M$  has as many columns as labels and as many rows as seeds) [164].

An interesting analogy between the circuit theory and random walks was established making the resolution of the problem simple and convenient for binary segmentation (background/foreground labels)[126]. The graph is viewed as an electrical circuit in which each edge is represented by a linear resistor (i.e. the edge weight is simulated to an electrical conductance). Seeds corresponding to background label are tied to the ground and each seed associated with the foreground are attached to a unit direct current ideal voltage source. The electrical potentials thus obtained in this circuit for each node are equal to the probability that a random walker sent from this node will reach a foreground node before reaching a background one. This approach could also be used to define the probabilities for all the labels by selecting one label at time and setting the seed nodes of the other labels grounded (i.e. potential is equal to 0) and then affecting each node to the label corresponding to the maximum probability value.

### 1.3.3.2 Heart Surface Segmentation

The heart and background labels are created from the previously estimated heart ellipsoid. The heart volume labels  $H$  is obtained by eroding the fitted ellipsoid thus to ensure that the kept volume is inside the heart and does not include any surrounding structures (e.g. liver or bones). The heart ellipsoid is also dilated to get the background labels.  $B$  is defined as the complementary of the dilated ellipsoid volume. A calculus domain is also defined using the difference between the dilated and the eroded ellipsoid volumes. This allows to reduce the search space and hence the computational time. Figure 1.16 shows an example of the heart labels.

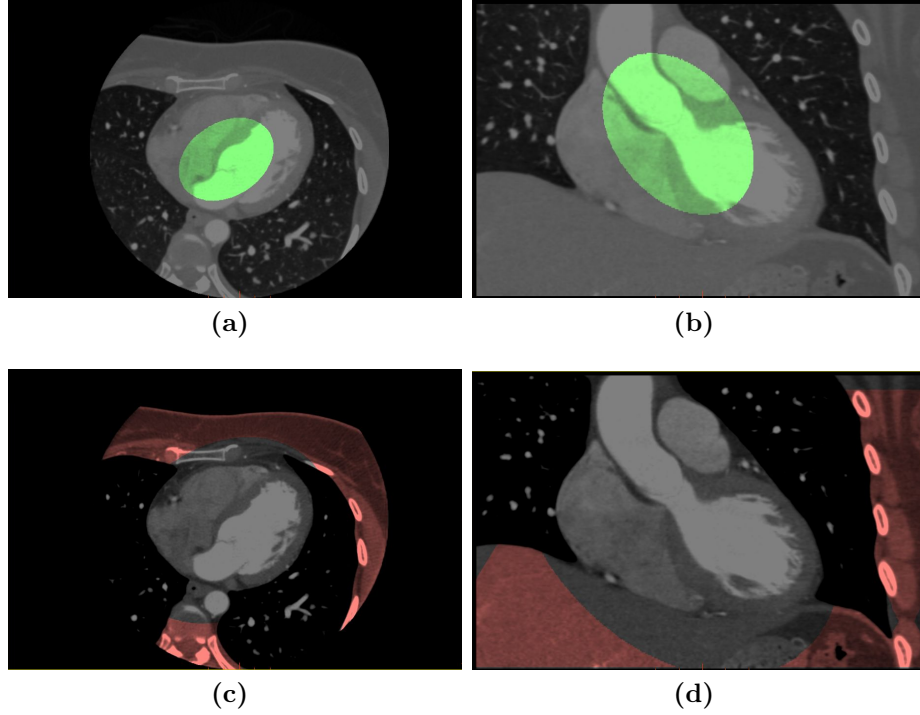


**Figure 1.16** – Heart labels creation: (a) and (b) Axial and coronal views of the heart inside labels. (c) and (d) Axial and coronal views of the heart background labels.

Practically, the RW problem is solved by minimizing the energy term:

$$E(x) = \sum_{e_{ij} \in E} \omega_{ij} (x_i - x_j)^2, s.t. x(H) = 1, x(B) = 0. \quad (1.20)$$

with  $x_i$  being the probability assumed for label H at node  $v_i$ . The heart segmentation  $s$  is thus obtained by thresholding the computed probability  $x$  as following:

$$s_i = 1 \text{ if } x_i \geq \delta, 0 \text{ if } x_i < \delta. \quad (1.21)$$

The final heart volume is obtained by performing a 2D dilation on the RW result to avoid truncating the coronaries. Figure 1.17 illustrates an example of the resulting heart segmentation. 2D views shows the heart delineation result compared to the original image. 3D rendering views allows to visualize the coronary arteries on the heart surface.

**1.3.3.2.1 Implementation Details** The Laplacian matrix models the interaction between all the nodes which leads to a large sparse linear system for which direct solver are not efficient in practice. A solution would be to factorize the laplacian matrix to a lower and higher triangular

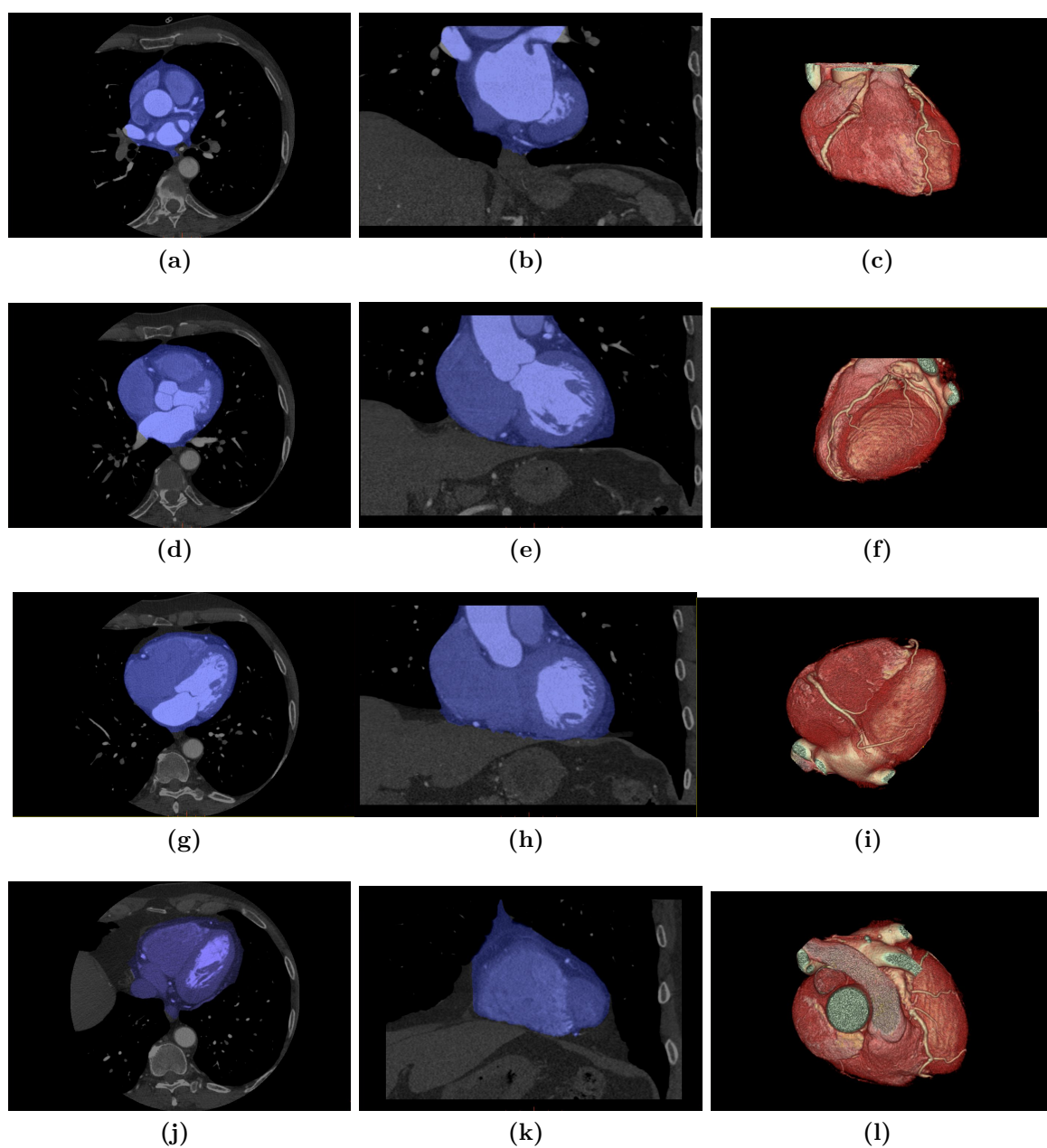


**Figure 1.17** – An example of automated heart isolation: Axial (first row), coronal (second row) and 3D rendering (third row) views of the heart volume labeled on the original volume..

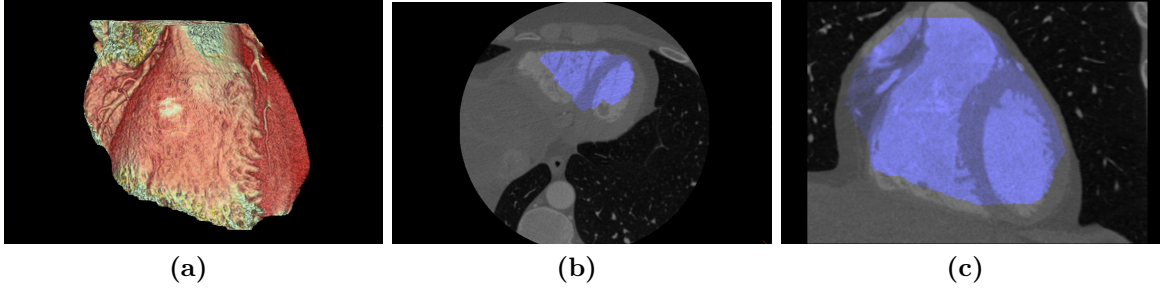


**Figure 1.18** – Modifying threshold value for sternum removal. The peripheral bones are removed but this induces some heart structure removal too.

matrix and perform a two stage resolution: a backward and a forward substitution [162] to solve the linear problem efficiently. This approach could be suitable for reasonable sizes (2D medical images with a size of  $256 \times 256$  could be handled by direct solvers). However, 3D images would result in extremely large Laplacian matrix (  $256 \times 256 \times 256$  voxels) which would require an impractical amount of time and memory to factorize the matrix and solve the problem by direct solvers. An alternative to direct solver for large linear systems resolution is the *Conjugate Gradient method*. This approach is an iterative approach specially designed for handling symmetric positive definite matrices [392]. The sparse nature of the system is exploited to improve the computational and storage efficiency: only the  $6 + 1$  bands of the laplacian matrix are stored. The volume is also down-sampled by 2 to reduce the computational domain without loss of precision.

#### 1.3.3.3 Extra Bones Removal

The previous heart mask volume (result of the random walker step) showed some false positive detection due to the inclusion of parts of the sternum and the spine bones. This is mainly due to the fact that these structures are very close to the heart volume and exhibit a relatively close probability values to the heart ones. Reducing the random walker probability threshold  $\delta$  could solve this problem. However, this would lead to cutting some cardiac structures (see figure 1.18).

To solve this problem, we propose a bone removal step in order to remove all the remaining bones in the final heart volume. First, a bright structures threshold is applied to the heart volume. This results in keeping blood pools and bones connected components. The heart blood pools are removed by applying a size-based connected components filtering (the same one as for the heart center estimation). Subsequently, small circular connected components are filtered (with size  $< S_{bones}$ ) thus resulting in keeping only eventual bones included in the heart

volume. A hole closing followed by a dilation is then applied on the resulting structures. The heart mask volume is hence obtained by removing the previous bones connected components. Finally, to avoid holes inside the heart volume due to some false positives a hole closing steps is applied. The different bones removal steps are illustrated in figure 1.19.

## 1.4 Experiments

### 1.4.1 Data

The heart delineation algorithm was tested on a 133 cardiac CT database. The database is divided in two subsets:  $S_1$  and  $S_2$  mainly coming from GE Healthcare’s LightSpeed VCT (64-slice Volume Computed Tomography) and GE’s Discovery CT750 HD (64-slice High Definition scanner). Volume size ranges from 164 to 373 slices with a slice size of 512x512 pixels. The in-plane resolution (resolution inside a slice) varies from 0,34 mm to 0,50 mm, while the out-of-plane resolution (the slice thickness) is 0.625 mm for all the volumes. The database contains both healthy and pathological cases. Calcified, soft and mixed plaques are present with different stenosis degrees. The database contains also some cases with the presence of stents and heart bypass. Generally, the database shows moderate and good image quality.

### 1.4.2 Manual Segmentation

For the evaluation, the database was annotated separately (two subsets of 72 and 61 images) by two different observers. Manual annotation of cardiac CT images is a time consuming task. Typically, a manual heart segmentation takes about 90 minutes depending on the image quality and field of view. For heart volume annotation, semi automatic tools were used to help accelerating the processing. First, an estimation of the heart mask is computed using an automatic tool based on a set of thresholds and morphological operations. Subsequently, the mask is manually corrected to add missing parts (e.g. coronaries, cavities and/or heart muscle) using a manual tool that allows to propagate the volume starting from a seed point into the missing regions based on region growing guided by appearance properties. Over-segmentation or false positive detections (e.g. sternum, livers, trunks) are also eliminated using a manual tool. Both 2D (axial, sagittal, coronal) views and 3D rendering volumes are used to adjust the heart volume. To be sure all the unwanted structures are suppressed, the observer changes the HU threshold on the 3D rendering view and eliminates eventual residues. Finally, the heart volume is saved and is then exported in a binary file and converted to a 3D triangulated mesh

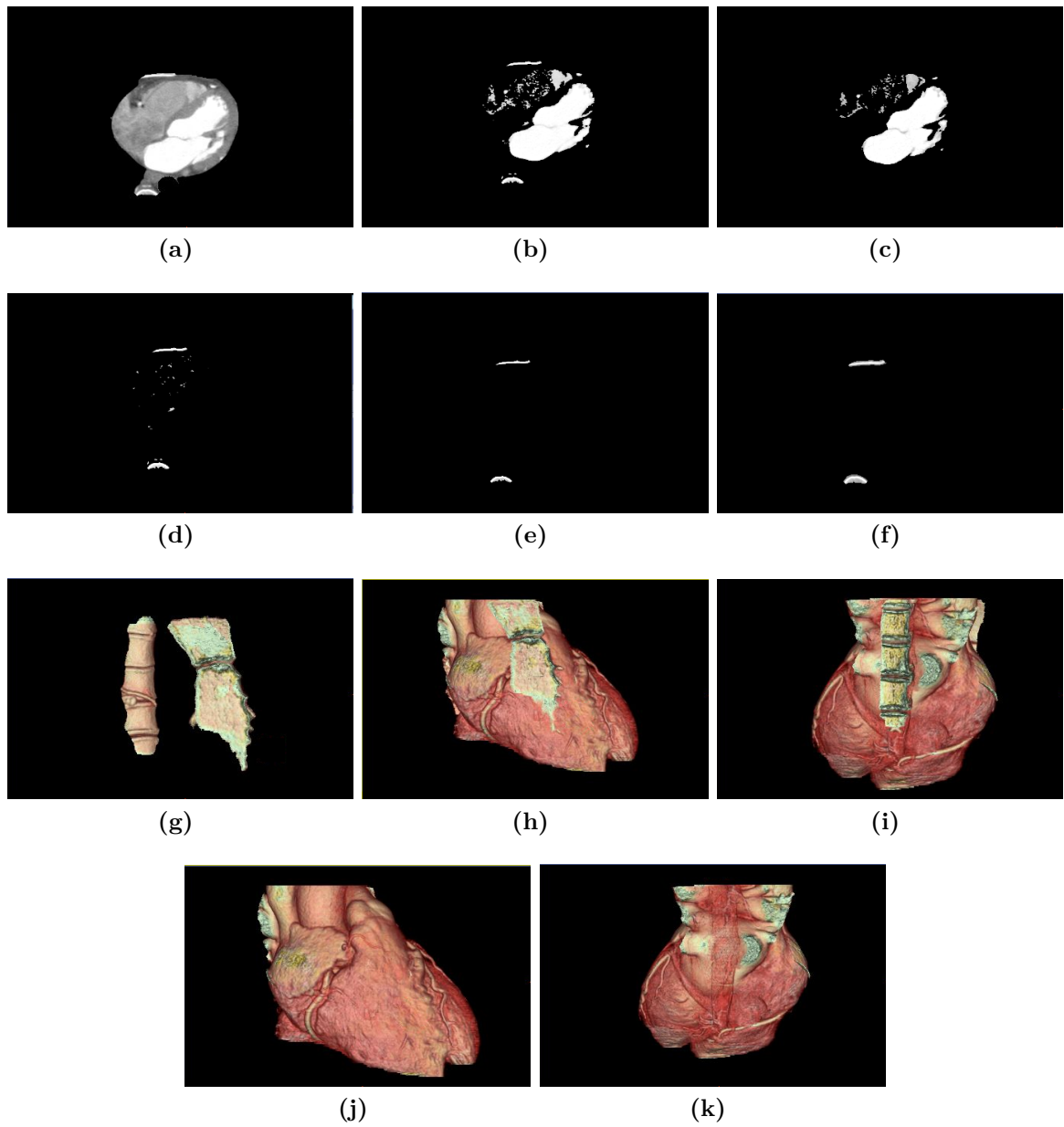


**Figure 1.19** – Extra bones removal: (a) - (f) 2D axial views showing the different processing steps. (g) 3D rendering of the detected bones. (h) - (k) 3D rendering views of the heart volume before and after bones removal. We clearly can state the impact of removing bones on clearing the heart surface views.

for further evaluations.

### 1.4.3 Evaluation measures

In order to assess the performance of our approach, we evaluated the automated heart masks using both quantitative and qualitative evaluations. Quantitative evaluation allows for an objective evaluation based on manually annotated *ground truths*. It is also a way to obtain a comparison with state-of-the art methods. However, this kind of comparison should be considered carefully because the evaluation are generally performed on different data sets and the ground truths are annotated by different observers with different experience levels. Moreover, quantitative evaluation may not properly represent the segmentation quality. In fact, it does not give a precise information about the impact of an over-segmentation or an under-segmentation on clinical outcome and consequently patients health. Therefore, a qualitative evaluation of the segmentation method was conducted in order to get more information about the performance of the algorithm against specific challenges (see section 1.1). Evaluation measures and metrics used for both evaluations are detailed in following sections 1.4.3.1 and 1.4.3.2.

#### 1.4.3.1 Quantitative Evaluation

First, the algorithm was evaluated quantitatively using the 133 CT images and their corresponding gold standard segmentation. In the literature, different evaluation methodologies are commonly used for the assessment of a given segmentation compared to a “ground truth” (see appendix C). We can distinguish two main categories of such techniques: (1) Volume-based measures and (2) Distance-based measures have been conducted. We have used a set of commonly used metrics for medical segmentation evaluation that are explained hereafter.

**1.4.3.1.1 Volume-based Evaluation** Volume-based measures are defined from the different True Positive (TP), False Positive (FP), True Negative (TN) and False Negative (FN) sub-regions of the segmentation result (see appendix C.1 for definitions). To compute corresponding sub-volumes, heart segmentation results and manual heart ground truths are converted to binary masks.

Let  $S$  be the binary segmentation result and  $G$  refer to the binary mask of the manually delineated ground truth. The corresponding TP, FP, TN and FN volumes are thus defined as follow:

$$V_{TP} = S \cap G ; V_{FP} = S - G ; V_{TN} = I - S - G \text{ and } V_{FN} = G - S.$$



First, *sensitivity*, *specificity*, *positive predictive value* (PPV) and *negative predictive value* (NPV) (see section appendix C for definitions) of the algorithm have been computed on both of the subsets  $S_1$  and  $S_2$  separately. In addition, *False negative volume fraction* (FNVF) and *False positive volume fraction* (FPVF) (see section C.1.1 for formulations) are also computed to assess the amount of false detections as a fraction of the ground truth volume. FPVF indicates the amount of the over-segmented tissues and FNVF corresponds to the fraction volume of the missed parts by the algorithm compared to the ground truth volume.

*Dice coefficient* is among measures that are commonly used to evaluate the performance of a segmentation approach [116, 396]. It assesses the similarity between the segmentation result and the manual segmentation (reference standard) by reporting the extent of the overlap between the two volumes. Its values range from 0 (no overlap) to 1 (total overlap). *Dice similarity coefficient* (DSC) is obtained using equation 1.22:

$$DSC(S, G) = \frac{2|S \cap G|}{|S| + |G|} \quad (1.22)$$

**1.4.3.1.2 Distance-based Evaluation** Secondly, distance based evaluation has been performed. Generally, distance measures quantify the error distance between the automated and manual segmentation surfaces. The *Haussdorf distance* is a mathematical metric usually used to measure the “closeness” of two sets of points that are subsets of a metric space. Let  $\mathcal{S}$  be the surface of the heart volume and  $\mathcal{G}$  be the surface of the corresponding ground truth. The Haussdorf distance is expressed as :

$$H(\mathcal{S}, \mathcal{G}) = \max \{h(\mathcal{S}, \mathcal{G}), h(\mathcal{G}, \mathcal{S})\} \quad (1.23)$$

with,

$$h(\mathcal{S}, \mathcal{G}) = \max_{a \in \mathcal{S}} \{\min_{b \in \mathcal{G}} \{d(a, b)\}\} \quad (1.24)$$

### 1.4.3.2 Qualitative Evaluation

In order to capture the accuracy of the proposed approach in heart isolation and obscuring surrounding structures removal, we conducted a qualitative evaluation using a subset of our database composed of 65 images randomly selected from both of the sets  $S_1$  and  $S_2$ . An expert has visually evaluated the quality of the segmented heart masks. The automatic heart masks have been scored with respect to two main criteria: 1) Removal of structures that may obscure the coronaries (i.e., sternum and ribs, liver, Spine) and 2) Inclusion of main cardiac



## Chapter 1. Automated Heart Mask Extraction

---

components (i.e, heart cavities, coronaries, ascending aorta and grafts if any). Hence, seven evaluation metrics have been defined to asses the performance of the algorithm:

- **Sternum Removal:** assesses if the sternum has been successfully removed or not
- **Liver Removal:** indicates if the liver was removed from the final heart mask or there is still some obscuring parts.
- **Spinal Removal:** assesses the spine removal
- **Cavities Inclusion:** attests whether the heart cavities are kept in the heart volume or not.
- **Ascending Aorta Inclusion:** this metric allows to evaluate the algorithm against the ascending aorta inclusion criteria which is relevant for cardiac diseases diagnosis.
- **Coronary Inclusion:** indicates whether the heart coronaries are included in the final heart volume or have been truncated.
- **Grafts Inclusion:** indicates whether the bypass graft (if there is any) is added to the segmented heart or if it was cut.

For each criterion, the given score ranges from 1(failure) to 3 (success). For false positives evaluation (Sternum, Liver and Spinal removal), the score assesses how much the structure is obscuring the coronaries and the heart surface. A score of 1 means that the removal has failed and that the kept parts are shadowing the heart structures. A score equal to 3 means that the obscuring organs have been successfully removed and that the resulting heart volume does not need to be adjusted. Similarly, for false negatives evaluation (Cavities Inclusion, Ascending Aorta Inclusion, Coronary Inclusion, Grafts Inclusion), a score of 1 means that an important part of the concerned feature is truncated (main coronaries, heart cavities...) , while a score of 3 means that no part is missing. A score of 2 indicates that small parts are missing and the the result is acceptable with reference to the concerned criteria.

**Table 1.4** – Qualitative evaluation: Overall segmentation quality classification

Grade	Segmentation Result
1	Failure (main parts of the heart are cut or too much false positive)
2	Acceptable (needs subsequent manual corrections)
3	Good (needs some minor corrections)
4	Very good (some extra structures not obscuring the heart surface)
5	Perfect

**Table 1.5** – Automated heart segmentation: computational time for each processing part

	Pre-processing	Heart model fitting	Heart volume segmentation	All
Mean	1,2	1,7	13,7	16,7
Min	1	0	5	8
Max	3	3	28	31

Moreover, an overall score is affected for each exam to assess the overall “Segmentation Quality”. Table 1.4 details the different possible scores classification for segmentation quality assessment.

## 1.5 Results

### 1.5.1 Computational time

Computational time is a critical issue in clinical applications that should be considered while developing any approach. All the tests was run on a 4 cores Intel(R) Xeon(R) CPU W3565 @ 3.20GHz, 8.00 GB (RAM) machine. A complete heart segmentation on a 512x512x203 cardiac CT exam takes around 16 seconds. The random walker iterations takes around 5 seconds to converge. Table 1.5 shows the mean, minimum and maximum value of the processing time for the main steps.

Heart volume segmentation (i.e. labels extraction, Random Walker iterations and the post-processing step) is the most consuming part (80 % of the overall processing time). This part could be further optimized to reduce the computational time. In fact, this is due to a non optimized step of ellipsoid volume extraction that could be considerably reduced to some few seconds.

### 1.5.2 Parameters Optimization

The proposed approach presents an important set of parameters that affects more or less the final segmentation result. In this section we detail the setting of the most important parameters used in our algorithm. We also explain the steps of some parameters optimization. Table 1.6 shows the optimized parameters values for the different heart segmentation steps.

Pre-processing step: For the optimization of the lungs, the aorta volumes and the heart center extraction, automated tests have been launched and the results have been stored using screen shots. This allowed for a visual inspection of the performance of this pre-processing steps and thus optimizing the different parameters.

## Chapter 1. Automated Heart Mask Extraction

**Table 1.6** – Automated heart segmentation: Parameters settings

Step	Part	Parameter	Value
<b>Pre-processing</b>	Lungs extraction	Lungs intensity thresholds	$T_{air} = -1000$ HU , $T_{lungs} = -500$ HU
		Lungs size threshold	$V_{lungs} = 40$ mL
	Descending Aorta extraction	Bright structures threshold	$T_{bright} = +110$ HU
		Aorta size range	$S_{aorta1} = 314$ mm <sup>2</sup> , $S_{aorta} = 600$ mm <sup>2</sup>
<b>Heart model fitting</b>	Heart Center extraction	Bright structures threshold	$T_{bright2} = 255$ HU
	Heart shell points extraction	Angular step (ray casting)	$\theta = 360$ deg /50
	Outliers removal	Outliers portion	$\alpha = 1/16$
		Second derivative threshold	$T_d = 2$
<b>Heart volume extraction</b>	Ellipsoid fitting	AFD coefficient	$\nu = 2.5$
	Random walker	Probability threshold	$\delta = 0.6$
		Dilation SE size	$S_{SE} = 4$
	Bones Removal	Connected component size	$S_{bones} = 125$ mm <sup>3</sup>

Heart model fitting: This step includes the heart points extraction, model-based outliers removal and iterative ellipsoid fitting. The angular sampling for the ray casting approach has been set in a way to get enough points for an accurate ellipsoid fitting. We fix this angular step to  $\theta = 360$  deg /50. Lower angular values lead to more biased models by the outliers and greater ones do not improve the result as much as they slow down the processing time. To set the second derivative threshold for the detection of the X and Y outliers, we tested different values and visualized the detected outliers for each value.  $T_d = 2$  gives the best compromise. For ellipsoid fitting,  $\nu$  have been chosen to give accurate fitting results after some iterations. In general, for  $\nu = 2.5$ , 2 or 3 iterations suffice to get a coherent ellipsoid that covers the heart volume. Visual inspection was also used to validate the performance of this step.

Heart volume extraction: For the optimization of this step, we have used the Receiver Operator Characteristic (ROC) curve [508]. While varying the Random Walker probability threshold  $\delta$  and the size of the 2D dilation structure element  $S_{SE}$ , we computed the different associated sensitivity and specificity values. This helped to find the best compromise between false positive and false negative detections. Figure 1.20 shows the obtained ROC curve. The best point (the nearest point to the upper left corner point (0,1)) is obtained for  $\delta = 0.6$  and  $S_{SE} = 2$ . The final heart segmentation with the bones removal step is displayed on figure 1.21. This final step allows to improve the algorithm performance (the green point is closer to the point (0,1)).

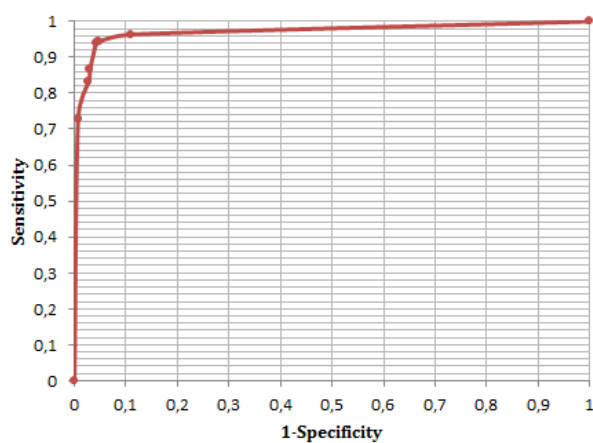


**Figure 1.20** – ROC Curve of heart segmentation: the different ROC points are obtained by varying the random walker threshold and the dilation size

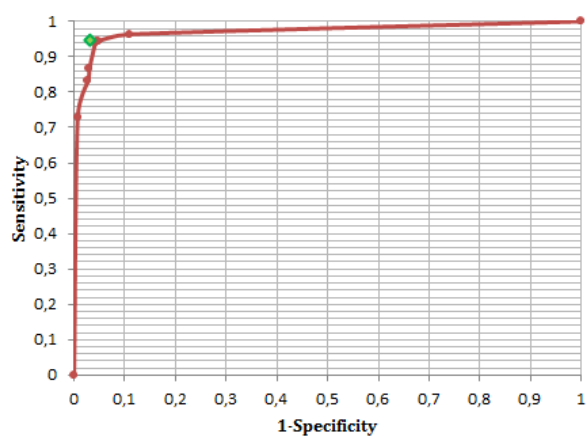


**Figure 1.21** – ROC Curve of heart segmentation: the bones removal step improves the heart segmentation quality (green point).

### 1.5.3 Quantitative evaluation results

Automated segmented heart volumes are stored in binary volume files with the same resolution. Those files have been used to compute the different evaluation volume-based measures using a C program developed under the PINK library [297]. For distance based measure, the segmented volumes are transformed to triangular meshes using the marching cube algorithm with the same parameters for all the datasets. The Hausdorff distance has been computed using the MESH program described in [20].

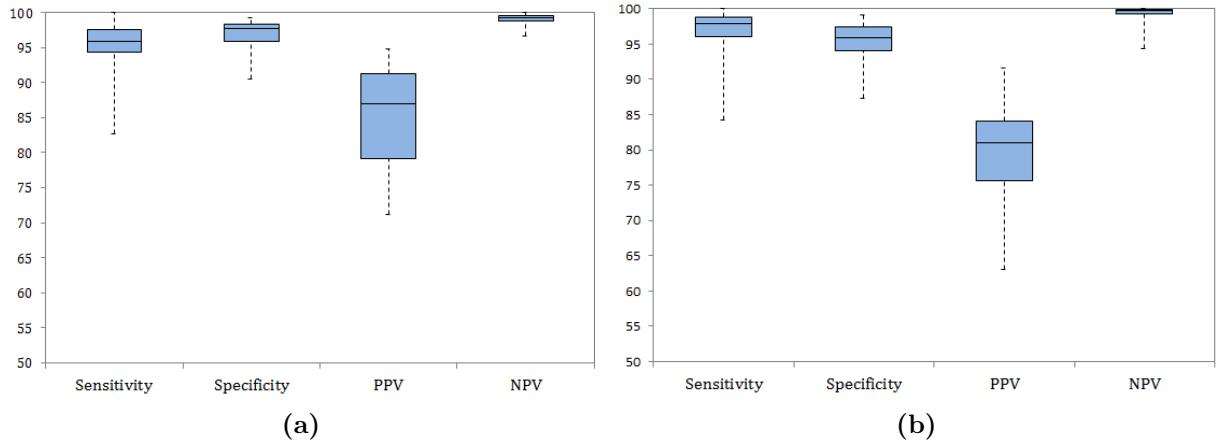
Table 1.7 shows the results of the fully automatic cardiac 3D quantitative evaluation by applying the metrics of section 1.4.3.1.1 to the automated segmentation volumes using the manually segmented gold standards. Results are provided for  $S_1$  and  $S_2$  separately, as well as the mean values for all the database. Summary box and whisker plots of sensitivity, specificity, PPV and NPV for both of the subsets are given in figure 1.22. The algorithm provides a mean sensitivity value of  $95,64 \pm 15,72$  and a specificity of  $96,11 \pm 12,78$ . This shows that our algorithm is able to accurately discriminate between heart voxels (true positives) and background voxels (true negatives). This result outperforms the result achieved by the work of [331]. For FNFP and FPVF a mean value of 0.05 and 0.2 are obtained respectively. This means that the algorithm has a tendency to overestimate the heart volume specially for  $S_2$ . The false positives volume is 4 times greater than false negative volume. This is mainly due to keeping some sternum liver parts.

**Table 1.7** – Quantitative evaluation: Sensitivity, specificity, PPV and NPV mean values and standard deviations for  $S_1$ ,  $S_2$  and the overall database

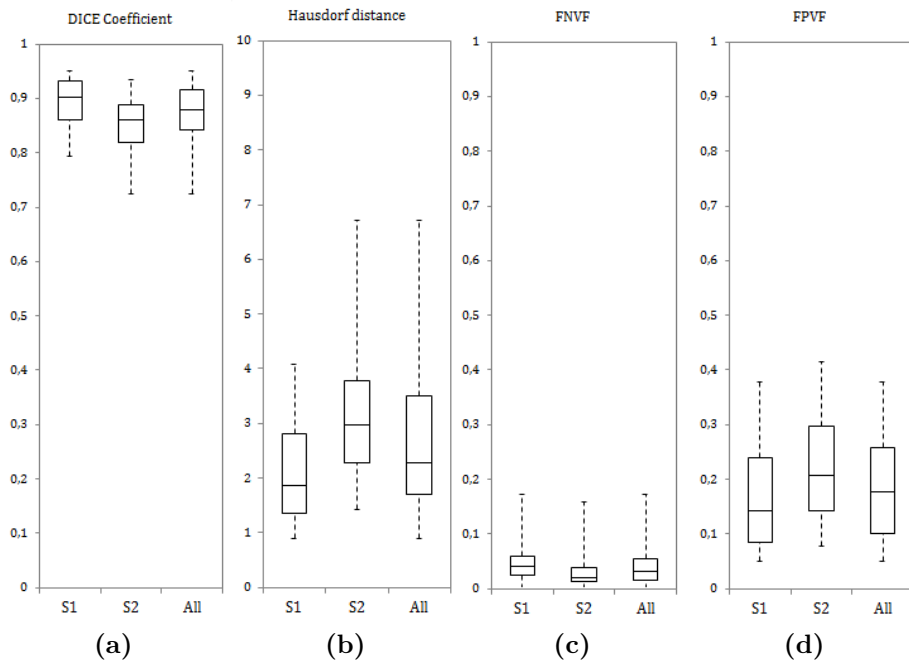
	Sensitivity	Specificity	PPV	NPV	FNVP	FPVF
$S_1$	$94,72 \pm 4,48$	$96,85 \pm 12,59$	$85,27 \pm 12,95$	$99,10 \pm 0,70$	$0,05 \pm 0,04$	$0,17 \pm 0,10$
$S_2$	$96,57 \pm 22,21$	$95,31 \pm 13,05$	$79,97 \pm 31,49$	$99,25 \pm 1,15$	$0,05 \pm 0,03$	$0,24 \pm 0,18$
<i>All</i>	$95,64 \pm 15,72$	$96,11 \pm 12,78$	$82,97 \pm 25,30$	$99,18 \pm 0,94$	$0,05 \pm 0,06$	$0,20 \pm 0,1$

Table 1.8 presents results of Dice coefficient and Hausdorff distance. An average Dice coefficient of  $0.87 \pm 0,17$  and a maximum distance error of  $2,67 \pm 1,43$  were obtained on the overall database. This meets the heart segmentation state of the art performances (see table 1.10). These results are displayed in the box and whisker plots of figure 1.23. Results shows that the algorithm is more accurate for the subset  $S_1$  than  $S_2$ . In fact,  $S_2$  always shows lower metrics than  $S_1$ . This reflects the sensitivity of any quantitative evaluation to the quality of manual ground truths. In fact, an inter-variability is always present between manual segmentation. This could be explained by different expertise level and different manual annotation protocols.

To inspect the surface-to-surface distance error, we visually analyzed the distance map of some exams showing high distances values. The distance maps are shown in figure 1.24.



**Figure 1.22** – Box plots of volume based evaluation metrics for data sets  $S_1$  and  $S_2$ .



**Figure 1.23** – Box plots of DICE coefficient, Hausdorff distance, FNVF and FPVF metrics for data sets  $S_1$  and  $S_2$ .

## Chapter 1. Automated Heart Mask Extraction

**Table 1.8** – Quantitative evaluation: DICE overlap measure and Hausdorff distance values for  $S_1$ ,  $S_2$  and the overall database

		Mean	Minimum	Q1	Median	Q3	Maximum
DICE	$S_1$	$0,89 \pm 0,12$	0,79	0,86	0,90	0,93	0,95
	$S_2$	$0,84 \pm 0,19$	0,72	0,81	0,86	0,88	0,93
	<i>All</i>	$0,87 \pm 0,17$	0,72	0,84	0,88	0,91	0,95
Distance	$S_1$	$2,07 \pm 0,96$	0,89	1,36	1,86	2,81	4,08
	$S_2$	$3,22 \pm 1,40$	1,43	2,27	2,96	3,79	6,70
	<i>All</i>	$2,67 \pm 1,43$	0,89	1,71	2,29	3,51	6,70

Maximum distances are mainly recorded around major vessel trunks and at the heart lower base because of remaining parts of the liver ( (figures a, b, c). Liver and vessel trunks are particularly hard to remove because the absence of clear edges delineating the heart surface around near these structures. Some cases showed also a high distance error due to the inclusion of some ribs (figure c).

The obtained results shows that quantitatively this method produces a reliable heart segmentation.

### 1.5.4 Qualitative evaluation results

To perform the qualitative evaluation, screen shots views of 3D rendering of the automated heart surface are saved from different angles to allow the visualization of the whole heart surface. These images are displayed in a web page where an observer could provide his evaluation for each exam and save the final evaluation in a file. Two experts have visually inspected these results. The obtained results are provided in table 1.9. The proposed approach is very robust against 5 criteria: Spinal removal, Cavities inclusion, Ascending aorta inclusion, Coronary inclusion, Grafts inclusion. One single case showed a truncated apex leading to a score of 2,98 for the cavities inclusion criterion. A score of 2.51 and 2.43 was obtained for sternum liver removal respectively. This confirms the quantitative results showing that the algorithm does over-estimate the heart volume. This also agrees with the distance error measured at these regions which are challenging because of the lack of contrast and their closeness to the heart surface.

The overall segmentation quality mean grade is of 3,94 with no failure cases. The distribution of the different scores are shown in figures 1.25 and 1.26. The algorithm shows a highly accurate segmentation quality in most cases. In fact, 70 % of the segmented volumes shows a grade between 4 and 5. 24 % of the results are acceptable and less than 5 % of the cases might need additional manual editions to remove some unwanted parts. Some examples of our result images are shown in Figure 1.27.

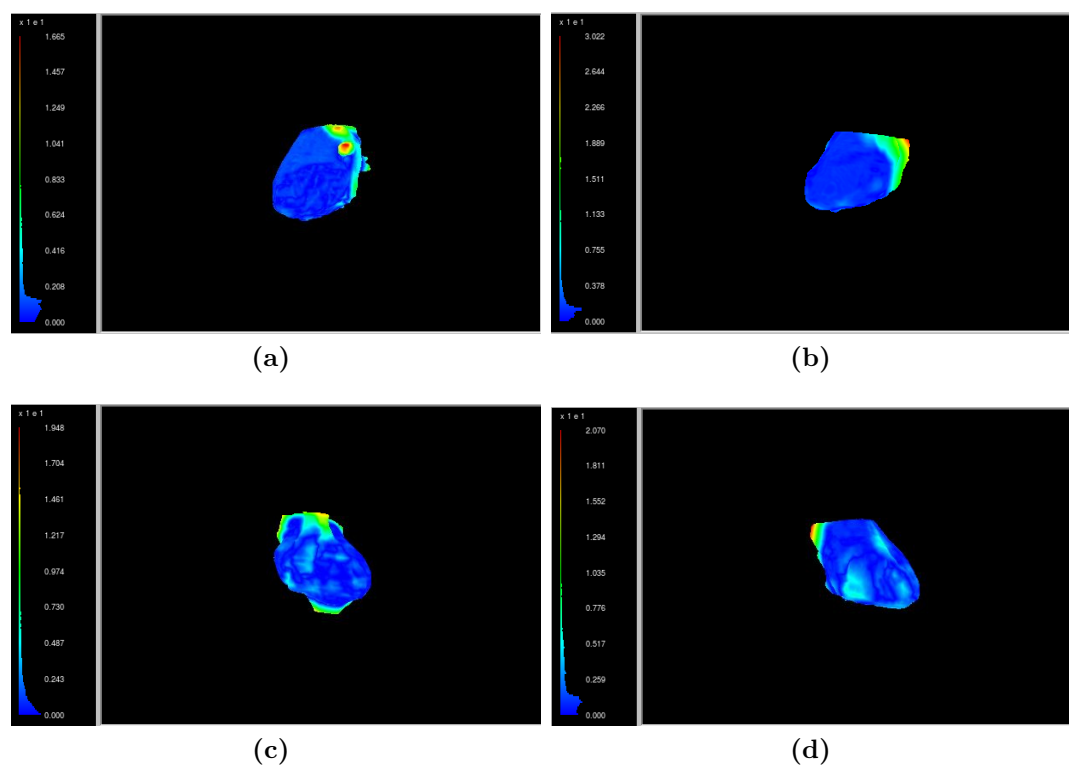


**Figure 1.24** – Distance maps of some segmented heart volumes exhibiting relatively high distance errors.

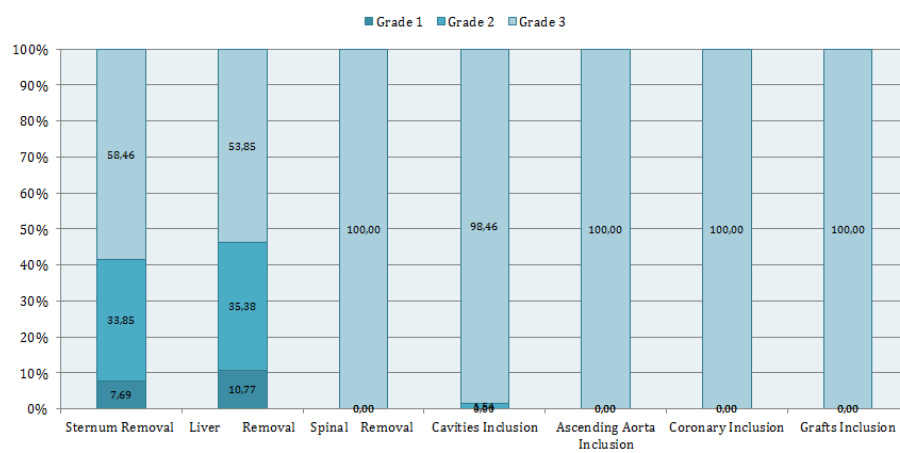


**Figure 1.25** – Qualitative Evaluation: distribution of the different grade classifications over the data set.



## Chapter 1. Automated Heart Mask Extraction

**Table 1.9** – Qualitative evaluation: Mean grade value of the different evaluation metrics

	Sternum removal	Liver removal	re-	Spinal removal	Cavities in- clusion	Ascending aorta inclusion	Coronary inclusion	Grafts inclusion	Segmentation quality
Grade	2,51	2,43		3,00	2,98	3,00	3,00	3,00	3,94

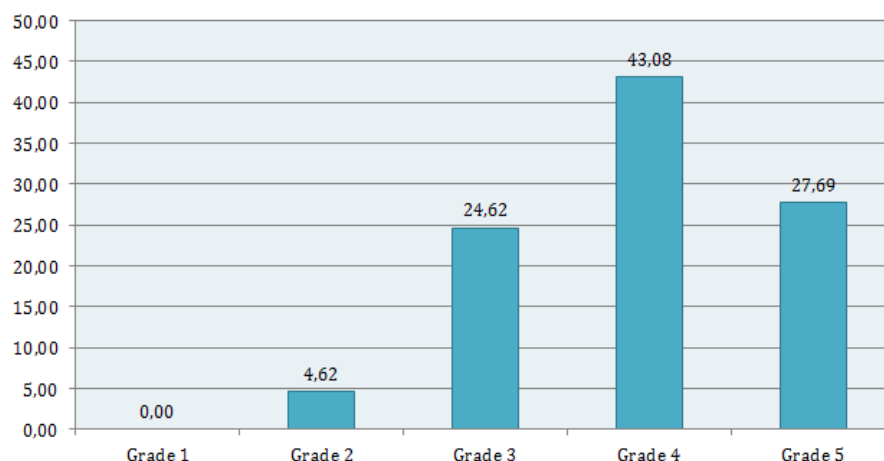


**Figure 1.26** – Qualitative Evaluation: Segmentation quality grade classification for all the database.

The qualitative and quantitative evaluations showed that our approach offers a level of accuracy and efficiency comparable to the best previously published approaches. Table 1.10 illustrates the comparison of the performance of our algorithm with state-of-the-art automated heart segmentation approaches in CT angiographies. Generally, our method performs as well as state-of the art approaches. Compared to the work of Funka-Lea et al. [154], our algorithm provides lower distance error. It also results in lower computational time than four works ([310], [431], [199] and [216]) and equal times as the [497]. We have to mention that some publications (e.g. [497], [216]) computed the mean distance error which is logically lower than the Hausdorff distance. Moreover, we have to note that the previous evaluations have been performed on different databases. Thus, comparing such evaluations should be done carefully as the data sets necessarily present some differences in acquisition protocols and reconstruction parameters. Moreover, the ground truths being annotated by different observers, this induces a subsequent variability between the different evaluations. A conclusive and objective comparison should thus be performed using the same database.

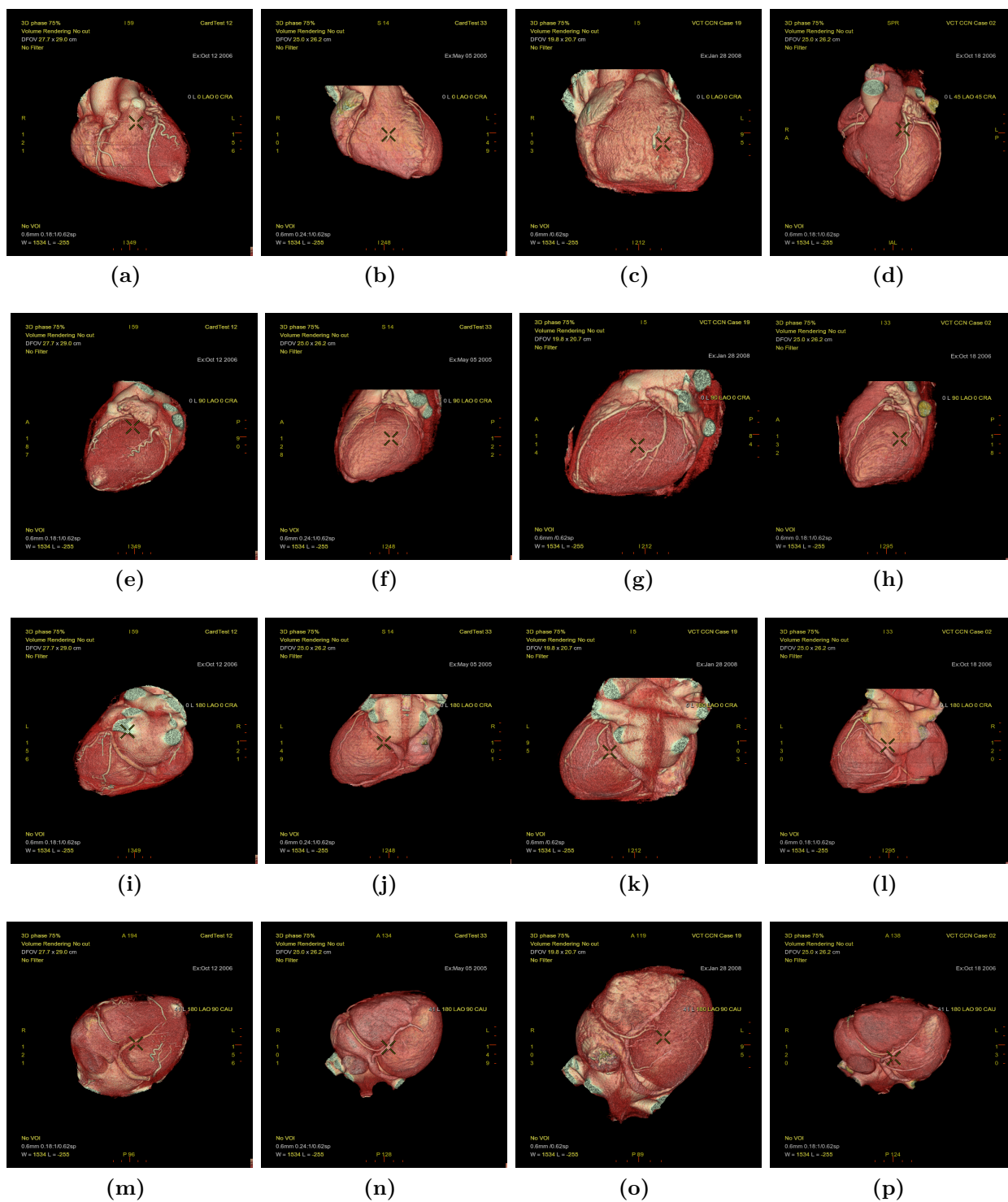


Figure 1.27 – Examples of heart segmented volumes.

**Table 1.10** – Comparison of the previous works on heart isolation CT angiography

Work	data	Error	Overlap	Processing time
<a href="#">Moreno et al. [310]</a>	10	6.4 mm	NA	4min (down-sampled) 17h original
<a href="#">van Rikxoort et al. [431]</a>	14 target images	NA	$0.8733 \pm 0.0363$	30 min
<a href="#">Ecabert et al. [132]</a>	28	$0.82 \pm 1.00$ mm	NA	10-30 sec
<a href="#">Isgum et al. [199]</a>	14 data set	NA	$0.88 \pm 0.03$	15 min
<a href="#">Funka-Lea et al. [154]</a>	70	5.5 mm	NA	20 sec
<a href="#">Kirisli et al. [216]</a>	251	$1.25 \pm 1.73$ mm	0.95	25 min
<a href="#">Zhong et al. [497]</a>	589 (288 patients)	1.91 mm	NA	1-5 sec
Our approach	133	$2,67 \pm 1,43$ mm	$0,87 \pm 0,17$	8-31 sec

---

---

## Chapter 2

---

# Coronaries Artery Segmentation

### Contents

---

<b>1.1 Cardiac Anatomy</b>	<b>3</b>
1.1.1 The Cardiovascular System Anatomy	3
1.1.2 Cardiovascular Lesions	11
1.1.3 Treatments	17
<b>1.2 Cardiac Medical Imaging</b>	<b>18</b>
1.2.1 Conventional Coronary Angiography	20
1.2.2 Intra Vascular UltraSound	21
1.2.3 Computed Tomography Angiography	22
<b>1.3 Cardiac Computed Tomography</b>	<b>30</b>
1.3.1 Cardiac CT: Advantages and Limitations	32
1.3.2 Coronary Assessment using CT Angiography	35
<b>1.4 Our Approach</b>	<b>45</b>
1.4.1 Context of the thesis	45
1.4.2 Our Contribution	46
1.4.3 Thesis Outline	51

---

Coronary arteries segmentation consists in the isolation the coronary artery tree from the surrounding cardiac structures. Such step is very useful for visualization of the arteries, abnormalities detection and quantification in large 3D data. Thanks to the development of the CT angiography acquisition and reconstruction techniques, improved image quality and spatial

resolution can be achieved hence allowing to better capture the coronary arteries. However, regarding the small size of coronary arteries (ranging from 5mm to less than 1 mm in distal parts), the current CT resolution (approximately 0.4 to 1.4) is still not sufficient to robustly extract the coronary vessel. Besides, coronary segmentation or extraction is still a challenging task owing to the close heart chambers having the same intensity ranges as the coronary lumen, motion artifacts, calcium blurring and severe artery stenosis. Therefore, several successful approaches developed for other vascular structures extraction are not suited for coronary segmentation. For instance, methods based on deformable models (see section 2.4.2.2) presented satisfactory results for extracting different anatomical structures in medical data, but their adaption to extract narrow structures as artery vessels is difficult. Hence, special algorithms have been dedicated for coronary arteries extraction using specific knowledge.

Hereafter, we first review some of recent works on coronary arteries segmentation in section 2.1. In the second section, we present a novel coronary enhancement filter based on the Shape Tree and path openings. Finally, we will present and discuss results different approaches for vessel lumen segmentation. Results are evaluated using the online evaluation framework described in [215].

## 2.1 Coronary arteries segmentation: A brief Review

Recently, several algorithm specifically designed for the coronary arteries segmentation have been published. Two major categories can be identified: methods that segment the coronary lumen in one pass without a need for the vessel centerline estimation, and methods that need to determine a vessel centerline (automatically or manually) and then extract the vessel lumen surface. The second category can furthermore be divided into two sub-categories: approaches that first determine (or take as input) a vessel centerline that extract the vessel border (surface evolution), and approaches that iteratively extract the vessel lumen center points and the corresponding vessel contours (i.e. tracking approaches).

### 2.1.1 Direct segmentation approaches

Methods that segment the coronary lumen in one single pass include region-growing [39, 85] and combination of morphological operators [45, 47]. In [85] a first estimation of the probable location of coronary arteries is extracted using a 3D region growing approach. Then, based on the dilation by 3 voxels of the probable location, the coronary final detection is performed by applying a one-level discrete wavelet transformation to each slice of the CTA volume. The au-

### 2.2.1 Coronary arteries segmentation: A brief Review

---

thors used only the LH and HL sub-bands to extract the accurate coronaries. Visual inspection indicates that the approach shows promising result but no quantitative evaluation is performed to assess the robustness of the approach specially to extract abnormal vessel segments. [Bock et al.](#) proposed a progressive region growing approach controlled by a growth front monitoring technique. To control the segmentation and correct local leakage artifacts, the approach uses the knowledge about the growth behavior within tubular structures as well as the knowledge about contrast decrease during the vessel course. [Renard and Yang \[355\]](#) also used locally adaptive region growing by computing local statistics for the appearance of lumen voxels to separately segment the lumen and arterial wall. In [\[47\]](#), an automatic approach combining the gray-level hit-or-miss transform and region-growing is presented. A semi-automated algorithm based on morphological grayscale reconstruction through 2D slice images devoted to the extraction of the 3D coronary artery tree is also proposed in [\[270\]](#).

While showing interesting results with high scale vessels, Hessian based filtering often fails to detect coronary vessels. Two major limitations consist in: 1) the relatively small scale of these arteries and 2) the challenging configurations when anomalies such as plaques or stent grafts are present. For the first case, noise can affect the filter result. In the second one, vessels with abnormalities present an appearance with different image patterns and contrast the healthy one. Therefore, learning based approaches are combined to Hessian based filters to improve detection performance as in [\[217\]](#). In this work, a two stage approach is proposed to automatically extract coronary vessels. First, a set of vessel candidate points is extracted using a learning based approach. At each search position, the object location is estimated using the Hessian matrix. Then the object is classified as a vessel or non-vessel on the basis of its appearance using the Adaboost algorithm. Features are extracted using Haarlike filtering. Finally, a coronary tree shape model (composed of 30 discrete nodes sampled from three major coronary arteries and two coronary veins) is fitted to the detected candidates using an optimization procedure. The final coronary tree centerlines are evaluated using the Rotterdam Coronary Artery Algorithm Evaluation Framework described in [\[379\]](#). However, no information is provided about how one single coronary tree model can handle all coronaries anatomical variations. Other improved vesselness measure has been proposed in [\[474\]](#). They propose to add a local geometric feature based on ray casting to discriminate between the false step-edge responses and the positive vessel responses in Frangi's vesselness measurement.

[Mohr et al. \[305\]](#) proposed an automated algorithm for coronary lumen segmentation using level-sets with additional tissue classification. To detect and remove calcified plaque, they use an explicit calcium extraction step based on an intensity threshold. The calcium threshold value is determined for each vessel within the data by an unsupervised classification technique.

Yang et al. [475] proposed a method to segment the left coronary artery. The approach first classifies the volumetric data into three homogenous regions and finds the one filled with blood. Then a level set model is started at the ostia and operates on the previously extracted blood pool volume to extract the coronary artery and obtain a 3D geometric model of the coronary with subvoxel accuracy. Later, the authors propose a hybrid approach for segmentation of coronary arteries using multi-scale vessel filtering and a Bayesian probabilistic approach in a level set image segmentation framework [476]. An initial estimation of the coronary vessels is obtained from the multiscale vessel filter response. The obtained surface then evolves to detect the exact vessel boundary using an improved evolution model of implicit surfaces.

///A region-based active contour method was used to segment the major coronary arteries in [447]. Centerlines of the coronary arteries are then extracted by mesh contraction. The calcified stenosis were identified using deformed circularity and convex hull deficiency. However the above system did not predict severely affected coronary arteries. Later, the authors proposed an active contour method, which uses global and local intensity statistics to segment the coronary artery in [445]. Correction scheme was developed to remove kissing vessel artifacts and this approach was able to segment only major branches of the arterial tree.

In [272], a novel model-guided segmentation approach based on a Markov random field formulation with convex priors is proposed. Similarly to their previous work [271], an explicit calcium extraction step is incorporated. Besides, the new approach provides robust surface regularization suitable for coronary lumen segmentation by adopting the general Markov random field formulation to tubular segmentation. Such formulation assures the preservation of the tubular structure of the coronary lumen and avoids any post processing to eliminate outliers. In [357], a shape-based segmentation and visualization technique for quantitative analysis of atherosclerotic plaques in coronary artery disease is presented. It uses two surface representations, one for the contrast filled vessel lumen and a second one for the vascular wall.

In the last years, graph-based technique, such as graph cuts [50], random walker [164] and power-watershed [95] have become a group of popular image segmentation methods. Graph based approaches have also been extensively used for coronary segmentation tasks as in [291, 500, 501]. However shrinking bias (Graph Cuts) and sensitivity to seed point locations (Random walker), are still the classical issues of graph-based approaches presenting a barrier for the use of such approaches to segment elongated structures such as vessel, especially when presenting a complex tree structure. Moreover, the intensity feature generally used for the construction of the graph might be not suited for coronary vessel segmentation. In fact, the intensity can significantly change along the vessel and distal parts may present lower intensity values, hence causing segmentation leakage to the surrounding structures. Therefore, some methods

### 2.2.1 Coronary arteries segmentation: A brief Review

---

combined graph based approaches with vessel shape priors. In [380], a semi automated approach for coronary segmentation based on graph cuts is presented. The authors proposed a new edge-weighting function depending on the intensity of the centerline. Segmented regions not belonging to coronary vessels are subsequently removed using an iterative weighted kernel regression approach. Besides, to overcome shrinkage bias and sensitivity to seed point locations, Zhu and Chung [500] proposed a graph-based segmentation approach based on a new tubularity Markov tree model (TMT), which works as both new energy function and graph construction method. Thanks to vessel data fidelity obtained with TMT, shrinking bias and sensitivity to seed point location can be avoided. In [502] an other graph-based method for segmenting 3D vessel trees is proposed. The proposed approach exploits an adaptive cylinder flux based connectivity framework formulated using random walks. The used connectivity framework allows to obtain a global optimal segmentation of the coronaries without extracting the vessel skeleton or any other ROI. Moreover it solves the classical issues of the graph-based methods mentioned above.

Learning based schemes were also used to extract the coronary tree in 3D CT datasets. [496] proposed a machine learning based vesselness measure that exploits the rich domain specific knowledge embedded in an expert-annotated dataset. A set of geometric and image features are extracted and sent to a probabilistic boosting tree classifier. A high score is given to voxels inside the artery and a low score to those lying outside. This score is considered as a vesselness measure that can be used for coronary lumen segmentation.

#### 2.1.2 Centerline-based segmentation approaches

Some approaches dedicated to coronary vessel segmentation were designed by combining a centerline extraction scheme with a surface extraction technique [251, 253, 453]. Lesage et al. [251] developed a recursive Bayesian model for the delineation of coronary arteries from 3D cardiac CTA and utilized a discrete minimal path technique as the optimization scheme. The approach simultaneously optimizes the vessel centerline and the associated lumen radius on a 4D space+scale graph. It incorporates prior knowledge on radius variations and derives the local data likelihood from a multiscale, oriented gradient flux-based feature. Similarly, Li and Yezzi [253] presented a 4D minimal path technique to simultaneously extract 3D tubular surfaces and their centerlines by incorporating an additional non-spatial dimension into the search space. The idea is to represent the vessel not only as a 3D curve but as a 4D one, where each 4D point represents a 3D sphere center coordinates and its radius value. The vessel surface is then obtained as the the envelope of the family of extracted spheres. However,



such approaches can only segment one single vessel and hence do not handle branching vessels. Moreover, a pair as starting and ending points are required to extract the vessel branch. The whole coronary tree can be entirely extracted by manually selecting the different branches. An other approach consists in automatically detecting branching points (i.e. junction) and iteratively track the different branches. This approach is proposed in [254], as an extension of the work described in [253], to detect 3D multi-branch tubular structure and corresponding centerlines by iteratively searching 4D key points. After the key points are located, iteratively, the branches are identified by finding structures between all adjacent key point pairs. Zhao and Bhotika [492] recently introduced an adaptive patient-specific vessel intensity model used within a sequential Monte Carlo vessel tracking framework. The proposed model is built from local intensity histograms and combines both the vessel and background models into the vessel likelihood measure. Starting from one single point, the intensity model is dynamically updated as a function of the vessel radius, hence allowing to track long and thin vessels. In [491], the authors proposed to incorporate a statistical bifurcation method into the tracking process hence allowing to track all the vessel tree by recursively tracking branches and detecting junctions. In [80, 82], a second order vessel tensor is constructed from directional intensity measurements inspired from diffusion tensor image modeling. The vessel tensor is initialized at a single seed point inside the vessel and drives the segmentation of the whole vessel tree by automatically detecting branching points by clustering the direction vectors generated by the tensors. The centerline of the vessel as well as its thickness is extracted.

Level sets were also used in [444] to extract the coronary lumen boundaries. The authors used a level set-based segmentation method guided by an implicit 3D cylindrical vessel model generated from the input centerlines. After the level set evolution is run for a number of iterations, a new centerline is extracted and the vessel diameter is re-estimated in order to update the vessel model. The steps of level set evolutions and vessel centerline update are repeated until convergence. However as one single radius is considered per cross-section to regulate the contour evolution, abrupt changing contours due to the presence of severe plaques might not be captured.

In their recent work on coronary stenosis detection, Shahzad et al. [389, 390] proposed a graph-cut based algorithm using probabilities derived from sampling around the vessel centerline to extract the coronary lumen contours. The resulting graph-cut segmentation is discrete and contains some outliers. Hence, the graph-cut lumen boundary is smoothed and outliers are removed with a robust kernel regression approach. However, as no special treatment for calcium removal is planned, the approach shows moderate segmentation accuracy for diseased arteries when evaluated on the online Rotterdam evaluation framework described in [215].

### 2.2.1 Coronary arteries segmentation: A brief Review

---

Lugauer et al. [271] proposed a learning-based boundary detector. First, potential lumen boundary positions are detected using a radial dense ray-casting started at centerline points with a machine learning algorithm to extract the boundary likelihood along each ray. To enhance the approach robustness against calcified plaques, a calcium exclusion step is applied by analyzing the lumen boundary positions. Finally, an optimal vessel lumen surface is generated from the boundary candidates using a tubular surface optimization scheme followed by a refinement step [253]. In [376], a supervised shape-based segmentation method is described. The approach learns the geometry and appearance of vessels in medical images from annotated data and uses this knowledge to segment the vessels in unseen images. The vessel boundaries are segmented in a coarse-to-fine fashion. First, they are roughly estimated with multivariate linear regression, using image intensities sampled in a region of interest around the initial centerlines. Subsequently, the position of the boundaries is refined with a robust nonlinear regression technique, using image intensities sampled on the boundary of the rough segmentation.

Centerline-based segmentation schemes ensures that the lumen surface of all tagged branches (i.e. branches corresponding to the input centerlines) are segmented. However, segmentation robustness of such approaches is conditioned by the accuracy of the provided vessel centerline. In fact, as the segmentation process relies on the provided set of centerlines, all missing branches in the input tree will not be segmented. Besides, inaccurate centerline points position will affect the final vessel border. To solve the problem of sensitivity to the initial centerline position, iterative vessel borders and centerline refinement may be used as in [444, 453] or a correction step can be added after the centerline extraction step as in [389].

The particular scale and topology of the coronary arteries incited authors to design specific approaches for coronaries segmentation. However, several proposed algorithm tends to have limited success with complicated configurations (e.g. presence of severe lesions, complex shape). Hence, important details on the coronary artery system may be lost during the segmentation process and the final result may not be satisfactory for a relevant analysis. User interaction could be considered to solve such problems (manual edition of the segmentation result, correction of the vessel centerline, etc...). However, such solution can be very time-consuming and not suitable for a rapid and efficient clinical use.

Most of the published works on coronary arteries extraction have been evaluated qualitatively [47, 266, 270, 355, 377, 453]. In these works, the coronary arteries extraction is evaluated visually and scored with reference to different defined criteria. In [270, 453], the segmentation accuracy is evaluated based on the number of correct vessel extractions. Moreover, in [270], the results are categorized following the image quality and amount of disease. Despite qualitative evaluation is important to assess the quality of the segmentation approach visually, a

quantitative evaluation of such approaches compared to manually annotated data by experts is mandatory in order to efficiently judge the accuracy of the proposed method. Some authors evaluated the ability of their proposed approaches [217, 474, 500] to correctly extract the coronary branches by using the online evaluation framework described in [379]. This framework allows to compare the centerline derived from the coronary segmentation to those manually extracted. However, such evaluation gives only an idea about the ability of the proposed approach to extract the annotated branches, and offers no information about the accuracy of the extracted vessel surface.

In [476], the coronaries segmented contours were compared against expert delineated contours on two datasets. The used measure to compare the two contours is the average mean distance error. Recently, Kirişli et al. [215] proposed an other online framework allowing to evaluate the coronary arteries segmentation accuracy. To the better of our knowledge, this is the only public framework allowing to compare coronary segmentation results to a manual segmentation ground truth, as well as comparing the obtained results with other works. Several recent works used the proposed framework in order to evaluate the accuracy of their approaches as [218, 271, 272, 305, 389, 444].

Table 2.1 presents a review of some coronary segmentation approaches. The main idea of the approach as well as the user interaction involved by the approach are reported. For the evaluation process we precise the number of patients (i.e. number of CT images), the evaluation methodology and metrics used by the authors. Besides, we mention for each approach the type of coronary arteries that are segmented.

## 2.2.1 Coronary arteries segmentation: A brief Review

**Table 2.1** – An overview of the qualitatively and quantitatively evaluated CTA coronary artery segmentation approaches. For qualitative evaluation “Visual inspection” indicates that the quality of the segmentation result was assessed visually and judged as satisfactory or not. For qualitative evaluation the metric used is mentioned.

Work	Approach	User Inter.	Patients	Evaluation	Arteries
Chen et al. [85]	Region Growing and DWT	Auto.	NA	Visual inspection	RCA, LAD,LCX
Kitamura et al. [217]	Learning based detection using Hessian analysis	Auto.	32	Overlap	RCA, LAD, LCX and a side-branch
Lesage et al. [251]	4D Bayesian maximal paths	Semi-auto.	51	Ov <sup>1</sup> , AD <sup>2</sup> and AR <sup>3</sup>	Complete Tree
Li and Yezzi [253]	4D minimal path extraction	Semi-auto.	5	Voxel-wise similarity indices	Complete Tree
Luengo-Oroz et al. [270]	Morpho. operators on 2D Slices	Semi-auto.	9	Number of correct extractions	LAD & LCX
Lugauer et al. [271]	Learning based ray casting	Auto.	48	Dice, MSD <sup>4</sup> , MAXSD <sup>5</sup>	Complete Tree
Mohr et al. [305]	Tissue classification with level set approach	Auto.	48	Dice, MSD <sup>4</sup> , MAXSD <sup>5</sup>	Complete Tree
Schaap et al. [380]	Graph cuts with robust kernel regression	Semi-auto.	12	Dice, ASSD <sup>6</sup> , AMCD <sup>7</sup>	Two main arteries with a side branch
Schaap et al. [376]	Learning based segmentation using geometric and intensity features	Semi-auto.	83	Visual inspection and RMSD <sup>8</sup>	One vessel
Shahzad et al. [390]	Graph-cuts and robust kernel regression	Auto.	48	Dice, MSD <sup>4</sup> , MAXSD <sup>5</sup>	Complete Tree
Wang et al. [444]	Implicit Model-Guided Level Sets	Auto.	48	Dice, MSD <sup>4</sup> , MAXSD <sup>5</sup>	Complete Tree
Wesarg and Firlle [453]	Morpho. Mat. , filtering and thresholding	Semi-auto.	12	Number of correct extractions	3 vessels
Yang et al. [476]	Bayesian driven implicit surfaces	Auto.	7	Mean distance error	LM, LAD, LCX and RCA
Yang et al. [474]	Modified Frangi’s vesselness	Auto.	32	Overlap	RCA, LAD,LCX
Zheng et al. [496]	machine learning based vesselness	Auto.	14	Detection rate vs FP rate	Complete Tree
Zhu and Chung [502]	Random walks with adaptive cylinder flux	Semi-auto.	NA	Visual inspection	RCA, LAD,LCX

<sup>1</sup>Overlap

<sup>2</sup>Average Distance

<sup>3</sup>Average Radius

<sup>4</sup>Mean Squared Distance

<sup>5</sup>Max Squared Distance

<sup>6</sup>Average symmetric surface distance

<sup>7</sup>Average maximum contour distance

<sup>8</sup>root mean squared landmark-to-surface distance

### 2.2 A Coronary Enhancement Filter using the Shape Tree and Path Openings

Tubular elongated and thin structures filtering has motivated several research in the past years. Thin object refer to objects exhibiting at least one dimension much smaller than the other(s). This particular field of image filtering has motivated a number of applications in several domains as fiber extraction [122], road network detection [429] and vessel segmentation [47, 412]. Due to their nature, thin object are easily corrupted by noise and partial volume effects. Besides, the complex topology of some thin objects as human vessels, tortuous and spatial sparsity constitute some subsequent challenges.

Coronary artery filtering is still particularly difficult, despite the continuous improvement of spatial resolution of cardiac CT images. In fact, coronary arteries are very thin tortuous tubular structures organized in a tree-like network and prone to noise. Besides, these small vessels often present pathological anomalies which modify their tubular structures and implies some discontinuities along the object. Therefore, applied filters would not have the wanted response at such regions. Junction points shall also be considered carefully when applying and analyzing thin object filters. Moreover, CT cardiac images are 3D datasets presenting a huge amount of data which implies computational issues. In general, coronary arteries filtering aims to enhance the vascular structure while reducing/removing noise. It is considered as an important pre-processing step for the accurate segmentation of the whole coronary tree.

In this section, we propose an approach for coronary arteries enhancement based on robust path opening and the use of the Shape Tree. In section 2.2.1, we review the basic notions of Hessian based filters, Path Opening and Shape Tree. In the following sub-section, we present the proposed enhancement filter. The preliminary results are finally presented and discussed.

#### 2.2.1 Preliminaries

In this section, we briefly recall the theoretical foundations for the proposed enhancement filter and some of techniques used during the tests. We first start with the hessian based filters, extensively used in the literature of vascular structures enhancement and segmentation. Second, we review the basic notions of path opening operators, a set of new operators that showed interesting filtering results while overcoming hessian based filters limitations. Finally, we recall the basic notion of component tree based filters and review a new approach of filtering based on the shape space [472].

## 2.2.2 A Coronary Enhancement Filter using the Shape Tree and Path Openings

### 2.2.1.1 Hessian based enhancement filter

Different hessian-based vessel enhancement filters have been proposed in the literature [149, 267, 373] applicable in different modalities (i.e. 3D CT and MRA) and for different vessels enhancement and detection (i.e. cerebral, carotids and cardiac). Hessian filters are metrics using second order derivatives (at different scales) to detect tubular-like structures by combining the eigenvalues of the Hessian matrix. First the hessian matrix is built by computing the second order Gaussian derivatives at scale  $\sigma$  as following:

$$\mathcal{H} = \begin{bmatrix} \frac{\partial^2 I_\sigma}{\partial x^2} & \frac{\partial^2 I_\sigma}{\partial x \partial y} & \frac{\partial^2 I_\sigma}{\partial x \partial z} \\ \frac{\partial^2 I_\sigma}{\partial y \partial x} & \frac{\partial^2 I_\sigma}{\partial y^2} & \frac{\partial^2 I_\sigma}{\partial y \partial z} \\ \frac{\partial^2 I_\sigma}{\partial z \partial x} & \frac{\partial^2 I_\sigma}{\partial z \partial y} & \frac{\partial^2 I_\sigma}{\partial z^2} \end{bmatrix} \quad (2.1)$$

where,

$$\frac{\partial^2 I_\sigma}{\partial x^2} = I(x) * \frac{\partial^2 G(\sigma, x)}{\partial x^2} \quad (2.2)$$

with  $G(x, \sigma)$  being a Gaussian function with standard deviation  $\sigma$ .

Afterward, the hessian matrix is decomposed into eigenvalues  $\lambda_1$ ,  $\lambda_2$  and  $\lambda_3$  such as  $|\lambda_1| < |\lambda_2| < |\lambda_3|$ . The obtained eigenvalues are subsequently analyzed to determine a likelihood of  $x$  belonging to tubular structure (i.e. vessel). Hence, the following hypothesis shall be satisfied: (a)  $\lambda_1 \approx 0$ , (b)  $\lambda_2 \approx \lambda_3 < 0$  and (c)  $|\lambda_1| \ll |\lambda_2|$ . The proposed filters differs in how they verify the different hypothesis and define the *vesselness* measure. In this work, we used the vessel-likelihood defined by Sato et al. [373]:

$$\mathcal{S}_\sigma(x) = \begin{cases} \sigma^2 |\lambda_3| \left( \frac{\lambda_2}{\lambda_3} \right)^\xi \left( 1 + \frac{\lambda_1}{|\lambda_2|} \right)^\tau & , \lambda_3 < \lambda_2 < \lambda_1 < 0 \\ \sigma^2 |\lambda_3| \left( \frac{\lambda_2}{\lambda_3} \right)^\xi \left( 1 - \rho \frac{\lambda_1}{|\lambda_2|} \right)^\tau & , \lambda_3 < \lambda_2 < 0 < \lambda_1 < \frac{|\lambda_2|}{2} \end{cases} \quad (2.3)$$

where  $\xi \geq 0$  influences cross-section asymmetry,  $\tau \geq 0$  controls the sensitivity to blob-like structures,  $0 < \rho \leq 1$  controls sensitivity to the tubular object curvature, and  $\sigma$  normalizes responses across scales.

As stated previously, the Hessian-based filter uses Gaussian derivatives applied at different scales. The choice of  $\sigma$  is important as it determines the size of the tubular structures we want to capture. Large scales tends to deform original objects at detection and lose details. On the other hand, using too small scales emphasize details but they are more prone to producing spurious responses to noise and small features around the vessel. Hence, it would be more interesting to apply the hessian filter at different successive scales to capture a larger range of tubular structures sizes. Meaningful scales should be selected, as it is computationally expensive to process along all possible scale values. The final vesselness function is defined for each point  $x$  of the image as the best response over the different scales at this point:

$$\mathcal{V}(x) = \max_{\sigma} v(x, \sigma) \text{ with } \sigma_{min} \leq \sigma \leq \sigma_{max} \quad (2.4)$$

This family of filters is widely used in the context of tubular structures enhancement and detection. Its main advantages are, first, that the Hessian is fast to compute, especially when using optimized algorithms. Besides, this approach allows by applying a simple threshold on the vesselness measure to remove all undesirable structures. However, it does suffer also from some limitations, that are particularly annoying in the case of pathological coronaries segmentation. Its first limitation is that the computation of the Hessian is based on a local measurement in neighborhood of each element of volume. The vesselness measure drops quickly at the extremities of tubular structures, which is the case with the presence of severe stenosis. Moreover, hessian based approaches involves the selection of the scale of the objects to be detected (i.e. the size of the neighborhood to be considered). Objects having the target shape but at a slightly different scale won't be selected by the filter. In the case of coronary arteries, the vessel scale changes along the tree and hence even if we use two different scales for the hessian, vessels of intermediate scales might be deteriorated. Therefore, the objects that will be filtered are tightly determined by the selected scale.

### 2.2.1.2 Path Openings

Morphological filters are filters allowing to extract features corresponding to a particular shape. Such filters compute the response of each point (pixel or voxel) by combining the values of neighboring points defined by a given structuring element. In order to filter linear bright structures on a dark background in an image, the standard approach is to compute the infimum of opening by straight line segments covering a large range of orientations [395]. The resulting opening operator is an isotropic operator if the length of the linear structuring element are defined to be independent of the direction. Unfortunately, in real world, thin and elongated

### 2.2.2 A Coronary Enhancement Filter using the Shape Tree and Path Openings

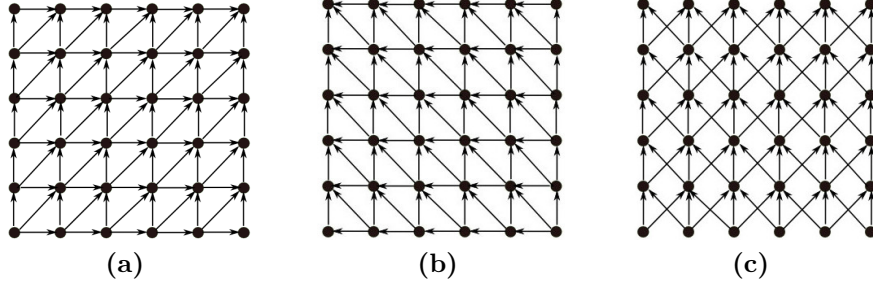


**Figure 2.1** – Examples of adjacency graphs: (a) SW-NE 90° graph (b) SE-NW 90° graph (c) S-N 90° graph

structures are rarely perfectly straight. Consequently, linear segment-based operators are not suitable to extract locally non-straight features as coronary vessels.

To overcome such a limitation of straight lines operators, path operators were introduced in [67, 179]. These new filters increase the flexibility of the structuring element and hence have the ability to adapt to local image features. Consequently, a set of narrow, flexible and oriented structuring elements is generated given a length  $L$  and an adjacency relation. This defines the global orientation of the path. As a result, path opening is a filter that allows to remove bright structures (brighter than local neighbors) that do not contain a path of at least a given length  $L$  and orientation. This is done by assigning to each voxel the highest grey level where a path of length  $L$  can be formed. The theory on path opening operator is detailed in [180].

A path is a connected 1D line on the image, composed of a succession of nodes linked by edges. For a 3D image, nodes are voxels and the edges are defined by a given adjacency relation. The adjacency relation is typically derived from the connectivity relation between neighboring voxels. It defines the orientation to follow in order to add successors to the path. For 2D cases, four adjacency relations are commonly used. In figure 2.1, we illustrate some examples of adjacency graph.

Let  $X$  represent the input image domain. A spatial oriented graph  $(X, \rightarrow)$  is constructed on  $X$  by defining an adjacency relation  $x \rightarrow y$ . This means that one can go from  $x$  (successor) to  $y$  (predecessor). A path  $\mathbf{a}$  of length  $L$  and orientation  $\theta$  is defined as a set  $\sigma(\mathbf{a})$  of  $L$  points of  $X$  connected in the direction defined by the orientation  $\theta$ . Figure 2.2 shows an example of a path of length 6 with a S-N 90° adjacency. A path can hence be defined as following:

$$\sigma(\mathbf{a}) = \{a_1, a_2, \dots, a_L\} \text{ such as } a_i \rightarrow a_{i+1} \quad (2.5)$$

Let  $\Pi_L$  be the set of paths of length  $L$ . We refer to the set of paths of length  $L$  defined on



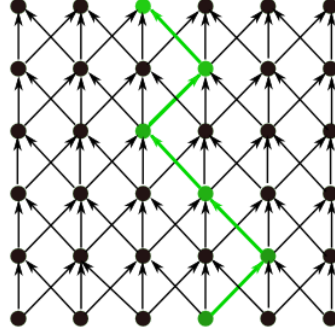


**Figure 2.2** – A valid path of length 6 on a S-N 90° graph.

X by  $\Pi_L(X)$ :

$$\Pi_L(X) = \{ \mathbf{a} \in \Pi_L : \sigma(\mathbf{a}) \subseteq \Pi_L \} \quad (2.6)$$

A binary path opening by a path of length  $L$  is hence defined as the union of all paths of length  $L$  contained in X:

$$\alpha_L(X) = \cup \{ \sigma(\mathbf{a}) : \mathbf{a} \in \Pi_L(X) \} \quad (2.7)$$

Consequently, a path opening keeps all points of X belonging to at least one path of length  $L$ . Definition of path opening of grey-level images is hence straightforward. A grey-level path opening can be defined by threshold decomposition. Let  $I$  be a grey level image defined on the domain X. The grey scale path opening might be computed by stacking the results of all binary path openings from the lowest to the highest threshold value. For each voxel, the assigned output value corresponds to the highest threshold value for which the binary operator remains true. In practice, grey level thresholds are not processed one by one. Path length statistics are stored when processing up levels. Figure 2.3 shows an example of a binary path opening on a 2D image with a path of length 5 with a graph adjacency of figure c.

Path openings showed promising results compared to conventional opening by reconstruction with a linear segment as structuring element by adding more flexibility in the constraint. However, path openings might fail to extract the correct local orientation when the data is contaminated with noise. Such problem is frequent with high resolution images as CT angiography. In order to allow short discontinuities along the detected paths, Robust Path Opening (RPO) has been proposed in [92]. Such operators tolerate gaps up to some maximal allowed length  $K$ . In figure 2.4, we illustrate the difference between the use of path opening operators and RPOs to extract incomplete linear bright structures. As mentioned before, coronary arteries might

## 2.2.2 A Coronary Enhancement Filter using the Shape Tree and Path Openings

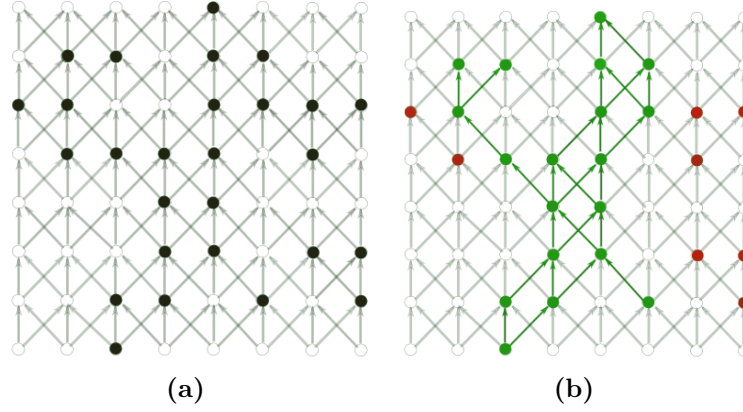


**Figure 2.3** – A 2D example of a set  $X$  and its path opening  $\alpha_5(X)$ : (a) The initial set  $X$  (in black) defined on a S-N  $90^\circ$  graph. (b) The path opening result in green. Eliminated points are highlighted in red.

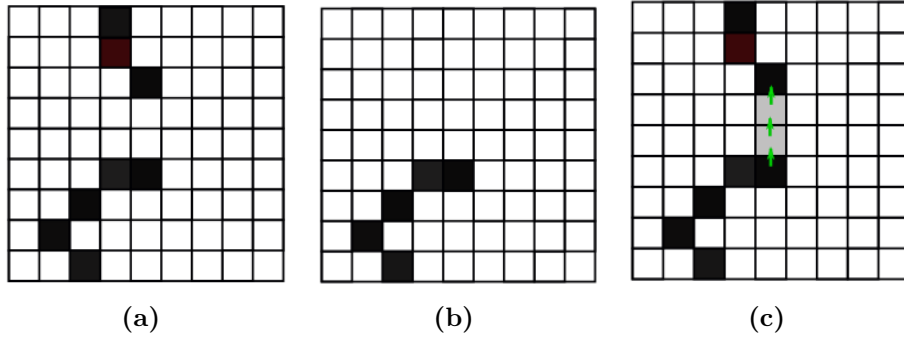


**Figure 2.4** – A toy example of extraction of a disconnected linear bright path using path opening and robust path opening: (a) Disconnected path (b) Path opening with  $L = 5$  (c) Robust path opening with  $L = 5$  and  $K = 2$

be frequently disconnected by the presence of soft or calcified plaques, or by presence of noisy points. Hence we decided to use robust path openings in order to enhance coronary arteries while reconstructing missing gaps.

### 2.2.1.3 Shape Tree

Initially, mathematical morphology operators were developed based on the use of structuring elements, that defines the size and the shape of the neighboring of a given pixel [386]. However, the use of such structuring elements induces some limitations, mainly their tendency to deform contours and as they do not respect the object connectivity. Such limitations motivated the development of a new family of morphological operators based on attributes rather than elements as proposed [55, 370]. Such operators, called *connected operators*, are based on the notion of

connectivity that defines the immediate neighbors of a pixel given a connectivity scheme (the 4- and 8-connectivity for 2-D images and 6-, 18- and 26-connectivity for 3-D images). Connected operators act by merging elementary regions called flat zones (i.e. connected regions where the grey-level is constant). Unlike element based operators, these operators cannot create new contours nor deform their initial positions. They have, hence, good contour-preservation properties and are capable of low-level filtering as well as higher-level object recognition.

A first strategy for connected operators creation relies on a reconstruction process involving a first simplification step, using a classical filtering tool and then a reconstruction step. The second and most popular strategy to define connected operators is based on a hierarchical region-based representation of the input image. Therefore, a component tree (e.g. level sets) of the input image is constructed in a first step. Different trees were proposed in the literature as the max/min trees [372] and the inclusion tree [306]. Such trees are equivalent to the original image as it can be reconstructed from its associated tree.

Then, filtering involves the design of a shape-based attribute computed on each node of the tree and keeping only the nodes presenting sufficiently a strong attribute value. Several attributes might be used in order to detect objects of a particular shape in an image. Such objects can be represented by one or several connected components of the tree. The goal is hence to select these nodes and remove the other non significant ones by the use of adapted attributes. We can distinguish two types of attributes: increasing and non increasing ones.

**2.2.1.3.1 Increasing Attributes** The attribute evolves monotonically when traveling through a branch. It depends only on the characteristics of the node and not on in the image. Examples include:

- **Height:** Corresponds to the difference between the max and min grey value on the node.
- **Air:** Corresponds to the number of points of the node with a grey value equal to the node height.
- **Volume:** Corresponds to the total number of points of the node. It can be computed as the sum of the airs of the different grey values included in the node.

The input image can easily be filtered using a threshold on such attributes. In fact, as the attribute is increasing, children of an inactive node are also inactive. Hence, to reconstruct the filtered image, we just have to remove all the inactive nodes. For example, the area opening is an operator that filters the image using the air attribute to remove all objects with an air value

## 2.2.2 A Coronary Enhancement Filter using the Shape Tree and Path Openings

lower than a given threshold, while preserving the objects contours (unlike the area opening by reconstruction operator).

**2.2.1.3.2 Non Increasing Attributes** Such attributes do not evolve monotonically along a given branch on the tree. It depends on the node own characteristics specific to the image features like its geometry or its texture. This type of attributes is more suitable for specific segmentation tasks. Geometric attributes are mainly computed based on the inertia matrix whose eigenvalues characterize the relative length of the main axes of the object and thus its shape. The main advantage of these attributes is that they are invariant to scale, thereby they allow selecting objects according to their shape and not size. This is very useful to isolate structures composed of several components with similar shape but whose scale varies, which is the case of arteries coronary.

This tensor is defined on the set of points of a connected component C with  $V(C)$  = Volume of the component and  $\bar{x}$ ,  $\bar{y}$ ,  $\bar{z}$ , , the coordinates of its center of gravity:

$$I(C) = \begin{bmatrix} I_{xx}(C) & I_{xy}(C) & I_{xz}(C) \\ I_{yx}(C) & I_{yy}(C) & I_{yz}(C) \\ I_{zx}(C) & I_{zy}(C) & I_{zz}(C) \end{bmatrix} \quad (2.8)$$

with:

$$\begin{aligned} I_{xx}(C) &= \sum_C (x - \bar{x})^2 + \frac{V(C)}{12} \\ I_{yy}(C) &= \sum_C (y - \bar{y})^2 + \frac{V(C)}{12} \\ I_{zz}(C) &= \sum_C (z - \bar{z})^2 + \frac{V(C)}{12} \\ I_{xy}(C) &= I_{yx}(C) = \sum_C (x - \bar{x})(y - \bar{y}) \\ I_{xz}(C) &= I_{zx}(C) = \sum_C (x - \bar{x})(z - \bar{z}) \\ I_{yz}(C) &= I_{zy}(C) = \sum_C (y - \bar{y})(z - \bar{z}) \end{aligned}$$

A set of attributes can hence be computed, with  $\lambda_1 > \lambda_2 > \lambda_3$  the eigenvalues of  $I$ :

- **Non compacity** :  $I_1 = \frac{Tr(I)}{V^{\frac{5}{3}}}$

- **Elongation 1**:  $E_1 = \left| \frac{\lambda_1}{\lambda_2} \right|$

$$\text{-Elongation 2: } E_2 = \left| \frac{\lambda_1}{\sqrt{\lambda_2 \times \lambda_3}} \right|$$

$$\text{-Flatness 1: } F_1 = \left| \frac{\lambda_2}{\lambda_3} \right|$$

$$\text{-Flatness 2: } F_2 = \left| \frac{\sqrt{\lambda_1 \times \lambda_2}}{\lambda_3} \right|$$

Attributes computation can be performed recursively during the construction of the component tree. At each step, when a new point is added to a node or two nodes are merged, the node attribute is updated by adding the contribution of the new element(s) to the previously computed one.

The simplest way to filter the tree consists in pruning the tree by removing all the nodes having an attribute value lower than a threshold, as well as all of its descendant. This pruning rule is straightforward if the attribute is increasing on the tree (i.e. the computed attribute is always stronger for the ancestors of the node). If the chosen criterion is not increasing, the pruning strategy is not straightforward. In fact, the descendants of a node to be removed have not necessarily to be removed. In this case, several pruning strategies can be used (min, max, Viterbi) as detailed in [371]. Finally, the output image can be reconstructed from the pruned tree.

Figure 2.5 shows an example of the max tree constructed from the grey-scale input image. The different connected components are theoretically obtained by applying increasing successive threshold values to the input image. As we can see on figure f, each node of level  $n$  is included in a precedent node of level  $n - 1$ . The component tree can be build by considering a flood-filling approach. The approach starts at the root and performs a depth-first flooding process to build the final tree. The dual tree of the max tree, i.e. the min tree can be constructed by starting by the highest grey value (giving the tree root) and proceeding in the decreasing sens until reaching the lowest grey level (reaching the tree nodes). The second algorithm used for efficiently constructing component trees is based on the union-find approach [413], which was first introduced into connected filtering as an efficient means to perform area openings [319].

As mentioned earlier, pruning strategy consists generally in removing nodes of the tree for which the computed attribute is lower than a given threshold (with different possible decision about the node childs) . However, such a thresholding approach does not take into account the intrinsic parenthood relationship of the tree (two different objects might be selected on the same branch). Besides, by using a unique threshold value, it is often impossible to extract all the wanted objects. In fact, objects of interest might present different energy values between

### 2.2.2 A Coronary Enhancement Filter using the Shape Tree and Path Openings

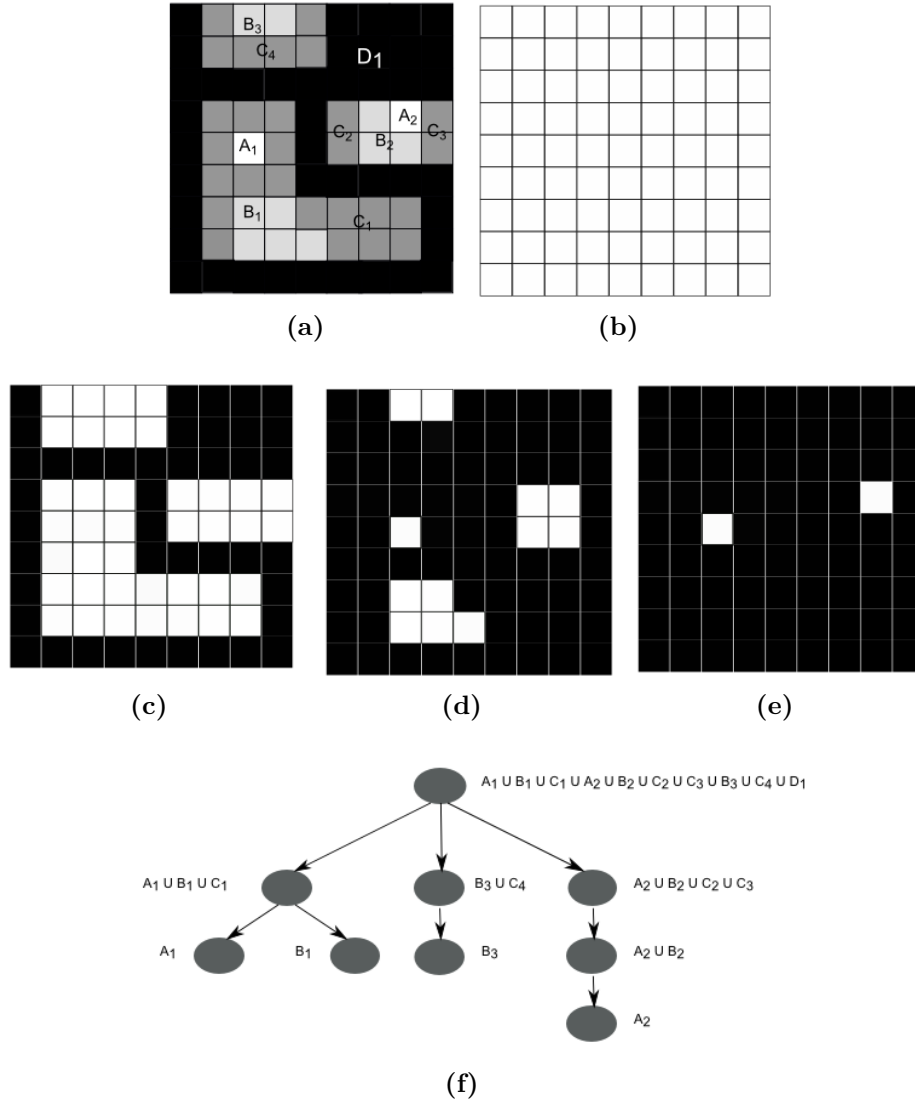


**Figure 2.5** – A toy example of the extraction of the max tree of a grey level image: (a) Input Image (b)-(e) Different connected components of the image at different threshold values (f) Correspondent max tree.

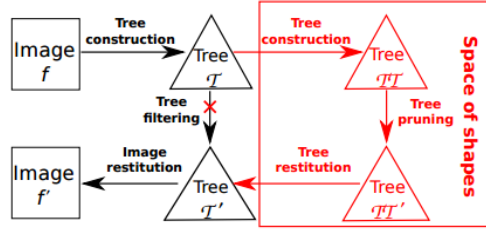


**Figure 2.6** – Image filtering using the classical connected operators (the black path) and the shape space based approach (the black+red path). Illustration material from [472].

different branches.

Recently, Xu et al. [472] presented a robust method to remove components of a given tree. The idea is to apply a connected filter on the component tree itself, seen as a weighted graph with a neighborhood relationship given by the parenthood relationship; A node's neighbors are its parent and its children, and the weight is given thanks to the chosen criterion. Consequently, the filtering is done not in the space of the image, but on the space of shapes made by all the components of the image. A max tree can hence be built on the component tree, and an increasing criterion (on the second tree) can be used to robustly remove unwanted components. This new approach allows to keep active nodes as well as their local neighborhood in the space of shapes rather than keeping only nodes with an attribute value higher than a given threshold. Hence, if we look for elongated structures, we will select nodes significantly elongated compared to their neighbors in the shape space, as well as its neighboring elongated nodes. This approach is more robust than simple pruning of the tree of components, as it selects meaningful nodes compared to their context, and do not use a single threshold value which would not select all wanted objects as it depends on the scale of the computed attribute on a given branch.

Figure 2.6 shows the process of image filtering using the classical connected (the black path) operators and the new proposed approach in [472] (the black+red path). Let  $\mathcal{A}$  be the probability for a component of the input image to be of a given shape. The minima of the shape space are hence, components that are less probable to be of that shape type compared to their context (i.e. children and parent). Considered as a weighted graph, the tree  $\mathcal{T}$ , can thus be presented by a second component tree  $\mathcal{T}\mathcal{T}$  (a min tree for example) where the leaves are represented by minima of  $\mathcal{A}$  on  $\mathcal{T}$ . Therefore, pruning leaves of  $\mathcal{T}\mathcal{T}$  corresponds to removing components of  $\mathcal{T}$  that are less likely to be of the searched shape measured by  $\mathcal{A}$ . To select the significant nodes on  $\mathcal{T}\mathcal{T}$ , the authors used the extinction value of minima [427]. Such measure quantifies the persistence of a given node compared to its neighbors along its branch on the shape tree. If we are looking for nodes that minimizes (maximizes) a given attribute energy,

### 2.2.2 A Coronary Enhancement Filter using the Shape Tree and Path Openings

---

we will isolate all nodes presenting local minima (maxima) in their local context (see [472] for more details).

Finally, the complete processing scheme is described in figure 2.6. After constructing the component tree  $\mathcal{T}$  of the input image  $f$ , we transform the resulting tree to the space of shapes by constructing the tree  $\mathcal{T}\mathcal{T}$ . Then, we filter the new tree using the extinction value in the shape space to obtain the filtered tree  $\mathcal{T}\mathcal{T}'$ . Finally, we reconstruct the tree component  $\mathcal{T}'$  and the resulting filtered image  $f'$ . Pruning the second tree of shapes consist in keeping the significant neighborhood of minima (or maxima) with an extinction value higher than a given threshold. We can also compute an other attribute on the second tree, as the height of a component in the shape space or the volume of the connected component of  $\mathcal{T}\mathcal{T}$  corresponding to the number of pixels of this set of components in the original image. Such attributes allows to increase the selectivity of the defined filter.

Hereafter, we will present an application of the morphological filtering in shape space to extract coronary vessels in cardiac CT angiographies.

### 2.2.2 The enhancement filter

In this section, we propose a new approach for coronary vessel segmentation based on morphological filtering in the shape space. Most robust approaches (see section 2.1) dealing with direct coronary segmentation are based on extracting image features (intensity or geometric) to extract blood vessels [217, 305]. One popular approach is based on the computation of a vesselness measure (e.g. using the Hessian matrix) to extract a set of seeds and then propagate to extract the complete coronary tree. Such approach is currently used in different commercial tools, notably the automated coronary segmentation protocol embedded in the GE Volume Viewer software. However, as mentioned earlier, such approaches are tightly depending on local intensity variation and sensitive to the selected scale. Moreover, low responses around junction points and pathological regions enhances the need to look for an alternative solution to filter coronary arteries in CT angiography. Using connected filters seem to be a promising approach.

As mentioned above, component-tree have been previously used for medical images segmentation/enhancement, mainly for CT/MR angiography [71, 72, 457] and cerebral MRI [123]. Some methods were devoted to one specific step of the segmentation process as markers selection as in [123]. Others were designed to filter the processed image and remove unwanted parts leading to a first step of segmentation that needs further cleaning [457]. Meanwhile, proposed approaches, which deals with a full segmentation problem by using components tree, focused only on simple shape objects segmentation (typically circular or elliptical 2D features). There-



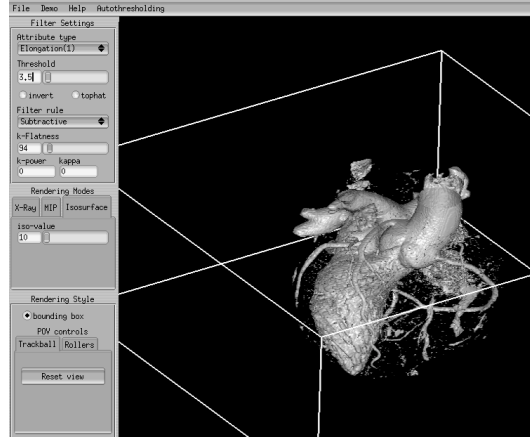


**Figure 2.7** – Cardiac CT angiography filtering using the elongation attribute computed on the max tree.

fore, the problem of automatically extracting complex 3D objects based on the use of a set of knowledge elements on the target structure is still an active issue in the field of component-tree-based methods.

A first step in this work was to quickly evaluate the state of the art of component-tree based segmentation tools for extracting coronary arteries. In this context, we used the publicly available demonstration program for combined attribute filtering and visualization based on Max-Trees [2]. This software provides a GUI to segment 3D volumes based on Max-Tree filtering. It offers a set of attributes based on inertia moments and radial moments [220]. Different pruning strategies are also proposed. The tool allows to interactively select the attribute threshold value. It hence allowed to observe that two attributes provided the best segmentation results: Elongation and Non compactness. Figure 2.7 shows the result of filtering a 3D volume of cardiac CT using the elongation attribute. It shows that this criterion allows to keep important parts of the coronary arteries. Meanwhile, such filtering keeps a considerable amount of noise and the major cardiac contrasted structures as the trunks and the ventricle. Hence, using a simple threshold based filtering on the max tree of the image is not suited for coronary isolation. A subsequent step of filtering to remove unwanted structure and to disconnect coronaries from other blood pool structures is mandatory to obtain an accurate result. Besides, using a simple threshold to filter the tree based on a non increasing criterion seems to give unsatisfactory results. Therefore, we propose to use the shape space tree as an interesting alternative.

### 2.2.2.1 Evaluation process

In order to evaluate the results of the different steps of the proposed approach, we compare the filtered result to a ground truth segmentation of the corresponding coronaries. We used a subset

### 2.2.2 A Coronary Enhancement Filter using the Shape Tree and Path Openings

---

of 11 CT cardiac images. The ground truth segmentation is obtained by first automatically segmenting the coronaries volume, and manually adding missing parts. To compare the two segmentation, we use the sensitivity and the PPV metrics. these metrics allows to assess the amount of correct detections (sensitivity), and the amount of false positives (PPV). This metrics are first used to quickly tune the approach parameters by eliminating aberrant values (corresponding to very low PPV or sensitivity values). Nevertheless, visual inspection is still necessary to judge the type of false positive and differentiate between noise and other anatomical structures like cavities that can be removed easily using adapted segmentation algorithms.

#### 2.2.2.2 Shape Tree construction

To compute the shape tree of cardiac CT volumes, we first extended the work of [Xu et al. \[472\]](#), initially in 2D, to 3D cases. This extension was straightforward using the C++ library Milena [\[269\]](#). However, a cardiac CT volume is a stack of  $N$  2D short images of size  $512 \times 512$ .  $N$  is typically between 160 and 300, allowing to cover all the heart volume. Such amount of data to be processed involves a considerable memory consumption and limits the use of this approach. In fact, when computing some complicated attributes on the component tree, such as inertia moments, we frequently encountered memory issues. The main reason for such issue is that the used library is not suited for manipulating CT angiography images. In fact, such images contains several inactive voxels ( $I(x) = 0$ ) that needlessly occupy memory resources and increase the computational time. A better storage structure adapted for CT volumes will help solving this memory problem.

To fix the out-of-memory problem, we proposes some adaptations. This was important given the number of attributes we will compute and the size of processed images. The first idea was to reduce the processed amount of data to improve the approach performances by dividing the input volume to subsets of 2D slices. Each subset of images is processed and filtered separately and then merged to obtain the final result. However, this strategy will divide the artery coronaries into segments that can be confused, at a small scale, to reconstruction noise. Hence, the final result will contain much more false positives having similar geometric properties as coronaries. The second possible way to simplify the input image was to divide the image into disjoint and adjacent 3D sub-volumes. The same limitation as the previous approach raises. Finally, we decided to extract a ROI of the input image without dividing it. Therefore, for each cardiac image, we extract the heart masque as described in our previous work [\[289\]](#). This choice allows to: 1) Crop the image and reduce the amount of data to be processed and hence improve the approach performances, and 2) Improve the approach robustness by reducing the amount of

false positives having similar appearance characteristics to coronaries as the pulmonary vessels, since we remove all surrounding organs of the heart.

Subsequently, in order to reduce processing time and memory consumption, was to reduce the gray values range considered for the computation of the max tree. Initially, if we consider all the CT values of the input image, the grey values range from 0 to 5000 typically. This involves important computational time and a more complex tree to be processed. Therefore, we propose to reduce the values range only to the blood pool class values. In fact, a CT angiography presents a rich 3D volume containing several heterogeneous structure classes (soft tissues, air, blood pools). By selecting only the blood pool class (higher than 1000), we significantly reduce the size of the component tree, and hence the computational time and the allocated memory space.

Finally, by applying the two previous strategies we were able to reduce the computational time by 1/4. Practically, it takes about 2 minutes to process a  $512 \times 512 \times 160$  volume on a 4 cores Intel(R) Xeon(R) CPU W3565 @ 3.20GHz, 8.00 GB (RAM).

To filter the coronaries we used the approach proposed in [472]. First, we construct a max tree on the automatically extracted heart by using a 6-connectivity. In fact, we observed that by using 18- and 26-connectivities, the applied filter was less selective and more noise was included in the final result. Then, we construct a second min tree on the first one. As explained previously, we used the extinction value computed on local maxima to filter the second tree.

We first proceed to filtering the image by using only the max tree in order to see the difference with the shape space filtering. Therefore, we start by computing a set of attributes on the max components tree, adapted to the segmentation of coronary arteries. We have tested some of the increasing (Volume, Air and Height) and non increasing attributes (Non-compactness, Elongation and flatness) presented in section 2.2.1.3. The non compactness measures how much the object deviates from a spherical shape. For a given volume, this attribute is minimal for a sphere, and increases rapidly as the object becomes more elongated. The inertia tensor eigenvalues measure the length of the principal axes of the objects. Hence, elongation measures, based on the combination of these eigenvalues, allow the selection of elongated components by giving priority to the principal axis. Flatness selects elongated and flat components

After a visual inspection, we concluded that the best results are obtained with the first measure of elongation  $E_1$ . Figure 2.8 shows the result of a cardiac image example filtered using the max tree. The two images are obtained by applying two different threshold values on the elongation attribute.

We evaluated the filtering approach on a set of 11 cardiac CT exam. It was very challenging to determine the best threshold value allowing to robustly extract the coronaries while mini-

## 2.2.2 A Coronary Enhancement Filter using the Shape Tree and Path Openings

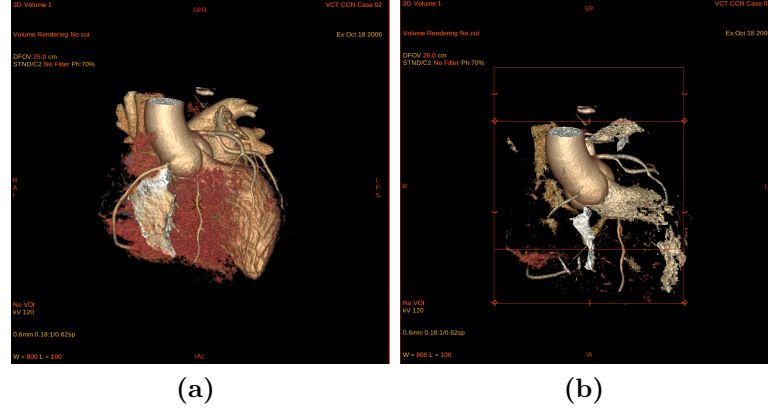


**Figure 2.8** – Image filtering using the max tree and the elongation attribute with a connectivity  $C_6$ : (a)  $h = 2$  (b)  $h = 5$

mizing the amount of kept noise. This is illustrated on figure 2.8, where relatively two close threshold values (2 and 5) yield to different segmentation results. Therefore, we conclude that filtering the image based only on the max tree is not suited for coronary extraction. We filter, hence, the image in the shape space as proposed in [472]. To filter the second tree, we tested three different approaches as illustrated in table 2.2.

**Table 2.2** – Coronary arteries filtering using different attributes on the tree of shapes

	Attribute		
	None	$e_{height}$	$e_{vol}$
Sensitivity	0,97	0,59	0,81
PPV	0,02	0,26	0,16

We observed that the simple filtering based on the extinction value was not enough to achieve an efficient filtering; The neighborhood of selected nodes was systematically too large. However, it is possible to compute some increasing attributes on the tree of shapes to constraint adding a node to the neighborhood of a significant maxima. We tested the attributes volume ( $e_{vol}$ ) and height ( $e_{height}$ ) on the tree of shapes and it was the volume attribute, combined to the extinction value, that gave the most interesting results (see figure 2.9).

These first tests showed that the use of the shape space tree to filter the image allowed to increase the robustness of the proposed filter. In fact, more parts of the coronaries are selected by this filter. However, as we can see on figure 2.9, an important amount of noise is still kept on the final result. Therefore, some strategies of noise reduction and coronary enhancement were tested.

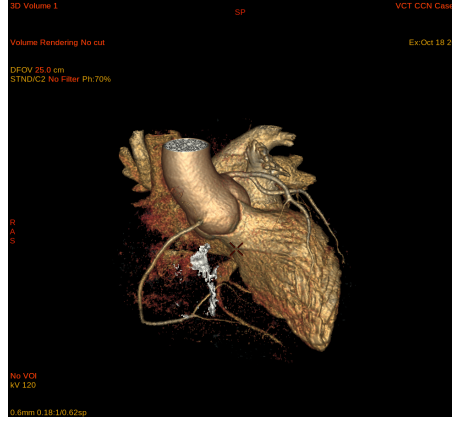


**Figure 2.9** – Filter on masque

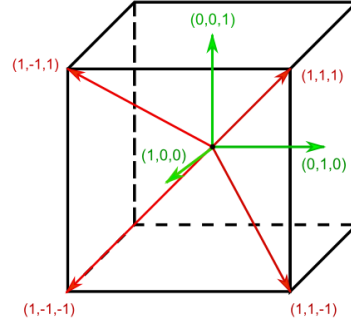
### 2.2.2.3 Image filtering for noise reduction using robust path openings

After the previous tests, we deduced that processing the initial image in order to reduce noise and enhance the structures of interest (i.e. coronary arteries) is necessary. Two approaches have been compared. The first enhancement filter is based on the computation of the Sato vesselness to highlight tubular structures. Therefore, we applied the hessian-based filter for two different scales (1.5 and 3). The maximum response of both of the filters was used as a masque for the tree-based filter described in the previous section. However, its use is still not ideal since we are again faced with limitations namely the dependence to scale and local variations that we are trying to avoid through the proposed approach.

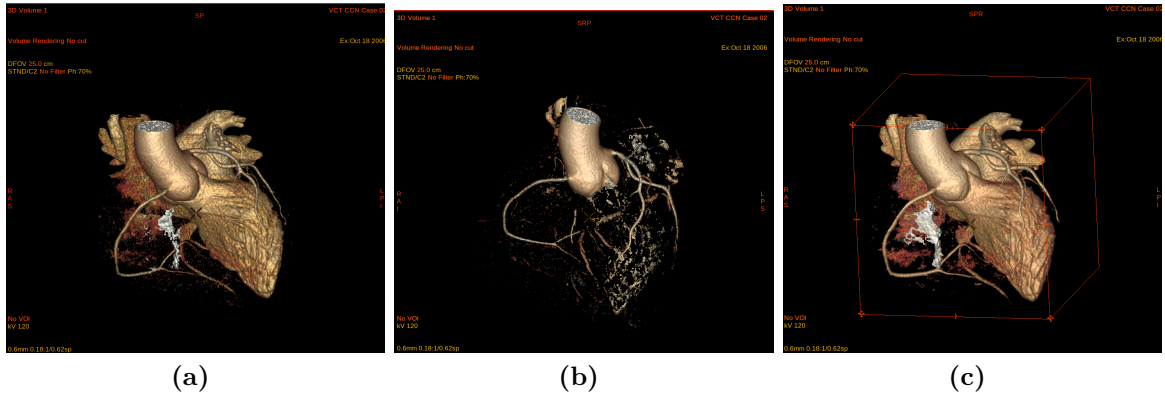
The second filter deals perfectly with the previous limitations. It is based on path openings (section 2.2.1.2). For this, we used the Robust Path Openings (RPOs) described in [92]. The approach computes the path opening of the input image along the 7 main orientations of the discrete space  $\mathbb{Z}$ . The orientations include the three principal directions corresponding to the vectors of the orthogonal basis  $(0, 0, 1)$ ,  $(0, 1, 0)$ ,  $(1, 0, 0)$ , and the four principal diagonals  $(1, 1, 1)$ ,  $(1, 1, -1)$ ,  $(1, -1, 1)$ ,  $(1, -1, -1)$ . We allowed a disconnection of  $K = 2$  along the filtered paths to deal with noise.

Figure 2.11 shows the results obtained after adding a pre-filtering step of the input image. By using the hessian based enhancement filter, we were able to remove all connected vascular structures to the coronaries as the main trunks and the heart cavities. However, an important amount of noise is still present at the final result (corresponding to structures having high responses to the hessian filter as the left ventricle borders). However, by applying the robust path opening based filter, we were able to keep more part of the coronaries that were eliminated by the hessian based filtering (see figure 2.11). The major outcome of this filter is the ability

## 2.2.2 A Coronary Enhancement Filter using the Shape Tree and Path Openings



**Figure 2.10** – The 7 directions used for the robust path opening.



**Figure 2.11** – Image pre-filtering using the hessian and the robust path opening filters. Results of the extraction of the coronary arteries are obtained by applying a shape space filtering on the pre-filtered image: (a) Image filtered using no pre-filtering step (b) Image filtered using the hessian enhancement filter and the RPO based enhancement filter (c).

to enhance tubular structures while being scale invariant and robust to noise.

Furthermore, in order to improve the robustness of the whole filtering chain against noisy structures kept because they verify the filtering criteria, we propose to combine more than an attribute to be more representative of the coronaries structure. In fact, coronary arteries are elongated structures with a significant volume compared to noisy elongated structures. We, hence, choose to weight the elongation attribute using the air and volume attributes of the corresponding components. The result of this weighting strategies are compared to the previous results in figure 2.12. We can clearly see that the amount of noise has considerably decreased compared to filtering the original image without an enhancement step and by only filtering the tree based on the elongation attribute. 2D cross sections of the cardiac volume are shown to compare the amount of remaining noise.

The final complete scheme of the proposed approach is described in figure 2.13.

## Chapter 2. Coronaries Artery Segmentation

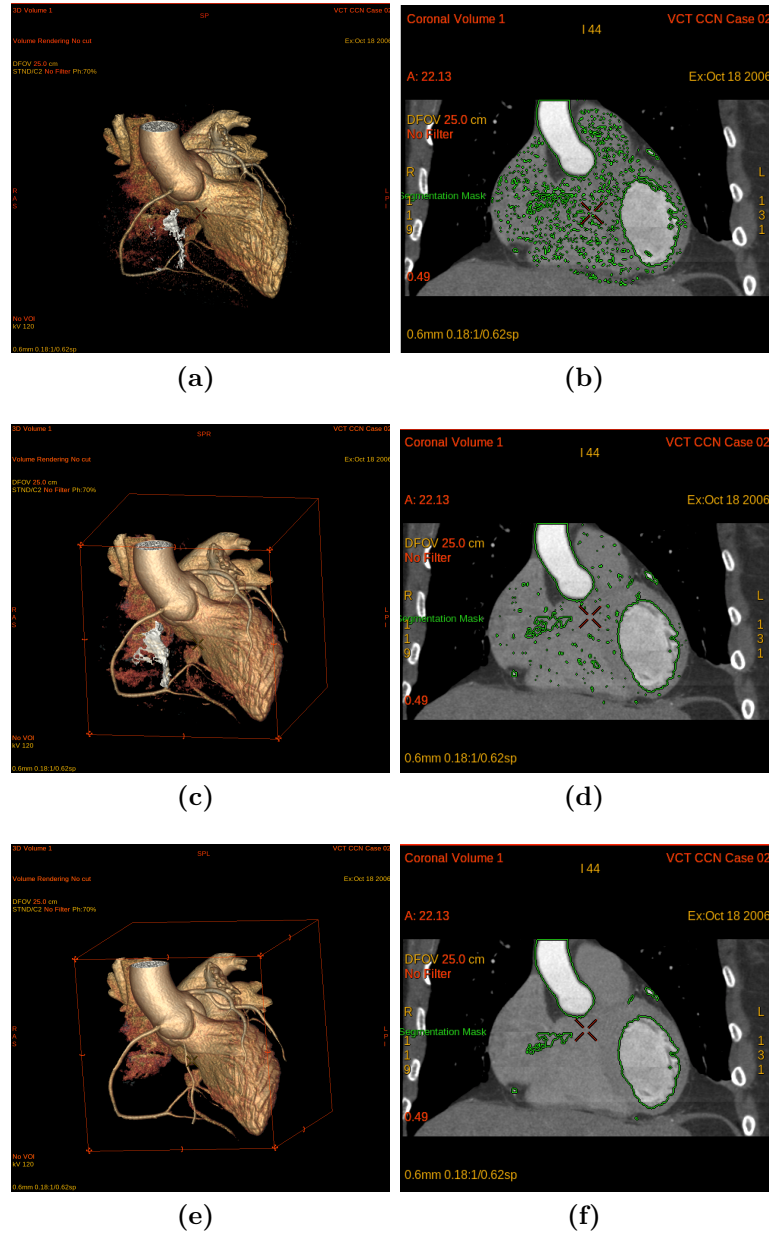


**Figure 2.12** – Noise reduction using weighted elongation attribute with the component volume ((e), (f)). Results of image filtering using the original image with no enhancement with the elongation attribute ((a), (b)) and the RPO based enhancement filter with the elongation attribute ((c), (d)).



### 2.2.2 A Coronary Enhancement Filter using the Shape Tree and Path Openings

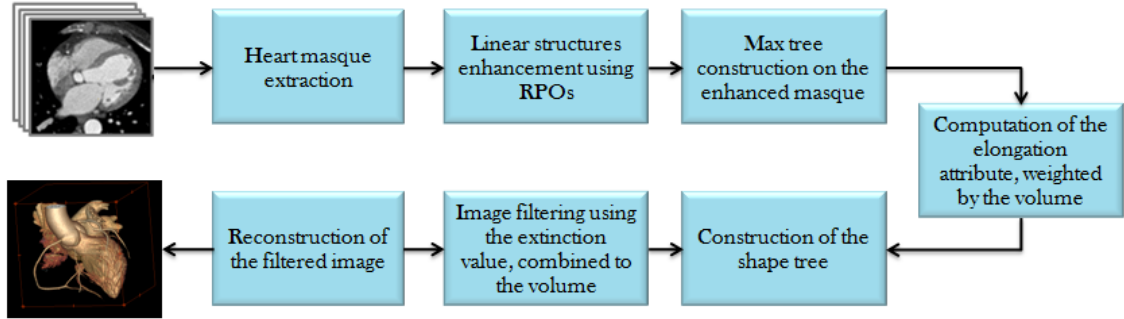


**Figure 2.13** – The cardiac image filtering for coronary segmentation flowchart.

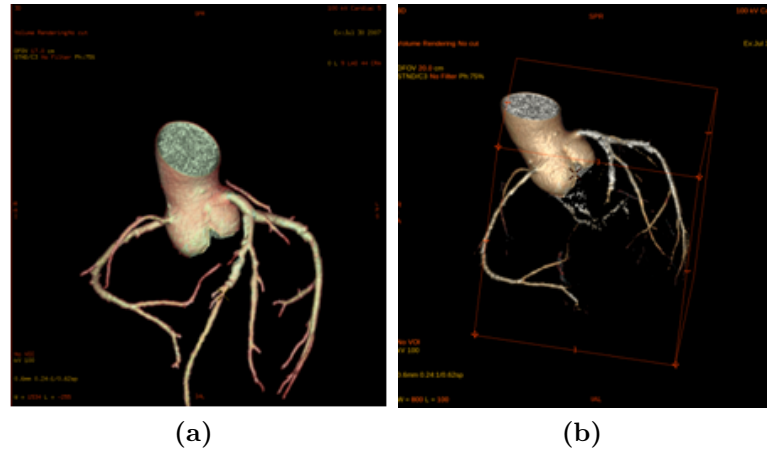


**Figure 2.14** – Challenging case with several calcified plaque disconnecting the coronary arteries (a) Coronary tree ground truth (b) Automatically segmented coronary tree. An post-processing step was applied to remove the remaining heart cavity.

### 2.2.3 Preliminary Results and Discussion

As we can state by visually analyzing previous results, the proposed approach suffers from a major limitation; An important amount of false positive is still present in the final result, corresponding to cardiac cavities and major trunks (pulmonary arteries and aorta). Such anatomies can easily be removed by applying appropriate cavities segmentation algorithms, in a post-processing step. Besides, some pathological coronary segments were missing on a case (see figure 2.14). The corresponding plaque was a calcified one, causing a disconnection of the corresponding coronary arteries. A path with more flexible noise amount would help to reconnect such coronaries.

The proposed approach presents promising results for automated coronary arteries segmentation. To quantify the obtained results, we compared the automated segmentation results to



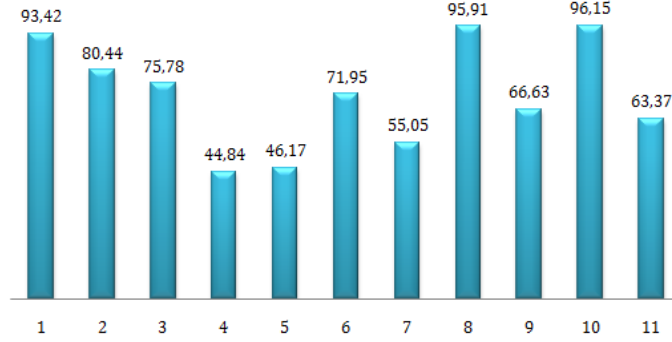


**Figure 2.15** – Overlap measure obtained on the 11 cardiac datasets.

manual segmentation. In order to assess the amount of correctly extracted coronaries, we compute the overlap measure between the coronary arteries of the ground truth and the automated segmented ones. Results on the 11 datasets are shown in figure 2.15. The approach shows a mean overlap measure of more than 71.

The presented work emphasizes the fact that automatic segmentation of complex objects like coronary arteries based on the use of component-tree-based methods, obviously remains an open methodological problem. Such filters are interesting as they are shape preserving and do not amplify noise. However, the proposed approach depends on a set of parameters that need to be optimized. Robust path openings seem to be efficient in order to enhance elongated structures. The major asset of this approach is that it is scale independent. However, it mainly suffers for its combinatorial complexity. In a next step, it would be interesting to test the recent work of Merveille et al. [293] on ranking the directional response of the path operator in order to differentiate between blob like and tubular structure. Besides, the use of more elaborated knowledge based attributes in order to extract coronaries might help to increase the approach robustness.

### 2.3 Statistic-based Vessel Lumen Segmentation

In this section, we proposed a centerline-based approach to automatically extract vessel lumen volume. As explained in section 2.1.2, such methods utilize the previously extracted vessel centerlines to quantify the vessel lumen contours. Hereafter, we are only interested by the lumen quantification step. The vessel centerlines can be obtained using one of the techniques explained in 2.4.1. The proposed approach is based on a seeded segmentation approach to extract the vessel lumen volume. Our main concern is to accurately extract vessel lumen seeds

while excluding non luminal textures such as calcified and non calcified plaques. To evaluate the performances of the proposed approaches, we used the publicly available database and the corresponding coronary arteries centerlines provided by team Rcadia in the context of the Rotterdam coronary arteries challenge [215].

First, we review the state of the art approach used for coronary arteries lumen extraction, in the GE Volume Viewer software. Second, we explain a novel approach for robust vessel lumen markers extraction based on the use of scan specific adaptive vessel statistics. Finally, we present the quantitative evaluation results of vessel lumen contours extraction using two different segmentation algorithms. Results have been obtained through the online evaluation framework described in [215].

#### 2.3.1 State of the art coronary arteries segmentation and lumen extraction

The current state of the art algorithm used for coronary arteries lumen extraction, in the GE Volume Viewer software, is based on the use of automatically extracted coronary centerlines to quantify the lumen contours. It uses a watershed process based on gray-level gradients and markers, as proposed in [296]. First, a mask is extracted using a region growing to be used as a maximum estimate of the vessel volume that the watershed result should not overgrow. The region growing step is constrained by a threshold on the gray value increase when including a new point, computed from the local vessel statistics. This allows to avoid including bones and calcification in the mask volume. The same mask is also used to extract the background labels. Next, the vessel centerlines are used as vessel markers to initiate the watershed process.

The output volume of the watershed step (figure 2.16) is used as a 3D binary input, to extract the vessel lumen contours. The vessel centerlines are used as a guide for the extraction and the quantification of the 2D cross section vessel lumen contours at different location of the vessel. For each point of the centerline, we compute a vectorial (set of 3D points) contour of the cross section from the previously segmented object as described in figure 2.17. To provide a better precision and avoid blocky contours at a voxel level, we derive a sub-voxelic contour. Therefore, a sub-pixel iso-density curve is extracted by using a threshold density value  $d_T$  derived from the median voxel value on the previously extracted contour. The sub-pixel iso-densities curve is computed using linear interpolation between voxel grey values to refine the curve position. Thus for each contour point, with a grey level  $d_c$ , we detect the neighboring point having a grey value  $d_n$  such as  $d_T$  is lying between  $d_c$  and  $d_n$ . Then a displacement  $\delta$  is

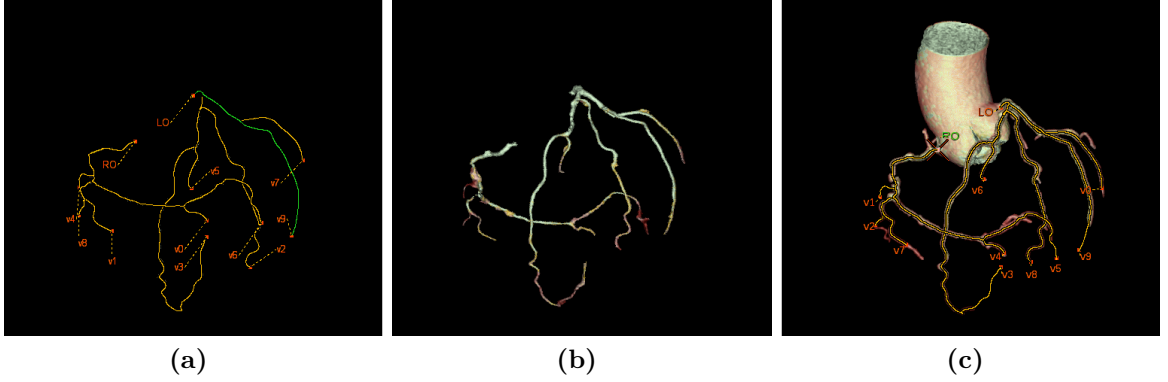


**Figure 2.16** – Coronary artery tree segmentation: (a) The provided coronaries centerlines used as vessel markers to initiate the watershed process. (b) The resulting coronary arteries lumen volume used to compute the lumen contours. (c) The coronary arteries tree rendering with the centerlines and the ascending aorta.

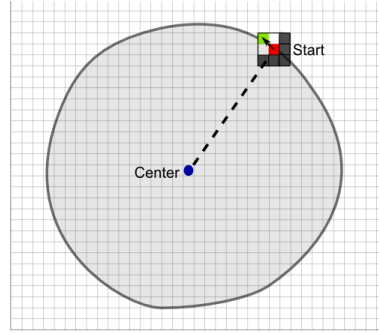


**Figure 2.17** – Vessel lumen Quantification: For each vessel cross section a 2D ray casting is used to find the starting point of the section contour, i.e. the first point outside the watershed volume. Then, we look for the next contour point in a restricted neighborhood of the current point. The process stops when the starting point is reached for the second time.

computed to refine the contour point:

$$\delta = \frac{d_T - d_c}{d_n - d_c} \quad (2.9)$$

This approach was used in the context of stenosis detection as described in section 2. However, it presented moderate performances for accurate stenosis detection and lumen quantification; It mainly suffers for erroneous pathological vessel lumen estimation. In fact, a major drawback for this approach is the use of vessel centerlines as markers to segment the vessel lumen. Consequently, if the used centerline goes through a vessel lesion, the resulting vessel lumen segmentation will be biased. Besides, this method uses a region growing step to define the lumen mask. However, this mask usually present leakages around low intensity regions (i.e. soft

plaques and distal vessel). This is mainly due to the fact that only local statistics are used to constraint the region growing process and hence this yields to miss-estimating local thresholds. Additionally, no specific treatment is planned to remove soft coronary plaques from the lumen mask and this yields to including such lesions in the final segmentation result. Hereafter, we propose a novel approach using scan specific statistics to extract a vessel lumen mask that can be used in a seeded based segmentation approach to robustly extract and quantify the vessel lumen volume.

### 2.3.2 Vessel lumen mask extraction using adaptive statistics

For an accurate segmentation of the vessel lumen volume, a robust handling of the coronary lesions is mandatory. Due to the fact that coronary lesions can present intensities similar to those captured inside the vessel lumen, they are often erroneously included in the lumen segmentation. However, they are not part of the vessel blood-flowing lumen and hence must be removed from the lumen segmentation result in order to get a reliable segmentation for stenosis analysis. Previous works used thresholding and tissue classification to remove calcified plaques before segmenting the vessel lumen [271, 305, 460]. However, no specific treatment was planned for soft plaques, although these lesions are more challenging to remove because they exhibit similar intensities to coronary arteries. Therefore, we propose to use a vessel statistics based approach to eliminate the plaques from the coronary lumen, before applying a segmentation step. As shown in figure 2.18, plaques/lumen borders are characterized by an intensity value change. Hence, calcified and soft plaques borders can be detected using appropriate threshold values.

In order to build a vessel intensity model, we propose an adaptive approach that automatically extracts a data-driven intensity appearance model of the coronary arteries lesions. Using the same static vessel model for all the patients is not possible, due the significant inter-patient variability. In fact, several studies showed that using different dilutions of contrast material for multislice CT leads to significantly different attenuation in lumen and associated plaques. The plaque attenuation clearly varies with the luminal one and hence the intra-coronary attenuation should be taken into account to estimate the different plaques intensities. Besides, the plaque intensities varies significantly with the choice of reconstruction kernel and protocol timing. Therefore, we propose to automatically determine scan-specific intensity thresholds for both calcified and non calcified plaques from luminal attenuation.

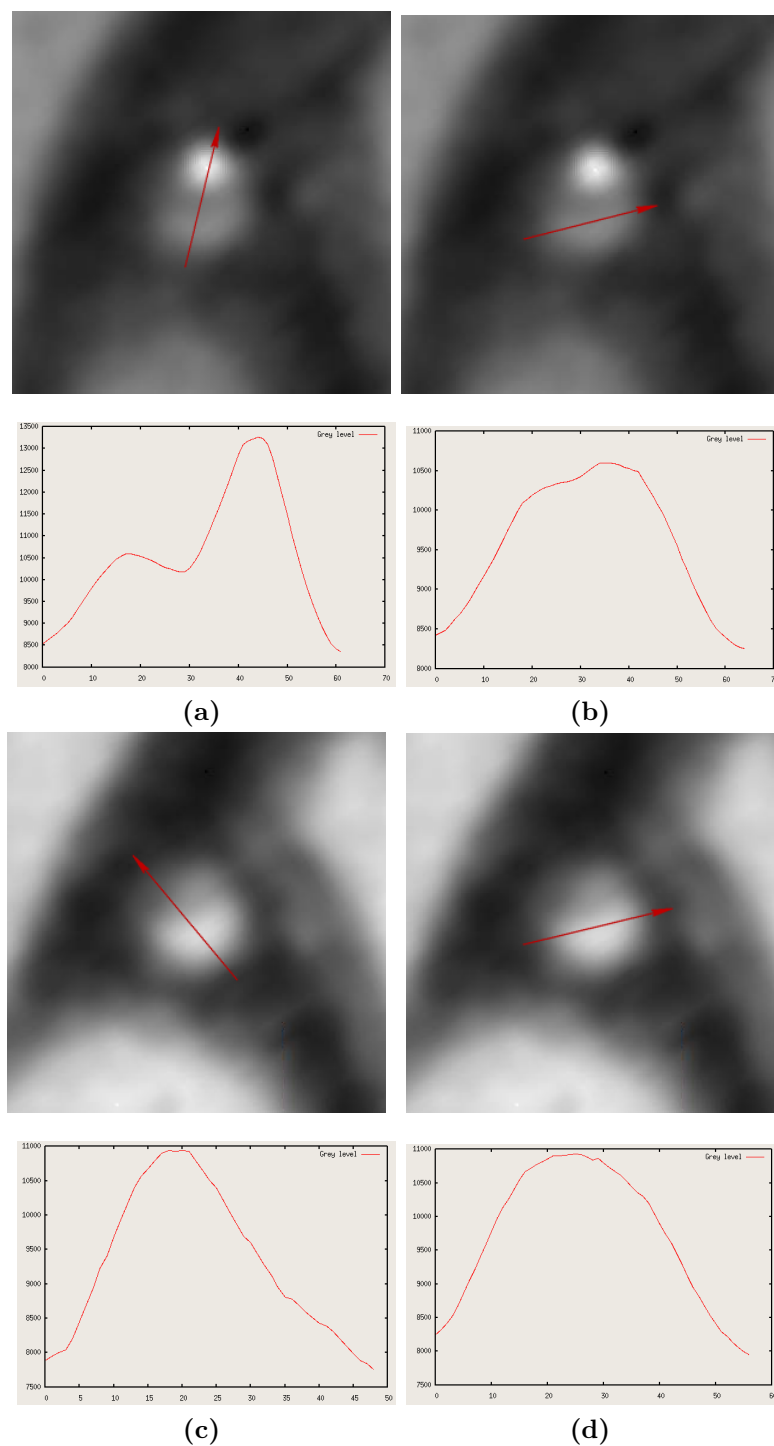


**Figure 2.18** – 2D vessel cross section intensity profiles are shown for normal (a)-(c) and pathological (b)-(d) cases with the corresponding ray directions. Normal ray profiles has maximal intensity values near to the vessel center and lower values near the lumen border. Intensity profiles along pathological tissues show different patterns. For calcified lesions, a second and higher peak is detected at the center of the calcified region. On the contrary, soft lesions showed lower intensity values than the vessel lumen hence involving a drop of the ray intensity profile. The two borders can be delineated by using adequate threshold values.

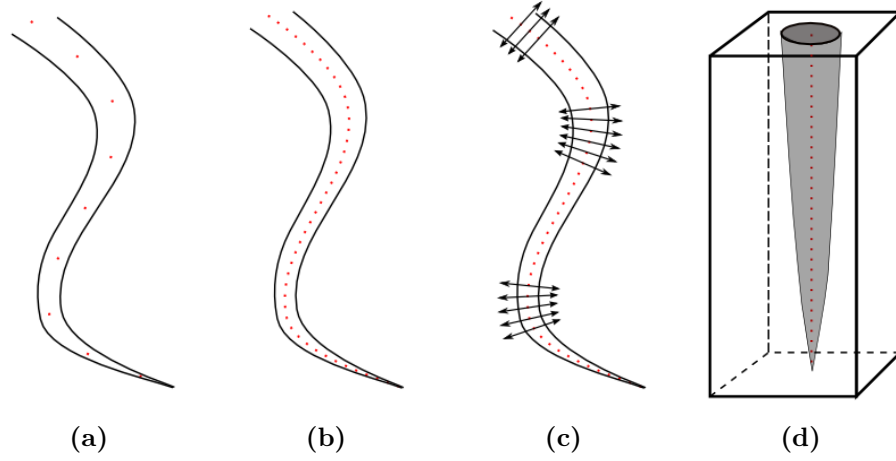


**Figure 2.19** – Vessel reformatting volume generation: (a) The provided vessel centerline. (b) The resampled centerline. (c) The 2D vessel cross-sections stacked to construct the final vessel warped volume (d).

### 2.3.2.1 Reformatted vessel volume extraction

In order to provide a resampled version of the original CTA image, while reducing the processing time and memory use we propose to work on a warped volume of the vessel. This volume corresponds to an orthogonal image stack of the corresponding vessel known as the reformatting vessel volume (see figure 2.19). First, the vessel centerline is resampled in order to get a homogenous inter-slice distance and avoid image distortion. The provided centerlines are resampled to obtain an inter-slice resolution of  $0.1mm$ . For each point on the vessel centerline we extract a slice orthogonal to the vessel path using a tricubic interpolation. We adjust the size of the extracted 2D slices such that it covers an area that is big enough to show the cross-section of vessel with a maximum diameter value. Thus, the 2D window can safely be restricted to  $16mm \times 16mm$ . The in-plane resolution was also set to  $0.1mm$ . Hence, for each vessel, we extract an isotropic warped volume composed of a set of parallel stack of 2D cross sections of the vessel as shown in figure 2.19.

### 2.3.2.2 Vessel lumen marker extraction

First, the algorithm is initialized by extracting the ascending aorta volume using a set of thresholding and connected component analysis. The aorta volume is then used in order to determine the normal blood pool attenuation. The uniform normal blood pool region is filtered using a median filter to reduce noise amount. Then, we compute the corresponding image

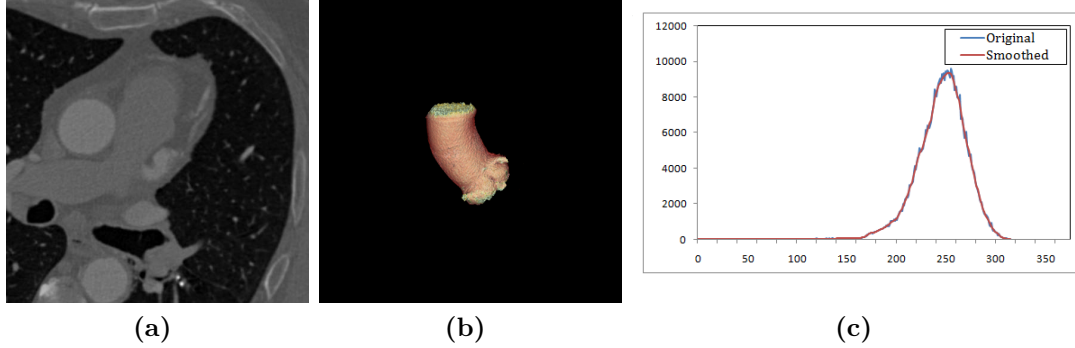


**Figure 2.20** – Ascending aorta extraction (b) from image (a), followed by histogram extraction and smoothing (c) for initial vessel statistics computation.

histogram as shown in figure 2.20. A Gaussian smoothing is applied on the aorta histogram.

Then, we extract the normal blood pool value as the peak value  $M_{Aorta}$  of the resulting Gaussian-like curve. Additionally, we compute the standard deviation value of the smoothed aorta histogram  $std_{Aorta}$ . Using these two values, we define the upper and lower contrast intensities as following:

$$\begin{aligned} L &= M_{Aorta} - k \times \sigma_{Aorta} \\ U &= M_{Aorta} + k \times \sigma_{Aorta} \end{aligned} \quad (2.10)$$

These two values represent the lower and upper threshold values for the normal blood pool class around the aorta. To calculate scan-specific thresholds in order to eliminate calcified and non calcified plaques on coronary arteries, we should adapt the previously extracted thresholds by considering the scan-specific variation in contrast distribution through the coronary arteries. In fact, as we can see on figure 2.21, the luminal intensity decreases along the coronary artery. First, we smooth the vessel lumen central attenuation using a gaussian kernel in order to remove unwanted fluctuation due to the presence of coronary lesions or noisy points. The resulting curve is shown on figure 2.21. It describes the overall decrease of the vessel lumen attenuation from proximal points to distal ones. Thus, for a point  $i$  on the vessel centerline, we define the non calcified and calcified plaques thresholds as following:

$$\begin{aligned} NCP_i &= A_i - \kappa \times (A_0 - L) \\ CP_i &= A_i + \kappa \times (U - A_0) \end{aligned} \quad (2.11)$$

### 2.2.3 Statistic-based Vessel Lumen Segmentation

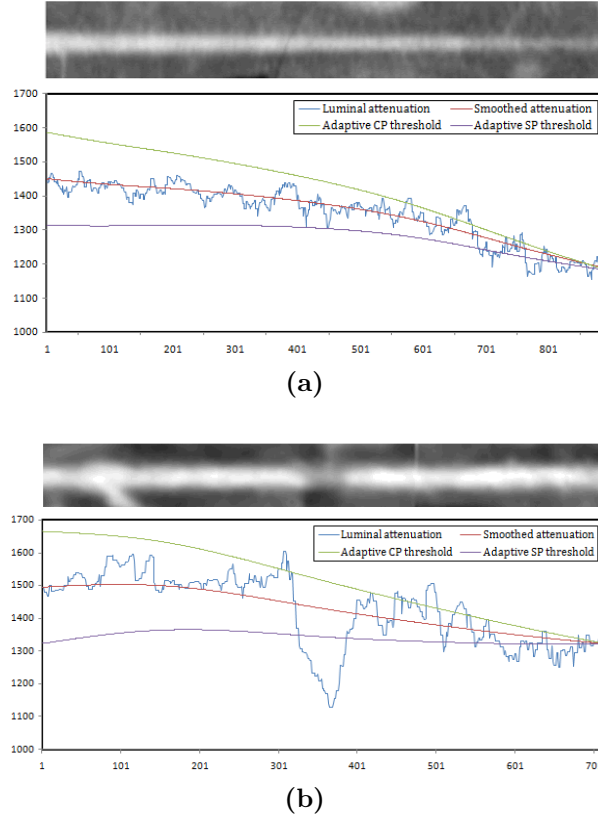


**Figure 2.21** – Adaptive thresholds for calcified and non calcified plaques extraction for a healthy (a) and diseased vessel (b).

with,

$$\kappa = 1 - i/n \quad ; \quad n \text{ being the length of the vessel.} \quad (2.12)$$

The previous thresholds are used in order to create a vessel mask while excluding coronary lesions. The extracted mask is further used in a seed based segmentation framework to extract the final vessel lumen. To automatically determine a robust marker of the vessel lumen, we propose a ray casting based approach to search radially for the vessel lumen boundaries using the soft plaques and calcified adaptive thresholds. Using a cylindrical coordinate system, a slice in the warped vessel volume is represented by the coordinate  $z$ . A point on the corresponding 2D cross section is defined by an angle  $\theta$  and a radial position  $\rho$ . For each slice of the reformatted volume,  $K$  rays of a maximum length of  $R$  equidistant points are generated. To avoid possible bias caused by noisy points, we define a local neighborhood for border points search. For each point on the directed ray, the neighborhood is inspected to determine whether it belongs to a



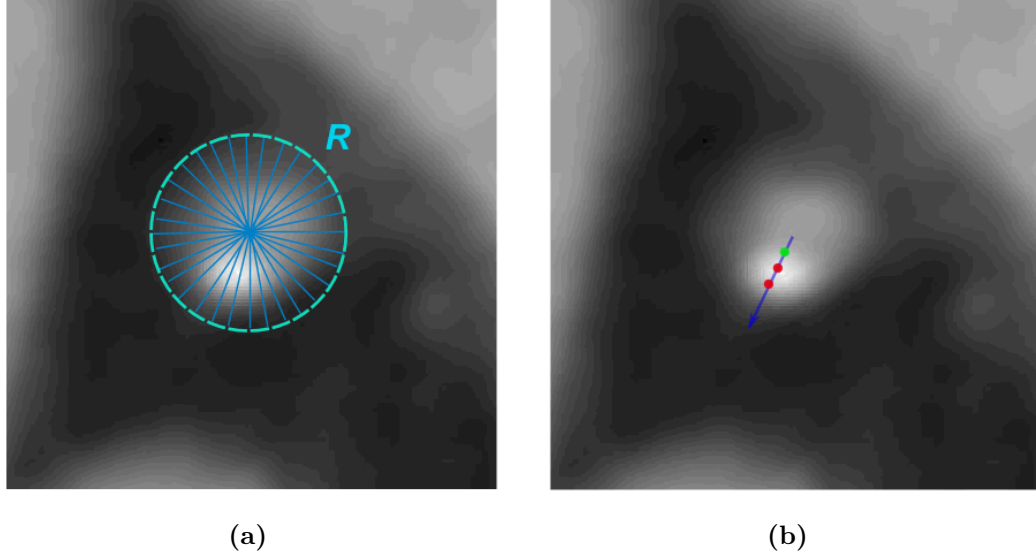


**Figure 2.22** – 2D lumen boundaries extraction using adaptive thresholds: (a) Rays of a maximum radius  $R$  are traced around the vessel centerline point. (b) A point on the ray and the associated neighboring pattern to detect lumen border.

coronary lesion border or not. Hence, a point is classified as a lumen/calcified plaque border point if it shows a gray value higher than the calcified plaque threshold, as well as its two successive neighbors (figure 2.22). Similarly, we use the soft plaque threshold to determine lumen/non calcified plaques borders. The detected border points are hence stored as the vessel slice contour points.

To maintain accuracy and consistency, we constrained the ray casting step by defining a maximum radius,  $R$ , for the search of the border points at each slice. This allows to stop the search for challenging cases and avoid going into unwanted structures. To be robust against vessel scale changes, we update this maximum radius value along the vessel path. Hence, for each slice  $i$ , a maximum search radius  $R_i$  from the coronary centerline is defined by continuously decreasing the value from proximal to distal sections. In order to be sure we cover the whole vessel, we started at radius value of  $4.5\text{ mm}$ . Furthermore, since cardiac CT images are often noisy, the resulting contours are quite noisy too (figure 2.23). Therefore, we apply a final contour smoothing step based on the smoothing of neighboring radius values of each 2D slice.

Figure 2.24 shows examples of extracted vessel masks using the previous approach. Vessel masks were extracted in vessel warped volumes (section 2.3.2.1) and then projected in the 3D original image volume. We compare the results of the vessel lumen masks extraction using static scan specific thresholds (extracted based only on the aorta histogram) and adaptive scan

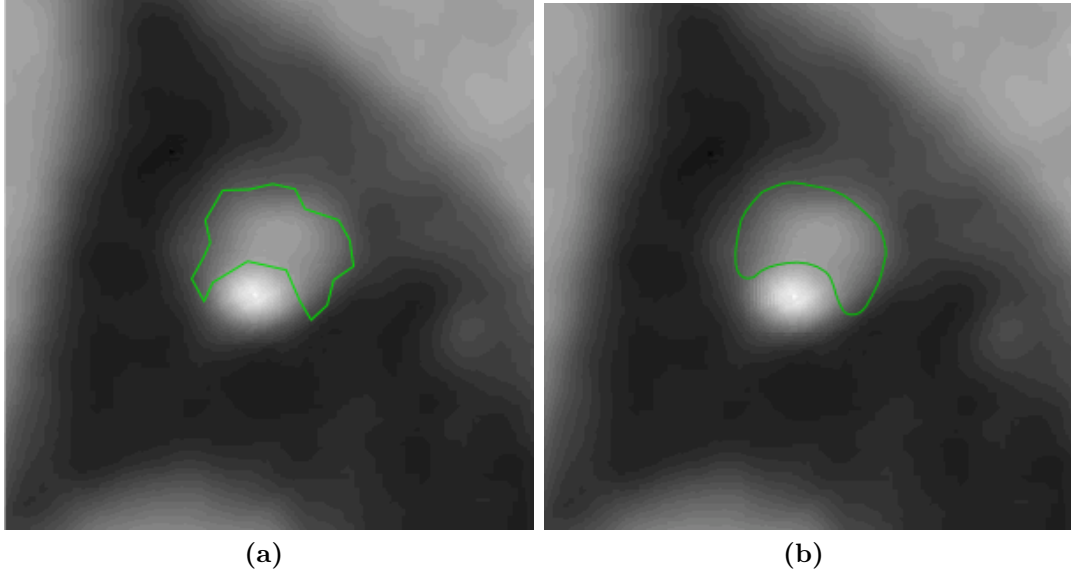


**Figure 2.23** – A post smoothing step to avoid noisy contours: Original (a) and smoothed (b) contour.

thresholds using the vessel lumen attenuation variation. As illustrated, the adaptive thresholds allow to obtain a more accurate vessel lumen markers by elimination vessel lesions and avoiding leakage into neighboring structures. This is mainly observed near to distal vessels where lumen intensities are very similar to surrounding tissues. In the first case a soft plaque was also eliminated using the proposed approach.

### 2.3.3 Vessel Segmentation and evaluation results

#### 2.3.3.1 Vessel segmentation using seed-based algorithms

Seeded segmentation approaches are commonly used in medical images analysis [97]. They allow to integrate a prior high-level knowledge on the vessel location by using a binary or probabilistic indicator function that denotes whether we are inside or outside the target object. Binary indicators are a set of seeds or markers, used to initiate the segmentation process, and mark the object foreground and background. The performance of seeded segmentation approaches heavily relies on the selection of seed points. Wrong seeds lead to erroneous segmentation results. In fact, different seed points sets can yield different segmentation results. Most commonly used seed-based segmentation techniques are Graph Cuts [50], Random Walkers [164] and the Watershed Transform performed in different ways [100, 295, 437].

In order to overcome graph cuts and watersheds issues, we propose to use the Random walker algorithm for vessel lumen segmentation. The algorithm details are described in section

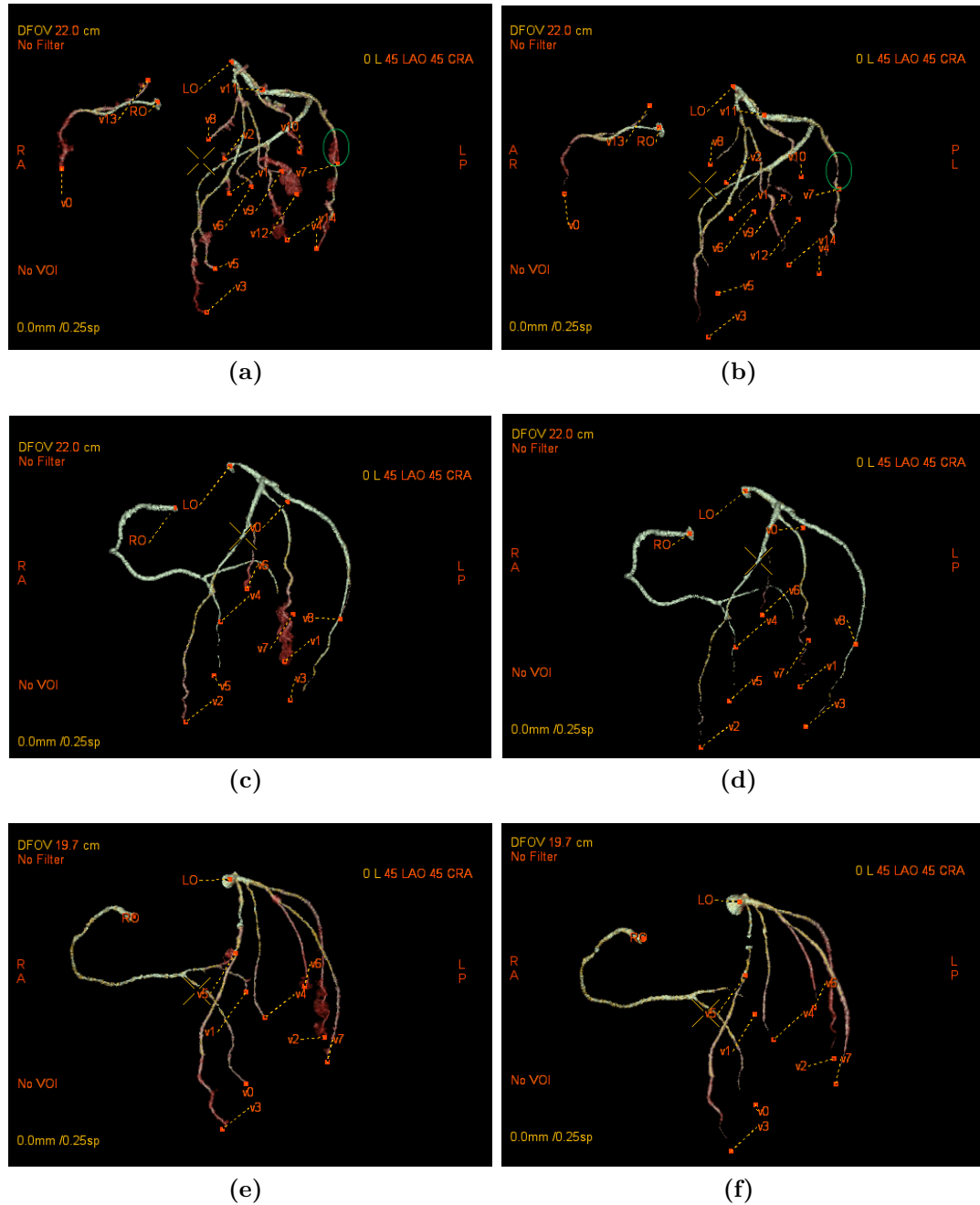


**Figure 2.24** – Examples of coronary vessels masks extraction using static patient specific thresholds ((a) (c) (e)) and adaptive patient specific thresholds ((b) (d) (f)). Adaptive thresholds allow to obtain more accurate vessel lumen markers by removing leakage and lesion inclusion.

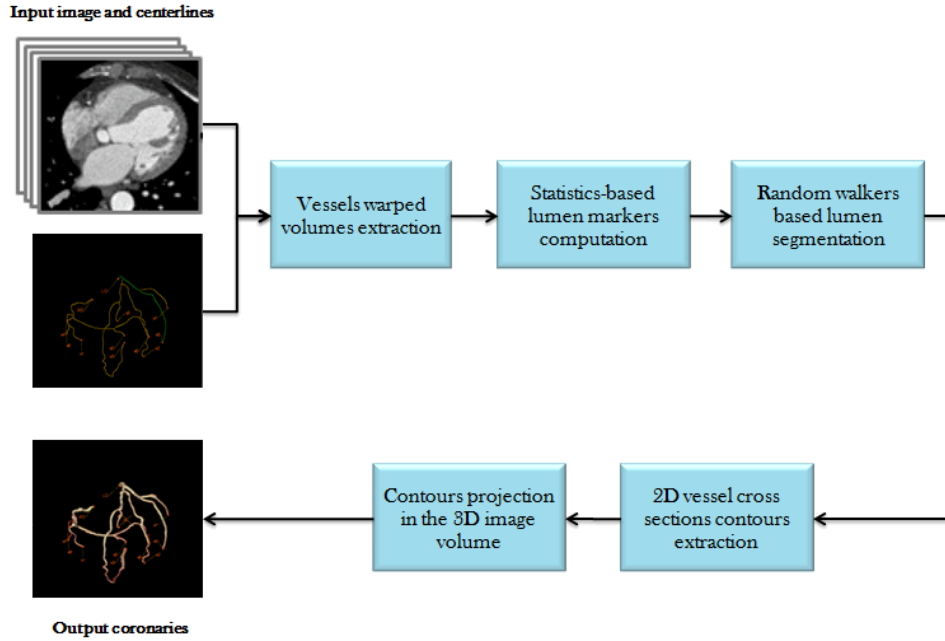


**Figure 2.25** – Overall lumen segmentation flowchart.

**1.3.3.1.** Segmentation is performed on warped vessel volumes. The vessel lumen seeds are marked using the previously extracted lumen mask. The background seeds are created from the vessel lumen by computing the complementary of the dilated lumen mask. Once the vessel lumen volume is segmented, we extract the 2D cross section contours by using a ray casting approach. The same approach described in section 2.3.1 is used. The obtained contours are furthermore radially smoothed to avoid noisy points. Finally, the obtained contours are dumped into the original 3D image volume and the complete coronary tree is hence extracted. The overall lumen segmentation steps are presented in figure 2.25.

Figure 2.26 shows some extracted coronary vessels for different datasets of the training database of the Rotterdam coronary arteries segmentation challenge.

#### 2.3.3.2 Quantitative evaluation results

In order to quantify the lumen segmentation results, we used the online Coronary Artery Stenoses Detection and Quantification Evaluation Framework described in [215]. Therefore, we provide a unique 3D surface describing the complete coronary artery tree. This online framework allows to evaluate the accuracy of coronary arteries lumen segmentation by comparing the provided 3D coronaries model with a segmentation obtained by averaging three manual observers segmentation, using three different evaluation measures:

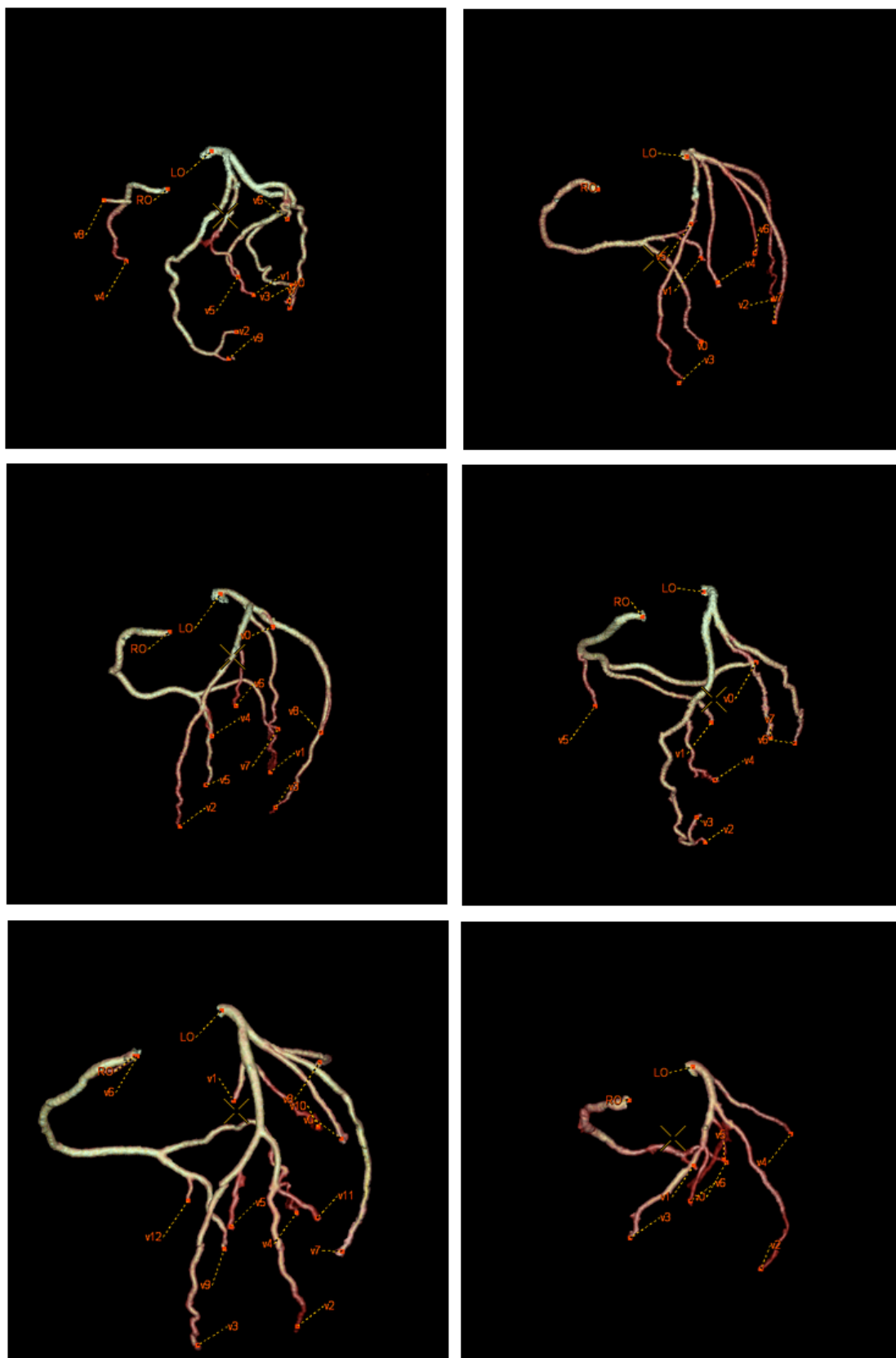


**Figure 2.26** – 3D example of coronary lumen segmentation results of datasets 16, 14, 13, 12, 01 and 05.

### 2.2.3 Statistic-based Vessel Lumen Segmentation

- Root mean squared distance (MSD) between the manual and automated 3D vessel lumen surface
- Hausdorff distance (MAXSD) between the two surfaces
- 3D Dice coefficient to measure the overlap between the reference standard and the automated segmentation

Healthy and diseased vessel segments are considered separately during the evaluation process. We have to mention that the following results are obtained on the training databases. Results on the testing database can be disclosed only once to avoid training on the testing database.

First, we evaluated the segmentation results obtained by varying the constant multiplying the standard deviation in equation 2.10. The evaluated segmentation is the output mask extracted using the scan specific adaptive thresholds with the ray casting approach performed in warped vessel volumes, without applying a further segmentation step. Table 2.3 show the obtained evaluation for  $k = 1.5$ ,  $k = 2.5$  and  $k = 3$ . We found that 2.5 yielded the better results. This value was subsequently used for the following tests.

**Table 2.3** – Vessel lumen mask extraction using different k values.

	DICE Diseased	DICE Healthy	MSD Diseased	MSD Healthy	MAXSD Diseased	MAXSD Healthy
<b>k = 3</b>	0.55	0.57	0.68	0.80	6.85	7.63
<b>k = 2.5</b>	<b>0.57</b>	<b>0.62</b>	<b>0.65</b>	<b>0.67</b>	<b>6.74</b>	<b>8.08</b>
<b>k = 1.5</b>	0.53	0.61	0.78	0.69	6.99	8.49

In order to evaluate the contribution of the use of the warped vessel volumes to segment the coronary lumen, we compared the proposed approach with a segmentation technique using the same seeds extraction idea but performed on the 3D original volume. Results are presented in table 2.4. As we can state, working on reformatted vessel volumes allows to obtain more accurate and precise lumen segmentation results for both healthy and pathological vessels.

Table 2.5 shows the evaluation results of the state of the art approach (section 2.3.1) and the proposed approach. The new approach clearly offers better performances with reference to the three evaluation metrics and for both healthy and diseased vessels. These results reflect the contribution of the use of more intelligent seeds in accurately extracting vessel lumen contours. Besides, as shown previously, the use of warped volumes allowed to improve these performances by adding more precision. This is a valuable contribution especially for thin object segmentation

## Chapter 2. Coronaries Artery Segmentation

**Table 2.4** – Vessel lumen segmentation performances evaluation using the reformatted vessel volumes and the original images.

	DICE Diseased	DICE Healthy	MSD Diseased	MSD Healthy	MAXSD Diseased	MAXSD Healthy
<b>Vessel reformatted volumes</b>	0.65	0.74	0.49	0.46	4.41	5.52
<b>3D original volumes</b>	0.59	0.58	0.52Å	0.63Å	4.67Å	5.90Å

using limited image spatial resolution. Such improvements are also important as they allow to more accurately detect and quantify coronary lesions.

**Table 2.5** – Comparison of state of the art approach and the proposed one.

	DICE Diseased	DICE Healthy	MSD Diseased	MSD Healthy	MAXSD Diseased	MAXSD Healthy
<b>State of the art approach</b>	0.48	0.45	0.68	0.84	5.07	5.93
<b>Proposed approach</b>	0.65	0.74	0.49	0.46	4.41	5.52

Finally, our approach present state of the art performance as compared to the other approaches evaluated on the same online framework. We obtained similar overlap measures to *Observer2*, for both healthy and diseased segments. Besides, we obtained similar MSD values for healthy and pathological segments as compared to the two approach [271] and [305]. Meanwhile, our approach presented lower performances with reference to the Hausdorff distance as compared to other approaches and observers. However, we have to keep on mind that the presented results are obtained on a subset of the testing database. This database was used for training the algorithms presented in [271] and [272]. Hence, the obtained results by these approaches should be considered carefully as they might be biased by the training step.

**Table 2.6** – Coronary lumen segmentation performances as compared to state of the art approaches and the three observers.

	DICE Diseased	DICE Healthy	MSD Diseased	MSD Healthy	MAXSD Diseased	MAXSD Healthy
<a href="#">Lugauer et al. [272]</a>	0.75	0.77	0.27	0.32	1.96	2.79
Observer3	0.76	0.80	0.24	0.19Å	3.07	3.25
<a href="#">Lugauer et al. [271]</a>	0.72	0.74	0.28	0.35	2.02	2.88
Observer1	0.74	0.79	0.26	0.26	3.29	3.61
<a href="#">Mohr et al. [305]</a>	0.73	0.75	0.29	0.45	1.87	3.73
Observer2	0.66	0.73	0.31	0.25	2.70	3.00
<b>Proposed approach</b>	0.65	0.74	0.49	0.46	4.41	5.52

#### 2.3.4 Conclusions and future work

In this section, we proposed an automated approach for coronary arteries lumen extraction from vessel centerlines. We proposed a novel approach for vessel seeds extraction that seems to be more accurate for seed based segmentation than the use of the vessel centerlines as markers. The approach has been evaluated on a subset of 18 cardiac exam and showed state of the art performances. We have to mention that the segmentation results are conditioned by the provided vessel centerlines quality. Missing branches will yield to miss-segmentation of the coronary tree. In the future, we plan to further improve the segmentation quality by using a more robust segmentation framework by using the Power Watershed proposed in [96]. Besides, we propose to build and test a probabilistic indicator function for vessel seeds rather than a binary one, using scan specific vessel statistics. Finally, we will submit lumen segmentation results as well as stenosis detection using the new vessel segmentation approach on the testing database of the Rotterdam challenge in order to perform a better and fair comparison.





## Part III

# Methods for Automated Coronary Arteries Stenosis Detection



---

---

# Chapter 1

---

## Previous work and Evaluation framework

### Contents

---

<b>2.1</b>	<b>Image Pre-processing</b>	<b>54</b>
2.1.1	Downsampling	54
2.1.2	Image filtering for noise reduction	55
2.1.3	Tubular structures enhancement	55
<b>2.2</b>	<b>Image Pre-segmentation</b>	<b>57</b>
2.2.1	Delineation of anatomical region of interest	57
2.2.2	Abnormalities removal	58
2.2.3	Seeds extraction	58
<b>2.3</b>	<b>Vessel modeling</b>	<b>60</b>
2.3.1	Intensity Models	60
2.3.2	Geometry Models	62
2.3.3	Hybrid Models	63
<b>2.4</b>	<b>Vessel features extraction</b>	<b>64</b>
2.4.1	Centerline extraction	67
2.4.2	Vessel extraction	73

---

Coronary arteries inspection using CT angiographies is a time consuming task and requires a level of expertise in coronary CT analysis and interpretation. It has been established that acquiring moderate expertise in coronary CT angiography interpretation may take more than one year [347]. Interpretation results are also subject to observer variability. Besides, the gold

standard for stenosis detection and quantification is a 2D imaging modality. Hence, stenosis detection and quantification is mainly based on a 2D measure of the diseased section diameter (usually the minimum value). However, by using 3D CT cardiac angiography more possibilities are provided for stenosis quantification. In fact the stenosis degree can be quantified using the cross section area in addition to the minimum, maximum or mean diameter values. This induces more variability in stenosis detection and quantification as each measure might provide different stenosis degrees. Subsequently, the CT image quality could be degraded by several artifacts caused by heart and respiratory motion, and presence of some blurring vessel abnormalities and surrounding structures (calcifications, stents, heart cavities). As a result, the diagnosis quality and accuracy could be affected [347]. Therefore, computer-aided extraction of coronary arteries lesions is appreciated to aid the visual analysis of CT images and lesion detection thus allowing to reduce the evaluation time and observers variability.

Many computer-aided algorithms for detecting and diagnosing arterial abnormalities have been developed for medical imaging. Proposed algorithms were dedicated for the detection of different lesion types such as carotids stenosis in MR [147, 194, 479] or CT modality [173, 409, 506], and aortic [40, 104] or brain aneurysm [182, 183]. Meanwhile, less methods have been dedicated to coronary arteries lesions. In fact, detecting and quantifying coronary lesions are particularly challenging and tedious tasks mainly due to the limited spatial resolution and the relatively small size of coronary vessels and the associated lesions. Moreover, coronary lesions present a highly complex topology (complex shapes) with a wide nature variability (calcified, soft and mixed plaques) that could not be easily captured using a single simple approach.

In this chapter we present two different approaches for automated coronary lesions detection in CT angiography. In section 1.1, we review state-of-the-art methods for coronary lesions detection. We first expose the specific models utilized in the literature to detect vascular lesions (Section 1.1.1). Then, we present coronary lesions dedicated approaches in section 1.1.2 and 1.1.3. In section 2, a first approach using lumen segmentation and healthy vessel model reconstruction is proposed. However, this approach suffers from some limitations related to the quality of lumen segmentation step. In fact, the robustness of the approach is conditioned by the lumen contours extraction which is challenging giving to the limited spatial resolution of cardiac CT and coronary arteries motion. Therefore, we later propose a second approach for stenosis detection in section 3. This approach is based on a machine learning technique to detect coronary lesions using scale invariant features. The main goal is to overcome the previous approach limitation due to the lumen segmentation step by focusing on modeling and detecting the coronary lesions rather than detecting the resulting lumen narrowing. We compared the performance of these two approaches using the same evaluation framework [215] and prove that

learning based approaches are more robust against false positive detection and allows to get a better true positive detection rate.

## 1.1 Coronary Arteries Lesions Detection

Recently, efforts have been made towards (semi-)automatic detection and quantification of coronary artery lesions in cardiac CT angiography. Coronary arteries lesion detection problem mainly refers to the localization of vessel abnormalities causing a lumen narrowing (stenosis) that might limit the heart blood flow. A stenosis being the result of a plaque formation on the vessel wall, two possible approaches have been defined to solve this problem in general: 1) Detect the resulting lumen narrowing, 2) Detect the plaque causing the narrowing. The first approach is mainly based on a healthy vessel lumen modeling and thus extracting the lesions as being a deviation from the constructed model. The second approach aims to model the vessel lesion by identifying its main characteristics. However, due to a large topological (extent, eccentricity) and appearance (calcified, soft and mixed) variability, it is very hard to capture all the lesions configurations using a single model. Therefore, most of the proposed algorithms was designed to track one single type of lesions. Some of the proposed approaches only focus on 1) calcified plaques detection [357, 423, 453], others on 2) soft plaque lesions [355] or 3) both of them [161, 212, 417]. To deal with this problem, researchers have utilized machine learning approaches aiming to detect different types of lesions using one single approach.

### 1.1.1 Pathology Models

Authors have tried to detect vessel pathologies using prior information about the target lesion. In fact, several models have been defined to capture the pathology characteristics. Both appearance and geometric properties were used. However, due to a wide variability of cardiac pathologies anatomy, it seems to be very challenging to detect those anomalies only based on simple models. Following, we cite some defined models in the literature to capture specific properties, hence allowing to discriminate between different types of vascular pathologies.

#### 1.1.1.1 Stenosis

Stenosis are generally characterized by their specific geometric shape corresponding to a laminar narrowing due to a plaque formation. The most intuitive and classical way is to detect those anomalies as sudden decrease of lumen radius value [147, 193, 373, 506] in a post processing stage after a robust lumen segmentation step. These approaches do not deal with the plaque

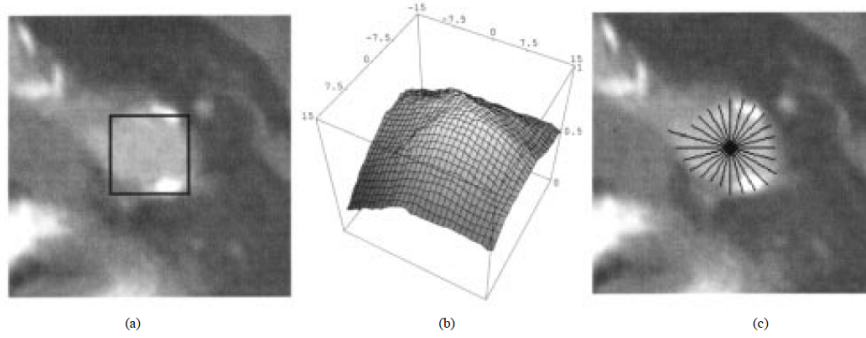


**Figure 1.1** – 2D Ray-casting to detect vessel wall points while excluding the calcified plaques using a gradient threshold. Illustration from the work of [Wink et al. \[460\]](#).

type characterization in general; The same model is used to detect stenosis caused by a calcified and a soft plaque. In [262], the work proposed by [Sato et al. in \[373\]](#) to detect tubular structures (vessels) was refined to detect stenosis by defining a new measure of double cone-like shapes (see Figure 1.2). Stenosis have also been detected based to the resulting blood flow limitation by simulating the coronary arteries blood flow using a coherent coronary tree segmentation (section 1.1.2.4).

### 1.1.1.2 Calcification

Calcifications are an advanced stage of the atheroma plaque development process. At this stage, the plaque is mainly composed of calcium which makes them appear as bright structures stack to the vessel wall. Based on this appearance characteristic, the most commonly used approach to detect those structures is to use appropriate thresholds [454] of CT values combined to a set of morphological operations. [Wink et al. \[460\]](#) proposed a 2D ray casting approach to detect calcified plaques on the vessel wall based on gradient threshold (figure 1.1). This allowed to exclude the calcification from the vessel contour and robustly estimate the vessel lumen center. Features based on size, shape, location, and appearance models are also defined to distinguish between true calcification candidates and other false detection that can look like calcified plaques [198, 235, 236, 463].

### 1.1.1.3 Aneurysm

Aneurysms have been located as a local deviation from the vessel model as in [261, 460]. In fact, to the best of our knowledge, there is no specific model proposed for aneurysms due to their shape variability. However, in [104], abdominal aortic aneurysms are detected using an active shape model formulation learned from a set of training data. Morphological criteria were also

defined to detect aneurysm by analyzing the vessel surface curvature [211]. Geodesic Active Region Model combined with non-parametric region-based information was used to segment brain aneurysms in [182, 183]. Similarly to stenosis, those lesions could also be detected as local increase of the vessel wall volume or radius.

In general, vascular abnormalities could be detected as being deviations from a healthy vessel model [466]. Based on the real vessels segmentation, a corresponding *healthy* vessel model is used to extract the vessel abnormalities thus avoiding to deal with these complex shapes. This approach is generic and allows to detect both stenotic and aneurysmal regions. Similarly, tubular deformable models were registered onto the vessel lumen. This allows to detect normal, stenotic and aneurysmal regions [206]. The main advantage of such approaches is that they do not focus on abnormalities modeling and thus are able to detect a wide range of heterogeneous lesions. However, these class of approaches are dependent on the vessel lumen segmentation quality. In fact, they require a topological and morphological coherent vessel segmentation to be able to accurately estimate the healthy vessel model and hence detect vascular abnormalities. However, we have to mention that aneurysmal coronary lesions present an exceedingly rare clinical entity and are in majority related to a coronary atherosclerosis causing a positive remodeling.

Next we will focus on proposed approaches for coronary lesions detection in the literature. We will only focus on methods dealing with coronary stenosis or plaque detection. We present these works based on the main idea designed to detect the target coronary lesion. Section 1.1.2 deals with *ad hoc* approaches aiming to directly model a given type of lesion to be detected. Second, we present a set of *learning based* approaches proposed to deal with the lesions heterogeneity problem.

### 1.1.2 Rule-based Approaches

In this section, we review proposed rule-based approaches for automated coronary lesions detection and quantification. These approaches are directed towards lesions specific patterns identification using explicitly designed heuristics based on previously defined lesions models (i.e. appearance and geometric models). Hereafter, we present the state-of-the-art approaches classified following the heuristic used to detect the target lesion. First, the most used approach in the literature, based on the vessel lumen segmentation, is exposed. Then, we review some intensity and geometry-based approaches. Finally, a new emergent class of approaches based on the simulation of coronary blood flow is presented.



### 1.1.2.1 Lumen Segmentation based Approaches

Early works addressing the coronary stenosis detection and quantification challenge mainly focused on an accurate vessel lumen delineation step in order to extract stenotic areas using different approaches [18, 171]. The first most commonly used idea is to reconstruct an expected normal vessel lumen using the real segmented lumen. For this purpose, several authors proposed to extract a “healthy” lumen diameter (or radius/area) by applying various regression techniques to the real lumen radii profile. Comparing the two diameter profiles, stenotic areas could hence be detected and quantified. Linear regression approaches are commonly used to estimate the expected lumen radii profile [63, 80, 141, 305, 333]. In [63], stenoses are determined by manually placing a proximal and distal reference on the coronary vessel segment to be analyzed, after a lumen segmentation step. The algorithm estimates a normal tapering of the corresponding segment. Stenoses are then detected by assessing the difference between the segmented lumen contours and the normal proximal-to-distal tapering of the segment. In addition, a tissue-based analysis of the area between the vessel wall and the lumen contour allows to identify the composition of the associated lesion (i.e. calcified or soft plaque). However this approach suffers from a low sensitivity and PPV values. The method proposed in [141] needs the artery endpoints as inputs. First, the lumen surface is extracted using a Fast-Marching algorithm followed by a continuous 3D surface reconstruction step based on a Right Generalized Cylinder model. Then, stenoses are detected and quantified by comparing the reconstructed lumen surface to an “idealized” profile obtained from a linear regression of the radii of the most reliable contours. However, several errors are produced due to their segmentation approach; Their approach seems to be not robust against false positive detection. In [333], the authors proposed a semi-automated hybrid approach for coronary stenoses detection and quantification. The coronary arteries are segmented combining the Hessian matrix based “vesselness” filter with three dimensional region growing algorithm. Similarly to the previous approaches, stenosis are detected and quantified by estimating the vessel diameter at each centerline location via plane fitting, and applying linear regression analysis on the estimated diameter profile. In [208], a piecewise least squares line fitting is used to determine the “normal” luminal diameters from the scan. The regression is performed separately on each segment to take into account the normal drop of radius values after each bifurcation. Lesions extraction is performed in several steps, mainly based on the computation of stenosis degrees by the comparison of the two diameters profiles. The algorithm keeps only stenosis with a narrowing degree higher than 25%. In [135], stenoses are detected and quantified by comparing the extracted lumen area with the second order regression of the lumen area over the vessel length. To avoid erroneous de-

tections due to the partial volume effect, the intensity of boundary voxels is contrasted against the myocardium and the left ventricle intensities. The same approach was also used in the work of [Shahzad et al. \[390\]](#). A graph cut based segmentation is used to extract the coronary lumen volume. Furthermore, an expected healthy lumen diameter profile is computed using a weighted Gaussian kernel regression. Hence, stenotic regions are detected by using the healthy profile as a reference.

An other possible approach for stenosis detection based on the lumen radii analysis, is to compare the stenotic lumen section to a non stenotic (i.e. healthy) proximal or/and distal references in the same vessel. In [\[479\]](#), an approach for carotid artery stenosis detection in MRA data is detailed. To extract the vessel surface, authors used a mesh that deforms toward high gradient values while maintaining a smoothness criteria. To detect the stenosis, the vessel skeleton and the radii are extracted using an organized region growing. The stenotic region is manually selected by putting two seed points. The region growing process is applied to determine the maximum sphere passing inside the region thus determining the vessel radii. The stenosis is then estimated by comparing the radius in the stenotic region with the radius of a healthy section selected manually. [Cetin et al. \[81\]](#) proposed a method based on 1D analysis of the vessel radii variation to detect vessel stenosis. First, a tensor model for tubular structure segmentation is used to extract the vessel centerline and thickness. Possible stenoses regions are detected as the intervals for which the radius constitutes a valley. Therefore, the estimated radius profile is smoothed using a Gaussian filtering. Then the start and end points of the stenosis are determined by analyzing the energy profile of the radius derivative. In a similar approach, [Wang et al. \[447\]](#) computed the circularity and the convex hull deficiency to describe the shape of the coronary arteries cross sections. These features are then used to automatically detect and identify the presence of calcified stenoses.

Being located within the vessel wall, coronary plaque lesions can also be detected by analyzing the volume enclosed between the inner and outer vessel contours. In [\[161, 355, 423\]](#), both the outer boundary of the vessel and the lumen contours are delineated. Thus, plaque lesions are detected as hypo-dense areas between the inner and the outer wall of the vessel. [Rinck et al. \[357\]](#) used a shape-based segmentation approach to extract the inner and outer vessel surfaces and then analyze the deviation between the two volumes. The method may, however, need additional user interaction to accurately compute plaque volumes by placing a seed point before and after each plaque. An iterative model-based variational approach is applied in [\[161\]](#) to delineate the blood vessel external boundary and lumen. The approach detects both calcified and soft plaques. Calcified lesions are segmented by hysteresis based adaptive thresholding. Soft (non-calcified) plaque lesions are detected as hypo-dense areas without calcium between

the external vessel boundary and lumen. The proposed approach was tested by different clinical trials and compared to human interpretation of the coronary CTA [161]. At a per study level, the approach showed a high sensitivity value above 80%. However, a lower PPV values have been obtained (between 20% and 80%). Toumoulin et al. [423] used a level set approach to detect both the inner and outer wall of a vessel in CT data sets and were therefore able to identify calcified plaques.

The proposed framework by Renard and Yang [355, 356] relies also on the separate segmentation of the lumen and arterial wall of the major arteries by applying a statistical model-based segmentation approach. Soft plaques are identified by examining the effective cross-section areas of the lumen and its surrounding wall surfaces. The soft plaque detection criterion is based only on area difference which makes the method prone to errors. Similarly, in [239] active contours driven by spatially localized probabilistic models are employed to extract the vessel surfaces from the inside-out and the outside-in. The proposed framework uses a scale parameter to restrict the statistical characteristics of the vessel into local regions. By identifying areas where the inner and outer contours do not meet, soft plaques are detected. Tested on 8 datasets (4 datasets with soft plaques and 4 healthy datasets), the approach showed interesting results for plaque detection. However, the technique should be improved in order to be able to detect the plaque lesions robustly. Wang et al. [444] incorporated an implicit 3D vessel model to guide the level sets propagation defined on initial set of centerline points. After the evolution of the level sets, new centerline points are extracted and a new vessel diameter is then quantified. A new vessel model is hence redefined. Propagation and redefinition are repeated until convergence. To extract and quantify stenosis, the inner and outer vessel walls are extracted using the same scheme with different parameters.

Generally, the previous techniques are still highly depending on the lumen segmentation quality. Indeed, any over estimation or under estimation of the vessel segmentation could lead to false positive and/or false negative detections. The coronary lumen (and outer wall) delineation step is challenging for several reasons: The size of coronary artery vessels, the limited CTA resolution and the partial volume effect are the main reasons making the segmentation of the lumen difficult. To deal with this problem some authors proposed to process a more precise segmentation of the lumen by generating sub-voxelic contours from a segmented lumen volume [291] or by sub-sampling the initial volume and generating reformatted vessel volumes [208]. Moreover, segmentation approaches based on gradient variation to delineate the lumen boundaries are prone to failure near bifurcations and around soft plaques because of the loss of signal. In [305], the authors used level-sets with additional tissue classification and calcium exclusion in order to get an accurate lumen segmentation. Other works proposed to post-process

the resulting segmentation to eliminate detected outliers [389, 390].

#### 1.1.2.2 Intensity-based Approaches

An other category of proposed methods focused on directly extracting the vessel pathology based on appearance properties. [Lor and Chen \[265\]](#) used a concentric model derived from Gaussian distribution to detect both the vessel lumen and the coronary plaques. Kalman filtering is used for quantitative evaluation of the vessel diameter stenosis. Finally, a Bayes classifier is used to determine the stenosis degree based on the posterior probability of severity conditioned on stenosis percentage and plaque type of the training data. In [113, 115], the authors presented a semi-automated algorithm for volumetric quantification of non-calcified and calcified plaques from coronary CTA. The algorithm uses scan-specific attenuation thresholds for lumen, non-calcified plaques (NCP), calcified plaques (CP) and epicardial fat to delineate non-calcified and calcified plaques. The algorithm shows interesting correlation with manual quantification performed by two different readers. However, this approach relies on manual selection of start and end points of regions to be analyzed and it needs a user defined region of interest to compute the scan specific thresholds which may influence the computation of these values. The approach was further improved in [207, 208] for the detection of obstructive and non obstructive plaque lesions in the three main coronary arteries (LAD, LCX and RCA). The method needs a coronary mask as input to extract the vessel centerlines. The vessel lumen is then segmented using scan-specific threshold levels of calcified and non-calcified plaques with a recursive region growing approach. In the work of [Wesarg et al. \[454\]](#) calcified plaques are dynamically excluded from the vessel segmentation during centerline extraction. Then, stenosis candidates are detected by analyzing the vessel diameter variation. Subsequently, the local neighborhood of the detected candidates is analyzed to determine whether the detected lumen reduction is due to a calcified plaque or is just a false detection. However, this approach suffers from several drawbacks: It is strongly dependent on the user manually placed seed points on the arteries and detected lesions are not segmented and no quantitative analysis is presented. In [374], the authors used an intensity-based technique involving a registration step to extract a set of calcified plaques candidates using both contrast enhanced and non-contrast enhanced CT images. In spite of presenting interesting results (a sensitivity of 85.5% and a PPV of 87.8%), their method can lead to unnecessary radiation exposure because of the use of both contrasted and non contrasted CT scans. In [471], calcified plaques detection for calcium scoring estimation in non contrasted chest CT is performed by thresholding the filtered volume and removing small detected regions. Subsequently, a region based analysis allows to remove

false detections located at the aortic valve and the mitral valve regions. Komatsu et al. [223] proposed a visual aid for manual detection of calcified and soft plaque lesions in CT angiography. The approach provides a “Plaque Map” based on the color-based isometric lines method and the Bird’s Eye View, to color the relevant limit of CT numbers and show the 3D-contour images. In [107], potential calcium plaque are extracted by identifying connected regions that exceed a given threshold. A stochastic model based approach is applied to estimate the partial content of calcium for accurate quantification of calcium amount in the coronary arteries. For hypo-dense plaque lesions detection, Makrogiannis et al. [276] introduced a non parametric dissimilarity measure to define a local indicator function for the likelihood of belonging to the foreground object. Prior distribution of intensity and low-level image information have been incorporated. The likelihood function has been used as a speed function in a level set formulation to extract hypo-dense regions associated with soft plaques. In [258], a quantitative intensity-based analysis of the vessel wall is proposed for non calcified plaques detection. The method is based a mathematical morphology (Voxel-Map) performed on a three-dimensional coronary tree model which detects coronary walls in a similar approach as IVUS. This results in a 3D coronary artery wall model directly showing the composition of plaque attenuation that are associated with its severity [258].

### 1.1.2.3 Second Derivative based Approaches

Frangi et al. proposed a model-based approach to quantify carotids stenosis in MRA data sets [147]. A filter to enhance vascular structures is defined based on the eigenvalues of the Hessian matrix computed for each voxel of the image. Then, a deformable model is used to segment the vessel and thus quantify the stenosis using luminal diameter reduction. However, the hessian based filter would fail near to stenotic regions as the local shape deviates from a healthy tubular structure. As a result, the previous approach will fail to enhance stenotic regions. In [262], an orthonormal set is obtained by linearly combining the second order derivative estimators with energy normalizing coefficients and a new *conus-like* shape is included to describe the stenosis (Figure 1.2). Based on the new shape space a stenosis detection condition is proposed: three parameters are set to discriminate against other shapes than the double cone shape.

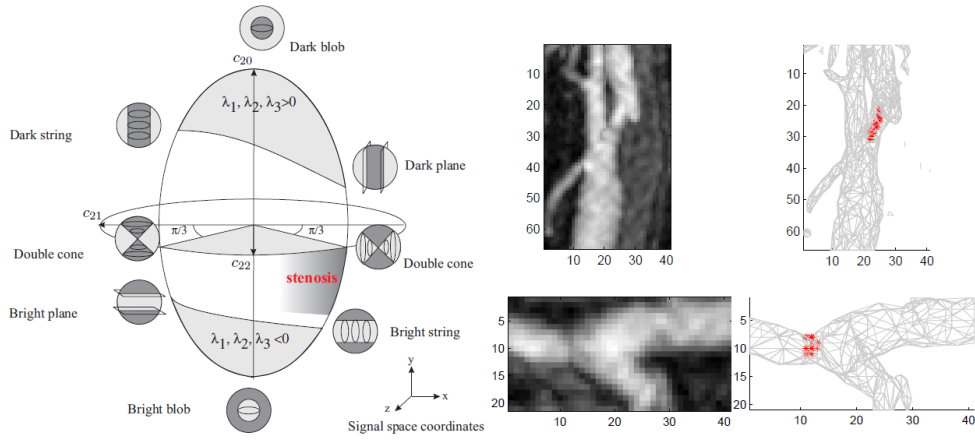


**Figure 1.2** – Stenosis detection using hessian based approach: (Left) The non-redundant shape-space for second order 3D variations proposed by [262]. (Right) Maximum Intensity Projection (MIP) of two stenotic regions in an MRA dataset, wire-frame representation with stars denoting the stenotic area.

**Table 1.1** – Ad hoc approaches for (semi-)automated detection of coronary arteries lesions. SP refers to soft plaques and CP to calcified ones.

Work	User	Inter	Modality	Approach	Target lesion	data	Evaluation	Results
Broersen et al. [63]	semi-auto.		contrasted CT	lumen seg. + healthy profile reconstruction	Hybrid	30	per lesion	sensitivity = 27.7% PPV = 31%
Cetin et al. [81]	auto.		contrasted CT	lumen seg. + Gemoetric features analysis	Hybrid	11	NA	NA
Dey et al. [115]	semi-auto.		non contrasted CT	Intensity models	Hybrid	24	per lesion	correlation = 0.90-0.94
Eslami et al. [135]	semi-auto.		contrasted CT	lumen seg. + healthy profile reconstruction	Hybrid	30	per lesion	sensitivity = 51% PPV = 4%
Flórez Valencia et al. [141]	semi-auto.		contrasted CT	lumen seg. + healthy profile reconstruction	Hybrid	30	per lesion	sensitivity = 15% PPV = 5%
Goldenberg et al. [161]	auto.		contrasted CT	inner/outer wall delineation	Hybrid	49-398	per patient	sensitivity > 80% PPV = 20-80%
Kang et al. [208]	semi-auto.		contrasted CT	lumen seg.+ Inensity models + healthy profile reconstruction	Hybrid	42	per segment	sensitivity = 93% specificity = 81% PPV = 52%
Lankton et al. [239]	semi-auto.		contrasted CT	inner/outer wall delineation	SP	8	per lesion	sensitivity = 87.5% PPV = 100%
Lor and Chen [265]	semi-auto.		contrasted CT	Lumen seg. + Intensity and geometry features analysis	Hybrid	30	per lesion	sensitivity = 32% PPV = 3%
Mohr et al. [305]	auto.		contrasted CT	lumen seg. + healthy profile reconstruction	Hybrid	30	per lesion	sensitivity = 51% PPV = 16%
Öksüz et al. [333]	semi-auto.		contrasted CT	lumen seg. + healthy profile reconstruction	Hybrid	30	per lesion	sensitivity = 17% PPV = 26%
Renard and Yang [355]	semi-auto.		contrasted CT	inner/outer wall delineation + geometric features analysis	SP	2	NA	NA
Saur et al. [374]	auto.		angio and native CT	Intensity and geometric models	CP	127	per lesion	sensitivity 85.5% PPV = 87.8%
Shahzad et al. [389]	semi-auto.		contrasted CT	lumen seg. + healthy profile reconstruction	Hybrid	30	per lesion	sensitivity = 55% PPV = 27%
Toumoulin et al. [423]	semi-auto.		4-slices CT	inner/outer wall delineation	CP	6	NA	NA
Wang et al. [444]	auto.		contrasted CT	inner/outer wall delineation	Hybrid	30	per lesion	sensitivity = 11% PPV = 33%
Wesarg et al. [454]	semi-auto.		contrasted CT	lumen seg. + Gemoetric features analysis	CP	10	per lesion	sensitivity = 98%
Wang and Liatsis [446]	auto.		contrasted CT	lumen seg. + Gemoetric features analysis	CP	NA	NA	NA

#### 1.1.2.4 FFRs Estimation Approaches

**Fractional Row Reserve (FFR)** is a lesion-specific technique to determine the functional significance of a coronary stenosis. It corresponds to the ratio of the pressure distal to a stenotic region to the pressure before the stenosis. A wire is used to determine the maximal coronary blood flow down a vessel in the presence of a stenosis compared to the maximal flow in the hypothetical absence of the stenosis. An FFR of 0.75 means that the corresponding stenosis caused 25% drop in the vessel blood flow. However, the relation between coronary stenosis severity and myocardial ischemia is not causal. In fact, some severe stenosis could be functionally non-significant. The FFR measure allows to determine the culprit lesion of an ischemia and thus defines the narrowed coronary that needs to be revascularized [343]. An important advantage of this technique is that it allows to detect the important stenosis and allows to simultaneously stent the diseased vessel. Nevertheless, this technique is an invasive procedure for which a non-invasive alternative is highly appreciated.

Thanks to recent advances in image-based modeling and computational fluid dynamics, it is possible today to non-invasively compute the fractional flow reserve using only CTA scans called  $\text{FFR}_{CTA}$  [414]. The computation the FFR from CTA is based on a combination of anatomy, physiology and fluid dynamics. First, an anatomic model of the coronary vessels is mandatory. Generally, this model is extracted from the CT images using segmentation techniques that might be refined manually; The coronary tree topology is defined, plaques are detected and vessel lumen is delineated. Second, the inflow and outflow boundary conditions reflecting the patient-specific physiology are extracted. Finally, the coronaries flow and pressure are computed by solving the governing equations of fluid dynamics. The scientific foundation for non invasive  $\text{FFR}_{CTA}$  computation are detailed in the work of Taylor et al. [414].

This approach have shown promising performances for ischemic stenosis detection compared to invasive FFR [224, 288, 301, 486]. However, these studies have been limited to stable patients. An interesting study would assess the performance of  $\text{FFR}_{CTA}$  to evaluate bypass grafts or instant restenosis. Moreover, the accuracy of  $\text{FFR}_{CTA}$  could be limited by moderate CT scan quality (e.g. presence of calcification, motion artifacts). In fact, a perfect coronary arteries model is mandatory for an accurate  $\text{FFR}_{CTA}$  estimation. A subsequent limitation could be the variability of the physiological model between populations and patients which may lead to biased  $\text{FFR}_{CTA}$  values [414].

Table 1.1 presents the different heuristic-based approaches proposed to detect coronary artery lesions in different modalities. For each method, the table reports the user interaction level, the used modality, the used approach and the target lesion type. Besides, details about



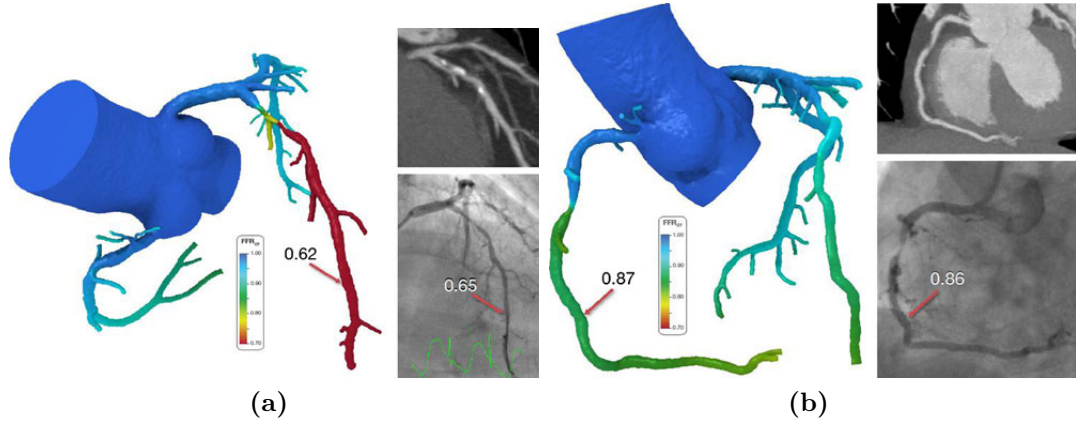


**Figure 1.3** – Two cases showing the accuracy of  $FFR_{CTA}$  compared to invasive FFR. Case (a) shows a nonfunctionally significant stenosis at the LAD with a computed  $FFR_{CTA}$  of 0.62. This value is confirmed using invasive angiography that shows an FFR of 0.65. Case (b) shows a non hemodynamically significant stenosis with an  $FFR_{CTA}$  of 0.87. The FFR measured using invasive angiography was of 0.86. Illustrations from [414].

the evaluation process and results of each approach are reported. Even if it is difficult to compare such approaches (different modalities, different target lesions and evaluation metrics), this table gives an insight of the state-of-the-art methods accuracy.

### 1.1.3 Learning-based Approaches

In the last few years, pattern recognition and classification systems became popular for specific object detection. In fact, they are used to solve several practical problems in clinical applications such as breast and lung cancer diagnosis. Recently, this technique has been used for coronary arteries lesions detection [303, 416, 505]. Thereby, we may overcome lumen segmentation quality related issues. Some of the proposed approaches deals with a specific target lesion (calcified, soft plaques) and thus utilizes specific features capturing the target abnormality characteristics [64, 198, 236, 259, 451]. On the other hand, some approaches were designed to deal with different type of lesions by using a mixture of features to cover the different configurations [212, 416, 419]. Calcified plaques within the coronary artery present a marker of the degree of underlying atheromatous involvement of that vessel. Therefore, automated tools for detection and quantification of coronary calcifications are proposed to assist the clinician during the calcium scoring step. Such methods allow to reduce the manual burden and the diagnosis time, which would be especially useful for large-scale screening. A large set of (semi-)automated approaches has been proposed trying to solve the problem of coronary artery calcifications detection in native (non-contrasted) or/and contrasted CT scans. Approaches are generally

designed following a two stage framework. First a set of calcified lesions candidates is extracted from the processed volume. Then, a classifier is used to discriminate between true positives (coronary calcifications) and false positives including bones, metal stents or any other metallic objects (see figure 1.4). In [64], a two stage non supervised classification approach was proposed to detect calcified lesions in electron beam CT images. First, the algorithm mines the calcified lesions characteristics and identifies a subset of optimal lesion features that will be used for classification. Second, a two stage clustering approach is applied to differentiate between arterial and non arterial calcifications. This work was extended in [65] using a supervised [Support Vector Machines \(SVM\)](#) based approach and a modified heart-centered coordinate system to align the different data sets. Similarly, using non contrasted EBCT angiography, [Kurkure et al. \[235, 236\]](#) used a two stages hierarchical supervised learning method for classification of candidate regions. The method learns an ensemble of classifiers at each stage, where each classifier is a cost-sensitive learner trained on a distinct asymmetrically sampled data subset. In the first stage, the method distinguishes between arterial (the coronary and the aortic) calcifications and other similar dense regions. At a second stage, coronary arteries calcifications are distinguished from aortic calcifications. However, the performance of this method are not assessed on multi-detector CT data sets, the most commonly used modality for cardiac lesions assessment. [İşgum et al. \[198\]](#) used specific features to automatically detect coronary calcification using a two-stage classification system from non-contrast-enhanced, ECG-gated Multi-slice Computed Tomography data. Candidates for coronary calcifications are first extracted by thresholding and connected component labeling. For classification, the features used were computed based on the size, shape, location, and appearance of the candidate regions. A two-stage classification system with a [K-Nearest Neighbor \(K-NN\)](#) classifier and a feature selection scheme was finally deployed to detect the true coronary artery calcifications. However, their classifiers were biased by the use of unbalanced training data containing a larger number of false candidates. In [\[463\]](#), an automated system for coronary calcium scoring in non enhanced CT angiography is presented. First, a set of coronary calcification candidates is extracted using appropriate threshold and connected components analysis. Then, a machine learning approach (Extra Trees [\[157\]](#)) is applied to distinguish between true coronary calcifications and other false positives using shape, intensity and spatial features. The system proposed a guided review post-processing step to reduce the amount of false positives. In [\[303\]](#), a rotation invariant sampling pattern was designed to extract calcified plaques on coronary arteries. For training, two different supervised learning techniques were tested: the [Probabilistic Boosting Tree \(PBT\)](#) and the [Random Forest \(RF\)](#) method. Both methods output a probability that a given point along the coronary centerline falls in the calcified region. The detection is restricted to the three main coronary arteries

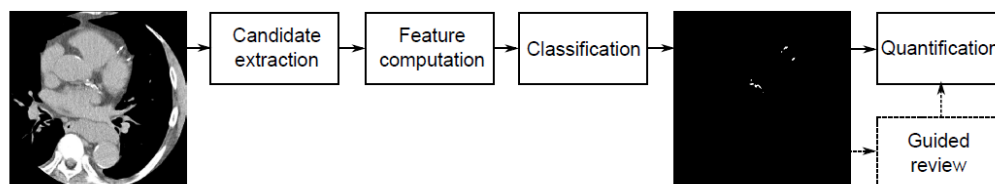


**Figure 1.4** – Automatic calcified coronary lesions extraction and quantification pipeline: First, the algorithm starts by identifying a set of calcification candidates. Appropriate features are computed to describe each of the previous candidates. Following, a trained classifier is used to distinguish between true calcifications and false detections. A review step is proposed in order to validate/suppress suspicious calcification that the classifier could not label with a high confidence. The final calcium score can thus be computed. Illustration from [463]

which makes the detection poor near bifurcation points. In the work of Li et al. [259], coronary calcification are detected using 22 characterizing features to train a SVM classifier. Using a four classification stages scheme, different candidates are detected and classified applying different features group. The system seems to perform better with reference to a patient basis analysis (whether a patient contains coronary calcifications or not) than using a vessel basis analysis (whether a coronary artery or a coronary branch contains calcifications).

Contrary to calcified lesions, fewer works have been dedicated to soft plaque extraction using learning based approaches. An automated approach was proposed in [451] to detect non-calcified plaques in coronary arteries. The approach starts with candidates selection by analyzing the 2D topology of the vessel wall gradient field. Then a Linear Discriminant Analysis (LDA) classifier is built with a set of 15 features (geometric features and 6 gray-level features) to compute a non-calcified plaque likelihood.

Other hybrid approaches have focused on coronary arteries stenosis identification which allows to detect all types of coronary plaques. Suzuki et al. [404] used a multilayer neural network for coronary artery stenosis in quantitative coronary angiography (QCA) using the normalized vessel diameters and cross-sectional areas as inputs. Tested on 30 QCA data sets, this approach achieved a correlation of 0,89 between the automatically estimated stenosis degree and the clinicians diagnosis. Toledano et al. [419] used a supported vector machine approach to learn and detect coronary artery stenosis in Multi-detector computed tomography (MDCT) images. The vessel is extracted in the corresponding curved image using image morphology and the boundaries are then estimated using dynamic programming. Soft and calcified plaques are detected separately using different multi-scale descriptors estimated at each point of the vessel centerline. Teßmann et al. [417] proposed a learning based classification approach that

uses local and global features for both calcified and non-calcified plaques detection using a multi-class variant of AdaBoost. However, this approach suffers from high false positive and negative detection rates. Moreover, the algorithm does not provide a threshold suitable for the segmentation and quantification of calcified plaques. In [212], severe stenosis are detected by a four-step approach including a learning-based centerline verification step and a lumen cross section estimation step using random regression forests. The stenosis candidates are detected based on lumen cross section radii. Finally, using the same classifiers as in [303], stenosis candidates are classified into “calcified”, “non calcified” and “mixed” plaques. Duval et al. [131] used rotation invariant features extracted inside a circular ROI around the centerline points. A RF classifier is used to detect the stenotic points. More precisely, five random forests are used per centerline point corresponding to the point itself and its four neighbors. A stenosis is considered to be present only if the five random forests agree. Similarly to [416] and [303], intensity and Haar-like features are used to train the classifier and detect the pathologies. The same classifier is also utilized in [80] to detect the stenosis coordinates along the coronary vessel using intensity-based and geometric features. Zuluaga et al. [507] proposed a semi-supervised learning based approach based on SVM to detect both calcified and non-calcified plaques using only healthy labeled samples and a large mixture set of unlabeled samples coming from both healthy and diseased sampled. The proposed framework allows to extend the training datasets using a new validated data set. However, this could induce a regression if the user validates a misclassified sample.

Table 1.2 presents the different learning-based approaches proposed to detect coronary artery lesions. For each method, the table reports the user interaction level, the used modality, the learning approach and the target lesion. Besides details about the evaluation process and results of each approach are reported. Even if it is difficult to compare such approaches (different modalities, target lesions and evaluation metrics), this table gives an insight of the state-of-the-art methods variability.

**Table 1.2** – Learning based approaches for (semi-)automated detection of coronary arteries lesions

Works	User Inter	Modality	Learning approach	Target lesion	data	Evaluation	Results
<a href="#">Tefmann et al. [417]</a>	automatic	Contrasted CT	Multi-class AdaBoost	Hybrid	45	per vessel	Sensitivity = 95.5% Specificity = 76.9%
<a href="#">Toledano et al. [419]</a>	semi-automatic	Contrasted CT	Support vector machines	Hybrid	21	per lesion	Sensitivity>90% Specificity>90%
<a href="#">Zuluaga et al. [505]</a>	automatic	Contrasted CT	Semi-supervised support vector machines	Hybrid	15	per lesion	Sensitivity = 89.8%
<a href="#">Kelm et al. [212]</a>	automatic	Contrasted CT	Random Forest (for plaque characterization)	Hybrid	229	per vessel	Sensitivity = 97.62% Specificity = 67.14% NPV = 99.77%
<a href="#">Cetin and Unal [80]</a>	semi-automatic	Contrasted CT	Random Forest	Hybrid	42	per lesion	Sensitivity = 53% PPV = 26%
<a href="#">Duval et al. [131]</a>	automatic	Contrasted CT	Random Forest	Hybrid	42	per lesion	Sensitivity = 43% PPV = 8%
<a href="#">Brunner et al. [64]</a>	automatic	EBCT	Unsupervised Classification based on the Hopkins test	Calcified plaques	16	per patient	Accuracy = 84%
<a href="#">Brunner et al. [65]</a>	semi-automatic	Non contrasted EBCT	Support vector machines	Calcified plaques	30	per segment	Sensitivity = 77.94 % Specificity = 96.57 %
<a href="#">İşgum et al. [198]</a>	automatic	Non contrasted CT	Two stage K-NN classifier	Calcified plaques	76	per lesion	Sensitivity = 73.8%
<a href="#">Kurkure et al. [236]</a>	semi-automatic	Non contrasted EBCT	Support vector machines	Calcified plaques	105	per scan	Accuracy = 98.27 % Sensitivity = 92.07 % Specificity = 98.62%
<a href="#">Mittal et al. [303]</a>	automatic	Contrasted CT	Probabilistic Boosting tree and Random Forest	Calcified plaques	165	per lesion	Sensitivity = 81% FPs per scan = 0,3
<a href="#">Li et al. [259]</a>	automatic	Contrasted CT	Support vector machines	Calcified plaques	55	per vessel	Accuracy = 83.64% Sensitivity = 81.50% Specificity = 84.09%
<a href="#">Wolterink et al. [463]</a>	automatic	non contrasted EBCT	Extra Trees	Calcified plaques	164	per patient	Sensitivity = 86%
<a href="#">Suzuki et al. [404]</a>	automatic	QCA	Multilayer Neural Network	Coronary stenosis	30	per lesion	Correlation = 0.89
<a href="#">Wei et al. [451]</a>	automatic	Contrasted CT	Linear discriminant analysis classifier	Soft plaque	62	per lesion	AUC value = 0.85

#### 1.1.4 Discussion

In this section, we reviewed most of the proposed techniques to deal with the problem of coronary arteries lesions detection and quantification. Depending on the lesion type and the kind of information to be quantified, several approaches have been proposed that can be summarized as illustrated in figure 1.5. The first family of presented approaches (ad-hoc approaches) tried to directly detect abnormalities by identifying and modeling these lesions' particularities. The bigger part of these approaches was dedicated to detect the vessel stenosis resulting from the plaque formation rather than detecting and characterizing the associated plaque lesion. Therefore they mainly focused on the vessel lumen geometry modeling and analysis to detect the vessel regions showing a lumen narrowing. Some methods proposed to reconstruct a healthy vessel lumen to be used as a reference for stenosis detection from the real vessel lumen profile by applying different regression approaches. However, creating such a healthy lumen profile is not trivial because of the complexity of the vessel structure and the related pathologies. Moreover, performing a regression along the whole vessel would necessary lead to erroneous detection due to the abrupt change of vessel radius after each bifurcation. Besides, using line fitting to estimate the vessel radii profile is not very robust as the normal vessel radii do not necessarily correspond to a straight line. Other approaches proposed to use a healthy (proximal and/or distal) reference section of the target vessel to detect and quantify the vessel stenosis. But the choice of this reference is very critical and can hence affect the detection and the quantification of the stenosis if not correctly selected. For this reason, some authors preferred to leave the reference selection task to the user rather than automatically select a section that could lead to false detections. An alternative to using healthy reference for stenotic region detection is to analyze other features computed for each vessel section such as circularity and eccentricity. All the previous approaches rely on an accurate lumen segmentation and contours delineation. Hence, the stenosis detection robustness is tightly related to the quality of the lumen segmentation which is particularly challenging due to limited spatial resolution, coronary artery motion and complex and variable coronary artery anatomies. We have also to notice that these approach mainly focus on severe stenosis extraction (causing  $>50\%$  of narrowing), hence it could miss coronary lesions that do not cause an obstructive lumen narrowing but that might be clinically relevant. Besides, being based on the lumen narrowing, most of these approaches would fail to detect vessel lesions associated to a positive remodeling.

An other subset of proposed approaches have focused on plaque detection and identification. As the plaque lesions are located within the vessel wall, these approaches was directed towards the vessel wall extraction and analysis. The basic idea is to extract both of the vessel inner

and outer vessel walls. Such approaches allows for the detection of the different plaque lesion types (calcified, non-calcified and mixed) and the quantification of the generated vessel stenosis. Such approaches are also robust against coronary plaques inducing positive vessel remodeling. Nevertheless, this task is still challenging for the same reasons, related to the accuracy of the vessel walls segmentation, detailed above. The two surface have to be accurate enough to be able to delineate the small lesions volumes which is not that easy due to the CT limited resolution compared to the plaques size.

Some other works tried to detect specific lesion types by using prior appearance models. Being heterogeneous by nature, it was difficult to define a single model that captures all the possible lesions. Therefore, most of the proposed approaches were rather dedicated to identify and segment one type of lesions. Being relatively easy to detect, the vast majority of works deals with calcified plaques detection for calcium scoring or related stenosis detection. Some of these approaches was only applied to non contrasted CT and hence are not suitable for contrasted CT. However, non-calcified lesions are more vulnerable and prone to rupture and need to be accurately detected in order to estimate the development stage of this plaque and its risk of rupture. Fewer works have focused on soft plaques modeling and extraction. These approaches were mainly based on extracting soft plaques intensity properties to delineate the lesion volume in contrasted CT. They generally offer a tool to visualize and analyze soft plaques composition. However, they are not able to differentiate between the different types of soft plaques. This is mainly a drawback of the CT technology. Moreover, such approaches need subsequent user interaction to define regions of interest needed for the extraction of the soft plaques. However, intensity-based approaches usually utilize specific modality techniques which are more suitable for the target lesion detection (e.g. non contrasted EBCT for calcification detection and contrast enhanced CT for soft plaque detection). This makes difficult to extend them to other modalities in order to be combined to simultaneously detect all plaques types. A possibility would be the use of different CT acquisitions (i.e. with and without contrast enhancement) but this would lead to exposing the patient to increased radiation doses. Dual source CT could be a solution for this problem if it was available in all medical centers.

The second family of available methods have made use of machine learning techniques to simultaneously tackle the different types of lesions. Most of these approaches use supervised classification schemes. Therefore, to be able to accurately detect all topologies of coronary plaques, such methods need a reliable, well balanced training set covering all possible pathological behaviors. Nevertheless, collecting such labeled data is time consuming and the accuracy of the manual annotation is prone to be affected by the inter-observers variability and different expertise level. Some attempts was directed towards the use of unsupervised classification

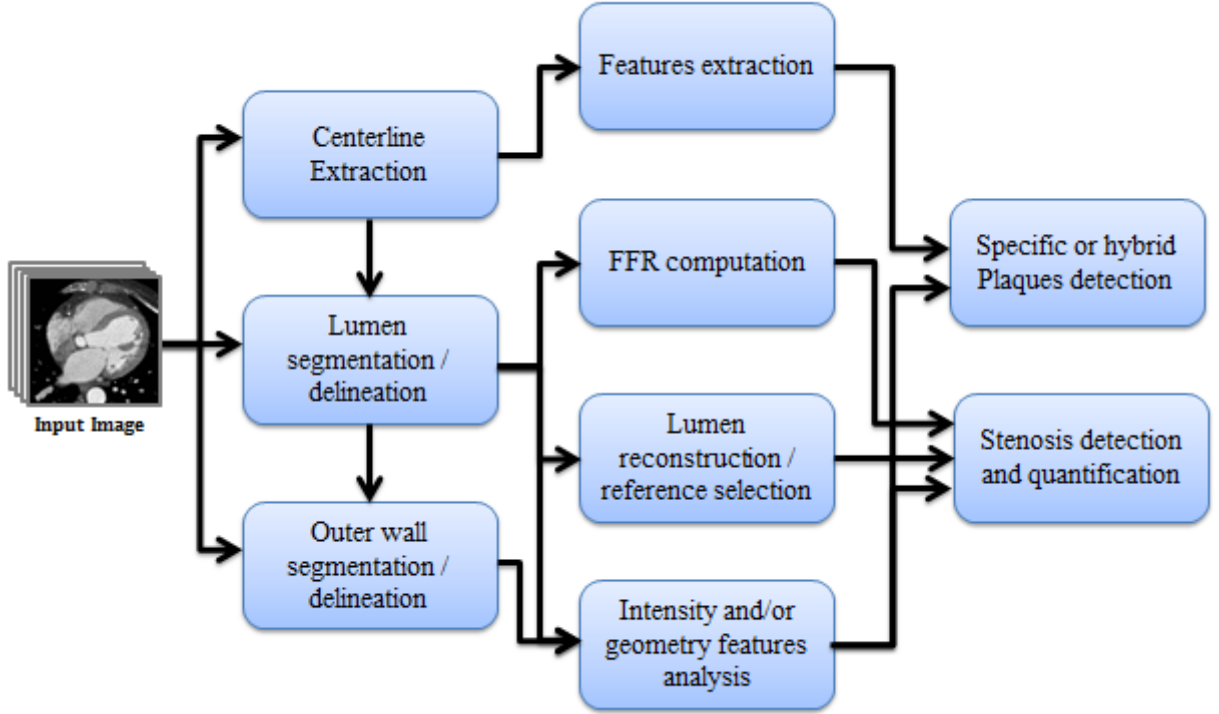


**Figure 1.5** – An overview of the proposed workflows in the previously published works on coronary arteries plaque lesions detection and quantification.

schemes but they showed relatively high rate of false positive detections.

Subsequently, methods for coronary arteries lesions extraction are generally based on coronary vessel centerlines (e.g. for vessel reformatted volumes extraction, ROIs definition, lumen reconstruction) and are hence affected by these centerlines quality. In the following, we propose two different frameworks for automated coronary arteries lesions detection based on a vessel lumen segmentation and reconstruction approach, and a learning based approach trying to overcome the limitation of the above mentioned approaches.

## 1.2 Materials and Evaluation Framework

The evaluation of previously cited methods is usually performed using different databases, metrics and criteria (per segment, vessel or patient evaluation). Therefore, making a fair comparison of these works remains difficult. Recently, Kirişli et al. [215] introduced an algorithm evaluation framework precisely dedicated to solving this problem: The Coronary Artery Stenoses Detection and Quantification Evaluation Framework. This framework is publicly available online at



the following address <http://coronary.bigr.nl/stenoses>. It provides an online evaluation framework of different challenges: Stenosis Detection, Stenosis detection and quantification, and Stenosis detection, quantification and lumen segmentation.

### 1.2.1 Data

The framework provides 48 multi-vendor cardiac CTA datasets of symptomatic patients aged between 41 and 80 years old consisting of 32 (67%) males. The datasets were acquired in three different medical centers on different CT scanners: (1) The Erasmus University Medical Center (Erasmus MC, Rotterdam, The Netherlands) using a dual-source CT scanner (Somatom Definition, Siemens, Forchheim, Germany), (2) The University Medical Center Utrecht (UMCU, Utrecht, The Netherlands) on a 64-slice CT scanner (Brilliance 64, Philips Medical Systems, Best, the Netherlands), and (3) The Leiden University Medical Center (LUMC, Leiden, The Netherlands) using a 320-slice CT scanner (Aquilion ONE 320, Toshiba Medical Systems, Tokyo, Japan). The enhanced CT images were reconstructed at the mid-to-end diastolic phase using retrospective or prospective ECG gating. Besides, for each patient, a non-enhanced CT scan is performed to assess the coronary calcium score (CCS) using a dedicated software. Patients have been hence selected based on their CCS (between 0 and 400) and distributed over 5 coronary calcium score risk categories in order to have a representative database [215]. More details about patient selection, image acquisition and reconstruction can be found on the framework website.

Every patient underwent both CTA and Conventional Coronary Angiography (CCA) examinations. Eighteen of the 48 CTA images were made available with CTA and [Quantitative Coronary Angiography \(QCA\)](#) reference standards for training purposes. For the remaining 30 datasets, only the CTA images were made available. These datasets were used for testing the proposed algorithms using the online framework. Patients in both of the training and testing database have been selected in a way to cover different vendors, CCS categories and stenosis degrees. The distribution of patients over the two sets is explained in [215].

### 1.2.2 Reference Standards

The CTA datasets were annotated by three independent experienced observers, blinded to the QCA results, from Erasmus MC, University Medical Center Rotterdam. The final ground truth was provided via a consensus reading described in [215]. Using the axial, MPR and curved MRP views, the coronary arteries were analyzed with reference to the 17 modified AHA coronaries model (see appendix B). Segments with a diameter lower than 1.5 mm were excluded from the

analysis. For each dataset, lesions with a luminal narrowing higher than 20% are reported. For each detected lesion, the plaque type (calcified, non calcified or mixed), the stenosis location and the quantitative stenosis grading (Normal, Mild, Moderate, Severe or Occluded) based on the stenosis degree were reported by the observers. Finally, a segment with at least one reported significant stenosis (i.e. with a luminal narrowing higher than 50%) was scored as having a significant coronary artery disease [215].

The CCA reference standards were provided by an observe, who was blinded to CTA annotations, using QCA. Using CCA datasets, each coronary segment of the modified 17-segment AHA classification was identified, assessed and classified as healthy or diseased. The detected stenosis are quantified using the angiographic views and was classified as significant if the luminal narrowing degree exceeded the 50%.

For lumen segmentation reference standards, three independent observers have assessed a set of selected vessel segments using CTA images. For each patient, the set of the selected segments is composed of all segments having a significant stenosis and three others randomly selected segments in each of the main coronary arteries. To manually delineate the coronaries lumen contours, the observers used manually refined vessel centerlines to draw the longitudinal contours on curved MPR views. Using these contours, the final cross sectional contours are extracted and refined.

As a result, for each dataset the QCA and CTA stenosis detection and quantification ground truth as well as the lumen segmentation on the CTA images were extracted. For more details on reference standards extraction please refer to the website of the challenge.

## 1.2.3 Evaluation Measure for Stenosis Detection and Quantification

Evaluation of computer aided diagnostic (CAD) approaches is a crucial step as it allows to assess the robustness of the proposed approach and its usefulness in a clinical context. However this evaluation depends on some parameters such as the quality of the ground truth used to evaluate the results, the evaluation measures end the definitions of what would be considered as a true sdetection and a false detection.

### 1.2.3.1 Definitions

The performance of a CAD system are often quantitatively evaluated based on their accuracy rate (i.e. percentage of significant lesions correctly detected by the CAD). Different measures have been used to assess a system accuracy as the sensitivity, specificity, false positive rate. However, in order to define and compute such measures, terms of true positive (TP), false pos-

## Chapter 1. Previous work and Evaluation framework

itive (FP), true negative (TN) and false negative (FN) detections should be defined. Generally, TP corresponds to the correctly detected positive samples (with abnormalities) and TN indicates the correctly classified negative patterns. FP refers to the erroneously classified negative patterns, and FN to missed positive samples.

There is no unique clear definition of those terms in the literature for coronary arteries lesions detection. Previously published works used different definitions of these measures to evaluate their proposed approaches. Such measurement could be defined based on different precision levels: a per-patient [18, 64, 161, 463, 471], per-vessel [18, 212, 258, 416], per-segment [65, 80, 131, 208] or per-lesion level [199, 419, 505]. Table 1.3 reports the different descriptions proposed in the literature using per-patient, per-vessel and per-segment analysis. We have to notice that the definition of a *lesion* depends on the coronary lesion targeted by the proposed approach. For instance, a lesion could refer to a calcified plaque, a soft plaque, a hybrid plaque (with or without a related stenosis), a stenosis or only a significant stenosis.

**Table 1.3** – Definition of TP, TN, FP and FN measures proposed in the literature for stenosis detection evaluation in CT angiography.

Analysis	Description	
Per patient	TP	A patient with at least one lesion reported in the ground truth and detected by the system
	TN	A patient with no lesion reported neither in the ground truth nor by the system
	FP	A patient with at least one lesion detected by the system but not reported in the ground truth
	FN	A patient with at least one lesion reported in the ground truth but missed by the system
Per vessel	TP	A vessel with at least one lesion reported in the ground truth and detected by the system
	TN	A vessel with no lesion reported neither in the ground truth nor by the system
	FP	A vessel with at least one lesion detected by the system but not reported in the ground truth
	FN	A vessel with at least one lesion reported in the ground truth but missed by the system
Per segment	TP	A segment with at least one lesion reported in the ground truth and detected by the system
	TN	A segment with no lesion reported neither in the ground truth nor by the system
	FP	A segment with at least one lesion detected by the system but not reported in the ground truth
	FN	A segment with at least one lesion reported in the ground truth but missed by the system

This ambiguity and diversity in defining previous measure terms lead to a wide range of evaluation frameworks and an additional variability between the proposed approaches performances. As a result, the comparison of such approaches is not possible. Meanwhile, the definition of previous measures is more complicated for a lesion-based analysis. First, the definition of the different measures depends on type of the target lesion as stated before. However, some ambiguities raises related to a non clear statement about the detection of other non

targeted lesions. For instance, some of the hybrid approaches (that target different types of lesions) are only focusing on the detection of calcified and soft plaques detection and no precise information are provided about the classification of a mixed plaques. Other approaches that focus on the detection of coronary stenosis du to calcified plaques do not state the performance of the approach against soft plaque related stenosis. Moreover, in several works, no details are given on the definition of what would be considered as a true negative (TN). For example, for a lesion-based analysis, a true positive is the truly detected lesion reported by an observer. But, it is more complicated to define what is a true negative. However, this measure is important and crucial for the estimation of the specificity of the detection system.

Patient based analysis are not robust enough to allow an accurate evaluation of an approach performance; A positive scan could be detected even with an erroneous detected lesion. Vessel and segment based analysis are more accurate as they allow to call the attention of the physician to the diseased vessel or segment. A clinically relevant and interesting measure of detected abnormalities would be based on the number of the detected lesions. In fact, this allows to get a precise idea about the accuracy of a classification system and fairly compare it to a clinician performance.

Hereafter, we use a segment and lesion based analysis, provided by the automated evaluation framework, to assess the ability of the proposed approaches to detect and quantify *significant stenosis* ( $> 50\%$  of lumen narrowing) with reference to QCA and CTA reference standards respectively. The use of this framework allows as to fairly compare our works to state-of-art approaches submitted to the challenge. Table 1.4 details the used definitions of the TP, FP, TN and FN measures.

#### 1.2.3.2 Evaluation measures

**1.2.3.2.1 Stenosis Detection** The framework uses two reference standards (*QCA* and *CTA*) to evaluate the ability of an algorithm to discriminate a significant stenosis from a non significant one. For each data, the centers of all detected significant lesions by the algorithm are reported. Vessel portions with a diameter lower than 1.5 mm are discarded from the evaluation.

For each reference standard, two metrics are used to evaluate the performance of the stenosis detection algorithm: *the Sensitivity* rate and *Positive Productive Value* (PPV) rate using equations 1.1 and 1.2 respectively:

$$\text{Sensitivity} = \frac{\text{TP}}{\text{TP} + \text{FN}} \quad (1.1)$$

## Chapter 1. Previous work and Evaluation framework

**Table 1.4** – Segment-based (compared to QCA reference standards) and lesion-based (compared to CTA reference standards) definitions of TP, TN, FP and FN detections for coronary arteries significant stenosis detection using the framework described in [215].

Analysis Reference		Description
Per segment (QCA)	TP	A segment with at least one significant stenosis detected by the system and the reference
	TN	A segment with no significant stenosis reported either by the system or the reference
	FP	A segment with at least one significant stenosis detected by the system while no significant stenosis were reported in the QCA reference
	FN	A segment with at least one significant stenosis reported in the reference but missed by the system
Per lesion (CTA)	TP	A significant stenosis detected by the system and matches a significant reference stenosis.
	TN	A non significant stenosis detected by the system and that does not matches any of the non significant stenosis of the reference or a non significant stenosis reported in the reference but missed by the system
	FP	A significant stenosis detected by the system and matches no significant stenosis in the reference
	FN	A significant stenosis reported in the reference but missed by the system (either reported as a non significant or not detected at all)

$$PPV = \frac{TP}{TP + FP} \quad (1.2)$$

First, segment-based detection rates are examined compared to QCA references. Consequently, a segment is considered as being diseased if it contains at least one severe stenosis. A reported classification result is accepted as being a true positive if it shows at least one lesion in this segment. Second, lesion-based detection rates using CTA references are examined. A reported stenosis is considered to be a true positive if it is also reported by the consensus of the three experts (see table 1.4). The automatically reported stenosis needs thus to be matched to one of the 17-AHA segment, for the segment-based evaluation, and to a reference stenosis for the lesion-based evaluation. The matching steps are presented in figure 1.6. Details on the matching procedure are also available on the challenge website (<http://coronary.bigr.nl/stenoses>). As a result, the algorithm is ranked with reference to each evaluation metric separately (4 ranks) and a final total rank overall the metrics and the patient is provided to allow to compare the different approaches.

**1.2.3.2.2 Stenosis Quantification** For the stenosis quantification evaluation, both CTA and QCA reference standards are used. For each detected stenosis, the percentage of the lumen narrowing detected by the algorithm is reported. The stenosis degree is reported as a value ranging from 0 to 100% with 0 corresponds to a non stenotic region and 100 implies

### 1.1.2 Materials and Evaluation Framework

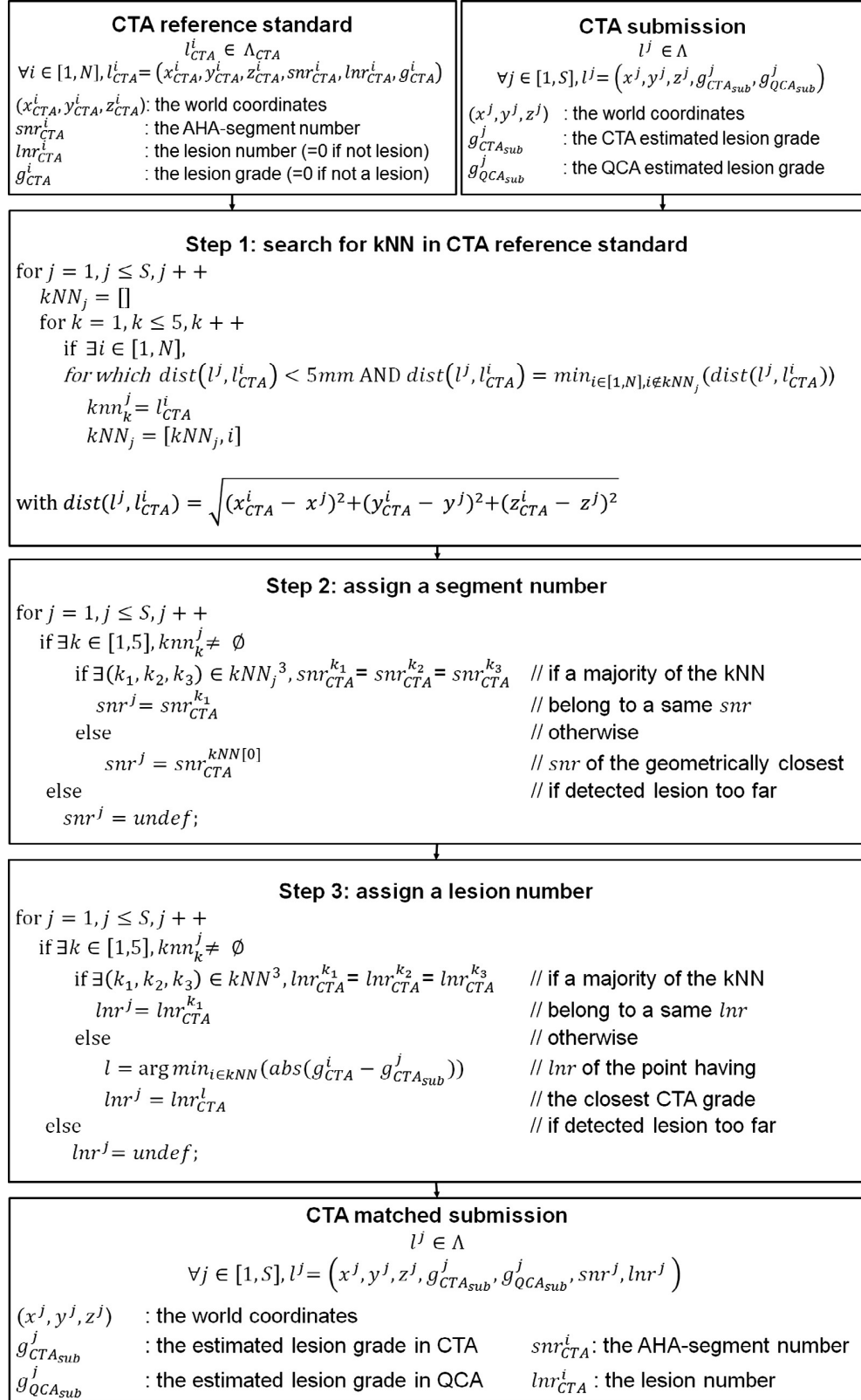


**Figure 1.6** – Matching procedure of the reported stenosis to a segment and lesion number. Illustration from reference [215]

a total occlusion. For the segment-based analysis (i.e. with reference to the QCA ground truth), the lumen diameter reduction of each of the coronaries segments (cf. the modified 17-AHA segments model) corresponds to the maximum lumen narrowing of all his stenosis. The *absolute average difference* (AAD, eq. 1.3) and the *root mean squared difference* (RMSD, eq. 1.4) over the reported lumen diameter stenosis (by the evaluated algorithm) and the true lumen diameter reduction (reported by the observer) are used to evaluate the stenosis quantification with reference to the QCA reference standards for all patients.

$$\text{AAD} = \frac{\sum_{i=1}^S |g_i - g_i^{ref}|}{S} \quad (1.3)$$

$$\text{RMSD} = \sqrt{\frac{\sum (g_i - g_i^{ref})^2}{S}} \quad (1.4)$$

where  $g_i^{ref}$  corresponds to the QCA stenosis reference standard,  $g$  is the stenosis grade reported by the algorithm, and  $S$  the number of considered segments.

For the lesion-based analysis, each stenosis reported by the algorithm is assigned to the corresponding stenosis grade (mild, moderate, severe, occluded). The *weighted Kappa* value [91] is used to evaluate the stenosis performance overall the patients with reference to the CTA standards references. It assesses the difference agreement between the observed lumen narrowing and the one reported by the algorithm.

More details about the computation of the previous metrics are available in the work of Kirişli et al. [215].

---

---

## Chapter 2

---

# A two-stage Automatic Coronary Arteries Stenoses Detection

### Contents

---

<b>1.1</b>	<b>Prior Knowledge and Challenges . . . . .</b>	<b>87</b>
1.1.1	Prior Knowledge: Anatomic and Appearance Priors . . . . .	87
1.1.2	Heart Isolation Challenges . . . . .	88
<b>1.2</b>	<b>Related Work . . . . .</b>	<b>90</b>
<b>1.3</b>	<b>Overview of the Proposed Approach . . . . .</b>	<b>94</b>
1.3.1	Pre-processing Step . . . . .	95
1.3.2	Heart Model Fitting . . . . .	99
1.3.3	Heart Volume Extraction . . . . .	113
<b>1.4</b>	<b>Experiments . . . . .</b>	<b>120</b>
1.4.1	Data . . . . .	120
1.4.2	Manual Segmentation . . . . .	120
1.4.3	Evaluation measures . . . . .	122
<b>1.5</b>	<b>Results . . . . .</b>	<b>125</b>
1.5.1	Computational time . . . . .	125
1.5.2	Parameters Optimization . . . . .	125
1.5.3	Quantitative evaluation results . . . . .	128
1.5.4	Qualitative evaluation results . . . . .	130

---



In this section we present a lumen segmentation based approach for automated stenosis detection in CT angiographies. This work is dedicated to extract all significant stenosis caused by soft, calcified or mixed plaques. Figure 2.1 shows an example of the target lesions. The proposed approach is described in figure 2.2.

In this work we propose a two-step severe cardiac stenoses detection approach. The coronary arteries tree is constructed from a set of automatically extracted vessel centerlines; A lumen segmentation algorithm is applied to extract the lumen volume from the vessel centerlines. To detect severe stenosis, first, we used the geometric model of a stenosis to detect suspicious areas by reconstructing the healthy lumen profile. Secondly, we applied a false positives removal step, based on lesions appearance properties. Hereafter, we will detail the different steps.

### 2.1 Artery Coronaries Tree Construction

To construct the coronary artery tree, we need a set of coronary centerlines as input. Several techniques for automatic vessel centerline tracing in the literature could be used for this purpose (see section 2.4.1.2). For this work, we used the automatically extracted centerlines, provided by the Rcadia Team, as input to our algorithm. A hessian based filter and a tracking approach is utilized to extract the coronary arteries centerlines. Details of the extraction scheme are provided in [30, 161]. The centerlines are provided for each branch separately. Therefore, we need to process the set of centerlines in order to construct a connected coronary tree. First, the right and left sub-trees of the coronaries are defined from the input centerlines. The right and left ostia are hence computed from the starting points of the different sub-trees; the two ostia are defined as the barycenter of left and right sub-trees starting points respectively. Since the centerlines are provided per vessel branches (they start at the coronaries ostia and ends at different leaf points), they result in multiple overlapping parts. Thus, the input centerlines are processed and divided in a set of disjoint smaller segments. For this reason, we traverse the different centerlines in order to detect all the bifurcation points. Starting from leaf points (ending points), an intersection is detected if two centerlines points are separated by a distance lower than a threshold  $T_{bif}$  (we set  $T_{bif}$  to 1 voxel).

Figure 2.3 shows an example of merging three different branch centerlines. Starting from the first vessel (V1), we identify the first vessel it intersects (V2). Then we check if V2 intersects an other vessel before intersecting V1 (in this case V3). We repeat the same process on V3. Here

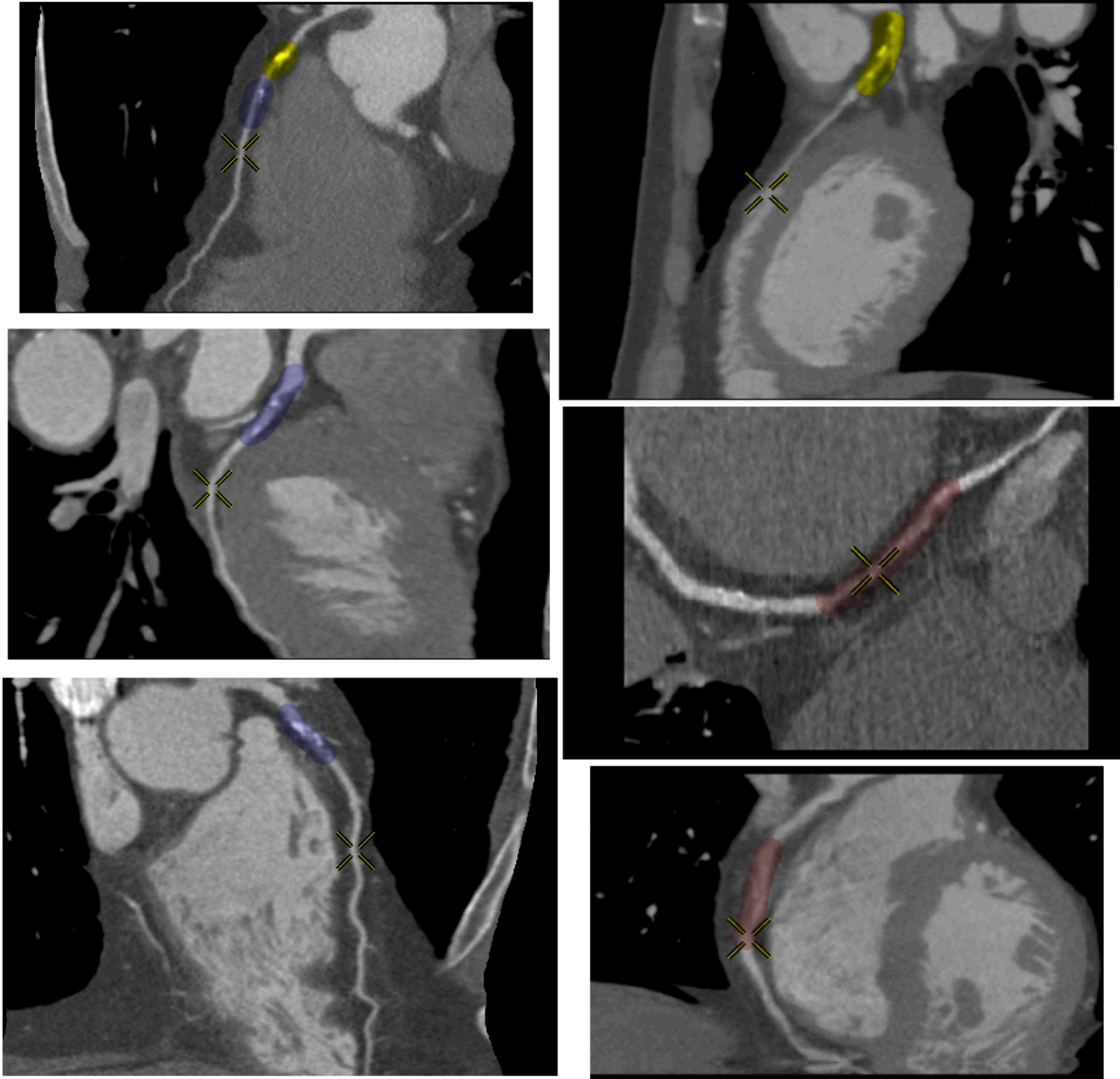


**Figure 2.1** – Examples of different target lesions to be detected in the challenge database. Calcified plaques are highlighted in yellow, soft plaques in red and mixed plaques in blue.

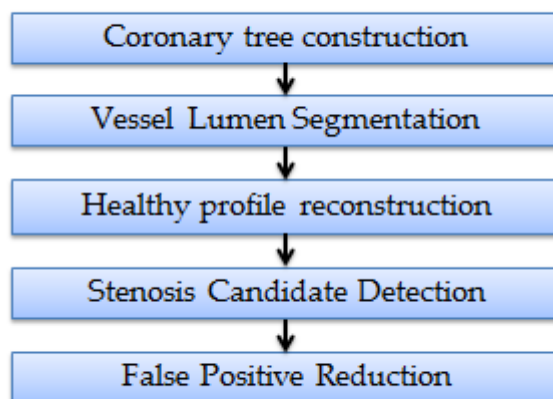


**Figure 2.2** – Overview of the lumen based stenosis detection approach

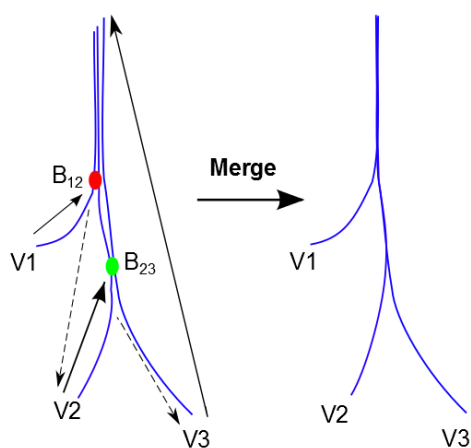


**Figure 2.3** – Example of merging 3 different branches with overlapping segments.

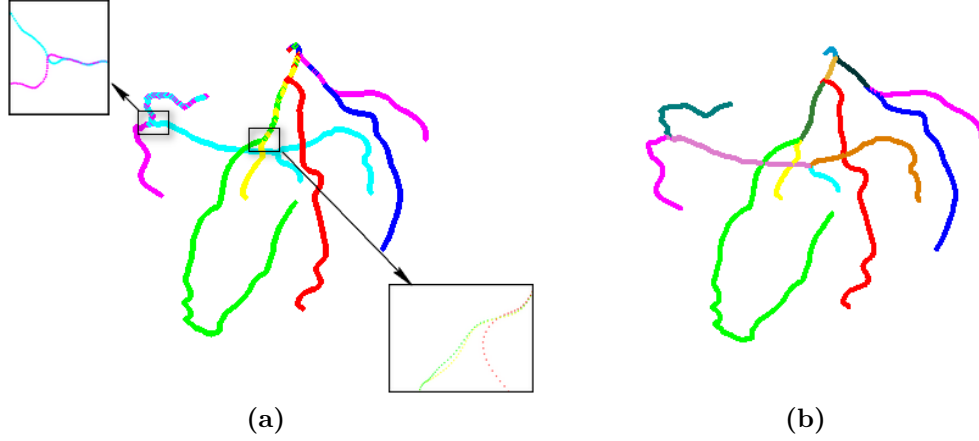


**Figure 2.4** – Coronary artery tree merging. (a) The original coronaries centerlines presenting overlapping segments with multiple centerline points (each branch is illustrated using a different color). (b) Resulting coronary arteries tree organized in a set of disjoint segments (each segment is represented by a different color).

we see that V3 does not intersect any other vessel, so we start by merging the two vessels V2 and V3 by setting the common segment of the two vessels (above  $B_{23}$ ) to the mean of the two vessels centerlines. Then we merge this resulting segment with V1. Furthermore, we apply a hamming filter, with a window size of  $w = 5$ , to smooth the centerlines and avoid discontinuity around junctions.

Figure 2.4 shows the constructed coronaries tree for dataset 09. Thus, the final coronaries tree is organized in a set of disjoint segments. The whole tree analysis is performed by segment traversing starting from each leaf and stopping if a bifurcation with a longer branch is reached. Once the vessel tree is constructed, we define a local geometry for each point on the vessel centerline. First, the tangent at a point is computed as the direction defined by its neighboring points (on the centerline). A hamming filter is used to smooth the centerline tangents and avoid discontinuities around bifurcation points. Then, cross sectional planes are defined using the vessel centerline tangents by getting the plane normal to the vessel tangent at each point and computing two vectors perpendicular to the tangent of the vessel. As a result, for each point of the vessel centerline we define a geometry matrix containing the tangent ( $R_3$ ) and the cross section vectors ( $R_1$  and  $R_2$ ) as shown in figure 2.5.

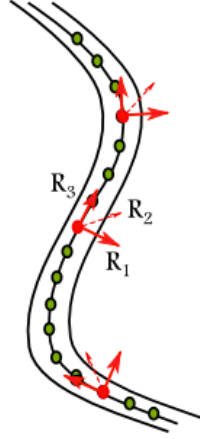


**Figure 2.5** – Geometry definition for each centerline points.  $R_1$  and  $R_2$  are used to define the cross section planes.

## 2.2 Vessel Lumen Contours Extraction and Diameter Quantification

Based on the prior anatomical knowledge stating that a stenosis corresponds to lumen diameter reduction, investigating the inner vessel wall diameter variation would be relevant to detect and identify stenotic regions. To extract vessel lumen volume and quantify the 2D cross sections we used the method previously described in section 2.3.1. This approach employs a watershed based process initiated by the coronary arteries centerlines to extract the vessel lumen volume. Then, using the binary segmented lumen volume, the 2D lumen borders are extracted at different locations along the vessel by computing subvoxelic contours. Once the vessel lumen contours extraction is processed, the section area is measured and used for stenosis detection and quantification.

For stenosis detection, we choose to use the cross sectional area as it is more robust against vessel stenosis topology variations. In fact, coronary atherosclerosis plaques being often eccentric and non symmetric, the associated vessel lumen cross section would not be necessarily circular. As a result, lumen diameter (min or mean values) could not be considered as an accurate indicator of the stenosis degree as it could result in an erroneous estimation of the lumen narrowing. Meanwhile, the use of lumen cross section area provides more information about the stenosis severity as it is in correlation with the blood rate flowing through this cross section.

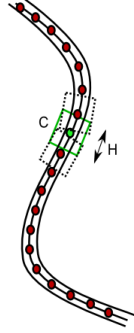


**Figure 2.6** – Vessel area quantification: for each center point the correspondent section area is set to the median value of all the section area inside the box of height  $H$ .

To improve robustness against erroneous section quantification, we apply a local median filter on the vessel lumen section area profile. We use a 3D box of height  $H$  (typically 11 voxels), centered at the centerline point to be quantified, and we set the active vessel section area to the median of area values of all the sections included inside the box (figure 2.6):

$$\text{Area}_i = \text{median}\{\text{Area}_j; i - \frac{H}{2} \leq j \leq i + \frac{H}{2}\} \quad (2.1)$$

## 2.3 Stenosis Detection

To detect coronary stenosis, we propose a two stage approach combining geometric and intensity features analysis. Therefore, based on the area profile of the estimated lumen cross sections, we reconstruct a *synthetic* area profile to be used as a “healthy lumen” reference. To be robust against abrupt changes in lumen cross section area after each bifurcation, the profile reconstruction is performed for each segment separately. The lumen profile reconstruction is performed by applying a robust regression on the segment area profile. The extracted (real) profile is first analyzed to remove the outliers corresponding to erroneous vessel cross section quantification. Centerline points having a lumen cross section area higher than a defined threshold  $T_a$  are considered to be outliers and are removed from the set of points on which the regression step is performed. To set the threshold value  $T_a$ , we compute the median value  $m_{area}$  of all the lumen section areas along the whole vessel. The threshold value is set to:

$$T_a = m_{area} + 1.5 * \sigma_{area} \quad (2.2)$$

$\sigma_{area}$  is the standard deviation value of the lumen cross section areas. Once the outliers are

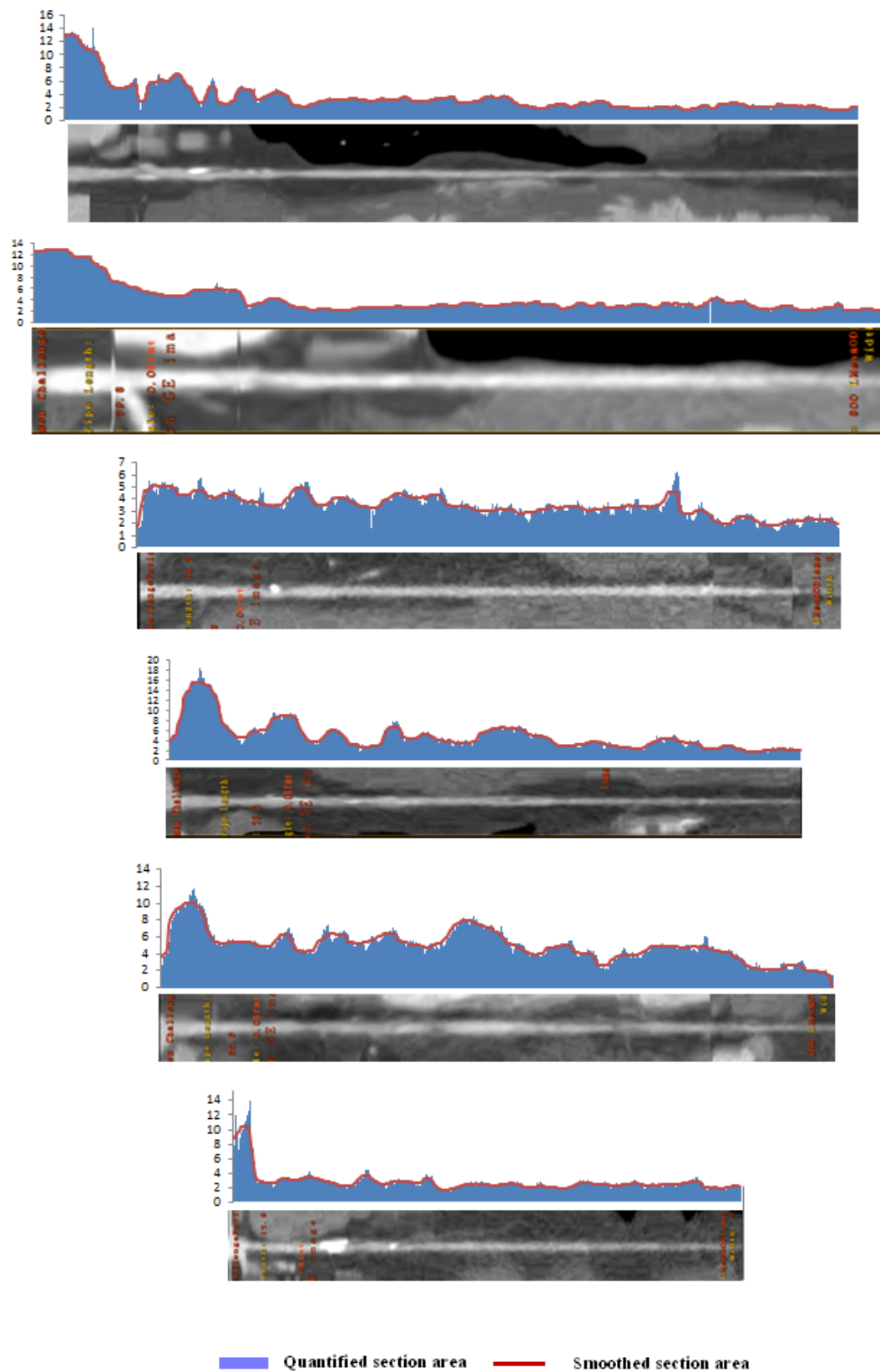


**Figure 2.7** – Examples of vessel lumen quantification showing the real (in blue) and the smoothed (in red) vessel lumen cross sections area profiles.

detected and removed, we apply a linear regression on the cleaned profile. Let  $x_i$  be a centerline point index on a vessel segment and  $y_i$  the observed real lumen cross section area for this point. We assume that, for each vessel segment,

$$\mathbf{Y} = \mathbf{X}\beta + \epsilon \quad (2.3)$$

with,

$$\mathbf{Y} = \begin{pmatrix} y_1 \\ y_2 \\ \vdots \\ y_n \end{pmatrix}; \quad \mathbf{X} = \begin{pmatrix} 1 & x_1 \\ 1 & x_2 \\ 1 & \vdots \\ 1 & x_n \end{pmatrix}; \quad \beta = \begin{pmatrix} \beta_1 \\ \beta_2 \end{pmatrix} \quad and \quad \epsilon = \begin{pmatrix} \epsilon_1 \\ \epsilon_2 \\ \vdots \\ \epsilon_n \end{pmatrix}$$

The goal is to find the straight line,

$$\mathbf{L} = \mathbf{X}\beta \quad (2.4)$$

that fits the best the previous set of points by minimizing the sum of least squares errors. Figure 2.8 shows the reconstructed healthy lumen profile  $a_{healthy}$  for a vessel with calcified, mixed and soft plaques.

Afterward, we compute the stenosis degree (grade) for each center point by comparing the real section area to the synthetic/healthy value (figure 2.9).

$$S_{Grade} = 100\% \times \left(1 - \frac{a_{real}}{a_{healthy}}\right) \quad (2.5)$$

Only points having a stenosis grade higher than a given threshold  $S_{degree}$  are flagged. The value of this threshold depends on the severity of the stenosis we want to rule out. For this work, we extract all points presenting a stenosis degree higher than  $S_{degree} = 50\%$  of the expected value (i.e. significant stenosis). We set this value to 40% and not 50% (the fixed value for sever stenosis as stated by the challenge organizers) to allow a margin error that could occur due to an overestimation of the vessel lumen. Once we have computed this first set of stenotic area, we propagate the flagged points to extract the whole lesion area by detecting the start



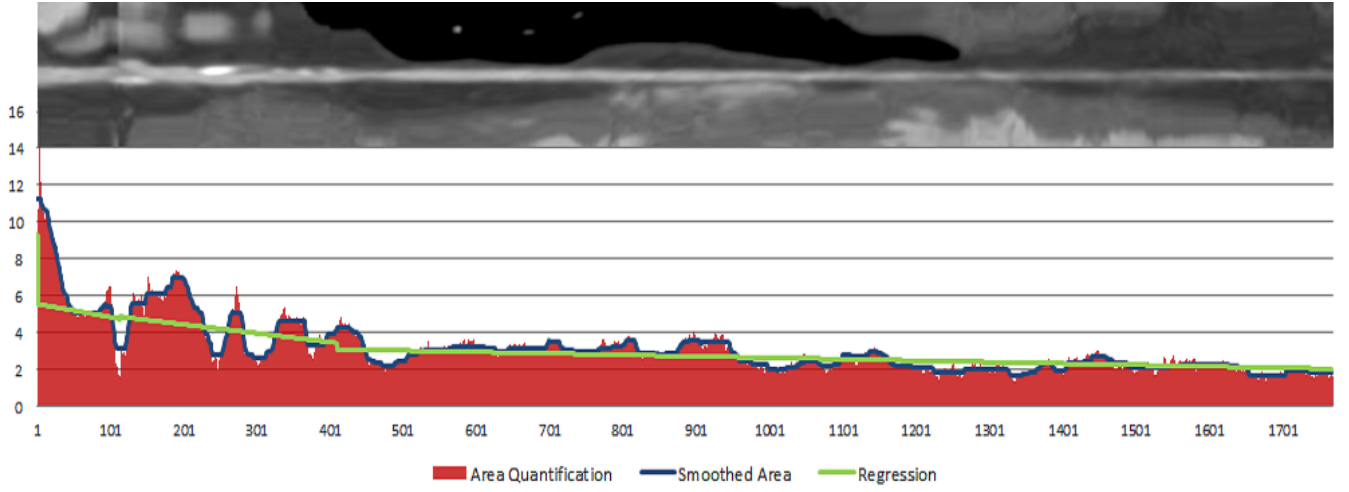


**Figure 2.8** – Vessel area profile reconstruction: Original and smoothed vessel area profile per 2D section (in red and blue respectively). The vessel theoretic profile is constructed using a robust linear regression (in green).

and end point of the lesions. Those extremity points are detected if the real value crosses the expected value. The center of the stenosis is set to the center of the section with the smallest area (i.e. the higher stenosis degree). An example of flagged stenotic regions is shown in figure 2.9. At the end of this first step we have computed a set of stenosis candidates, however likely to contain false positives. Thus, we propose to use of additional information about the lesion appearances to filter the erroneous positive detections (i.e. false positives) from this set.

In addition to the analysis of the vessel section area, we propose to use additional vessel statistics in order to improve the accuracy of lesion detection. Indeed, atheromatous lesion plaques are characterized by their appearance in CT angiography as detailed in section 1.1.1. Hence, we define a cylindrical ROI centered at each centerline point to analyze the vessel neighboring in order to detect present plaques. To allow the ROI to cover the whole vessel wall and hence to include the vessel lesions, the size of this cylinder is defined based on the local size of the vessel section. The ROI width is hence set to the local width of the vessel cross section dilated by 3 voxels to include the vessel wall. The height of the ROI is fixed to 11 voxels. To capture the intensity variation around each points on the vessel centerline, we compute the difference between the maximum (**max**) and minimum (**min**) grey level values inside the corresponding ROI. Besides, this variation is weighted with reference to the distance of each point from the root of the corresponding vessel branch. This allows to avoid considering irrelevant high variations at vessel distal parts where the signal to noise ratio became relatively high. Finally, among all the lesion candidates detected at step 1, we keep only the candidates

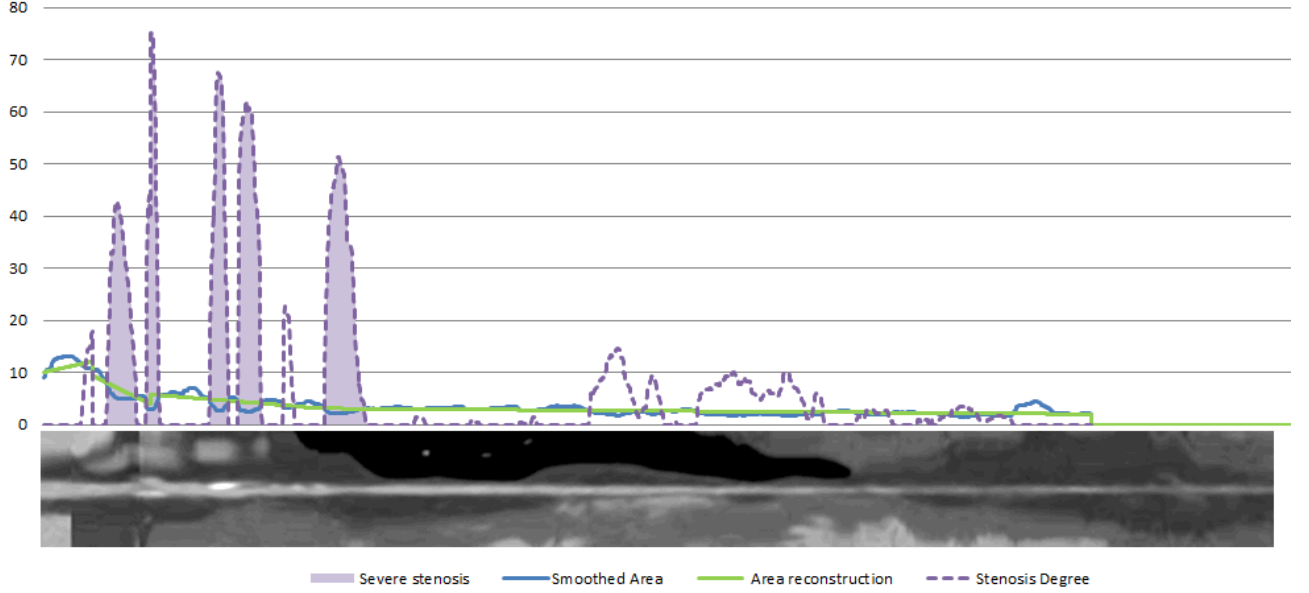


**Figure 2.9** – Stenoses detection and quantification using the healthy reconstructed vessel lumen cross section area profile. Several stenosis are detected but only five of them are flagged as severe stenosis.

verifying the following condition:

$$w_i * (\mathbf{max} - \mathbf{min}) > \alpha * \sigma_{dev} \quad (2.6)$$

where  $\sigma_{dev}$  corresponds to the standard deviation of the gray value along the whole vessel branch and  $w_i$  is the corresponding weight of position  $i$  on the vessel centerline.  $\alpha$  is set empirically to 2.5. Figure 2.10 illustrates some examples of intensity variations along vessels with different lesion types. We can notice that the different plaque types regions exhibit relatively high variation values compared to healthy segments.

For each detected stenosis in the final set at the end of step 2, the proximal and distal extremities as well as the lesion extent are marked on the lumen and curved views. The detected lesions are also highlighted on the 3D rendering view of the coronary arteries tree allowing the user to get a quick overview on the different coronaries condition (figure 2.11).

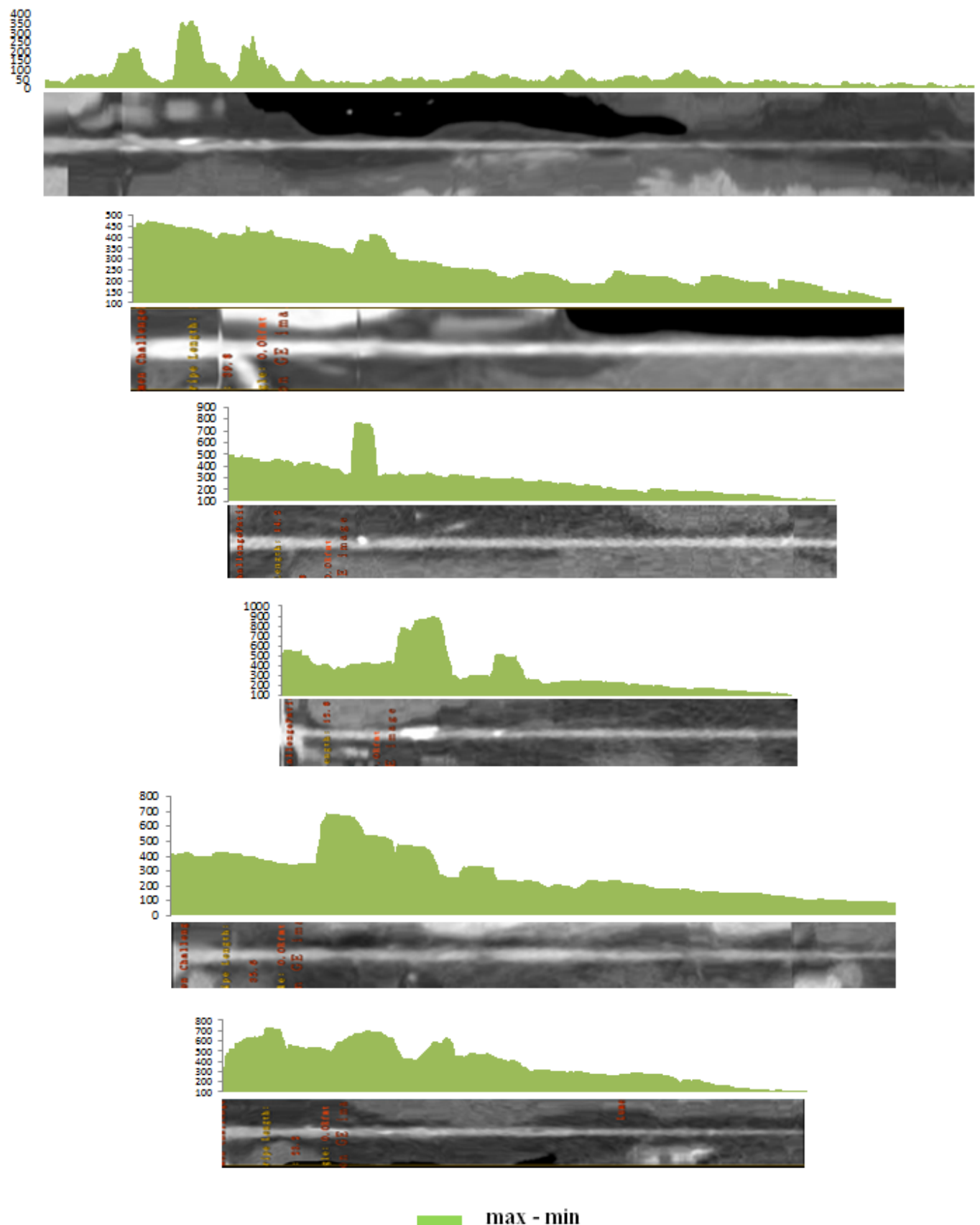


**Figure 2.10** – Examples of computed intensity variations along some diseased branches.

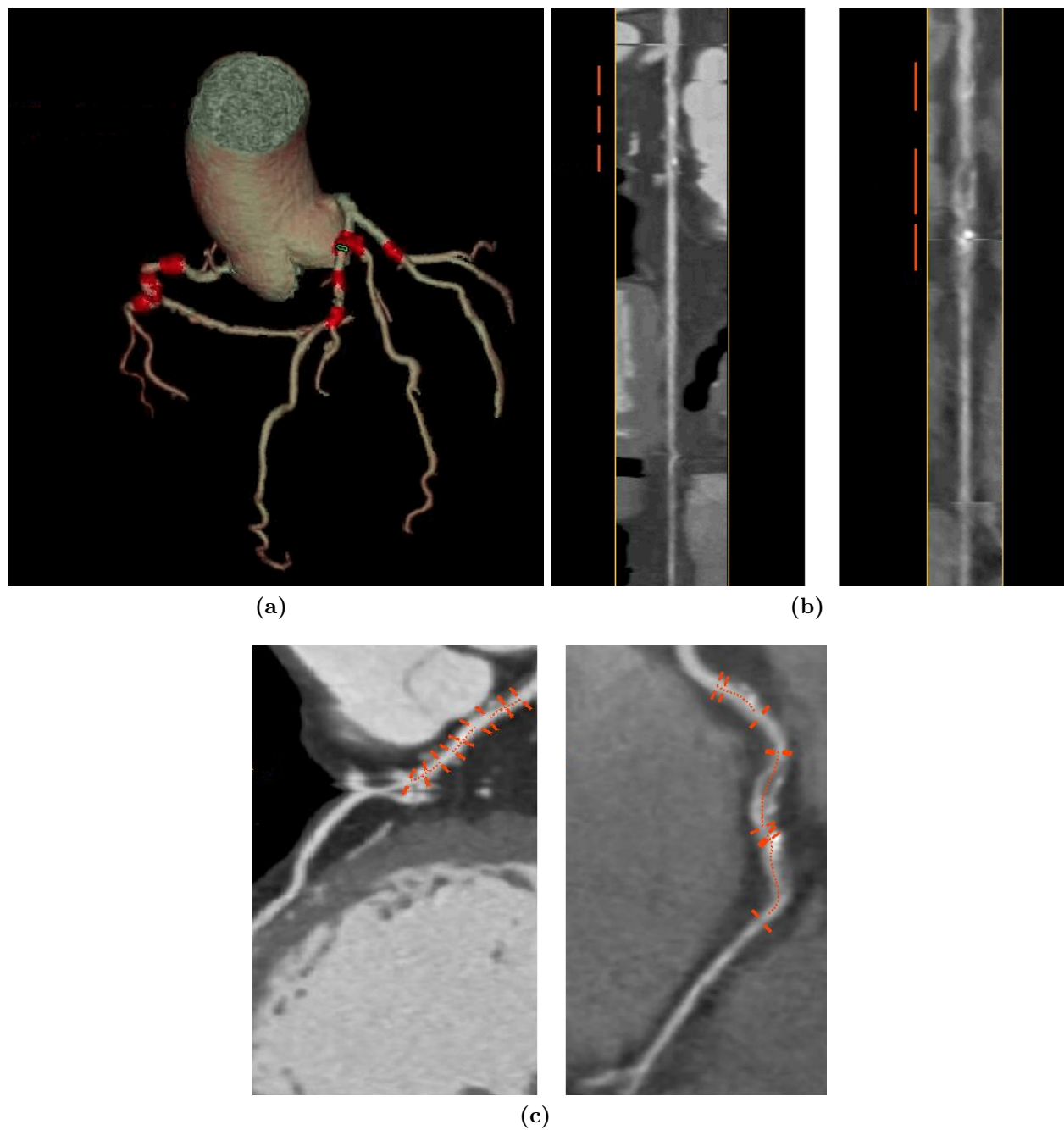


**Figure 2.11** — Stenosis detection for dataset 09: (a) 3D rendering of the coronary tree with detected stenosis highlighted in red. (b) Lumen views of the left anterior descending artery and the right artery coronary (c) Curved view of the left anterior artery and the right. Detected stenotic areas are marked in between two red segments.

## 2.4 Evaluation for MICCAI 2012 coronary artery stenosis detection challenge

We have tested our algorithm on the 48 multi-vendor CTA datasets of typical patients provided by the MICCAI Stenosis detection/quantification and lumen segmentation challenge. As explained in section 1.2, the database is composed of 18 training datasets, with QCA and CTA reference standards, and 30 other testing datasets. The mean overall processing time of our method is 1 minute, including the lesion detection process that takes 10 seconds on a 4-core Intel(R) Xeon(R) CPU 5160 at 3.00GHz computer, with 4.00 GB (RAM).

The stenosis detection results are evaluated compared to the CTA and QCA references separately. The metrics considered are the sensitivity, which assesses the proportion of actual severe stenoses which are correctly identified, and the PPV, corresponding to the proportion of positive detection that are true positives (see section 1.2.3). Tables 2.1 and 2.2 shows the obtained results on the training and the testing database separately. The overall results are depicted in table 2.3.

**Table 2.1** – Performance of the proposed approach for severe stenosis detection on the training database. Results are compared to the three observers and their consensus. Evaluation is performed by segment (compared to QCA) and lesion analysis (compared to CTA).

	QCA		CTA	
	Sens. (%)	P.P.V. (%)	Sens. (%)	P.P.V. (%)
CTA Consensus	64.0	64.0	100.0	100.0
Observer1	72.0	48.6	92.6	56.8
Observer2	76.0	65.5	81.5	73.3
Observer3	52.0	68.4	63.0	73.9
Our approach	60.0	19.5	48.1	8.3

Table 2.4 shows the evaluation results for the training datasets after each step of the stenoses detection algorithm. For the first step, we obtained a sensitivity of 68% as compared to QCA references and 44.4% as compared to CTA. However the obtained PPV for the QCA and CTA based evaluation was of 11.6% and 5.0% respectively. These scores are related to the high amount of FPs reported by our section area analysis (i.e. first step). With the two steps detection approach, we were able to reduce the amount of FPs from 130 to 62 as compared to QCA and from 228 to 143 as compared to CTA. This allows to improve the PPV rates for both of CTA and QCA (8.3% compared to CTA and 19.5% w.r.t QCA). Besides, the sensitivity per lesion analysis increased to 48.1% while the sensitivity per segment decreases to 60.0%. The

## 2.2.4 Evaluation for MICCAI 2012 coronary artery stenosis detection challenge

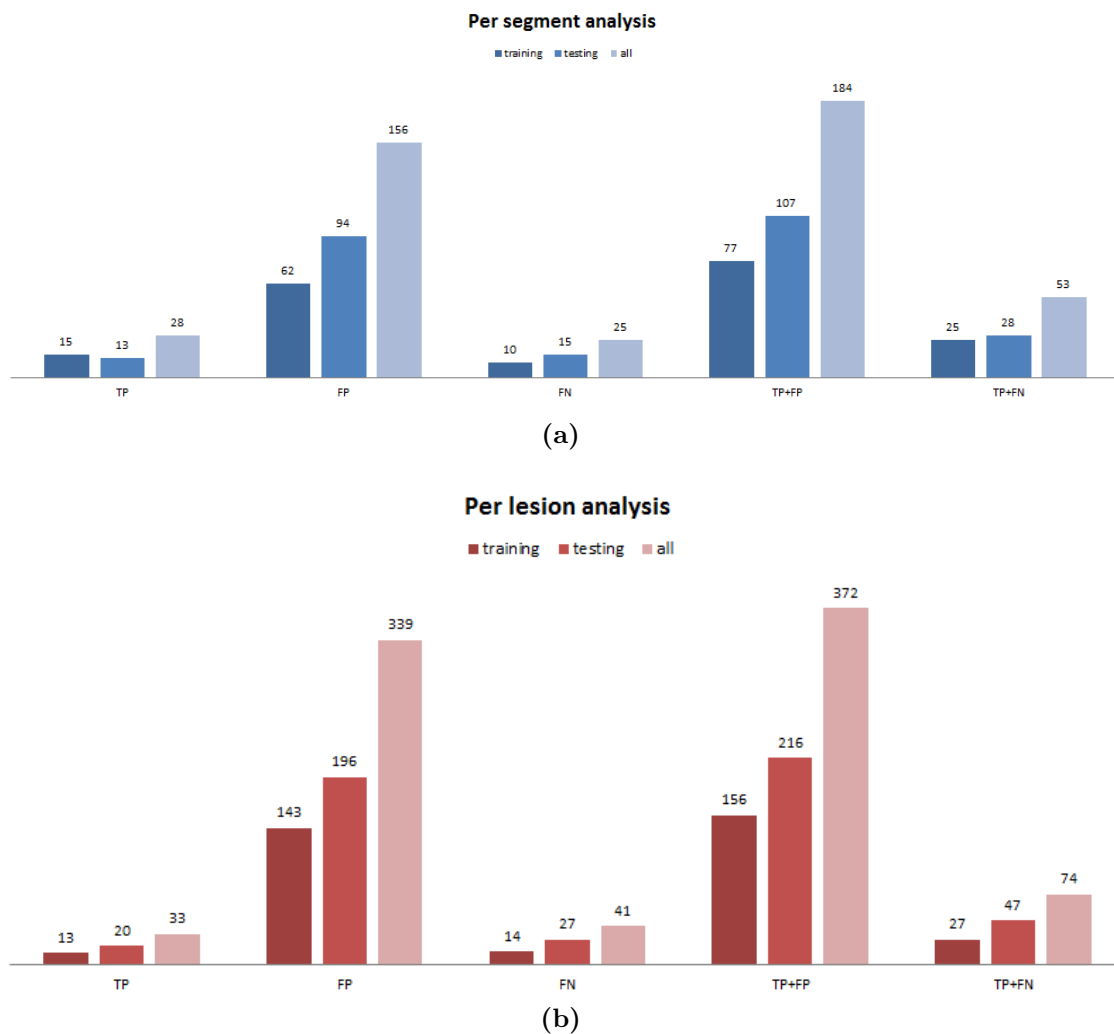


**Figure 2.12** – Coronary arteries severe stenosis detection performance: True positive (TP), false positive (FP), false negative (FN) and true negative (TN) rates with reference to the QCA (a) (segment-based analysis) and CTA (b) (segment-based analysis) reference standards. Values are illustrated for the training and the testing databases as well as for the whole database.

## Chapter 2. A two-stage Automatic Coronary Arteries Stenoses Detection

**Table 2.2** – Performance of the proposed approach for severe stenosis detection on the testing database. Results are compared to the three observers and their consensus. Evaluation is performed by segment (compared to QCA) and lesion analysis (compared to CTA).

	QCA		CTA	
	Sens. (%)	P.P.V. (%)	Sens. (%)	P.P.V. (%)
CTA Consensus	82.1	52.3	100.0	100.0
Observer1	85.7	40.0	83.0	60.9
Observer2	75.0	51.2	70.2	80.5
Observer3	64.3	42.9	66.0	59.6
Our approach	46.4	12.1	42.6	9.3

**Table 2.3** – Performance of the proposed approach for severe stenosis detection on the 48 datasets. Results are compared to the three observers and their consensus. Evaluation is performed by segment (compared to QCA) and lesion analysis (compared to CTA).

	QCA		CTA	
	Sens. (%)	P.P.V. (%)	Sens. (%)	P.P.V. (%)
CTA Consensus	73.6	56.5	100.0	100.0
Observer1	79.2	43.3	86.5	59.3
Observer2	75.5	57.1	74.3	77.5
Observer3	58.5	50.8	64.9	64.0
Our approach	52.8	15.2	44.6	8.9

**Table 2.4** – Evaluation of the first and second steps results on the training datasets. The first step corresponds to the stenosis candidates extraction using only the lumen area reduction. The second step corresponds to the false positive removal step using appearance properties.

	QCA (per segment)				CTA (per lesion)			
	TP	FP	Sens (%)	PPV (%)	TP	FP	Sens (%)	PPV (%)
First Step	17	130	68.0	11.6	12	228	44.4	5.0
Second step	15	62	60.0	19.5	13	143	48.1	8.3

#### 2.2.4 Evaluation for MICCAI 2012 coronary artery stenosis detection challenge

---

later value change is due to the fact that two segments were detected as true positives because a FP lesion was reported inside them.

The obtained results on the testing database showed a sensitivity of 46.4% compared to QCA references and 42.6% compared to CTA. These moderate scores are mainly related to an erroneous vessel section area quantification step. In fact, we have noticed that the contours were erroneous for some lesions which lead to miss-classifying the related stenosis. Erroneous vessel quantification could be explained by some anomalies in the vessels centerline that were not perfectly centered inside the vessel lumen and biased by some of the vessel lesions, which biases the watershed final result. A more robust contour extraction approach should improve the detection accuracy. Similarly, this approach provides low PPV values of 12.1% and 9.3% on the testing database, per segment and per lesion respectively. This is explained by the number of FPs that are still remaining after the second step. Besides the erroneous detections related to the lumen quantification and/or the centerlines quality, the FPs amount is also related to the way the TPs/TNs are classified. To evaluate the results, the software sets as FP any lesion we detect with the proposed algorithm that have a reference degree lower than 50%. However setting such hard threshold is not robust due to the inter-observer variability and the limited resolution of CT angiography that does not allow to differentiate between 40, 50 and 60% stenosis. In fact, by removing the threshold of 50% for TP/FN classification and considering all stenosis degrees reported in the reference standard, the amount of the FPs per lesion moves from 143 to 96 per lesion and from 62 to 48 per segment on the training dataset. This work has been published during the “3D Cardiovascular Imaging: a MICCAI segmentation challenge” workshop organized in conjunction with the 15th International Conference on Medical Image Computing and Computer Assisted Intervention (MICCAI) [291]. The propose approach ranked third among 11 algorithms during the on-site evaluation.





---

---

## Chapter 3

---

# Learning-based Detection of Severe Coronary Stenoses

### Contents

---

<b>2.1</b>	<b>Coronary arteries segmentation: A brief Review . . . . .</b>	<b>136</b>
2.1.1	Direct segmentation approaches . . . . .	136
2.1.2	Centerline-based segmentation approaches . . . . .	139
<b>2.2</b>	<b>A Coronary Enhancement Filter using the Shape Tree and Path Openings . . . . .</b>	<b>144</b>
2.2.1	Preliminaries . . . . .	144
2.2.2	The enhancement filter . . . . .	155
2.2.3	Preliminary Results and Discussion . . . . .	163
<b>2.3</b>	<b>Statistic-based Vessel Lumen Segmentation . . . . .</b>	<b>164</b>
2.3.1	State of the art coronary arteries segmentation and lumen extraction .	165
2.3.2	Vessel lumen mask extraction using adaptive statistics . . . . .	167
2.3.3	Vessel Segmentation and evaluation results . . . . .	173
2.3.4	Conclusions and future work . . . . .	179

---

Machine learning techniques have been extensively used for aided medical diagnostic. However, fewer works have tried to solve the problem of coronary arteries lesions detection using machine learning approaches, comparing to heuristic based ones. Besides, as stated in section 1.1.3, most of the approaches that tried to employ machine learning for vascular lesion detection have focused on one single lesion type detection. The popularity and the proven good

performance of such approaches in several medical domains, have motivated the investigation of their ability to detect coronary arteries plaques (with different nature) in CT angiography. Nevertheless, the first motivation to this work is to prove that learning based approaches are able to overcome the limitation of rule-based techniques for detecting all coronary pathologies types (using one single approach). In fact, the heterogeneity of such lesions makes difficult the modeling and the detection of all plaque types by applying simple heuristic-based approaches. Moreover, explicit approaches usually detect stenosis based on lumen (and vessel outer wall) segmentation, which makes the robustness of the detection approach tightly conditioned by the segmentation step accuracy. Machine learning approaches are a promising alternative for such techniques.

In this section, we propose a fully automated learning-based method for coronary artery stenosis detection and quantification. The approach utilizes the [Random Forest \(RF\)](#) classifier to detect severe stenosis based on lesion-specific features. It can be divided into three main steps: (1) Features extraction, (2) Classifier training and (3) Stenosis detection and Quantification. The algorithm needs the artery coronaries centerlines as input. We used the same centerlines set as described in [section 2.1](#). As mentioned previously, these branches centerlines are processed by applying a merging algorithm to create the left and right coronaries trees. Thus, the final coronaries tree is organized in a set of disjoint segments corresponding to the 17-AHA-segments model. The analysis of the whole tree is then performed by segment traversing starting from each leaf and stopping if a bifurcation with a longer branch is reached.

Before explaining the different steps of this work, we first propose to have an overview of machine learning approaches principles and basic ideas.

### 3.1 Machine Learning Approaches in Medical Context

Machine learning is a scientific discipline that constitutes a sub-field of computer science and statistics, integrating different approaches such as artificial intelligence, combinatorial optimization and probability theory. It deals with the design of systems able to automatically learn from specific data (called *training data*) and experience, making them able to recognize complex patterns and make intelligent decisions. Learning based classification systems are employed in a wide variety of practical problems where explicit rule-based algorithms performance seems to be unsatisfactory. Fields of applications include computer vision, search engines, bio-informatics and medical diagnosis. For a review of popular machine learning methods and their applications, one could refer to the works of [Dutton and Conroy \[130\]](#) and [Kubat et al. \[233\]](#).

### 3.3.1 Machine Learning Approaches in Medical Context

---

Depending on the input data type and the desired outcome of the learning algorithm, machine learning techniques can model a problem differently. This defines different learning styles that could be used to categorize machine learning algorithms. We mainly identify three categories:

- **Supervised learning:** For this category, learning algorithms are trained using labeled examples for which the desired outputs are known. The task of the machine learning algorithm is to find a relationship between the input data and the associated known output values that will be used to predict new outputs from unlabeled data. Hence, the training database is composed of a set of pairs  $(\mathbf{x}_i, y_i)$  where  $\mathbf{x}_i$  is an input object and  $y_i = f(\mathbf{x}_i)$  the corresponding desired (i.e. known) output value. By analyzing the training data, the supervised learning algorithm tries to estimate the function  $f$  that maps each input object to a coherent output. This inferred function will be used to map and classify new *unseen* instances correctly. The algorithm should be able to generalize from the labeled data to the unseen data in the best way (e.g. classification and regression problems). This type of approaches needs the training data set to be sufficiently large. Support vector machines (SVMs) [94], and Decision Trees [360] are some examples of supervised learning algorithms.
- **Unsupervised learning:** Contrary to supervised learning algorithms, unsupervised learning approaches operate on unlabeled training data (i.e. without any information on the output result). The aim of such approaches is to extract a model by determining the hidden structures present in the input data (e.g. clustering model). Example algorithms include Hidden Markov Models [27] and K-means clustering [145].
- **Semi-supervised learning:** The input data are a mixture of a small amount of labeled data (representing one class) and a larger set of unlabeled examples. It falls between the two previous learning categories: As for the supervised learning, the data represents a desired prediction problem, but the algorithm should subsequently learn the data structure to organize the different samples. It has been found that combining such labeled and unlabeled data can improve the learning accuracy. Moreover, this allows to reduce the cost associated with the labeling process and use easily available unlabeled data. Examples are Self training and Graph-based algorithms [83].

Others learning categories include Deep learning [382] and Reinforcement Learning [204].

In the last decades, machine learning algorithms have been intensively applied on medical imaging datas ets. In fact, medical image processing community is more and more interested

by investigating the usability of machine learning in medical context which led, for instance, to the introduction of several workshops on this subject<sup>1 2</sup>. It is used to help solving prognostic problems such as prediction of a disease progression, therapy planning and support, and patient management. Moreover, machine learning has been utilized for diagnostic purpose to analyze medical data in order to detect abnormalities and alarm the medical expert. Hence resulting in a better clinical monitoring, an improved quality of medical care and enable diagnosis in real time. Below, we summaries the most successfully used algorithms for computer aided diagnosis: The Supported Vector Machines (SVMs), The Boosting algorithms and the Random Forest classifier (RF).

### 3.1.1 Supported Vector Machines

SVM is one of the most widely used forms of an ensemble learning method [44, 94, 433]. They are supervised learning models used for classification and regression analysis. Given a training set of examples belonging to two different classes, an SVM algorithm outputs a model that allows to assign a new unlabeled sample to one of the two classes which makes it a discriminative (binary) classifier. The output model is defined by a *hyperplane* (or a set of hyperplanes in a high- or infinite-dimensional space) that separates the two categories, in a representative space, thus forming the wider possible gap between the two training classes points. The estimated hyperplane gives the largest minimum distance, named *margin*, to the training examples thus ensuring a low generalization error of the classifier. To classify a new example, first the sample is mapped into the same space as learning data and then assigned to the corresponding category depending on which side of the hyperplane it falls on.

Let's suppose that the two classes to be discriminated are linearly separable in a given higher-dimensional space. A 2D simplified representation of the classification problem is illustrated in figure a. Several lines could be used to separate the two categories but there exists only one line that allows to separate the training data into two distinct classes while minimizing the classification errors. The algorithm should find the hyperplane that maximizes the minimum margin as illustrated in figure c. If we formally define a hyperplane by the following expression:

$$f(\mathbf{x}) = \beta_0 + \beta^T \mathbf{x} \quad (3.1)$$

---

<sup>1</sup>The international workshop on Machine Learning in Medical Imaging, MICCAI conference <http://mlmi2014.web.unc.edu/>

<sup>2</sup>Machine Learning for Clinical Data Analysis, The International Conference on Machine Learning conference <http://icml.cc/2012/workshops/>.

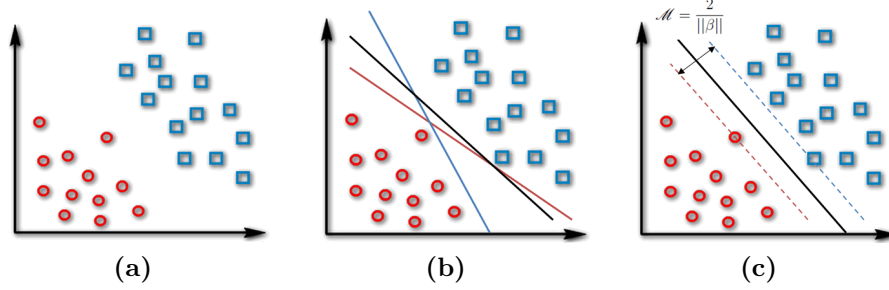


**Figure 3.1** – Supported vector machines classifier: (a) A 2D example of linearly separable data. (b) The two classes could be separated using multiple lines. But being too close to some training data such lines are more sensitive to noise and will not generalize correctly. (c) The better hyperplane separating the two training subsets is the one maximizing the margin distance as it will be able to better classify new samples that are close to the current decision boundary.

the margin  $\mathcal{M}$ , equal to twice the distance to the closest examples, is expressed by:

$$\mathcal{M} = \frac{2}{\|\beta\|} \quad (3.2)$$

Hence, maximizing  $\mathcal{M}$  is equivalent to minimizing the constrained function  $L(\beta)$ :

$$\min_{\beta, \beta_0} L(\beta) = \frac{1}{2} \|\beta\|^2 \text{ subject to } y_i(\beta^T \mathbf{x}_i + \beta_0) \geq 1 \quad \forall i, \quad (3.3)$$

where  $y_i$  represents the label of the training example  $\mathbf{x}_i$ . The constraint expresses the requirement that the hyperplane should classify correctly the training data. To obtain the weight vector  $\beta$  and the bias  $\beta_0$  defining to the optimal hyperplane, the previous Lagrangian optimization could be solved using Lagrange multipliers.

Supported vector machines were also extended for non linear classification in [44]. Other extensions have been proposed to use the SVMs approaches for multi-class classification by reducing the single multi-class problem into multiple binary classification problems [127]. SVMs were used in medical context for several practical applications [159, 209, 348] including coronary lesions detection [65, 236, 505, 507].

### 3.1.2 Boosting Algorithms

Boosting algorithms are an ensemble of supervised machine learning methods relying on the principle of generating a majority voting prediction from a set of individual classifiers [287]. Most boosting algorithms consists of combining weak classifiers, giving at least a slightly better

accuracy than a random classification, to finally obtain a strong classifier. For that, a weighted training set is used for the learning stage; A positive weight  $w_i$  is assigned for each training data example  $\mathbf{x}_i$ . Initially all the weights are set to 1 and a first learning is performed yielding to a first hypothesis  $h_1$ . The resulting classifier will correctly classify some of the training data examples and erroneously classify the others. The training data is hence re-weighted: the weights of the miss-classified examples is increased while the correctly classified ones lose weight. As a result the next weak classifier will focus more on examples that the previous hypothesis miss-classified in order to perform a better classification. Using this new weighted training samples, a new hypothesis is created. This iterative process is repeated  $T$  times ( $T$  is a parameter of the boosting algorithm) (figure 3.2). The final strong classifier  $\mathcal{H}$  is a combination of all weak hypothesis  $h_t$  weighted with reference to their performance on the overall training data sets:

$$\mathcal{H}(\mathbf{x}) = \sum \alpha_t h_t(\mathbf{x}) \quad (3.4)$$

where  $\alpha_t$  is the weight associated to the weak hypothesis  $h_t$  depending on their accuracy of classification.

The most well known boosting algorithm is the Adaptive Boosting algorithm usually named by *AdaBoost*. It was introduced by Freund and Schapire in 1995 [150] and became very popular as it was the first boosting algorithm that adjusts adaptively to the weak learners. Given a distribution  $\vec{p}$  over the training samples, the algorithm calls a weak learner and gets back a weak hypothesis  $h$ . At each iteration, a new set of weights is assigned to the training examples based on the classification error of the weak classifier. Hence a new distribution is defined using the set of weights and a new weak classifier is called. The algorithm combines the different weak hypothesis by summing their probabilistic prediction [150]. The AdaBoost can also be easily extended to multi-class classification [69, 150]. Boosting have been used in different medical imaging related works as in [493, 498, 499] and more precisely for coronary lesions detection in [303, 416, 417].

### 3.1.3 Random Forests

The Random Forests classifier (RF) is an ensemble of decision trees that output one prediction value corresponding to the class that is the mode of the different trees output classes.

Decision trees are hierarchical piecewise models, used for multiple variable analysis in or-

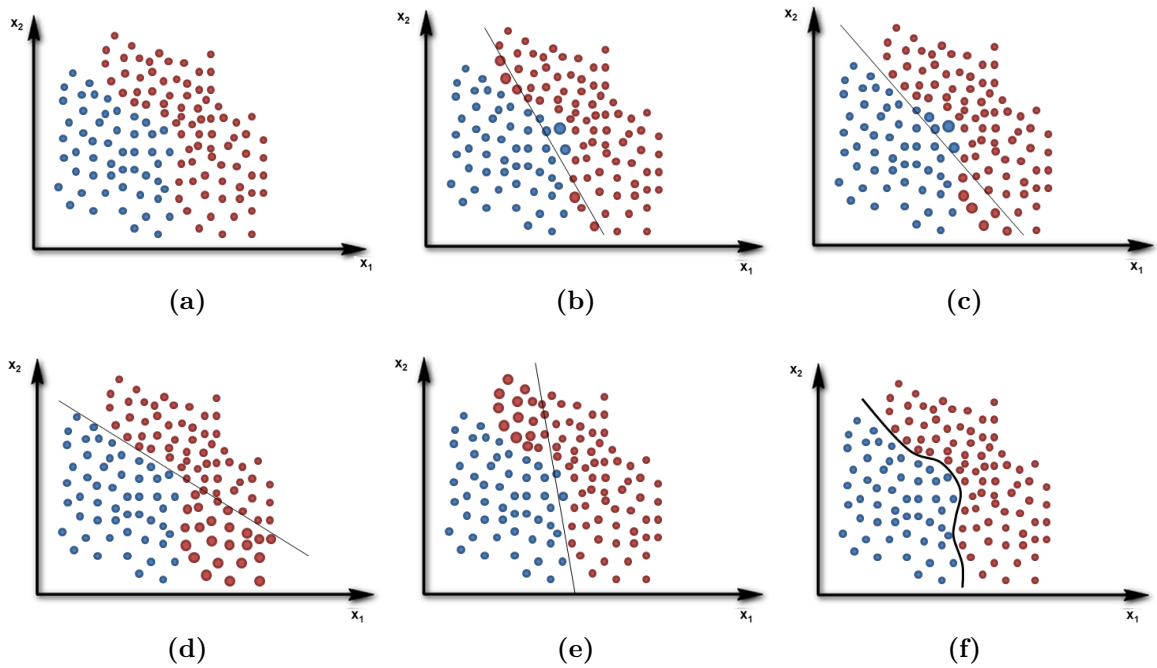


**Figure 3.2** – Boosting algorithm: (a) A 2D example of training data for a 2-class classification. (b)-(e) Examples of some weak classifiers iteratively created by the boosting algorithm to construct the final strong classifier. After each weak classifier, the training data is re-weighted giving a higher weight to misclassified samples. (f) The final strong classifier as a weighted combination of weak hypothesis allowing to accurately separate the two classes.



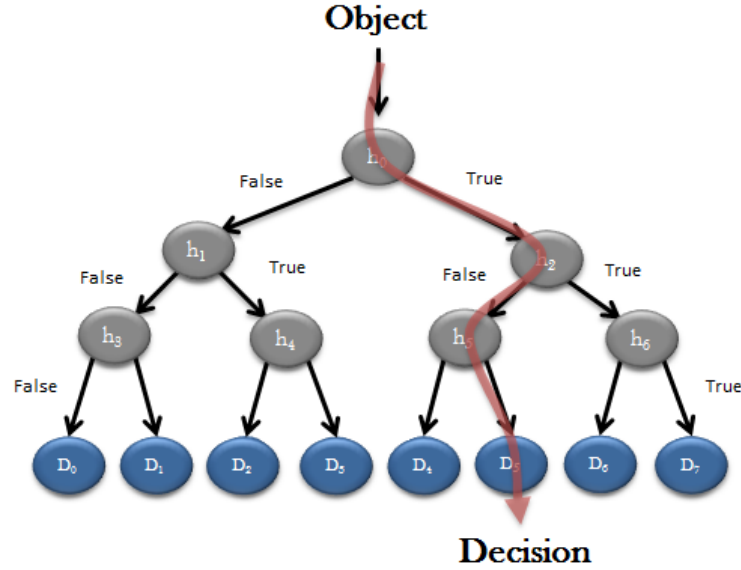


**Figure 3.3** – Decision tree constitutes a set of hierarchically organized nodes (gray) with ending leaves (blue). Each node corresponds to a test function ( $h_i$ ) used to decide whether to send the input data to the left child node or to the right one. Each path on the tree leads to a leaf point corresponding to a final decision  $D_i$  (prediction) on the input object.

der to make a final decision for an input object (figure 3.3). It uses a tree-like graph which internal nodes represents a test on one or some of attributes (i.e. features) of the input object. Depending on the test result (*True* or *False*), the object is sent to the right or the left child node of the current node. This process is repeated until reaching a final node (i.e. leaf) giving a prediction on the input data. The path from the root point to one leaf constitutes the classification rules. Decision trees are used for classification but also regression problems [59]. Efforts have been made to construct (i.e. train) powerful decision trees from training data for specific tasks. Training a decision tree corresponds to define the nodes split functions (i.e. test functions) by optimizing a given energy term using the training data and their corresponding labels. However, used as single entities, decision trees are not practical for high dimensional data. Meanwhile, as stated previously, it has been proven that combining an ensemble of (weak) learners yields to accurate and strong classifiers (e.g. boosting algorithms, section 3.1.2).

Based on combining ensemble learning and decision trees, the idea of constructing ensembles of randomly trained decision trees (i.e. *random decision forests*) rose. Hence, a random forest is a set of decision trees grown separately using a random subset of the input training data [58]. This design was influenced by the idea of random subspaces selection for tree training, proposed in [186]. The final output class is obtained by averaging all tree outputs. Randomness is also injected in the training process of each tree; To compute the node split function models, random

### 3.3.1 Machine Learning Approaches in Medical Context

---

subsets of features are used instead of using all the computed features in the training subset. The idea of searching over a random subset of the training data features when splitting a node of each single tree was first introduced in the work of [Amit and Geman \[14\]](#) for handwritten digit recognition. Similarly, the mean of the tree probabilities is used as the tree ensemble output. The Random Forest algorithm was first formulated by Leo Breiman [58] and combines the idea of “bagging”, where a random selection of examples from the training set is used to grow each tree of the ensemble [57], with a random features selection to split the data on each node. This approach seems to perform comparably to state-of-the-art learning based techniques [77]. Recently, forest-based techniques have been extensively used in computer vision [101, 394] and medical imaging fields [80, 303, 308, 398].

The random forest algorithm, as any other learning based approach, is composed of a learning (training) stage and a testing stage. The forest is composed of  $T$  trees ( $Tree_t$ ), with different or similar depths  $d_t$ . Let  $S$  refer to the overall training data set. Thus,  $S$  corresponds to a set of  $N$  data element  $\mathbf{x}_i$  and their corresponding labels  $y_i$ .

$$\mathbf{S} = \{(\mathbf{x}_1; y_1), (\mathbf{x}_2; y_2), \dots, (\mathbf{x}_N; y_N)\} \quad (3.5)$$

$\mathbf{x}_i$  is an  $M$ -dimensional vector containing the extracted features used for the split function optimization during the training step and to parse the trees during the testing stage. The features are extracted from the raw data (e.g. a 3D medical image) in order to represent the data in a different meaningful space (named *features space* and denoted  $\mathcal{F}$ ). The definition of such features space depends on the problem to be solved and are very important for the robustness of the random forest classifier. We will discuss this later in section 3.2. Since the different trees use different random subsets of training data,  $S_0^t$  will refer to the subset of data used during the learning of the tree  $Tree_t$ .  $S_i^t$  denotes the subset of training data reaching the node  $i$  of the tree  $t$ .

**3.1.3.0.3 Training step** The training step is an off-line stage during which the different parameters of the classifier are optimized, i.e. the nodes splitting functions and the leaves predictors.

The split (i.e. test) functions of the different nodes are a key feature of the Random Forest classifier. These functions correspond to different weak learners, that are learned automatically from the set of annotated (labeled) input data. A test function  $h_i$  is a binary function proper to each node  $i$ , used to split the input set of data  $S_i$  into two subsets  $S_i^R$  and  $S_i^L$  according to

the result of the test (figure a).

$$h(\mathbf{x}, \theta_i) \in \{0, 1\} \quad (3.6)$$

The training stage is mainly dedicated to determine the type and the parameters  $\theta_i$  of the split function by optimizing a given objective function defined on a subset of the training data. At each node, and using  $m$  randomly selected features, the algorithm learns the best function that allows to divide the incoming training set  $S_i$ .

$$\theta_i = \arg \max_k IG(S_i, S_i^L, S_i^R, \theta_k) \quad (3.7)$$

The choice of the objective function  $IG$  used for the definition of an optimized split function depends on the target task. A possible choice is to define  $IG$  as being the *information gain* obtained by splitting the input data set into  $S_i^R$  and  $S_i^L$ . This allows to define the best split function resulting in the two purest split subsets, i.e. each resulting subset contains only training data from one single class [101]. When training the  $i^{th}$  node, only a subset of the sample vector feature is selected to estimate the split function parameters. The set of features is selected randomly which allows to guarantee a low correlation level between the different trees (the trees are trained using different data examples selected randomly) while enhancing the efficiency (using random subsets reduces the search space dimension) [58].

The final step in the learning stage is to learn the leaves predictors that will be used during the testing stage to predict the class of each new sample. For classification, each final node contains the empirical distribution over all the classes of the training data samples having reached that leaf. The probabilistic leaf predictor for tree  $Tree_t$  is then denoted by:

$$P_t(c|\mathbf{x}); c \text{ being the class index} \quad (3.8)$$

The leaf output could also be set as the Maximum A-Posteriori (MAP) estimate obtained by:

$$c = \arg \max_c P_t(c|\mathbf{x}) \quad (3.9)$$

### 3.3.1 Machine Learning Approaches in Medical Context

---

During the training step, the structure shape is also being learned while learning the nodes parameters. The final tree structure depends on the used criteria to stop growing the branches. Most commonly, tree expansion is stopped when the trained tree reached a maximum depth  $d_{max}$ . Growing could also be stopped when a node contains a small number of training points, i.e. using a threshold on the training subset size. We can also choose to stop the tree growing if the remaining training points exhibit high similarity with reference to the selected attributes.

By the end of the training stage, each node is associated to an optimum weak learner and each leaf corresponds to a defined predictor, thus allowing to predict the class of any new unlabeled vector.

**3.1.3.0.4 Testing step** After the training step, a forest with  $T$  optimized trees is constructed. All the trees were trained independently and with random subset of labeled data and features leading to a high accuracy of classification. For the testing step, a new previously unseen vector  $\mathbf{v}$  is sent to set of the forest trees. For each tree, starting at the root node, the test sample is pushed through the different branches until reaching one leaf (see figure 3.5). The testing step could be performed by sending the test sample simultaneously to all the forest trees (in parallel), thus allowing to achieve better computational efficiency.

By traversing a trained tree, a set of hierarchical tests is applied to the input vector using the previously learned weak classifiers. At each node, the unseen data will be sent to the left or right branch depending on the result of the associated test function applied to  $\mathbf{v}$ . This step is repeated until the sample reaches a final node. Hence, the class label of the input vector is determined using the predictor associated to the reached leaf. This results in getting several predictions (decisions) for the input data for tree of the forest. To get a single final forest predictor, all the trees predictions are combined together in several possible ways. In figure 3.5, the final tree prediction is obtained by averaging all trees predictors:

$$P(c|\mathbf{v}) = \frac{1}{T} \sum_{t=1}^T P_i(c|\mathbf{v}) \quad (3.10)$$

The overall forest predictor could also be defined as the normalized product of all the trees predictors. However, this operation is more sensitive to noisy trees predictions. In fact, averaging the different trees posteriors has the advantage of being more robust to noise.

In conclusion, random decision forests are highly depending on the selection of the different parameters of the model. As explained previously, several parameters interferes in the construction of the classifier model. The most critical ones are related to the:

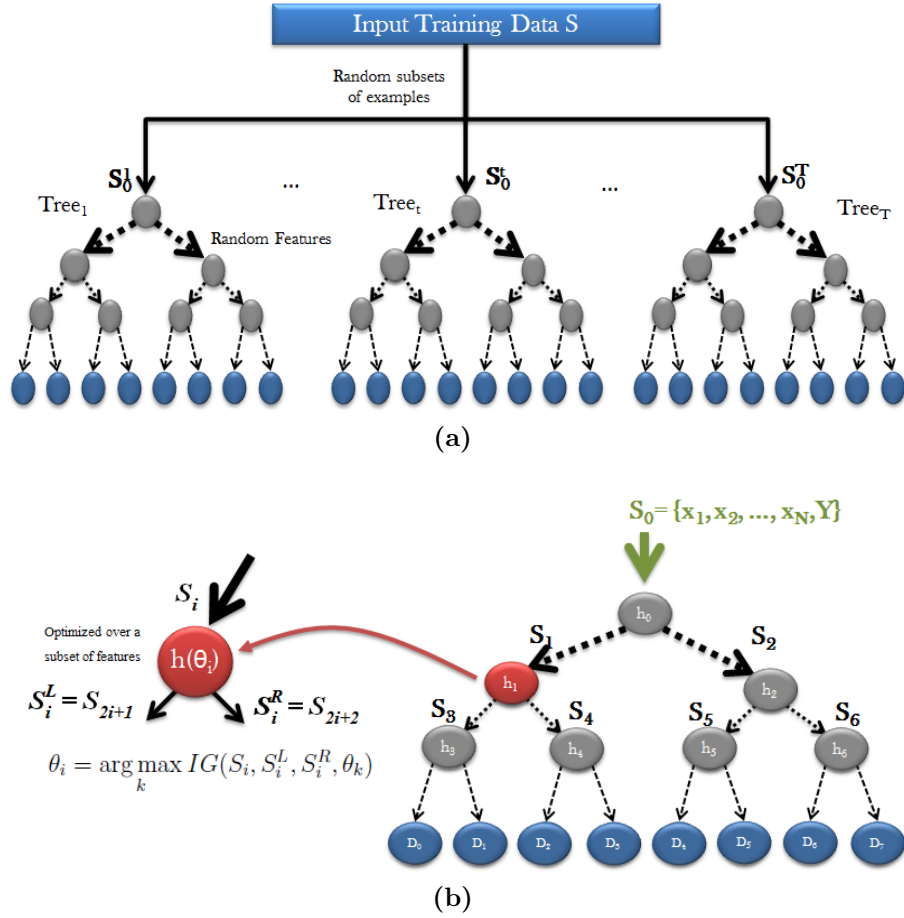


**Figure 3.4** – Training stage: (a) Each tree is trained using a *randomly* selected subset of input labeled data. The trees are grown separately until reaching a stopping condition (details in the text). (b) To train a single decision tree, a subset of learning data is used as input (here denoted  $S_0$ ). For each node  $i$ , a set of *randomly* selected features of the vector  $\vec{x}$  is employed for optimizing the parameters of the split function  $h_i$  by maximizing a given energy function  $IG$ . The input data set  $S_i$  is then split into two disjoint sets  $S_i^R$  and  $S_i^L$ , subsequently used to grow the children nodes. Internal nodes are illustrated in gray and final leaves in blue.

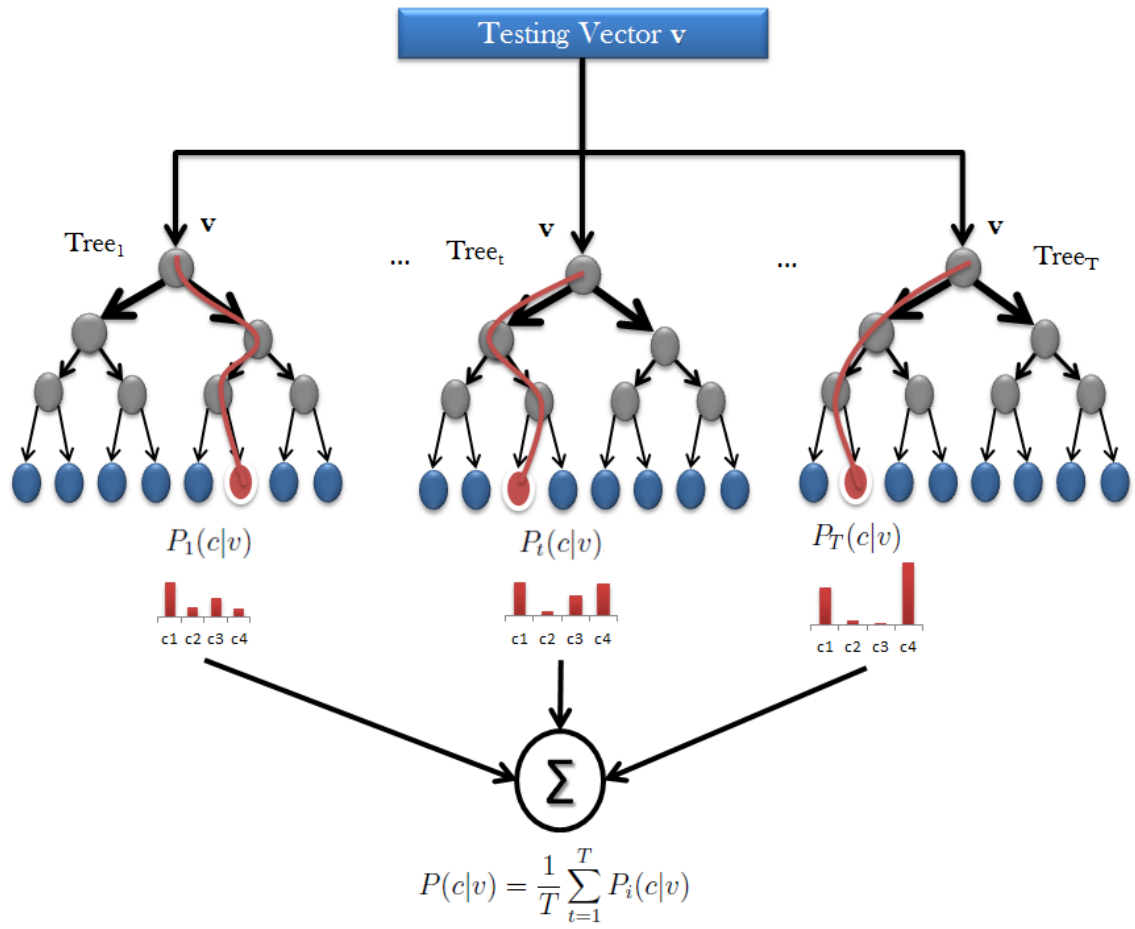


**Figure 3.5** – Random Forest testing stage

- Forest structure: number of trees  $T$ , maximum tree depth  $d_{max}$
- Nodes training: choice of the objective function to be optimized  $IG$ , choice of the weak learners model  $\theta$ , number of selected features for model estimation  $m$ .
- Features definition and extraction for a specific application.

These previous parameters setting have a direct affect on the algorithm predictive accuracy and the computational efficiency. Next, we discuss the features extracted for coronary lesions detection.

### 3.2 Features Extraction for Coronary Lesions Modeling

In order to detect coronary lesions using a learning based approach, we first need to define an accurate description of a stenosis using a set of features. The set of features is encapsulated into a vector that will be used by the learning approach.

This step is very crucial to ensure the robustness of the classification approach. In fact, for a learning based approach to be accurate and able to generalize from the training data, the selected features should be discriminative and allow to characterize the target class. Therefore, we focused on defining special image features that allow to capture the stenosis properties at different scales. For this purpose we defined a pattern description that approximates the local vessel shape and allows to capture its abnormalities. Shape patterns are usually employed to approximate an anatomical structure in medical context. They are generally designed in a way to fit the target object shape based on prior knowledge, to guide a feature extraction scheme. Such shape models have been used for polyps detection in [424], heart cavities extraction in [493] and liver segmentation in [238].

However, coronary arteries lesions do not exhibit a typical unique shape that could be easily modeled by a sampling template. Calcified and soft plaques present heterogeneous properties that could not be generalized to a unique form description. In fact, using CT angiography, soft plaques could not be precisely delineated and are mainly detected due to the resulting lumen narrowing. Meanwhile, calcified plaques, even if being easier to visualize, are not that easy to model. In general, coronary plaques present highly variable shape, location, eccentricity and characteristics that are not easy to predict and estimate by simply transforming a predefined template. Hence, in order to accurately model a lesion within a coronary artery, we need to extract adequate features from the raw data.

### 3.3.2 Features Extraction for Coronary Lesions Modeling

---

A major point of interest is the scale size of the chosen shape pattern to describe the coronary lesion; It should be able to capture sufficient context information to accurately determine the vessel condition. One choice could be to model the coronary branch as a whole. However, this modeling is unlikely to provide precise information on the anomaly location and extent as it will classify the whole vessel as being healthy or diseased. In fact, vascular lesions are often located in a short segment of the vessel (compared to the whole vessel length). On the other hand, if we tackle the problem on a per-slice level, this could induce higher false detection rates that could be due to noisy vessel section and the lack of information about the surrounding vessel sections. These characteristic observations should be considered for the lesion shape model design. The shape pattern should cover only a portion of the vessel and should be large enough to be able to capture the plaque volume. Besides, the background tissues surrounding the vessel should be excluded as much as possible to not disturb the lesion detection process. The shape model should hence only include the local vessel volume to insure that no false lesions, due to the vessel surrounding tissues, could be detected by the algorithm.

We propose to exploit the naturally cylindrical shape of coronary vessels in order to achieve the previously stated constraints and define a shape pattern that sufficiently captures the local vessel condition. Therefore, we define a cylindrical segment ROI that fits the vessel local shape. Straight cylindrical patterns with fixed size were used in previous works [80, 303, 417]. In [303], authors mainly focused in detecting calcified plaques using intensity-based features. In [417], a multi-scale approach using patterns at different scales was proposed. However, patterns at high scales do not respect the local curvature of the vessels, which makes the approach prone to failure as it is likely to include undesired structure surrounding the vessel. Cetin et al. [80] used fixed cylinder height and radii and thus the approach is no longer scale invariant. Our approach combines robustness against scale variance and vessel curvature. Furthermore, the centerline is sub-sampled in order to create overlapped cylindrical patterns. The sampling model is then used to extract a set of features that will be used to drive the training and the classification steps. As a result, each sampling point along the vessel centerline will be classified as “healthy” or “diseased”.

#### 3.2.1 Vessel sampling using the cylindrical pattern

If we represent the vessel cross section by a 2D circular pattern (as shown in figure 3.7), the local vessel artery shape could be modeled using a cylindrical shape. The proposed pattern should include the vessel lumen as well as the vessel wall. This ensure that the plaque lesion, if any, is well included in the sampling pattern and thus could be captured by the defined



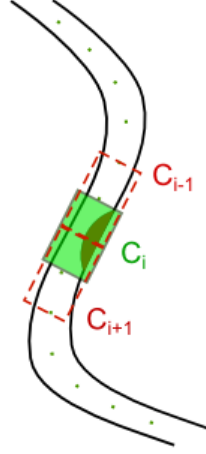


**Figure 3.6** – Example of a lesion located at the bounding of two successive patterns  $C_{i-1}$  and  $C_{i+1}$ . Adding an overlapping pattern  $C_i$  allows to insure that at least one of the cylindrical patterns includes the lesion and thus it could be captured by the extracted features.

features. Hence, the vessel is discretely approximated by using a set of cylindrical sampling segments defined on each point on the vessel centerline. As a result the whole vessel shape and curvature are covered (see figure a). The vessel centerline is sampled with a sampling step allowing to create overlapping cylindrical patterns along the vessel. This overlap between the successive ROIs allows to ensure that small stenosis are well included in at least one of the sampling patterns and so can be correctly classified (illustrated in figure 3.6).

However, a vessel coronary present a varying (decreasing) size from the coronary root to the leaf (distal region). Thereby, a static pattern with a fixed size is not appropriate to accurately fit the vessel volume; A large pattern is convenient to ensure that we include locally all the vessel volume but this will result in including vessel surrounding structures at distal segments. On the other hand, if we set the pattern size to be small enough to ensure that we do not include other non-vascular structures at distalities, this pattern will not include the totality of the vessel volume at proximal segments (it will be too small to cover the vessel lumen and walls). As a result, proximal lesion plaques could be missed. To the best of our knowledge, the only work (among the learning based approaches for lesions detections detailed in section 1.1.3) that treated this problem is the work of [Teßmann et al. \[417\]](#). In this work, the authors used a multi-scale feature extraction scheme using different cylindrical patterns with different scales. However, this approach is still not robust to the vessel curvature. As high scale patterns do not fit the vessel curvature while lower scale patterns are not large enough to capture a whole

### 3.3.2 Features Extraction for Coronary Lesions Modeling

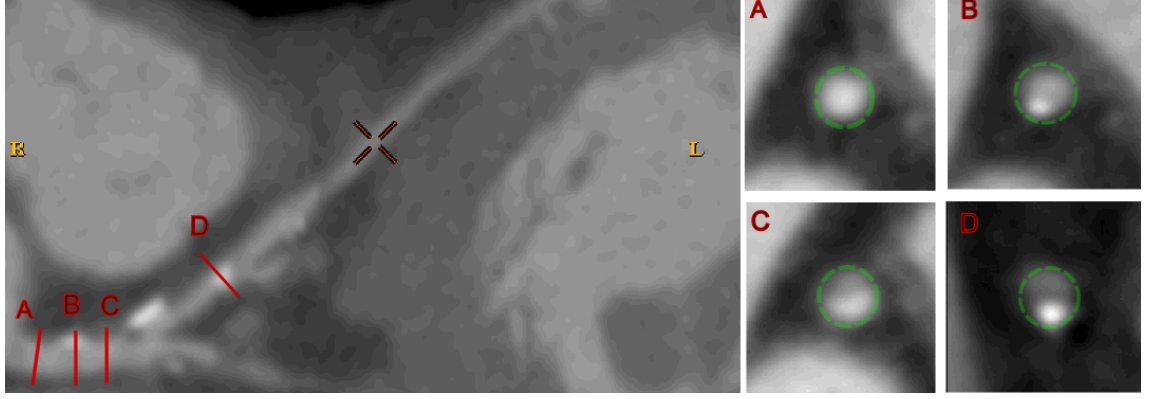


**Figure 3.7** – Example of vessel with different plaque types (soft and calcified). Cross sections A, B, C and D of the vessel are shown on the right images. The slices shows a healthy section (A), two calcified sections (B and D) and a section with a soft plaque (C). The vessel cross section are fairly approximated by circular sections.

lesion. To ensure a scale invariance of the extracted features along the whole vessel, we chose to derive the size of the model pattern from the healthy vessel size. Doing so, we ensure that the proposed pattern includes the vessel lumen and wall while excluding all other surrounding structure. To quantify the vessel lumen area we use the same approach described in section 2.2. After a watershed-based approach for vessel lumen segmentation and 2D contours extraction, a robust regression approach is applied on the lumen cross section diameter profile for each branch in order to get an estimation of the healthy lumen diameter profile  $D_{healthy}$ . We used the healthy lumen profile instead of the real profile to be able to include the vessel wall and lesions inside the pattern. In fact, a plaque lesion may cause a lumen narrowing and thus if we build our pattern size based on the real lumen profile, the plaque will not be located inside the pattern. Hence, for each centerline point, the estimated diameter value is used to compute the cylindrical pattern parameters. As a result, the cylindrical pattern is represented by:

$$\mathbf{C}_i(\phi, \mathbf{z}) = \begin{pmatrix} \frac{D_i}{2} \cos(\phi) \\ \frac{D_i}{2} \sin(\phi) \\ -\frac{H}{2} + z \end{pmatrix}_{\{R_1, R_2, R_3\}_i} \quad (3.11)$$

where  $D_i = (1 + 20\%) * D_{healthy}$  and  $z \in [0, H_i]$ .  $H_i$  corresponds to the height of the cylindrical pattern and is set to  $H_i = 2 * D_i$ .  $D_{healthy}$  is the reconstructed lumen diameter at point  $i$  on the centerline. This model represents a straight cylinder defined on the vessel cross section geometry at point  $i$  (see figure a) with a varying size form proximal to distal points on

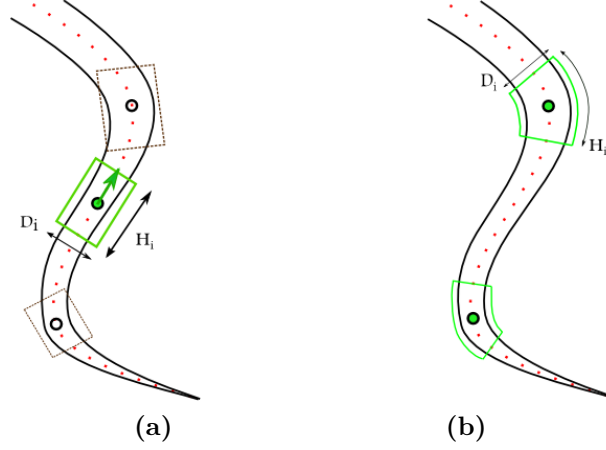


**Figure 3.8** – Vessel sampling pattern: (a) A straight cylindrical pattern with varying height  $H_i$  and width  $D_i$ . This model is not accurate to sample highly curved segments of the vessel (examples in dashed lines). (b) To deal with curved regions along the vessel, we propose to use a curved cylindrical model that locally fits the vessel curvature. This allows to avoid including undesirable surrounding structures and missing some vessel regions which could bias the classification of the corresponding point.

the vessel. This model is more robust against vessel scale variation, contrary to previous works where the size (height and width) of the cylindrical pattern was set to fixed value.

However, since the vessel shape is not perfectly tubular, we deform the cylindrical model in order to fit the local vessel curvature. This is done by using a “curved” cylindrical pattern instead of a straight one. To construct the curved pattern, we fit the cylinder straight axis to the curved vessel centerline. To do so, we use the different local vessel geometry to define each cross section of the vessel instead of defining the whole cylindrical pattern using one single geometry (i.e. the three axis of the center point  $i$ ). As a result, the pattern is now defined as a set of circular cross sections  $S_z$ , each defined on the cross section plane of the vessel.

$$\mathbf{S}_z(\phi) = \begin{pmatrix} \frac{D_i}{2} \cos(\phi) \\ \frac{D_i}{2} \sin(\phi) \\ -\frac{H}{2} + z \end{pmatrix}_{\{R_1, R_2, R_3\}_z} \quad (3.12)$$

The resulting cylinder pattern is shown in figure b. Figure b shows an illustration of the proposed pattern applied to a whole vessel. Unlike the straight cylindrical pattern, the scale varying curved pattern allows to fit the real size of the vessel and thus avoid including non desirable structures while ensuring to cover the important vessel regions.

As coronary lesions have no specific size or shape, we need to divide our pattern into

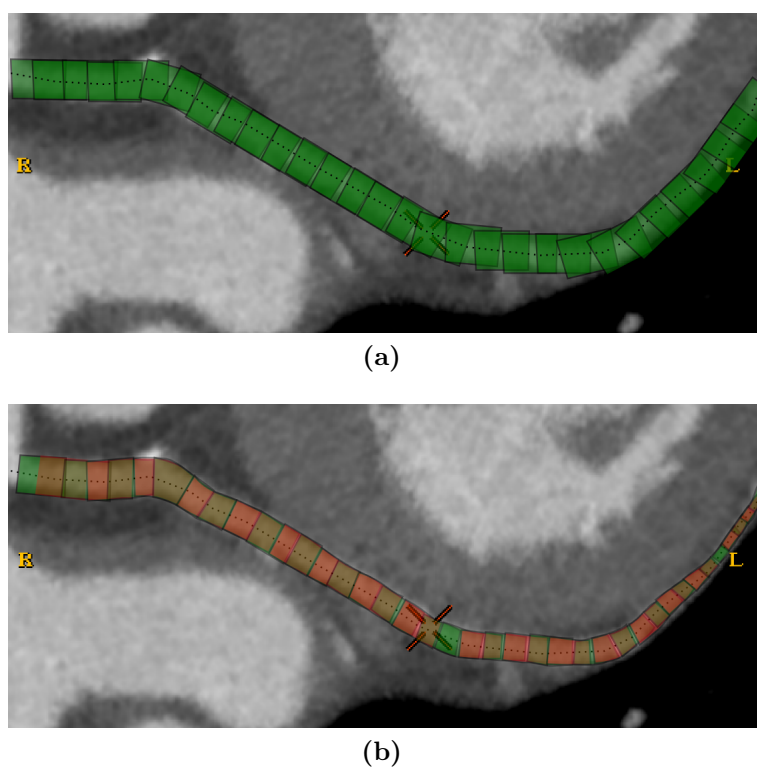


**Figure 3.9** – Schematic vessel sampling using the (a) straight and (b) curved cylindrical patterns. The curved varying pattern offers a better overlap with the vessel volume while minimizing the inclusion of undesirable surrounding structures (specially at distal segments of the vessel).

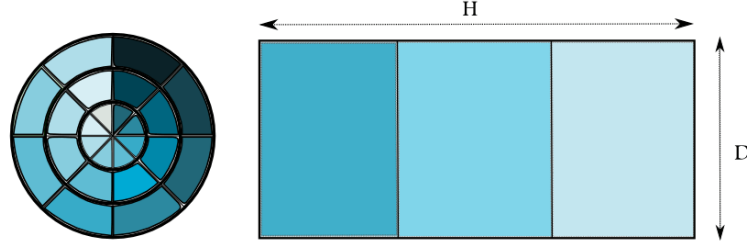


**Figure 3.10** – Schematic illustration of the different sub-regions (radial on the left and longitudinal on the right) defined in the cylindrical pattern.

different regions in order to capture the stenosis characteristic properties at different scales and positions. In the sequel, we will use a straightened cylindrical pattern, for illustration and explanation, instead of a curved one for simplicity. To extract the features values, the cylindrical pattern is partitioned into radial and longitudinal sub-regions. First, the pattern is divided into 3 cylindrical disjoint and equal parts along its main axis as shown in figure 3.10. Each part, is further partitioned into 8 cones and each cone into 3 sub-regions thus resulting in 24 2-dimensional sub-regions (per cross section) and 72 3-dimensional sub-region (along the z-axis) per pattern (see figure 3.10). For each 2D cross section of the pattern, samples are generated using polar coordinates by exploiting the basic radial shape of the proposed pattern (figure 3.11). Each sample is characterized by its polar coordinates as follow:

$$\mathbf{s}(\rho, \phi, \mathbf{z}) = \begin{pmatrix} \rho \cos(\phi) \\ \rho \sin(\phi) \\ -\frac{H}{2} + z \end{pmatrix}_{\{R_1, R_2, R_3\}_z} \quad (3.13)$$

with,

$$\rho = \frac{D_i}{2 * N_{radius}} * j; \quad j \in [0, N_{radius}] \quad (3.14)$$

$$\phi = \frac{2 * \Pi}{N_{angle}} * k; \quad k \in [0, N_{angle}] \quad (3.15)$$

$$z = \frac{H_i}{N_{section}} * l; \quad l \in [0, N_{section}] \quad (3.16)$$

$N_{radius}$  is the number of samples along a given radius of the cylindrical pattern cross section.

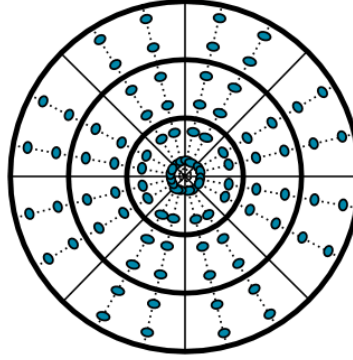


**Figure 3.11** – An illustration of the sampling of a 2D slice of the cylindrical pattern. The sampling results in 4 points per 2D sub-region.

$N_{angle}$  corresponds to the number of radial segments (i.e. arcs) used to sample the cross section. Finally,  $N_{section}$  defines the number of the cross sections used to sample the cylindrical pattern along its main axis. For our curved pattern, for each cross section, we use the local center point geometry  $\{R_1, R_2, R_3\}$  to extract the sampling points. This modeling exploits the 3D extent of the vascular structure and allows to extract relevant context information inside of each cylindrical ROI in order to get a coherent description of the vessel segment condition. This approach is more robust than just using a 2-dimensional features extraction scheme (i.e. on 2D cross sections), as the later one does not contain enough information about adjacent vessel parts which could lead to erroneous detections. Besides, the adaptive scale of the pattern take into account the natural size reduction along the vessel from its root to the most distal parts from the aorta.

### 3.2.2 Features selection

To increase the robustness of any supervised learning algorithm, the selected features should sufficiently capture the characteristic properties of the underlying classes of the data. The computed features utilizes the image properties and employs some mathematical mechanism used to highlight lesion/lumen specificities. They are extracted at different sub-regions separately or by combining several sub-regions of the previously detailed cylindrical region of interest. Thus, we define two types of computed features: *local features* and *global features*. Local features are features computed in the 3D sub-regions defined previously. Global features are computed only once per each cylindrical pattern. The different features allows to capture a lesion at different locations around the vessel and at different scales.

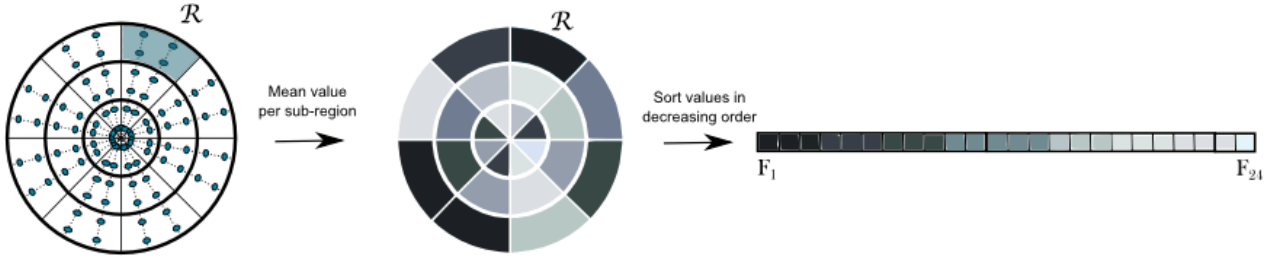


**Figure 3.12** – Mean gray values extraction and sorting in order to create a rotational invariance of these features. Each feature value corresponds to the mean intensity value inside of one of the sub-regions. Higher values are represented with darker colors. The set of feature values is sorted and then added to the feature values vector.

### 3.2.2.1 Local Features

For each of the 3D sub-regions of the cylindrical pattern, a set of image-based and geometric feature values are extracted. First, we extract intensity-based features inside each of the 3D sub-regions. Intensity-based features are commonly used for lesion detection as in [80, 416, 417]. They exploits the image appearance properties to capture intensity discontinuities that may occur due to the presence of a lesion plaque. For each sampling point  $s$  of the pattern, the image intensity value, denoted  $I$ , is extracted. A tricubic interpolation on the CT dataset is used to generate sub-voxelic value for samples inside small sub-regions. As a result, the *mean gray value* inside each sub-region  $\mathcal{R}$  is computed and stored into the feature vector. To be robust against lesion position around the vessel axis, we sorted these values in decreasing order so that high values and low values are always represented by the same features (figure 3.12). Hence, attenuation values representing a lesion are always kept at the same position on the features vector and as a result the classifier becomes insensitive to the lesion position. This ensures a rotation invariance with respect to these features by keeping only the relevant information related to the intensity value (representing a calcified or a soft plaque) while discarding the location information around the vessel (which is not determinant to know wheter a stenosis is present inside the current pattern or not).

However, previous features are particularly significant for calcified plaques as they exhibit high intensity values compared to vessel lumen ranges. Thus, the associated stenosis can be easily discerned using simple intensity-based features as they deviate form the normal vessel lumen ranges. Meanwhile, detecting soft plaques using only the previous features seems to be challenging as this type of plaques exhibit low intensity values making such lesions hardly discernible from the vessel surrounding tissues. Therefore, in order to detect the related gray value attenuation we compute a set of Haar-like features.

### 3.3.2 Features Extraction for Coronary Lesions Modeling

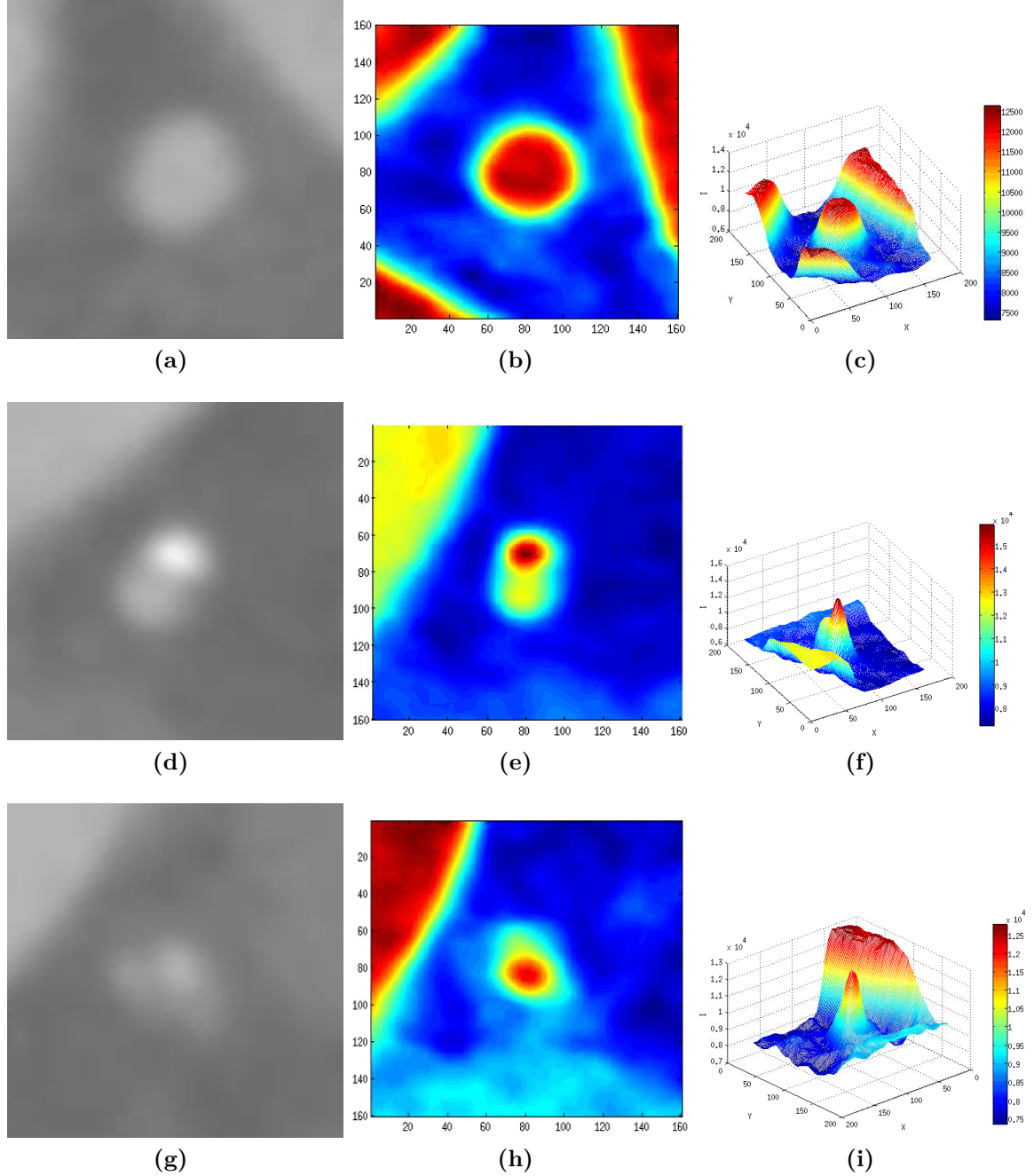


**Figure 3.13** – Intensity variation of 2-D cross sections of some coronary arteries - First column presents a normal cross-section (a), a cross-section with a calcification (a) and a cross-section with a soft plaque (a). 2D views of pseudo-color intensity plots of the same cross sections are shown in column 2. The third column shows a 3D view of the same intensity plots. Pseudo-color maps are generated by scaling the cross section data between its minimum and maximum values.



As mentioned previously, soft and calcified plaques present different attenuation value ranges than the vessel lumen (see figure 3.13). Therefore, when a stenosis (due to any type of lesion plaque) is present, a meaningful intensity discontinuity occurs inside the diseased vessel part. To capture such disparity, we use a range of feature values based on the computation of *radial* and *longitudinal gradients* between neighboring local sub-regions of the pattern. We first compute the difference between the gray values of each two opposite sub-regions (i.e.  $\mathcal{R}_1$  and  $\mathcal{R}_2$ ) and parts (i.e.  $\mathcal{P}_1$  and  $\mathcal{P}_2$ ) as shown in figure 3.14. As a lesion is generally located at one side of the vessel volume part, this feature allows to highlight the dissimilarity between the healthy and diseased regions of the vessel located at opposite sides of the model pattern. Computing these differences overall the sub-regions and parts allows the features to be invariant with reference to the lesion location around the vessel. We additionally compute the difference between the sum of the intensity values of each two crowns (i.e.  $\mathcal{C}_1$  and  $\mathcal{C}_2$ ) as illustrated on the same figure. We also compute  $F_{H_{crowns}}$  as the difference between the medial crown intensity and the sum of the inner and the outer crowns intensities.

$$F_{H_{ij}} = I_{\mathcal{R}_i} - I_{\mathcal{R}_j}; \quad (3.17)$$

$$F_{H_{ij}} = I_{\mathcal{P}_i} - I_{\mathcal{P}_j}; \quad (3.18)$$

$$F_{H_{ij}} = I_{\mathcal{C}_i} - I_{\mathcal{C}_j}; \quad (3.19)$$

$$F_{H_{crowns}} = I_{\mathcal{C}_1} + I_{\mathcal{C}_3} - I_{\mathcal{C}_2} \quad (3.20)$$

with,

$$I_{\mathcal{R}} = \sum_{s \in \mathcal{R}} I(s) \quad (3.21)$$

Moreover, to be rotation invariant and to ensure an overlap between each two neighbor regions, we rotate the cylindrical pattern by an angle of  $\Pi/8$  to create an overlap between the different parts and we re-compute all the previous local features once again (figure 3.15). Hence, the overall robustness of the approach is further increased.

Subsequently, we compute longitudinal gradients over the vessel pattern as illustrated in figure 3.16. These features mainly allow to capture a lesion by comparing healthy sections to diseased portions of the vessel. They are particularly helpful for detecting lesions causing total occlusions. In fact, such lesion plaques occupy the whole vessel cross section and hence the radial features will fail to detect any discontinuity as the pattern cross sections (mainly

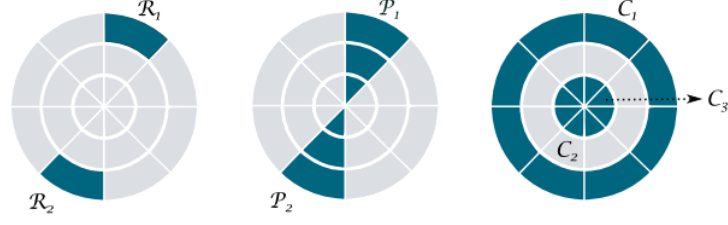


**Figure 3.14** – Illustration of radial gradients features calculation using Haar-like patterns. The difference between the two dark regions is computed as a feature for each pair of regions. The difference intensity value between the light crown and the sum of the two dark ones is also used as a Haar-like feature.

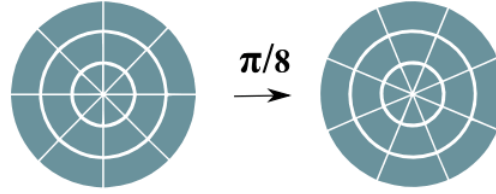


**Figure 3.15** – Cylindrical pattern rotation to enhance the rotation invariance around the vessel center.

containing the lesion) will present homogenous intensity values. Such radial and longitudinal gradients features approximates the Haar-like features, very popular for object recognition and first proposed in [439]. Contrary to the original Haar-like filters utilizing rectangular patterns, we extracted these features using cylindrical patterns to sufficiently capture the structure of the vessels.

$$F_{H_4} = I_{SC_1} - I_{SC_2}; \quad (3.22)$$

$$F_{H_5} = I_{SC_3} + I_{SC_5} - I_{SC_4}; \quad (3.23)$$

#### 3.2.2.2 Global Features

Global features are features computed all over the pattern and reported only once per each centerline point. Similarly to local features, we first compute a set of intensity based global features including the *mean*, *minimum* and *maximum* values inside the cylindrical pattern. Moreover, in order to assess the variation of the attenuation value and hence the homogeneity of the tissue inside the pattern, we compute the *variance*, the *standard deviation* as well as the *mean average deviation* and *median average deviation* over all the samples of the pattern. Subsequently, for each pattern, we compute the histogram of the sampling points intensities

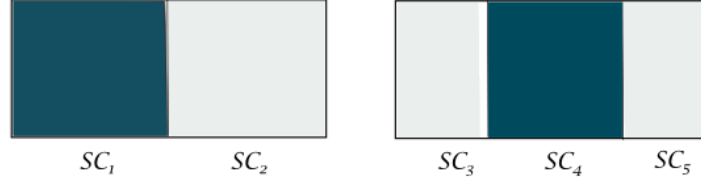


**Figure 3.16** – Illustration of longitudinal gradients features calculation similar to the well known Haar-like features. For the left, the difference between the dark and light regions is computed as a feature to assess the presence of a lesion inside one of the two sub-regions. For the right, the feature corresponds to the difference intensity value between the two bright sub-regions and the dark one. This allows to capture a lesion located at the center of the pattern.

ranging from 0 HU (the minimum attenuation value for soft plaques as explained in section 1.3.0.3) and 600 HU (the maximum attenuation value for calcified plaques). Each histogram is composed of 40 equal bins with a bin-width of 15 HU. This allows to capture the amount of high or low gray values corresponding to calcified or soft plaques. Using the histogram, we hence extract 40 features  $F_{Histo_i}$  defined by:

$$F_{Histo_m} = \#(B_m); \text{ with } B_m = \{v; limit_m \leq v < limit_{m+1}\} \quad (3.24)$$

$$(3.25)$$

The use of the histogram aims at keeping only the relevant information concerning the potential presence of plaques causing the stenosis without focusing on their position inside the cylindrical pattern. This helps the classifier to be more robust against lesion position around the vessel axis. Examples of histogram extracted around different lesion plaque types are shown in figure 3.17.

Additionally to intensity-based features used to describe the appearance of the local vessel pattern, we propose to use geometric-based features in order to describe the local shape of the vessel. Hence, we first use the vessel lumen radius estimated using the approach described in section 2.2. In fact, the approximate lumen radius value is a meaningful feature to be used in order to represent the lumen narrowing for stenotic points. For each cylindrical pattern, we report the lumen radius value computed at its central point. Though, this value varies by decreasing along the vessel branch from the root point to the distal segments. Besides, at the same location along the same vessel the lumen radius is likely to vary from one patient to another. Therefore, to avoid the intra- and inter-patient variance and be robust against the point position along the branch, we normalized this feature using the mean radius value along

### 3.3.2 Features Extraction for Coronary Lesions Modeling

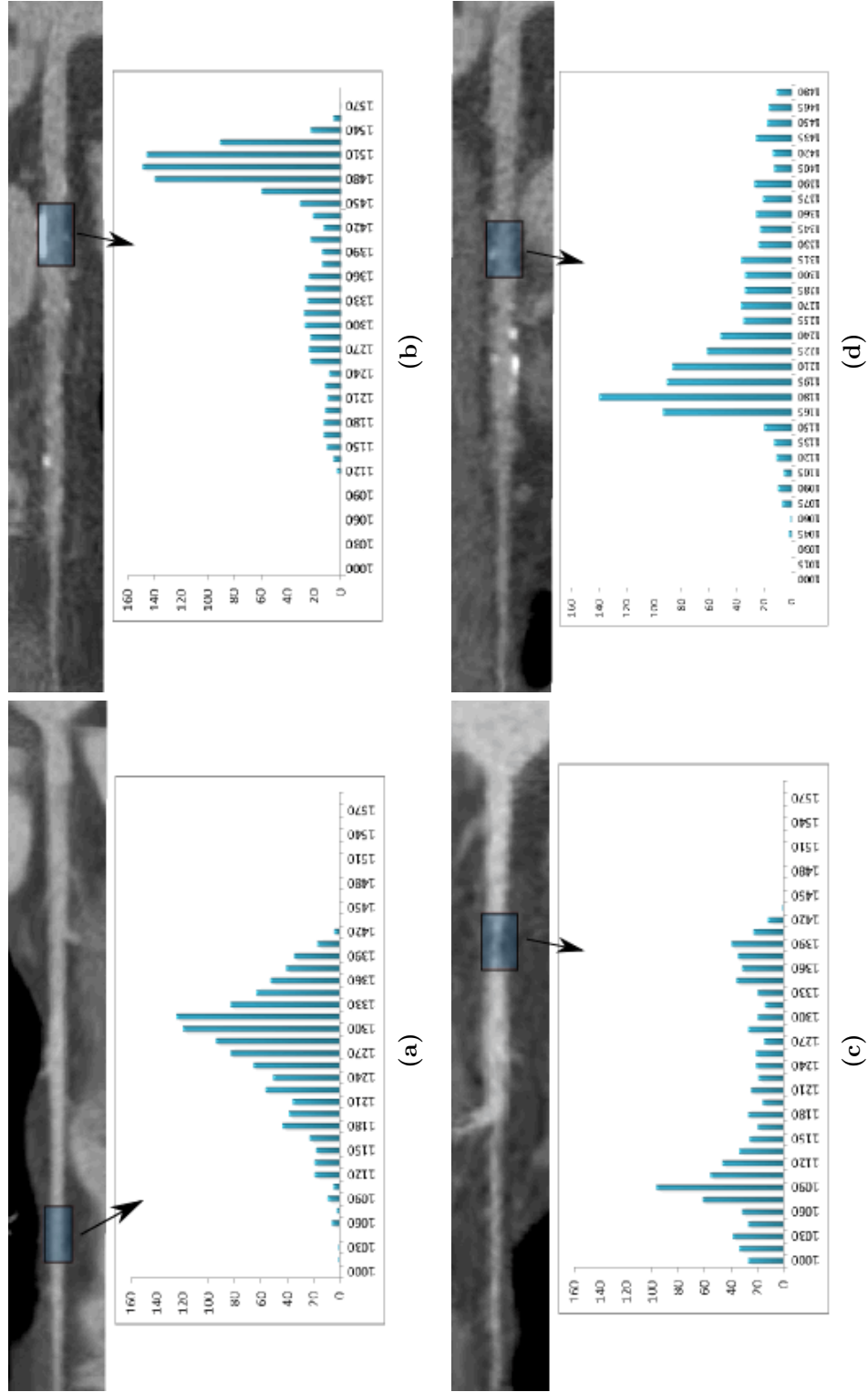


**Figure 3.17** – Intensity histogram of a sampling pattern located at a diseased vessel segment with (a) normal, (b) calcified, (c) soft and (d) mixed plaque. All the histograms contain 40 bins ranging from 0 HU to 600 HU.

the corresponding branch  $\hat{r}$ .

$$F_r = \frac{r_i}{\hat{r}} \quad (3.26)$$

$$(3.27)$$

To locally describe the shape of the lumen vessel, we also propose to compute a vascular enhancement-based feature using the hessian eigenvalues. Such filters provide a good response at normal lumen positions while providing poor responses deviating from the normality at diseased lumen points. This is due to deviation of the lumen shape from a local tubular structure near to coronary lesion (i.e. lumen stenosis). Even if this could present a limitation to the application of such filters for lumen enhancement and segmentation, this weakness could be used to detect lumen anomalies. The hessian based filter is descibed in section 2.2.1.1. In the context of coronary lesions detection, we computed the Hessian matrix and the associated eigenvalues at 3 different scales for each vessel centerline point  $p_i$ . For a normal vessel cross-section (i.e. nearly symmetric cross section), the two eigenvalues are expected to have similar magnitudes and the same sign (positive as the vessel lumen is brighter than the surrounding tissue). The *Sato vesselness* measure is hence reported per cylindrical pattern as a geometric feature.

However, a major problem related to the intensity-based features is that gray values may differ between two different exams because of varying acquisition parameters. Therefore, the previously explained, local and global, intensity-based features are normalized using the mean intensity value inside the aorta. For this, the aorta volume is automatically segmented and the mean intensity value overall the segmented volume is computed and used to normalize all the intensity-based features.

### 3.3 Stenosis detection using the Random Forest Classifier

Recently, there has been an increasing interest in using Random Forests for medical images processing [80, 131, 303, 308, 398]. They have demonstrated to be better or at least comparable to other state-of-the-art methods in classification applications [58], and more specifically for coronary lesions detection task as shown in [303]. While achieving state-of-the-art results, the popularity of Random forests is mainly due to their high computational efficiency during both

training and classification steps. Besides, they can easily be parallelized, which makes them interesting for multi-core and GPU implementations. Furthermore, compared to other ensemble methods such as boosting, RFs are inherently multi-class and are more robust to label noise. Therefore, we decided to use the random forest algorithm for automatically detecting coronary lesions. As explained in section 3.1.3, the random forest classifier is an ensemble of  $T$  individual decision trees learned using random sampling points from  $N$  input data. The final decision is obtained from a consensus over all the trees. In each tree, each split node uses the same number of  $m$  randomly selected features (from  $M$  computed features) to output the local decision.

#### 3.3.1 Training Step

During the training phase, we first create the training database to build the decisions trees. The training database is a feature key that defines the robustness of any supervised learning based approach. It should include sufficiently representative samples of both of the classes we want to discriminate. Coronary plaque lesions exhibit various shape, extent, position and appearance properties leading to wide range of observable configurations. Hence, the better is to ensure that different possible figures are covered and present in the training database. This allows the approach to correctly identify the different lesions types and configurations. On the other hand, we have to ensure that there is no risk of over-fitting<sup>3</sup>. Over-fitting could occur when the training database is unbalanced and does not contain all the possible instances. Meanwhile, the training database should not be too large in order to avoid high training and testing computational time.

To build our training database, samples are selected from the 18 training data sets provided by the MICCAI challenge organizers [215]. These data sets were carefully selected in a order to be representative of the different coronary arteries lesions types and configuration occurring in clinical practice. Table 3.1 presents the lesion types reported in the training data sets. We can see that the three types (soft, calcified and mixed plaques) are equally present. The distribution of all the coronary stenosis degrees over the training data sets is summerized in table 3.2. The database contains 103 lesions varying from non significant (i.e.  $<20\%$ ) to total occlusion (i.e.  $> 95\%$ ). The framework focuses only on the detection of severe lesions on a cardiac CT angiography. Hence, only stenosis with a degree higher than 50% are considered.

---

<sup>3</sup>Over-fitting is a practical difficulty that could occur for a decision tree based model (or many other predictive models). It happens when the learning approach continues developing hypothesis to reduce the training dataset classification error at the cost of providing poor classification results on the unseen testing dataset. Hence, the resulting decision model tightly depends on insignificant features of the training instances which are difficult to generalize on the testing data sets. As s result the classifier loses his power of prediction on new samples.

### Chapter 3. Learning-based Detection of Severe Coronary Stenoses

---

Figure 3.18 shows the distribution of the coronary lesions reported by the CTA observers over the different lesion types and stenosis degrees, on the training database. We can notice that more than half of the reported lesions do not correspond to severe stenosis and hence could not be used to train the classifier.

**Table 3.1** – Coronary plaque types distribution over the 18 training data sets.

	Plaque Type		
	Soft	Calcified	Mixed
dataset00	0	0	0
dataset01	1	0	0
dataset02	1	0	0
dataset03	0	2	0
dataset04	2	4	3
dataset05	4	1	4
dataset06	2	2	1
dataset07	5	2	3
dataset08	0	2	4
dataset09	4	4	3
dataset10	4	3	2
dataset11	4	9	3
dataset12	0	0	0
dataset13	0	5	2
dataset14	0	2	2
dataset15	5	0	1
dataset16	1	3	1
dataset17	0	0	2
All	33	39	31

To construct the training database, we select samples from the two classes: *pathological* and *healthy* points (i.e. sampling patterns). A pathological sample corresponds to a stenotic point with a narrowing degree higher than 50%. In the provided data sets, 27 lesions are marked as severe ones. We include all the corresponding vessel points to the training database. On the other hand, the number of healthy vessel points is largely greater than the number of pathological ones. Therefore, we construct our training database in a way to include:

- All the pathological points reported by the observers and presenting a stenosis with more than 50% of lumen narrowing denoted by ( $S_{Pat}$ ).
- A set of non pathological points equally selected over all the 18 training data sets denoted

### 3.3.3 Stenosis detection using the Random Forest Classifier

**Table 3.2** – Coronary stenosis degrees distribution over the training data sets.

	Stenosis Degree					All
	1-19%	20%-49%	50%-69%	70%-94%	95%-100%	
dataset00	0	0	0	0	0	0
dataset01	1	0	0	0	0	1
dataset02	0	1	0	0	0	1
dataset03	0	2	0	0	0	2
dataset04	0	6	2	1	0	9
dataset05	0	6	3	0	0	9
dataset06	0	3	1	1	0	5
dataset07	0	6	2	2	0	10
dataset08	0	5	0	1	0	6
dataset09	0	9	2	0	0	11
dataset10	0	5	2	1	1	9
dataset11	0	14	1	0	1	16
dataset12	0	0	0	0	0	0
dataset13	0	7	0	0	0	7
dataset14	0	2	2	0	0	4
dataset15	0	4	2	0	0	6
dataset16	0	4	0	0	1	5
dataset17	0	1	1	0	0	2
All	1	75	18	6	3	103



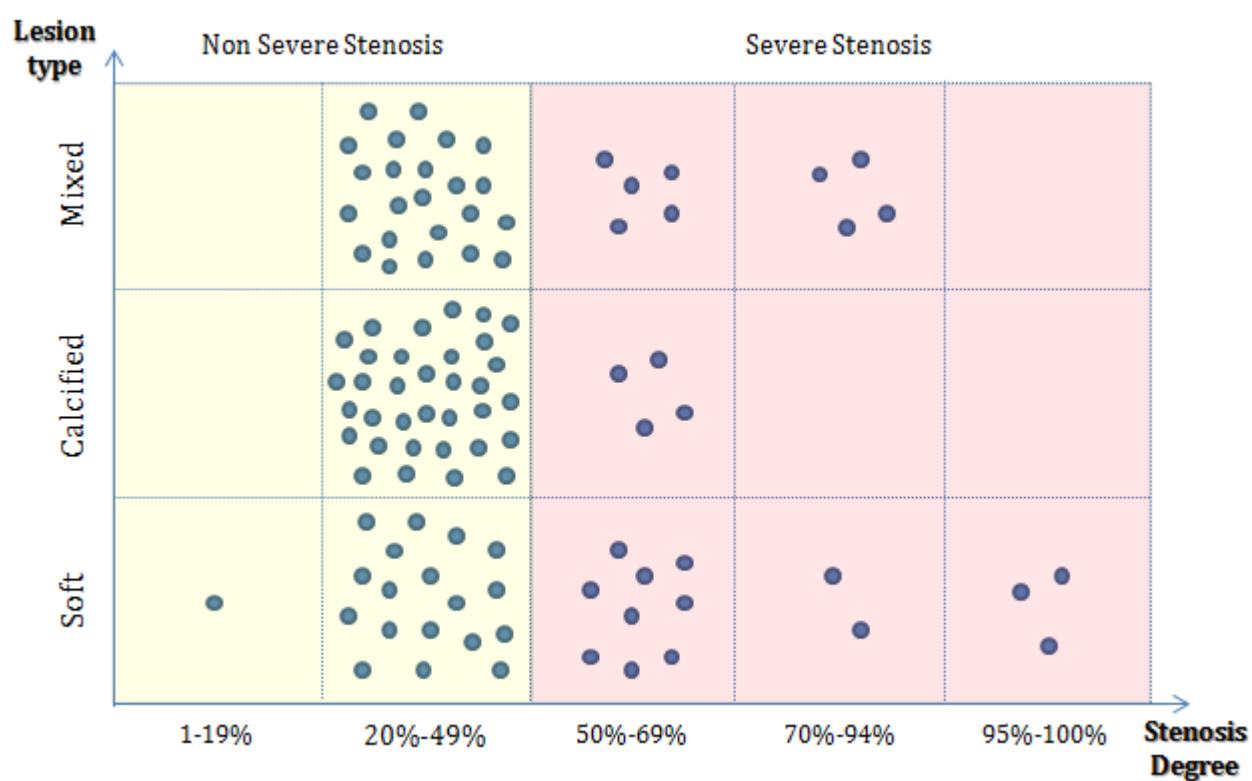


**Figure 3.18** – Distribution of the reported coronary lesions by the CTA observers over the different lesion types and stenosis degrees. Only 27 over 103 lesions correspond to severe stenoses.

### 3.3.3 Stenosis detection using the Random Forest Classifier

---

by  $(S_{NPat})$ .

While the number of stenotic sampling points is fixed (by the ground truth), the set of non pathological points could be selected using different distributions based in two main definitions. In fact, compared to pathological point (i.e. with a lumen narrowing greater than 50%), a non pathological point could be defined as: 1) a non stenotic point (i.e. 0-19% of lumen narrowing) or 2) a stenotic point with a lumen narrowing between 20 and 49% (i.e. non-severe stenosis). Hence, we tested several training databases using the following possible non pathological class samples selections:

- $(S_{NPat})$  contains all the healthy points (i.e. 0-19% of lumen narrowing) of the 18 training exams.
- $(S_{NPat})$  contains all the non severe stenotic points (i.e. 20-49% of lumen narrowing) of the 18 training exams.
- $(S_{NPat})$  contains a subset of  $N$  healthy points of the 18 training exams ( $N$  varying from 30 to 200).
- $(S_{NPat})$  contains a subset of  $N$  points with a lumen narrowing lower than 50% (including healthy points and non severe stenosis) over the 18 training exams ( $N$  varying from 30 to 200).

Using the leave-one-out-cross validation, we concluded that the best classification performance is obtained by using the third definition of the healthy class samples with  $N = 50$ . Results of this step of optimization will be shown in section 3.4. Then, the previously explained features are computed around each selected sampling point and used to train the Random Forest classifier. Hence, the training database is presented as a  $N \times (M+4)$  matrix.  $N$  corresponds to the total number of training samples (healthy and pathological points).  $M$  represents the number of computed features. The matrix contains 4 extra columns corresponding to: the training exam identifier, the vessel branch label, the point 3D world coordinates (x, y, z) and the sample class ( $H$  for healthy and  $P$  for pathological).  $F_i$  corresponds to the  $i^{th}$  feature value computed at each point. The composition of the training database is illustrated in figure 3.19.

Besides, the performance of the random forest for the given training data set depends on the forest design parameters: tree depth  $D$ , number of trees  $T$ , and number of randomly selected features  $m$  to consider at each node to find the best split. The parameters of the classifier were optimized over the training database. Details of these parameters optimization are given in

Exam	Branch	Point	Class	Feature <sub>1</sub>	...	Feature <sub>M</sub>
$E_1$	$B_1$	$(x_1, y_1, z_1)$	H	$F_1$	...	$F_M$
$E_1$	$B_1$	$(x_2, y_2, z_2)$	P	$F_1$	...	$F_M$
...	...	...	...	...	...	...
$E_1$	$B_2$	$(x_{45}, y_{45}, z_{45})$	P	$F_1$	...	$F_M$
...	...	...	...	...	...	...
$E_i$	$B_j$	$(x_k, y_k, z_k)$	H	$F_1$		$F_M$
...	...	...	...	...	...	...
$E_{18}$	$B_L$	$(x_N, y_N, z_N)$	H	$F_1$	...	$F_M$

Figure 3.19 – The structure of the training dataset.

section 3.4.1.3. By the end of the training step, the resulting classifier is stored to be used for the testing step using an unseen exam samples.

### 3.3.2 Testing Step

Second, the detection of severe stenosis is possible by running the previously trained classifier on a new unseen dataset (testing step). Therefore, the same features are extracted on the new exam. For each point on the vessel centerline, we define the cylindrical pattern using the local vessel geometry and size and compute the set of local and global features detailed in section 3.2. For each sampling point  $i$ , we get a vector of features  $\mathbf{v}_i$  describing the local vessel appearance and geometric properties. As a result, we obtain a set of feature vectors for the testing exam, that we send to the random forest classifier to be processed. The classifier considers each feature vector (corresponding to a single point on a vessel branch) separately. To classify this new instance using the random forest trees, the unseen vector is sent to the root node of all the trees separately and then traverse the whole tree by traveling downward to the left or right node depending on the function test result. Finally, each tree gives a vote, depending on the leaf node reached by the instance, that corresponds to the probability of this sample to belong to a given class. The final predicted class probabilities of an input sample is computed as the **mean** predicted class probabilities of the trees in the forest. For coronary lesions, we used two different classes: *pathological* and *healthy*. For each point of the coronaries' centerlines, the classifier provides a pair of probability values. We propose thus to focus on the pathological class probability.

For each branch, we reconstruct the pathological class probability profile by concatenating the final predicted probabilities for each point on this vessel branch. Figure 3.20 shows an example of the output profile of a vessel branch. As we can state, such profile is difficult

### 3.3.3 Stenosis detection using the Random Forest Classifier

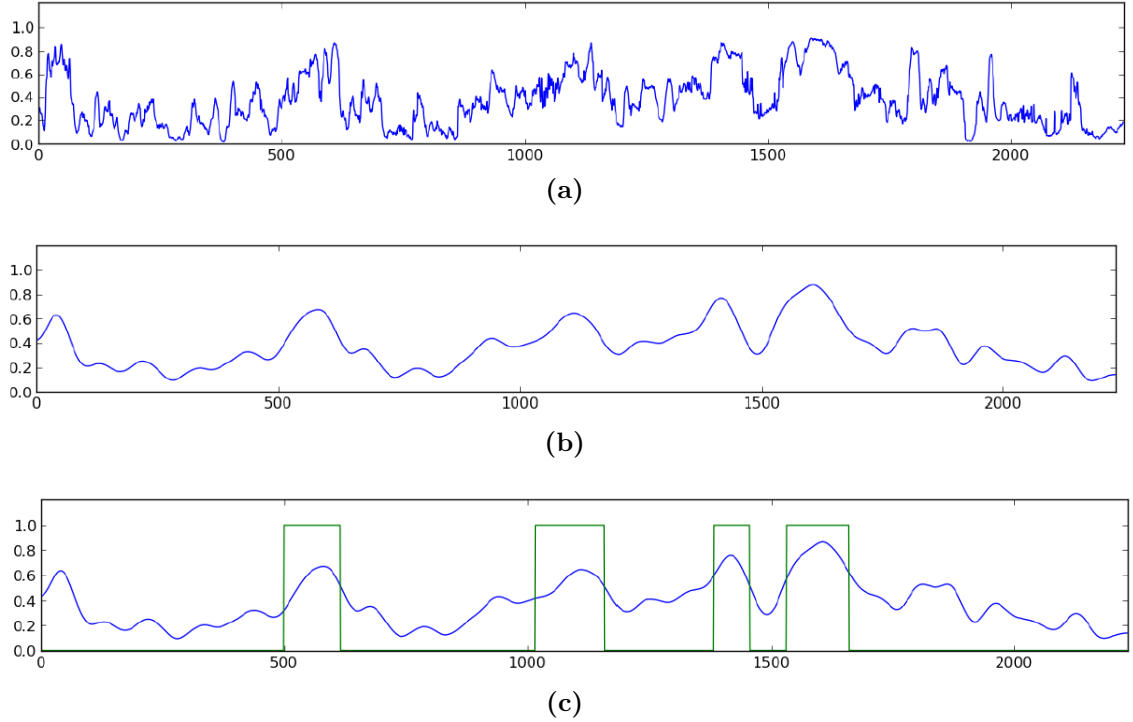


**Figure 3.20** – Output probability profile processing: (a) The output probability profile for the pathological class along a vessel branch (i.e. the horizontal axis corresponds to the point position along the vessel path). (b) The smoothed probability profile after applying the Hann filter. (c) The severe stenosis ground truth (green line) displayed on the smoothed profile. We can see that the annotated stenosis correspond to peak of the probability profile. Hence the classifier is able to recognize the marked stenosis. This profile is obtained on an annotated dataset that was excluded from the training database (cross validation leaving-one-out process).

to exploit as it is very noisy. We should hence process the output probabilities in order to smooth the branch probabilities profile and extract the stenotic regions. Therefore, for each branch profile, we apply a *Hann filter* with a window width of 40. This allows to smooth the probability profile by removing spurious small fluctuations while keeping meaningful peaks. The remaining peaks correspond to probably stenotic regions (see figure 3.20).

#### 3.3.2.1 Stenotic regions flagging

The next step consists in extracting the stenotic vessel regions and define the stenosis center. Two strategies have been tested for this task. The first one consists in detecting the stenotic area of the vessel by simply thresholding the probability profile. Hence we only keep the connected component corresponding to a probability of belonging to the pathological class higher than  $T_{prob}$  (see figure 3.21). The choice of this threshold value is critical as it affects directly the performance of the detection approach (i.e. the sensitivity and the PPV values).

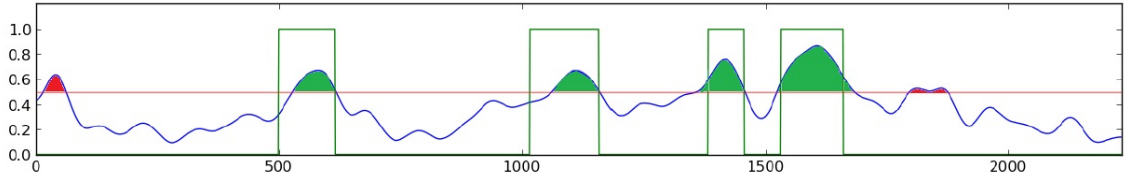


**Figure 3.21** – Stenotic regions detection using a single threshold. Using a threshold value of 50 (red line) allows to detect all the stenosis reported by the consensus of readers (the detected regions are marked in green) but it also leads to the detection of three false detections marked in red. The ground truth stenosis are shown using the green line.

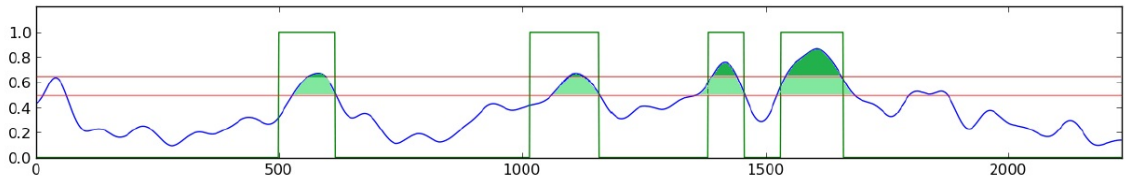


**Figure 3.22** – Stenotic regions detection using hysteresis thresholding. A first high threshold allows to select the surely stenotic regions (in dark green). Second the selected connected components are propagated to including neighboring stenotic point with a probability higher than  $T_{prob2}$  (in light green). Using such approach false positives are eliminated thanks to the first high threshold. The ground truth stenosis are shown using the green line.

In fact, increasing the value of  $T_{prob}$  leads to lower the amount of false positives while could increase the number of false negatives (i.e. missed stenoses). Meanwhile, low values of  $T_{prob}$  allows to detect more stenosis (i.e. true positives) but induces an increase of false positive detections. A set of cross validation tests have been performed using the training database in order to optimize this threshold value. Details of this optimizations are given in section 3.4. To overcome these limitations due the use of a one single threshold, we propose to use a double thresholding based approach. Hence, two different thresholds  $T_{prob1}$  and  $T_{prob2}$  are defined as  $T_{prob1} > T_{prob2}$ . First, points with a probability higher than  $T_{prob1}$  are identified as sure stenotic points. Second, neighboring points of the selected connected components having a probability higher than  $T_{prob2}$  are added to the previously stenotic regions (see figure 3.22). This second threshold allows to better detect the stenosis starting and ending edges as they do not necessary exhibit high probability values. This method thus ensures to better detect the whole stenotic regions since only high probability points are selected thanks to the first threshold  $T_{prob1}$ , while their surrounding extremities are added thanks to the second lower threshold  $T_{prob2}$ . This approaches allows also to avoid isolated non stenotic false positive that are eliminated by the use of the high threshold  $T_{prob1}$ . Similarly to the previous approach, these thresholds are optimized using a cross validation leave on out process. Results are reported in section 3.4.

### 3.3.3 Stenosis detection using the Random Forest Classifier

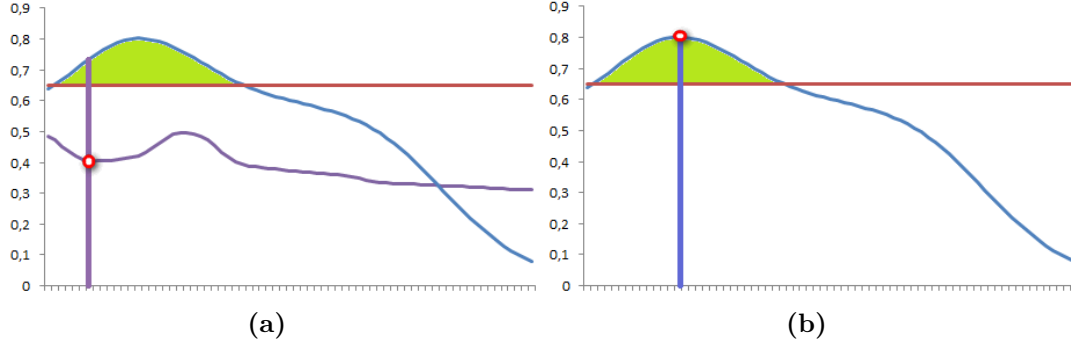


**Figure 3.23** – Stenosis Center Extraction: The probability profile is illustrated in blue. In (a), the center point is defined as the vessel point showing the minimum cross section area value. The flagged stenotic region is displayed in green and the corresponding cross section area profile is drawn in purple. The straight line indicates the extracted stenosis center. In (b), the center point is extracted as the point having the maximum probability value. The two approaches give two distinct points.

#### 3.3.2.2 Stenosis center extraction

The previous step results in a set of stenotic regions flagged per vessel branch. This offers an information about the extent of each lesion. However, an other important information about coronary lesions is the stenosis center. This center corresponds to the section of the stenotic vessel region presenting the maximum lumen narrowing (i.e. the minimum lumen area). It is used to compute the stenosis degree with reference to a healthy vessel section. Besides, this center is the only information reported by the approach and used the automated evaluation framework to validate the stenosis detection process as explained in [215].

To extract this stenosis center, we tested two different approaches. The first approach gets use of the lumen cross section area information. Based on the automated lumen segmentation and quantification, the stenosis center is reported as the point presenting the minimum lumen section area among all the points of the flagged vessel region (figure a).

Since the automatically extracted lumen area is not perfect, the previous approach could lead to erroneous stenosis centers. Therefore, we propose to use the probability profile; The stenosis center is hence defined as the point showing the highest probability value along the flagged connected component. In fact, we have noticed that for each detected region, there exits at least one maximum point. We assume that at this point, showing the highest probability, the local vessel portion represents a good stenotic pattern model and hence corresponds to the stenosis center.

The two approaches are optimized and compared using a cross validation over the learning database. The results of the different tests are detailed in section 3.4. Based on this series of

tests, the second approach seems to provide better detection results.

### 3.3.3 Stenosis Quantification

Finally, quantitative information about the previously detected stenosis are derived such as the percent of diameter-stenosis. The detected stenosis candidates are hence graded using the automatically segmented vessel lumen. The stenosis degree reflects the percent of vessel narrowing relative to an assumed healthy (i.e. normal) vessel section. The choice of such reference is very crucial for the stenosis degree computation; Erroneous references lead to erroneous stenosis degrees. Generally, the stenosis degree is quantified using one single healthy vessel reference immediately adjacent to the stenotic region as following:

$$S_d = 100\% \times \left(1 - \frac{a_{min}}{a_h}\right) \quad (3.28)$$

with  $a_{min}$  the minimal section area and  $a_h$  the healthy section area.

However, using one single reference may lead to quantification errors if the healthy section is not correctly selected. If it is located too far from the diseased lesion, the comparison of the two sections is not conclusive as the stenosis degree is miss-estimated. If the healthy section is erroneously selected downstream the stenosis might be under-estimated. On the other side, if the healthy reference is selected upstream, the lumen narrowing could be over estimated (due to the normal vessel diameter tapering). To minimize the influence of the healthy reference selection, we propose to use a double reference approach. Therefore, a proximal and distal adjacent healthy references are selected for each detected stenosis. These references are defined as the first neighboring healthy points (i.e. not detected by the approach as diseased points) of the flagged stenotic regions (see figure a).

For each detected stenosis, we compute both of the CTA and QCA grades as required by the evaluation framework. Hence, for each stenosis center point  $i$  detected at the previous step, we compute the flagged stenosis minimum cross section area  $a_{min}$  and the minimum cross section diameter  $d_{min}$ . Then, the two grades are computed as following:

$$S_{CTA} = 100\% \times \left(1 - \frac{a_{min}}{a_p + w * (a_d - a_p)}\right) \quad (3.29)$$

where,

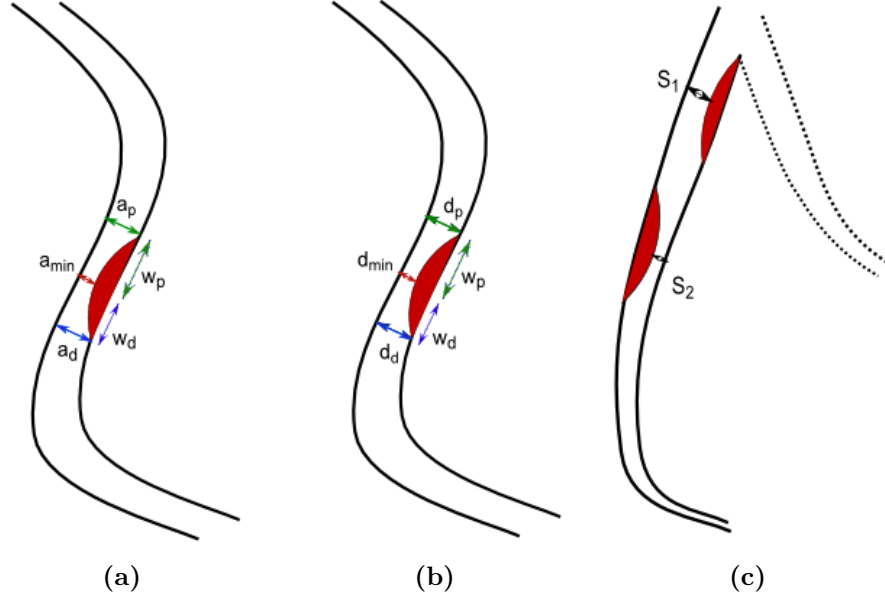


**Figure 3.24** – Stenosis quantification for (a) the CTA (per lesion) and (b) QCA (per segment) evaluation. (c) The segment stenosis corresponds to the maximum lumen narrowing induced by all the stenosis located at that segment.

$a_d$  and  $a_p$  corresponds to proximal and distal references (i.e. healthy points) section areas used to quantify the stenosis degree.

$$S_{QCA} = 100\% \times \left(1 - \frac{d_{min}}{d_p + w * (d_d - d_p)}\right) \quad (3.30)$$

where,  $d_d$  and  $d_p$  corresponds to proximal and distal references vessel section diameters.  $d_{min}$  is the diseased region minimum diameter value.

with,

$$w = \frac{w_p}{w_p + w_d} \quad (3.31)$$

For each segment, the stenosis degree corresponds to the maximum of all the stenosis degrees included in that segment as illustrated in figure c.



### 3.3.4 Implementation

The implementation of the presented approach implied a large amount of work devoted to parameter tuning, validation and optimization of strategies. The previous algorithm was developed in C++ and integrated into a clinical diagnosis prototype of the GE Volume Viewer software. The prototype is totally automated and allows to perform coronary lesions detection of any unseen 3D CT data exam using automatically extracted vessel centerlines.

The first version of the prototype was mainly developed to be tested and evaluated on the challenge database with the provided centerlines. Hence, no pre-processing was necessary to extract the centerlines needed to perform the feature extraction and the classification step. This version was used to optimize and tune the different parameters over the training database. The developed module implements the feature extraction strategies and acts as the connection to the Random Forest classifier. The first step consists of extracting the features along the coronary vessels of a given exam. The extraction steps are illustrated in algorithm 2.

---

**Algorithm 2:** Feature Extraction

---

```
input : cardiac CT exam  $E$ , Coronary Branches Centerlines  $CL$ , Lumen radii  $R$   
output:  $F$  the exam features  
  for all Coronary branch  $B$  do  
    for all Segment  $S$  of  $B$  do  
      if  $S$  has not been visited yet then  
        for all  $x$  along  $S$  do  
           $C = \text{DefineCylindricalPattern}(x, R)$   
           $F_x = \text{ComputeFeatures}(C)$   
           $F \leftarrow F \cup F_x$ ;  
        end for  
      end if  
    end for  
  end for  
Return  $F$ 
```

---

The feature extraction step is run on all the training data sets. The extracted features are stored to create the database used to train the classifier. Once the features are extracted for all the training data sets, we proceed to the creation of learning database using pathological and healthy samples. This step as well as the Random Forest training step are performed off-line by using a Python script. The Random Forest implementation used in this module is based on the freely available version of the **scikit-learn Python** based framework(<http://scikit-learn.org/stable/index.html>). This module allows a very flexible implementation and evaluation

### 3.3.3 Stenosis detection using the Random Forest Classifier

---

of the various parameters of the Random Forest algorithm. To facilitate the communication between the C++ and the Python parts of the module, we used the Boost Python library hence allowing to bind C++ to Python programs in a mostly-seamless fashion. The training scheme is described in the following algorithm:

---

**Algorithm 3:** Classifier training

---

**input** : Sets of features of the learning data sets  $F$   
**output**: The trained classifier  $RF$

$S \leftarrow \emptyset$   
**for all** set  $F$  of features of a training data set **do**  
     $H = \text{ExtractHealthySamples}(F)$   
     $P = \text{ExtractPathologicalSamples}(F)$   
     $S \leftarrow S \cup H \cup P$   
**end for**

$RF = \text{TrainClassifier}(S);$   
**Return**  $RF$

---

Once the training step performed, the obtained classifier is serialized and stored in a file for later use during classification phases. All trees constructed during learning are thus preserved. Then, during the testing step, the serialized classifier is reloaded in order to classify the new unseen exam.

The algorithm 4 describes the different steps of an unseen exam processing. First, the different features are extracted for all the coronary vessels points. Then, the different obtained samples are sent to the classifier using a C++/Python interface. The trained classifier affects a probability of being pathological to each vessel point. Once, all the samples are classified, the probability profile of each branch is constructed and processed, and then the stenosis candidates are extracted. The final step consists in computing each stenosis measurement (center point, degree, start and end points). The detected stenoses and their measures are then displayed on the different views.

This work lead to two different prototypes. The first version was dedicated to work on the MICCAI challenge database. We hence used automatically generated centerlines provided by the challenge organizers to extract the different features. Results of evaluating this work on the Rotterdam Coronary Artery Algorithm Evaluation framework are presented in section 3.4.2.1. These results were published in our work [292]. Second, this work was extended in order to be able to fully automatically detect coronary lesions on any unseen cardiac CT exam without using any inputs (i.e. vessel centerlines). Therefore, the final version works in conjunction with the automated heart extraction and coronary segmentation explained in previous chapters.

---

**Algorithm 4:** Testing phase
 

---

**input** : Unseen cardiac CT exam  $E$ , Coronary vessels centerlines  $CL$ , Lumen radii  $R$ , Serialized classifier  $RF$   
**output**: Detected Stenosis  
 $F = \text{ExtractFeatures}(E, CL, R)$   
**for all** Branch  $B \in CL$  **do**  
   **for all** sample  $x \in B$  **do**  
    $P_x = \text{Classify}(x, F)$   
   add  $P_x$  to the vector of probabilities of the branch  $B$   $P_B$   
**end for**  
 $P_{BS} = \text{SmoothProbabilityProfile}(P_B)$   
 FlagStenoticRegions( $P_{BS}$ )  
 $C_S = \text{ExtractStenosesCenter}(P_{BS}, R)$   
 ComputeStenosesDegrees( $C_S, R$ )  
**end for**  
 DisplayStenosis()

---

The final framework also utilizes an already existing module of Volume Viewer for automated centerline extraction. The final flowchart of the developed prototype is shown in figure 3.25. This prototype has been further quantitatively and qualitatively evaluated on a GE cardiac CT database (section 3.4.2.2).

The algorithm is launched by selecting a CTA dataset and pressing one button that allows to load the exam and launch the processing (figure 3.26). Then, the whole chain, consisting of heart segmentation, coronary detection, centerline extraction, lumen quantification and features extraction and classification, runs automatically with no additional user interaction or

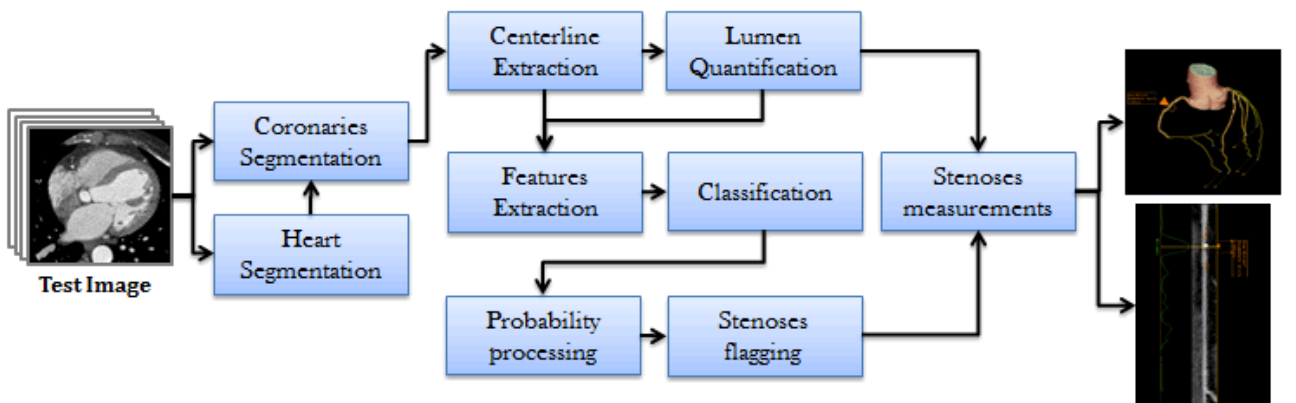


**Figure 3.25** – The prototype flowchart developed for the automated coronary stenosis detection.

### 3.3.3 Stenosis detection using the Random Forest Classifier

---

parameters setting. Once the classification step is performed and the output probability result is processed, the stenosis center as well as the stenosis degree are computed.

The set of detected stenosis is then displayed by adding bookmarks at each stenosis. The bookmark defines the starting and ending points of the lesion, detected automatically, as well as the center of the stenosis and its grade. The stenoses are displayed on a 3D volume rendering of the coronaries tree. Besides, the lumen, curved and cross section views are displayed allowing the user to visualize the straightened vessel volume and the desired cross sectional planes in order to better inspect the detected stenoses. Detected stenoses are also marked on these different views as shown in figure 3.27. The user could switch between the different vessels views to visualize the different detected lesions. Moreover, for each selected vessel branch, the output probability profile of belonging to the pathological class is displayed along the vessel lumen view thus allowing to compare the probability profile variation to the vessel appearance directly. The user could hence visualize suspicious regions having relatively high probability values that are not detected by the algorithm. Two examples of automated stenosis detection are shown in figure 3.28.

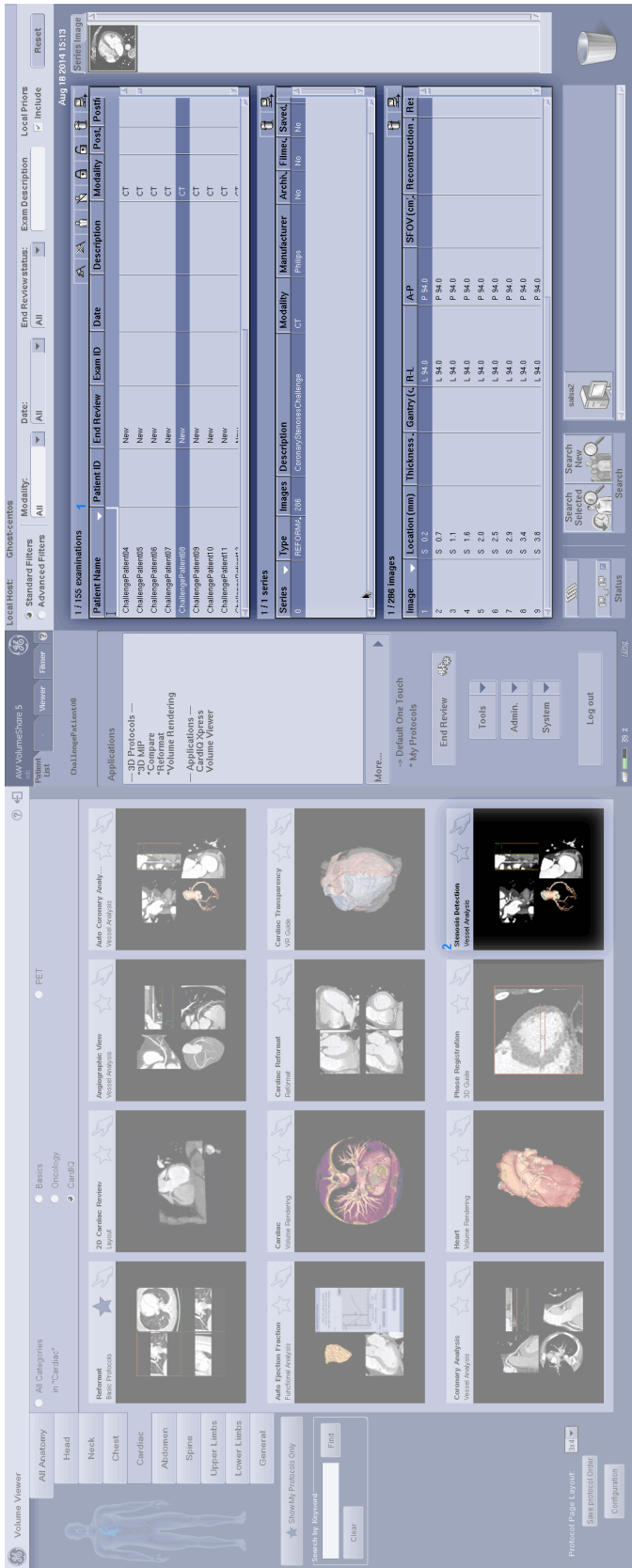


**Figure 3.26** – The prototype is launched by clicking on the icon (2) after selecting the wanted exam from the list of available exams in (1). This work is developed as a prototype of the Volume Viewer software.

### 3.3.3 Stenosis detection using the Random Forest Classifier

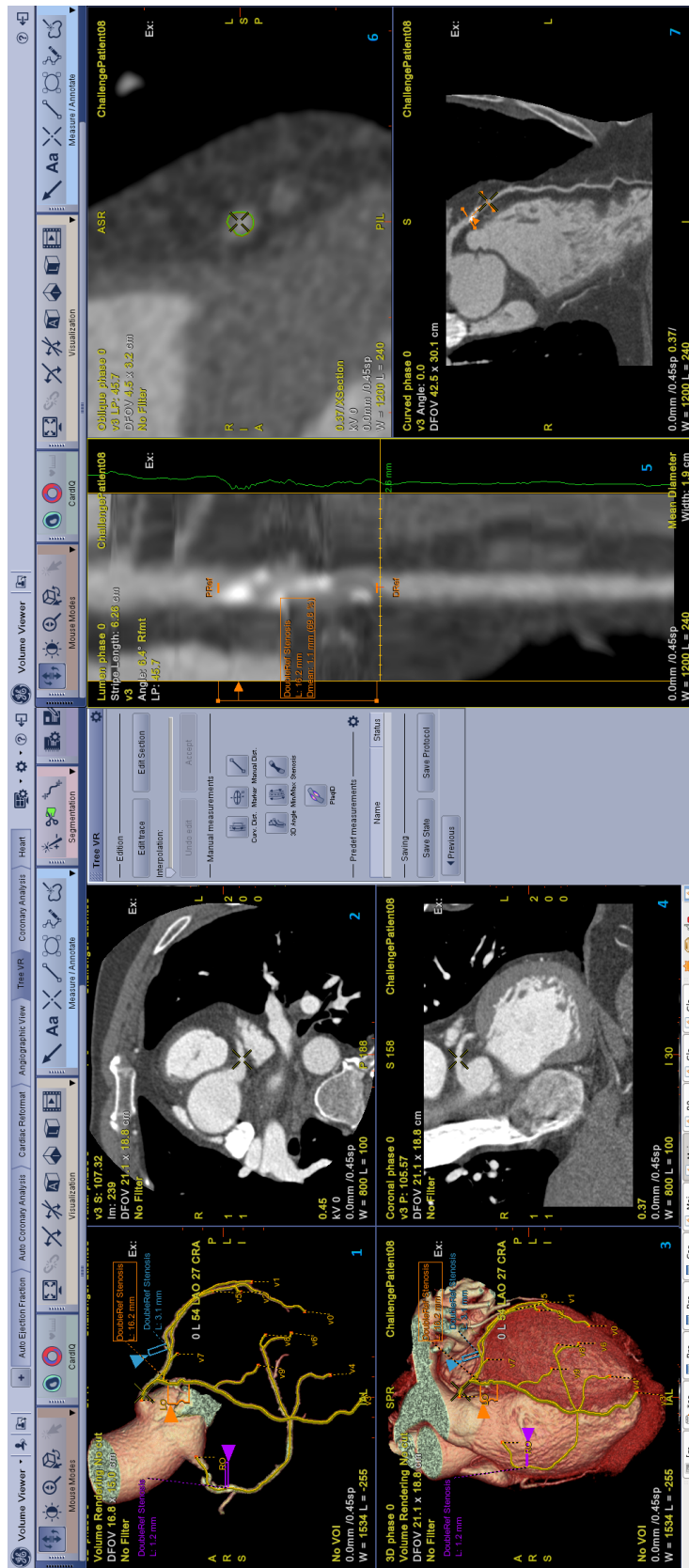


**Figure 3.27** – An overview of the developed automated prototype for coronary stenosis detection. The 3D views of the segmented artery coronary tree and the heart are shown in views 1 and 3. Views 2 and 4 show the coronal and axial views of the original volume. The detected stenosis are marked using different color codes per lesion on the different views. Lumen, cross section and curved views of the diseased vessel branch are displayed on right view ports (5, 6 and 7). The green profile along the vessel lumen shows the mean vessel diameter. The user could switch the displayed profile to visualize the corresponding probability profile. The stenosis degree as well as the stenosis proximal and distal references are detailed on each stenosis bookmark.

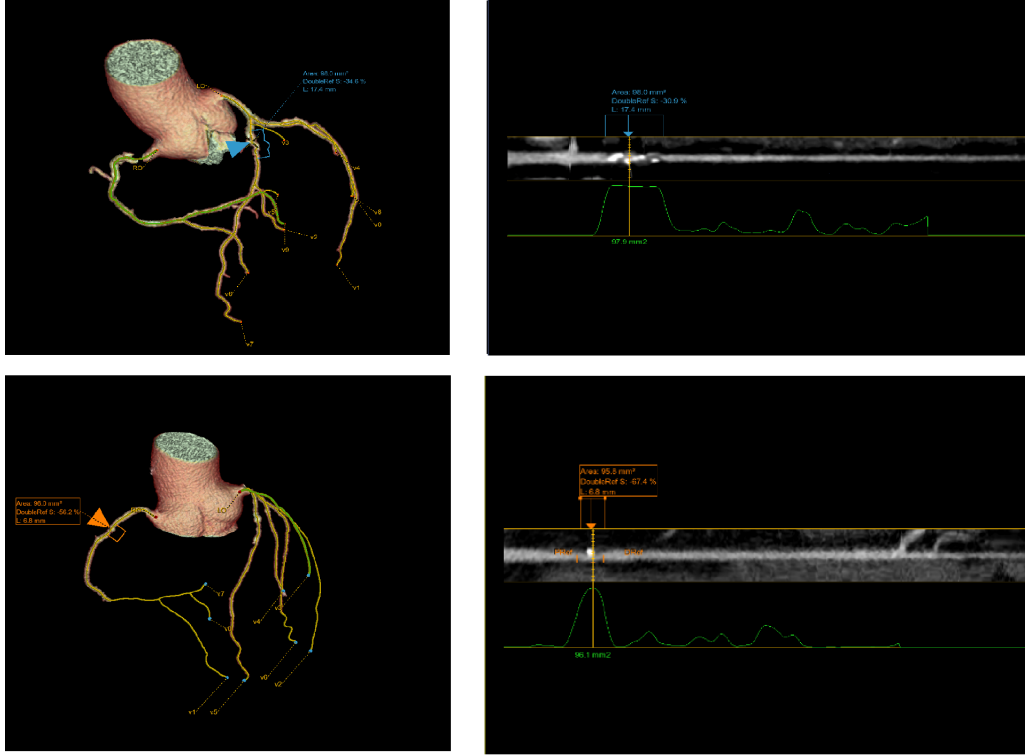


**Figure 3.28** – Automatic Stenosis detection on two diseased branches from two different cases: Patient 08 (First row) and Patient 14 (second row). 3D View of the artery coronary tree with marked detected stenosis (left), Lumen view of a diseased branch showing the probability profile in green with a peak at a severe stenosis (right).

### 3.4 Experiments and Results

The proposed algorithm have been evaluated using the training and testing databases of the publicly available Coronary Artery Stenoses Detection and Quantification Evaluation Framework described in section 1.2. The training database was used to train the Random Forest classifier as well as to optimize the different parameters of the algorithm. The testing database have been used to evaluate the optimized algorithm and get the final performance on unseen data.

The present section is devoted to describe all the required elements for the evaluation of the proposed methodology described in this chapter. First, we specify the configuration and the parameters tuning of the used classifier. Later, we present the evaluation results of the proposed approach on unseen data bases.

### 3.4.1 Parameter Tuning and Experimental Setup

For the parameters optimization steps, we used the leave-one-out cross validation method. It involves keeping one exam of the training database to validate the approach and use the remaining 17 exams to train the classifier. This is repeated until all the 18 exams had been used for validation. This allows to simply and quickly test and optimize the algorithm parameters using only the training database.

The first optimization step of our approach was dedicated to the cylindrical vessel pattern parameters as explained in section 3.2.1. Typical values are  $N_{radius} = 8$ ,  $N_{angle} = 16$  and  $N_{section} = 11$ . These sampling parameters were optimized over the training data set. Optimized values lead to a number of 4 sample points per 2-dimensional sub-region ( a sub-region on the cross section) and a total of 1056 ( $4 \times 24 \times 11$ ) sampling points per pattern. Next, the extracted features, the training database, the classifier parameters and a set of additional parameters are optimized.

#### 3.4.1.1 Features Selection

One important parameter of any learning based approach is the selection of a set of meaningful features that allow to better capture the lesion characteristics to robustly detect all coronary pathologies. The selected features should adequately describe the different types of stenosis that are present in CTA images and be able to generalize easily to other unseen data. Different sets of features have been extracted and tested on the training database as explained in section 3.2. The first tests were dedicated to a restricted number of features including only 7 global intensity-based features (minimum, maximum, mean value, variance, standard deviation, mean average deviation, median average deviation and the central point intensity values). These tests were not conclusive as they lead to high false positive rates and moderate true positive rates. Hence, we used the partitioned cylindrical pattern in order to better capture the presence or not of a vessel lesion. This led to 27 additional local features (12 sub-region means and 15 triangular stats) as detailed in section 3.2. Subsequently, we introduced the histogram-based features with various bins widths. We also added the central point radius value and the hessian intensity computed over different scales, as two geometric features to describe the lumen narrowing induced by the vessel lesion. Afterward, we created an overlap between the different pattern sub-regions by rotating the cylindrical pattern in order to cover all possible lesion positions around the vessel. To increase the robustness of the algorithm against inter-patient variance, we normalized all the intensity based features. Moreover, we extracted two additional longitudinal gradients to detect the lesion along the vessel pattern. The different tests have



## Chapter 3. Learning-based Detection of Severe Coronary Stenoses

been created by sequentially adding and optimizing a new type of features to the previously optimized ones. Finally, the tests are compared based on the online evaluation framework and the best set of features is selected based on the overall average rank (as compared to the CTA and QCA references).

Table 3.3 details the composition of 7 tested features sets. In figure 3.29 and 3.30, we illustrate the obtained classification results using these features sets, optimized over the training data sets. These tests were mainly dedicated to evaluate the two geometric features (mean radius and hessian-based features), the optimization of the histogram width as well as the creation of the overlap and the normalization of the intensity based features.

**Table 3.3** – Composition of 7 tested features sets using the partitioned cylindrical pattern.

Set	Extracted Features
$\mathcal{F}_1$	8 Global intensity features + 37 local features + global histogram of 40 bins + radius
$\mathcal{F}_2$	8 Global intensity features + 37 local features + global histogram of 60 bins + radius
$\mathcal{F}_3$	8 Global intensity features + 37 local features + overlap + global histogram of 40 bins + radius
$\mathcal{F}_4$	8 Global intensity features + 37 local features + overlap + global histogram of 40 bins + radius + hessian intensity
$\mathcal{F}_5$	8 Global intensity features + 37 local features + 2 longitudinal gradients + overlap + global histogram of 40 bins + normalized radius + Normalized intensity features
$\mathcal{F}_6$	8 Global intensity features + 37 local features + 2 longitudinal gradients + overlap + global histogram of 60 bins + radius + Normalized intensity features
$\mathcal{F}_7$	8 Global intensity features + 37 local features + 2 longitudinal gradients + overlap + global histogram of 40 bins + radius + Normalized intensity features

Based on the submitted tests to the online evaluation framework, we concluded that the set  $\mathcal{F}_5$  gives the best classification results on the training data sets. The partitioning of the cylindrical pattern allowed to capture more information about the vessel lesions and hence increased the detection rates. On the other side, the hessian based feature was not conclusive. In fact the use of this feature leads to high false positive per patient rates as shown in figure 3.29.

### 3.4.1.2 Training database creation

As explained in section 3.3.1, different compositions of the training database are possible. In order to determine the best training database, we tested different instances and submitted the classification results using the online evaluation framework. The different subsets are obtained by varying the amount and nature of non pathological samples. First, we created a training data set by considering all the healthy samples (i.e. points, along the coronary vessels of all the training data sets, tagged as non diseased by the observers). This choice is represented

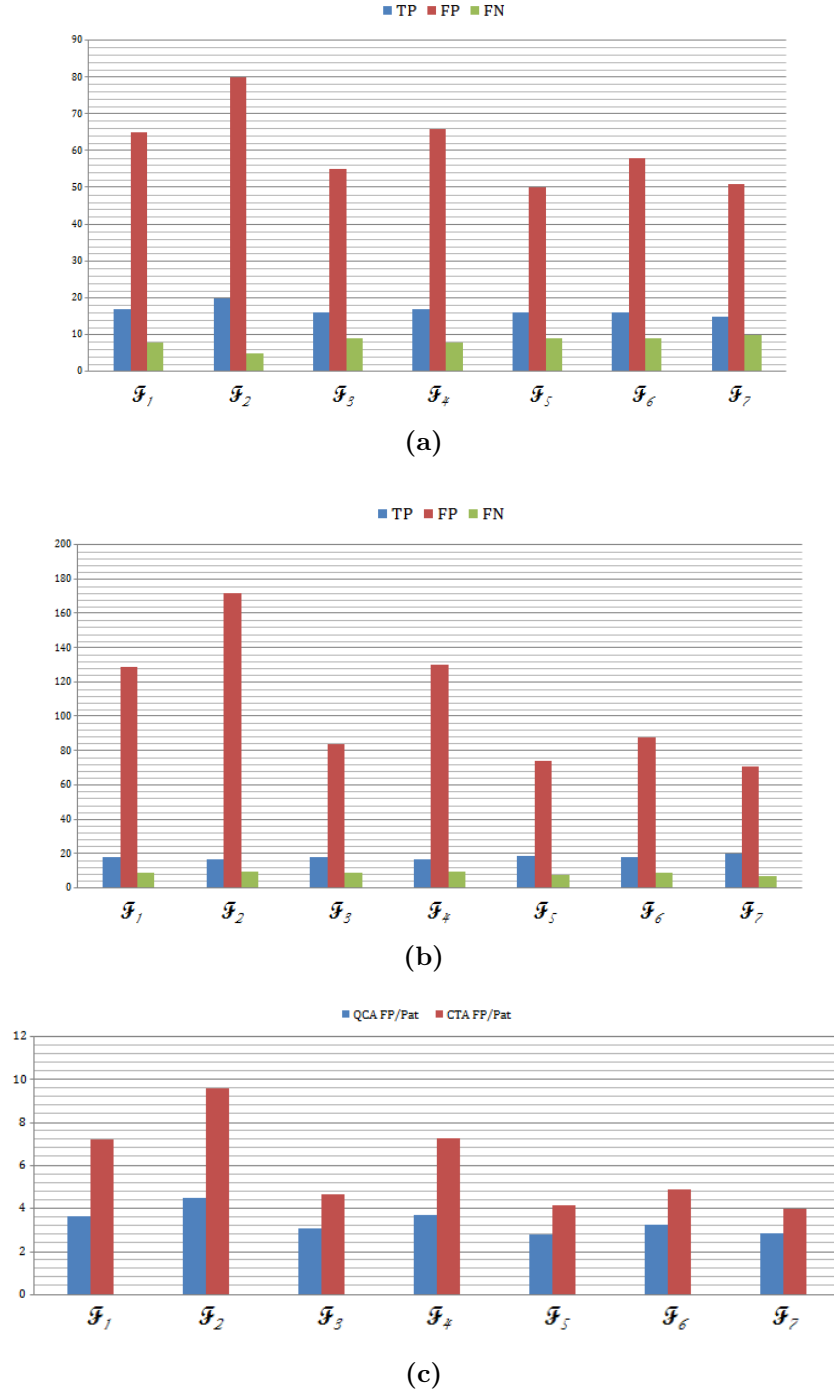


**Figure 3.29** – 7 different sets of features have been extracted over the training data sets. The sets are compared using the per lesion (CTA) and per segment (QCA) evaluations. (a) and (a) shows the QCA and CTA true positives, false positives and false negatives rates. In (c) the false positive per patient rates (compared to the QCA and CTA references) are shown.

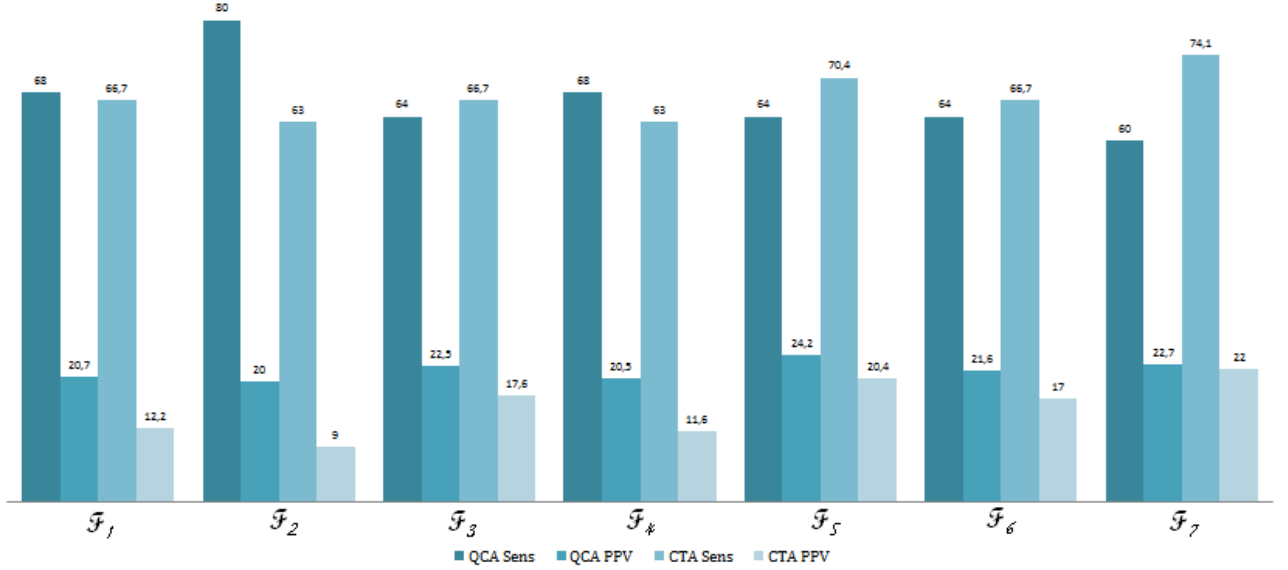


**Figure 3.30** – Sensitivity and PPV values compared to the QCA and CTA references for the 7 sets of features.  $\mathcal{F}_5$  shows the best overall performances.

by the first training database  $S_1$  on figure 3.31. However, the classifier is only supposed to detect severe stenosis (i.e.  $> 50\%$ ). Hence, to efficiently detect such diseases and distinguish between severe and non severe stenosis, the training database should include both of the classes. Therefore, a second training database (subset  $S_2$ ) was created by including only the two classes of diseased points: (1) the severe stenosis and (2) the non severe stenotic points. However, such training dataset is not perfectly representative of non severely stenotic class as it does not contain healthy samples. Therefore, we create a third training database  $S_3$  containing  $N$  points equally selected among healthy and non severe stenotic points. Finally, we considered an ensemble of training databases by including only a number  $N$  of healthy points to learn the non severe stenotic class. We have tested different values of  $N$  to determine the optimal value leading to the better classification of the severe stenosis on the training data sets. Results of  $N = 30$  and  $N = 50$  are presented in figure 3.32 for subsets  $S_4$  and  $S_5$ . Figure 3.33 illustrates the obtained ranks with reference to the four evaluation metrics by the five training subsets compositions.

Based on the comparison of the different results using the previously proposed sets of training, we conclude that the better classification performances are obtained by using the training database  $S_5$ , i.e. composed of 50 healthy samples and including all the severe stenosis.

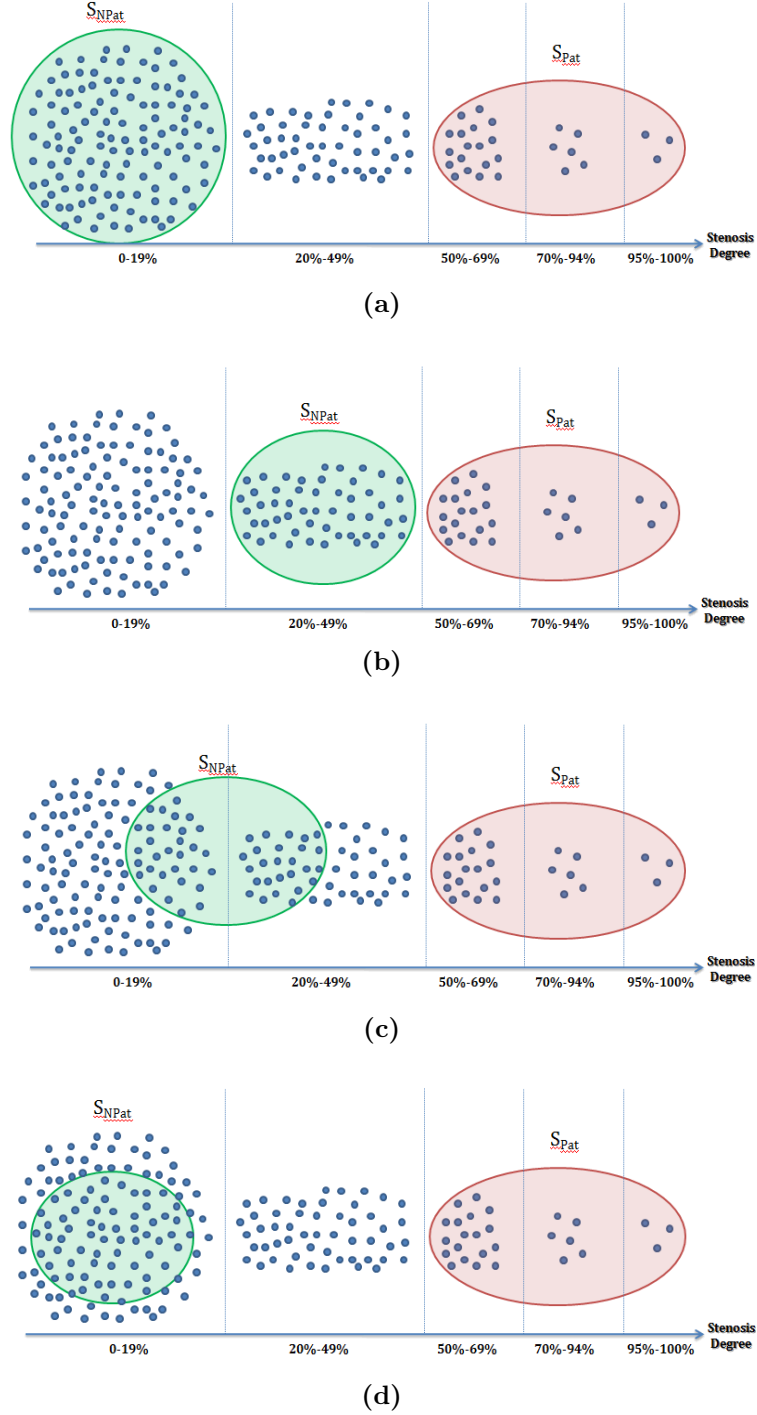


**Figure 3.31** – Composition of different training databases for stenosis detection. (a) All the healthy points are included into the training database with the pathological points ( $S_1$ ). (b) The non pathological class is constructed used only the stenotic points with a degree lower than 50% ( $S_2$ ). (c) A set of N points selected from healthy and non severe stenotic points is used as non pathological samples ( $S_3$ ). Finally (d), a set of N points selected only from the healthy class is selected to designate the non pathological class ( $S_4$  and  $S_5$ ).

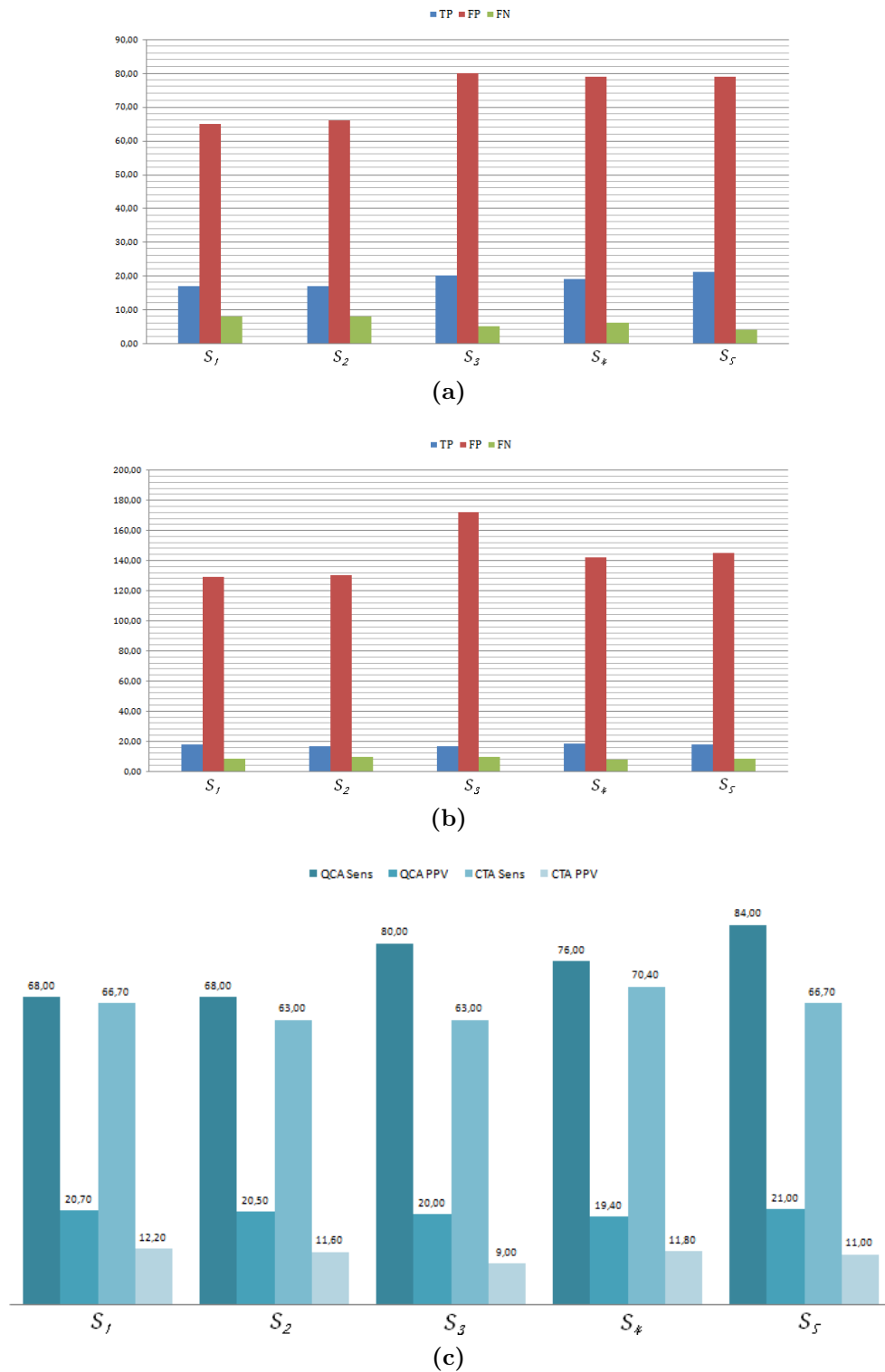


**Figure 3.32** – Comparison of different training databases for stenosis detection: (a) shows the distribution of the segments detected as diseased over the TP, FP and FN classes (i.e. per segment analysis) for different training databases ( $S_1$  to  $S_5$ ). In figure (b) the distribution of the detected lesions (i.e. per lesion analysis), by the proposed approach, over the TP, FP and FN classes is illustrated using the same training databases. The sensitivity and PPV for both the CTA and QCA based analysis for each training database are presented in figure (c).

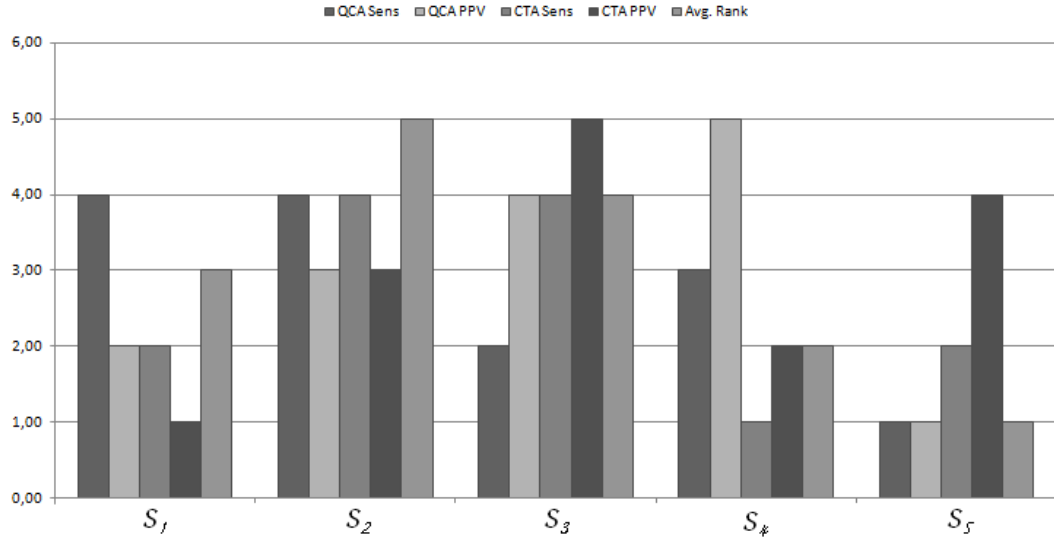


**Figure 3.33** – Obtained ranks by the different training databases. The best overall rank is obtained by subset  $S_5$ .

**Table 3.4** – Random Forest parameters setting

Parameters	Tested values
Number of estimators (i.e. trees) $T$	100, 500, 1000, 1500
Number of features for the split $m$	$\frac{M}{2}$ , $\sqrt{M}$ , $\log_2(M)$
Split function Criterion	<i>Gini function, entropy</i>

#### 3.4.1.3 Random Forest classifier parameters selection

The used implementation of the Random Forest classifier allows to instantiate a classifier with a set of variable parameters. The interface offers a set of 12 tunable parameters. We mainly focused on the optimization of 4 principle parameters: (1) Number of estimators  $T$ , (2) Number of features to consider when looking for the best split at each node  $m$ , (3) The criterion function to measure the quality of a node split and (4) The maximum depth of the trees. The ensemble of tested parameters values for the Random Forest are summerized in table 3.4.

In order to optimize the previous random forest intrinsic parameters, we have used the ROC curves (see section C.1.1.7). Such curves allowed to determine the best set of parameters offering the better performances over the training data sets. In figure 3.34, we illustrate three ROC curves used to optimize the Random Forest classifier parameters. Each curve corresponds to a different set of values of  $T$  (the number of trees in the forest) and the number of features considered at each node split  $m$ . Each curve is obtained by increasing the probability threshold from 0 to 1.

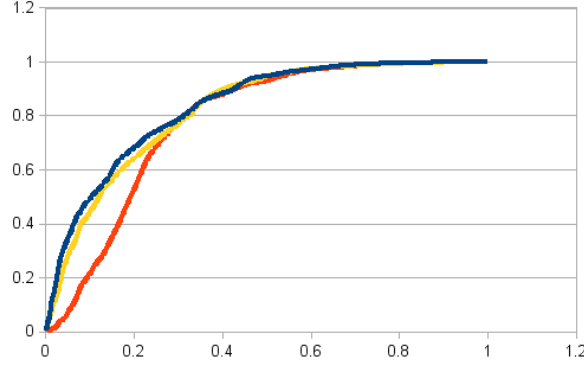


**Figure 3.34** – ROC Curves used to optimize the Random Forest classifier parameters. Each curve corresponds to a set of parameters from table 3.4. Parameters value presented by the blue curve gives the better performance.

We have also compared the overall evaluation results obtained by the online evaluation framework to define the best set of parameters. Figure 3.35 shows the obtained results for five different tested sets of parameters.

Based on the previous tests on the training database, we choose to use the **Shannon Entropy** as a criterion to measure the information gain and quality of each node split [391]. Subsequently, we set  $T$  to **1000** and  $m$  to **sqrt(M)** ( $M$  being the number of all the features used for training the classifier). We choose not to set the depth value of the trees, instead the nodes are expanded until all leaves are pure. These parameters setting is represented by submission  $\mathcal{P}_4$  on figure 3.35.

### 3.4.1.4 Output probability profile processing

The choice of the training database and the classifier's intrinsic parameters is very crucial to determine the performances of the proposed approach. However, there exist additional parameters that affects the classification results. The processing of the output probability is important in order to efficiently extract the stenotic regions as explained in section 3.3.2.1; The output profile is smoothed using a Hann filter. Different smoothing window widths varying from 40 to 400 are tested to optimize this parameter over the training data sets using a cross validation process (see table 3.5). Per segment and per lesion sensitivity and PPV values of the different submissions are shown in figure 3.36. Based on this set of tests, the best classification performances were obtained using a window width of 40.

### 3.3.4 Experiments and Results

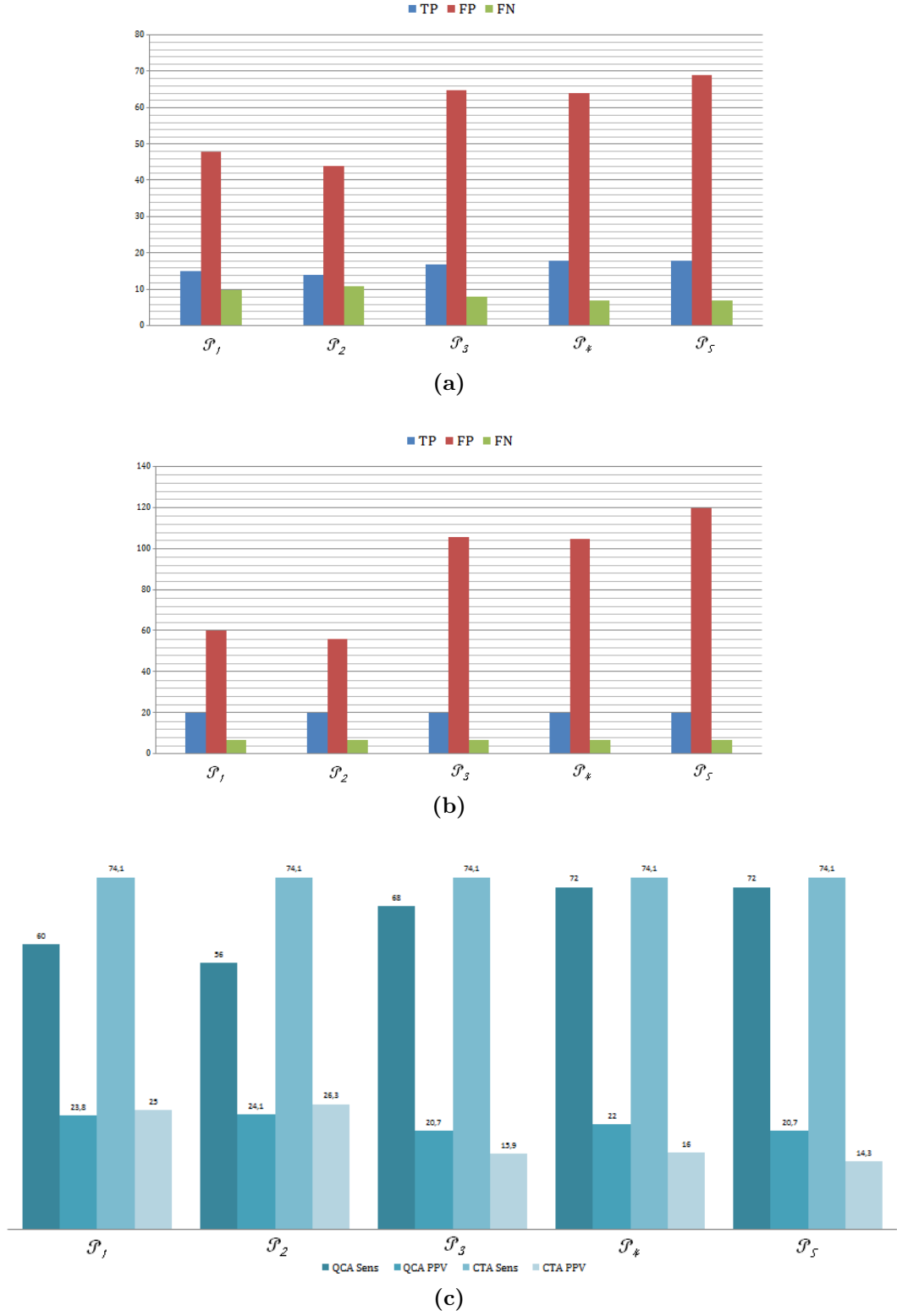


**Figure 3.35** – Optimization of the Random Forest classifier intrinsic parameters over the training data sets. The rates of the per lesions and per segments TP, FP and FN are shown in (a) and (b). The CTA and QCA sensitivity and PPV values are shown in (c).



**Table 3.5** – Random Forest output probability profile smoothing. Variation of the window width and comparison of the classification results over the training database. The overall rank of the submission is modified in order to compare only these three submissions.

	QCA			CTA			Modified Rank
	TP	FP	FN	TP	FP	FN	
$w_{smmoth} = 40$	<b>18</b>	65	<b>7</b>	<b>17</b>	114	<b>10</b>	1
$w_{smmoth} = 100$	17	66	8	<b>17</b>	130	<b>10</b>	2
$w_{smmoth} = 400$	7	<b>28</b>	18	8	<b>38</b>	19	3

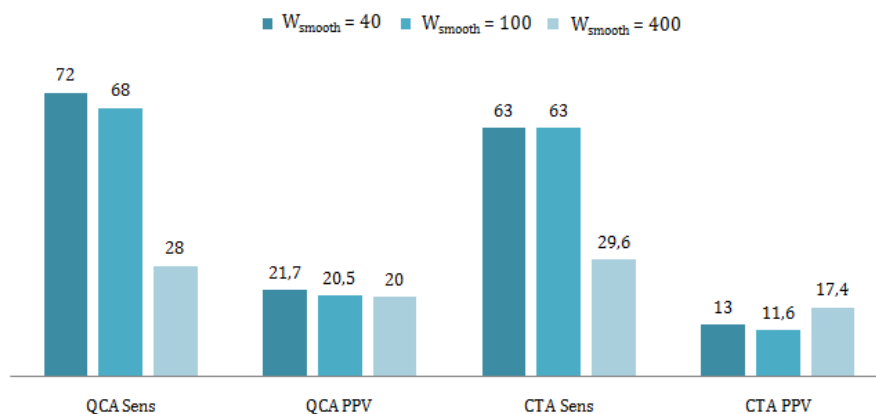


**Figure 3.36** – Severe and non severe stenosis classification performances for three different smoothing parameters. The per lesion and per segment sensitivity and PPV values are presented for the three submissions.

#### 3.4.1.5 Stenosis threshold optimization

Once the optimal smoothing window size has been set, the probability threshold value should be selected in order to extract stenotic regions. The choice of the threshold value is very important as it allows to decide whether a point should be included as a pathological vessel point or not. Hence, we tested different values in order to define the optimal threshold value. We used a leave-one-out cross validation process to test the different values on the training data sets. For each exam, we train the classifier on the remaining 17 exams. The vessel points of the unseen exam are processed using the trained classifier. The output probability profile is then processed for each coronary branch separately and the chosen threshold value is applied to the processed profile in order to flag the stenotic points. Figure 3.37 shows the classification results for different threshold values ranging from 50 to 80 . Submission results are listed with reference to their average ranking.

Based on the previous submissions, the probability threshold value has been set to 50 corresponding to the first threshold  $T_1$  on figure 3.37. However, we observed that such choice gives a relatively high false positive rates. Meanwhile, increasing the threshold values will lead to missing some stenosis. Hence we decided to use a two-threshold based approach in order to robustly detect stenotic regions while reducing false detections.

A set of double threshold values have been tested and their classification results evaluated using the Rotterdam evaluation framework. Obtained results are detailed in figure 3.38. The best performances over the training data sets are obtained by setting  $T_{prob_1}$  to 70 and  $T_{prob_2}$  to 50 (corresponding to the first test).

The choice of the threshold values allows to define the stenotic regions to be flagged (i.e. the extent of the lesion). However, we subsequently need another characteristic of the vessel lesion to be evaluated: its center point. In fact, this point is the only information reported to the evaluation framework. Therefore, we tested two strategies to extract such point as detailed in section 3.3.2.2. Figure 3.39 shows the comparison of the two strategies performances. As illustrated, the maximum probability strategy allows to have a better per lesion detection rates. This is mainly due to the moderate lumen quantification quality that leads to erroneous estimations of the stenosis center.

Hereafter, we report results of the developed approach tested using two different unseen testing databases.



**Figure 3.37** – Optimization of the probability threshold value for stenosis detection. FP, TP and FN rates are shown for both a per segment (a) and a per lesion (b) evaluation for different threshold values. The corresponding sensitivity and PPV values are presented in (c).

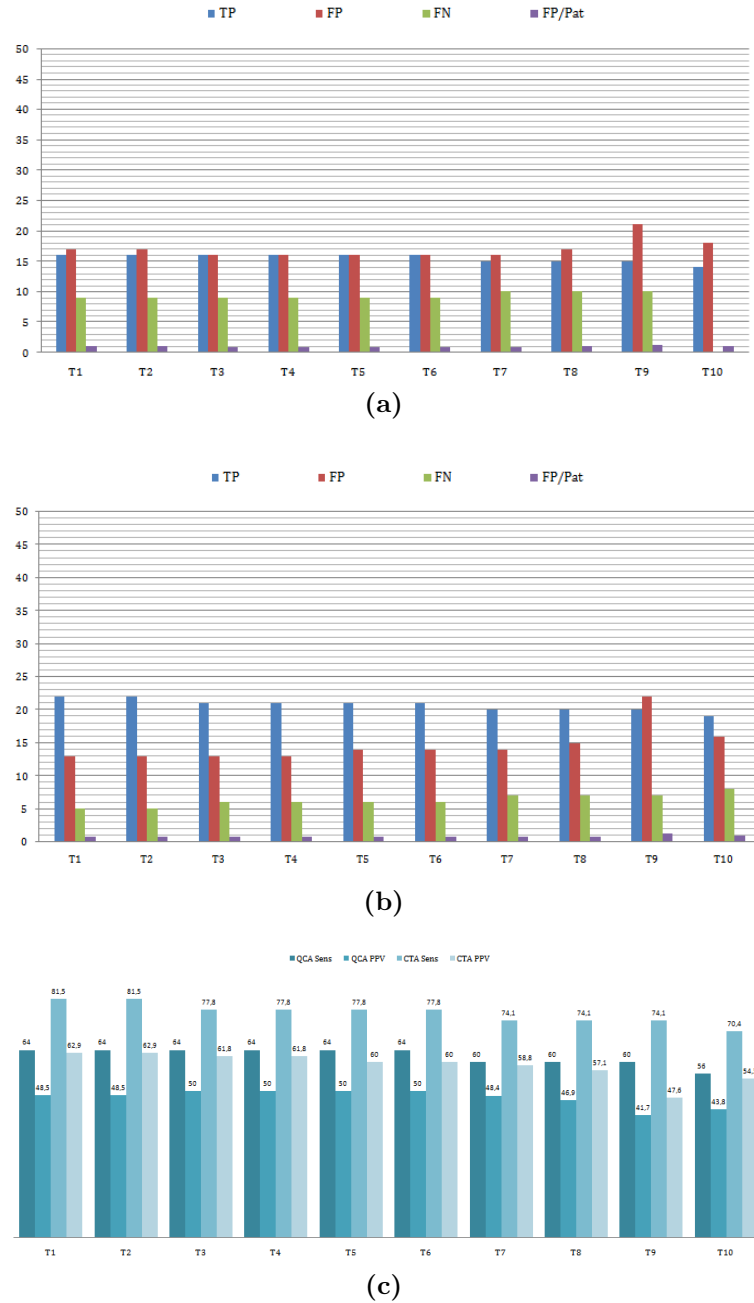
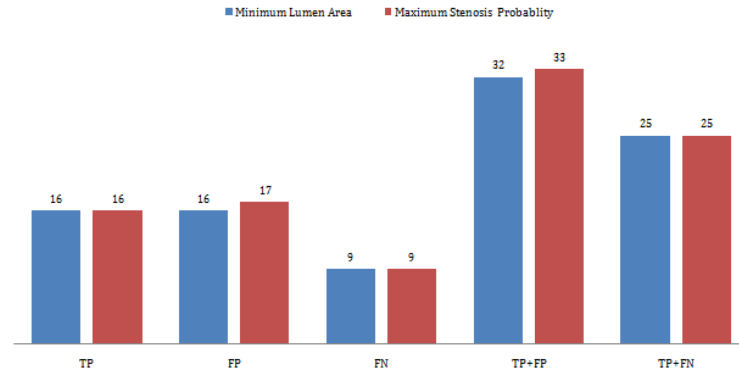
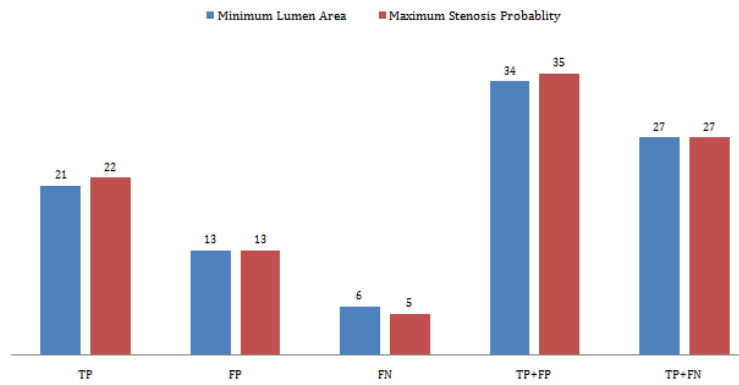


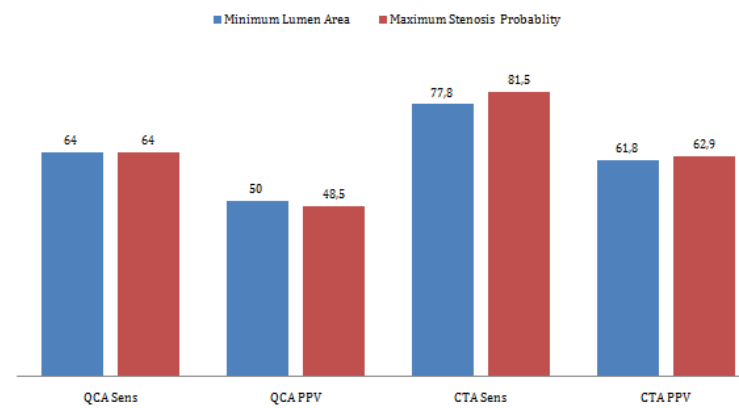
**Figure 3.38** – Stenotic regions detection by using a two-thresholds based approach. FP, TP and FN rates as well as the FP per patient rates, are shown for both a per segment (a) and a per lesion (b) evaluation for different couples of threshold values. The corresponding sensitivity and PPV values are presented in (c).



(a)



(b)



(c)

**Figure 3.39** – Stenosis center extraction strategy selection: FP, TP and FN rates are shown for both a per segment (a) and a per lesion (b) evaluation of both of the strategies. The corresponding sensitivity and PPV values are presented in (c). The maximum probability strategy gives a better classification result.

### 3.4.2 Results

First, we have evaluated the proposed algorithm using the testing database of the Rotterdam Coronary Challenge (section 3.4.2.1). Details about the database and the evaluation framework are given in section 1.2. This first evaluation was lesion- and segment-based allowing to compare the performances of the approach to the work of other teams on the same database. However, the online evaluation framework is restricted to the detection of severe stenosis and rejects any non severe (i.e.  $<50\%$ ) lesion which leads to relatively high false positive rates. Besides, as the evaluation results details are not accessible, we do not have details about the failure cases of the proposed approach. Hence, we decided to evaluate our algorithm separately on a second database in section 3.4.2.2.

#### 3.4.2.1 Evaluation on the Rotterdam Coronary Artery Algorithm Evaluation Framework

Two versions of the proposed approach have been tested using the online evaluation framework. The first version  $V_1$  was published in our work [292] during the SPIE Medical Imaging conference 2014. This version used a single probability threshold value to detect stenotic regions. Afterward, this work was further improved leading to a second version  $V_2$ . The new version was dedicated to reduce the amount of false positives by using a two-threshold based approach. The evaluation results of both of the versions are detailed in tables 3.6, 3.7 and 3.8.

**Table 3.6** – Per segment evaluation results (TP, FP, FN and FP/Pat values) of severe stenosis detection obtained by the two approaches  $V_1$  and  $V_2$  on the training and testing databases of the Rotterdam Coronary Artery Algorithm Evaluation Framework

Database		TP	FP	FN	TP+FP	TP+FN	FP/pat
<b>Training</b>	$V_1$	18	64	7	82	25	3,55
	$V_2$	16	22	9	38	25	1,22
<b>Testing</b>	$V_1$	16	126	12	142	28	4,2
	$V_2$	15	38	13	53	28	1,26
<b>All</b>	$V_1$	34	190	19	224	53	3,95
	$V_2$	31	60	22	91	53	1,25

The first version was able to detect 18 among 25 diseased segments on the training data sets, leading to a QCA sensitivity score of 72%. Second, lesion-based detection rates using CTA references are examined. On the 27 annotated severe stenosis from the 18 training data sets, 20 have been correctly reported by our algorithm which corresponds to a CTA sensitivity of

**Table 3.7** – Per lesion evaluation results (TP, FP, FN and FP/Pat values) of severe stenosis detection obtained by the two approaches  $V_1$  and  $V_2$  on the training and testing databases of the Rotterdam Coronary Artery Algorithm Evaluation Framework

Database		TP	FP	FN	TP+FP	TP+FN	FP/pat
<b>Training</b>	$V_1$	20	105	7	125	27	5,83
	$V_2$	22	21	5	43	27	1,16
<b>Testing</b>	$V_1$	26	200	21	226	47	6,66
	$V_2$	19	46	28	65	47	1,53
<b>All</b>	$V_1$	46	305	28	351	74	6,35
	$V_2$	41	67	33	108	74	1,39

**Table 3.8** – Per segment and Per lesion evaluation results (Sensitivity and PPV values) of severe stenosis detection obtained by the two approaches  $V_1$  and  $V_2$  on the training and testing databases of the Rotterdam Coronary Artery Algorithm Evaluation Framework

Database		QCA (per segment)		CTA (per lesion)	
		Sens. (%)	P.P.V. (%)	Sens. (%)	P.P.V. (%)
<b>Training</b>	$V_1$	72	22	74,1	16
	$V_2$	64	42,1	81,5	51,2
<b>Testing</b>	$V_1$	57,1	11,3	55,3	11,5
	$V_2$	53,6	28,3	40,4	29,2
<b>All</b>	$V_1$	64,2	15,2	62,2	13,1
	$V_2$	58,5	34,1	55,4	38

74.1% (Table 3.8). Meanwhile, we obtained 16% for CTA PPV score and 22% QCA PPV score. Subsequently, evaluation have been performed using 30 unseen CTA data. The algorithm was able to correctly detect 16 among 28 diseased vessel segment, corresponding to 57.1% of CTA sensitivity. 26 lesions among 47 annotated stenosis have been reported by the evaluated version which leads to a CTA sensitivity of 55.3%. Similarly to the training data sets, moderate PPV values have been obtained with compared to QCA and CTA references (11,3 % and 11,5%). An analysis of the reported false positive types allowed to define some strategies in order to avoid such high amounts of false positives (126 false positives for the per segment evaluation and 200 for the per lesion one, on the testing data base). As a result, we submitted a second classification result using the second version (based on the double probability threshold).

The proposed new version of the algorithm is able to detect 16 over the 28 diseased segments of the training data base (i.e. a sensitivity of 64%), and 22 among the 27 annotated severe stenosis (i.e. a sensitivity of 81.5%). On the testing data sets, a sensitivity of 53,6% has been obtained compared to QCA references. The per lesion sensitivity value was of 40,4%. We notice that using the new strategy of setnosis flagging, we were able to reduce the false positive rates. For instance, for a per lesion evaluation on the overall database, the new approach miss-classifies only 67 false positive lesions against 305 using the old approach. In fact, the current version offers better PPV values compared to the one published in our work previous work [292]. Compared to QCA, a PPV value of 34.1% have been performed overall the data sets. Meanwhile a PPV of 38% was obtained with reference to CTA ground truths (Tables 3.8).

**Table 3.9** – Evaluation results of the three proposed methods on severe stenosis detection compared to the observers’ consensus.

Method	QCA				CTA			
	TP	FP	FN	TN	TP	FP	FN	FP/pat
CTA consensus	23	21	5	345	47	0	0	0
Observer 1	24	36	4	330	39	25	8	0,8
Observer 2	21	20	7	346	33	8	14	0,3
Observer 3	18	24	10	342	31	21	16	0,7
Melki et al. [291]	13	94	15	272	20	196	27	7
Melki et al. [292]	16	126	12	240	26	200	21	6,6
$V_2$	15	38	13	328	19	46	28	1,5

Compared to our first work on automated stenosis detection published in [291], this prototype presents more interesting evaluation results on the same data sets as shown in table 3.9. The new version of the prototype shows a better FP per patient score as compared to the



## Chapter 3. Learning-based Detection of Severe Coronary Stenoses

previous ones (only 1.5 FP/Patient against more than 6 FP/Patient for the older prototypes). This result is important as it indicates that the obtained false positive rates are still reasonable for a clinical use of the prototype.

Tables 3.10 and 3.11 summarize the results of the different works that have been submitted and evaluated using the online evaluation framework on the testing database and the overall database (testing+training). The proposed approach ranked fourth among the 16 tested approaches. Based on these results, we can clearly notice that our approach achieved state of the art performances. For a per segment basis, our approach presented a better sensitivity value than the work of Kitamura et al. [217] and the same as Cetin and Unal [80]. In terms of PPV, we obtained a better PPV value than the works of Cetin and Unal [80] and Lugauer et al. [271]. Similarly, for the per lesion evaluation, our work offers a better PPV value than both of the previous works.

**Table 3.10** – Results of severe stenosis detection of the Rotterdam Coronary Challenge: comparison of the 16 submitted methods. Evaluation was performed on the 30 testing data sets.

Method	Cat.	QCA				CTA				Avg. rank
		Sensitivity		PPV		Sensitivity		PPV		
		%	Rank	%	Rank	%	Rank	%	Rank	
CTA Consensus	Min User	82,1	2	52,3	1	100	1	100	1	1,2
Observer2	Min User	75	3	51,2	2	70,2	3	80,5	2	2,5
Observer1	Min User	85,7	1	40	5	83	2	60,9	3	2,8
Observer3	Min User	64,3	5	42,9	4	66	4	59,6	4	4,2
Kitamura et al.[218]	Automatic	35,7	15	32,3	6	51,1	7	33,3	5	8,2
Lugauer et al.[271]	Automatic	60,7	6	24,6	8	46,8	11	25	12	9,2
Cetin et al. [81]	Min User	53,6	10	19,2	12	53,2	6	26	10	9,5
Our Appraoch	Automatic	53,6	10	28,3	7	40,4	14	29,2	8	9,8
Lugauer et al.[272]	Automatic	53,6	10	22,1	11	48,9	10	27,7	9	10
Mohr et al. [305]	Automatic	57,1	7	14,4	14	51,1	7	15,7	14	10,5
Melki et al. [292]	Automatic	57,1	7	11,3	18	<b>55,3</b>	5	11,5	15	11,2
Wang et al. [444]	Automatic	25	17	<b>50</b>	3	10,6	20	<b>33,3</b>	5	11,2
Eslami et al. [135]	Min User	<b>67,9</b>	4	9,4	19	51,1	7	4	19	12,2
Duval et al. [131]	Automatic	57,1	7	12,2	16	42,6	12	7,6	17	13
Broersen et al. [63]	Automatic	25	17	18,9	13	27,7	16	31	7	13,2
Shahzad et al. [389]	Min User	28,6	16	24,2	9	21,3	17	23,3	13	13,8
Öksüz et al. [333]	Min User	21,4	19	22,2	10	17	18	25,8	11	14,5
Melki et al. [291]	Automatic	46,4	14	12,1	17	42,6	12	9,3	16	14,8
Lor and Chen [265]	Min User	50	13	13,9	15	31,9	15	3	20	15,8
Flórez Valencia et al. [141]	Min User	17,9	20	8,5	20	14,9	19	4,8	18	19,2

### 3.3.4 Experiments and Results

**Table 3.11** – Results of severe stenosis detection of the Rotterdam Coronary Challenge: comparison of the 16 submitted methods. Evaluation was performed on the 48 training and testing data sets.

Method	Cat.	QCA				CTA				Avg. rank
		Sensitivity		PPV		Sensitivity		PPV		
		%	Rank	%	Rank	%	Rank	%	Rank	
CTA Consensus	Min User	73,6	3	56,5	2	100	1	100	1	1,8
Observer2	Min User	75,5	2	57,1	1	74,3	3	77,5	2	2
Observer1	Min User	79,2	1	43,3	4	86,5	2	59,3	4	2,8
Observer3	Min User	58,5	11	50,8	3	64,9	5	64	3	5,5
Cetin et al. [81]	Min User	60,4	9	28,3	10	<b>67,6</b>	4	37	6	7,2
Kitamura et al.[218]	Automatic	47,2	14	<b>41,7</b>	5	60,8	7	36,3	7	8,2
Our Appraoch	Automatic	58,5	11	34,1	9	55,4	9	<b>38</b>	5	8,5
Lugauer et al.[271]	Automatic	62,3	6	27,5	11	54,1	11	26	11	9,8
Lugauer et al.[272]	Automatic	60,4	9	27,4	12	59,5	8	30,3	10	9,8
Melki et al. [292]	Automatic	<b>64,2</b>	4	15,2	18	62,2	6	13,1	15	10,8
Mohr et al. [305]	Automatic	<b>64,2</b>	4	18,7	15	54,1	11	16,8	14	11
Duval et al. [131]	Automatic	62,3	6	15,6	16	55,4	9	10,7	16	11,8
Shahzad et al. [389]	Min User	37,7	16	38,5	6	27	17	32,8	9	12
Broersen et al. [63]	Automatic	30,2	18	26,7	13	33,8	15	35,2	8	13,5
Wang et al. [444]	Automatic	32,1	17	36,2	8	18,9	19	24,1	12	14
Eslami et al. [135]	Min User	62,3	6	11,9	19	47,3	13	4,2	19	14,2
Öksüz et al. [333]	Min User	28,3	19	36,6	7	<b>14,9</b>	20	21,2	13	14,8
Melki et al. [291]	Automatic	52,8	13	15,2	17	44,6	14	8,9	17	15,2
Lor and Chen [265]	Min User	47,2	14	20,2	14	31,1	16	<b>4</b>	20	16
Flórez Valencia et al. [141]	Min User	<b>20,8</b>	20	<b>9,8</b>	20	21,6	18	5,5	18	19

**Table 3.12** – (Semi-) Automated severe stenosis detection performance of the 16 public methods submitted to the evaluation framework.

	QCA Sen	QCA PPV	CTA Sen	CTA PPV
Mean	44,42	20,23	37,91	19,41
Standard deviation	16,13	10,59	15,14	11,12
Minimum	17,9	8,5	10,6	3
Q1	27,7	12,175	26,1	8,875
Median	51,8	19,05	42,6	24,15
Q2	57,1	24,3	51,1	28,075
Maximum	67,9	50	55,3	33,3

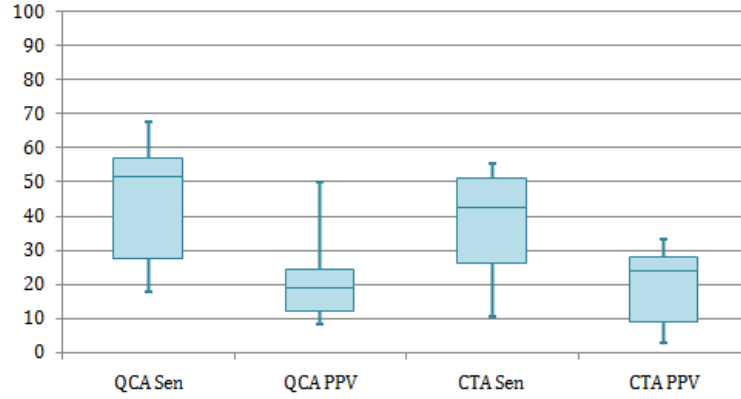


**Figure 3.40** – Sensitivity and PPV values distribution as compared to QCA and CTA reference standards.

When analyzing the different proposed methods, we can state that there exists no approach that managed to obtain high score with reference to the 4 criteria. In fact, methods that obtained the best PPV values (e.g. [Wang and Liatsis \[445\]](#)), presented the lowest sensitivity values, with reference to table 3.10. Similarly, methods that were scored the best with reference to the sensitivity rate, obtained lower PPV values (e.g. [Eslami et al. \[135\]](#)). The best approach was the one that managed to get moderate values for the four scores, i.e. the work of [Kitamura et al. \[217\]](#).

Figure 3.40 shows the distribution of the obtained sensitivity and PPV scores per comparison to QCA and CTA references, on the testing data sets. Clearly, all the automated methods provides better detection rates as compared to QCA than CTA references. This is mainly due to the fact that a method could correctly detect a pathological segment while missing the exact lesion location. Lower CTA scores are mainly explained by the fact that giving the exact location and degree of the detected stenosis is challenging when using CTA images. A stenosis could be missed only because the method provides a center that does not within the range of the reference standard which could explain the relatively low sensitivity CTA scores. The reported stenosis will also be considered as a FP. Besides, if the method reports a stenosis with a degree slightly lower than 50%, the stenosis will be classified as a FP. Which explains some of the false positive detections reported by the automated methods.

However, even if the proposed approach seems to provide good PPV values compared to other methods, we was interested by explaining such moderate rates. In fact, an analysis of the reported false positives by our algorithm on the training data sets showed that these low scores can be attributed to different reasons. First, around 15% of false positives are located in branch bifurcation area. It is mainly due to the fact that the cylinder pattern direction

in that case is not precise enough and thus the ROI sometimes overlaps with other vessel surrounding structures. Second, nearly 23% of reported false positives are located at distal parts of coronaries where the lumen quantification fails and leads to erroneous cylinder patternâ€™ radius that exceeds the vessel one. Besides, the quality of the CT data became too poor at distal segments and hence affect the detection of vessel lesions. In the two previous cases, we extract features outside coronaries, which leads to classification errors. Moreover, 32% of false positives values are in fact mild and moderate stenosis ( $< 50\%$  narrowing), classified by our method as true positives while the framework rates them as false positives. The addition of an accurate lumen narrowing quantification step on each stenosis reported by the algorithm would help to better discriminate severe and non-severe stenoses. Finally, the proposed approach seems to merge close stenosis in one single lesion (about 10%). Hence, the reported stenosis center does not correspond to a stenosis center reported by the observers. Such error leads also to some false negatives. Based on this analysis, it appears that only the remaining 20% of the reported false positives are due to the a miss-classification by our algorithm that could be related to the centerline quality. We can thus consider that the PPV for both CTA and QCA evaluation can be improved by handling bifurcations and distal segments separately and by adding a further step to discard non-severe stenoses based on a robust quantification step.

Several reasons could also explain the obtained sensitivity results by the proposed methods. The first limitation that we have noticed, is the vessel centerline quality. In fact, all the proposed algorithms depend on the provided centerlines. If a diseased vessel is missing, the approach would not be able to detect it. Moreover, our approach is based on the hypothesis that the given centerline is well centered at the vessel lumen to be able to correctly capture the vessel wall lesions. However, for some vessel segments, the centerline were biased by the presence of a lesion. In fact, automated coronary tracking is a very challenging task due to the relatively small size of these vessels. Therefore a correction step of the automatically extracted centerlines is mandatory to ensure that all the centerlines are correctly located at the vessel lumen center.

Moreover, we have to mention that the three observers performance for coronary stenoses detection and quantification as compared to CTA reference standard should be interpreted with caution. In fact, as the reference standards was derived from a consensus of these three readers, their performance can be biased to their advantages. Therefore we cannot fairly compare the submitted methods to the performance of the three observers. Instead, to compare the automated detection of stenosis to a manual annotation based on a CTA reference standard, the manual CTA detection should be obtained from a different observer than the ones involved in the consensus reading.

Besides, the evaluation framework does suffer from a set of limitations that affect the final results obtained by the different methods. First, as we can state by examining the scores of the three observers, there exists a clear incoherence between QCA and CTA references. In fact, the CTA consensus is not perfectly in agreement with the QCA reference standard. This could be explained by two major factors; First, the consensus is obtained based on the observation of three independent observers, and is hence subject to inter-observers variability. Second, there exists some detection and/or quantification mismatches between the two modalities. A severe stenosis might be easily detectable in CCA modality but not visible using CTA images due to their limited resolution. Besides, using CCA, a moderate stenosis can be over estimated and hence classified as a severe stenosis, for instance by using wrong references to estimate the QCA stenosis degree. Reversely, a stenosis might be overestimated using CTA modality, which may occur due to a booming or motion artifact, while the corresponding segment does not present any real severe lesions when inspected using CCA images. Such mismatches between the two modalities makes challenging to get high detection scores as compared to QCA references, since all the proposed approaches use CTA data to extract the lesions.

Second, another limitation of the evaluation framework is the stenosis matching procedure between the automatically detected stenosis and the references standards. To evaluate the detection performance of the approach, we have to report only the stenosis location of the center, generally corresponding to the maximum narrowing along the detected lesion. No precisions are given about the procedure to extract such point by the organizers. Moreover such point definition depends on the lumen quantification quality as we need the lumen radii value to determine the maximum narrowing. Hence, this may result in mismatches between the stenosis center detected by the method and the reference standard; Even if the corresponding lesion have been detected by the method, if the reported stenosis center does not lie within the range of the reference standard, it will be classified as a false positive and the reference standard as a false negative. Moreover, if the method provides a large lesion while the reference standard indicates a series of smaller stenosis (at the same vessel), there will be mismatch. As explained in [215], in the best case, only one of the reference stenoses will be correctly matched, if the provided center point lies within the range of one of the small reference stenoses. Therefore, we believe that the evaluation framework could be modified in order to include a better matching procedure. A slice based evaluation seems to be more robust in order to determine whether a method is able to correctly detect the annotated lesions or not. As shown in figure 3.41, the evaluation could be performed by considering a per slice evaluation procedure. As a result, the detection method provides a series of slices corresponding to the detected stenosis and the framework matches each slice with the reference standards. Such process is more precise than

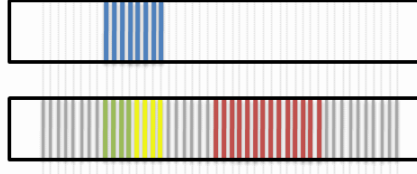


**Figure 3.41** – A slice-based evaluation scheme: Blue slices refers to the reference standard annotated by the observers. True Positive slices (reported by the method) are marked in green while false negative ones are depicted in yellow. False positive detections are marked in red and true negative slices (non diseased) are depicted in grey.

a center point based one.

An additional limitation of the evaluation framework is the use of a hard threshold value to discriminate a severe stenosis from a non severe one. In fact, the observers have used hard classification of the detected lesions into five categories depending on their stenosis degree. However, an automated method may grade a lesion as a stenosis of 49%, while the observers grades the same lesion as being moderate and the QCA reveals a stenosis degree of 52%. As a result, the corresponding approach will be penalized and the corresponding lesion will be classified as a FN, although the grade computed by the approach is close to the reference standards' one. In fact, stenosis grading using CTA is subject to a margin of error as the modality resolution is limited at narrowed vessels. Besides, a stenosis grade could vary depending on the selection of healthy landmarks. Hence, it is difficult to differentiate between a 45 % and 50 % stenosis degree. A solution would be to use more flexible categories by adding a margin error of 5% to each category border, so that a method would not be penalized while missing or reporting borderline stenoses.

### 3.4.2.2 Evaluation on a GE database

Additionally to the Rotterdam testing database, the final version of the previous learning based stenosis detection algorithm has been tested on clinically relevant CTA data sets. The new unseen database  $\mathcal{B}_1$  is composed of 31 CTA images coming from GE Healthcare's LightSpeed VCT (64-slice Volume Computed Tomography) and GE's Discovery CT750 HD (64-slice High Definition scanner). The images have been analyzed by different observers and all present stenoses have been annotated manually. For each CTA data, the main 17 segments are inspected and the detected lesions are reported. For each lesion, the observer reports the type (calcified, soft, mixed) and grade category of the stenosis (Normal, Mild, Moderate, Severe or Occluded). Thereby, a ground truth database was generated containing the position, type and grade of every lesion present in the CTA images.

**Table 3.13** – Lesion distribution within the two testing databases.

	Lesion Type					Stenosis Degree		
	Calcified	Soft	Mixed	Stent	All	Non Severe	Severe	All
$B_1$	39	19	42	9	100	54	34	88
$B_2$	18	12	42	0	72	40	32	72

The 31 CTA images with 193 annotated coronary artery branches were used for a first set of evaluation. The evaluation was performed per Branch and Patient basis. A branch is considered as true positive if it was detected by the method and it contains at least one lesion. A False negative branch is a diseased branch missed by the algorithm. Similarly, a TP patient is a patient having at least one lesion and detected by the automated method. This testing database contains 119 diseased vessels with 100 lesions (see table 3.13). Among the 100 lesions, only 88 presented a visible lumen narrowing (i.e. a lumen stenosis): 54 are non severe stenosis and 34 are severe one. The remaining 12 lesions are associated to a positive remodeling of the vessel wall and present hence no stenosis. The evaluation of the proposed method has been performed on the 17-AHA coronary segments, if they have been correctly segmented and tracked by the automated segmentation and tracking tool. The detection results are summarized in table 3.14. On the 119 diseased branches, 86 were correctly detected leading to sensitivity of 72.2%. The method detected only 9 false positives corresponding to a PPV value of 90.5%. For a per patient basis, the proposed approach has a sensitivity of 84% and a PPV of 100%.

**Table 3.14** – Per Branch and Per patient evaluation results using  $B_1$

	TP	FP	FN	TN	Sensitivity (%)	Specificity (%)	PPV (%)
<b>Branch Based</b>	86	9	33	65	72.20	87.80	90.50
<b>Patient Based</b>	21	0	4	6	84	100	100

Subsequently, in order to get a more precise evaluation of the proposed approach, we performed a segment-based evaluation using a sub-database  $B_2$  of  $B_1$  defined only of 11 CTA images. Therefore the algorithm was applied to 92 automatically extracted coronary artery centerlines. From these vessels, a total of 25 was healthy and 67 contained one or more lesions. The automatically extracted vessels contained a total of 98 segments with 35 diseased segments and 63 healthy ones. The selected CTA data sets contains only lesions inducing a lumen narrowing (see table 3.13). In total, 72 stenotic lesions were present on the segmented vessels where 18 of them were calcified plaques, 12 were soft plaques and 42 were mixed plaques. Applied to

$B_2$ , the method was able to detect 27 among the 35 diseased segment which corresponds to a sensitivity of 77.14%. 5 segments have been reported by the algorithm as diseased while they contain no lesions. This results of a specificity of 92% and a PPV value of 84.38%. As with the previous database, the vessel-based and patient-based detection rates were examined. From the 67 pathological vessel branches, 47 have been properly classified by the method. Only one branch was wrongly detected as diseased. Hence, obtained sensitivity and specificity values are 70.15% and 96.00% respectively. Additionally, 8 of the 11 diseased patients was correctly classified. This amounts to an overall correct detection rate of 72.0% and a PPV of 100%. Results are summarized in table 3.15.

**Table 3.15** – Per segment, Per Branch and Per patient evaluation results using  $B_2$

	TP	FP	FN	TN	Sensitivity (%)	Specificity (%)	PPV (%)
<b>Segment Based</b>	27	5	8	58	77,14	92,06	84,38
<b>Branch Based</b>	47	1	20	24	70,15	96,00	97,92
<b>Patient Based</b>	8	0	3	0	72,7	100	100

Even though the whole coronary tree is analyzed for the lesion detection task, unlike other state of the art methods [207, 208, 303, 355] that focus only on the three major coronary arteries, classification times are still low. Performing CAD on the automatically extracted coronary tree takes around 5 seconds on a standard PC hardware. This time is clearly much lower than the one required by a clinician to manually annotate the different vessels. The whole processing chain, together with the heart segmentation and coronary tree extraction and tracking, takes about 20 to 30 seconds to generate the final diagnosis. The processing time may vary with the size of the cardiac CT dataset and the complexity of the extracted coronary tree. This time may be further optimized by using a C++ code for the classification task instead of the Python one. In fact, the trained classifier being serialized, it might be reloaded using a C++ code embedded in the voxtool library. The whole proposed chain is fully automated, requiring no user interaction to generate the final results. Examples of the quality of the detection results and the accuracy of the approach are presented in figures 3.42, 3.43, 3.44 and 3.45.



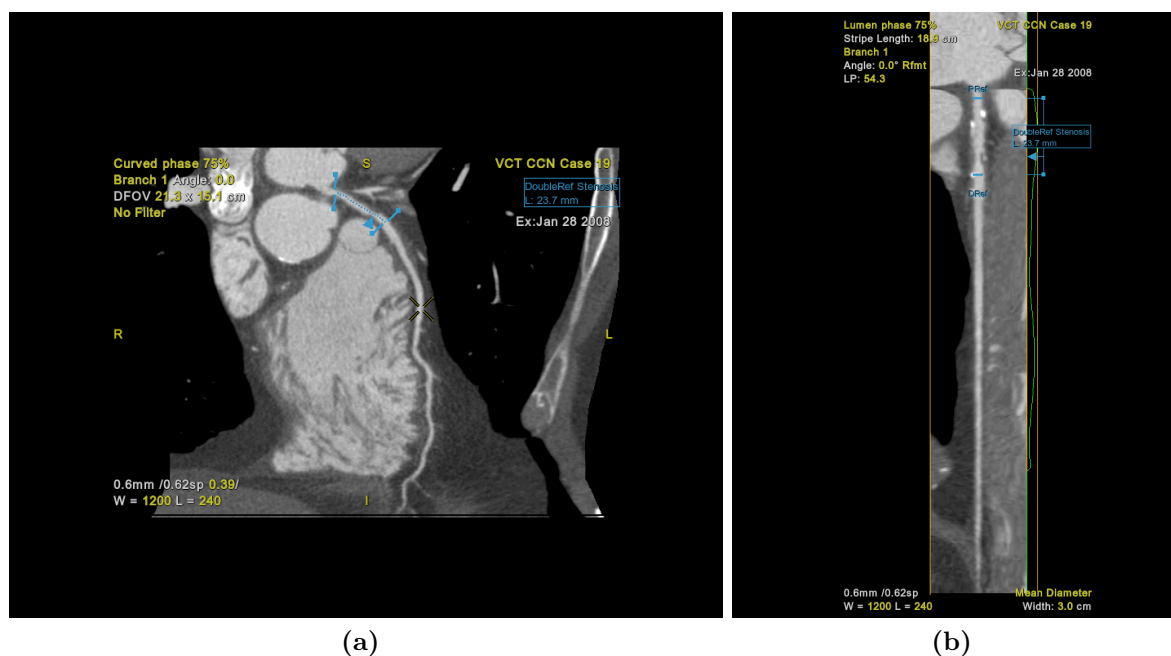


**Figure 3.42** – Coronary lesions detection results on a diseased LAD branch showing soft and calcified plaques. Detected lesions are marked using blue bookmarks. The proximal and distal references as well as the minimum lumen narrowing are marked.

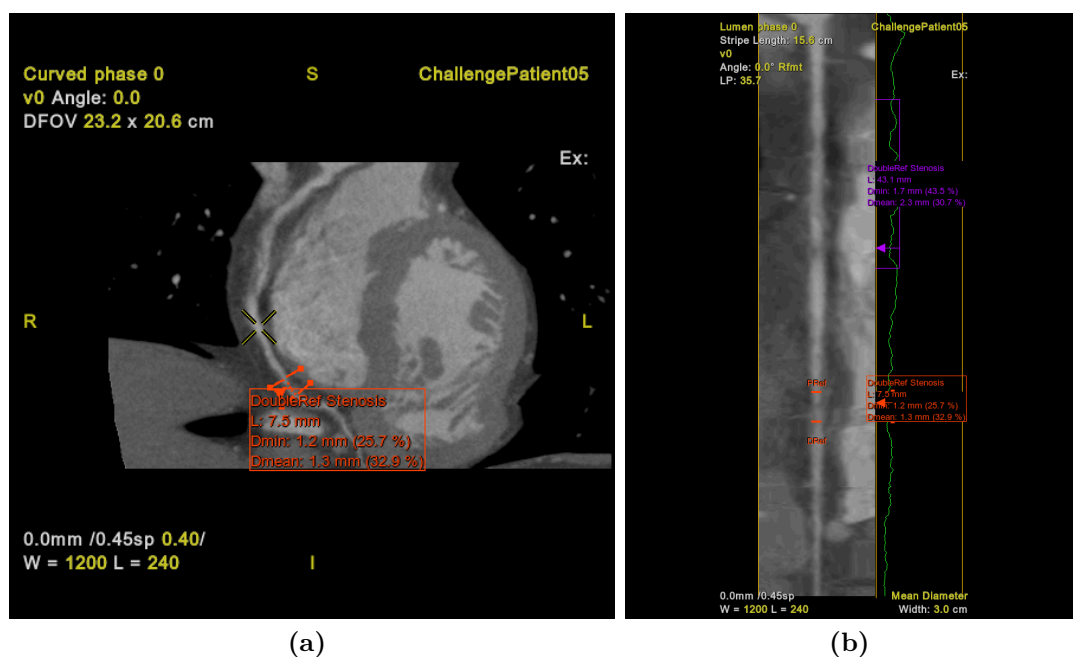


**Figure 3.43** – Coronary lesions detection results on a diseased RCA branch showing soft plaques. Two different lesions are detected and are marked in purple and red bookmarks. The proximal and distal references as well as the minimum lumen narrowing of each lesion are shown.

### 3.3.4 Experiments and Results

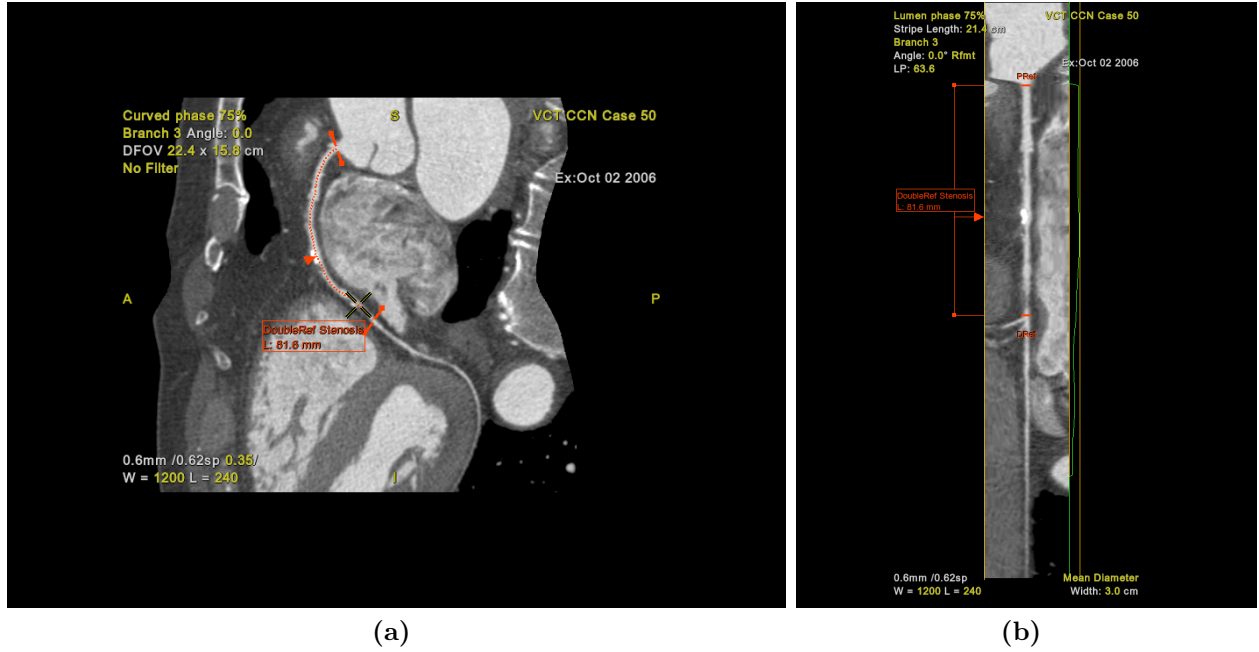


**Figure 3.44** – Coronary lesions detection results on a diseased RCA branch with mixed, calcified and soft plaques. The different lesions are detected and are marked using a red bookmark. The proximal and distal references as well as the minimum lumen narrowing of each lesion are shown.

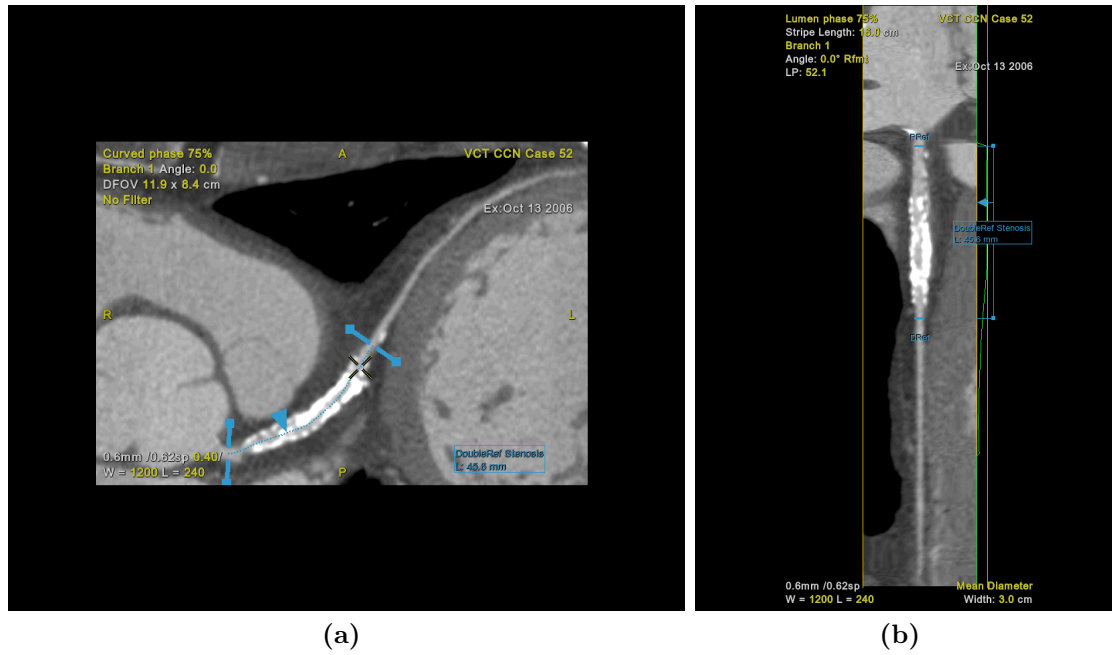


**Figure 3.45** – Coronary lesions detection results on a diseased RCA branch with calcified plaques and a stent that covers the proximal segment. The detected stent is marked using a blue bookmark.



## Part IV

# Conclusions and Future Work



---

## Contents

---

<b>2.1</b>	<b>Coronary arteries segmentation: A brief Review . . . . .</b>	<b>136</b>
2.1.1	Direct segmentation approaches . . . . .	136
2.1.2	Centerline-based segmentation approaches . . . . .	139
<b>2.2</b>	<b>A Coronary Enhancement Filter using the Shape Tree and Path Openings . . . . .</b>	<b>144</b>
2.2.1	Preliminaries . . . . .	144
2.2.2	The enhancement filter . . . . .	155
2.2.3	Preliminary Results and Discussion . . . . .	163
<b>2.3</b>	<b>Statistic-based Vessel Lumen Segmentation . . . . .</b>	<b>164</b>
2.3.1	State of the art coronary arteries segmentation and lumen extraction .	165
2.3.2	Vessel lumen mask extraction using adaptive statistics . . . . .	167
2.3.3	Vessel Segmentation and evaluation results . . . . .	173
2.3.4	Conclusions and future work . . . . .	179

---

This PhD thesis deals with automated analysis of coronary arteries for lesions detections and quantification using CT angiography data. We have developed algorithms adapted to this context and allowing to reduce the time, cost and risk related to conventional coronary angiography. This work involves a multi-disciplinary interaction, which allowed us to better understanding the problems to be treated and acquire additional knowledge helpful for solving them. In particular, our approaches benefit from anatomical knowledge in order to improve the accuracy and robustness of the different steps of the processing. This knowledge is integrated in the different algorithms at different levels; to initialize the process, guide the segmentation, characterize the target structures and reduce false detections. We were hence able to simplify the proposed algorithms, increase their effectiveness and make them more robust and accurate. Our major concern when developing these approaches was to ensure their applicability in a clinical context by verifying that they meet the target performances. Therefore, we dedicated a major part of this thesis to study and validate (qualitatively and quantitatively) the proposed approaches. In order to make the proposed solutions useful in daily clinical practices, our main objectives were:

- 
- Propose algorithms for cardiac CT analysis using techniques that combine automation, efficiency and robustness.
  - Improve some existing processing steps (e.g. heart segmentation, lumen delineation) that affect the final stenosis detection results.
  - Validate and analyze the proposed prototype qualitatively and quantitatively by combining several metrics.

In the next sections, we first summarize the main contributions of this work that we organize following three different main topics. Then, we recall the major limitations of the proposed approaches and expose possible solutions to overcome them.

---

# Chapter 1

---

## Achieved work

### 1.1 Automated heart delineation

In chapter 1, we have presented and evaluated an automated model-based approach for heart isolation in cardiac CT angiography. The proposed technique is mainly composed of a first step of fitting of the geometrical model of the heart (represented by a 3D ellipsoid), followed by a refinement step to delineate the final heart volume. To fit the geometric model, a set of points is extracted on the heart surface. To eliminate contaminated points, in order to avoid biasing the fitting process, a backward outliers removal step is performed. Afterward, a novel two-stage ellipsoid fitting is proposed to estimate the best ellipsoid covering the heart volume. Subsequently, as the heart is not perfectly elliptic, a supervised graph based technique using Random Walkers (RW) is utilized to refine the heart's delineation. A final step of extra bones removal is applied to clean up the final heart volume. This work has been validated on 133 healthy and pathological CT cardiac images. According to a quantitative and qualitative evaluation on two different sets, the proposed method appears to be an accurate and robust technique for heart segmentation. In fact, an average Dice coefficient of  $0.87 \pm 0.17$  and a maximum distance error of  $2.67 \pm 1.43$  were obtained. Besides, 70 % of the segmented volumes shows a very good or perfect segmentation quality.

This work could be used in different clinical applications such as cardiac and vascular diseases investigation or for real-time interventional procedures guiding. The result of heart segmentation could be used to define the heart short and long axis and generate the different views of the heart chambers. It can be used to clearly visualize the coronary arteries running on the surface of the heart. Furthermore, the masque is usually utilized as an input volume for automated cardiac structures segmentation (coronaries and heart chambers) hence reducing the overall processing time as well the amount of false detections.



### 1.2 Coronary arteries extraction

We have elaborated a novel coronary arteries extraction approach robust to local perturbation and that overcomes the scale related problems. The approach first uses Robust Path Opening to enhance linear structures of a given length with a given amount of noise. Then a component tree filtering approach is applied to extract the coronary arteries. A set of attributes were computed over the constructed tree and evaluated to determine the best ones allowing to robustly capture the coronary arteries. By combining two different attributes we were able to filter major parts of the coronary arteries while reducing the noise amount. The approach showed promising results for coronary arteries extraction compared to a hessian based approach. Compared to ground truth segmentation, the approach shows a mean overlap measure of more than 71.

### 1.3 Automated coronary stenosis detection

#### 1.3.1 A two-stage Automatic Coronary Arteries Stenoses Detection

In this work, a fully automated algorithm to rule out coronary stenotic area using 3D cardiac CT angiography is presented. The approach is based on lumen segmentation and quantification to detect stenotic regions caused by all types of plaques (soft, calcified or mixed). A first set of stenosis candidates are extracted by analyzing the vessel lumen diameter profile. Then, this set is cleaned up. To remove the outliers, geometric and intensity-based features are used to characterize coronary plaques and stenosis. This work has been evaluated using the Rotterdam Coronary Challenge [215]. It was also evaluated on site during the MICCAI conference (2012) and ranked third. Results show that this tool can be used as a first reader to indicate segments with high likelihood of severe stenosis.

#### 1.3.2 Learning-based Detection of Severe Coronary Stenoses

A learning-based approach for automatic detection of coronary arteries lesions in cardiac CT data is presented. The technique uses a robust multiscale vessel specific pattern to extract a set of rotation invariant features along the vessel centerlines. As input we used the automatically extracted centerlines provided by team Rcadia [30, 161]. We used the Random Forest as a classifier to learn the coronary stenosis from a set of 18 training datasets. The approach was evaluated on the remaining 30 datasets of the Rotterdam challenge.

This approach shows promising results for coronary artery stenosis detection based on the MICCAI stenosis detection challenge evaluation framework. It ranks third among 12 submitted

### 1.1.3 Automated coronary stenosis detection

---

algorithms and shows similar performances to the two best works. This shows the potential of machine learning based approaches in resolving the stenosis detection problem against segmentation based approaches. Detection results were also evaluated on a set of GE Healthcare cardiac images by using a vessel-based and segment-based evaluations. The approach showed a sensitivity of 77.14%, a specificity of 92% and a PPV value of 84.38% for a per segment analysis. A fully automated prototype useful in clinical context is developed based on this technique. It could be used as an automated tool to help clinicians quickly highlight severe stenosis (~10 seconds).



---

## Chapter 2

---

### Limitations and Perspectives

General limitations for the proposed techniques are mainly related to the quality of CT images. In fact, coronary arteries are relatively tiny tubular structures that are quickly affected by noise present in the image. This affects segmentation approaches as well as stenosis detection techniques. Besides, the image quality could be degraded by several artifacts caused by heart and respiratory motion, and presence of some blurring vessel abnormalities and surrounding structures (calcifications, stents, heart cavities). A subsequent limitation of the use of CT images is the current spatial resolution not allowing to clearly visualize and accurately process coronary branches with low scale size. The limited resolution can also affect the stenosis degree quantification.

#### 2.1 Automated heart delineation

The most sensitive step of the heart segmentation approach is the initialization and fitting of the geometric model. If the ellipsoid initially includes non cardiac structures, the final results might be not satisfactory. In fact, as we use this geometric model to label the heart volume for the Random walker based segmentation, if an unwanted structure is already included in the initial marker of the heart, it will be present at the final segmented volume. This what happens with ribs. This structures are too close the heart anatomy and are often included in the final result. Moreover, some other surrounding structures of the heart (e.g. liver, major trunks) might be included because the contact regions are absent or weak. In fact, because of the lack of contrast and their closeness to the heart surface, such structures are difficult to remove.

This issue can be addressed by adding an interactive tool allowing the user to adjust the fitted model if necessary. This type of edition tools is often used for clinical applications and adds a flexibility to the proposed tool. Future work will focus on automatically removing the

remaining pulmonary veins and ascending aorta that can obscure the root of the coronaries. Moreover, we plan to further reduce the processing time for the heart segmentation by implementing a multi-grid and parallel approach for the RW and use a more robust statistical approach for the outliers removal.

## 2.2 Coronary arteries extraction

The proposed method yields promising results for coronary arteries filtering. However, some points of improvement are planned to increase the approach robustness. Major tasks for future work should include computational time reduction and the removal of unwanted kept structures in the final segmented masque. We plan to use a more robust implementation of the tree construction algorithm that would be more adapted for cardiac CT processing. In fact, these images present a considerable number of inactive voxels that do not need to be processed. Such implementation would help to reduce the computational time and the complexity of the approach. Furthermore, we propose to add an automated steps of false positive removal from the final segmentation result. This step includes heart cavities major vessel (pulmonary arteries) removal. Finally, the approach suffers from a major weakness when dealing with pathological cases. We observed some missing coronary parts due to the presence of a severe stenosis resulting in missing the coronary segment beyond the stenosis. In order to solve this limitation, a constrained region growing can be performed in order to reconnect the missing parts. The proposed approach could also be tested in order to filter other type of human vascular structures

## 2.3 Automated coronary stenosis detection

### 2.3.1 A two-stage Automatic Coronary Arteries Stenoses Detection

Based on the evaluation results, our approach mainly suffers from a considerable number of false positives. Besides, some of the significant stenosis were missed by the algorithm. The amount of false positive and false negative can be discussed regarding the evaluation process criteria used to perform such classification. However, one major drawback of this approach is its sensitivity to the lumen segmentation quality. In fact, the approach is mainly based on the quantification of the lumen diameter (or area) to extract the stenotic points. Any error on the lumen segmentation might induce a false (positive or negative detection). Therefore, as future work we will use the improved lumen segmentation approach in order to improve the lesion detection accuracy.

### 2.3.2 Learning-based Detection of Severe Coronary Stenoses

Even if the approach presented very promising results based on both qualitative and quantitative evaluations, some aspects need to be improved for using the proposed prototype in clinical practice. One major drawback of such approaches is that its performances directly relies on the quality of the input centerlines. Unfortunately, the used centerlines provided by the team Rcadia presents some anomalies. First, we noticed that some significant branches of major coronaries are sometimes missing. This is crucial when a stenosis has been reported by the observers at this missing branch. It will be reported as a false negative by the evaluation framework, while our approach will never be able to detect it. Besides, visual inspection revealed that these centerlines have problems around severe stenosis or occlusions. Some centerlines end prematurely if a severe lesion is encountered. Finally, the quality of vessel centerlines is very critical for an accurate feature extraction. In fact, the designed vessel pattern supposes that the provided centerline is well centered at the vessel lumen in order to be able to capture the region features. Any perturbation along the vessel centerline will lead to erroneous features extraction. This currently happens near to calcified plaques where the centerline is biased by the plaque intensities. Therefore, a centerline correction step seems to be mandatory in order to increase the performances of the proposed approach.

Furthermore, a current drawback of the method is that the definition of one unique threshold value for the probability profile for all the exams is difficult. An interesting solution will be the proposition of a dynamic threshold selection using an interactive tool available via the graphical user interface. Besides, a thorough analysis of the impact of the used features on the final classification result should be performed in order to determine most relevant ones. As future work, we also plan to enrich the learning database by including new annotated coronary lesions. In fact, the relatively limited amount of training data can be considered as a weakness of the current version of our algorithm. It would also be interesting to test other learning-based schemes as the active learning. This will allow to continuously learn from new data examined by the user. Besides, miss-classifications would be corrected by the radiologist and could thus lead to an improvement of the approach accuracy. However, this should be used carefully in order to not deteriorate the prototype performances. Only high qualified users should be able to add a new training data and correct a false classification.

Finally, automatic stenosis detection and quantification is still challenging specially because it is hard to accurately discriminate between severe and non-severe stenosis using a hard 50% threshold. In fact, it is not possible to accurately differentiate between a 45% and a 53% stenosis degree, given the current resolution of the used CT scanners. A possible solution would be to

## Chapter 2. Limitations and Perspectives

---

use a more flexible approach for reporting detected stenosis. The idea is to allow reporting a suspicious detected stenosis, using a color code with regard to their probability to be a severe lesion.

# Part V

## Appendix





---

---

# Appendix A

---

## Publications

Some of the work described in this manuscript have been the subject of previous publications:

### Journals

- I. Melki, H. Talbot, J.Cousty, C.Pruvot, J. Knoploch, L.Launay, L.Najman. A hybrid algorithm for automatic heart delineation in CT angiography. *International Journal of Computer Assisted Radiology and Surgery* 28, pp 37-38.
- H. A. Kiriçli, M. Schaap, C. T. Metz, A. S. Dharampal, W. B. Meijboom, S. L. Papadopoulou, A. Dedic, K. Nieman, M. A. De Graaf, M. F. L. Meijs, M. J. Cramer, A. Broersen, S. Cetin, A. Eslami, L. Flórez-Valencia, K. L. Lor, B. Matuszewski, I. Melki, B. Mohr, I. Oksüz, R. Shahzad, C. Wang, P. H. Kitslaar, G. Unal, A. Katouzian, M. Orkisz, C. M. Chen, Frédéric Precioso, Laurent Najman, S. Masood, D. Unay, L. Van Vliet, R. Moreno, R. Goldenberg, E. Vuçini, G. P. Krestin, W. J. Niessen, T. Van Walsum. Standardized evaluation framework for evaluating coronary artery stenosis detection, stenosis quantification and lumen segmentation algorithms in computed tomography angiography.. *Medical Image Analysis*, 2013, 17 (8), pp. 859-876.

### Conferences

- I. Melki, H. Talbot, J.Cousty, C.Pruvot, J. Knoploch, L.Launay, L.Najman. A hybrid algorithm for automatic heart segmentation in CT angiography. In *Image Processing (ICIP), 2012 19th IEEE International Conference on* (pp. 2013-2016).
- I. Melki, C. Cardon, N. Gogin, H.Talbot, L. Najman. Learning-based automatic detection of severe coronary stenoses in CT angiographies. In *SPIE Medical Imaging. International Society for Optics and Photonics*, 2014, pp. 903536-903536-9.

## Publications

---

- I. Melki, H. Talbot, J.Cousty, C.Pruvot, J. Knoploch, L.Launay, L.Najman . Automatic Coronary Arteries Stenoses Detection in 3D CT angiography. Proc. MICCAI Workshop 3D Cardiovascular Imaging: A MICCAI Segmentation, 2012.

---

## Appendix B

---

### American Heart Association Coronary segmentation

Coronary anatomy varies greatly from one person to another. For a better description and communication of the coronary arteries findings, the use of a standardized coronary arterial tree nomenclature is required. In this context, the [AHA](#) proposed a standard coronary segmentation model that represents the most frequently encountered coronary segments and that optimizes the correspondence and communication between the different cardiac imaging modalities.

#### B.1 Left ventricle segmentation

Several imaging modalities are used for the assessment of the left ventricle function, the myocardial perfusion and coronary lesion inspection. This includes echocardiography, coronary angiography (CA), cardiac computed tomography (CCT), cardiac magnetic resonance (CMR), single photon emission tomography (SPECT) and positron emission computed tomography (PET). Despite the technical differences between those modalities, they tend to image and display the myocardium and its surrounding cavities [? ]. To facilitate the intra- and cross-modality communication and comparison for clinical application and research, the American Heart Association (AHA) proposes a set of consensus recommendations for the display and the visualization of cardiac images. The heart should be oriented and displayed using the long axis of the left ventricle and selected planes oriented at 90 degrees angles relative to the long axis. A standardized nomenclature of *short axis*, *vertical long axis* and *horizontal long axis* -corresponding to the traditional *short-axis*, *apical 2-chamber*, and *apical 4-chamber* planes of the 2D echocardiography- should be used to describe the 3 perpendicular cardiac planes for all the modalities (see figure [A.1](#)). The left ventricle muscle could be divided into a variable number of segments [? ? ]. The first developed model was a 15-segment model proposed by Austen et al. [? ] to describe the left ventricle anatomy. Based on an autopsy study, precise data on mass and size of the myocardium were derived. It allowed for a repartition of the myocardial mass into basal (35%), mid-cavity (35%), and apical (40%) thirds perpendicular to the left ventricle long axis [? ]. Thus, a

standard 17-segment model of the left ventricle was established based on this anatomic finding. Figure A.1 shows the circumferential location and names of the 17 segments. The basal and mid-cavity thirds are segmented into six 60 degrees parts each. The apical slice was divided into four equal segments of 90 degrees each. The 17th segment corresponds to the left ventricle apex, the extreme tip of the ventricle where the cavity is no longer available. The AHA recommends the use of this left ventricle model for the analysis of the ventricle function and myocardium perfusion.

## B.2 Coronary arteries territories assignment

Despite the tremendous anatomic variability of coronary arteries, the AHA recommends to assign each individual segment of the left ventricle to a specific coronary artery territory. Figure A.2 shows the assignment of the 17 segments of the left ventricle to one of the three main coronary arteries: LAD, LCX and RCA. Segments 1, 2, 7, 8, 13, 14, and 17 are supplied with the LAD artery. Segments 3, 4, 9, 10, and 15 are assigned to the RCA distribution. Segments 5, 6, 11, 12, and 16 are assigned to the LCX artery. The greatest variability occurs at the apical cap (segment 17), which can be supplied by any of the three arteries. This assignment between the left ventricle segments and the coronary arteries distribution facilitates the detection of corresponding coronary lesions.

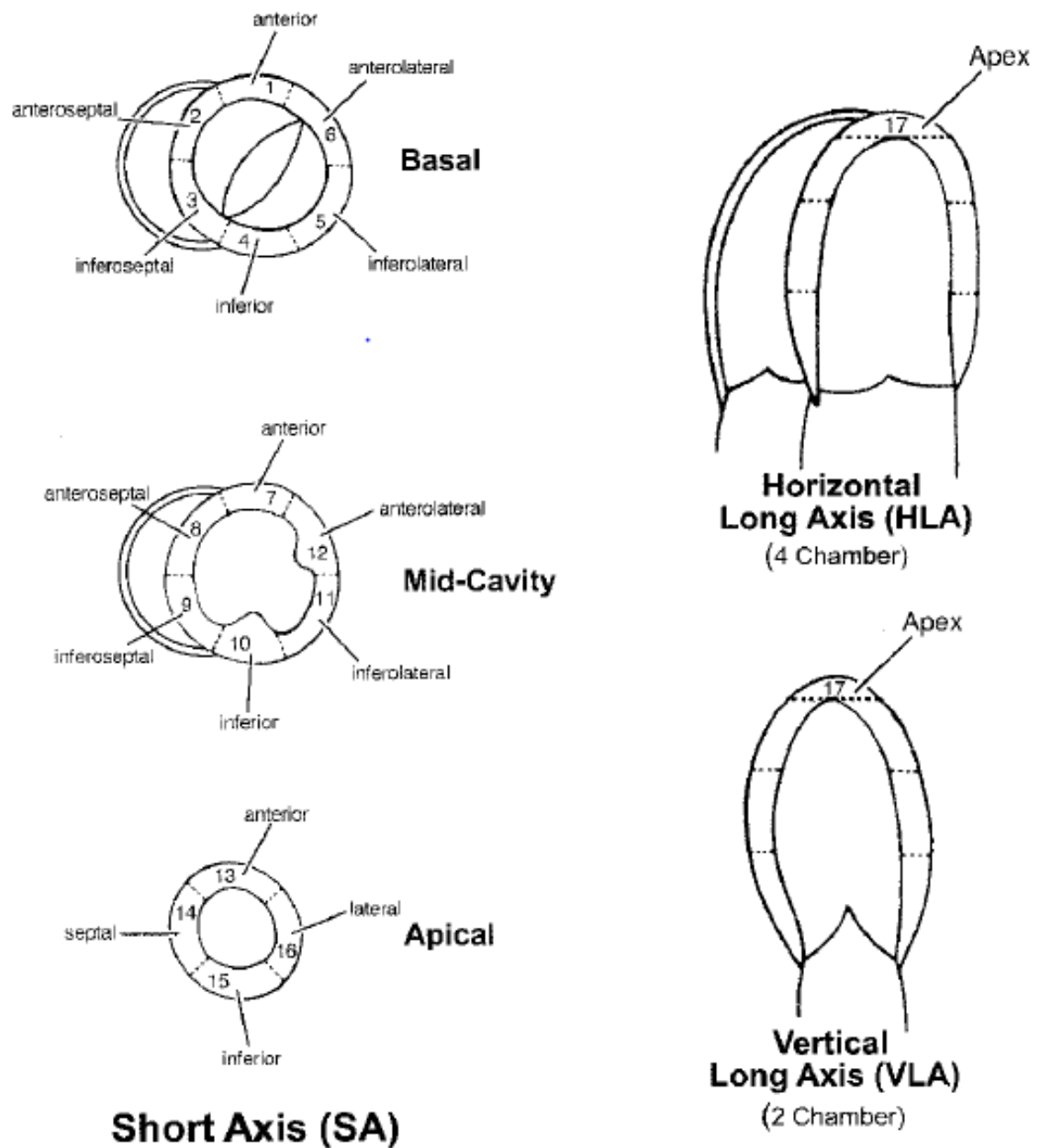


**Figure A.1** – Views of the long vertical axis, long horizontal axis and the short axis planes showing the recommended basal, mid-cavity and basal slices with the corresponding 17-segments. Illustration from [? ]

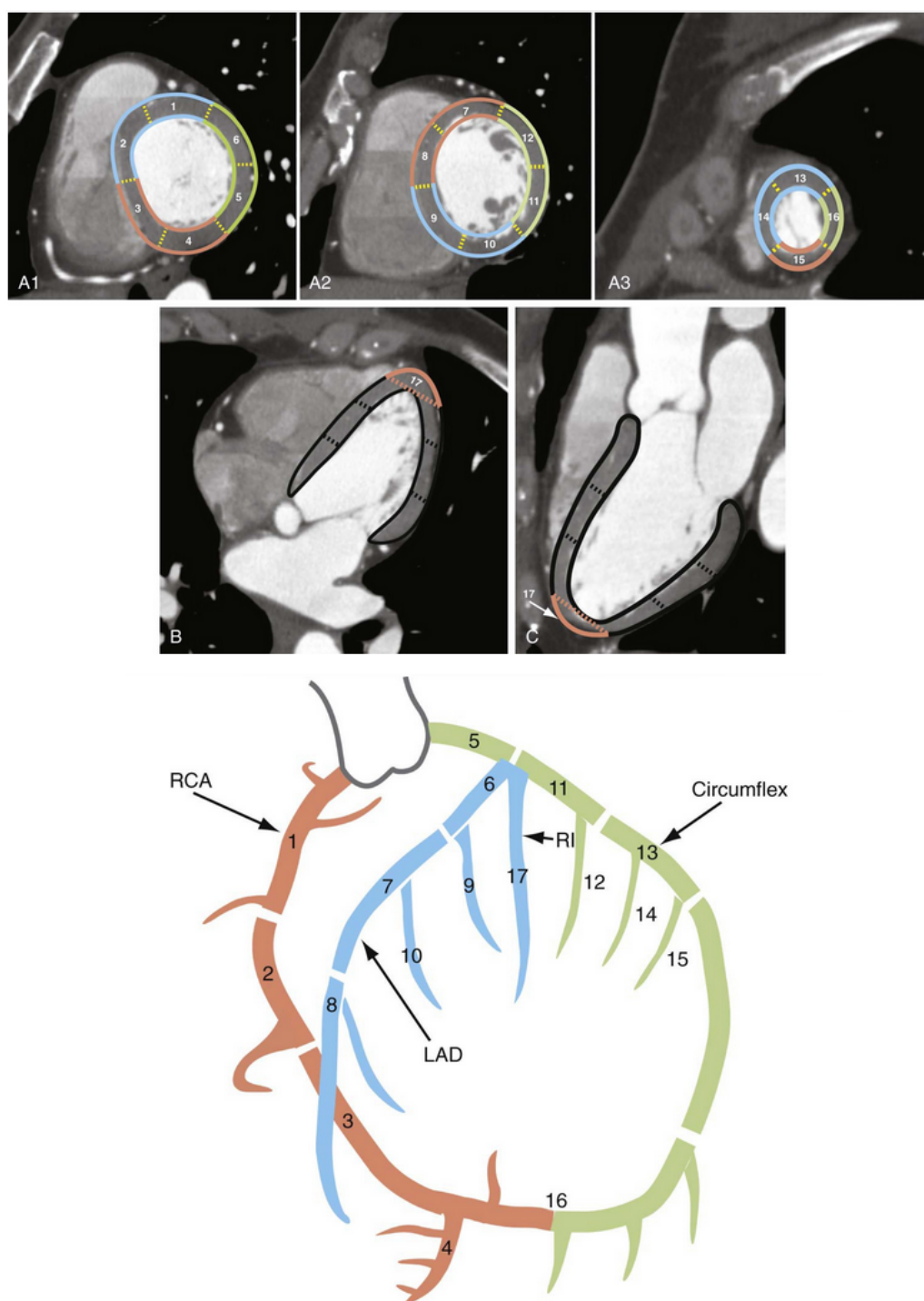


**Figure A.2** – Assignment of the 17 segments of the left ventricle to the RCA (red), LAD (blue) and LCX (green). A1, A2 and A3 shows the axial views of the basal, mid-cavity and the apical thirds of left ventricle on a CT angiography with the corresponding AHA segments. B and C shows the horizontal and vertical long axis of the left ventricle displaying the ventricle apex (segment 17). Bottom: Segmental anatomy of coronary arteries corresponding to the modified AHA 17-segment model of the left ventricle. With considering that there is a great variability in blood supply of different segments, the individual segments are assigned to each coronary artery territories. Illustration from [? ]

## B.2 Coronary arteries territories assignment

Segment Number	Myocardial segment nomenclature	Associated coronary segment nomenclature
1	Basal Anterior	RCA proximal
2	Basal Anteroseptal	RCA mid
3	Basal Inferoseptal	RCA distal
4	Basal Inferior	right posterior descending
5	Basal Inferolateral	main stem
6	Basal Anterolateral	LAD proximal
7	Mid-Anterior	LAD mid
8	Mid-Anteroseptal	LAD distal
9	Mid-Inferoseptal	first diagonal
10	Mid-Inferior	second diagonal
11	Mid-Inferolateral	LXC proximal
12	Mid-Anterolateral	obtuse marginal
13	Apical Interior	LCX distal
14	Apical Septal	LCX posterolateral branch
15	Apical Inferior	LCX posterior descending branch
16	Apical lateral	RCA posterolateral branch
17	Apex	ramus intermedius branch

**Table A.1** – The 17 myocardial segments with the recommended nomenclature for the left ventricle and the corresponding coronary arteries segmentation for tomographic imaging of the heart





---

# Appendix C

---

## Measures for Automated Segmentation Evaluation of medical imaging

Image processing and object/background segmentation are the first steps towards quantitative medical images analysis. In fact, many interesting approaches have been proposed, in the literature, for organs or pathologies segmentation using different modalities. While a great effort has been dedicated to designing new innovative algorithms, fewer works have been dedicated to an appropriate validation framework for this techniques. The first goal of medical image segmentation is to propose algorithms able to produce accurate segmentation results that meet the targets of the wanted application. Therefore, the quality of the segmentation must be assessed to be sure that the proposed approach accomplished the wanted task and is accurate enough to be used in clinical applications. Generally, a manual segmentation of the target object is performed by one or several experts and the result (consensus of the different manual segmentation if more than one expert) is considered as "gold standard" to evaluate the automated segmentation. A large number of measures are available to evaluate the segmentation quality with reference to the manual segmentation (i.e. gold standard). Those techniques can be extensively divided into two main categories: (1) Volume-based measures and (2) Distance-based measures. Hereafter, we will explain the different most used measures in image processing fields.

### C.1 Volume Based Measures

Let  $I(x, y, z) : \mathbb{R}^3 \mapsto \mathbb{R}$  be a 3D medical image and  $S(I(x, y, z)) : \mathbb{R}^3 \mapsto \Omega, \Omega = 0, 1$  a binary segmentation of  $I$ . If we define  $G(I(x, y, z)) : \mathbb{R}^3 \mapsto \Omega$  as the ground truth (i.e. a gold standard annotated by an expert), we can thus classify each voxel  $(x, y, z)$  of the segmented image  $S$  into one of the four following classes (figure A.1):

- True positive: if  $S(x, y, z) = 1 \wedge R(x, y, z) = 1$  (correctly identified)
- False positive: if  $S(x, y, z) = 1 \wedge R(x, y, z) = 0$  (incorrectly identified)

		Ground Truth	
		Positive	Negative
Segmentation	Positive	TP	FP
	Negative	FN	TN

**Table A.1** – Confusion matrix

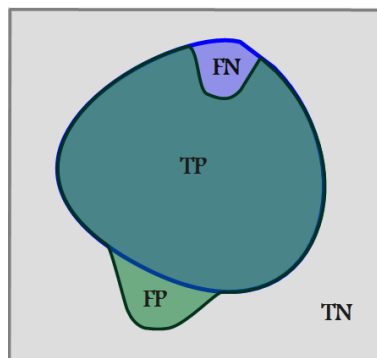


**Figure A.1** – An example of a segmentation with the distribution of false positives, true positives, true negatives and false negatives. Both the segmentation  $S$  (green) and the ground truth  $G$  (blue) are illustrated.

- True negative: if  $S(x, y, z) = 0 \wedge R(x, y, z) = 0$  (correctly rejected)
- False negative: if  $S(x, y, z) = 0 \wedge R(x, y, z) = 1$  (incorrectly rejected)

Hence four statistical parameters can be defined: number of **TP**, number of **FP**, number of **TN** and number of **FN**. A confusion matrix can be used to summarize the four values:

Several statistical parameters can be thus derived to assess the segmentation result accuracy.

## C.1.1 Statistical measures

### C.1.1.1 Sensitivity

Sensitivity of an algorithm refers to its ability to correctly identify the wanted object from its background. It is defined as the percentage of true positives detected correctly and is expressed from the previous definition of true positives and false negatives volumes:

$$\text{sensitivity} = \frac{\text{Volume of true positives}}{\text{Volume of true positives} + \text{Volume of false negatives}} \quad (\text{C.1})$$

$$= \frac{|V_{TP}|}{|V_{TP}| + |V_{FN}|} \quad (\text{C.2})$$

### C.1.1.2 Specificity

Specificity of an algorithm refers to the method's ability to exclude a condition correctly. It represents the percentage of true negatives detected correctly and is expressed as:

$$\text{Specificity} = \frac{\text{Volume of true negatives}}{\text{Volume of true negatives} + \text{Volume of false positives}} \quad (\text{C.3})$$

$$= \frac{|V_{TN}|}{|V_{TN}| + |V_{FP}|} \quad (\text{C.4})$$

### C.1.1.3 Positive productive value

Positive Productive value (PPV) corresponds to the proportion of true positives inside the segmented area (included in the ground truth segmentation). It evaluates the performance of the method against false positive detections.

$$\text{PPV} = \frac{\text{Volume of true positives}}{\text{Volume of true positives} + \text{Volume of false positives}} \quad (\text{C.5})$$

$$= \frac{|V_{TP}|}{|V_{TP}| + |V_{FP}|} \quad (\text{C.6})$$

### C.1.1.4 Negative productive value

Negative Productive value (NPV) corresponds to the proportion of true negatives inside the segmented object's background (not included in the ground truth segmentation). It evaluates the performance of the method against false negative detection.

$$\text{NPV} = \frac{\text{Volume of true negatives}}{\text{Volume of true negatives} + \text{Volume of false negatives}} \quad (\text{C.7})$$

$$= \frac{|V_{TN}|}{|V_{TN}| + |V_{FN}|} \quad (\text{C.8})$$

### C.1.1.5 Fraction of false negative

This measure is expressed as a fraction of the ground truth volume. Fraction of false negatives (FFN) denotes the fraction of tissue that was missed by the approach. It is formulated as following:

$$\text{FFN} = \frac{\text{Volume of false negatives}}{\text{Volume of true positives} + \text{Volume of false negatives}} \quad (\text{C.9})$$

$$= \frac{|V_{FN}|}{|V_{TP}| + |V_{FN}|} \quad (\text{C.10})$$

### C.1.1.6 Fraction of false positive

This measure is expressed as a fraction of the ground truth volume. Fraction of false positives (FFP) indicates the fraction of volume that was falsely segmented by the approach. It is formulated as following:

$$\text{FFP} = \frac{\text{Volume of false positives}}{\text{Volume of true positives} + \text{Volume of false negatives}} \quad (\text{C.11})$$

$$= \frac{|V_{FP}|}{|V_{TP}| + |V_{FN}|} \quad (\text{C.12})$$

### C.1.1.7 Receiver Operator Characteristic curve

A receiver operating characteristic (ROC) curve of a binary classification system is a graphical plot that shows the variation of the performance of the system as a decision threshold is varied. The ROC curve is a graph of sensitivity (y axis) vs. 1 - specificity (x axis). Each segmentation result represents one point in the ROC space. The curve is delimited by two points B(0,0) and C (1,1) representing two particular cases. Point B corresponds to the case where the system detects no positive cases (sensitivity = 0) and detects all the negative cases (specificity = 1). Point C corresponds to the situation where the system classifies all the instance as positive detections. Thus, all positive cases are detected (sensitivity = 1) while all negative cases are missed (specificity = 0). The perfect classification system corresponds to the point A (0,1). In fact, for this case no false positives (sensitivity = 1) or false negatives (specificity = 1) are detected.

The ROC curve analysis allows to select the optimal cutoff value that provides the better trade off between the system sensitivity and specificity (best classifying point). The choice of this point depends on the costs of detecting false positives and false negatives as well as the prevalence of the class to be detected (i.e., the proportion of presence of true positives and true negatives in the initial set to be classified) [? ]. In fact, depending on the application of the system, positive and negative miss-classification may not be considered with the same cost. For pathology detection systems, miss-classifying a positive case as false negative is more crucial than miss-classifying a negative case as false positive. Therefore, sensitivity would be preferred to specificity in this case.

To graphically determine the best point, we need first to define the slope value  $s$  based on the false positive and false negative cost, and the prevalence value  $P$ :

$$s = \left( \frac{\text{False positives cost}}{\text{False negatives cost}} \right) \times \frac{1 - P}{P} \quad (\text{C.13})$$

$$(\text{C.14})$$

The best classifying point corresponds to the point where a line with the above slope  $s$  touches the

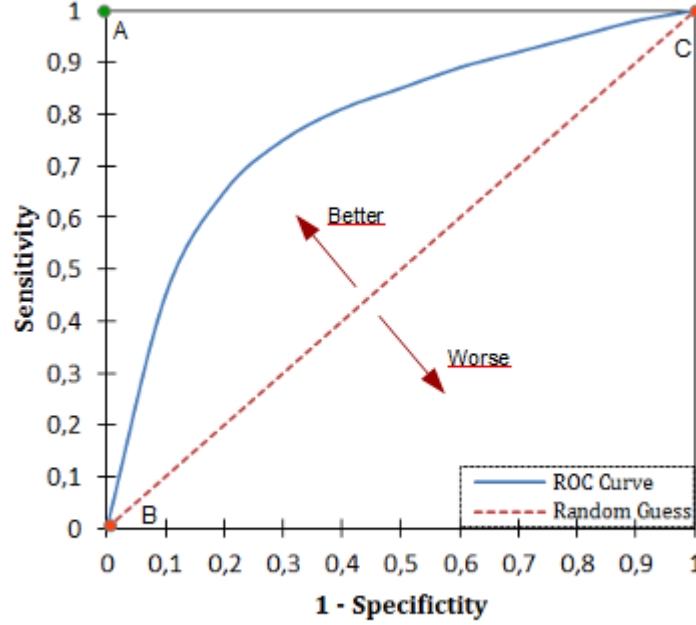


**Figure A.2** – A ROC curve illustration showing particular classification cases.

ROC curve moving down from above to the left [? ]. When the costs are equal and the prevalence is of 0.5, the best point corresponds to the intersection point of the ROC curve and the line parallel to the diagonal.

## C.1.2 Overlap Measures

### C.1.2.1 Dice similarity coefficient

Dice similarity Coefficient (DSC) is a spatial volume-based measure that quantifies the overlap between two given binary regions [? ? ]. It is expressed using the following formula:

$$DSC = \frac{2 * |S \cap G|}{|S| + |G|} \quad (C.15)$$

$$= \frac{2 * |V_{TP}|}{(|V_{FP}| + |V_{TP}|) + (|V_{FN}| + |V_{TP}|)} \quad (C.16)$$

Thus, dice coefficient represents the size of the union of the two sets  $S$  and  $G$  ( $|S \cap G|$ ) divided by the average size of the two sets ( $\frac{|S| + |G|}{2}$ ). The dice values ranges from 0 to 1. A value of 0 indicates no overlap between the two sets; a value of one indicates that the two sets are in perfect agreement. Higher values of DSC indicates that the segmented result matches better the ground truth than lower

values of DSC.

### C.1.2.2 Jaccardi Index

Also known as Tanimoto coefficient, Jaccardi index is an other similarity measure used to compare two sets [? ]. It is expressed as following:

$$J = \frac{|S \cap G|}{|S \cup G|} \quad (C.17)$$

$$= \frac{2 * |V_{TP}|}{|V_{FP}| + |V_{TP}| + |V_{FN}|} \quad (C.18)$$

It represents the ratio of the size of the intersection of S and G to the size of their union. Similarly to the dice coefficient, the Jaccardi index ranges from 0 to 1.

## C.2 Distance based measures

Let  $\mathcal{S}$  denotes the surface of the segmented object  $S$  and  $\mathcal{G}$  the surface of the corresponding ground truth  $G$ . Distance based evaluation measures quantify the distance between the segmentation result and the ground truth surfaces  $\mathcal{S}$  and  $\mathcal{G}$ . Hausdorff distance and Mean absolute distance are among the distances used for segmentation evaluation.

### C.2.1 Distance of Hausdorff

The *directed* Hausdorff distance between two non empty, closed and bounded sets  $\mathcal{S}$  and  $\mathcal{G}$  corresponds to the maximum distance of  $\mathcal{S}$  to the nearest point in  $\mathcal{G}$ . Formally, the Hausdorff distance is a maximum distance defined as:

$$h(\mathcal{S}, \mathcal{G}) = \max_{a \in \mathcal{S}} \{ \min_{b \in \mathcal{G}} \{ d(a, b) \} \} \quad (C.19)$$

where  $a$  and  $b$  are points of  $\mathcal{S}$  and  $\mathcal{G}$  respectively and  $d(a, b)$  is a metric distance that could be defined as the Euclidean distance for simplicity. This distance can be obtained in two stages: First, for each point  $a$  in  $\mathcal{S}$  compute the minimum distance to all points in  $\mathcal{G}$ . Second, the maximum of all this minimums is obtained as the Hausdorff distance of the set  $\mathcal{S}$  to the set  $\mathcal{G}$ . However, this definition of Hausdorff distance is asymmetric (directed). In general :

$$h(\mathcal{S}, \mathcal{G}) \neq h(\mathcal{G}, \mathcal{S}) \quad (C.20)$$

Therefore, a more accurate definition of the distance Hausdorff would be:

$$H(\mathcal{S}, \mathcal{G}) = \mathbf{max} \{h(\mathcal{S}, \mathcal{G}), h(\mathcal{G}, \mathcal{S}) \} \quad (\text{C.21})$$

The last definition is generally used to compute the Hausdorff distance *between* two sets. This measure allows to quantify the mismatch between two sets by computing the distance of the point of  $\mathcal{S}$  that is farthest from any point in  $\mathcal{G}$  and vice versa. So, if the Hausdorff distance between  $\mathcal{S}$  and  $\mathcal{G}$  is  $h$  then all the points of the set  $\mathcal{S}$  are at a distance lower than or equal to  $h$  and vice versa.

### C.2.2 Mean absolute distance

The mean (or average) absolute distance  $m$  of a surface  $\mathcal{S}$  to another surface  $\mathcal{G}$  corresponds to the mean of all minimum distance values separating the points of the set  $\mathcal{S}$  from the set  $\mathcal{G}$ .

$$m(\mathcal{S}, \mathcal{G}) = \frac{1}{|\mathcal{S}|} \sum_{a \in \mathcal{S}} \min_{b \in \mathcal{G}} \{d(a, b)\} \quad (\text{C.22})$$

First, for each point  $a$  in  $\mathcal{S}$ , the minimum distance to the surface  $\mathcal{G}$  is computed. The average of all these distances gives the average absolute distance of  $\mathcal{S}$  to  $\mathcal{G}$ . This calculation is not symmetric. Therefore, as for the Hausdorff distance, we compute the average absolute distance of  $\mathcal{G}$  to  $\mathcal{S}$ . The final average symmetric absolute distance *between*  $\mathcal{S}$  and  $\mathcal{G}$  is obtained by combining the two previous average distances.

$$M(\mathcal{S}, \mathcal{G}) = \mathbf{max} \{m(\mathcal{S}, \mathcal{G}), m(\mathcal{G}, \mathcal{S}) \} \quad (\text{C.23})$$

The mean absolute distance between two surface  $\mathcal{S}$  and  $\mathcal{G}$  tells us about how much these two surfaces differs on average. This value is 0 for a perfect segmentation.





---

# Bibliography

- [1] Wikipedia, open-content encyclopedia. URL [http://en.wikipedia.org/wiki/Main\\_Page](http://en.wikipedia.org/wiki/Main_Page). 12, 21
- [2] Mtdemo: a volume visualization package with attribute filtering, 2008. <http://www.cs.rug.nl/~michael/MTdemo/>. 156
- [3] Cardiovascular diseases (CVDs) - Fact sheet N317, March 2013. 1
- [4] Layers of blood vessels, accessed: May 20 2014. URL <http://studentosteopathicmedicine.tumblr.com/post/22209552918/layers-of-blood-vessels>. xvii, 6
- [5] Stephan Achenbach. Cardiac CT: state of the art for the detection of coronary arterial stenosis. *Journal of cardiovascular computed tomography*, 1(1):3–20, 2007. xix, 30, 36, 42
- [6] Stephan Achenbach, Werner Moshage, Dieter Ropers, Jörg Nossen, and Werner G Daniel. Value of electron-beam computed tomography for the noninvasive detection of high-grade coronary-artery stenoses and occlusions. *New England Journal of Medicine*, 339(27):1964–1971, 1998. 28
- [7] Stephan Achenbach, Stefan Ulzheimer, Ulrich Baum, Marc Kachelrieß, Dieter Ropers, Tom Giesler, Werner Bautz, Werner G Daniel, Willi A Kalender, and Werner Moshage. Noninvasive coronary angiography by retrospectively ecg-gated multislice spiral ct. *Circulation*, 102(23):2823–2828, 2000. 28
- [8] Stephan Achenbach, Fabian Moselewski, Dieter Ropers, Maros Ferencik, Udo Hoffmann, Briain MacNeill, Karsten Pohle, Ulrich Baum, Katharina Anders, Ik-kyung Jang, et al. Detection of calcified and noncalcified coronary atherosclerotic plaque by contrast-enhanced, submillimeter multidetector spiral computed tomography a segment-based comparison with intravascular ultrasound. *Circulation*, 109(1):14–17, 2004. 32
- [9] David Adalsteinsson and James A Sethian. A fast level set method for propagating interfaces. *Journal of computational physics*, 118(2):269–277, 1995. 81

## Bibliography

---

- [10] R. Adams and L. Bischof. Seeded region growing. *IEEE Transactions on Pattern Analysis and Machine Intelligence*, 16:641–647, 1994. ISSN 0162-8828. doi: <http://doi.ieeecomputersociety.org/10.1109/34.295913>. [74](#)
- [11] G. Agam and C. Wu. Probabilistic modeling-based vessel enhancement in thoracic ct scans. *Proc. IEEE Conf. Comput. Vision and Pattern Recognit.*, pages 684–689, 2005. [56](#), [57](#), [61](#), [70](#)
- [12] G. Agam, S.G. Armato III., and C. Wu. Vessel tree reconstruction in thoracic ct scans with application to nodule detection. *IEEE Trans. Med. Imaging*, 24 (4):486–499, 2005. [56](#), [57](#), [70](#)
- [13] Arthur S Agatston, Warren R Janowitz, Frank J Hildner, Noel R Zusmer, Manuel Viamonte, and Robert Detrano. Quantification of coronary artery calcium using ultrafast computed tomography. *Journal of the American College of Cardiology*, 15(4):827–832, 1990. [28](#)
- [14] Yali Amit and Donald Geman. Shape quantization and recognition with randomized trees. *Neural computation*, 9(7):1545–1588, 1997. [237](#)
- [15] Ben Appleton and Hugues Talbot. Efficient path openings and closings. In *Mathematical Morphology: 40 Years On*, volume 30 of *Computational Imaging and Vision*, pages 33–42. Springer-Verlag, Dordrecht, 2005. [82](#)
- [16] Yadon Arad, Louise A Spadaro, Ken Goodman, Alfonso Lledo-Perez, Scott Sherman, Gail Lerner, and Alan D Guerci. Predictive value of electron beam computed tomography of the coronary arteries 19-month follow-up of 1173 asymptomatic subjects. *Circulation*, 93(11):1951–1953, 1996. [28](#)
- [17] Armin Arbab-Zadeh and John Hoe. Quantification of coronary arterial stenoses by multidetector ct angiography in comparison with conventional angiographymethods, caveats, and implications. *JACC: Cardiovascular Imaging*, 4 (2):191–202, 2011. [42](#), [43](#)
- [18] Elisabeth Arnoldi, Mulugeta Gebregziabher, U Joseph Schoepf, Roman Goldenberg, Luis Ramos-Duran, Peter L Zwerner, Konstantin Nikolaou, Maximilian F Reiser, Philip Costello, and Christian Thilo. Automated computer-aided stenosis detection at coronary ct angiography: initial experience. *European radiology*, 20(5):1160–1167, 2010. [188](#), [206](#)
- [19] Go AS, Mozaffarian D, Roger VL, Benjamin EJ, Berry JD, Blaha MJ, Dai S, Ford ES, Fox CS, Franco S, Fullerton HJ, Gillespie C, Hailpern SM, Heit JA, Howard VJ, Huffman MD, Judd SE, Kissela BM, Kittner SJ, Lackland DT, Lichtman JH, Lisabeth LD, Mackey RH, Magid DJ, Marcus GM, Marelli A, Matchar DB, McGuire DK, Mohler ER 3rd, Moy CS, Mussolino ME, Neumar RW, Nichol G, Pandey DK, Paynter NP, Reeves MJ, Sorlie PD, Stein J, Towfighi A, Turan TN, Virani SS, Wong ND, Woo D, Turner MB ; on behalf of the American Heart Association Statistics Committee, and Stroke Statistics Subcommittee. Heart disease and stroke statistics–2014 update: a report from the american heart association statistics committee and stroke statistics subcommittee. *Circulation*, 129:28–292, 2014. [1](#)
- [20] Nicolas Aspert and Touradj Ebrahimi. Mesh: measuring errors between surfaces using the hausdorff distance. In *ICME*, volume 1, 2002. [128](#)

- 
- [21] W Gerald Austen, JE Edwards, RL Frye, GG Gensini, VL Gott, LS Griffith, DC McGoon, ML Murphy, and BB Roe. A reporting system on patients evaluated for coronary artery disease. report of the ad hoc committee for grading of coronary artery disease, council on cardiovascular surgery, american heart association. *Circulation*, 51(4):5–40, 1975. xvii, 11
- [22] Sheldon Axler, Pamela Gorkin, and Karl Voss. The Dirichlet problem on quadratic surfaces. *Math. Comput.*, 73(246):637–651, 2004. 115
- [23] S.R. Aylward and E. Bullitt. Initialization, noise, singularities, and scale in height ridge traversal for tubular object centerline extraction. *Medical Imaging, IEEE Transactions on*, 21(2):61–75, 2002. ISSN 0278-0062. 71
- [24] Stephen R. Aylward, Susan Weeks, and Elizabeth Bullitt. Analysis of the parameter space of a metric for registering 3d vascular images. In *MICCAI*, pages 932–939, 2001. 67
- [25] Christian Bauer and Horst Bischof. Edge based tube detection for coronary artery centerline extraction. *The Midas Journal. MICCAI Workshop -Grand Challenge Coronary Artery Tracking*, 2008. 73
- [26] Christian Bauer and Horst Bischof. Extracting curve skeletons from gray value images for virtual endoscopy. In *Medical Imaging and Augmented Reality*, pages 393–402. Springer, 2008. 62, 72
- [27] Leonard E. Baum and Ted Petrie. Statistical inference for probabilistic functions of finite state markov chains. *The Annals of Mathematical Statistics*, 37(6):1554–1563, 12 1966. 231
- [28] Christoph R Becker, Konstantin Nikolaou, Michael Muders, Gregor Babaryka, Alexander Crispin, U Joseph Schoepf, Udo Loehrs, and Maximilian F Reiser. Ex vivo coronary atherosclerotic plaque characterization with multi-detector-row ct. *European radiology*, 13(9):2094–2098, 2003. xviii, 33
- [29] Mark H. Beers, Robert S. Porter, and Thomas V. Jones. *The Merck Manual of Diagnosis and Therapy*. Medical Services, USMEDSA, USHH, 2004. 11
- [30] G. Begelman, R. Goldenberg, S. Levanon, S. Ohayon, and E. Walach. Creating a blood vessel tree from imaging data, July 19 2011. URL <http://www.google.com/patents/US7983459>. US Patent 7,983,459. 212, 308
- [31] Rami Ben-Ari and Dror Aiger. Geodesic active contours with combined shape and appearance priors. *Lecture Notes in Computer Science*, 5259:494–505, 2008. 79
- [32] Irad Ben-Gal. Outlier detection. In *Data Mining and Knowledge Discovery Handbook*, pages 131–146. Springer, 2005. 100
- [33] Giles Bertrand. Simple points, topological numbers and geodesic neighborhoods in cubic grids. *Pattern recognition letters*, 15(10):1003–1011, 1994. 62
- [34] Josef Bigün and JM Hans du Buf. N-folded symmetries by complex moments in gabor space and their application to unsupervised texture segmentation. *Pattern Analysis and Machine Intelligence, IEEE Transactions on*, 16(1):80–87, 1994. 55

## Bibliography

---

- [35] Thomas O. Binford. Visual perception by computer. In *Proceedings of the IEEE Conference on Systems and Control (Miami, FL)*, 1971. 63
- [36] Biology-Forums. Location of the heart within the mediastinum of the thoracic cavity, accessed: May 15, 2014. URL <http://biology-forums.com/index.php?action=gallery;sa=view;id=8517>. xvii, 8
- [37] A. Blake, C. Rother, M. Brown, P. Perez, and P. Torr. Interactive image segmentation using an adaptive gmmrf model. In *in ECCV*, pages 428–441, 2004. 114
- [38] H Blum. A transformation for extracting new descriptors of shape. *Models for the Perception of Speech and Visual Form*, MIT Press, pages 362–380, 1967. 62, 72
- [39] Susanne Bock, Caroline Kühnel, Tobias Boskamp, and Heinz-Otto Peitgen. Robust vessel segmentation. In *Medical Imaging*, pages 691539–691539. International Society for Optics and Photonics, 2008. 136, 137
- [40] Osman Bodur, Leo Grady, Arthur Stillman, Randolph Setser, Gareth Funka-Lea, and Thomas O'Donnell. Semi-automatic aortic aneurysm analysis. In *Medical imaging*, pages 65111G–65111G. International Society for Optics and Photonics, 2007. 184
- [41] C. Boldak, Y. Rolland, and C. Toumoulin. An improved model-based vessel tracking algorithm with application to computed tomography angiography. *Biocybernetics And Biomedical Engineering*, 23:41–63, 2003. 63, 70
- [42] Fred L Bookstein. Fitting conic sections to scattered data. *Computer Graphics and Image Processing*, 9(1):56–71, 1979. 108
- [43] Gunilla Borgefors, Ingela Nystrom, and Gabriella Sanniti Di Baja. Computing skeletons in three dimensions. *Pattern Recognition*, 32:1225–1236, 1999. 62, 73
- [44] Bernhard E Boser, Isabelle M Guyon, and Vladimir N Vapnik. A training algorithm for optimal margin classifiers. In *Proceedings of the fifth annual workshop on Computational learning theory*, pages 144–152. ACM, 1992. 232, 233
- [45] Tobias Boskamp, Daniel Rinck, Florian Link, Bernd Kummerlen, Georg Stamm, and Peter Mildenerger. New vessel analysis tool for morphometric quantification and visualization of vessels in ct and mr imaging data sets. *Radiographics*, 24:287–297, 2004. xx, 60, 61, 73, 75, 136
- [46] S. Bouix, K. Siddiqi, and A. Tannenbaum. Flux driven automatic centerline extraction. *Medical Image Analysis*, 9(3):209–221, 2005. 62, 72, 73
- [47] Bessem Bouraoui, Christian Ronse, Joseph Baruthio, Nicolas Passat, and Ph Germain. Fully automatic 3d segmentation of coronary arteries based on mathematical morphology. In *Biomedical Imaging: From Nano to Macro, 2008. ISBI 2008. 5th IEEE International Symposium on*, pages 1059–1062. IEEE, 2008. 74, 82, 136, 137, 141, 144
- [48] Douglas P Boyd and Martin J Lipton. Cardiac computed tomography. *Proceedings of the IEEE*, 71(3):298–307, 1983. 27

- 
- [49] Y. Boykov and V. Kolmogorov. Computing geodesics and minimal surfaces via graph cuts. In *Computer Vision, 2003. Proceedings. Ninth IEEE International Conference on*, pages 26–33 vol.1, oct. 2003. [114](#)
- [50] Yuri Boykov, Olga Veksler, and Ramin Zabih. Fast approximate energy minimization via graph cuts. *ICCV*, pages 377–384, 1999. [57](#), [138](#), [173](#)
- [51] Yuri Boykov, Olga Veksler, and Ramin Zabih. Fast approximate energy minimization via graph cuts. *Pattern Analysis and Machine Intelligence, IEEE Transactions on*, 23(11):1222–1239, 2001. [91](#)
- [52] Y.Y. Boykov and M.-P. Jolly. Interactive graph cuts for optimal boundary and region segmentation of objects in n-d images. In *Computer Vision, 2001. ICCV 2001. Proceedings. Eighth IEEE International Conference on*, volume 1, pages 105–112 vol.1, 2001. [114](#)
- [53] Hans-Jürgen Brambs and Andrik J Aschoff. Noninvasive coronary angiography with 16-detector row ct: effect of heart rate. *Radiology*, 234:86–97, 2005. [27](#)
- [54] C Brasselet, F Addad, and A Lafont. Qu’est-ce qu’une sténose coronaire significative? *La Lettre du cardiologue*, (352):32–36, 2002. [16](#)
- [55] Edmond J. Breen and Ronald Jones. Attribute openings, thinnings, and granulometries. *Comput. Vis. Image Underst.*, 64(3):377–389, November 1996. [149](#)
- [56] JF Breen, PF Sheedy 2nd, RS Schwartz, AW Stanson, RB Kaufmann, PP Moll, and JA Rumberger. Coronary artery calcification detected with ultrafast ct as an indication of coronary artery disease. *Radiology*, 185(2):435–439, 1992. [28](#)
- [57] Leo Breiman. Bagging predictors. *Mach. Learn.*, 24(2):123–140, August 1996. [237](#)
- [58] Leo Breiman. Random forests. *Machine learning*, 45(1):5–32, 2001. [236](#), [237](#), [238](#), [256](#)
- [59] Leo Breiman, Jerome Friedman, Charles J Stone, and Richard A Olshen. *Classification and regression trees*. CRC press, 1984. [236](#)
- [60] David J Brenner and Eric J Hall. Computed tomography - an increasing source of radiation exposure. *New England Journal of Medicine*, 357(22):2277–2284, 2007. [25](#)
- [61] Markus M Breunig, Hans-Peter Kriegel, Raymond T Ng, and Jörg Sander. Lof: identifying density-based local outliers. In *ACM Sigmod Record*, volume 29, pages 93–104. ACM, 2000. [101](#)
- [62] Harald Brodoefel, Christof Burgstahler, Ilias Tsiflikas, Anja Reimann, Stephen Schroeder, Claus D Claussen, Martin Heuschmid, and Andreas F Kopp. Dual-source ct: Effect of heart rate, heart rate variability, and calcification on image quality and diagnostic accuracy 1. *Radiology*, 247(2):346–355, 2008. [31](#)
- [63] Alexander Broersen, P Kitslaar, Michel Frenay, and Jouke Dijkstra. Frenchcoast: fast, robust extraction for the nice challenge on coronary artery segmentation of the tree. In *In Proceedings of MICCAI workshop "3D cardiovascular imaging: a MICCAI segmentation challenge."*, 2012. [188](#), [194](#), [292](#), [293](#)

## Bibliography

---

- [64] Gerd Brunner, Uday Kurkure, Deepak R Chittajallu, Raja P Yalamanchili, and Ioannis A Kakadiaris. Toward unsupervised classification of calcified arterial lesions. In *Medical Image Computing and Computer-Assisted Intervention–MICCAI 2008*, pages 144–152. Springer, 2008. [196](#), [197](#), [200](#), [206](#)
- [65] Gerd Brunner, Deepak R Chittajallu, Uday Kurkure, and Ioannis A Kakadiaris. Toward the automatic detection of coronary artery calcification in non-contrast computed tomography data. *The international journal of cardiovascular imaging*, 26(7):829–838, 2010. [197](#), [200](#), [206](#), [233](#)
- [66] Antoni Buades, Bartomeu Coll, and Jean-Michel Morel. A review of image denoising algorithms, with a new one. *SIAM Journal on Multiscale Modeling and Simulation*, 4(2):490–530, 2005. [56](#)
- [67] Michael Buckley and Hugues Talbot. Flexible linear openings and closings. In *Mathematical Morphology and its Applications to Image and Signal Processing*, pages 109–118. Springer, 2000. [147](#)
- [68] Matthew J Budoff, Ronald J Oudiz, Conrad P Zalace, Hamid Bakhsheshi, Steven L Goldberg, William J French, Tapan G Rami, and Bruce H Brundage. Intravenous three-dimensional coronary angiography using contrast enhanced electron beam computed tomography. *The American journal of cardiology*, 83(6):840–845, 1999. [28](#)
- [69] Peter Bühlmann and Torsten Hothorn. Boosting algorithms: Regularization, prediction and model fitting. *Statistical Science*, pages 477–505, 2007. [234](#)
- [70] Elizabeth Bullitt and Stephen R. Aylward. Volume rendering of segmented tubular objects. In *MICCAI*, pages 161–168, 2001. [67](#), [70](#)
- [71] Benoît Caldaïrou, Benoît Naegel, and Nicolas Passat. Segmentation of complex images based on component-trees: Methodological tools. In *Mathematical Morphology and Its Application to Signal and Image Processing*, pages 171–180. Springer, 2009. [155](#)
- [72] Benoît Caldaïrou, Nicolas Passat, and Benoît Naegel. Attribute-filtering and knowledge extraction for vessel segmentation. In *Advances in Visual Computing*, pages 13–22. Springer, 2010. [82](#), [155](#)
- [73] Paul S Calhoun, Brian S Kuszyk, David G Heath, Jennifer C Carley, and Elliot K Fishman. Three-dimensional volume rendering of spiral ct data: Theory and method 1. *Radiographics*, 19(3):745–764, 1999. [39](#)
- [74] Oscar Camara, Gaspar Delso, Olivier Colliot, Antonio Moreno-Ingelmo, and Isabelle Bloch. Explicit incorporation of prior anatomical information into a nonrigid registration of thoracic and abdominal ct and 18-fdg whole-body emission pet images. *Medical Imaging, IEEE Transactions on*, 26(2):164–178, 2007. [87](#)
- [75] J.F. Carrillo, M. Hernández Hoyos, E.E. Davila-Serrano, and M. Orkisz. Recursive tracking of vascular tree axes in 3d medical images. *Int J Comput Assisted Radiol Surg*, 1(6):331–339, 2007. [70](#)



- [76] Juan F. Carrillo, Maciej Orkisz, and Marcela Hernández Hoyos. Extraction of 3d vascular tree skeletons based on the analysis of connected components evolution. *Computer Analysis of Images and Patterns*, 3691:604–611, 2005. 70, 72
- [77] Rich Caruana, Nikos Karampatziakis, and Ainur Yessenalina. An empirical evaluation of supervised learning in high dimensions. In *Proceedings of the 25th international conference on Machine learning*, pages 96–103. ACM, 2008. 237
- [78] C Castro, MA Luengo-Oroz, A Santos, and MJ Ledesma-Carbayo. Coronary artery tracking in 3d cardiac ct images using local morphological reconstruction operators. *The Insight Journal*, 4, 2008. 57, 58, 59, 82, 92
- [79] Manuel D Cerqueira, Neil J Weissman, Vasken Dilsizian, Alice K Jacobs, Sanjiv Kaul, Warren K Laskey, Dudley J Pennell, John A Rumberger, Thomas Ryan, Mario S Verani, et al. Standardized myocardial segmentation and nomenclature for tomographic imaging of the heart a statement for healthcare professionals from the cardiac imaging committee of the council on clinical cardiology of the american heart association. *Circulation*, 105(4):539–542, 2002.
- [80] Suheyly Cetin and Gozde Unal. Automatic detection of coronary artery stenosis in cta based on vessel intensity and geometric features. In *Proc. of MICCAI Workshop 3D Cardiovascular Imaging: a MICCAI segmentation, Challenge*, 2012. 140, 188, 199, 200, 206, 237, 243, 250, 256, 292
- [81] Suheyly Cetin, Gozde Unal, and Muzaffer Degertekin. An automatic branch and stenoses detection in computed tomography angiography. In *Biomedical Imaging (ISBI), 2012 9th IEEE International Symposium on*, pages 582–585. IEEE, 2012. 189, 194, 292, 293
- [82] Suheyly Cetin, Ali Demir, Anthony Yezzi, Muzaffer Degertekin, and Gozde Unal. Vessel trac-tography using an intensity based tensor model with branch detection. *Medical Imaging, IEEE Transactions on*, 32(2):348–363, 2013. 140
- [83] Olivier Chapelle, Bernhard Schölkopf, Alexander Zien, et al. *Semi-supervised learning*, volume 2. MIT press Cambridge, 2006. 231
- [84] Jian Chen, Yoshinobu Sato, and Shinichi Tamura. Orientation space filtering for multiple orientation line segmentation. *IEEE Transactions on Pattern Analysis and Machine Intelligence*, 22:417 – 429, 1998. 55
- [85] Shuo-Tsung Chen, Chao-Yu Huang, and Chung-Ming Chen. Automatic segmentation of coronary arteries based on region growing and discrete wavelet transformation. In *Computing, Measurement, Control and Sensor Network (CMCSN), 2012 International Conference on*, pages 5–8, July 2012. 136, 143
- [86] A.Y.S. Chia, M.K.H. Leung, HL. Eng, and S. Rahardja. Ellipse detection with hough transform in one dimensional parametric space. In *Proc. IEEE ICIP*, pages 333 –336, 2007. 106
- [87] Grahams Child. Endo dysfunction athero.png - this file is licensed under the creative commons attribution-share alike 3.0 unported license., accessed: May 20 2014. URL [http://en.wikipedia.org/wiki/File:Endo\\_dysfunction\\_Athero.PNG](http://en.wikipedia.org/wiki/File:Endo_dysfunction_Athero.PNG). xvii, 13



## Bibliography

---

- [88] A. C. S. Chung, J. A. Noble, P. E. Summers, and M. Brady. 3D vascular segmentation using MRA statistics and velocity field information in PC-MRA. *In Information Processing in Medical Imaging - IPMI*, 2082 of Lecture Notes in Computer Science:461–467, 2001. [61](#)
- [89] A.C.S. Chung and J.A. Noble. Statistical 3d vessel segmentation using a rician distribution. *Proc. Med. Image Comput. Assist. Interv.*, pages 82–89, 1999. [61](#)
- [90] Robert Cierniak and Mike Butynski. *X-ray computed tomography in biomedical engineering*. Springer, 2011. [xviii](#), [23](#), [24](#), [25](#), [26](#), [27](#)
- [91] Jacob Cohen. Weighted kappa: Nominal scale agreement provision for scaled disagreement or partial credit. *Psychological bulletin*, 70(4):213, 1968. [210](#)
- [92] François Cokelaer, Hugues Talbot, and Jocelyn Chanussot. Efficient robust d-dimensional path operators. *Selected Topics in Signal Processing, IEEE journal of*, 6(7):830–839, 2012. [48](#), [148](#), [160](#)
- [93] Stéphane Cook, Alexander Walker, Olivier Hügli, Mario Togni, and Bernhard Meier. Percutaneous coronary interventions in europe: prevalence, numerical estimates, and projections based on data up to 2004. *Clinical Research in Cardiology*, 96:375–82, 2007. [1](#)
- [94] Corinna Cortes and Vladimir Vapnik. Support-vector networks. *Machine Learning*, 20(3):273–297, 1995. ISSN 0885-6125. doi: 10.1007/BF00994018. [231](#), [232](#)
- [95] C. Couprie, L. Grady, L. Najman, and H. Talbot. Power watersheds: A unifying graph based optimization framework. *IEEE Transactions on Pattern Analysis and Machine Intelligence*, 2009. [138](#)
- [96] C. Couprie, L. Grady, L. Najman, and H. Talbot. A new image segmentation framework: Powerwatersheds. *International Symposium on Mathematical Morphology*, pages 53–55, 2009. [179](#)
- [97] Camille Couprie, Laurent Najman, and Hugues Talbot. Seeded segmentation methods for medical image analysis. In *Medical Image Processing*, pages 27–57. Springer, 2011. [173](#)
- [98] Michel Couprie, David Coeurjolly, and Rita Zrour. Discrete bisector function and Euclidean skeleton in 2D and 3D. *Image and Vision Computing*, 25(10):1519–1698, October 2007. [73](#)
- [99] Richard Courant and David Hilbert. *Methods of Mathematical Physics*, volume 2. John Wiley and Sons, 1989. [115](#)
- [100] J. Cousty, G. Bertrand, L. Najman, and M. Couprie. Watershed cuts: thinnings, shortest-path forests and topological watersheds. *IEEE Transactions on Pattern Analysis and Machine Intelligence*, 2009. [113](#), [173](#)
- [101] Antonio Criminisi, Jamie Shotton, and Ender Konukoglu. Decision forests: A unified framework for classification, regression, density estimation, manifold learning and semi-supervised learning. *Foundations and Trends in Computer Graphics and Vision: Vol. 7: No 2-3, pp 81-227*, 2012. [237](#), [238](#)

- 
- [102] A.J. Culyer. *Encyclopedia of Health Economics*. Elsevier Science & Technology Books, 2014. ISBN 9780123756787. [22](#)
- [103] M. de Bruijne, B. van Ginneken, M. A. Viergever, and W. J. Niessen. Adapting active shape models for 3d segmentation of tubular structures in medical images. *Information Processing in Medical Imaging*, 2732:136–147, 2003. [62](#)
- [104] de Bruijne M., B. van Ginneken, W. Niessen, M. Loog, and M. Viergever. Modelbased segmentation of abdominal aortic aneurysms in cta images. *SPIE Medical Imaging*, 5032:1560–1571, 2003. [62](#), [184](#), [186](#)
- [105] R B Dean and W J Dixon. Simplified statistics for small numbers of observations. *Analytical Chemistry*, 23(4):636–638, 1951. [102](#)
- [106] K. Deguchi, T. Izumitani, and H. Hontani. Detection and enhancement of line structures in an image by anisotropic diffusion. *Pattern Recognition Letters*, 23(12):1399–1405, 2002. [55](#)
- [107] Jamshid Dehmeshki, Xujiong Ye, D Amin, Maryam Abaei, XinYu Lin, and Salah D Qanadli. Volumetric quantification of atherosclerotic plaque in ct considering partial volume effect. *Medical Imaging, IEEE Transactions on*, 26(3):273–282, 2007. [192](#)
- [108] M.A.M. Den Dekker, K. De Smet, G.H. De Bock, R.A. Tio, M. Oudkerk, and R. Vliegenthart. Diagnostic performance of coronary ct angiography for stenosis detection according to calcium score: Systematic review and meta-analysis. *European Radiology*, 22(12):2688–2698, 2012. [31](#)
- [109] T. Deschamps and L.D. Cohen. Fast extraction of minimal paths in 3D images and applications to virtual endoscopy. *Medical Image Analysis*, 5(4), 2001. [xx](#), [67](#), [68](#)
- [110] Maxime Descoteaux, Louis Collins, and Kaleem Siddiqi. Geometric flows for segmenting vasculature in mri: Theory and validation. In Christian Barillot, DavidR. Haynor, and Pierre Hellier, editors, *Medical Image Computing and Computer-Assisted Intervention — MICCAI 2004*, volume 3216 of *Lecture Notes in Computer Science*, pages 500–507. Springer Berlin Heidelberg, 2004. ISBN 978-3-540-22976-6. [80](#)
- [111] Robert C Detrano, Terence M Doherty, Michael J Davies, and Herbert C Stary. Predicting coronary events with coronary calcium: pathophysiologic and clinical problems. *Current problems in cardiology*, 25(6):369–402, 2000. [30](#)
- [112] Marc Dewey, Andrea L Vavere, Armin Arbab-Zadeh, Julie M Miller, Leonardo Sara, Christopher Cox, Ilan Gottlieb, Kunihiro Yoshioka, Narinder Paul, John Hoe, et al. Patient characteristics as predictors of image quality and diagnostic accuracy of mdct compared with conventional coronary angiography for detecting coronary artery stenoses: Core-64 multicenter international trial. *AJR. American journal of roentgenology*, 194(1):93, 2010. [31](#)
- [113] Damini Dey, Tracy Callister, Piotr Slomka, Fatma Aboul-Enein, Hidetaka Nishina, Xingping Kang, Heidi Gransar, Nathan D Wong, Romalisa Miranda-Peats, Sean Hayes, et al. Computer-aided detection and evaluation of lipid-rich plaque on noncontrast cardiac ct. *American Journal of Roentgenology*, 186(6 Supplement 2):407–413, 2006. [191](#)

## Bibliography

---

- [114] Damini Dey, Cynthia J Lee, Muneo Ohba, Ariel Gutstein, Piotr J Slomka, Victor Cheng, Yasuyuki Suzuki, Shoji Suzuki, Arik Wolak, Ludovic Le Meunier, et al. Image quality and artifacts in coronary ct angiography with dual-source ct: initial clinical experience. *Journal of cardiovascular computed tomography*, 2(2):105–114, 2008. [31](#)
- [115] Damini Dey, Victor Y Cheng, Piotr J Slomka, Ryo Nakazato, Amit Ramesh, Swaminatha Gurudevan, Guido Germano, and Daniel S Berman. Automated 3-dimensional quantification of noncalcified and calcified coronary plaque from coronary ct angiography. *Journal of cardiovascular computed tomography*, 3(6):372–382, 2009. [191](#), [194](#)
- [116] Lee R Dice. Measures of the amount of ecologic association between species. *Ecology*, 26(3):297–302, 1945. [123](#)
- [117] E. W. Dijkstra. A note on two problems in connexion with graphs. *Numerische Mathematik*, 1:269–271, 1959. [67](#)
- [118] Engin Dikici, O'Donnell Thomas, Grady Leo, and White Richard. Coronary artery centerline tracking using axial symmetries. *The Insight Journal*, 2008. [68](#)
- [119] Wilson DL and Royston DD znd Noble JA znd Byrne JV. Determining x-ray projections for coil treatments of intracranial aneurysms. *IEEE Trans Med Imaging.*, 18(10):973–80, Oct 1999. [61](#)
- [120] JT Dodge, B Greg Brown, Edward L Bolson, and Harold T Dodge. Lumen diameter of normal human coronary arteries. influence of age, sex, anatomic variation, and left ventricular hypertrophy or dilation. *Circulation*, 86(1):232–246, 1992. [xxxv](#), [11](#), [12](#)
- [121] Dokladal, P. Lohou C., Perroton L., and Bertrand G. Liver blood vessels extraction by a 3-d topological approach. *MICCAI*, pages 98–105, 1999. [75](#)
- [122] Petr Dokládál and Dominique Jeulin. 3-d extraction of fibres from microtomographic images of fibre-reinforced composite materials. In *Mathematical Morphology and Its Application to Signal and Image Processing*, pages 126–136. Springer, 2009. [144](#)
- [123] Petr Dokládál, Isabelle Bloch, Michel Couprie, Daniel Ruijters, Raquel Urtasun, and Line Gärner. Topologically controlled segmentation of 3d magnetic resonance images of the head by using morphological operators. *Pattern Recognition*, 36(10):2463–2478, 2003. [155](#)
- [124] Olivio F Donati, Paul Stolzmann, Lotus Desbiolles, Sebastian Leschka, Sebastian Kozerke, André Plass, Christophe Wyss, Volkmar Falk, Borut Marincek, Hatem Alkadhi, et al. Coronary artery disease: Which degree of coronary artery stenosis is indicative of ischemia? *European journal of radiology*, 80(1):120–126, 2011. [35](#)
- [125] V. Doré and M. Cheriet. Robust nl-means filter with optimal pixel-wise smoothing parameter for statistical image denoising. *IEEE Transactions on Signal Processing*, 57:1703–1716, 2009. [55](#)
- [126] Peter G. Doyle and J. Laurie Snell. *Random Walks and Electric Networks*. Mathematical Association of America, Washington, DC, 1984. [116](#)

- 
- [127] Kai-Bo Duan and S Sathiya Keerthi. Which is the best multiclass svm method? an empirical study. In *Multiple Classifier Systems*, pages 278–285. Springer, 2005. [233](#)
- [128] Alice Dufour, Nicolas Passat, Benoît Naegel, and Joseph Baruthio. Interactive 3d brain vessel segmentation from an example. In *Biomedical Imaging: From Nano to Macro, 2011 IEEE International Symposium on*, pages 1121–1124. IEEE, 2011. [82](#)
- [129] Alice Dufour, Olena Tankyevych, Benoît Naegel, Hugues Talbot, Christian Ronse, Joseph Baruthio, Petr Dokládál, and Nicolas Passat. Filtering and segmentation of 3d angiographic data: Advances based on mathematical morphology. *Medical image analysis*, 17(2):147–164, 2013. [82](#)
- [130] David M Dutton and Gerard V Conroy. A review of machine learning. *The Knowledge Engineering Review*, 12(04):341–367, 1997. [230](#)
- [131] Matthieu Duval, Elodie Ouzeau, Frederic Precioso, and Bogdan Matuszewski. Coronary artery stenoses detection with random forest. In *3D Cardiovascular Imaging: A MICCAI segmentation challenge*, 2012. [199](#), [200](#), [206](#), [256](#), [292](#), [293](#)
- [132] O. Ecabert, J. Peters, H. Schramm, C. Lorenz, J. Von Berg, M.J. Walker, M. Vembar, M.E. Olszewski, K. Subramanyan, G. Lavi, and J. Weese. Automatic model-based segmentation of the heart in ct images. *Medical Imaging, IEEE Transactions on*, 27(9):1189–1201, Sept 2008. ISSN 0278-0062. [91](#), [93](#), [134](#)
- [133] Ayman El-Baz, Aly A Farag, Georgy Gimel’farb, Mohamed A El-Ghar, and Tarek Eldiasty. A new adaptive probabilistic model of blood vessels for segmenting mra images. In *Medical Image Computing and Computer-Assisted Intervention–MICCAI 2006*, pages 799–806. Springer, 2006. [61](#)
- [134] Raimund Erbel, Stefan Möhlenkamp, Susanne Moebus, Axel Schmermund, Nils Lehmann, Andreas Stang, Nico Dragano, Dietrich Grönemeyer, Rainer Seibel, Hagen Kälisch, et al. Coronary risk stratification, discrimination, and reclassification improvement based on quantification of subclinical coronary atherosclerosis—the heinz nixdorf recall study. *Journal of the American College of Cardiology*, 56(17):1397–1406, 2010. [30](#)
- [135] Abouzar Eslami, Amin Aboee, Zardosht Hodaei, Mandana Javanshir, Stephane Carlier Moghadam, Amin Katouzian, and Nassir Navab. Quantification of coronary arterial stenosis by inflating tubes in ct angiographic images. In *3D Cardiovascular Imaging: A MICCAI segmentation challenge*, 2012. [188](#), [194](#), [292](#), [293](#), [294](#)
- [136] Hongqin Fan, Osmar R. Za’ane, Andrew Foss, and Junfeng Wu. A nonparametric outlier detection for effectively discovering top-n outliers from engineering data. In *PAKDD’06*, pages 557–566, 2006. [101](#)
- [137] Jiahua Fan, Frank Dong, Paavana Sainath, Jiang Hsieh, Xiangyang Tang, Thomas Toth, Baojun Li, Peter Crandall, Robert Senzig, and Adam Dixon. Image quality evaluation of a lightspeed ct750 hd computed tomography system. In *SPIE Medical Imaging*, pages 72584S–72584S. International Society for Optics and Photonics, 2009. [25](#)

## Bibliography

---

- [138] Fastcoexist.com. This machine can 3-D scan your insides in a single heartbeat, January 3 2014. [25](#)
- [139] A. Fitzgibbon, M. Pilu, and R.B. Fishe. Direct least-squares fitting of ellipses. *PAMI, IEEE Transactions on*, 21:476–480, 1999. [106](#), [108](#)
- [140] N. Flasque, M. Desvignes, J.-M. Constans, and M. Revenu. Acquisition, segmentation and tracking of the cerebral vascular tree on 3D magnetic resonance angiography images. *Medical Image Analysis*, 5(3):173–183, September 2001. [70](#), [72](#)
- [141] Leonardo Flórez Valencia, Maciej Orkisz, RA Corredor Jerez, JS Torres González, EM Correa Agudelo, Claire Mouton, and M Hernández Hoyos. Coronary artery segmentation and stenosis quantification in CT images with use of a right generalized cylinder model. In *Proceedings of MICCAI workshop "3D cardiovascular imaging: a MICCAI segmentation challenge*, 2012. [188](#), [194](#), [292](#), [293](#)
- [142] C. Florin, N. Paragios, and J. Williams. Globally optimal active contours, sequential monte-carlo and on-line learning for vessel segmentation. *Eur. Conf. Comput. Vision*, pages 476–489, 2006. [63](#)
- [143] Charles Florin, Romain Moreau-Gobard, and Jim Williams. Automatic heart peripheral vessels segmentation based on a normal mip ray casting technique. In *Medical Image Computing and Computer-Assisted Intervention–MICCAI 2004*, pages 483–490. Springer, 2004. [57](#), [59](#), [91](#), [99](#)
- [144] Charles Florin, Nikos Paragios, and Jim Williams. Particle filters, a quasi-monte carlo solution for segmentation of coronaries. *Proc. Med. Image Comput. Assist. Interv.*, pages 246–253, 2005. [61](#), [63](#)
- [145] E. W. Forgy. Cluster analysis of multivariate data: efficiency versus interpretability of classifications. *Biometrics*, 21:768–769, 1965. [231](#)
- [146] A.F. Frangi, W.J. Niessen, R.M. Hoogeveen, T. van Walsum, and M.A. Viergever. Model-based quantitation of 3-d magnetic resonance angiographic images. *Medical Imaging, IEEE Transactions on*, 18(10):946–956, 1999. [62](#), [63](#), [78](#)
- [147] A.F. Frangi, W.J. Niessen, P.J. Nederkoorn, O.E.H. Elgersma, and M.A. Viergever. Three-dimensional model-based stenosis quantification of the carotid arteries from contrast-enhanced mr angiography. In *Mathematical Methods in Biomedical Image Analysis, 2000. Proceedings. IEEE Workshop on*, pages 110 –118, 2000. [62](#), [69](#), [78](#), [184](#), [185](#), [192](#)
- [148] A.F. Frangi, W.J. Niessen, and M.A. Viergever. Three-dimensional modeling for functional analysis of cardiac images, a review. *Medical Imaging, IEEE Transactions on*, 20(1):2 –5, jan 2001. ISSN 0278-0062. [90](#)
- [149] AlejandroF. Frangi, WiroJ. Niessen, KoenL. Vincken, and MaxA. Viergever. Multiscale vessel enhancement filtering. In WilliamM. Wells, Alan Colchester, and Scott Delp, editors, *Medical Image Computing and Computer-Assisted Intervention – MICCAI – 98*, volume 1496 of *Lecture Notes in Computer Science*, pages 130–137. Springer Berlin Heidelberg, 1998. [xx](#), [xxi](#), [56](#), [62](#), [64](#), [65](#), [76](#), [79](#), [145](#)

- 
- [150] Yoav Freund and Robert E Schapire. A decision-theoretic generalization of on-line learning and an application to boosting. In *Computational learning theory*, pages 23–37. Springer, 1995. 234
  - [151] Hichem Frigui and Raghu Krishnapuram. A robust competitive clustering algorithm with applications in computer vision. *Pattern Analysis and Machine Intelligence, IEEE Transactions on*, 21(5):450–465, 1999. 77
  - [152] O. Friman, M. Hindennach, and H.-O. Peitgen. Template-based multiple hypotheses tracking of small vessels. *Biomedical Imaging: From Nano to Macro, 2008. ISBI 2008. 5th IEEE International Symposium on*, pages 1047–1050, May 2008. xx, 54, 55, 58, 64, 70, 71
  - [153] Ola Friman, Milo Hindennach, Caroline Kuhnel, and Heinz-Otto Peitgen. Multiple hypothesis template tracking of small 3d vessel structures. *Medical Image Analysis*, 14(2):160 – 171, 2010. URL <http://www.sciencedirect.com/science/article/pii/S1361841509001479>. 69, 70
  - [154] Gareth Funka-Lea, Yuri Boykov, Charles Florin, M-P Jolly, Romain Moreau-Gobard, Rana Ramaraj, and Daniel Rinck. Automatic heart isolation for ct coronary visualization using graph-cuts. In *Biomedical Imaging: Nano to Macro, 2006. 3rd IEEE International Symposium on*, pages 614–617. IEEE, 2006. 92, 93, 96, 98, 99, 132, 134
  - [155] R. Gan, A.C.S. Chung, W.C.K. Wong, and S.C.H. Yu. Vascular segmentation in three-dimensional rotational angiography based on maximum intensity projections. *Proc. IEEE Int. Symp. Biomed. Imaging*, pages 133–136, 2004. 57
  - [156] S Gang, L Min, L Li, L Guo-Ying, X Lin, J Qun, and Z Hua. Evaluation of CT coronary artery angiography with 320-row detector CT in a high-risk population. *Evaluation*, 85(1013), 2012. 31
  - [157] Pierre Geurts, Damien Ernst, and Louis Wehenkel. Extremely randomized trees. *Machine learning*, 63(1):3–42, 2006. 197
  - [158] E Ghersin, D Litmanovich, A Kerner, A Engel, and T Hayek. Elongated eccentric soft coronary plaque: Major diagnostic pitfall on quantitative coronary angiography overpowered by computed tomography coronary angiography and intravascular ultrasound. *Australasian radiology*, 50(3): 267–270, 2006. 34
  - [159] Shashikant Ghumbre, Chetan Patil, and Ashok Ghatol. Heart disease diagnosis using support vector machine. In *International Conference on Computer Science and Information Technology*, 2011. 233
  - [160] Tom Giesler, Ulrich Baum, Dieter Ropers, Stefan Ulzheimer, Evelyn Wenkel, Maria Mennicke, Werner Bautz, Willi A Kalender, Werner G Daniel, and Stephan Achenbach. Noninvasive visualization of coronary arteries using contrast-enhanced multidetector CT: influence of heart rate on image quality and stenosis detection. *American Journal of Roentgenology*, 179(4):911–916, 2002. 27
  - [161] Roman Goldenberg, Dov Eilat, Grigory Begelman, Eugene Walach, Eyal Ben-Ishai, and Nathan Peled. Computer-aided simple triage (CAST) for coronary ct angiography (CCTA). *International journal of computer assisted radiology and surgery*, 7(6):819–827, 2012. 185, 189, 190, 194, 206, 212, 308



## Bibliography

---

- [162] Gene H. Golub and Charles F. Van Loan. *Matrix computations (3rd ed.)*. Johns Hopkins University Press, Baltimore, MD, USA, 1996. [119](#)
- [163] R. Gong, S. Wörz, and K. Rohr. Segmentation of coronary arteries of the human heart from 3d medical images. In *Workshop Bildverarbeitung für die Medizin*, pages 66–70, 2003. [70](#)
- [164] L. Grady. Random walks for image segmentation. *PAMI, IEEE Transactions on*, 28:1768–1783, 2006. [114](#), [116](#), [138](#), [173](#)
- [165] N. Grammalidis and M.G. Strintzis. Head detection and tracking by 2-d and 3-d ellipsoid fitting. In *Computer Graphics International, 2000. Proceedings*, pages 221–226, 2000. [xxii](#), [106](#), [108](#), [110](#)
- [166] P.M. Gregson. Automatic segmentation of the heart in 3d mr images. In *Electrical and Computer Engineering, 1994. Conference Proceedings. 1994 Canadian Conference on*, pages 584–587 vol.2, Sep 1994. [92](#), [93](#)
- [167] Marie-Louise Grønholdt, Aase Wagner, Britt M Wiebe, Jon U Hansen, Torben V Schroeder, Jens E Wilhjelm, Markus Nowak, and Henrik Sillesen. Spiral computed tomographic imaging related to computerized ultrasonographic images of carotid plaque morphology and histology. *Journal of ultrasound in medicine*, 20(5):451–458, 2001. [30](#)
- [168] Frank E. Grubbs. Procedures for detecting outlying observations in samples. *Technometrics*, 11(1):1–21, 1969. [100](#), [102](#)
- [169] Joachim Gruettner, Christian Fink, Thomas Walter, Mathias Meyer, Paul Apfaltrer, U Joseph Schoepf, Joachim Saur, Tim Sueselbeck, Dominik Traunwieser, Richard Takx, et al. Coronary computed tomography and triple rule out ct in patients with acute chest pain and an intermediate cardiac risk profile. part 1: impact on patient management. *European journal of radiology*, 82(1):100–105, 2013. [34](#)
- [170] M Akif Gülsün and Hüseyin Tek. Robust vessel tree modeling. In *Medical Image Computing and Computer-Assisted Intervention–MICCAI 2008*, pages 602–611. Springer, 2008. [67](#), [68](#), [69](#), [81](#)
- [171] Ethan J Halpern and David J Halpern. Diagnosis of coronary stenosis with ct angiography: comparison of automated computer diagnosis with expert readings. *Academic Radiology*, 18(3):324–333, 2011. [188](#)
- [172] Ethan J Halpern, Michael P Savage, David L Fischman, and David C Levin. Cost-effectiveness of coronary ct angiography in evaluation of patients without symptoms who have positive stress test results. *American journal of roentgenology*, 194(5):1257–1262, 2010. [34](#)
- [173] K Hameeteman, Maria A Zuluaga, Moti Freiman, Leo Joskowicz, Olivier Cuisenaire, L Flórez Valencia, Mehmet Akif Gülsün, Karl Krissian, Julien Mille, Wilbur CK Wong, et al. Evaluation framework for carotid bifurcation lumen segmentation and stenosis grading. *Medical Image Analysis*, 15(4):477–488, 2011. [184](#)
- [174] M. Sabry Hassouna, A. A. Farag, S. Hushek, and T. Moriarty. Cerebrovascular segmentation from tof using stochastic models. *Medical Image Analysis*, 10(1):2–18, 2006. [61](#)

- 
- [175] M.S. Hassouna and A.A. Farag. On the extraction of curve skeletons using gradient vector flow. *Proc. of ICCV*, pages 1–8, 2007. [62](#), [72](#)
- [176] M.S. Hassouna, A.A. Farag, S.G. Hushek, and T. Moriarty. Statistical-based approach for extracting 3d blood vessels from tof-myra data. *Proc. Med. Image Comput. Assist. Interv.*, pages 680–687, 2003. [57](#), [61](#)
- [177] Jörg Hausleiter, Tanja Meyer, Martin Hadamitzky, Maria Zankl, Pia Gerein, Katharina Dörler, Adnan Kastrati, Stefan Martinoff, and Albert Schömig. Non-invasive coronary computed tomographic angiography for patients with suspected coronary artery disease: the coronary angiography by computed tomography with the use of a submillimeter resolution (cactus) trial. *European heart journal*, 28(24):3034–3041, 2007. [31](#)
- [178] D M Hawkins. *Identification of outliers*. Monographs on Applied Probability and Statistics. Springer, Dordrecht, 1980. [100](#)
- [179] Henk Heijmans, Michael Buckley, and Hugues Talbot. Path-based morphological openings. In *Image Processing, 2004. ICIP'04. 2004 International Conference on*, volume 5, pages 3085–3088. IEEE, 2004. [147](#)
- [180] Henk Heijmans, Michael Buckley, and Hugues Talbot. Path openings and closings. *Journal of Mathematical Imaging and Vision*, 22:107–119, 2005. [10.1007/s10851-005-4885-3](#). [147](#)
- [181] G. T. Herman. Image reconstruction from projections. *Real-Time Imaging*, 1(1):3 – 18, 1995. [22](#)
- [182] Monica Hernandez and Alejandro F. Frangi. Non-parametric geodesic active regions: Method and evaluation for cerebral aneurysms segmentation in 3dra and cta. *Medical Image Analysis*, 11(3):224 – 241, 2007. [184](#), [187](#)
- [183] Monica Hernandez, Alejandro F. Frangi, and Guillermo Sapiro. Three-dimensional segmentation of brain aneurysms in cta using non-parametric region-based information and implicit deformable models: Method and evaluation. In Randy E. Ellis and Terry M. Peters, editors, *Medical Image Computing and Computer-Assisted Intervention - MICCAI 2003*, volume 2879 of *Lecture Notes in Computer Science*, pages 594–602. Springer Berlin / Heidelberg, 2003. [184](#), [187](#)
- [184] M. Hernández Hoyos, M.A. Zuluaga, M. Lozano, J.C. Prieto, P. Douek, I.E. Magnin, and M. Orkisz. Coronary centerline tracking in ct images with use of an elastic model and image moments. In *MICCAI Workshop - Grand Challenge Coronary Artery Tracking*, pages 8 on-line: <http://hdl.handle.net/10380/1401>, New York City, USA, September 2008. Midas Journal, Midas Journal. [57](#), [70](#), [72](#)
- [185] Marcela Hernandez-Hoyos. *Segmentation anisotrope 3D pour la quantification en imagerie vasculaire par résonance magnétique (in french)*. PhD thesis, Ecole Doctorale des Sciences de l'Ingénieur de Lyon, CREATIS UMR-CNRS, 5515, Lyon, France., 2002. [62](#), [64](#), [70](#), [78](#)
- [186] Tin Kam Ho. The random subspace method for constructing decision forests. *Pattern Analysis and Machine Intelligence, IEEE Transactions on*, 20(8):832–844, 1998. [236](#)



## Bibliography

---

- [187] Vincent B. Ho and Gautham P. Reddy. *Cardiovascular Imaging*, volume 1. Elsevier Health Sciences, 2010.
- [188] Victoria J. Hodge and Jim Austin. A survey of outlier detection methodologies. *Artificial Intelligence Review*, 22:2004, 2004. [100](#)
- [189] Udo Hoffmann, Fabian Moselewski, Ricardo C Cury, Maros Ferencik, Ik-kyung Jang, Larry J Diaz, Suhny Abbara, Thomas J Brady, and Stephan Achenbach. Predictive value of 16-slice multidetector spiral computed tomography to detect significant obstructive coronary artery disease in patients at high risk for coronary artery disease patient-versus segment-based analysis. *Circulation*, 110(17):2638–2643, 2004. [31](#)
- [190] Udo Hoffmann, Quynh A Truong, Jerome L Fleg, Alexander Goehler, Scott Gazelle, Stephen Wiviott, Hang Lee, James E Udelson, and David Schoenfeld. Design of the rule out myocardial ischemia/infarction using computer assisted tomography: a multicenter randomized comparative effectiveness trial of cardiac computed tomography versus alternative triage strategies in patients with acute chest pain in the emergency department. *American heart journal*, 163(3):330–338, 2012. [34](#)
- [191] Godfrey N Hounsfield. Computed medical imaging. *Journal of computer assisted tomography*, 4(5):665–674, 1980. [22](#), [24](#), [27](#)
- [192] Marcela Hoyos, Piotr Orlowski, Ewa Piatkowska-Janko, Piotr Bogorodzki, and Maciej Orkisz. Vascular centerline extraction in 3d mr angiograms for phase contrast mri blood flow measurement. *International Journal of Computer Assisted Radiology and Surgery*, 1:51–61, 2006. 10.1007/s11548-006-0005-0. [70](#)
- [193] Marcela Hoyos, Jean-Michel Serfaty, Albinka Maghiar, Catherine Mansard, Maciej Orkisz, Isabelle Magnin, and Philippe Douek. Evaluation of semi-automatic arterial stenosis quantification. *International Journal of Computer Assisted Radiology and Surgery*, 1:167–175, 2006. 10.1007/s11548-006-0049-1. [185](#)
- [194] Marcela Hernández Hoyos, Maciej Orkisz, Philippe C. Douek, and Isabelle E. Magnin. Assessment of carotid artery stenoses in 3d contrast-enhanced magnetic resonance angiography, based on improved generation of the centerline. *MGEV*, 14:349–378, January 2005. [184](#)
- [195] P.C Hrimpton, Miller H.C, Lewis M.A, and Dunn M. Doses from computed tomography (ct) examinations in the uk. *Review*, 2003. [22](#)
- [196] Walter Huda and Awais Vance. Patient radiation doses from adult and pediatric ct. *AJR*, 188: 540–546, 2007. [22](#)
- [197] B. Iglewicz and D.C. Hoaglin. *How to detect and handle outliers*. ASQC basic references in quality control. ASQC Quality Press, 1993. ISBN 9780873892476. [100](#), [102](#), [103](#)
- [198] Ivana Išgum, Annemarieke Rutten, Mathias Prokop, and Bram Van Ginneken. Detection of coronary calcifications from computed tomography scans for automated risk assessment of coronary artery disease. *Medical Physics*, 34(4):1450–1461, 2007. [186](#), [196](#), [197](#), [200](#)

- 
- [199] Ivana Isgum, Marius Staring, Annemarieke Rutten, Mathias Prokop, Max A Viergever, and Bram van Ginneken. Multi-atlas-based segmentation with local decision fusion—application to cardiac and aortic segmentation in ct scans. *Medical Imaging, IEEE Transactions on*, 28(7): 1000–1010, 2009. [90](#), [91](#), [93](#), [132](#), [134](#), [206](#)
- [200] P. Jaccard. *Nouvelles recherches sur la distribution florale*. Bulletin de la Société vaudoise des sciences naturelles. Impr. Réunies, 1908.
- [201] Wen Jin, Anthony K. H. Tung, Jiawei Han, and Wei Wang. Ranking outliers using symmetric neighborhood relationship. In *In PAKDD*. Springer, 2006. [101](#)
- [202] Thorsten RC Johnson, Konstantin Nikolaou, Bernd J Wintersperger, Alexander W Leber, Franz von Ziegler, Carsten Rist, Sonja Buhmann, Andreas Knez, Maximilian F Reiser, and Christoph R Becker. Dual-source ct cardiac imaging: initial experience. *European radiology*, 16(7):1409–1415, 2006. [27](#), [30](#)
- [203] Thorsten RC Johnson, Christian Fink, Stefan O Schönberg, and Maximilian F Reiser. *Dual energy CT in clinical practice*, volume 201. Springer, 2011. [25](#)
- [204] Leslie Pack Kaelbling, Michael L Littman, and Andrew W Moore. Reinforcement learning: A survey. *Journal of Artificial Intelligence Research*, 4:237–285, 1996. [231](#)
- [205] Christoph Kaiser, Jens Bremerich, Sabine Haller, Hans Peter Brunner-La Rocca, Georg Bongartz, Matthias Pfisterer, and Peter Buser. Limited diagnostic yield of non-invasive coronary angiography by 16-slice multi-detector spiral computed tomography in routine patients referred for evaluation of coronary artery disease. *European heart journal*, 26(19):1987–1992, 2005. [31](#)
- [206] Dong-Goo Kang, Dae Chul Suh, and Jong Beom Ra. Three-dimensional blood vessel quantification via centerline deformation. *Medical Imaging, IEEE Transactions on*, 28(3):405–414, 2009. [187](#)
- [207] Dongwoo Kang, Piotr Slomka, Ryo Nakazato, Victor Y Cheng, James K Min, Debiao Li, Daniel S Berman, C-C Jay Kuo, and Damini Dey. Automatic detection of significant and subtle arterial lesions from coronary ct angiography. In *SPIE Medical Imaging*, pages 831435–831435. International Society for Optics and Photonics, 2012. [191](#), [299](#)
- [208] Dongwoo Kang, Piotr J Slomka, Ryo Nakazato, Reza Arsanjani, Victor Y Cheng, James K Min, Debiao Li, Daniel S Berman, C-C Jay Kuo, and Damini Dey. Automated knowledge-based detection of nonobstructive and obstructive arterial lesions from coronary ct angiography. *Medical physics*, 40(4):041912, 2013. [188](#), [190](#), [191](#), [194](#), [206](#), [299](#)
- [209] Savvas Karatsiolis and Christos N Schizas. Region based support vector machine algorithm for medical diagnosis on pima indian diabetes dataset. In *Bioinformatics & Bioengineering (BIBE), 2012 IEEE 12th International Conference on*, pages 139–144. IEEE, 2012. [233](#)
- [210] Michael Kass, Andrew Witkin, and Demetri Terzopoulos. Snakes: Active contour models. *International Journal of Computer Vision*, 1:321–331, 1988. 10.1007/BF00133570. [78](#)
- [211] Y. Kawata, N. Niki, and T. Kumazaki. An approach for detecting blood vessel diseases from cone-beam ct image. *Proc. IEEE Int. Conf. Image Process.*, 2:500–503, 1995. [187](#)

## Bibliography

---

- [212] B Michael Kelm, Sushil Mittal, Yefeng Zheng, Alexey Tsymbal, Dominik Bernhardt, Fernando Vega-Higuera, S Kevin Zhou, Peter Meer, and Dorin Comaniciu. Detection, grading and classification of coronary stenoses in computed tomography angiography. In *Medical Image Computing and Computer-Assisted Intervention–MICCAI 2011*, pages 25–32. Springer, 2011. [185](#), [196](#), [199](#), [200](#), [206](#)
- [213] Stefan Kiechl and Johann Willeit. The natural course of atherosclerosis : Part ii: Vascular remodeling. *Arterioscler Thromb Vasc Biol*, 19:1491–1498, 1999. [15](#)
- [214] Cemil Kirbas and Francis KH Quek. Vessel extraction in medical images by 3d wave propagation and traceback. In *Bioinformatics and Bioengineering, 2003. Proceedings. Third IEEE Symposium on*, pages 174–181. IEEE, 2003. [64](#), [75](#)
- [215] HA Kirişli, M Schaap, CT Metz, AS Dharampall, WB Meijboom, SL Papadopoulou, A Dedic, K Nieman, MA de Graaf, MFL Meijs, et al. Standardized evaluation framework for evaluating coronary artery stenosis detection, stenosis quantification and lumen segmentation algorithms in computed tomography angiography. *Medical Image Analysis*, 17(2):859–876, 2013. [xxvi](#), [xxxvi](#), [48](#), [49](#), [50](#), [136](#), [140](#), [142](#), [165](#), [175](#), [184](#), [203](#), [204](#), [205](#), [208](#), [209](#), [210](#), [257](#), [265](#), [296](#), [308](#)
- [216] Hortense A Kirişli, Michiel Schaap, Stefan Klein, Lisan A Neefjes, Annick C Weustink, Theo Van Walsum, and Wiro J Niessen. Fully automatic cardiac segmentation from 3d cta data: a multi-atlas based approach. In *SPIE Medical Imaging*, pages 762305–762305. International Society for Optics and Photonics, 2010. [90](#), [91](#), [93](#), [132](#), [134](#)
- [217] Y. Kitamura, Yuanzhong Li, and W. Ito. Automatic coronary extraction by supervised detection and shape matching. In *Biomedical Imaging (ISBI), 2012 9th IEEE International Symposium on*, pages 234–237, May 2012. [137](#), [142](#), [143](#), [155](#), [292](#), [294](#)
- [218] Yoshiro Kitamura, Yuanzhong Li, Wataru Ito, and Hiroshi Ishikawa. Coronary lumen and plaque segmentation from cta using higher-order shape prior. In Polina Golland, Nobuhiko Hata, Christian Barillot, Joachim Hornegger, and Robert Howe, editors, *Medical Image Computing and Computer-Assisted Intervention – MICCAI 2014*, volume 8673 of *Lecture Notes in Computer Science*, pages 339–347. Springer International Publishing, 2014. [142](#), [292](#), [293](#)
- [219] Pieter H. Kitslaar, Michel Frenay, Elco Oost, Jouke Dijkstra, and Berend Stoel. Connected component and morphology based extraction of arterial centerlines of the heart (cocomobeach). In *The MIDAS Journal: MICCAI Workshop–Grand Challenge Coronary Artery Tracking*, 2008. [57](#), [58](#), [60](#), [71](#), [72](#), [74](#), [92](#)
- [220] Fred N Kiwanuka and Michael HF Wilkinson. Radial moment invariants for attribute filtering in 3d. In *Applications of Discrete Geometry and Mathematical Morphology*, pages 68–81. Springer, 2012. [156](#)
- [221] Edwin M Knox and Raymond T Ng. Algorithms for mining distance-based outliers in large datasets. In *Proceedings of the International Conference on Very Large Data Bases*, pages 392–403. Citeseer, 1998. [101](#)

- 
- [222] Thomas Markus Koller, Guido Gerig, Gabor Szekely, and Daniel Dettwiler. Multiscale detection of curvilinear structures in 2-d and 3-d image data. In *Computer Vision, 1995. Proceedings., Fifth International Conference on*, pages 864–869. IEEE, 1995. [55](#), [63](#)
- [223] Sei Komatsu, Atsushi Hirayama, Yosuke Omori, Yasunori Ueda, Isamu Mizote, Yasuo Fujisawa, Masayoshi Kiyomoto, Toshiaki Higashide, and Kazuhisa Kodama. Detection of coronary plaque by computed tomography with a novel plaque analysis system, ‘plaque map’, and comparison with intravascular ultrasound and angiography. *Circulation Journal*, 69(1):72–77, 2005. [192](#)
- [224] Bon-Kwon Koo, Andrejs Erglis, Joon-Hyung Doh, David V Daniels, Sanda Jegere, Hyo-Soo Kim, Allison Dunning, Tony DeFrance, Alexandra Lansky, Jonathan Leipsic, et al. Diagnosis of ischemia-causing coronary stenoses by noninvasive fractional flow reserve computed from coronary computed tomographic angiogram results from the prospective multicenter discover-flow (diagnosis of ischemia-causing stenoses obtained via noninvasive fractional flow reserve) study. *Journal of the American College of Cardiology*, 58(19):1989–1997, 2011. [195](#)
- [225] Grigorios Korosoglou, Dirk Mueller, Stephanie Lehrke, Henning Steen, Waldemar Hosch, Tobias Heye, Hans-Ulrich Kauczor, Evangelos Giannitsis, and Hugo A Katus. Quantitative assessment of stenosis severity and atherosclerotic plaque composition using 256-slice computed tomography. *European radiology*, 20(8):1841–1850, 2010. [31](#)
- [226] ERWIN Kreyszig. *Applied Mathematics*. Wiley Press, 1979. [102](#)
- [227] K. Krissian, G. Malandain, and N. Ayache. Directional anisotropic diffusion applied to segmentation of vessels in 3d images. *Scale-Space Theory in Computer Vision*, pages 345–348, 1997. [55](#)
- [228] K. Krissian, G. Malandain, N. Ayache, R. Vaillant, and Y. Troussel. Model-based multiscale detection of 3d vessels. *Computer Vision and Pattern Recognition, IEEE Computer Society Conference on*, pages 722–727, 1998. [68](#)
- [229] Karl Krissian. Flux-based anisotropic diffusion applied to enhancement of 3-d angiogram. *Medical Imaging, IEEE Transactions on*, 21(11):1440–1442, 2002. [55](#)
- [230] Karl Krissian and Sara Arencibia Garcia. A minimal cost path and level set evolution approach for carotid bifurcation segmentation. *Insight Journal*, 2009. [60](#), [67](#), [72](#)
- [231] Karl Krissian, Grégoire Malandain, Nicholas Ayache, Régis Vaillant, and Yves Troussel. Model-based detection of tubular structures in 3d images. *Computer Vision and Image Understanding*, 80(2):130 – 171, 2000. [56](#), [63](#), [64](#)
- [232] Karl Krissian, Hrvoje Bogunovic, Jose Maria Pozo, Maria Cruz Villa-Uriol, and Alejandro Frangi. Minimally interactive knowledge-based coronary tracking in cta using a minimal cost path. *The Insight Journal*, 2008. [58](#), [67](#), [72](#), [74](#), [75](#)
- [233] Miroslav Kubat, Ivan Bratko, and Ryszard Michalski. A review of machine learning methods. In Ryszard S. Michalski, Ivan Bratko, and Miroslav Kubat, editors, *Machine Learning and Data Mining; Methods and Applications*. John Wiley & Sons, Inc., 1996. [230](#)

## Bibliography

---

- [234] Axel Kuettner, Tobias Trabold, Stephen Schroeder, Anja Feyer, Torsten Beck, Ariane Brueckner, Martin Heuschmid, Christof Burgstahler, Andreas F Kopp, and Claus D Claussen. Noninvasive detection of coronary lesions using 16-detector multislice spiral computed tomography technology: initial clinical results. *Journal of the American College of Cardiology*, 44(6):1230–1237, 2004. [31](#)
- [235] U Kurkure, DR Chittajallu, G Brunner, R Yalamanchili, and Kakadiaris IA. Detection of coronary calcifications using supervised hierarchical classification. In *2nd MICCAI Workshop on Computer Vision for Intravascular and Intracardiac Imaging*, New York, Sept. 10 2008. [186](#), [197](#)
- [236] Uday Kurkure, Deepak R Chittajallu, Gerd Brunner, Yen H Le, and Ioannis A Kakadiaris. A supervised classification-based method for coronary calcium detection in non-contrast ct. *The International Journal of Cardiovascular Imaging*, 26(7):817–828, 2010. [186](#), [196](#), [197](#), [200](#), [233](#)
- [237] Caroline Lacoste, Gérard Finet, and Isabelle E. Magnin. Coronary tree extraction from x-ray angiograms using marked point processes. *IEEE International Symposium on Biomedical Imaging*, 2006. [63](#)
- [238] Hans Lamecker, Thomas Lange, and Martin Seebass. A statistical shape model for the liver. In *Medical Image Computing and Computer-Assisted Intervention MICCAI 2002*, pages 421–427. Springer, 2002. [242](#)
- [239] Shawn Lankton, Arthur Stillman, Paolo Raggi, and Allen R Tannenbaum. Soft plaque detection and automatic vessel segmentation. In *Probabilistic Models For Medical Image Analysis 2009*, pages 25–33. Georgia Institute of Technology, 2009. [190](#), [194](#)
- [240] M. Law and A. Chung. Three dimensional curvilinear structure detection using optimally oriented flux. *Eur. Conf. Comput. Vision*, pages 368–382, 2008. [56](#)
- [241] M. Law and A. Chung. Efficient implementation for spherical flux computation and its application to vascular segmentation. *IEEE Trans. Image Process*, 18 (3):596–612, 2009. [56](#)
- [242] W. K. Law and A.C.S. Chung. Segmentation of vessels using weighted local variances and an active contour model. In *Computer Vision and Pattern Recognition Workshop, 2006. CVPRW '06. Conference on*, pages 83–83, 2006. [80](#)
- [243] V.F. F. Leavers. *Shape Detection in Computer Vision Using the Hough Transform*. Springer-Verlag New York, Inc., Secaucus, NJ, USA, 1992. [106](#)
- [244] Alexander W Leber, Andreas Knez, Carl W White, Alexander Becker, Franz von Ziegler, Olaf Muehling, Christoph Becker, Maximilian Reiser, Gerhard Steinbeck, and Peter Boekstegers. Composition of coronary atherosclerotic plaques in patients with acute myocardial infarction and stable angina pectoris determined by contrast-enhanced multislice computed tomography. *The American journal of cardiology*, 91(6):714–718, 2003. [34](#)
- [245] Alexander W Leber, Andreas Knez, Alexander Becker, Christoph Becker, Franz von Ziegler, Konstantin Nikolaou, Carsten Rist, Maximilian Reiser, Carl White, Gerhard Steinbeck, et al. Accuracy of multidetector spiral computed tomography in identifying and differentiating the

- composition of coronary atherosclerotic plaques : a comparative study with intracoronary ultrasound. *Journal of the American College of Cardiology*, 43(7):1241–1247, 2004. [30](#), [31](#)
- [246] Alexander W Leber, Andreas Knez, Alexander Becker, Christoph Becker, Maximilian Reiser, Gerhard Steinbeck, and Peter Bookstegers. Visualising noncalcified coronary plaques by ct. *The international journal of cardiovascular imaging*, 21(1):55–61, 2005. [32](#)
- [247] Alexander W Leber, Alexander Becker, Andreas Knez, Franz von Ziegler, Marc Sirol, Konstantin Nikolaou, Bernd Ohnesorge, Zahi A Fayad, Christoph R Becker, Maximilian Reiser, et al. Accuracy of 64-slice computed tomography to classify and quantify plaque volumes in the proximal coronary system: a comparative study using intravascular ultrasound. *Journal of the American College of Cardiology*, 47(3):672–677, 2006. [30](#), [32](#)
- [248] J. Lee, P. Beighley, E. Ritmana, and N. Smith. Automatic segmentation of 3D micro-CT coronary vascular images. *Medical Image Analysis*, 11(6):630–647, December 2007. [59](#), [70](#)
- [249] Boudewijn P. F. Lelieveldt, Rob J van der Geest, M Ramze Rezaee, Johan G. Bosch, and Johan H. C. Reiber. Anatomical model matching with fuzzy implicit surfaces for segmentation of thoracic volume scans. *Medical Imaging, IEEE Transactions on*, 18(3):218–230, 1999. [90](#), [93](#)
- [250] David LESAGE. *Models, Features and Extraction Schemes for Vascular Segmentation: Application to the delineation of Coronary Arteries from 3D Computed Tomography Data*. PhD thesis, ISEcole Nationale Supérieure des Télécommunications Spécialité : Signal et Images, 2009. [64](#), [66](#)
- [251] David Lesage, Elsa D Angelini, Isabelle Bloch, and Gareth Funka-Lea. Bayesian maximal paths for coronary artery segmentation from 3d ct angiograms. In *Medical Image Computing and Computer-Assisted Intervention–MICCAI 2009*, pages 222–229. Springer, 2009. [139](#), [143](#)
- [252] Hua Li and A. Yezzi. Vessels as 4d curves: Global minimal 4d paths to extract 3d tubular surfaces. In *Computer Vision and Pattern Recognition Workshop, 2006. CVPRW '06. Conference on*, pages 82–82, 2006. [68](#)
- [253] Hua Li and A. Yezzi. Vessels as 4-d curves: Global minimal 4-d paths to extract 3-d tubular surfaces and centerlines. *Medical Imaging, IEEE Transactions on*, 26(9):1213–1223, Sept 2007. [139](#), [140](#), [141](#), [143](#)
- [254] Hua Li, Anthony Yezzi, and Laurent Cohen. 3d multi-branch tubular surface and centerline extraction with 4d iterative key points. In *Medical Image Computing and Computer-Assisted Intervention–MICCAI 2009*, pages 1042–1050. Springer, 2009. [140](#)
- [255] Qiang Li, Shusuke Sone, and Kunio Doi. Selective enhancement filters for nodules, vessels, and airway walls in two-and three-dimensional ct scans. *Medical physics*, 30(8):2040–2051, 2003. [56](#)
- [256] Rongxin Li and Sébastien Ourselin. Accurate curvilinear modeling for precise measurements of tubular structures. *Proc. Digital Image Comput: Tech. Appl*, pages 243–252., 2003. [62](#), [64](#), [78](#)
- [257] Yin Li, Jian Sun, Chi-Keung Tang, and Heung-Yeung Shum. Lazy snapping. In *ACM SIGGRAPH 2004 Papers*, SIGGRAPH '04, pages 303–308, New York, NY, USA, 2004. ACM. [114](#)



## Bibliography

---

- [258] Ying Li, Wei Chen, Kaijun Liu, Yi Wu, Yonglin Chen, Chun Chu, Bingji Fang, Liwen Tan, and Shaoxiang Zhang. A voxel-map quantitative analysis approach for atherosclerotic noncalcified plaques of the coronary artery tree. *Computational and mathematical methods in medicine*, 2013, 2013. [192](#), [206](#)
- [259] Zhenwei Li, Xiaoli Yang, and Jianguo Zhang. A coronary calcification detection scheme using contrast enhanced ct dataset. *Journal of Information & Computational Science*, 10:15:4835–4847, 2013. [196](#), [198](#), [200](#)
- [260] Peter Libby, Paul M. Ridker, and Attilio Maseri. Inflammation and atherosclerosis. *Circulation, American Heart Association*, 105:1135–1143, 2002. [11](#)
- [261] Qingfen Lin. *Enhancement, Detection, and Visualization of 3D Volume Data*. PhD thesis, Dept. EE, Linköping University, 2003. [xx](#), [56](#), [64](#), [65](#), [69](#), [76](#), [186](#)
- [262] Qingfen Lin and Per-Erik E. Danielsson. Stenosis detection using a new shape space for second order 3d-variations. In *IPMI '01: Proceedings of the 17th International Conference on Information Processing in Medical Imaging*, pages 388–394, London, UK, 2001. Springer-Verlag. [xxv](#), [186](#), [192](#), [193](#)
- [263] M. Lindenbaum, M. Fischer, and A. M. Bruckstein. On gabor contribution to image enhancement. *Pattern Recognition*, 27:1–8, 1994. [55](#)
- [264] H. Lombaert, Yiyong Sun, L. Grady, and Chenyang Xu. A multilevel banded graph cuts method for fast image segmentation. In *Computer Vision, 2005. ICCV 2005. Tenth IEEE International Conference on*, volume 1, pages 259 – 265 Vol. 1, oct. 2005. doi: 10.1109/ICCV.2005.13. [114](#)
- [265] Kuo-Lung Lor and Chung-Ming Chen. Probabilistic model based evaluation of coronary artery stenosis on computed tomography angiography. In *Proceedings of MICCAI workshop "3D cardiovascular imaging: a MICCAI segmentation challenge*, 2012. [191](#), [194](#), [292](#), [293](#)
- [266] C. Lorenz, S. Renisch, T. Schlathoelter, and T. Buelow. Simultaneous segmentation and tree reconstruction of the coronary arteries in msct images. *Society of Photo-Optical Instrumentation Engineers (SPIE) Conference Series*, 5031:167–177, May 2003. [76](#), [141](#)
- [267] Cristian Lorenz, I.-C. Carlsen, Thorsten M. Buzug, Carola Fassnacht, and Jürgen Weese. Multi-scale line segmentation with automatic estimation of width, contrast and tangential direction in 2d and 3d medical images. In *Proceedings of the First Joint Conference on Computer Vision, Virtual Reality and Robotics in Medicine and Medical Robotics and Computer-Assisted Surgery, CVRMed-MRCAS '97*, pages 233–242, London, UK, UK, 1997. Springer-Verlag. [64](#), [145](#)
- [268] L. M. Lorigo, O. D. Faugeras, W. E. L. Grimson, R. Keriven, R. Kikinis, A. Nabavi, and C. F. Westin. Curves: Curve evolution for vessel segmentation. *Medical Image Analysis*, 5(3):195 – 206, 2001. [xxi](#), [68](#), [79](#), [80](#)
- [269] EPITA LRDE. The olena image processing platform, 2007–2012. <http://olena.lrde.epita.fr>. [157](#)

- [270] Miguel A Luengo-Oroz, María J Ledesma-Carbayo, JJ Gómez-Diego, Miguel A García-Fernández, Manuel Desco, and Andrés Santos. Extraction of the coronary artery tree in cardiac computer tomographic images using morphological operators. In *Functional Imaging and Modeling of the Heart*, pages 424–432. Springer, 2007. [137](#), [141](#), [143](#)
- [271] Felix Lugauer, Jingdan Zhang, Yefeng Zheng, Joachim Hornegger, and B. Michael Kelm. Improving accuracy in coronary lumen segmentation via explicit calcium exclusion, learning-based ray detection and surface optimization. In *Proc. SPIE*, volume 9034, pages 90343U–90343U–10, 2014. [138](#), [140](#), [141](#), [142](#), [143](#), [167](#), [178](#), [292](#), [293](#)
- [272] Felix Lugauer, Yefeng Zheng, Joachim Hornegger, and B Michael Kelm. Precise lumen segmentation in coronary computed tomography angiography. In *Medical Computer Vision: Algorithms for Big Data*, pages 137–147. Springer, 2014. [138](#), [142](#), [178](#), [292](#), [293](#)
- [273] Michael Lynch, Ovidiu Ghita, and Paul F Whelan. Automatic segmentation of the left ventricle cavity and myocardium in mri data. *Computers in biology and medicine*, 36(4):389–407, 2006. [90](#)
- [274] Renke Maas and Rainer H. Boger. Old and new cardiovascular risk factors: from unresolved issues to new opportunities. *Atherosclerosis Supplements*, 4(4):5 – 17, 2003. Proceedings of the First International Symposium on ADMA as a Cardiovascular Risk Factor; Hamburg, October 4-6, 2002. [12](#)
- [275] Erica Maffei, C Martini, C Tedeschi, P Spagnolo, Alessandra Zuccarelli, Teresa Arcadi, A Guaricci, Sara Seitun, AC Weustink, NR Mollet, et al. Diagnostic accuracy of 64-slice computed tomography coronary angiography in a large population of patients without revascularisation: registry data in nstemi acute coronary syndrome and influence of gender and risk factors. *La radiologia medica*, 116(7):1014–1026, 2011. [31](#)
- [276] Sokratis Makrogiannis, Rahul Bhotika, JamesV. Miller, Jr. Skinner, John, and Melissa Vass. Nonparametric intensity priors for level set segmentation of low contrast structures. In Guang-Zhong Yang, David Hawkes, Daniel Rueckert, Alison Noble, and Chris Taylor, editors, *Medical Image Computing and Computer-Assisted Intervention - MICCAI 2009*, volume 5761 of *Lecture Notes in Computer Science*, pages 239–246. Springer Berlin Heidelberg, 2009. [192](#)
- [277] R. Manniesing and W. Niessen. Local speed functions in level set based vessel segmentation. *Proc. Med. Image Comput. Assist. Interv.*, 3216:475–482, 2004. [61](#), [76](#)
- [278] R. Manniesing, B. K. Velthuis, M. S. van Leeuwen, I. C. van der Schaaf, P. J. van Laar, and W.J. Niessen. Level set based cerebral vasculature segmentation and diameter quantification in ct angiography. *Medical Image Analysis*, 10(2):200–214, 2006. [80](#)
- [279] R. Manniesing, M. A. Viergever, and W. J. Niessen. Vessel enhancing diffusion: A scale space representation of vessel structures. *Medical Image Analysis*, 10:815–825, 2006. [55](#)
- [280] Riccardo Marano, Francesco De Cobelli, Irene Floriani, Christoph Becker, Christopher Herzog, Maurizio Centonze, Giovanni Morana, Gian Franco Gualdi, Guido Ligabue, Gianluca Pontone, et al. Italian multicenter, prospective study to evaluate the negative predictive value of 16-and 64-slice mdct imaging in patients scheduled for coronary angiography (nimiscad-non invasive



## Bibliography

---

- multicenter italian study for coronary artery disease). *European radiology*, 19(5):1114–1123, 2009. [31](#)
- [281] S. Matsuo, Y. Nakamura, T. Matsumoto, I. Nakae, Y. Nagatani, R. Takazakura, M. Takahashi, K. Murata, and M. Horie. Visual assessment of coronary artery stenosis with electrocardiographically-gated multislice computed tomography. *The International Journal of Cardiovascular Imaging*, 20(1):61–66, 2004. [2](#)
- [282] Christian M Matter, Matthias Stuber, and Matthias Nahrendorf. Imaging of the unstable plaque: how far have we got? *European heart journal*, 30(21):2566–2574, 2009. [35](#)
- [283] Tim McInerney and Demetri Terzopoulos. A dynamic finite element surface model for segmentation and tracking in multidimensional medical images with application to cardiac 4d image analysis. *Computerized Medical Imaging and Graphics*, 19(1):69–83, 1995. [90](#)
- [284] Tim McInerney and Demetri Terzopoulos. Medical image segmentation using topologically adaptable surfaces. In Jocelyne Troccaz, Eric Grimson, and Ralph Mösges, editors, *CVRMed-MRCAS’97*, volume 1205 of *Lecture Notes in Computer Science*, pages 23–32. Springer Berlin Heidelberg, 1997. [78](#)
- [285] W Bob Meijboom, Matthijs FL Meijs, Joanne D Schuijf, Maarten J Cramer, Nico R Mollet, Carlos AG van Mieghem, Koen Nieman, Jacob M van Werkhoven, Gabija Pundziute, Annick C Weustink, et al. Diagnostic accuracy of 64-slice computed tomography coronary angiography: a prospective, multicenter, multivendor study. *Journal of the American College of Cardiology*, 52(25):2135–2144, 2008. [31](#)
- [286] E. Meijering, W. Niessen, J. Weickert, and M. Viergever. Evaluation of diffusion techniques for improved vessel visualization and quantification in three-dimensional rotational angiography. *Proc. Med. Image Comput. Assist. Interv.*, pages 177–185, 2001. [56](#)
- [287] Ron Meir and Gunnar Rätsch. An introduction to boosting and leveraging. In *Advanced lectures on machine learning*, pages 118–183. Springer, 2003. [233](#)
- [288] Simone Melchionna, Stefania Fortini, Massimo Bernaschi, Mauro Bisson, Nahyup Kang, and Hyong-Euk Lee. From medical imaging to computer simulation of fractional flow reserve in four coronary artery trees. In *SPIE Medical Imaging*, pages 903535–903535. International Society for Optics and Photonics, 2014. [195](#)
- [289] I. Melki, H. Talbot, J. Cousty, C. Pruvot, J. Knoplioch, L. Launay, and L. Najman. A hybrid algorithm for automatic heart segmentation in ct angiography. In *Image Processing (ICIP), 2012 19th IEEE International Conference on*, pages 2013–2016, Sept 2012. [46](#), [47](#), [94](#), [157](#)
- [290] Imen Melki, Hugues Talbot, Jean Cousty, Laurent Najman, Céline Pruvot, Jérôme Knoplioch, and Laurent Launay. A hybrid algorithm for automatic heart delineation in CT angiography. In *Computer Assisted Radiology and Surgery - CARS’2012*, pages S37–S38, France, 2012. [47](#), [94](#)
- [291] Imen Melki, Hugues Talbot, Jean Cousty, Céline Pruvot, Jérôme Knoplioch, Laurent Launay, and Laurent Najman. Automatic coronary arteries stenoses detection in 3d ct angiography. In *Proceedings of MICCAI workshop "3D cardiovascular imaging: a MICCAI segmentation challenge"*, 2012. [49](#), [138](#), [190](#), [227](#), [291](#), [292](#), [293](#)

- 
- [292] Imen Melki, Cyril Cardon, Nicolas Gogin, Hugues Talbot, and Laurent Najman. Learning-based automatic detection of severe coronary stenoses in ct angiographies. In *SPIE*, 2014. 46, 49, 269, 289, 291, 292, 293
- [293] Odyssee Merveille, Hugues Talbot, Laurent Najman, and Nicolas Passat. Tubular structure filtering by ranking orientation responses of path operators. In *Computer Vision–ECCV 2014*, pages 203–218. Springer, 2014. 164
- [294] C. Metz, M. Schaap, A. van der Giessen, T. van Walsum, and W. Niessen. Semi-automatic coronary artery centerline extraction in computed tomography angiography data. *International Symposium on Biomedical Imaging - ISBI*, pages 856–859, 2007. 75
- [295] Fernand Meyer. Un algorithme optimal pour la ligne de partage des eaux. In *Proceedings 8th Congress AFCET*, volume 2, pages 847–857, Lyon, France, 1991. 113, 173
- [296] Fernand Meyer and Serge Beucher. Morphological segmentation. *Journal of Visual Communication and Image Representation*, 1(1):21–46, September 1990. 165
- [297] Hugues Talbot et al. Michel Couprie, Laszlo Marak\*. The pink image processing library (<http://pinkhq.com>). 128
- [298] J. Mille, R. Boné, and L.D. Cohen. Region-based 2d deformable generalized cylinder for narrow structures segmentation. *Proc. Eur. Conf. Comput. Vision., Springer*, pages 392–404, 2008. 78
- [299] Julien Mille and Laurent D. Cohen. Deformable tree models for 2d and 3d branching structures extraction. *IEEE Computer Society Conference on Computer Vision and Pattern Recognition Workshops*, 2009. xx, 54, 56, 62, 69, 78
- [300] Julie M Miller, Carlos E Rochitte, Marc Dewey, Armin Arbab-Zadeh, Hiroyuki Niinuma, Ilan Gottlieb, Narinder Paul, Melvin E Clouse, Edward P Shapiro, John Hoe, et al. Diagnostic performance of coronary angiography by 64-row ct. *New England Journal of Medicine*, 359(22): 2324–2336, 2008. 31, 35
- [301] James K Min, Bon-Kwon Koo, Andrejs Erglis, Joon-Hyung Doh, David V Daniels, Sanda Jegere, Hyo-Soo Kim, Allison M Dunning, Tony DeFrance, Alexandra Lansky, et al. Usefulness of noninvasive fractional flow reserve computed from coronary computed tomographic angiograms for intermediate stenoses confirmed by quantitative coronary angiography. *The American journal of cardiology*, 110(7):971–976, 2012. 195
- [302] S.C. Mitchell, J.G. Bosch, B.P.F. Lelieveldt, R.J. van der Geest, J.H.C. Reiber, and M. Sonka. 3-d active appearance models: segmentation of cardiac mr and ultrasound images. *Medical Imaging, IEEE Transactions on*, 21(9):1167–1178, sept. 2002. 90
- [303] S. Mittal, Y. Zheng, B. Georgescu, F. Vega-Higuera, S.K. Zhou, P. Meer, and D. Comaniciu. Fast automatic detection of calcified coronary lesions in 3d cardiac ct images. In *Proceedings of the First international conference on Machine learning in medical imaging. MLMI’10*, pages 1–9, Berlin, Heidelberg, 2010. Springer-Verlag. 196, 197, 199, 200, 234, 237, 243, 256, 299

## Bibliography

---

- [304] Sadaaki Miyamoto, Hidetomo Ichihashi, and Katsuhiro Honda. Algorithms for fuzzy clustering. *Methods in c-Means Clustering with Applications*. Kacprzyk J, editor Berlin: Springer-Verlag, 2008. [77](#)
- [305] Brian Mohr, Saad Masood, and Costas Plakas. Accurate lumen segmentation and stenosis detection and quantification in coronary cta. In *Proceedings of 3D Cardiovascular Imaging: a MICCAI Segmentation Challenge Workshop*, 2012. [137](#), [142](#), [143](#), [155](#), [167](#), [178](#), [188](#), [190](#), [194](#), [292](#), [293](#)
- [306] Pascal Monasse and Frederic Guichard. Fast computation of a contrast-invariant image representation. *IEEE Transactions on Image Processing*, 9(5):860–872, 2000. [150](#)
- [307] J Montagnat. *Deformable Modelling for 3D and 4D Medical Image Segmentation*. PhD thesis, Sophia Antipolis University, Nice, France, 1999. [63](#)
- [308] Albert Montillo, Jamie Shotton, John Winn, Juan Eugenio Iglesias, Dimitri Metaxas, and Antonio Criminisi. Entangled decision forests and their application for semantic segmentation of ct images. In *Information Processing in Medical Imaging*, pages 184–196. Springer, 2011. [237](#), [256](#)
- [309] A Moreno, C Maki Takemura, O Colliot, O Camara, and I Bloch. Heart segmentation in medical images using the fuzzy spatial relation "between". In *Information Processing and Management of Uncertainty in Knowledge-Based Systems, IPMU*, pages 2052–2059, 2006. [91](#)
- [310] A Moreno, Celina Maki Takemura, Olivier Colliot, Oscar Camara, and Isabelle Bloch. Using anatomical knowledge expressed as fuzzy constraints to segment the heart in ct images. *Pattern Recognition*, 41(8):2525–2540, 2008. [91](#), [93](#), [132](#), [134](#)
- [311] WE Moshage, Stephan Achenbach, Bernd Seese, Kurt Bachmann, and Markus Kirchgeorg. Coronary artery stenoses: three-dimensional imaging with electrocardiographically triggered, contrast agent-enhanced, electron-beam ct. *Radiology*, 196(3):707–714, 1995. [28](#)
- [312] Sadako Motoyama, Masayoshi Sarai, Hiroto Harigaya, Hirofumi Anno, Kaori Inoue, Tomonori Hara, Hiroyuki Naruse, Junichi Ishii, Hitoshi Hishida, Nathan D Wong, et al. Computed tomographic angiography characteristics of atherosclerotic plaques subsequently resulting in acute coronary syndrome. *Journal of the American College of Cardiology*, 54(1):49–57, 2009. [xviii](#), [32](#)
- [313] Graham Mowatt, Jonathan A Cook, Graham S Hillis, Shonagh Walker, Cynthia Fraser, Xueli Jia, and Norman Waugh. 64-slice computed tomography angiography in the diagnosis and assessment of coronary artery disease: systematic review and meta-analysis. *Heart*, 94(11):1386–1393, 2008. [35](#)
- [314] B. Naegel, C. Ronse, and L. Soler. Using grey-scale hit-or-miss transform for segmenting the portal network of the liver. *Computational Imaging and Vision*, 30:429–440, 2005. [74](#)
- [315] Benoît Naegel, Nicolas Passat, and Christian Ronse. Grey-level hit-or-miss transforms—part i: Unified theory. *Pattern Recognition*, 40(2):635 – 647, 2007. [75](#)
- [316] Benoît Naegel, Nicolas Passat, and Christian Ronse. Grey-level hit-or-miss transforms—part ii: Application to angiographic image processing. *Pattern Recognition*, 40(2):648–658, 2007. [82](#)

- [317] Morteza Naghavi. *Asymptomatic Atherosclerosis: Pathophysiology, Detection and Treatment*. Springer, 2010. 30
- [318] P.S. Nair and A.T. Saunders Jr. Hough transform based ellipse detection algorithm. *PRL*, 17: 777 – 784, 1996. 106
- [319] Laurent Najman and Michel Couprie. Building the component tree in quasi-linear time. *Image Processing, IEEE Transactions on*, 15(11):3531–3539, 2006. 152
- [320] Iraj Nazeri, Payman Shahabi, Mahmood Tehrai, Babak Sharif-Kashani, and Alireza Nazeri. Impact of calcification on diagnostic accuracy of 64-slice spiral computed tomography for detecting coronary artery disease: a single center experience. *Archives of Iranian Medicine (AIM)*, 13(5), 2010. 31
- [321] Koen Nieman, Filippo Cademartiri, Pedro A Lemos, Rolf Raaijmakers, Peter MT Pattynama, and Pim J de Feyter. Reliable noninvasive coronary angiography with fast submillimeter multislice spiral computed tomography. *Circulation*, 106(16):2051–2054, 2002. 31
- [322] Wiro Niessen, Alexander van Swijndregt, Bernard Elsmann, Onno Wink, Max Viergever, and Willem Mali. Enhanced artery visualization in blood pool mra: Results in the peripheral vasculature. In Attila Kuba, Martin Šámal, and Andrew Todd-Pokropek, editors, *Information Processing in Medical Imaging*, volume 1613 of *Lecture Notes in Computer Science*, pages 340–345. Springer Berlin, Heidelberg, 1999. 71, 81
- [323] Lung NIH: National Heart and Blood Institute. Heart attack nih.gif, accessed: 20 May 2014. URL <http://www.nhlbi.nih.gov/health/health-topics/topics/heartattack/>. xvii, 16
- [324] Nicholas MI Noble, Derek LG Hill, Marcel Breeuwer, Julia A Schnabel, David J Hawkes, Frans A Gerritsen, and Reza Razavi. Myocardial delineation via registration in a polar coordinate system. In *Medical Image Computing and Computer-Assisted Intervention–MICCAI 2002*, pages 651–658. Springer, 2002. 90
- [325] T. O’Donnell, T.E. Boulton, X.-S. Fang, and A. Gupta. The extruded generalized cylinder: a deformable model for object recovery. In *Computer Vision and Pattern Recognition, 1994. Proceedings CVPR ’94., 1994 IEEE Computer Society Conference on*, pages 174–181, Jun 1994. doi: 10.1109/CVPR.1994.323826. 63
- [326] T. O’Donnell, M.-P. Dubuisson-Jolly, and A Gupta. A cooperative framework for segmentation using 2d active contours and 3d hybrid models as applied to branching cylindrical structures. *IEEE Int. Conf. Comput. Vision*, pages 454–459, 1998. 62
- [327] National Institute of Health. Anatomy of the heart, accessed: May 15, 2014. URL [http://www.nhlbi.nih.gov/health//dci/Diseases/hhw/hhw\\_anatomy.html](http://www.nhlbi.nih.gov/health//dci/Diseases/hhw/hhw_anatomy.html). xvii, 9, 10
- [328] National Institute of Health. Coronary artery bypass graft, accessed: May 15, 2014. URL <http://www.nhlbi.nih.gov/health/health-topics/images/cabg.jpg>. xvii, 19
- [329] National Institute of Health. Diagram of coronary angioplasty and stent placement, accessed: May 15, 2014. URL [http://www.nhlbi.nih.gov/health/dci/Diseases/Angioplasty/Angioplasty\\_WhatIs.html](http://www.nhlbi.nih.gov/health/dci/Diseases/Angioplasty/Angioplasty_WhatIs.html). xvii, 18

## Bibliography

---

- [330] National Institute of Health. Diagram of coronary angioplasty, accessed: May 15, 2014. URL [http://www.nhlbi.nih.gov/health/dci/Diseases/Angioplasty/Angioplasty\\_WhatIs.html](http://www.nhlbi.nih.gov/health/dci/Diseases/Angioplasty/Angioplasty_WhatIs.html). xvii, 18
- [331] M.G. Oghli, A. Fallahi, and M. Pooyan. 3-d heart segmentation on ct images using superellipsoid model fitting. In *Electrical Engineering (ICEE), 2012 20th Iranian Conference on*, pages 1567–1570, May 2012. 91, 93, 128
- [332] Bernd M. Ohnesorge, Thomas G. Flohr, Christoph R. Becker, Andreas Knez, and Maximilian F. Reiser. *Multi-slice and Dual-source CT in Cardiac Imaging: Principles - Protocols - Indications - Outlook*. Springer, 2006. xviii, 29, 38, 39, 41
- [333] İlkey Öksüz, Devrim Ünay, and Kamuran Kadıpaşaoğlu. A hybrid method for coronary artery stenoses detection and quantification in cta images. In *Proceedings of 3D Cardiovascular Imaging: a MICCAI Segmentation Challenge Workshop*, 2012. 188, 194, 292, 293
- [334] Sílvia Delgado Olabarriaga, Marcel Breeuwer, and Wiro J Niessen. Minimum cost path algorithm for coronary artery central axis tracking in ct images. In *Medical Image Computing and Computer-Assisted Intervention-MICCAI 2003*, pages 687–694. Springer, 2003. 67
- [335] K. Palagyi, E. Sorantin, E. Balogh, A. Kuba, C. Halmai, B. Erdohelyi, and K. Hausegger. A sequential 3d thinning algorithm and its medical applications. *Insana, M.F., Leahy, R.M. (eds.) IPMI 2001. LNCS, Springer, Heidelberg*, 2002:409–415, 2001. 62, 73
- [336] Spiros Papadimitriou, Hiroyuki Kitagawa, Phillip B. Gibbons, and Christos Faloutsos. Loci: Fast outlier detection using the local correlation integral. In *ICDE*, pages 315–, 2003. 101
- [337] N. Passat, C. Ronse, J. Baruthio, J.-P. Armspach, C. Maillot, and C. Jahn. Region-growing segmentation of brain vessels: An atlas-based automatic approach. *Journal of Magnetic Resonance Imaging*, 21(6):715–725, 2005. 57, 60, 75
- [338] Nicolas Passat, Christian Ronse, Joseph Baruthio, J-P Armspach, and J Foucher. Watershed and multimodal data for brain vessel segmentation: Application to the superior sagittal sinus. *Image and Vision Computing*, 25(4):512–521, 2007. 82
- [339] Simone Perandini, N Faccioli, A Zaccarella, TJ Re, and R Pozzi Mucelli. The diagnostic contribution of ct volumetric rendering techniques in routine practice. *The Indian journal of radiology & imaging*, 20(2):92, 2010. 37, 41
- [340] P. Perona. Orientation diffusions. *IEEE Trans. Image Processing*, pages 457–467, 1998. 55
- [341] P. Perona and J. Malik. Scale space and edge detection using anisotropic diffusion. *IEEE, Trans. Patt. Anal. Mach. Intell.*, 12:629–639, 1990. 55
- [342] C. Petitjean and J.N. Dacher. A review of segmentation methods in short axis cardiac MR images. *Medical Image Analysis*, 15(2):169 – 184, 2011. 90
- [343] Nico H.J. Pijls, Bernard de Bruyne, Kathinka Peels, Pepijn H. van der Voort, Hans J.R.M. Bonnier, Jozef Bartunek, and Jacques J. Koolen. Measurement of fractional flow reserve to assess the functional severity of coronary-artery stenoses. *New England Journal of Medicine*, 334(26):1703–1708, 1996. PMID: 8637515. 195

- 
- [344] R. Poli and G. Valli. An algorithm for real-time vessel enhancement and detection. *Comput. Meth. Prog. Biomed*, 52:1–2, 1996. [55](#)
- [345] Bernhard Preim and Dirk Bartz. *Visualization in medicine: Theory, Algorithms, and Applications*. Morgan Kaufmann, 2007. [xviii](#), [24](#), [27](#), [37](#), [38](#)
- [346] S Josevin Prem, MS Ulaganathan, and G Kharmega Sundararaj. Segmentation of the heart and great vessels in ct images using curvelet transform and multi structure elements morphology. *International Journal of Engineering and Innovative Technology*, 1:122–18, 2012. [90](#)
- [347] Francesca Pugliese, MG Myriam Hunink, Katarzyna Gruszczynska, Filippo Alberghina, Roberto Malagó, Niels van Pelt, Nico R Mollet, Filippo Cademartiri, Annick C Weustink, Willem B Meijboom, et al. Learning curve for coronary ct angiography: What constitutes sufficient training? 1. *Radiology*, 251(2):359–368, 2009. [183](#), [184](#)
- [348] Santi Wulan Purnami, Jasni Mohamad Zain, and Abdullah Embong. Data mining technique for medical diagnosis using a new smooth support vector machine. In *Networked Digital Technologies*, pages 15–27. Springer, 2010. [233](#)
- [349] X. Qian, M. P. Brennan, D. P. Dione, W. L. Dobrucki, M. P. Jackowski, C. K. Breuer, A. J. Sinusas, and X. Papademetris. A non-parametric vessel detection method for complex vascular structures. *Medical Image Analysis*, 13(1):49–61, 2009. [61](#)
- [350] Johann Radon. On the determination of functions from their integral values along certain manifolds. *Medical Imaging, IEEE Transactions on*, 5(4):170–176, 1986. [23](#)
- [351] Gilbert L. Raff, Chair, Aiden Abidov, Stephan Achenbach, Daniel S. Berman, Lawrence M. Buxt, Matthew J. Budoff, Victor Cheng, Tony DeFrance, Jeffrey C. Hellinger, and Ronald P. Karlsberg. {SCCT} guidelines for the interpretation and reporting of coronary computed tomographic angiography. *Journal of Cardiovascular Computed Tomography*, 3(2):122 – 136, 2009. [xxxv](#), [38](#), [41](#), [42](#), [43](#), [44](#), [45](#)
- [352] Sridhar Ramaswamy, Rajeev Rastogi, and Kyuseok Shim. Efficient algorithms for mining outliers from large data sets. In *ACM SIGMOD Record*, volume 29, pages 427–438. ACM, 2000. [101](#)
- [353] Gautham P Reddy, Daniel M Chernoff, James R Adams, and Charles B Higgins. Coronary artery stenoses: assessment with contrast-enhanced electron-beam ct and axial reconstructions. *Radiology*, 208(1):167–172, 1998. [28](#)
- [354] Matthias Regenfus, Dieter Ropers, Stephan Achenbach, Christian Schlundt, Winfried Kessler, Gerhard Laub, Werner Moshage, and Werner G Daniel. Diagnostic value of maximum intensity projections versus source images for assessment of contrast-enhanced three-dimensional breath-hold magnetic resonance coronary angiography. *Investigative radiology*, 38(4):200–206, 2003. [39](#)
- [355] Félix Renard and Yongyi Yang. Image segmentation for detection of soft plaques in multidetector CT images. In *Image Analysis and Interpretation, 2008. SSIAI 2008. IEEE Southwest Symposium on*, pages 121–124. IEEE, 2008. [137](#), [141](#), [185](#), [189](#), [190](#), [194](#), [299](#)



## Bibliography

---

- [356] Félix Renard and Yongyi Yang. Image segmentation for detection of soft plaques in multidetector ct images. *IEEE Southwest Symposium on Image Analysis and Interpretation*, 2008. [190](#)
- [357] D. Rinck, S. Krüger, A. Reimann, and M. Scheuering. Shape-based segmentation and visualization techniques for evaluation of atherosclerotic plaques in coronary artery disease. In K. R. Cleary and R. L. Galloway, Jr., editors, *Medical Imaging 2006: Visualization, Image-Guided Procedures, and Display*, volume 6141 of *Society of Photo-Optical Instrumentation Engineers (SPIE) Conference Series*, pages 124–132, March 2006. [138](#), [185](#), [189](#)
- [358] Jos BTM Roerdink and Arnold Meijster. The watershed transform: Definitions, algorithms and parallelization strategies. *Fundamenta Informaticae*, 41(1):187–228, 2000. [113](#)
- [359] K. Rohr and S. Wörz. High-precision localization and quantification of 3D tubular structures. In *Biomedical Imaging: Nano to Macro, 3rd IEEE International Symposium on*, pages 1160–1163, 2006. [63](#)
- [360] Lior Rokach. *Data mining with decision trees: theory and applications*, volume 69. World scientific, 2008. [231](#)
- [361] Paul L. Rosin. A note on the least square fitting of ellipses. *Pattern Recognition Letters*, 14: 799–808, 1993. [108](#), [109](#)
- [362] Russell Ross. The pathogenesis of atherosclerosis: A perspective for the 1990s. *Nature*, 362(1): 801–809, 1993. [12](#)
- [363] Russell Ross and Valentin Fuster. The pathogenesis of atherosclerosis. In: *Fuster V, Ross R, Topol EJ, eds. Atherosclerosis and Coronary Artery Disease, Philadelphia, Pa: Lippincott-Raven*, pages 441–62, 1996. [12](#)
- [364] Carsten Rother, Vladimir Kolmogorov, and Andrew Blake. "grabcut": interactive foreground extraction using iterated graph cuts. In *ACM SIGGRAPH 2004 Papers, SIGGRAPH '04*, pages 309–314, New York, NY, USA, 2004. ACM. [114](#)
- [365] P. J. Rousseeuw and A. M. Leroy. *Robust regression and outlier detection*. John Wiley & Sons, Inc., New York, NY, USA, 1987. ISBN 0-471-85233-3. [101](#)
- [366] D. Rueckert, P. Burger, S.M. Forbat, R. Mohiaddin, and G.-Z. Yang. Automatic tracking of the aorta in cardiovascular mr images using deformable models. *IEEE Trans. Med. Imaging*, 16: 581–590, 1997. [78](#)
- [367] John A Rumberger, Patrick F Sheedy, Jerome F Breen, Lorraine A Fitzpatrick, and Robert S Schwartz. Electron beam computed tomography and coronary artery disease: scanning for coronary artery calcification. In *Mayo Clinic Proceedings*, volume 71, pages 369–377. Elsevier, 1996. [28](#)
- [368] Michiel L Sala, Maurice B Bizino, Jacob Amersfoort, Albert de Roos, and Hildo J Lamb. Computed tomography evaluation of cardiac structure and function. *Journal of thoracic imaging*, 29(3):173–184, 2014. [34](#)

- 
- [369] Ali Salavati, Farid Radmanesh, Kazem Heidari, Ben A Dwamena, Aine M Kelly, and Paul Cronin. Dual-source computed tomography angiography for diagnosis and assessment of coronary artery disease: systematic review and meta-analysis. *Journal of cardiovascular computed tomography*, 6(2):78–90, 2012. [31](#)
- [370] Philippe Salembier and Jean Serra. Flat zones filtering, connected operators, and filters by reconstruction. *Image Processing, IEEE transactions on*, 4(8):1153–1160, 1995. [149](#)
- [371] Philippe Salembier and Michael H. F. Wilkinson. Connected operators: A review of region-based morphological image processing techniques. *Ieee signal processing magazine*, 26(6):136–157, 2009. [152](#)
- [372] Philippe Salembier, Albert Oliveras, and Luis Garrido. Antiextensive connected operators for image and sequence processing. *Image Processing, IEEE Transactions on*, 7(4):555–570, 1998. [150](#)
- [373] Y. Sato, S. Nakajima, N. Shiraga, N. Atsumi, S. Yoshida, T. Koller, G. Gerig, and R. Kikinis. Three-dimensional multi-scale line filter for segmentation and visualization of curvilinear structures in medical images. *Medical Image Analysis*, 2(2):143 – 168, 1998. [56](#), [62](#), [64](#), [76](#), [145](#), [185](#), [186](#)
- [374] Stefan C Saur, Hatem Alkadhi, Lotus Desbiolles, Gábor Székely, and Philippe C Cattin. Automatic detection of calcified coronary plaques in computed tomography data sets. In *Medical Image Computing and Computer-Assisted Intervention–MICCAI 2008*, pages 170–177. Springer, 2008. [191](#), [194](#)
- [375] Patrick J Scanlon, David P Faxon, Anne-Marie Audet, Blase Carabello, Gregory J Dehmer, Kim A Eagle, Ronald D Legako, Donald F Leon, John A Murray, Steven E Nissen, et al. Acc/aha guidelines for coronary angiography123a report of the american college of cardiology/american heart association task force on practice guidelines (committee on coronary angiography) developed in collaboration with the society for cardiac angiography and interventions. *Journal of the American College of Cardiology*, 33(6):1756–1824, 1999.
- [376] M. Schaap, T. van Walsum, L. Neefjes, C. Metz, E. Capuano, M. de Bruijne, and W. Niessen. Robust shape regression for supervised vessel segmentation and its application to coronary segmentation in cta. *Medical Imaging, IEEE Transactions on*, 30(11):1974–1986, Nov 2011. [141](#), [143](#)
- [377] Michiel Schaap, Rashindra Manniesing, Ihor Smal, Theo Van Walsum, Aad Van Der Lugt, and Wiro Niessen. Bayesian tracking of tubular structures and its application to carotid arteries in cta. In *Proceedings of the 10th international conference on Medical image computing and computer-assisted intervention*, MICCAI’07, pages 562–570, Berlin, Heidelberg, 2007. Springer-Verlag. [61](#), [141](#)
- [378] Michiel Schaap, Ihor Smal, Coert Metz, Theo van Walsum, and Wiro Niessen. Bayesian tracking of elongated structures in 3d images. In Nico Karssemeijer and Boudewijn Lelieveldt, editors, *Information Processing in Medical Imaging*, volume 4584 of *Lecture Notes in Computer Science*, pages 74–85. Springer Berlin / Heidelberg, 2007. [61](#)



## Bibliography

---

- [379] Michiel Schaap, Coert T Metz, Theo van Walsum, Alina G van der Giessen, Annick C Weustink, Nico R Mollet, Christian Bauer, Hrvoje Bogunović, Carlos Castro, Xiang Deng, et al. Standardized evaluation methodology and reference database for evaluating coronary artery centerline extraction algorithms. *Medical image analysis*, 13(5):701–714, 2009. [137](#), [142](#)
- [380] Michiel Schaap, Lisan Neefjes, Coert Metz, Alina van der Giessen, Annick Weustink, Nico Mollet, Jolanda Wentzel, Theo van Walsum, and Wiro Niessen. Coronary lumen segmentation using graph cuts and robust kernel regression. In *Information Processing in Medical Imaging*, pages 528–539. Springer, 2009. [139](#), [143](#)
- [381] Nelson B Schiller, Pravin M Shah, Michael Crawford, Anthony DeMaria, Richard Devereux, Harvey Feigenbaum, Howard Gutgesell, Nathaniel Reichek, David Sahn, and Ingela Schnittger. Recommendations for quantitation of the left ventricle by two-dimensional echocardiography. american society of echocardiography committee on standards, subcommittee on quantitation of two-dimensional echocardiograms. *Journal of the American Society of Echocardiography: official publication of the American Society of Echocardiography*, 2(5):358–367, 1988.
- [382] Jürgen Schmidhuber. Deep learning in neural networks: An overview. *Neural Networks*, 61: 85–117, 2015. [231](#)
- [383] Stephen Schroeder, Andreas F Kopp, Andreas Baumbach, Christoph Meisner, Axel Kuettnner, Christian Georg, Bernd Ohnesorge, Christian Herdeg, Claus D Claussen, and Karl R Karsch. Noninvasive detection and evaluation of atherosclerotic coronary plaques with multislice computed tomography. *Journal of the American College of Cardiology*, 37(5):1430–1435, 2001. [30](#), [31](#), [34](#)
- [384] R. Sebbe, B. Gosselin, E. Coche, and B. Macq. Pulmonary arteries segmentation and feature extraction through slice marching. *Proc. ProRISC workshop on Circuits, Systems and Signal Process.*, 2003. [76](#)
- [385] M. Sermesant, C. Forest, X. Pennec, H. Delingette, and N. Ayache. Deformable biomechanical models: Application to 4d cardiac image analysis. *Medical Image Analysis*, 7(4):475 – 488, 2003. [Medical Image Computing and Computer Assisted Intervention](#). [90](#)
- [386] J. Serra. *Image analysis and mathematical morphology*. Academic, London, 1982. [57](#), [92](#), [149](#)
- [387] J. Sethian. A fast marching level set method for monotonically advancing fronts. In *Proceedings of the National Academy of Sciences*, volume 93(4), pages 1591–1595, 1996. [75](#)
- [388] J. Sethian. Fast marching methods. *SIAM review*, 41(2):199–235, 1999. [67](#)
- [389] Rahil Shahzad, Theo van Walsum, Hortense Kirisli, Hui Tang, Coert Metz, Michiel Schaap, Lucas van Vliet, and Wiro Niessen. Automatic stenoses detection, quantification and lumen segmentation of the coronary arteries using a two point centerline extraction scheme. In *3D Cardiovascular Imaging: a MICCAI Segmentation Challenge Workshop.*, 2012. [140](#), [141](#), [142](#), [191](#), [194](#), [292](#), [293](#)

- 
- [390] Rahil Shahzad, Hortense Kirişli, Coert Metz, Hui Tang, Michiel Schaap, Lucas van Vliet, Wiro Niessen, and Theo van Walsum. Automatic segmentation, detection and quantification of coronary artery stenoses on cta. *The international journal of cardiovascular imaging*, 29(8):1847–1859, 2013. [140](#), [143](#), [189](#), [191](#)
- [391] Claude Elwood Shannon. A mathematical theory of communication. *ACM SIGMOBILE Mobile Computing and Communications Review*, 5(1):3–55, 2001. [282](#)
- [392] Jonathan R Shewchuk. An introduction to the conjugate gradient method without the agonizing pain. Technical report cmucs-tr-94-125, Carnegie Mellon University, Pittsburgh, PA, USA, 1994. [119](#)
- [393] H. Shikata, Hoffman E.A., and M. Sonka. Automated segmentation of pulmonary vascular tree from 3d ct images. *Proc. SPIE Med. Imaging*, 5369:107–116, 2004. [56](#), [57](#), [64](#)
- [394] Jamie Shotton, Andrew Fitzgibbon, Mat Cook, Toby Sharp, Mark Finocchio, Richard Moore, Alex Kipman, and Andrew Blake. Real-time human pose recognition in parts from a single depth image. In *CVPR*. IEEE, June 2011. [237](#)
- [395] Pierre Soille and Hugues Talbot. Directional morphological filtering. *Pattern Analysis and Machine Intelligence, IEEE Transactions on*, 23(11):1313–1329, 2001. [146](#)
- [396] Thorvald Sørensen. {A method of establishing groups of equal amplitude in plant sociology based on similarity of species and its application to analyses of the vegetation on Danish commons}. *Biol. Skr.*, 5:1–34, 1948. [123](#)
- [397] Susan Standring. *Gray’s anatomy*, volume 39. Elsevier, Churchill Livingstone, 2008. [87](#)
- [398] Alexander Statnikov, Lily Wang, and Constantin F Aliferis. A comprehensive comparison of random forests and support vector machines for microarray-based cancer classification. *BMC bioinformatics*, 9(1):319, 2008. [237](#), [256](#)
- [399] Carsten Steger. Extracting curvilinear structures: a differential geometric approach. In *Eur. Conf. Comput. Vision*, volume 1, pages 630–641, 1996. [63](#)
- [400] Zhonghua Sun, ChengHsun Lin, Robert Davidson, Chiauhuei Dong, and Yunchan Liao. Diagnostic value of 64-slice ct angiography in coronary artery disease: a systematic review. *European journal of radiology*, 67(1):78–84, 2008. [30](#), [35](#)
- [401] Zhonghua Sun, GH Choo, and KH Ng. Coronary ct angiography: current status and continuing challenges. *British journal of radiology*, 85(1013):495–510, 2014. [34](#)
- [402] J. Suri, K. Liu, L. Reden, and S. Laxminarayan. A review on mr vascular image processing algorithms: acquisition and prefiltering. *IEEE Trans. Inf. Technol. Biomed.*, part I.6 (4):324–337, 2002. [56](#)
- [403] Jasjit S Suri. Computer vision, pattern recognition and image processing in left ventricle segmentation: The last 50 years. *Pattern Analysis & Applications*, 3(3):209–242, 2000. [90](#)

## Bibliography

---

- [404] Kenji Suzuki, Isao Horiba, Noboru Sugie, and Michio Nanki. Computer-aided diagnosis system for coronary artery stenosis using a neural network. In *Medical Imaging 2001*, pages 1771–1782. International Society for Optics and Photonics, 2001. [198](#), [200](#)
- [405] A. Szymczak, A. Tannenbaum, and K. Mischaikow. Coronary vessel cores from 3d imagery: A topological approach. *Proc. SPIE Med. Imaging*, 5747:505–513, 2005. [59](#)
- [406] Andrzej Szymczak. Vessel tracking by connecting the dots. *MICCAI*, 2008. [xx](#), [56](#), [57](#), [59](#), [60](#)
- [407] Hugues Talbot. Globally optimal surfaces by continuous maximal flows. In *Digital Image Computing: Techniques and Applications*, pages 987–996, 2003. [114](#)
- [408] Hugues Talbot and Ben Appleton. Efficient complete and incomplete path openings and closings. *Image and Vision Computing*, 25(4):416–425, April 2007. [82](#)
- [409] Hui Tang, T. van Walsum, R. Hameeteman, M. Schaap, A. van der Lugt, L.J. van Vliet, and W.J. Niessen. Lumen segmentation of atherosclerotic carotid arteries in cta. In *Biomedical Imaging (ISBI), 2012 9th IEEE International Symposium on*, pages 274–277, May 2012. [184](#)
- [410] Jian Tang, Zhixiang Chen, Ada Wai-Chee Fu, and David Wai-Lok Cheung. Enhancing effectiveness of outlier detections for low density patterns. In *Proceedings of the 6th Pacific-Asia Conference on Advances in Knowledge Discovery and Data Mining, PAKDD '02*, pages 535–548, London, UK, UK, 2002. Springer-Verlag. [101](#)
- [411] Olena Tankyevych. *Filtering of thin objects. Applications to vascular Image Analysis*. PhD thesis, University Paris Est, Laboratory of informatics Gaspard-Monge, Departement of informatics, October 2010. [56](#)
- [412] Olena Tankyevych, Hugues Talbot, Petr Dokládál, and Nicolas Passat. Direction-adaptive grey-level morphology. application to 3d vascular brain imaging. In *Image Processing (ICIP), 2009 16th IEEE International Conference on*, pages 2261–2264. IEEE, 2009. [82](#), [144](#)
- [413] Robert Endre Tarjan. Efficiency of a good but not linear set union algorithm. *Journal of the ACM (JACM)*, 22(2):215–225, 1975. [152](#)
- [414] Charles A Taylor, Timothy A Fonte, and James K Min. Computational fluid dynamics applied to cardiac computed tomography for noninvasive quantification of fractional flow reserve: scientific basis. *Journal of the American College of Cardiology*, 61(22):2233–2241, 2013. [xxv](#), [195](#), [196](#)
- [415] Huseyin Tek, M Akif Gulsun, Soizic Laguitton, Leo Grady, David Lesage, and Gareth Funka-Lea. Automatic coronary tree modeling. *The Insight Journal*, 2008. [68](#), [71](#)
- [416] Matthias Teßmann, Fernando Vega Higuera, Dominik Fritz, Michael Scheuering, and Günther Greiner. Learning-based detection of stenotic lesions in coronary ct data. In *Proceedings of the Vision, Modeling, and Visualization Conference 2008, VMV 2008*, Konstanz, Germany, October 8-10 2008. [196](#), [199](#), [206](#), [234](#), [250](#)
- [417] Matthias Teßmann, Fernando Vega-Higuera, Dominik Fritz, Michael Scheuering, and Günther Greiner. Multi-scale feature extraction for learning-based classification of coronary artery stenosis. In *SPIE 7260, Medical Imaging 2009: Computer-Aided Diagnosis*, February 27 2009. [185](#), [198](#), [200](#), [234](#), [243](#), [244](#), [250](#)

- 
- [418] Tietjen and Moore. Some grubbs-type statistics for the detection of outliers. *Technometrics*, 14 (3):583–597, (August 1972). [102](#)
- [419] Michal Toledano, Michael Lindenbaum, Jonathan Lessick, Robert Dragu, Eduard Gherdin, Ahuva Engel, and Beyar Rafael. Learning to detect coronary artery stenosis from multi-detector ct imaging. Technical report, Technion - Israel Institute of Technology, Department of Biomedical Engineering, 2006. [196](#), [198](#), [200](#), [206](#)
- [420] R. Toledo, X. Orriols, P. Radeva, X. Binefa, J. Vitria, C. Canero, and J.J. Villanueva. Eigen-snakes for vessel segmentation in angiography. In *Pattern Recognition, 2000. Proceedings. 15th International Conference on*, volume 4, pages 340–343, 2000. [78](#)
- [421] Ricardo Toledo, Xavier Orriols, Xavier Binefa, Petia Radeva, Jordi Vitria, and Juan José Villanueva. Tracking elongated structures using statistical snakes. In *Computer Vision and Pattern Recognition, 2000. Proceedings. IEEE Conference on*, volume 1, pages 157–162. IEEE, 2000. [78](#)
- [422] Philip HS Torr and David W Murray. Outlier detection and motion segmentation. In *Optical Tools for Manufacturing and Advanced Automation*, pages 432–443. International Society for Optics and Photonics, 1993. [102](#)
- [423] C Toumoulin, C Boldak, M Garreau, and D Boulmier. Coronary characterization in multi-slice computed tomography. In *Computers in Cardiology, 2003*, pages 749–752. IEEE, 2003. [185](#), [189](#), [190](#), [194](#)
- [424] Zhuowen Tu, Xiang Sean Zhou, Luca Bogoni, Adrian Barbu, and Dorin Comaniciu. Probabilistic 3d polyp detection in ct images: The role of sample alignment. In *Computer Vision and Pattern Recognition, 2006 IEEE Computer Society Conference on*, volume 2, pages 1544–1551. IEEE, 2006. [242](#)
- [425] J.A. Tyrrell, E. di Tomaso, D. Fuja, R. Tong, K. Kozak, R.K. Jain, and B. Roysam. Robust 3-D modeling of vasculature imagery using superellipsoids. *IEEE Transactions on Medical Imaging*, 26(2):223–237, February 2007. [xx](#), [61](#), [64](#), [70](#), [71](#)
- [426] Markus Unger, Thomas Pock, Werner Trobin, Daniel Cremers, and Horst Bischof. H.: Tvseg - interactive total variation based image segmentation. In *In: British Machine Vision Conference (BMVC, 2008*. [114](#)
- [427] Corinne Vachier. Extinction value: a new measurement of persistence. In *IEEE Workshop on Nonlinear Signal and Image Processing.*, June 1995. [154](#)
- [428] Leonardo Florez Valencia, Jacques Azencot, and Maciej Orkisz. Carotid arteries segmentation in ct images with use of a right generalized cylinder model. *The insight Journal, MICCAI*, 2009. [68](#)
- [429] Silvia Valero, Jocelyn Chanussot, Jon Atli Benediktsson, Hugues Talbot, and Björn Waske. Advanced directional mathematical morphology for the detection of the road network in very high resolution remote sensing images. *Pattern Recognition Letters*, 31(10):1120–1127, 2010. [144](#)

## Bibliography

---

- [430] Hans C van Assen, Rob J van der Geest, Mikhail G Danilouchkine, Hildo J Lamb, Johan HC Reiber, and Boudewijn PF Lelieveldt. Three-dimensional active shape model matching for left ventricle segmentation in cardiac ct. In *Medical Imaging 2003*, pages 384–393. International Society for Optics and Photonics, 2003. [90](#)
- [431] Eva M van Rikxoort, Ivana Isgum, Marius Staring, Stefan Klein, and Bram van Ginneken. Adaptive local multi-atlas segmentation: Application to heart segmentation in chest ct scans. In *Medical Imaging*, pages 691407–691407. International Society for Optics and Photonics, 2008. [90](#), [91](#), [93](#), [132](#), [134](#)
- [432] Dirk Vandermeulen, D. Delaere, Paul Suetens, Hilde Bosmans, and Guy Marchal. Local filtering and global optimization methods for 3-d magnetic-resonance angiography image enhancement. *SPIE*, 1808:274–288, 1992. [55](#)
- [433] Vladimir Naumovich Vapnik and Vlamimir Vapnik. *Statistical learning theory*, volume 2. Wiley New York, 1998. [232](#)
- [434] A. Vasilevskiy and K. Siddiqi. Flux maximizing geometric flows. *Pattern Analysis and Machine Intelligence, IEEE Transactions on*, 24(12):1565–1578, 2002. [80](#)
- [435] Bert Verdonck, L Bloch, Henri Maître, Dirk Vandermeulen, Paul Suetens, and Guy Marchal. Accurate segmentation of blood vessels from 3d medical images. In *Image Processing, 1996. Proceedings., International Conference on*, volume 3, pages 311–314. IEEE, 1996. [81](#)
- [436] Sara Vicente, Vladimir Kolmogorov, and Carsten Rother. Graph cut based image segmentation with connectivity priors. In *Computer Vision and Pattern Recognition, 2008. CVPR 2008. IEEE Conference on*, pages 1–8. IEEE, 2008. [114](#)
- [437] Luc Vincent and Pierre Soille. Watersheds in digital spaces: an efficient algorithm based on immersion simulations. *IEEE transactions on pattern analysis and machine intelligence*, 13(6): 583–598, 1991. [113](#), [173](#)
- [438] Luc M Vincent. Efficient computation of various types of skeletons. In *Medical Imaging V: Image Processing*, pages 297–311. International Society for Optics and Photonics, 1991. [73](#)
- [439] Paul Viola and Michael J Jones. Robust real-time face detection. *International journal of computer vision*, 57(2):137–154, 2001. [253](#)
- [440] Renu Virmani, Frank D Kolodgie, Allen P Burke, Andrew Farb, and Stephen M Schwartz. Lessons from sudden coronary death a comprehensive morphological classification scheme for atherosclerotic lesions. *Arteriosclerosis, thrombosis, and vascular biology*, 20(5):1262–1275, 2000. [30](#)
- [441] Renu Virmani, ALLEN P BURKE, FRANK D KOLODGIE, and Andrew Farb. Vulnerable plaque: the pathology of unstable coronary lesions. *Journal of interventional cardiology*, 15(6): 439–446, 2002. [14](#)
- [442] Shu-Yen Wan, Erik L Ritman, and William E Higgins. Multi-generational analysis and visualization of the vascular tree in 3d micro-ct images. *Computers in Biology and Medicine*, 32(2): 55–71, 2002. [73](#)

- 
- [443] Chunliang Wang and Orjan Smedby. An automatic seeding method for coronary artery segmentation and skeletonization in cta. *Insight Journal, MICCAI*, 2008. 56, 59, 73
- [444] Chunliang Wang, Rodrigo Moreno, and Orjan Smedby. Vessel segmentation using implicit model-guided level sets. In *3D Cardiovascular Imaging: A MICCAI segmentation challenge*, 2012. 140, 141, 142, 143, 190, 194, 292, 293
- [445] Yin Wang and P. Liatsis. Automatic segmentation of coronary arteries in CT imaging in the presence of kissing vessel artifacts. *Information Technology in Biomedicine, IEEE Transactions on*, 16(4):782–788, July 2012. 138, 294
- [446] Yin Wang and Panos Liatsis. A fully automated framework for segmentation and stenosis quantification of coronary arteries in 3D CTA imaging. In *Developments in eSystems Engineering (DESE), 2009 Second International Conference on*, pages 136–140. IEEE, 2009. 194
- [447] Yin Wang, Xinyu Meng, and Daobo Wang. Automated coronary artery analysis system in 3D CTA images. In *Biomedical Engineering and Informatics (BMEI), 2010 3rd International Conference on*, volume 1, pages 122–126, Oct 2010. 138, 189
- [448] Michael R Ward, Gerard Pasterkamp, Alan C Yeung, and Cornelius Borst. Arterial remodeling mechanisms and clinical implications. *Circulation*, 102(10):1186–1191, 2000. 15
- [449] GA Watson. Least squares fitting of circles and ellipses to measured data. *BIT Numerical Mathematics*, 39(1):176–191, 1999. 108
- [450] Roberto Wayhs, Allan Zelinger, and Paolo Raggi. High coronary artery calcium scores pose an extremely elevated risk for hard events. *Journal of the American College of Cardiology*, 39(2): 225–230, 2002. 30
- [451] Jun Wei, Chuan Zhou, Heang-Ping Chan, Aamer Chughtai, Smita Patel, Prachi Agarwal, Jean Kuriakose, Lubomir Hadjiiski, and Ella Kazerooni. Computerized luminal analysis for detection of non-calcified plaques in coronary ct angiography. In *SPIE Medical Imaging*, pages 90350R–90350R. International Society for Optics and Photonics, 2014. 196, 198, 200
- [452] J Weickert. Coherence-enhancing diffusion filtering. *Int. J. Comput. Vision*, 31:111–127, 1999. 55
- [453] Stefan Wesarg and Evelyn A. Firle. Segmentation of vessels: The corkscrew algorithm. *SPIE International Symposium on Medical Imaging*, 19(3):249–257, 2004. xx, 58, 60, 71, 75, 81, 139, 141, 143, 185
- [454] Stefan Wesarg, M. Fawad Khan, and Evelyn A. Firle. Localizing calcifications in cardiac ct data sets using a new vessel segmentation approach. *Journal of Digital Imaging*, 19(3):249–257, September 2006. 186, 191, 194
- [455] Ross T Whitaker. A level-set approach to 3d reconstruction from range data. *International journal of computer vision*, 29(3):203–231, 1998. 81
- [456] Wikipedia. IVUS of CAD, accessed: May 22 2014. URL [http://en.wikipedia.org/wiki/File:IVUS\\_of\\_CAD\\_\(1\).png](http://en.wikipedia.org/wiki/File:IVUS_of_CAD_(1).png). xviii, 21



## Bibliography

---

- [457] M.H.F. Wilkinson and M.A. Westenberg. Shape preserving filament enhancement filtering. *Proc. Med. Image Comput. Assist. Interv.*, pages 770–777, 2001. [55](#), [56](#), [82](#), [155](#)
- [458] Michael HF Wilkinson, Tsjipke Wijkstra, Gijs De Vries, and Michel A Westenberg. Blood vessel segmentation using moving-window robust automatic threshold selection. In *Image Processing, 2003. ICIP 2003. Proceedings. 2003 International Conference on*, volume 2, pages II–1093. IEEE, 2003. [76](#)
- [459] Dale L Wilson and J Alison Noble. Segmentation of cerebral vessels and aneurysms from mr angiography data. In *Information Processing in Medical Imaging*, pages 423–428. Springer, 1997. [77](#)
- [460] O. Wink, W.J. Niessen, and M.A. Viergever. Fast delineation and visualization of vessels in 3-d angiographic images. *Medical Imaging, IEEE Transactions on*, 19(4):337–346, April 2000. [xxi](#), [xxv](#), [62](#), [69](#), [70](#), [71](#), [81](#), [167](#), [186](#)
- [461] O. Wink, W.J. Niessen, and M.A. Viergever. Multiscale vessel tracking. *IEEE Trans. Med. Imaging*, 23(1):130–133, 2004. [67](#), [68](#)
- [462] Onno Wink, Alejandro F. Frangi, Bert Verdonck, Max A. Viergever, and Wiro J. Niessen. 3d mra coronary axis determination using a minimum cost path approach. *Magnetic Resonance in Medicine*, 47:1169–1175, 2002. [68](#)
- [463] Jelmer M Wolterink, Tim Leiner, Richard AP Takx, Max A Viergever, and Ivana Išgum. An automatic machine learning system for coronary calcium scoring in clinical non-contrast enhanced, ecg-triggered cardiac CT. In *SPIE Medical Imaging*, pages 90350E–90350E. International Society for Optics and Photonics, 2014. [xxvi](#), [186](#), [197](#), [198](#), [200](#), [206](#)
- [464] Wilbur C. K. Wong, Ronald W. K. So, and Albert C. S. Chung. Principal curves: a technique for preliminary carotid lumen segmentation and stenosis grading. *The MIDAS Journal - Carotid Lumen Segmentation and Stenosis Grading (Grand Challenge)*, 2009. [54](#), [58](#)
- [465] Wilbur C.K. Wong and Albert C.S. Chung. Toward interactive user guiding vessel axis extraction from gray-scale angiograms: An optimization framework. *MICCAI 2006, LNCS 4190*, pages 223–231, 2006. [69](#)
- [466] Wilbur CK Wong and Albert CS Chung. Augmented vessels for quantitative analysis of vascular abnormalities and endovascular treatment planning. *Medical Imaging, IEEE Transactions on*, 25(6):665–684, 2006. [62](#), [187](#)
- [467] S. Wörz and K. Rohr. Segmentation and quantification of human vessels using a 3-d cylindrical intensity model. *IEEE TRANSACTIONS ON IMAGE PROCESSING*, 16(8):1994–2004, August 2007. [xx](#), [61](#), [62](#), [64](#), [70](#)
- [468] Stefan Wörz and Karl Rohr. A new 3d parametric intensity model for accurate segmentation and quantification of human vessels. *MICCAI*, pages 491–499, 2004. [61](#)
- [469] Stefan Wörz and Karl Rohr. Cramér-rao bounds for estimating the position and width of 3d tubular structures and analysis of thin structures with application to vascular images. *Journal of Mathematical Imaging and Vision*, 30:167–180, 2008. 10.1007/s10851-007-0041-6. [64](#), [70](#), [71](#)

- 
- [470] Changhua Wu, Gady Agam, Arunabha S. Roy, and Samuel G. Armato. Regulated morphology approach to fuzzy shape analysis with application to blood vessel extraction in thoracic ct scans. *Proc. SPIE Med. Imaging*, 5370:1262–1270, 2004. [57](#)
- [471] Yiting Xie, Matthew D Cham, Claudia Henschke, David Yankelevitz, and Anthony P Reeves. Automated coronary artery calcification detection on low-dose chest ct images. In *SPIE Medical Imaging*, pages 90350F–90350F. International Society for Optics and Photonics, 2014. [191](#), [206](#)
- [472] Yongchao Xu, Thierry Géraud, and Laurent Najman. Morphological filtering in shape spaces: Applications using tree-based image representations. In *Pattern Recognition (ICPR), 2012 21st International Conference on*, pages 485–488. IEEE, 2012. [xxiii](#), [144](#), [154](#), [155](#), [157](#), [158](#), [159](#)
- [473] Pingkun Yan and Ashraf A. Kassim. Mra image segmentation with capillary active contour. In James S. Duncan and Guido Gerig, editors, *MICCAI*, volume 3749 of *Lecture Notes in Computer Science*, pages 51–58. Springer, 2005. [xxi](#), [80](#)
- [474] Guanyu Yang, Pieter Kitslaar, Michel Frenay, Alexander Broersen, Mark J Boogers, Jeroen J Bax, Johan HC Reiber, and Jouke Dijkstra. Automatic centerline extraction of coronary arteries in coronary computed tomographic angiography. *The international journal of cardiovascular imaging*, 28(4):921–933, 2012. [137](#), [142](#), [143](#)
- [475] Yan Yang, A. Tannenbaum, and D. Giddens. Knowledge-based 3d segmentation and reconstruction of coronary arteries using ct images. In *Engineering in Medicine and Biology Society, 2004. IEMBS '04. 26th Annual International Conference of the IEEE*, volume 1, pages 1664–1666, 2004. [61](#), [138](#)
- [476] Yan Yang, A. Tannenbaum, D. Giddens, and A. Stillman. Automatic segmentation of coronary arteries using bayesian driven implicit surfaces. In *Biomedical Imaging: From Nano to Macro, 2007. ISBI 2007. 4th IEEE International Symposium on*, pages 189–192, April 2007. [138](#), [142](#), [143](#)
- [477] Yibing Yang and Hong Yan. An adaptive logical method for binarization of degraded document images. *Pattern Recognition*, 33(5):787–807, 2000. [76](#)
- [478] J. Yi and J.B. Ra. A locally adaptive region growing algorithm for vascular segmentation. *International Journal of Imaging Systems and Technology*, 13(4):208–214, 2003. [75](#)
- [479] Peter J Yim, Rakesh Mullick, Ronald M Summers, Hani Marcos, Juan R Cebral, Rainald Lohner, and Peter L Choyke. Measurement of stenosis from magnetic resonance angiography using vessel skeletons. In *Proc. SPIE (Med. Imag.)*, volume 3978, pages 245–255. Citeseer, 2000. [184](#), [189](#)
- [480] P.J. Yim, J.J. Cebral, R. Mullick, H.B. Marcos, and P.L. Choyke. Vessel surface reconstruction with a tubular deformable model. *Medical Imaging, IEEE Transactions on*, 20(12):1411–1421, 2001. [78](#)
- [481] C. Zahlten, H. Jürgens, C. J. G. Evertsz, R. Leppek, H.-O. Peitgen, and K. J. Klose. Portal vein reconstruction based on topology. *European Journal of Radiology*, 19(2):96–100, 1995. [75](#)
- [482] C. T. Zahn. Graph-Theoretical Methods for Detecting and Describing Gestalt Clusters. *Transactions on Computers*, C-20(1):68–86, 1971. [113](#)



## Bibliography

---

- [483] Sebastian Zambal, Jiri Hladuvka, Armin Kanitsar, and K Bühler. Shape and appearance models for automatic coronary artery tracking. *The Insight Journal*, 4, 2008. [xx](#), [59](#), [72](#), [92](#)
- [484] F. Zana and J.-C Klein. Segmentation of vessel-like patterns using mathematical morphology and curvature evaluation. *IEEE Trans. Image Process*, 10 (7):1010–1019, 2001. [55](#), [56](#)
- [485] Pat Zanzonico, Lawrence N Rothenberg, and H William Strauss. Radiation exposure of computed tomography and direct intracoronary angiography risk has its reward. *Journal of the American College of Cardiology*, 47(9):1846–1849, 2006. [1](#)
- [486] Christopher K Zarins, Charles A Taylor, and James K Min. Computed fractional flow reserve (ffct) derived from coronary ct angiography. *Journal of cardiovascular translational research*, 6 (5):708–714, 2013. [195](#)
- [487] M. Zerroug and R. Nevatia. Three-dimensional descriptions based on the analysis of the invariant and quasi-invariant properties of some curved-axis generalized cylinders. *Pattern Analysis and Machine Intelligence, IEEE Transactions on*, 18(3):237–253, Mar 1996. [63](#)
- [488] Long-Jiang Zhang, Sheng-Yong Wu, Jing Wang, Ying Lu, Zhuo-Li Zhang, Shi-Sen Jiang, Chang-Sheng Zhou, and Guang-Ming Lu. Diagnostic accuracy of dual-source ct coronary angiography: The effect of average heart rate, heart rate variability, and calcium score in a clinical perspective. *Acta Radiologica*, 51(7):727–740, 2010. [31](#)
- [489] Shaoxiong Zhang, David C Levin, Ethan J Halpern, David Fischman, Michael Savage, and Paul Walinsky. Accuracy of mdct in assessing the degree of stenosis caused by calcified coronary artery plaques. *American Journal of Roentgenology*, 191(6):1676–1683, 2008. [31](#)
- [490] Yong Zhang, Kun Chen, and Stephen T.C. Wong. 3d interactive centerline extraction. *MICCAI*, 2008. [68](#)
- [491] Fei Zhao and R. Bhotika. Coronary artery tree tracking with robust junction detection in 3d ct angiography. In *Biomedical Imaging: From Nano to Macro, 2011 IEEE International Symposium on*, pages 2066–2071, March 2011. [140](#)
- [492] Fei Zhao, Rahul Bhotika, Paulo RS Mendonça, Nils Krahnstoeber, and James V Miller. Adaptive intensity models for probabilistic tracking of 3d vasculature. In *Biomedical Imaging: From Nano to Macro, 2010 IEEE International Symposium on*, pages 41–44. IEEE, 2010. [140](#)
- [493] Yefeng Zheng, Adrian Barbu, Bogdan Georgescu, Michael Scheuering, and Dorin Comaniciu. Fast automatic heart chamber segmentation from 3d ct data using marginal space learning and steerable features. In *Computer Vision, 2007. ICCV 2007. IEEE 11th International Conference on*, pages 1–8. IEEE, 2007. [234](#), [242](#)
- [494] Yefeng Zheng, A. Barbu, B. Georgescu, M. Scheuering, and D. Comaniciu. Four-chamber heart modeling and automatic segmentation for 3-d cardiac ct volumes using marginal space learning and steerable features. *Medical Imaging, IEEE Transactions on*, 27(11):1668–1681, Nov 2008. [90](#)

- 
- [495] Yefeng Zheng, Fernando Vega-Higuera, Shaohua Kevin Zhou, and Dorin Comaniciu. Fast and automatic heart isolation in 3d ct volumes: Optimal shape initialization. In *Machine Learning in Medical Imaging*, pages 84–91. Springer, 2010. [92](#)
- [496] Yefeng Zheng, Maciej Loziczonek, Bogdan Georgescu, S Kevin Zhou, Fernando Vega-Higuera, and Dorin Comaniciu. Machine learning based vesselness measurement for coronary artery segmentation in cardiac ct volumes. In *SPIE Medical Imaging*, pages 79621K–79621K. International Society for Optics and Photonics, 2011. [139](#), [143](#)
- [497] Hua Zhong, Yefeng Zheng, Gareth Funka-Lea, and Fernando Vega-Higuera. Automatic heart isolation in 3d ct images. In *Medical Computer Vision. Recognition Techniques and Applications in Medical Imaging*, pages 165–180. Springer, 2013. [92](#), [93](#), [132](#), [134](#)
- [498] S Kevin Zhou, Jie Shao, Bogdan Georgescu, and Dorin Comaniciu. Pairwise active appearance model and its application to echocardiography tracking. In *Medical Image Computing and Computer-Assisted Intervention–MICCAI 2006*, pages 736–743. Springer, 2006. [234](#)
- [499] Shaohua Kevin Zhou, Jinghao Zhou, and Dorin Comaniciu. A boosting regression approach to medical anatomy detection. In *Computer Vision and Pattern Recognition, 2007. CVPR’07. IEEE Conference on*, pages 1–8. IEEE, 2007. [234](#)
- [500] Ning Zhu and A.C.S. Chung. Graph-based optimization with tubularity markov tree for 3d vessel segmentation. In *Computer Vision and Pattern Recognition (CVPR), 2013 IEEE Conference on*, pages 2219–2226, June 2013. [138](#), [139](#), [142](#)
- [501] Ning Zhu and A.C.S. Chung. Optimal and efficient segmentation for 3d vascular forest structure with graph cuts. In *Image Processing (ICIP), 2013 20th IEEE International Conference on*, pages 1135–1139, Sept 2013. [138](#)
- [502] Ning Zhu and Albert CS Chung. Random walks with adaptive cylinder flux based connectivity for vessel segmentation. In *Medical Image Computing and Computer-Assisted Intervention–MICCAI 2013*, pages 550–558. Springer, 2013. [139](#), [143](#)
- [503] Leonid Zhukov, Zhaosheng Bao, Igor Guskov, John Wood, and David Breen. Dynamic deformable models for 3d mri heart segmentation. In *SPIE Medical Imaging*, volume 4684, pages 1398–1405, 2002. [90](#)
- [504] Steven W. Zucker. Region growing: Childhood and adolescence. *Computer Graphics and Image Processing*, 5(3):382 – 399, 1976. [74](#)
- [505] MA Zuluaga, IE Magnin, Delgado Leyton EJ, F Lozano, M Orkisz, et al. Automatic detection of abnormal vascular cross-sections based on density level detection and support vector machines. *International journal of computer assisted radiology and surgery*, 6(2):163–174, 2011. [196](#), [200](#), [206](#), [233](#)
- [506] Maria A. Zuluaga, Maciej Orkisz, Edgar J.F. Delgado Leyton, Vincent Dore, Alfredo Morales Pinzon, and Marcela Hernandez Hoyos. Adaptations of maracas algorithm to the segmentation of the carotid bifurcation and stenosis quantification in cta images. *Insight Journal, MICCAI*, 2009. [55](#), [184](#), [185](#)

## Bibliography

---

- [507] Maria A Zuluaga, Don Hush, Edgar JF Delgado Leyton, Marcela Hernández Hoyos, and Maciej Orkisz. Learning from only positive and unlabeled data to detect lesions in vascular ct images. In *Medical Image Computing and Computer-Assisted Intervention–MICCAI 2011*, pages 9–16. Springer, 2011. [199](#), [233](#)
- [508] Mark H Zweig and Gregory Campbell. Receiver-operating characteristic (roc) plots: a fundamental evaluation tool in clinical medicine. *Clinical chemistry*, 39(4):561–577, 1993. [126](#)